SVENSKA GEOFYSISKA FÖRENINGEN

VOLUME 7, NUMBER 3 **Tellus** AUGUST 1955

A QUARTERLY JOURNAL OF GEOPHYSICS

Artificial Snowfall from Mountain Clouds

By F. H. LUDLAM, Imperial College, London

(Manuscript received December 21, 1954)

Abstract

A tentative theory of provoking snowfall from simple orographic clouds is composed, using simplifying assumptions, and it is shown reasonable to suppose that winter snowfall on Central Swedish mountains might be substantially increased by skillful seeding of supercooled mountain clouds.

1. Introduction

During the winter in Scandinavia extensive low clouds often occur which are only several hundred metres thick and which give no precipitation. The clouds are composed of supercooled droplets, but the temperature is not low enough for an abundant natural formation of ice crystals, which could lead to the development of snow. Nor do the clouds contain persistent vertical motions of a magnitude sufficient to sustain any considerable precipitation, except in localities where the air stream containing the clouds flows over mountains. The possibility arises, as envisaged by BERGERON (1949), of introducing ice crystals into the clouds to the windward of mountain ranges, and so provoking snowfall over the mountains.

This possibility is examined in the following paragraphs. First, the rate of growth of a crystal formed in the cloud, and the likelihood of its settling upon the mountain, are considered. Next an estimate is made of the concentration of crystals corresponding to the greatest possible snowfall rate, and the practicability of producing this concentration is discussed. Estimates are made of the frequency of occasions in Jämtland suitable for seeding operations, the amount of snow which they might provide during a whole winter, and their cost. Finally, the problem of assessing their efficiency is considered.

2. The growth of ice crystals by diffusion

The rate of growth of an ice crystal by diffusion of vapour is usually represented by the equation

$$\frac{dm}{dt} = 4\pi SC\,k\triangle p \qquad (1)$$

where m is the mass of the crystal,

S is a factor depending upon the shape of the crystal (the electrical capacity, equal to $2\,r/\pi$ for a disc and to r for a sphere, r being the radius),

C is a velocity-coefficient expressing the increase of condensation due to the (settling) motion of the crystal through the environment,

k is the coefficient of diffusion of water vapour in air,

and $\triangle p$ is the difference between the vapour densities in the environment and at the crystal surface.

If the crystal grows in a supercooled cloud the vapour density in the environment is function only of the temperature. The vapour density at the crystal surface is not that corresponding to ice saturation at the air temperature, because the crystal is warmed a little by the latent heat of condensation. However, it may readily be shown that this effect causes the vapour density excess to become the difference $\triangle p'$ between the saturated vapour densities over liquid water and ice at the air temperature, reduced by a factor $(1 + kf)$ where f is a function dependent only upon the air temperature. The coefficient of diffusion k is a function of both air pressure and temperature, but in considering crystal growth at levels near mountain tops (about 1,000 m) we may consider the pressure to be 900 mb, and then the quantity $k\triangle p$ in equation (1) becomes F, equal to $k\triangle p'/(1 + kf)$ and a function of temperature only, as shown in Table 1:

Table 1.

Temperature, °C:	— 2	— 4	— 6	— 8	— 10	— 12	— 14	— 16	— 18
$10^8 \cdot F = 10^8 k \triangle p'/(1 + kf)$ g/cm sec:	1	2	2.5	3.1	3.4	3.8	3.7	3.6	3.4

The other terms in the equation are less satisfactorily handled, because of the variety of forms of ice crystals. When they are grown in supercooled clouds they have the form of hexagonal plates at temperatures between 0° C and — 5° C; at rather lower temperatures prisms and hexagonal columns occur, and between — 9° C and — 25° C plane dendritic and stellar crystals, and hexagonal plates are found. Crystals which grow while settling through air of a variety of temperatures have complex forms and often show intricate patterns of hollows and protruding arms, so that their bulk density may be as little as 0.5.

In the following paragraphs we shall consider the hexagonal plate to be the form typical of the range of temperatures concerned (about — 6 to — 15° C), and use a value of S equal to $2r/\pi$, regarding the crystal as equivalent to a circular disc of the same mean radius r. It is then necessary to consider the relation between m and r, or between r and the thickness a of the crystal. From the few available observations (SCHAEFER, 1947; REYNOLDS, 1952; MASON, 1953; and OKITA and KIMURA, 1954) it appears that $(2r/a)$ is about 3 when r is less than about 50 μ, but that this fraction increases to 10 or more for radii up to about 200 μ, the thickness of large crystals rarely exceeding 30—40 μ, and often lying in the range of 5—20 μ for large dendritic crystals of diameter up to about 1 mm or even more.

Appropriate values for the fall-speed and the coefficient C are equally uncertain. For spheres Frössling found

$$C = 1 + 0.23\,(Re)^{\frac{1}{2}},\ 2 < (Re) < 800$$

where (Re) is the Reynolds number. KINZER and GUNN (1951) confirmed this relation for freely falling and evaporating droplets over a range of (Re) from about 10^2 to 10^3, but found that the coefficient 0.23 in the relation was not constant at lower values, increasing to a maximum of about 0.45 for (Re) of 4, and then decreasing to practically zero for (Re) less than about 0.5. For discs and with $(Re) > 500$, POWELL (1940) found a velocity coefficient about equal to that for spheres; the coefficient for discs in the range of (Re) covered during crystal growth (about 1 to 50) is unknown, but can be assumed to be given by the Frössling equation.

For (Re) of about 1 or less the fall-speed of columnar or plate-like crystals is approximately the fraction 0.7 of the fall-speed of spheres of equal volume and density (MCKNOWN and MALAIKA, 1950). SCHAEFER (1947) observed the relation between the mass and fall-speed of crystals for values of (Re) exceeding about 5, from which it appears that plates of thickness 40 μ, and diameter 400 μ and 1 mm have fall-speeds of about 40 and 65 cm/sec respectively. These values are considerably higher than the value of about 30 cm/sec found by NAKAYA and TERADA (1935) for large plane dendritic crystals of diameter 1.5 to 6 mm, whose thickness was only about 10 μ. However, observations by the same authors on hexagonal plates and capped hexagonal columns gave fall-speeds varying between 32 and 95 cm/sec, with an average value of about 55 cm/sec.

In view of all the above uncertainties we introduce some simplifications. The first stages in the crystal growth we regard as best

represented by the experimental observations of REYNOLDS (1952), who produced crystals of diameter up to about 200 μ by dry-ice seeding of a cloud supercooled to — 18° C in a large cold box. It is not possible to produce larger crystals by this technique, since at this size the fall-speed reaches about 10 cm/sec and the crystals are soon precipitated from the cloud. The crystals settle upon the floor of the box in a variety of sizes; under these conditions hexagonal plates and plane dendritic crystals of mean diameter 150 μ and thickness 20—35 μ were grown in a period of about 90 sec. The largest of the observed crystals reached this size in about 70 sec. These growth-periods are considerably faster than would be deduced from equ. (1), assuming $C = 1$. MASON (1953), also found that small hexagonal plates (of diameter up to 50 μ) grown at — 2° C in a supercooled cloud had a growth rate about 50 % higher than that predicted by the equation. This discrepancy may be due to the presence of the cloud droplets, which, as pointed out by MARSHALL and LANGLEBEN (1954), act as nearby sources of vapour not envisaged in the simple diffusion theory.

We ignore the temperature variation of the quantity F, and adopt a mean value of $3.2 \times \times 10^{-8}$ g/cm sec as appropriate to the range of temperatures (— 6 to about — 15° C) in which we are interested. We consider the crystal growth in three stages. In the first, the radius reaches 75 μ in the period of 90 sec observed by Reynolds. At the end of this stage we assume the thickness to be 30 μ, and calculate a fall-speed of about 12 cm/sec ($Re \approx 1.1$). The assumed value for the growth period, t_1, is supported by SCHAEFER (1953), who observes that crystals grown in the supercooled cloud of a cold-box at — 10 to — 15° C attain diameters of 100—200 μ and fall-speeds of 10—50 cm/sec in less than a minute.

Evidently during the subsequent growth the thickness hardly changes, since plate crystals of thickness exceeding about 40 μ are apparently not found. We therefore assume that in the second stage of growth, during a period t_2, the thickness of the crystal increases uniformly to 40 μ as the radius increases to 200 μ. At this size the fall-speed calculated from the drag coefficient of a disc, and assuming a mean density of 0.7, is 33 cm/sec. However, beyond this size there is a characteristic slipping and fluttering motion during the fall of the crystal which probably results in a higher mean fall-speed, and in view of this and the value of about 30 cm/sec found by Nakaya and Terada for crystals of thickness only about 10 μ, we assume the mean fall-speed to remain constant, during the third growth stage, at the value of 40 cm/sec indicated by Schaefer's data.

The growth period during the second stage (radius 75 μ to 200 μ) is then obtained from the simplified equation

$$\frac{dm}{dt} = 8\, r\, C \times 3.2 \times 10^{-8}$$

together with some assumption concerning the velocity coefficient C and the relation between the mass and radius of the crystal.

Since during this period (Re) varies from 1.1 to about 10 we may assume for C a constant value of approximately 1.6. Assuming, also, that the thickness a is given by

$$a = 24 \times 10^{-4} + r/12.5$$

we have

$$m = 0.7\, \pi r^2\, (24 \times 10^{-4} + r/12.5) \text{ and}$$
$$dm = 0.7\, \pi\, (48 \times 10^{-4} r + 3\, r^2/12.5)\, dr$$

Equ. (1) then becomes

$$dt = \frac{0.7\, \pi\, (48 \times 10^{-4} + 3\, r/12.5)\, dr}{8 \times 1.6 \times 3.3 \times 10^{-8}}$$

which is readily integrated to give t_2, the period during which the radius increases from 75 to 200 μ, as

$$t_2 = 540 \text{ sec}$$

During the third stage the thickness remains 40 μ, so that

$$m = 0.7\, \pi r^2 \times 4 \times 10^{-3} \text{ and}$$
$$dm = 1.76 \times 10^{-2}\, r\, dr$$

Also, since the fall-speed remains 40 cm/sec

$$(Re) \approx 480\, r$$

and $$C \approx 1 + 0.23\, (Re)^{1/2} = 1 + 5\, r^{1/2}$$

Equation (1) then becomes

$$dt = \frac{1.76 \times 10^{-2}}{8 \times 3.2 \times 10^{-8}} \cdot \frac{dr}{1 + 5 r^{1/2}}$$
$$= 6.9 \times 10^{+4}\, (1 + 5\, r^{1/2})^{-1}\, dr$$

This equation may be integrated to give the period t_3 required for the growth to any particular size from an initial radius of 200 μ; the period for the entire growth is $(t_1 + t_2 + t_3)$, and is shown in Table 2, together with the distance settled relative to the air during the growth, calculated from the growth periods and the mean fall-speeds.

Table 2.

Mass, μg	Radius of droplet of same mass, μ	Radius of crystal, μ	Time, sec	Fall path, m
		200	630	180
14	150	400	1,400	480
32	200	600	2,000	740
56	240	800	2,600	970
88	275	1,000	3,200	1,200
127	310	1,200	3,700	1,400
172	345	1,400	4,200	1,600
225	380	1,600	4,600	1,770

We may remark that the values in this table are not seriously affected by changes in the shape assumed for the growing crystal. Thus, for example, if after the first growth-stage the crystal thickness is allowed to remain at 30 μ then the values in the last two columns are decreased by about 20 % and 30 % respectively (since both C and the fall-speed are reduced, while the crystals grow more rapidly). However, over much the greater part of the growth periods the calculations represent what can be regarded as a minimum likely growth rate. Particularly when the crystals are large, the growth rate may be greater by a substantial fraction, partly on account of underestimated velocity coefficients, and partly because of the presence of neighbouring vapour sources in the form of cloud droplets.

3. Results of experimental seeding of clouds

The results of several series of experiments in the seeding of layer clouds with dry ice in general support the values of Table 2, although they suggest that the development of snow and the fall of snow crystals may be more rapid than indicated by the table.

LANGMUIR (1948 b) describes the seeding (with dry ice) of a stratocumulus with base at 1,500 m (— 3° C) and top at 2,500 m (−9° C). Snow began to fall from the cloud 1,600 sec after the seeding; after 2,500 sec the investigating aircraft flew through the precipitation and found it to consist of "rather large snowflakes". After 2,800 sec these snowflakes had fallen to a level nearly 1 km below the cloud base; these values would be in accord with those in Table 2 if the crystals had originated at the cloud base level, but since in fact they formed and grew at considerably higher levels both the growth rate and fall-speed must have been greater than assumed in the calculations. The discrepancy may be partly due to the aggregation of individual crystals into clusters (snowflakes) of higher mean fall-speed. It will later be shown that crystal concentrations of the order 10^4 to $10^5/m^3$ are to be expected; such concentrations imply a mean crystal separation of only 2 to 5 cm, so that small variations in fall-speed and sideways motions are likely to result in crystal collisions and aggregation. A rough calculation shows that chance aggregates of 2 or 3 crystals are likely to collide with single crystals after a fall of about 50 m. LANGLEBEN's (1954) observations indicate that an aggregate of eight plate-crystals of radius 200 μ has a fall-speed of 60—100 cm/sec, and one of eight crystals of individual radius 600 μ a fall-speed of 70—110 cm/sec. The increased values of fall-speed above the constant value of 40 cm/sec assumed for individual crystals strongly favours continued aggregation, and causes the snow to descend about twice as rapidly as shown in Table 2, after about the first 500 seconds of growth. The adjusted values would be in better agreement with the results of the seeding experiment described by Langmuir.

SMITH (1949) has discussed the result of seeding with dry ice three examples of altocumulus (layer) clouds and two examples of small cumulus. Snow trails of individual small crystals fell from two of the altocumulus clouds, of thickness 300 and 450 m, beginning 550 and 700 sec after the seeding. The third cloud had a thickness of 600 m (temperature at base — 2°, at top — 7° C); snow streaks were first seen 1,000 sec after seeding and after 1,300 sec the whole cloud had become transformed to ice, with snow consisting of flakes up to 1 cm in diameter falling from its base. The two cumulus clouds were about 1,100 m thick (temperature at base — 3°, at top — 7°C); a small snow streak became visible below

the first cloud 600 sec after it was seeded, and by 750 sec the snow had become conspicuous down to 150 m below the cloud base, containing densely packed snowflakes of 2—5 mm diameter. The snow reached the ground, 550 m below the cloud base, 1,100 sec after the seeding. The seeding of a neighbouring cloud had a similar result; 1,000 sec afterwards snow streaks extended to 300 m below the cloud base, and on flying through the snow after 1,750 sec the aircraft found it to consist of densely packed flakes 2 to 5 mm in diameter. In the first three experiments the rate of fall of the first snow was estimated at $1^1/_2$, $2^1/_2$ and 4 m/sec, while in the last two it was 4 and 3 m/sec.

SHELLARD and GRANT (1951) describe the seeding of a stratocumulus 150 m thick, temperature — 9° C, which lay above another layer of supercooled cloud 1,800 m thick. Snow fell from the seeded area and was observed by radar to descend about 2,300 m within 1,900 sec of the seeding, and was later seen to reach the ground in "not very large flakes". From the shape of the snow trails as recorded on the radar and the known horizontal wind shear the fall-speed of the snow was calculated to be 1.3 m/sec in one trail and rather less in two others.

In the course of a series of similar experiments, AUFM KAMPE, WEICKMANN and KELLY (1953) observed on two occasions the size of snow crystals which fell from seeded stratocumulus clouds. On the first occasion the snowfall from the seeded area left a hole in the cloud which was about 2 km wide 1,800 seconds after the seeding. Later, snow crystals collected from snow trails at the edges of the expanding hole were found to be hexagonal plates and stars of about 1 mm diameter. These had fallen from cloud originally 470 m thick with a temperature of about — 15° C. On the second occasion a cloud about 900 m thick (temperature at base about — 5° C, at top — 8° C) was observed to be "snowing out violently" less than 1,500 sec after seeding, and when the snow area was investigated it was again found to contain crystals of about 1 mm diameter. On another occasion snow reached the ground 1,200 sec after the seeding of a cloud with base about 500 m (— 6° C) and top about 1,400 m (— 9° C) above the ground. The average fall-speed of the first snow crystals must therefore have exceeded 40 cm/sec.

HALL, HENDERSON and CUNDIFF (1953) provide photographs showing the development of snow from a seeded orographic cloud about 1,400 m thick (temperature at base 0° C, at top — 9° C). These show that the snow fell about 500 m below the cloud base within about 600 sec of the seeding.

All these results provide a strong support for the theoretical calculations. They show that the first snow settles more than 500 metres in periods of from 1,000 to 1,900 sec after the seeding, in accordance with the second row of Table 2, but suggest that when the crystals grow in high concentration over depths of several hundred metres they become aggregated into flakes which have fall-speeds about twice as great as the 40 cm/sec assumed in deriving the subsequent entries in the table.

4. Conditions for collisions between growing crystals and cloud droplets

Since we are concerned with the growth of crystals inside supercooled clouds the possibility must also be considered of the crystals colliding with droplets, and so growing by accretion as well as by condensation. The important factors here are the concentration of droplets lying in the path of a falling crystal, and its ability to collect them. Some of the droplets are wafted aside in the air flow around the crystals, and so only a fraction E of the projected area of the crystal is effectively swept of droplets. LANGMUIR (1948 a) has shown that E, at low (Re), is a function of a parameter

$$K = 0.22\, r_C^2\, v/r\eta$$

where r_C is the radius of the droplets, η is the coefficient of viscosity of air, and r is the radius of a *spherical* collector falling through the droplet cloud at a relative speed v. It can be anticipated that a disc has a catch at least as great as that of a sphere of equal cross section, so that r and v can be identified with the radius and fall-speed of the hexagonal-plate crystal. At values of (Re) of the order 1, Langmuir has found that E is given by the relation

$$E = \{1 + 0.75 \log 2K/(K - 1.214)\}^{-2}$$

For values of K less than 1.214, the efficiency of catch is zero and the crystal cannot collide

with any droplets. The calculated efficiency of catch is sensitive to the radius assumed for the cloud droplets, and some estimate must be made of the likely value.

Simple mountain clouds are formed by upward motions imparted to the air when the wind blows over the slopes, but often the orographic disturbance in the air flow is superimposed upon an already-existing system of shallow cumulus or stratocumulus clouds. Although away from the mountain such clouds may be well broken, near and over the mountain they become fused into a practically continuous layer with a considerably increased thickness. Inside such clouds, containing irregular or convective stirring motions, the concentration of liquid water increases with height above the base-level at a rate of about 1 g/m³ km. Typical droplet concentrations in clouds formed in unpolluted air vary between about 100 and 500/cm³, and under these conditions the bulk of the liquid water in the clouds is contained in droplets of radius greater than about 5 μ near the base-level, 6—8 μ a few hundred metres higher, and 10 μ about 1 km above the base.

If now we calculate the values of K and E for crystals of radius 75, 200, 400 and 800 μ falling through clouds consisting of droplets of radius 6, 8 and 10 μ, we obtain the values shown in Table 3.

Table 3. Efficiency of catch E of crystals of radius r falling through clouds of droplets of radius r_C.

r_C, microns:	6		8		10	
r, microns:	K	E	K	E	K	E
75, 200	0.96	0	1.7	0.15	2.7	0.3
400	0.48	0	0.85	0	1.3	0.15
800	0.24	0	0.42	0	0.65	0

We see from this table that only droplets of radius greater than 8 μ can be collected by the falling crystals. Droplets of this size in significant concentrations are likely to occur only in the upper parts of clouds at least several hundred metres thick, so that in general the accretion process is unlikely to contribute to the crystal growth. It is significant that in none of the experiments mentioned above are graupel structures, the typical accretion products, described; the snow is always found to consist of individual crystals or snow-flake aggregates. Inside clouds containing many droplets of radius greater than 8 μ, that is, inside the larger cumuliform clouds, it can readily be shown that accretion becomes effective when the crystals have radii approaching 200 μ, and then produces a substantial increase in their fall speed, so that the accretion soon makes the dominant contribution to the growth of the crystals. These then develop into roughly spherical aggregates of graupel or hail. Inside shallow layer clouds this development is unlikely to occur, and the typical precipitation is composed of individual or loosely-clustered ice crystals. The presence of the cloud droplets is important in seeding operations, however, in providing a source of crystals and in increasing their rate of growth by diffusion. They also represent a reservoir which tends to maintain saturation with respect to liquid water even in the absence of an updraught.

5. Conditions favourable for producing snowfall from mountain clouds

The rate of growth of snow crystals determines the scale of the conditions which are suitable for the artificial production of snow over mountains. The important circumstances are illustrated in Fig. 1, which represents the flow of air at a mean speed V over mountains. If clouds occur to windward of the mountains with internal temperatures lower than about —7° C, conditions are favourable for the production of ice crystals by the introduction of silver iodide smoke. If they are formed at a height h above the ground it can be assumed that they must settle an equal distance relative to the air in order to reach the surface of the mountain. In the first example in the diagram they are carried by the wind beyond the mountain tops before settling out of the cloud, so that their growth is interrupted and they are subject to evaporation. In the second example the distance D between the region where the air begins to sink in the lee of the mountain and the region in which the crystals form in the mountain cloud, is so large that the crystals settle out upon the summit or windward slopes of the mountain. The condition that this should occur is seen from Table 2 to be that the

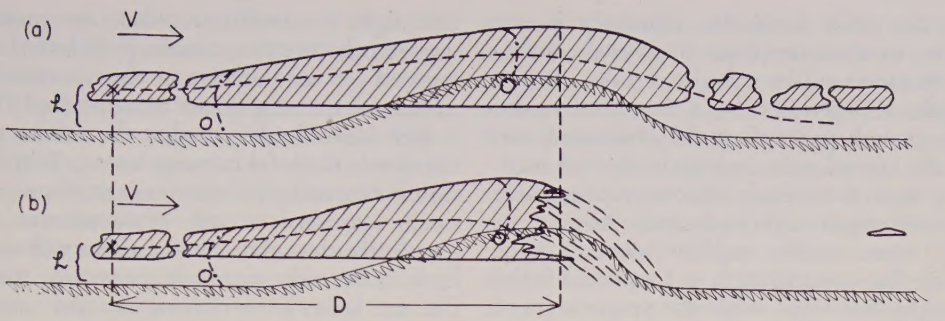

Fig. 1. Formation of snow in mountain clouds. An ice crystal introduced at a height h (several hundred m above ground) into clouds windward of the mountain has a trajectory shown by the pecked lines (partly lying within the region oo of orographic updraught). The crystal is initially a distance D from the region where air begins to descend in the lee of the mountain. In (a), (D/V), where V is the mean wind speed, is considerably less than 1,500 sec; the crystal attains a radius of less than about 200 μ, settles relative to the air less than 200 m, and evaporates in the lee of the mountain. In (b), (D/V) is rather more than 1,500 sec; the crystal attains a diameter of about 1 mm, settles relative to the air several hundred m, and thus is precipitated upon the mountain. If an appropriate concentration of crystals is introduced, each follows a similar trajectory, and the vapour condensed in the cloud is consumed in producing the snowfall, so that the mountain cloud disappears where the air begins to descend behind the mountain.

period D/V should be about 1,500 sec, assuming the height h to be several hundred metres. In winds of 5 to 15 m/sec this implies that the crystals should be introduced into the clouds at distances of some 8 to 23 km windward of the region where the air begins to descend behind the mountain. If the vapour condensed in the orographic updraught over the mountain is to be efficiently precipitated in the form of snow, the crystals should settle through at least the upper part of the region of updraught, practically completing their growth before arriving at the region of descending air.

The function of the updraught is to maintain the state of saturation with respect to liquid water, in which the snow crystals grow at the maximum possible rate. If all the water provided by the updraught, and that provided by the evaporation of the original cloud, is efficiently deposited as snow upon the mountain, then the cloud disappears in the region where descent of air begins, and the air remains clear in the lee of the mountain.

6. The concentration of snow crystals

If the crystals settling through the region of orographic updraught are to grow at the maximum rate, they must not be so numerous that the updraught is unable to maintain a state of water saturation. In air ascending under these conditions about 0.5 g/m^3 of water vapour is provided for condensation in a rise of 500 m. The rate of provision of vapour is therefore about $10^{-5}\ U$ g/m^3 sec, in an updraught of speed U cm/sec. A typical mean value of U in the region of orographic updraught is about $^1/_2$ m/sec. If the rate of vapour supply in such an updraught is equated to the rate of removal by the growth of N crystals/m^3, of radius about 500 μ, in air saturated with respect to liquid water, we obtain

$$\begin{aligned} Ndm/dt &= N \cdot 8\, r\, CF \\ &= N \times 0.4 \times 2.1 \times 3.0 \times 10^{-8} \\ &= N \times 2.5 \times 10^{-8} \end{aligned}$$

but $Ndm/dt = 50 \times 10^{-5}$

$\therefore\ N \approx 2 \times 10^4$

If the concentration of crystals introduced into the cloud should be less than this optimum value, then not all of the vapour provided by the orographic updraught is condensed upon the snow crystals; rather, the density of the droplet cloud increases towards the mountain tops, beyond which some evaporation occurs in the region where the air descends. The seeding operation does not then have the maximum possible efficiency.

On the other hand, the efficiency is not sensitive to concentrations of crystals somewhat in excess of the calculated value. If, for example, it is greater by a factor of 3, the crystal growth proceeds at the maximum rate until the crystal radii approach about 200 μ. At this stage the crystals remove vapour from an environment saturated with respect to liquid water more rapidly than vapour available for condensation is supplied by the updraught. For some while the evaporation of cloud droplets allows the rapid growth to continue, but when this evaporation is complete the vapour pressure and the growth rate fall to reach new steady values, in which the rate of increase of the crystal radii is about halved. This is not serious, however, for the crystals have already attained their maximum fall-speeds of about 40 cm/sec: the vapour provided by the orographic updraught is still efficiently deposited upon the snow crystals, and these reach the ground in about the same place, although individually they are smaller than in the instance where they have the concentration calculated above. Indeed, since under the reduced excess of vapour pressure the tabular form of growth may revert to a columnar mode, with a tendency for the fall-speed to increase, or because the increased concentration of crystals favours the formation of snowflake aggregates, the crystals may reach the ground more rapidly. It is hardly possible to say at what crystal concentration the stage of 'over-seeding' is reached, in which the crystals individually remain too small to reach the mountain surface before being carried well into its lee and subjected to evaporation. Since, however, even crystals of rather less than 200 μ radius have considerable fall-speeds (20—40 cm/sec), a crystal concentration excess by a factor of as much as 10 may not seriously reduce the efficiency of the seeding operation.

7. Performance of freezing-nucleus generators

The practicability of the seeding operation hinges on the necessity of providing crystal concentrations within the cloud of the order 10^4 to $10^5/m^3$. Very high concentrations of crystals can be introduced at all levels in a supercooled cloud by seeding from an aircraft with pellets of dry ice. Since, however, the seeding operations are imagined to occur over periods of several hours at a time, both by day and night in conditions when the mountain tops are obscured by clouds, it is clear that the method of seeding from the ground with smokes of freezing nuclei must be used. There is then some doubt whether the smoke enters the clouds in useful concentrations. Within the clouds themselves, if they consist of assembled small cumulus or of stratocumulus with practically clear skies above, there will usually be a moderately vigorous convective stirring. On at least some occasions such stirring extends to levels below the cloud base, but in their absence the turbulent stirring in moderately strong winds flowing over mountainous country must be relied upon to diffuse the smoke upwards. There are no adequate theories on which to base calculations of the rate of diffusion in a variety of likely conditions, and we can only refer to some empirical investigations carried out mainly in weather during which convection extended upwards from the ground.

In the work of Braham, Seely and Crozier (1952), the diffusion of an aerosol of fluorescent pigment, dispersed in particles of about 1 μ radius from a ground generator at the rate of about 3×10^{10}/sec, was examined. The particle concentrations observed by an aircraft downwind of the generator were reduced to those expected with a wind speed of 11 m/sec by multiplication with the fraction $11/V$, where V was the actual wind speed. This reciprocal law was established by Sutton (1947) for the diffusion of clouds near the ground over distances of a few hundred metres from a generator. After this correction the data showed that at heights of several hundred metres above the ground and at distances of 10—40 km from the generator the particles occurred in average concentrations of 100 to $200/m^3$. At distances beyond about 15 km the diffusion seemed to be relatively slow, suggesting that the eddies responsible for the diffusion are of scales much smaller than this (the convective motions may be expected to have dimensions of the order of 1 km or less). All the observations showed the width of the region over which concentrations of the above order were found was about half the distance from the generator. The results, which have been extended and improved by Crozier and Seely (1955), indicate that in a well-stirred atmosphere particles reach levels up to about

1 km above the ground at distances of about 20 km from the generator, in concentrations of the order of 10^{-8} S in winds of 5—20 m/sec, where S is the source strength in particles/sec.

In a similar investigation SMITH and HEFFERNAN (1954) used generators of silver iodide smoke, in which a solution of silver iodide in acetone was burnt in either a hydrogen or a kerosene flame. Both burners consumed silver iodide at the rate of about 200 g/hr; the hydrogen burner produced freezing nuclei active at — 7°, — 11° and — 20° to — 30° C at the rates of 5×10^{10}/sec, 5×10^{12}/sec and 10^{14}/sec respectively. The kerosene burner produced larger particles of silver iodide, and its rate of freezing nucleus generation was only about a tenth of that of the hydrogen burner. In an aircraft flown downwind of the generators samples of air were examined for freezing nuclei by chilling them in a cold box to produce supercooled clouds, and observing the numbers of ice crystals which formed. Measurements made upwind of the generator were used as a control.

The observations showed that a high proportion of the particles emitted from the hydrogen burner soon lost their efficiency as freezing nuclei: after 25 minutes exposure to the air the flux of effective nuclei was only one thousandth of the production of the burner. On the other hand the inactivation of nuclei from the kerosene burner was hardly detectable.

The phenomenon of inactivation of silver iodide nuclei has been studied by several investigators and attributed to photolysis at the surface of the particles. It has been related to exposure to sunshine and air of high humidity, but more recently BOLTON and QUERSHI (1954) appear to have found high air temperature to be the most important factor. Under the conditions of low temperature and general cloudiness in which freezing nuclei would be generated near mountain clouds in high latitudes the loss by inactivation is likely to be small. If so, it is reasonable to expect concentrations downwind of a generator using the more productive hydrogen flame to be greater by a factor of ten than those measured by Smith and Heffernan when the kerosene burner was used. Their observations show that in winds of about 10 m/sec the average concentrations of freezing nuclei active at about — 20° C, at heights of 500—800 m above ground and at distances of 10 to 15 km from the kerosene burner, were about 5×10^4/m^3. The source strength was about 3×10^{12}/sec, so that the dilution was in close agreement with that observed by Braham, Seely and Crozier.

On the basis of these results an efficient hydrogen burner whose nuclei do not suffer loss by inactivation produces corresponding concentrations of 10^3/m^3 active at — 7° C and 10^5/m^3 active at — 11° C. Thus providing that temperatures as low as — 10° C occur in the mountain clouds it is possible for one generator to provide the desired concentrations of crystals when it is placed some 10—40 km from the clouds in which the crystals are to be formed. If the temperature inside the clouds is anywhere considerably lower than — 11° C there may be some risk of providing too many crystals. In the present state of knowledge, however, there is no reliable basis for any discussion on the important subject of how to ensure the efficient production of artificial snowfall by control of generator output and positioning according to the particular meteorological situation. It can only be said that when clouds with internal temperatures below about — 10° C occur over the windward slopes of large mountains, then it is reasonable to expect that one generator at a distance of perhaps 40 km from the upper slopes can provide sufficient freezing nuclei to support an efficient artificial snowfall over a front of 10 to 20 km. Much experimental work would be needed to improve our understanding of how best to conduct such a seeding operation in a variety of meteorological situations.

The rate of diffusion of nucleus-smokes, and the magnitude and position of the mountain updraught, may be greatly influenced by hardly apparent details in the structure of the air stream (see, e.g. CORBY, 1954). The latter are also dependent upon the mountain shape: the most pronounced effects are caused by long ranges extending across the wind; isolated mountains, even though higher, are likely to produce weaker and less extensive orographic updraughts, and may therefore offer fewer opportunities of producing artificial snowfall. Consequently only a careful survey of conditions actually within a region where seeding operations are proposed can provide satisfactory data for an estimate of their feasibility and effect.

8. Quantitative estimate of artificial snowfall from mountain clouds

The maximum quantity of snow which can be obtained by seeding a mountain cloud is approximately the amount of water vapour condensed in the orographic updraught. This can be estimated by assuming that air near the ground is displaced upwards in the updraught by an amount about equal to the height of the mountain tops above the lowlands. In a typical example this displacement might be 500 m. If the general cloud base is 500 m above the low ground the surface air is brought just to saturation at its new level (assuming the lower layers are well stirred), preserving the cloud base at the same general level over the mountains. In air originally at the cloud base level the displacement condenses about 0.5 g/m^3 of water, and the average condensation in a column 500 m high is therefore 0.25 g/m^3. If this condensation in the lowest 500 m is removed by the fall of snow through the layer, and if the wind speed is V m/sec, then the snow behind each metre of the mountain flank facing the wind falls at the rate of 125 V g/sec. If the snow is spread over a path of 10 km in the wind direction the precipitation rate is 4.5×10^2 V mm/hr, or about $^1/_2$ mm/hr in a wind of 10 m/sec. This corresponds to an increase in snow depth at the rate of about 5 mm/hr. If the cloud base were only 300 m above the lowground, this maximum rate of snowfall is nearly doubled, and if in addition the thickness of the swept layer is 700 m, then it is trebled.

In the lee of the mountain the air is drier than it would be if it had not provided the artificial snowfall over the mountain. If widespread precipitation is reaching the ground in the lee of the mountain, it must suffer an increased loss by evaporation, equivalent to the amount of artificial snowfall. The effect of the seeding operation is then to transfer to the mountain a proportion of the precipitation which would otherwise fall, perhaps over a relatively large area, on lower ground in the lee of the mountain. Although the total precipitation over the entire region may not be increased significantly, it may be desirable to have more of it fall at high elevations, where for example as snow it can be stored until the end of the winter. On the other hand, if the artificial snowfall is produced when there is no general precipitation over the region in the lee of the mountain, then it can be claimed as a net increase for the entire region. It is doubtful if the mean annual precipitation of the whole earth can be increased by seeding, so that the increase over the mountains can then perhaps better be regarded as balanced by a very small decrease, quite undetectable, over a large part of the earth. This larger area may of course include oceans, in which any precipitation is wasted, and regions with a superabundance of rainfall.

9. Application to mountains of central Sweden

The annual yield of artificial precipitation from mountain clouds depends upon the frequency of occasions suitable for seeding operations. Observations of the kind, height, thickness, extent and temperature of clouds over mountains are necessary if an estimate of this frequency is to be made, but are not available in the usual climatological records. It is also desirable to have information on the disturbance in the wind flow produced by the mountains and the likely rate of diffusion of smoke from a nucleus generator, and to know whether or not natural precipitation occurs at an appreciable rate generally or over the mountain. In making plans for seeding operations in a particular area it is therefore necessary to make special meteorological observations and investigations for at least one or two seasons before an estimate of their possible result can be made.

As an illustration, however, we can use observations from the mountain weather-station of Blåhammaren, which is at a height of about 1,000 m above sea level in Jämtland, central Sweden, among mountains whose tops are mainly between about 1,000 and 1,500 m. The general level of the low ground is about 400 m. Particularly in maritime air masses, these mountains are often covered by extensive low clouds with a base about 800 m above sea level, and in the winter these clouds are supercooled. In such clouds the Blåhammaren station reports fog and rime. The rime frequently occurs also during snowstorms, suggesting that the natural snowfall does not efficiently remove all the vapour condensed in the orographic updraughts. We assume, however, that conditions suitable for seeding the

Table 4. Hours of fog (without snow or with snowfall less than 0.3 mm/hr) at Blåhammaren, during months Nov.-May, 1951—53 and 1952—53.

a) 1951—52

Mean wind speed $\bar{V}$:		Temperature, °C:											Total hours H, with temp. — 5° C or less	$H\bar{V}$
Beaufort force	m/s	— 3	— 4	— 5	— 6	— 7	— 8	— 9	— 10	— 11	— 12	— 13	less than — 13	
0	0.1			3							1			4	0
1	0.9							6						6	5
2	2.5			9	8	18	3		5			9	5	57	142
3	4.5	34	17	17	5	40		33	27					122	549
4	6.7	65	14	25	15	20	25	43	17			22		167	1,119
5	9.3	20	64	9	10	11	18	35	27	15		3		128	1,190
6	12.3	17		14	27	7	19	19	16					102	1,255
7	15.5	4	3	25	8	28		4	5					70	1,085
8	19.0			23			5						3	31	589
9	22.5									10				10	225
10	26.5						3							3	80
													$\Sigma H\bar{V}$:		6,239

b) 1952—53

0	0.1								2					2	0
1	0.9								6					6	5
2	2.5	10		5	13	12	30		30					90	225
3	4.5	6		41	3	26	38	75	56	15			7	261	1,175
4	6.7	18	12	31	44	27	26	63	22				3	216	1,448
5	9.3	9	106	39	35	34	51	6	14	26				205	1,907
6	12.3	22		3	9	26		16	6	1	9			70	860
7	15.5		20	3		7	12	29						51	790
8	19.0	11	3			4	6				12		3	25	475
9	22.5					2								2	45
10	26.5						4						10	14	371
													$\Sigma H\bar{V}$:		7,301

mountain clouds occur when Blåhammaren has fog with a temperature of — 5° C or below, but no snow or only snowfall at an average rate estimated to be less than 0.3 mm/hr. On some of these occasions the clouds may not have extended sufficiently high (a few hundred m above Blåhammaren) to provide the temperature of — 10° C necessary for the artificial production of sufficient concentrations of ice crystals. On the other hand there are likely to have been other occasions not included but suitable for seeding operations, when the cloud base was above the station, or when the station temperature was higher than — 5° C but the cloud tops were a kilometre or more above the station and therefore at a temperature below — 10° C. Table 4 shows the distribution of hours of fog according to temperature and wind speed during the winters 1951—52 and 1952—53.

If now it is assumed that the vertical displacement over a large mountain in this region amounts to 600 m and that the cloud base is on the average 400 m above the low ground, the rate of precipitation over a 10 km stretch of the mountain tops is found in the way described in section 8 to be $10^{-1}\ V$ mm/hr. Thus the maximum possible contribution of a seeding operation to the winter snowfall is one tenth of the sum of the entries in the final columns of each part of the table. This amounts to more than 600 mm in each winter, representing a snow-depth of a few metres. The average precipitation over the Jämtland mountains during the winter is according to climatic charts between about 350 and 450 mm (during each of these winters, however, the precipitation at Blåhammaren was about 600 mm).

Some support for the estimate of the artificial snowfall can be obtained from a picture (fig.

9) in a paper by Melin (1943). This shows a heap of rime which has fallen during a winter to the feet of a precipitation gauge at the top a 1,200 m mountain south of Jämtland. The heap appears to have a radius of about 2 m, and an average height of about 50 cm. It was collected by a gauge presenting an area of about $^1/_3$ m^2 to the wind. If it is assumed that the density of the heap and the efficiency of catch of the gauge are 0.5 g/cm^3 and 0.5 respectively, a simple calculation shows that if during riming conditions the corresponding amount of supercooled water in a column 600 m high had been removed over a path extending for 10 km along the wind, the average precipitation over the area would have been 300 mm.

It must be emphasized, of course, that this is only a tentative estimate of the maximum possible amount of the artificial snowfall, and that it could occur only over a limited mountain area, and does not represent a general increase of the same magnitude over the whole of a river catchment. The maximum amount of artificial precipitation can better be appraised by comparing its total volume with that of the spring flood in the rivers. The water-equivalent corresponding to the maximum artificial snowfall of 600 mm over a mountain chain extending 50 km across the prevailing winds is about 250×10^6 m^3. A typical river in this area with a catchment containing such a mountain chain, has a spring flood discharge of about $1{,}000 \times 10^6$ m^3 over a period of three months.

In the winter of 1953—54 the precipitation in Jämtland was much below normal. Weather observations are available not from Blåhammaren, but from Skurdalshöjden, which is on a hill about 20 km farther north, at a height of just under 800 m. An analysis of the fog observations, and also of records of rime deposited upon test bodies, provides an estimate of about 80 mm as the maximum artificial snowfall for this winter, or about 30×10^6 m^3 water over a large mountain group. The data are not satisfactory, however, because this station is only at about the average height of the cloud base in the winter, and so may not always experience fog when clouds suitable for seeding rest on the mountain tops. Equally the rime deposits are likely to be much smaller than those which would occur nearer the mountain tops, where the clouds contain more condensed water. The maximum artificial snowfall may be about proportional to the natural precipitation, but it is hardly possible to draw even tentative conclusions until more detailed observations are made.

10. The cost of seeding operations

In seeding operations over a mountain chain of this size a number of freezing nucleus generators would be placed at carefully chosen sites around the mountains, and it might be desirable to have some mobile generators. The cost of constructing generators is small compared with the cost of operating them, which amounts to about £ 1.3/hr. At any one time about five generators would be used, and a season's work on this scale is therefore likely to be composed of about 3,000 generator-hours with a total consumption of about 300 kg of silver and a cost of about £ 4,000. To this would be added the salaries of at least a pair of enthusiastic and skilled operators, and also minor expenditure, including the cost of transport for mobile generators and the operators, of forecast services, and of equipment and surveys needed for observing and analysing the results of the work.

Laboratory studies of the physical nature of particles in silver iodide smokes and of the process of inactivation may well lead to improvements in the design of generators and in the nucleating efficiency of their smokes, with substantial reduction of operating costs.

11. The problem of evaluating the results of seeding operations

The estimated maximum attainable increases in the mountain snow-cover and spring flood discharge of the rivers in the region considered amount respectively to about 100 % and 25 % of the normal values. Such increases would be easily noticeable. However, it must be emphasized that these estimates are tentative, and it is unlikely that present seeding techniques have a very high efficiency. More probably any artificial increases, at least at first, would be considerably smaller, and, indeed, smaller than the natural seasonal variations. There is about an even chance, for example, that the discharge in the upper reaches of the Jämtland rivers

during a three-month period including the spring flood departs from the normal by more than 15 %. Moreover, for the purpose of improving seeding techniques it is very desirable to be able to evaluate even smaller effects due to changes of method, and to be able to study the results of seeding in a variety of meteorological conditions. However, because conditions suitable for seeding are those in which natural snowfall often occurs, and because the effects sought are only as large or even smaller than common fluctuations due to natural and imperfectly understood causes, the difficulty of detecting them is a major problem.

The effects of seeding can be established only by statistical methods using some kind of control for comparison with natural, undisturbed conditions. Comparison is usually made with natural behaviour in the operation area, as shown by meteorological or other records, or with the natural behaviour simultaneously observed in neighbouring, unseeded areas. The methods may be combined by using the records to compare conditions in the several areas during both periods when seeding has and has not been performed. However, any method employing historical data, especially in mountainous areas, suffers from their extreme paucity and possibly also from the existence of climatic trends. The routine observations which are made even today are usually quite inadequate to determine the amount and distribution of precipitation over mountains. This is due to technical as much as to financial difficulties. For example snow-gauges have a number of imperfections and if exposed on mountains are difficult to reach and tend in winter weather. Surveys of the depth and water-equivalent of the snow-pack are also difficult and even dangerous, and are usually regarded as providing only an index of the general snow-cover, so that many hydrologists believe that the spring river-discharge can give a better measure of the winter snowfall. On the other hand if the results of seeding operations are sought only on a seasonal basis, then each individual experiment, of the series needed for statistical investigation, requires a year to perform.

There is thus urgent need for the development of evaluation techniques, and especially for the invention of techniques for detecting the effects of seeding individual cloud systems. These will spring from new ideas which are likely of arise only from improved understanding of precipitation processes, gained from detailed observation and intensive study of cloud and precipitation systems. Only by this means can the science of cloud physics achieve its purposes of improving the prediction of the weather, and of increasing man's ability to influence, and finally to control the weather.

Acknowledgement

This paper forms part of a researc hprogramme in cloud physics under development at the International Institute of Meteorology in Stockholm, with the support of Statens Tekniska Forskningsråd, Sweden, and the Munitalp Foundation, U. S. A.

REFERENCES

AUFM KAMPE, H. J., WEICKMANN, H. K., and KELLY, J. J., 1953: "Seeding experiments in supercooled stratus clouds", *Tech. Mem.* 1576, Signal Corps Engineering Lab., Fort Monmouth, N. J.

BERGERON, T., 1949: "The problem of artificial control of rainfall on the globe", *Tellus*, **1**, p. 1.

BOLTON, J. G., and QUERSHI, N. A., 1954: "Effects of air temperature and pressure on the decay of silver iodide", unpublished M.S. quoted by E. Bollay (1955): "Methods and results of large-scale applications of cloud seeding in the western United States", *Archiv f. Met., Geophys, Biokl.*, A, in the press.

BRAHAM, N. R., SEELY, B. K., and CROZIER, W. D., 1952: "A technique for tagging and tracking air parcels", *Trans. Amer. Geophys. Un.*, **33**, p. 825.

CROZIER, W. D., and SEELY, B. K., 1955: "Concentration distributions in aerosol plumes 3 to 22 miles from a point source", *ibid*, **36**, p. 42.

FRÖSSLING, N., 1938: "Über die Verdunstung fallender Tropfen", *Gerl. Beitr. Geophys.*, **52**, p. 170.

HALL, FERGUSON, HENDERSON, T J., and CUNDIFF, S. A., 1953: "Cloud seeding operations in the Bishop Creek, California, watershed", *Res. Pap. 36, U.S. Weather Bureau*, Washington, D.C.

KINZER, G. D., and GUNN, ROSS, 1951: "The evaporation, temperature and thermal relaxation-time of freely falling waterdrops", *J. Met.*, **8**, p. 71.

LANGLEBEN, M. P., 1954: "The terminal velocity of snowflakes" *Quart. J. R. Met. Soc.*, **80**, p. 174.

LANGMUIR, I., 1948 a: "The production of rain by a chain reaction in cumulus clouds at temperatures above freezing", *J. Met.*, **5**, p. 175.

— 1948 b: "Studies of the effects produced by dry ice seeding of stratus clouds", *Occ. Rep. 10, Project Cirrus*, G.E.C. Res. Lab., Schenectady, New York.

MARSHALL, J. S., and LANGLEBEN, M. P., 1954: "A theory of snow crystal habit and growth", *J. Met.*, **11**, p. 104.

MASON, B. J. 1953: "The growth of ice crystals in a supercooled water cloud", *Quart. J. R. Met. Soc.*, **79**, p. 104.

MCKNOWN, J. S., and MALAIKA, J., 1950: "Effects of particle shape on settling velocity at low Reynolds numbers", *Trans. Amer. Geophys. Un.*, **31**, p. 74.

MELIN, R., 1943: "Nederbörd och vattenhushållning inom Malmagens fjällområde", *Medd., Ser. Uppsatser* No. 44, Statens Met.-Hydrografiska Anstalt.

NAKAYA, U., and TERADA, T., 1953: *J. Fac. Sci.*, Hokkaido Imp. Univ., Ser. 2, **1**, p. 191.

OKITA, T., and KIMURA, K., 1954: "Ice crystal growth in the atmosphere", *J. Met. Soc. Japan*, Ser. II, **32**, p. 129.

POWELL, R. W., 1940: "Further experiments on the evaporation of water from saturated surfaces", *Trans. Inst. chem. Eng.*, **18**, p. 36.

REYNOLDS, S. E., 1952: "Ice crystal growth, *J. Met.*, **9**, p. 36.

SCHAEFER, V. J., 1947: "Properties of particles of snow..", *Trans. Amer. Geophys. Un.*, **28**, p. 587.

— 1953: *Final Rep., Project Cirrus*, Part. 1., G.E.C. Res. Lab., Schenectady, New York.

SHELLARD, H. C. and GRANT, D. R., 1951: "Results of an artificial nucleation experiment", *Met. Mag.*, **80**, p. 253.

SMITH, E. J., 1949: "Experiments in seeding cumuliform cloud layers with dry ice", *Australian J. Sci. Res.*, A, **2**, p. 78.

— and HEFFERNAN, K. J., 1954: "Airborne measurements of the concentration of natural and artificial freezing nuclei", *Quart. J. R. Met. Soc.*, **80**, p. 182.

SUTTON, O. G., 1947: "The problem of diffusion in the lower atmosphere", *Quart. J. R. Met. Soc.*, **73**, p. 257.

Salt Nuclei, Wind and Daily Rainfall in Hawaii

A. H. WOODCOCK[1] and W. A. MORDY[2]

(Manuscript received March 12, 1955)

Abstract

The discovery of large sea-salt particles at cloud levels led to the hypothesis that these particles act as nuclei on which raindrops initially form within clouds and to the suggestion that the amount of rainfall on an oceanic island might be a function of the number of the salt particles in the air. Exploratory observations of rain and airborne salt in Hawaii, which were intended to test this suggestion, are presented and discussed. These observations do not prove that greater numbers of salt nuclei are related to greater amounts of rain. They do, however, indicate that such a relationship may exist, and that additional field studies should be made which utilize the pertinent results of the present study.

Introduction

The presence of large sea-salt particles at cloud heights (WOODCOCK, 1952) and the recent theoretical indications of the possible role of large particles in the growth of raindrops by accretion (BOWEN, 1950; LANGMUIR, 1948; LUDLAM, 1951), caused us to suppose that the amount of rainfall from warm clouds might be related to the quantity of salt in the air. The physical basis for this supposition lies in the computations of the accretional growth of droplets made by LANGMUIR (1948). These computations show that large cloud drops should grow more rapidly than do smaller drops while falling through a cloud of much more numerous and smaller cloud droplets. The amount of water removed accretionally from clouds by drops falling through them might be expected, therefore, to be a function of the initial size of these drops and of the number, other relevant quantities being equal.

It seems most probable that the initially largest cloud drops form on the largest sea-salt nuclei, as indicated in the laboratory study of the condensational growth rates of sea-salt nuclei which was made by KEITH and ARONS (1954). Hence, it was thought that the amount of rain falling at a dominantly marine location might be related to the number of large salt nuclei in the air.

Ideas such as those sketched above led to the present study of the salt aerosols and the rainfall in Hawaii. It was felt that Hawaii would be a favorable marine location to test the rain-salt hypothesis, since the northeast trade-wind inversion tends to limit the vertical development of the clouds, producing more uniform cloud heights (RIEHL, YEH, MALKUS, LASEUR, 1951). A further factor in the selection of Hawaii for this study was the fact that U.S. Weather Bureau problems of forecasting shower rains had suggested that physical factors other than those routinely considered might be involved in the rain-forming processes (ANON, 1950).

[1] Contribution No. 757 of the Woods Hole Oceanographic Institution. This work was supported by the Office of Naval Research under contract Nonr-798 (00) (Nr-085-001).

[2] Meteorology Department, Pineapple Research Institute and Hawaiian Sugar Planters Association. Technical paper no. 232 of the Pineapple Research Institute.

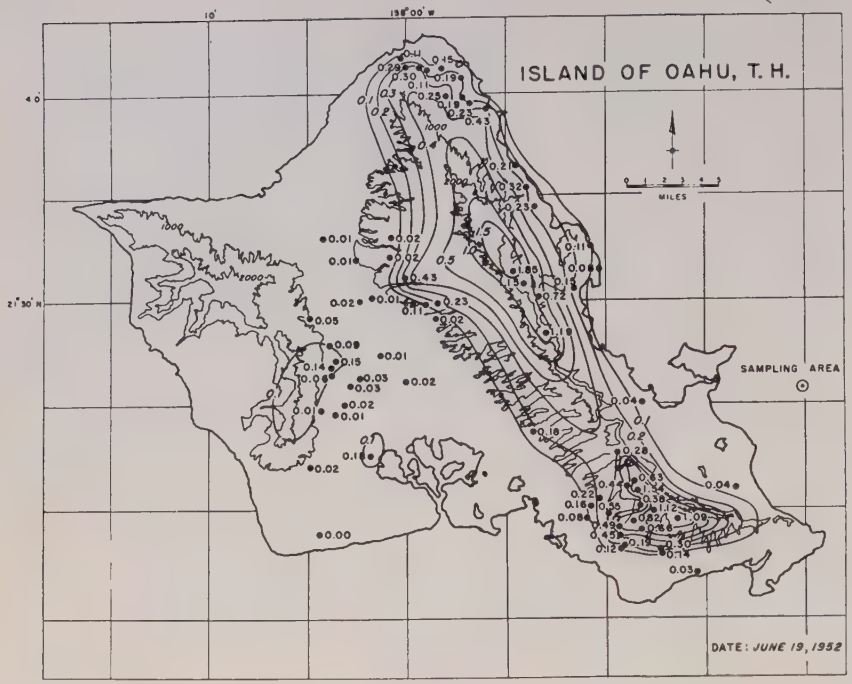

Fig. 1. Example of isohyetal maps used in deriving the total rain amounts shown on table 1, column 2. Rainfall amounts shown here are given in inches.

Numerous measurements of the quantity of salt nuclei in the air were made from aircraft over the sea on the windward side of the island of Oahu. An attempt is made here to relate this quantity of salt, which was usually sampled once a day, to the total amount of rain which fell on the island during each twenty-four hour period. These and other observations are presented in Table I and are discussed in sections 1, 2, 3, and 4 below.

Other properties of the air, such as mixing ratio, wind shear, instability, etc., which are potentially related to rainfall, are discussed briefly in sections 4 and 5, though they are not used directly in this exploratory study. These additional data are included in Table I so that other workers may examine their relevancy to the problem.

1. *Airbone salt particles*

The salt particles impinged upon and adhered to small glass sampling slides which were exposed to the atmosphere from aircraft. The slides were then taken to the laboratory, where particle diameters and numbers were determined with a microscope and at a controlled relative humidity of 90 %. At this relative humidity all salt nuclei were droplets, and the weights of salt in the individual droplets were computed from the droplet diameters. The detailed description of the techniques used to sample and measure the minute atmospheric salt particles has already been published and will not be discussed further in the present paper (Woodcock, Gifford, 1949; Woodcock, 1952).

On each flight an attempt was made to obtain the salt-nuclei samples at an altitude which was about one-hundred meters less than the altitude of the bases of the scattered local cumulus clouds but not necessarily under these clouds. The sampling position was over the sea and several miles up-wind (NE) of the island of Oahu (see Fig. 1). The air around and below the bases of the clouds had a higher water vapor and salt particle content than was found at greater altitudes in the cloud layer. It is supposed here that it is this lower air and its salt aerosols which flows into and forms the clouds. Thus the attempt here is to relate the quantities of the large salt aerosols present in the subcloud layer of air to the rain which subsequently falls from the clouds as the trade winds pass over the island.

Columns 3 and 4 of Table I show the salt amounts sampled on fifty-two flights, which

TABLE 1

Observations arranged in chronological order

1	2	3	4	5	6	7	8	9	10	11	12	13	14	15
Date	Total daily rainfall	Salt nuclei number l^{-1} of air	Salt nuclei weight m^{-3} of air	Cloud-base to-inversion distance	Wind shear 915—1,830 meters	Av. wind speed at cloud levels	Wind force	Av. wind direction at cloud levels	Mixing ratio near cloud-base altitudes	Mixing ratio in clear air at 1,525 m (from radiosonde)	Mixing ratio in clouds at 1,525 m	Instability; cloud-base-to inversion	Time of sampling flights	Minimum cloud-base altitude
	unit = 10^6 m^3	> 120 × 10^{-12} g	unit = 10^{-6} g	m	m sec^{-1}	m sec^{-1}		° true	gm/kg	gm/kg	gm/kg	cm^2	LCT	m
4 Jun 51	0.4	3.2	1.1	1700	2.0	5.7	3	57	13.0	7.8	12.1	1.42	13	640
5 Jun 51	0.8	4.7	1.4	1550	4.3	6.7	3.5	74	13.9	8.2	12.5	1.67	14	610
1 Jun 51	1.4	13.5	6.3	1360*	5.3	9.3	5	79	13.0	7.3	12.3	0.58	14	655
2 Jun 51	2.6	5.3	1.8	1920	3.0	8.2	5.5	71	12.8	7.1	12.3	1.55	11	580
3 Jun 51	0.8	18.6	6.0	1550	6.0	7.2	4	62	13.0	8.8	13.0	1.42	14	550
4 Jun 51	1.9	8.7	3.4	1260	2.6	11.3	4.5	70	13.6	9.1	13.2	1.03	10	560
5 Jun 51	3.7	11.5	5.0	1370	—	8.2	4.5	71	14.1	9.7	12.8	1.22	15	460
6 Jun 51	1.1	8.4	3.6	1160	3.2	9.3	4.5	65	13.6	9.6	12.3	1.16	10	510
7 Jun 51	0.8	6.1	2.0	1130	4.3	5.7	4	63	13.5	10.4	12.5	0.84	11	610
8 Jun 51	0.1	1.9	0.4	1100	3.0	3.1	3	74	13.7	10.8	13.4	0.65	14	640
9 Jun 51	0.3	3.2	1.0	1400	2.7	2.1	4	78	14.9	9.0	13.5	0.90	12	510
0 Jun 51	0.5	1.5	0.4	> 3000*	3.4	2.1	3	variable	14.5	7.2	13.2	—	08	460
6 Dec 51	2.7	3.7	1.2	2710*	4.3	7.2	3.5	83	12.2	7.2	11.5	1.35	14	700
7 Dec 51	2.3	2.7	1.0	2850	2.1	4.6	4	61	12.2	6.5	11.7	1.22	11	560
8 Dec 51	1.5	1.0	0.3	2220	4.0	6.2	3	65	11.2	8.0	11.4	0.77	10	400
9 Dec 51	6.0	7.4	3.8	> 3000*	5.6	5.7	5	88	11.3	8.5	12.0	—	14	855
2 Jan 52	3.5	4.5	1.5	> 3000*	3.8	9.3	3.5	86	15.6	10.3	13.5	—	09	335
3 Jan 52	9.9	11.3	8.1	> 3000*	3.8	11.8	6	89	14.4	9.5	12.4	—	09	460
4 Jan 52	0.6	21.5	16.4	425*	3.5	8.2	7	89	13.2	8.3	11.3	0.13	11	580
5 Jan 52	trace	18.0	13.0	305	4.2	10.3	7	95	8.1	6.0	10.2	0.19	10	940
8 Jan 52	11.0	12.1	4.9	2130	4.3	9.8	5	99	12.0	8.7	11.5	0.90	14	610
9 Jan 52	8.7	25.9	16.2	2090	4.7	12.9	6	83	12.5	10.5	12.0	0.90	15	655
1 Jan 52	6.7	23.3	13.2	2330*	8.2	17.0	7	90	10.6	5.2	11.1	2.12	10	870
2 Jan 52	1.2	47.0	31.0	730*	9.7	15.9	7	77	10.9	3.3	10.5	0.06	10	790
0 Feb 52	4.2	19.3	13.7	1830	4.7	13.9	6	94	13.0	9.4	11.7	0.39	11	510
5 Feb 52	3.5	0.3	0.1	> 3000*	5.3	2.6	1	variable	13.8	8.1	11.0	—	14	510
0 Feb 52	0.6	2.9	0.7	975	4.6	7.7	4	64	8.7	6.4	10.5	0.32	15	580
5 Feb 52	2.6	11.7	7.0	1620	3.1	6.7	4.5	85	10.9	8.8	11.5	1.10	14	790
0 Mar 52	3.2	28.3	11.2	> 3000*	4.2	12.9	5	74	11.5	7.3	11.0	—	14	685
2 Apr 52	1.9	10.3	4.2	1700	8.5	12.9	5	49	10.4	8.2	10.6	1.22	11	790
1 May 52	1.1	1.5	0.5	2200*	4.6	6.7	3	86	13.7	9.0	11.8	1.68	15	460
0 May 52	0.4	9.5	3.0	1130	4.0	9.8	4.5	77	12.6	6.8	12.3	1.29	14	640
6 Jun 52	3.7	16.9	6.5	1830	6.8	5.7	5	55	12.8	8.7	11.9	0.84	11—16	610
7 Jun 52	3.2	7.5	2.3	1980	5.0	6.3	3.5	78	11.6	9.2	12.5	2.38	10—16	700
8 Jun 52	6.0	9.0	4.1	2440	3.3	9.8	4	80	14.0	9.7	13.0	2.38	10—16	245
5 Jun 52	0.1	9.9	3.7	1190	3.3	10.8	4	90	13.2	7.2	12.2	1.42	10—16	610
6 Jun 52	4.0	10.9	3.3	1630	4.6	11.3	3.5	80	13.9	7.7	12.5	1.35	10—16	530
7 Jun 52	4.3	15.8	6.1	1720	—	11.3	4	73	15.0	7.8	13.0	1.35	10—16	440
8 Jun 52	2.7	12.3	5.3	1620	3.5	11.3	4.5	75	13.5	8.1	12.7	0.97	10—16	520
9 Jun 52	4.3	8.9	3.2	1920	4.8	5.7	4	81	13.0	10.6	13.1	0.97	10—16	670
0 Jun 52	1.3	5.1	2.0	1740	3.5	8.2	3.5	46	12.8	9.9	13.4	0.97	10—16	610
1 Jul 52	2.7	4.3	1.3	2160	3.1	9.3	3.5	88	13.7	8.9	12.9	2.00	10—16	550

* No temperature inversion observed on these days.

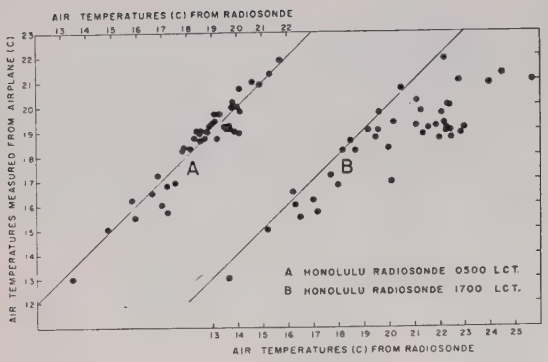
AIR TEMPERATURES (C) FROM RADIOSONDE
AIR TEMPERATURES MEASURED FROM AIRPLANE (C)
AIR TEMPERATURES (C) FROM RADIOSONDE
A
B
A HONOLULU RADIOSONDE 0500 LCT.
B HONOLULU RADIOSONDE 1700 LCT.

Fig. 2. Comparison of air temperatures observed from the salt-nuclei-sampling aircraft near cloud-base altitudes (see sampling area on fig. 1), with Honolulu radiosonde temperatures on the same day and at comparable altitudes.

were made on forty-two different days during 1951 and 1952. The quantities in these columns are limited to salt particles larger than $1.2 \times \times 10^{-10}$ grams. This limitation is due entirely to the fact that on many of the sampling days, and as a labor-saving step, only the larger nuclei on the sides were counted.

2. *Total rainfall measurements on Oahu*

Daily readings of many rain gages, scattered over the windward and central portions of the island, were used in drawing isoheytal maps for each of the forty-two days on which salt sampling flights were made. An example of these maps is shown in Figure 1. The rain data were assembled and the rain maps drawn by the second author, quite independently of the salt-nuclei-sampling activities of the first author.

Column 2 in Table I shows the values for total rainfall on Oahu, which were derived by planimeter-area measurements on the isoheytal maps. For instance the total rainfall obtained from the map shown in Figure 1 is 6×10^6 metric tons, a value derived by summing the products of the areas and the average rainfall amounts in each isohyetal contour. The rain amounts indicated in Table I were, in each case, collected in the time interval from 0800 LCT of one day to 0800 LCT of the following day. The date of the Hawaiian rain records is that of the day when the gages were read. In using these records here, however, it should be noted that the date of the preceding day is used; that is, the date when the salt-nuclei sample was taken. Thus the rainfall amount of 6×10^6 metric tons taken from the isoheytal map for 19 June 1952 (see Fig. 1), is listed in Table I as occurring on 18 June 1952.

3. *Inversion altitude and cloud-base-to-inversion distance*

In deriving the cloud-base-to-inversion distance, the minimum cloud-base altitude measurements (column 15) were used to mark the point where cloud temperatures would depart from the dry- lapse rate curves of the Honolulu soundings. This is illustrated in Figure 3. The point at which this cloud-lapse curve, or wet adiabat, intersects the dry bulb temperature line on the chart is taken as the altitude of the cloud tops. Cloud-base-to-inversion distance (column 5) is, therefore, simply the altitude of this intersection point minus cloud-base altitude, and is thought to represent roughly the maximum size of the clouds to be expected.

Inversion altitudes were taken from the Honolulu radiosonde records, using the soundings showing the maximum inversion altitudes observed at 0500 LCT. For example, the

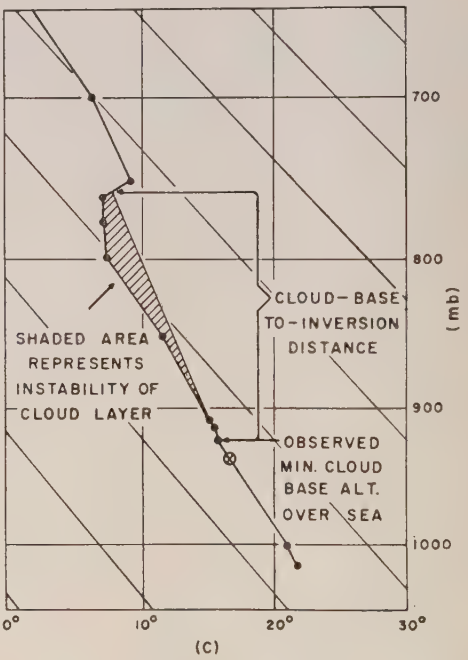

Fig. 3. Pseudo-adiabatic chart of Honolulu radiosonde record (1500Z, 26 February 1952) illustrating derivation of the cloud-base-to-inversion distances and the instability areas shown on table 1, columns 5 and 13. The circled X marks a temperature and pressure observed on the same day from aircraft over the windward sea.

20th value in column 5, Table I is based upon the radiosonde record of 0500 LCT on 6 January 1952, whereas the 20th rain record (column 2) is for the period 0800 LCT, 5 January 1952 to 0800 on the 6th. If the 0500 sounding of January 5 had revealed a higher inversion, then this sounding would have been used in deriving the value in column 5. The reason for this selection of the higher inversion altitude measured at the 0500 soundings is discussed below.

The 1700 LCT radiosonde temperature records were not used here because of the marked evidence on many days of local heating over the island which extended up to cloud heights, as shown in Figure 2, B. Thus it is thought that the 0500 soundings more nearly represent conditions over the sea and over the windward parts of the island where most of the rain falls.

On those days when no temperature inversion occurred, the cloud wet-lapse line usually intersected the radiosonde temperature line in a near-isothermal region. In Table I, column 5, the asterisks mark the days when the inversion was not present. On six of these days the altitude of the intersection of the lapse rate lines exceeded 3,000 m. In column 5 the cloud-base-to-inversion distances for these six days are given as $>$ 3,000 m.

The reason for selecting minimum cloud base altitude and maximum inversion altitudes for deriving the daily cloud-base-to-inversion distances, was the thought that these conditions would favor cloud growth, and that rain occurring during each 24 hour period would be most likely to occur during the periods of greatest potential vertical extent of the clouds. These distances are, however, somewhat uncertain, due to the question of how many hours any observed inversion or cloud base altitude may persist. This question is discussed in some detail later.

In deriving cloud-base-to-inversion distances, possible effects of the diurnal variation of inversion height (Leopold, 1948) are minimized by the consistent use of the 0500 LCT soundings[3].

[3] One exception to this rule was made on January 11, 1952, when a 1900 LCT sounding was used. This sounding, made one hour after sunset, showed none of the diurnal heating indications evident in most of the 1700 LCT soundings.

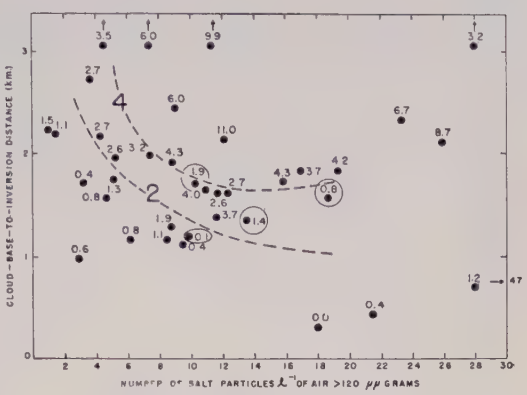

Fig. 4. Total daily amounts of rainfall on Oaho, expressed in units of 10^2 metric tons, related to the numbers of salt nuclei in the air and to the cloud-base-to-inversion distances. See text for further discussion.

4. *Winds and cloud-base altitudes*

The wind force at the sea surface was judged from the aircraft during sampling flights and is largely based upon the number, size and appearance of the white caps (breaking waves). The average winds at 915, 1,220, 1,525, and 1,830 meters altitude, were taken from the six-hourly records of the U.S. Weather Bureau at the Honolulu Airport. These wind velocities are given in columns 7 and 9, Table I.

The cloud-base altitudes shown in column 15, Table I, were measured from the airplane during a period of about one hour.

5. *Wind shear, stability and mixing ratios*

Among the various factors tending to reduce cloud growth and rain formation, the amount of shear present in the air through which the clouds must develop was thought to be important (Malkus, Scorer, 1955). Other factors, such as the instability of the clear air in the cloud layer and the difference in mixing ratios are given in Table I, columns 6, 10, 11, 12, and 13. Though these quantities are not used in the present paper, they are included here so that the reader may examine their relevance to the problem.

6. *Relating rainfall to cloud-base-to-inversion distance and to salt particle number*

Assuming that cloud-base-to-inversion distance and the number of salt particles might be the major factors causing variations in total

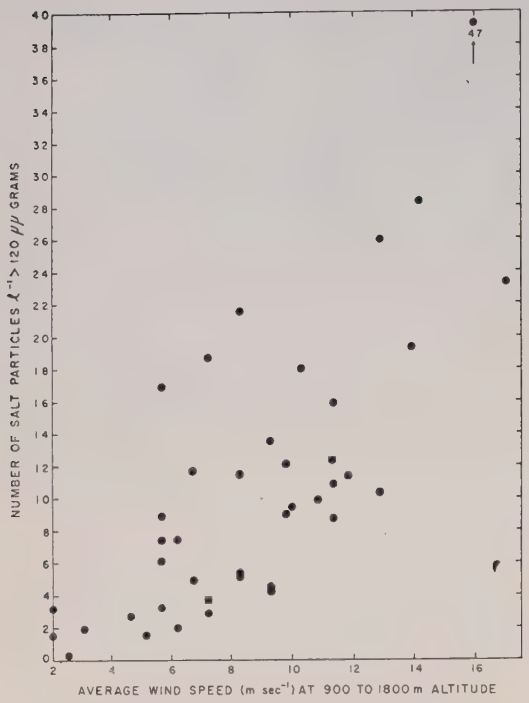

Fig. 5. Number of salt particles near cloud-base-altitudes, related to the average wind speed at altitudes between 900 and 1800 meters. (See WOODCOCK, 1953, for more detailed indication of dependence of salt nuclei upon wind).

rain amount, these three variables were plotted as shown in Figure 4[4].

The dashed lines on this figure are intended as an aid to the eye in roughly separating the values of rain amount into those less than two, those between two and four, and those greater than four. The units of rain amount equal 10^6 metric tons.

The most seriously divergent exceptions to the isoheytal pattern suggested by the dashed lines in Figure 4 are the rainfall amounts which are enclosed in circles. These observations will be discussed later. At the present time it is sufficient to point out that, with the above exceptions, the data in Figure 4 may be interpreted as indicating a crude quantitative relationship of the rainfall to the other variables on about two-thirds of the graph. For instance, note that increased values of cloud-base-to-inversion distance and of salt-nuclei number are generally attended by increased rainfall amounts, with a faint suggestion of an optimum rain amount in the middle range of nuclei number. On the right-hand portion of the figure the data are too sparse to justify an extension of the dashed isohyetal lines.

7. *Relating rainfall to cloud-base-to-inversion distance and to wind speed*

As shown in Figure 5 and in an earlier paper (WOODCOCK, 1953), the number of salt particles tends, however, to increase as the winds become stronger. Thus one might reasonably ask to what extent wind speed may contribute to rainfall. As a first test of the possible relationship of wind to rainfall, wind speed at cloud levels (see Table I, column 7) was substituted for salt-particle number on a diagram similar to Figure 4. The resulting distribution of values for rain amount is shown in Figure 6, and is clearly considerably less systematic than the distribution shown in Figure 4. Does this mean that wind has less effect upon rain in Hawaii than do the salt nuclei?

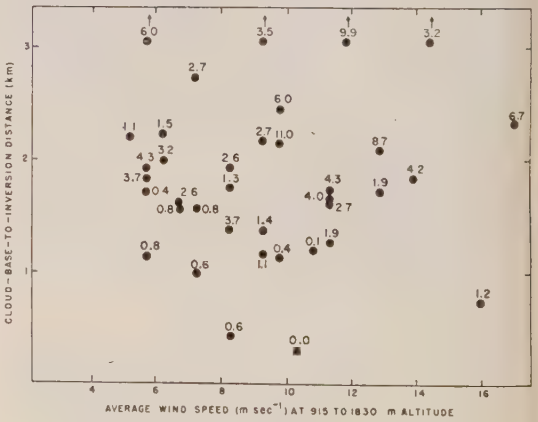

Fig. 6. Repetition of Figure 4, substituting wind speed at cloud levels for numbers of salt particles.

[4] The only data excluded from Figure 4 are those obtained on the five days when winds at cloud levels averaged less than 5 m sec^{-1} (see column 7, Table I). The reason for this exclusion is that low wind conditions favor a marked development of convective activity over the island during the daylight hours, thus making it very unlikely that the cloud-base-to-inversion distances, derived from the 0500 radiosonde temperature record, will represent the maximum cloud heights developed during the day.

The rainfall amounts on four of the six days when the cloud-base-to-inversion distance exceeded 3,000 meters, are simply plotted slightly above the maximum ordinate value (3,000 m) given in Figure 4.

In many of the previous studies of Hawaiian rainfall it has been pointed out that it is reasonable to expect increased rainfall with stronger winds, since these winds transport more moist air over the mountains. The amount of water vapor moving over the island daily should be nearly a linear funcion of wind speed, other factors remaining constant. Assuming that rainfall also might be a linear function of wind speed, the rainfall values plotted in Figure 4 were divided by the ratios of the observed wind speeds to the minimum wind speed of 5 m sec^{-1}. By this device it was hoped to subtract wind effects on rainfall from possible salt-nuclei effects. The resulting modified rain amounts are shown in Figure 7. It is interesting that the general pattern of distribution of rain amount shown in Figure 4 is still evident in Figure 7. In other words, increased values of cloud-base-to-inversion distance and of salt-nuclei number are still generally attended by increased rainfall amounts. Does this mean that the remaining pattern of change in rain amount with different values for salt-nuclei number is due to the effects of salt nuclei on rainfall?

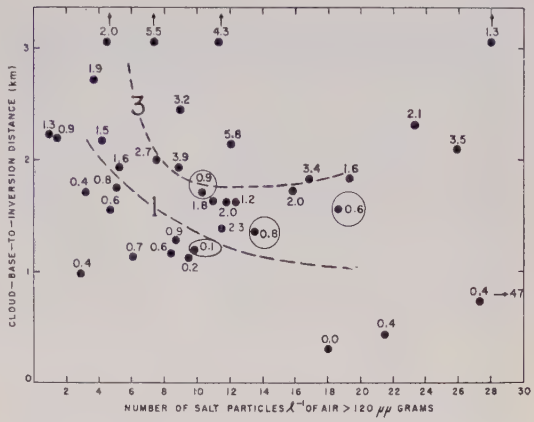

Fig. 7. The quotient of the total daily rain amounts and a function of wind speed, related to the number of salt nuclei in the air and to the cloud-base-to-inversion distances. See text for further discussion.

8. *Discussion*

The above questions cannot be answered at this time. The salt aerosols from the sea probably add still another variable to the already complex problem of Hawaiian rainfall. The contribution of wind to the daily rainfall in Hawaii remains unknown (Stidd, 1954 b) and there is at the present time little justification for assuming that rainfall might (or might not) be a simple linear function of wind speed, as was done in producing the "modified rain amounts" given in Figure 7. Further more detailed measurements are needed. The primary usefulness of the present study is that it further excites the curiosity about the role of salt nuclei in rain formation and it leads reasonably to pertinent suggestions about where, when and how future measurements should be made in an attempt to separate the wind and/or salt-aerosol contributions to rainfall.

In thinking about the possible significance of the distribution of values shown in Figure 4, it is well to remember that the twenty-four hour rainfall amounts represent an island-wide integration, whereas the values for number of salt particles and for cloud-base-to-inversion distances were usually taken from measurements obtained only once or twice a day and during relatively short periods of time. The proportion of each of the twenty-four hour periods during which these later values actually existed in the air over the island is of course unknown.

Changes in inversion height of as much as 1,000 m within a few hours have been indicated by Leopold (1948), and are occasionally evident in the Honolulu radiosonde records used in the present study. These changes will, of course, add uncertainty to the ordinate values in Figure 4, since these values are derived from the radiosonde records as described in section 3.

The usefulness of the cloud-base-to-inversion distances as a measure of cloud thickness and rainfall potential, probably depends upon the length of time these distances actually existed on the various sampling days. There is no adequate information about the hours of duration of any specific cloud-base-to-inversion distance, nor of the extent to which this duration is comparable from one sampling day to the next. In the absence of this information, further discussion of this point does not seem to be useful. It should be remarked, however, that Figures 4 and 7 suggest strongly that the cloud-base-to-inversion distances determined on the various days are related to the

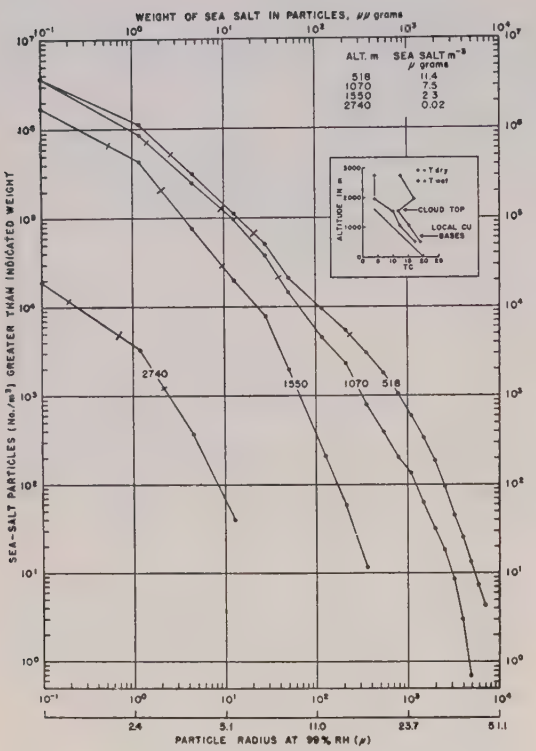

Fig. 8. An example of the decrease, with altitude, in the numbers of salt particles in Hawaii. Approximate position 21° 30′ N, 157° 40′ W; Time 1300 LCT, 30 May 1952. Surface wind 80 deg. force 4 to 5. Note that the region of cloud development is one of rapid decrease with height in the numbers of the larger nuclei. (The lines are drawn between the observed values as an aid to the eye in following the trends of the various observed distributions.)

rainfall. This result is thought to indicate that the durations of these distances are, on the average, sufficient to markedly influence the rainfall during each twenty-four hour period.

The amount of airborne salt also varies considerably during short periods of time. On ten of the days represented in Table I and Figures 4, 6, and 7, counts of salt nuclei were obtained at 1000 and 1600 hours, instead of the usual single observation per day. An average of these salt-particle counts is used in Figures 4 and 7. The ratios of the maximum to the minimum of these two values for salt-nuclei number averaged 1.56. On each of the remaining 27 days, when only one observation was made, the nuclei content of the air may have varied an equal or greater amount.

Thus it is evident that the two important quantities cloud-base-to-inversion distance and salt-nuclei number can be far from constant during a twenty-four hour period. It is thought that this lack of constancy may account for some of the observations which differ widely from the proposed pattern (see circled values of Figures 4 and 7). In view of the variability of the above quantities, it is rather surprising that there is any pattern in the distribution of the values in these figures. The suggestion of a pattern, despite the above variability, may be due to a real relationship between the quantities involved.

It is clear that numerous observations are needed throughout each twenty-four hour period in order to properly test the reality of the rainfall pattern suggested by Figures 4 and 7. At this early exploratory stage of this study, it does not seem fruitful to speculate about the meaning of this precipitation pattern and what it may imply about the rain-forming mechanism.

No consideration is given to the probable change in the slope of the cloud temperature-lapse line which would result from mixing of the cloud air with the environmental air during ascent. (Note on Fig. 3 that a wet lapse rate is assumed in the clouds.) This mixing would tend to decrease the cloud-top temperature and, as is evident from the gradient of salt-nuclei number in the cloud layer (see Figure 8), would also cause a reduction of the number of salt nuclei in the cloud. The omission of consideration of these variables here is due to the impression that their effect upon the rainfall amounts is of secondary importance in this preliminary study.

Solot (1950) and others have pointed out that wind speed determines the rate of moisture flow over the islands of Hawaii, and thus may directly affect rainfall intensity. Stidd (1954 a) has recently found evidence of a correlation of rainfall with the pressure over certain areas of the North Pacific and he suggests that this correlation is due to the influence of stronger trade winds in increasing rainfall. The fact that the number of salt nuclei in the air increases with increasing winds, poses a problem concerning the detailed nature of the effects of wind on rainfall. To what extent is the rainfall due to the amount of moist air or clouds flowing over the mountains and to what

extent is it due to the quantities of potential raindrop-forming nuclei which are in this air?

The salt nuclei show a persistent pattern of relationship to rain amount which is not revealed by wind speed and rain amount (compare Figures 4 and 7 to Figure 6). This apparent relationship of nuclei to rainfall may not be due, however, to quantitative effects of the number and size of salt particles upon the number and size of raindrops. It is possible that the determination of the number of the large salt nuclei in the air is a better measure of the 24 hour average wind speed over the sea and the mountains than are the Honolulu winds-aloft measurements. If this is true then Figures 4 and 7 may be interpreted as reflecting the wind effects upon total rainfall. The authors consider, however, that at the present stage of the study, these figures are clear evidence that salt nuclei will have to be considered in future studies of the Hawaiian rainfall problem.

Detailed short period studies, made during or immediately after rapid changes in wind speed, may supply an answer to this problem. It is expected that the changes in the quantities of airborne salt at cloud levels will be found to lag behind the changes of wind speed, due to the time requirements for the upward diffusion of the salt particles in the case of increased wind, or for their sedimentation when the wind is reduced. The duration of this time lag is uncertain, however. If the lag proves to be long enough, perhaps of several hours duration, it may be possible to answer the question of the contribution of salt nuclei to rain amount through the use of hourly measurements.

Most of the shower rains which occur on Oahu are produced by cumulus clouds which are immersed in and drifting with the trade-wind stream. Many, if not most, of these clouds are formed before arriving over the island, and from some of them rain is falling as they approach the island from over the windward sea. This rain often continues to fall as the clouds pass over the windward beaches and move inland to the mountains. The time these clouds remain over the island is thus a function of wind speed at cloud altitudes.

One effect of greater cloud speed is of course to increase the number of clouds passing over the island in a given twenty-four hour period. If orographic lifting of clouds and of the ambient air accounts for the increased rainfall in the mountain areas, and this seems to be generally accepted (see LEOPOLD, 1948; SOLOT, 1950; STIDD, 1954 b), then the greater the number of clouds streaming over the island in a day the greater the chances of rain formation. That presupposes, of course, that other rainforming factors are equal.

However, since it is assumed that the Hawaiian shower rains are formed by accretional and/or condensational growth processes, which may be critically time-dependent, it is possible that high winds may move the clouds off the mountain areas before the rain-forming processes, which bring about the rain excess in these areas, have time to proceed to completion. In this case one might expect a tendency towards a reduction of rain amount as winds exceed some optimum speed. This speed may be regarded as one which will cause a maximum number of clouds to be lifted over a mountain area within a given time, the duration of the lifted state being sufficient for a completion of the accretional and/or condensational growth processes. The rainfall and other data given here are not sufficiently numerous throughout the range of values given to indicate an optimum wind speed.

The authors are inclined to think that the increased rain amount which falls from the clouds behind the crest of the Koolau Mountain Range (see Figure 1 and HALSTEAD, LEOPOLD, 1948) is due in large part to the modification, over the mountains, of shower clouds which form over the windward sea and drift down upon the island in the trade-wind stream.

The night maximum of rain on Oahu, which has been noted by LEOPOLD (1948) and others, may be due to the night maximum of cloudiness over the sea noted by RIEHL (1947). Thus a night maximum of rainfall does not necessarily suggest a night maximum of nuclei or wind speed, as might be supposed from the present study.

YEH and others (1951) have suggested that wind direction will affect the rainfall on Oahu, due to the fact that the flow is sometimes parallel to the mountain ridges and sometimes normal. As can be seen in column 9, Table I, and in Figure 1, most of the wind directions were nearly normal to the long axis of the Koolau Range. This relative constancy

of the wind has caused us to ignore direction as one of the variables possibly affecting rainfall in this series of days.

Remarks about further study

In order to make a further test of the relationship of salt particles and/or wind to Hawaiian rainfall, it seems to be necessary to make additional measurements from aircraft. These measurements should be made over the sea, many kilometers upwind from the high-rainfall area on Oahu, and should include as many of the variables as possible. Four or more flights a day would be desirable, especially after a time of rapid change in wind speed.

An increase in the number of recording rain gages along the Koolau Range would add to the accuracy of the isoheytal maps. As shown in Figure 1, there are rather large areas in the high-rainfall regions of the mountain range where there are no gages. This relative sparsity of gages in this region adds a considerable uncertainty to the drawing of the isohyetal lines and hence to the total rainfall values derived from the maps. Errors due to this uncertainty add another factor to be considered in the evaluation of Figures 4, 5, and 7.

If further study confirms the general pattern of rainfall distribution suggested on Figures 4 and 7, the question of the forecast value of the measurements used in deriving this pattern will arise, and it will also become necessary to seek an explanation of the result in terms of the detailed mechanics of raindrop formation.

Acknowledgements

The authors want to thank Dr's Harry Wexler and Irving Langmuir, who originally suggested the study of salt nuclei and rain in Hawaii. The first author also wishes to express his appreciation of the skill, interest and effort of Mr. William Stearn and Mr. Wallace Waterhouse of Murray Air, Ltd., Honolulu, in the successful completion of the many airplane flights required in this study.

Mr. Larry Eber of the Pineapple Research Institute and Mr. Saul Price of the U.S. Weather Bureau, Honolulu, contributed much time and effort to this study by supplying numerous transcriptions of weather data.

REFERENCES

Anon, 1950: Physical basis for the production of rain in Hawaii (A statement by members of the forecast staff, U.S. Weather Bureau, Honolulu, Hawaii). Unpublished.

Bowen, E. G., 1950: The formation of rain by coalescence. *Austr. J. Sci. Res.*, A, 3, 193—213.

Halstead, M. H., and Leopold, L. B., 1948: Monthly median rainfall maps. Meteorology Dept., Pineapple Research Institute and Experiment Station, Hawaiian Sugar Planters Association, Honolulu, Hawaii, Report No. 2.

Keith, C. H., and Arons, A. B., 1954: The growth of sea-salt particles by condensation of atmospheric water vapor. *Jour. Met.*, **11**, 173—184.

Langmuir, Irving, 1948: The production of rain by chain reaction in cumulus clouds at temperatures above freezing. *J. Meteor.*, **5**, 175—192.

Leopold, Luna B., 1948: Diurnal weather patterns on Oahu and Lanai, Hawaii. *Pacific Science*, **2**, 81—95.

Ludlam, F. H., 1951: The production of showers by the coalescence of cloud droplets. *Quart. J. r. meteor. Soc.*, **77**, 402—417.

Malkus, Joanne Starr, and Scorer, R. S., 1955: The erosion of cumulus towers. *J. meteor.*, **12**, 43—57.

Riehl, H., Yeh, T. C., Malkus, J. S., and LaSeur, N. E., 1951: The northeast trade of the Pacific Ocean. *Quart. J. r. meteor. Soc.*, **77**, 598—626.

Riehl, Herbert, 1947: Diurnal variation of cloudiness over the subtropical Atlantic Ocean. *Bull. Amer. Met. Soc.*, **28**, 37—40.

Solot, Samuel B., 1950: Further studies in Hawaiian precipitation. Research paper No. 32, Weather Bureau, U.S. Department of Commerce, Washington, D.C.

Stidd, C. K., 1954 a: Objective Hawaiian rainfall estimates from mean 700 mb charts. To be published.

— 1954 b: Personal communication.

Woodcock, A. H., and Gifford, Mary M., 1949: Sampling atmospheric sea-salt nuclei over the ocean. *J. Marine Res.*, **8**, 177—197.

Woodcock, A. H., 1952: Atmospheric salt particles and raindrops. *J. Meteor.*, **9**, 200—212.

— 1953: Salt nuclei in marine air as a function of altitude and wind force. *J. Meteor.*, **10**, 362—371.

Yeh, T. C., Wallén, C. C., and Carson, J. E., 1951: A study of rainfall over Oahu. *Meteorological Monographs*, Vol. 1, No. 3, 34—46, Amer. Met. Soc., Boston 8, Massachusetts.

A Case Study of Jet Stream Clouds

By VINCENT J. SCHAEFER, The Munitalp Foundation, Inc. and
WILLIAM E. HUBERT[1], University of Stockholm

(Manuscript received December 23, 1954)

Abstract

Certain specific cloud forms are frequently associated with strong winds aloft. Investigation has shown that these clouds are usually observed in regions of strong horizontal and vertical wind shear, and in most cases in or above regions where negative absolute vorticity (dynamic instability) and low Richardson's numbers coincide. The small-scale details in jet stream clouds may be the result of turbulent motion in layers brought to or near saturation by large-scale vertical motions in the atmosphere. This paper contains a detailed study of a typical case.

Introduction

In an earlier article SCHAEFER (1953) presented pictures of four cloud types including specific forms of cirrus, cirrocumulus and altocumulus which are frequently associated with strong winds aloft. The use of cloud observations to locate wind maxima from the ground is limited, of course, to periods when lower clouds do not obscure the sky; however, high-flying aircraft do not experience this limitation and could undoubtedly make good use of such jet stream "indicators". One case wherein a commercial plane followed a cloud streak for 1,500 miles over the Atlantic has been brought to the writers' attention.

It seems unlikely that jet stream clouds are formed simply because the wind speed exceeds some critical value. We do know, however, that condensation may occur in the atmosphere if sufficient cooling takes place; this is synonymous in adiabatic processes to saying that ascending motion is required. It is well known that meridional circulations are associated with jetlets moving in a westerly current at a speed less than that of the maximum wind. Comparatively large-scale ascending motions are usually found, for instance, on the warm-air side of the jet stream entrance region.

The clouds which have come to be associated with jet streams are quite spectacular and the sky is frequently very chaotic in appearance. Reports from pilots indicate that the small-scale structure of these clouds might be due to turbulence elements. For this reason it was deemed desirable to study some of the more well-known atmospheric stability criteria in an attempt to find an explanation for the fine details observed in jet stream clouds.

Stability criteria

The jet stream has been defined as a narrow band of high wind speed embedded in a relatively quiescent surrounding atmosphere. Such a current is, therefore, characterized by strong wind shear, both horizontally and vertically, between the core and the surroundings. Several instability criteria which contain shearing terms (either horizontal or vertical) have been prominent in meteorological literature for the past 30 years. Three different criteria dealing with horizontal cyclonic, horizontal anticyclonic and vertical wind shear will be given particular consideration.

[1] Lieutenant, United States Navy. Present address Joint Numerical Weather Project, Washington, D.C. Any opinions expressed by Lt. Hubert are his own and do not reflect the views of the Navy Department at large.

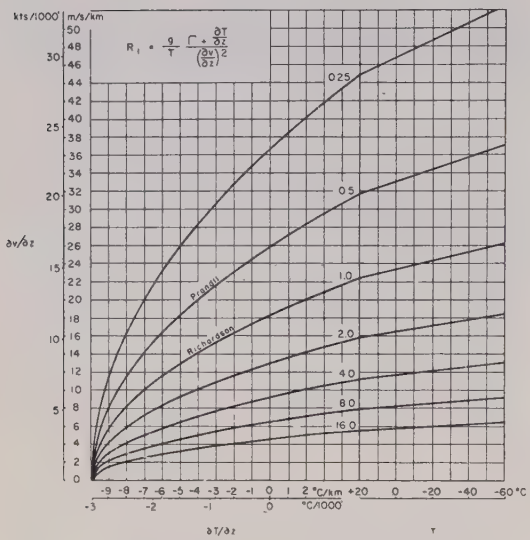

Fig 1. Graph of Richardson numbers (heavy solid lines) as function of lapse rate ($\partial T/\partial z$), vertical wind shear ($\partial v/\partial z$) and temperature (T).

Solberg (1939) has discussed the vanishing of the absolute vorticity in the case of transition to instability. The vertical component of the absolute vorticity in a zonal current (see Palmen 1948) is given by

$$\eta = -\frac{\partial u}{\partial y} + 2\,\omega \sin\phi + \frac{u}{R}\tan\phi \qquad (1)$$

Here η is the vertical component of the absolute vorticity, y the meridional coordinate (positive northward), ω the earth's angular velocity, ϕ the latitude, u the west wind speed and R the radius of the earth. If the sum of the relative vorticity and the earth's vorticity ($2\,\omega \sin\phi$) is negative, the motion is dynamically unstable. It appears possible to realize this type of instability on the south side of strong jet streams. This possibility is therefore of interest in our study of jet stream clouds and will be treated in more detail later on.

Another criterion for dynamic turbulence, this time in the zone of cyclonic shear to the north of a wind maximum, has been given by Arakawa (1951). According to his theory the criterical cyclonic shear, again for zonal flow, is given by

$$-\frac{\partial u}{\partial y} = \omega \sin\phi + \frac{2u}{R}\tan\phi \qquad (2)$$

This critical value is often realized in a narrow region (usually the upper frontal zone) just north of well-defined jet streams. Most of the cases of clear-air turbulence (eg. Hislop 1951, Berggren 1952 and Bannon 1952) have, in fact, been from this zone of strong cyclonic shear. The reason why clear-air turbulence and not turbulent-type clouds are usually found here will also be discussed later.

Richardson (1920) has developed a criterion for the increase or decrease of atmospheric turbulence where there is wind shear in the vertical. He postulates that turbulent flow will continue if the rate of supply of energy by eddy stresses is equal to or greater than the work done to maintain the turbulence against any stabilizing forces. The Richardson number is given by

$$R_i = \frac{g}{T}\,\frac{\dfrac{\partial T}{\partial z} + \Gamma}{\left(\dfrac{\partial \bar{v}_x}{\partial z}\right)^2 + \left(\dfrac{\partial \bar{v}_y}{\partial z}\right)^2} \qquad (3)$$

Here g is the acceleration of gravity, T the absolute temperature, $\partial T/\partial z$ the observed lapse rate and Γ the adiabatic lapse rate. The components of the vertical wind shear $\partial \bar{v}_x/\partial z$ and $\partial \bar{v}_y/\partial z$, should be evaluated from vector differences. In this paper the customary approximation

$$\left(\frac{\partial \bar{v}_x}{\partial z}\right)^2 + \left(\frac{\partial \bar{v}_y}{\partial z}\right)^2 \approx \left(\frac{\partial v}{\partial z}\right)^2 \qquad (4)$$

will be used throughout. By computing R_i from vertical cross sections and only in situations where the wind veers but slightly with height, it is assumed that this approximation is not too restrictive. The difficulty of assigning a critical value to the Richardson number is encountered here; different investigators have found values ranging from $^1/_4$ to unity. In figure 1 is presented a graph which permits rapid computation of Richardson numbers from vertical cross sections (dependent, o course, upon our assumption in equation 4). By entering the left hand portion of the graph with lapse rate and vertical wind shear as arguments, one immediately obtains R_i at $T = 20$ C. By first following a constant R_i to the vertical line corresponding to this temperature and then moving horizontally to the right, the corrected R_i at any other temperature

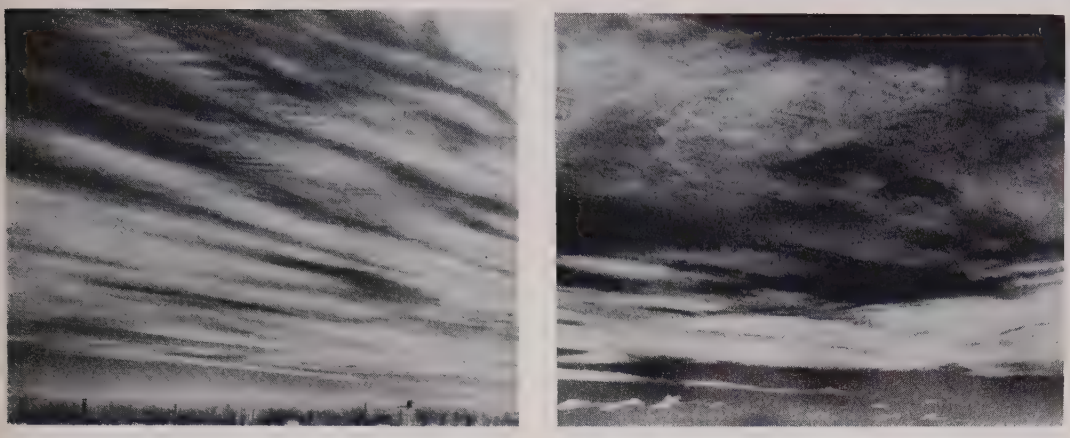

a b

Fig. 2. Cloud photographs taken at Schenectady, New York on 2 March 1953 (a) toward east at 1230 EST and (b) toward northeast at 1300 EST.

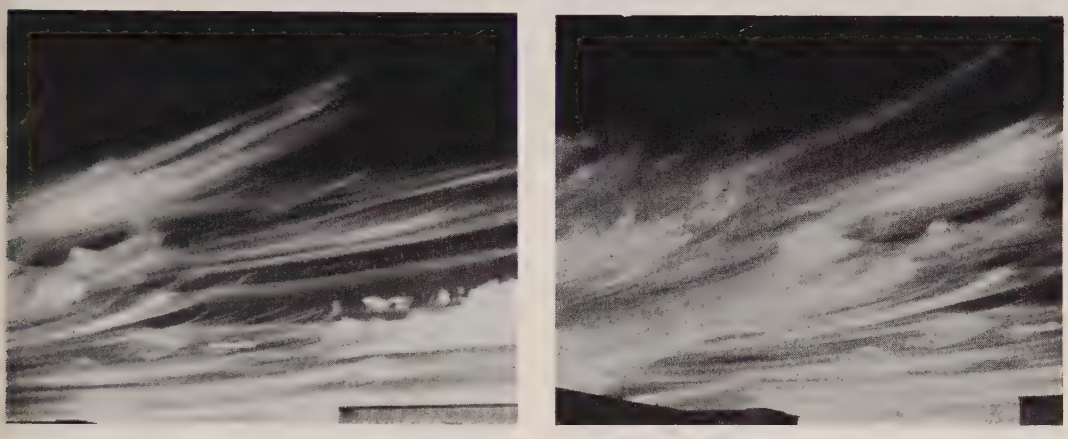

a b

Fig. 3. Cloud photographs taken at Schenectady, New York on 2 March 1953 at 1645 EST (a) toward north and (b) toward northwest.

is given. This figure clearly illustrates the importance of the vertical wind shear. It is self-evident that one should expect to find low Richardson numbers in the vicinity of jet streams; it is impossible to have a real jet without having both horizontal and vertical wind shear. The distribution of R_i with respect to well-defined wind maxima will be discussed for a typical case.

Through the use of the stability criteria which have been summarized above one might, therefore, hope to arrive at an explanation for the "turbulent motion" cloud types which have been observed in connection with jet streams. At least these three criteria, all based upon dynamic principles, offer a starting point in our investigation.

Turbulence and cloud formation

Obviously instability and the resulting turbulent motion do not necessarily mean that clouds will form. One needs only to look at the numerous reports of "clear-air turbulence" to realize that such is the case. Several factors seem to be of importance in this connection. The data collected by BARRETT and others (1949) using the dew-point hygrometer demonstrate the complexity of the moisture

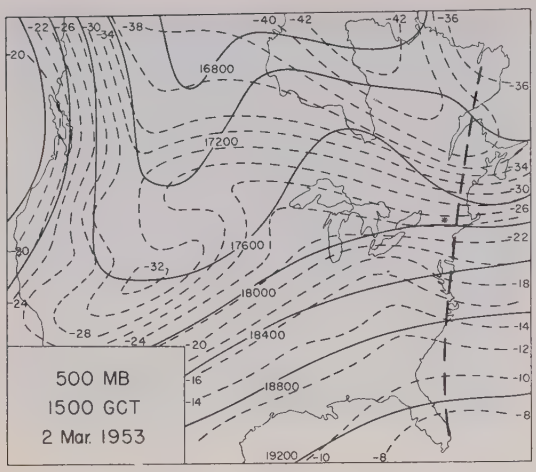

Fig. 4. 500-mb chart, 1500 GCT, 2 March 1953. Heavy solid lines, height contours at intervals of 400 feet. Thin dashed lines, isotherms at intervals of 4° Centigrade. Heavy dashed line, location of cross section. Star shows location of Schenectady, New York.

distribution at high levels in the atmosphere. Frequently the air is so dry that turbulent ascent clearly is unable to bring about condensation.

Vuorela (1953) has recently compleetd a study of the dew-point differences around jet streams over western Europe. His cross sections indicate that there is usually dry air on the cyclonic shear side of the jet stream in the region where clear-air turbulence is most frequently reported. There are exceptions, of course, and he has found cases where a narrow tongue of moist air extends vertically along the warm-air side of the polar front into the zone of strongest cyclonic wind shear. A few cases of jet stream clouds have also been observed here, but they are exceptions to the general rule.

Schaefer has noted that when jet stream clouds are present the sky to the northward is usually clear, and the visibility in this direction is extremely good. This suggests that the lateral circulation about the jet stream is thermally direct in these conditions. It has been shown by Riehl et al. (1952) that a lateral circulation of this sense should be found in the entrance zone of moving jetlets. Since the clouds discussed here are frequently visible from the ground, we can also conclude that the overall ascending motion cannot have persisted long enough to bring about condensation in a deep atmospheric layer. If, however, one or several thin layers were brought close to saturation by some large-scale ascending motion, condensation could then occur in the turbulent wave crests.

Flight observations in jet streams

During the past two years some extremely interesting first-hand observations of the physical nature of jet streams have been described by a senior pilot of the British Overseas Air Corporation. In two papers, Captain Bernard Frost (1953, 1954) has described his procedure for locating a jet stream maxima in the region between 18,000—25,000 feet. The first of his papers describes his temperature gradient method for approaching a jet stream. In his words, "The most valuable instrument used in locating the jet stream proved to be the outside air thermometer. ——— It was found that once in a strong wind at a certain level by flying exactly downwind the temperature remained unaltered and the wind speed remained unchanged. Further, an amazingly accurate guide for calculation of wind strength on either side of the jet stream (within altitude limits normally flown, viz., 15,000—25,000 feet) was that the wind *decreased some 8 knots for every degree Centigrade drop in temperature on the Polar (or cold) side and it decreased some 16 knots for every degree Centigrade rise in temperature on the Equatorial (or warm) side.*" Frost's first paper is illustrated with pictures of jet stream cloud types which are classic forms according to Schaefer. In his second paper, Captain Frost describes further and more detailed observations with special reference to cloud forms observed. His earlier observations and conclusions supplemented by those of his second paper are in complete agreement with the observations reported by Schaefer.

By private communication a detailed critique of Frost's original paper was presented by a group of Pan American pilots and navigators. Their experiences are also in complete agreement.

The case of 1—3 March 1953

On the morning of March 1, 1953 the sky over Schenectady, New York was completely cloudless with a deep blue color; the visibility was unlimited. Such clearness of air in eastern New York occurs only a few times a year.

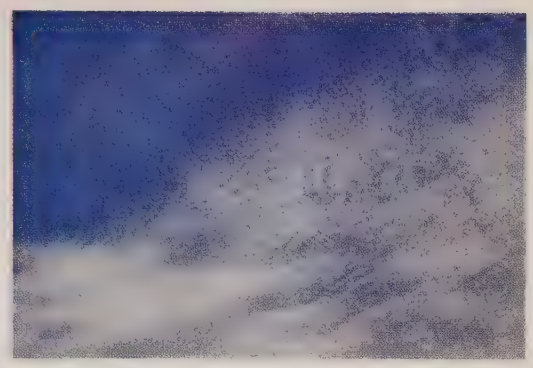

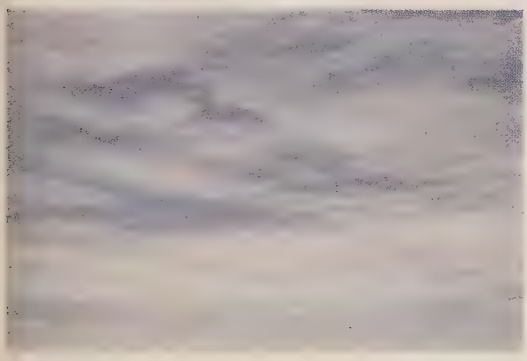

Fig 2 (cont.)

c Wave cloud at cirrus level, 1230 EST, March 2, 1953.

d Ripples in cirrus at 1231 EST, March 2, 1953.

e Ripples and billows at cirrus level, 1232 EST, March 2, 1953.

f Waves and banded cirrus, 1300 EST, March 2, 1953.

g Hole developing in banded cirrus, 1301 EST, March 2, 1953.

h Edge of large wave crest in cirrus, 1302 EST, March 2, 1953.

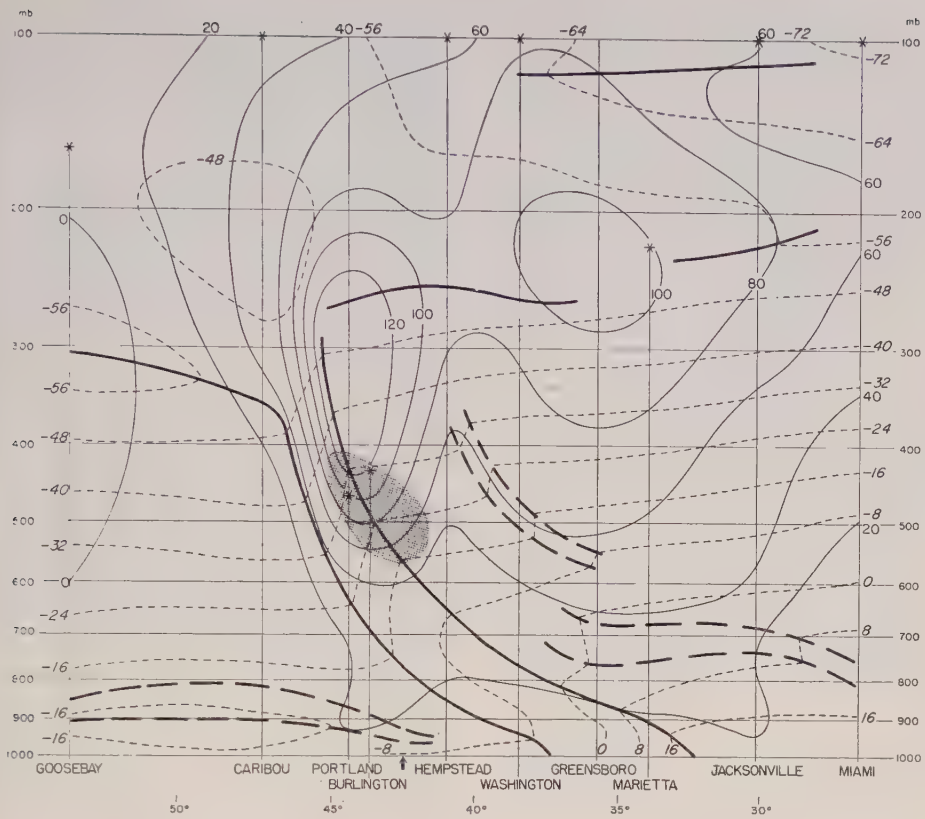

Fig. 5. Vertical cross section from Goose Bay, Labrador to Miami, Florida at 1500 GCT, 2 March 1953, along heavy dashed line in figure 4. Thin dashed lines, temperature (deg. C); thin solid lines, isotachs of observed wind component (knots) normal to section; heavy lines, frontal boundaires and tropopauses; stars, highest level to which wind observations were available; arrow, location of Schenectady. Region where Richardson numbers < unity shown by stippling.

The atmospheric electricity as measured by a point discharge collector was above 0.04 uA throughout the day. In late afternoon a few long lines of altocumulus appeared in the west, illuminated by the setting sun. At 1600 EST the maximum wind speed over Albany, New York was reported to be 220 knots.

On March 2, 1953 a most spectacular display of jet stream clouds was visible from Schenectady. Four large masses of cirrus containing ripples, waves and billows passed over during the day. The following account is taken from the observer's (Schaefer) notes: "These four cloud masses were apparently in the crests of traveling waves having a wave length of approximately 300 miles. Between crests occurred periods in which the sky was nearly cloudless. Such waves have been observed a number of times in association with high-velocity jet streams." In figures 2a through 2h are shown photographs taken shortly after noon on the 2nd of March, while figures 3a and 3b show two photographs taken at 1645 EST on the same day. Note that the earlier pictures show cloudless skies on the left side of the jet stream looking downstream. The atmospheric electricity was well above the level required to class it as Jet Stream Atmospherics.

In figure 4 is shown the 500 mb chart over North America at 1500 GCT, 2 March 1953. From the concentration of isotherms at this level, it is possible to locate a jet stream which extends from the Gulf of Alaska south of a deep trough over the southwestern United States and thence northeastward. There is also evidence of a second isotherm concentration

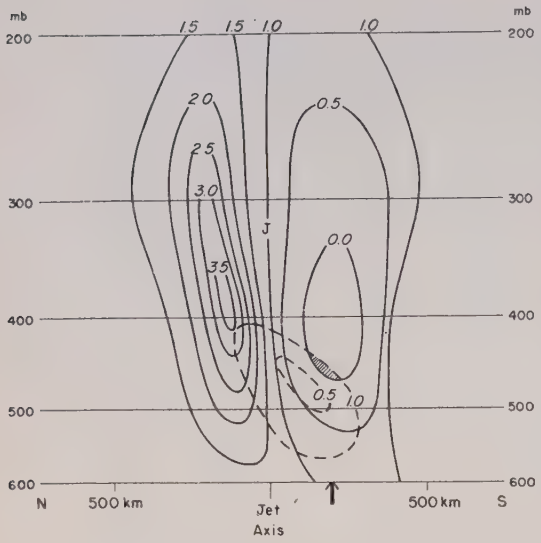

Fig. 6. Vorticity analysis in vicinity of polar-frontal jet in figure 5. Solid lines, component of absolute vorticity normal to constant pressure surfaces (units are multiples of $f = 2\omega \sin \phi$); dashed lines, isolines for Richardson numbers of 1.0 and 0.5. Cross hatching indicates zone where $R_i < 1$ and absolute vorticity < 0 coincide. Location of Schenectady shown by arrow.

extending across southern Canada toward the New England states. The location of Schenectady is shown on the chart by a star.

Figure 5 is a vertical cross section at 1500 GCT along the heavy dashed line in the preceding figure. All stations used in this cross section were projected onto this line using the direction of the 300 mb streamlines; the highest level to which observed winds were available at each station is shown by a small star and the location of Schenectady is depicted by the arrow at the bottom of the section. The isotach analysis (thin solid lines) was based primarily upon observed winds; however, geostrophic winds were used to complete the pattern at high levels over the polar-front jet stream. These isotachs give the wind speed in knots normal to the cross section. We see that there were actually two distinct wind maxima over the Atlantic coast at this time; furthermore, the polar front is strongly defined from the surface up to almost 300 mb. The clouds which were observed over Schenectady at this time were definitely to the south of the polar-frontal jet stream. This means that we can, in this case, neglect the criterion given by Arakawa which is applicable only to strong cyclonic shear. A cursory glance at the figure reveals, however, that there is a zone of strong horizontal wind shear to the south side of this jet stream; in addition, there is also the strong vertical shear which has been shown to be so important in Richardson's criterion.

The stippled area in figure 5 is the region in which equation 3 yields Richardson numbers less than unity. Figure 6 shows this same region of low R_i superimposed upon an analysis of the vorticity distribution around the polar-front jet stream. The vorticity was determined from figure 5 and represents the component of the absolute vorticity vertical to isobaric surfaces; the isopleths are labeled in multiples of $f = 2\omega \sin \phi$. Notice that the minimum Richardson number is less than 0.5, and that negative absolute vorticity is indicated in a zone to the south of the jet axis. It is of particular interest that directly over Schenectady (located by arrow) there is a zone where negative vorticity and $R_i < 1$ actually coincide (hatched area).

On March 3, 1953 the sky was nearly cloudless at sunrise with the air remaining dry and very clear. The sun was veiled with a dense haze of ice crystals. At 0815 EST thin lines of cirrus appeared in the west with masses of altocumulus billows following. This lower cloud deck was at 8,000 feet and the ice-crystal haze was between 30,000 and 38,000 feet. Rapid cloud movements continued into the evening with heavy sleet and freezing rain falling at Schenectady between 2200 and 2300 EST.

Conclusions

In the case studied here, Schenectady was clearly in the jet stream entrance zone and such is frequently the case when jet clouds are visible from the ground. It seems likely, therefore, that the ascending motion on the anticyclonic-shear side of the entrance due to the lateral circulation about the jet is important in transporting moisture to high levels in the atmosphere.

Examination of a number of jet stream cases has shown that most wind maxima associated with a strong polar front have an area of low Richardson's numbers in approximately the same location as shown in figure 5. Values as low as 0.15 have been computed. Furthermore, synoptic experience indicates that the absolute

vorticity is frequently negative on the right-hand side (looking downstream) of these jet streams. The fact that this area of dynamic instability overlaps the region of low Richardson's numbers in the majority of cases where jet stream clouds are observed may be significant. Turbulent motion could apparently account for the small-scale details inherent in the macro-structure, provided the air in a shallow layer is at or near the saturation point.

Lapse-time photographs of jet stream clouds occasionally reveal a rolling motion on a somewhat larger scale. Motion about horizontal axes parallel to narrow oceanic currents has already been postulated by Rossby (1954). It seems possible that this phenomenon may be detected in the atmosphere through the use of the lapse-time camera. It is hoped that the movies now being taken in the western United States will provide sufficient data for further investigation into the fine structure of jet streams.

REFERENCES

Arakawa, H., 1951: Possible heavy turbulent exchange between the extratropical tropospheric air and the polar stratospheric air. *Tellus*, **3**, pp. 208—211.

Barrett, E. W., Herndon, Lee R., and Carter, Howard J., 1949: A preliminary note on the measurement of water vapor content in the middle stratosphere. *J. Meteor.*, **6**, pp. 367—368.

Frost, B., December 1953: Flying in jet stream winds. *Shell Aviation News*, London, No. 186.

— September 1954: More about the Jet Stream. *Shell Aviation News*, London, No. 195.

Palmen, E., 1948: On the distribution of temperature and wind in the upper westerlies. *J. Meteor.*, **5**, pp. 20—27.

Richardson, L. F., 1920: The supply of energy from and to atmospheric eddies. *Proc. Roy. Soc.*, (A), **97**, pp. 354—373.

Riehl, H., et al., 1952: Forecasting in middle latitude. *American Meteorological Society Monograph*, No. 5, 80 pp.

Rossby, C.-G., 1953: A comparison of current patterns in the atmosphere and in the ocean basins. *Proc. U.G.G.I., 9th Gen. Assembly, Brussels, Autumn 1951.*

Schaefer, V. J., 1953: Cloud forms of the jet stream. *Tellus*, **5**, pp. 27—31.

Solberg, H., 1936: Le mouvement d'inertie de l'atmosphère stable et son rôle dans la théorie des cyclones. *Procès-verbaux de l'assoc. de météor., Un. géod. géophys. Inst. Edinbourg*, pp. 66—82.

Vuorela, Lauri A., 1953: On the air flow connected with the invasion of upper tropical air over Northwestern Europe. *Geophysica*, **4**, No. 3, pp. 105—130

The Mean Vertical Structure of the Jet Stream

By R. M. ENDLICH, S. B. SOLOT and H. A. THUR, Air Force Cambridge Research Center

(Manuscript received October 23, 1954)

Abstract

Mean vertical wind profiles were derived from observed wind soundings in jet stream regions using the "peak wind" as a reference level. These profiles show the greatest shears immediately above and below the level of the peak wind. Relationships were found between the average height of the peak wind and the heights of three characteristic tropopause types. A mean synoptic model of a jet stream having marked ageostrophic characteristics is presented.

Introduction

The major characteristics of the troposphere and lower stratosphere in the vicinity of jet streams were pointed out by a group of investigators at the University of Chicago (STAFF MEMBERS, 1947; PALMÉN and NAGLER, 1948). These characteristics are the tropopause discontinuities, the intense horizontal temperature gradients considerably below the jet stream core, and the associated frontal systems. The papers contain cross-sections, such as fig. 1, showing observed temperature fields and wind fields computed under the assumption of geostrophic motion. More recently, wind soundings and raobs to altitudes above 30,000 feet have increased in number and quality. In addition, aircraft reconnaissance has provided a limited number of detailed horizontal wind profiles (RIEHL and MAYNARD, 1954). It is the purpose of this paper to use these data to construct a synoptic model of the jet stream which will show the large scale features in greater detail than previous studies. This model will be used as a framework for study of the small scale structure of jet streams by means of data currently being gathered by Project Jet Stream (ENDLICH et al. 1954).

Data and Methods

Simultaneous soundings of wind and temperature for U.S. stations for the period November 1, 1952 through March 31, 1953, were selected from teletype data for stations which had wind soundings extending into the stratosphere and which reported a wind speed greater than 80 knots at one or more altitudes. This speed was chosen arbitrarily as the lower limit of jet stream conditions. The complete sample consisted of 261 pairs of observations. The wind data used consisted of the standard levels (at 5,000 ft intervals) at and above 20,000 ft. In addition, each report included a maximum observed wind, generally not at a standard level, which represented the strongest wind in the sounding. The latter was designated the "peak wind".

A pressure-height curve was constructed for each observation, and each wind report was tabulated against pressure. Using $p^{\star}$, the pressur at the peak wind, as a reference level, the data were rearranged and the speeds were linearly interpolated over 10 mb intervals. This form of the data was used in the summarizations which follow.

On the basis of their peak speeds, the

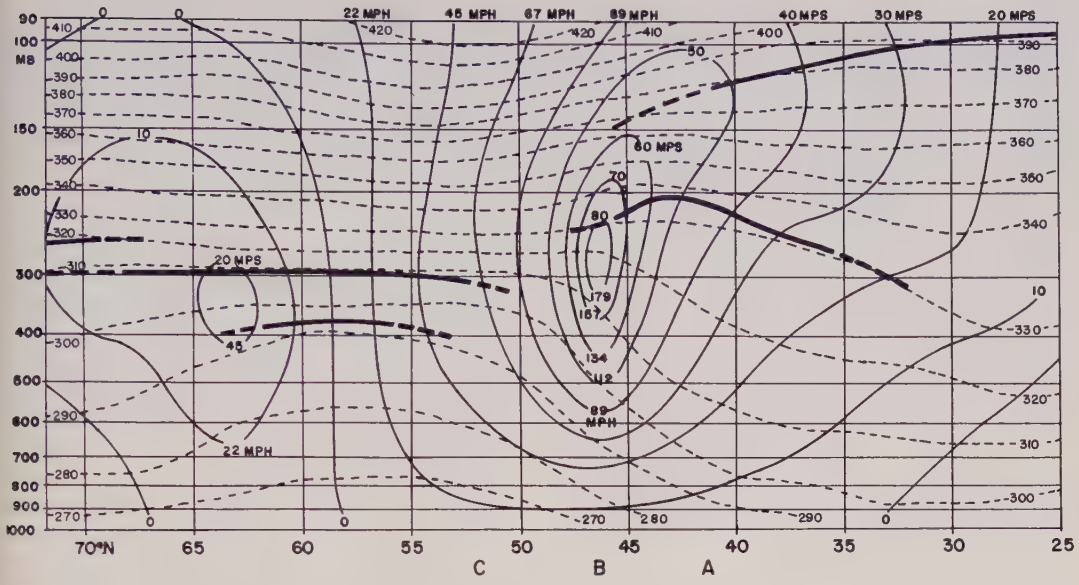

Fig. 1. A mean cross-section for 0300 GCT, November 30, 1946, showing the average distribution of geostrophic westerly wind and temperature over N. America from lat 25 N to 75 N in case of approximately straight westerly flow. Heavy lines indicate tropopause surfaces. Thin solid lines indicate the velocity of the westerly componen of the geostrophic wind (mps and mph). Dashed lines indicate potential temperature. (PALMÉN and NAGLER, 1948).t

soundings used were then divided into five equally frequent groups with the following ranges: 80 through 90 knots, 91—101, 102—112, 113—135 and > 135 knots. (The strongest wind in the sample was 266 knots.) Average vertical profiles were computed for each group for pressures in the range from $p^{\star}$ + 260 mb to $p^{\star}$ — 100 mb. To compensate for missing data at the highest altitudes, averages were calculated according to the method of SOLOT and DARLING (1954).

Discussion

The distribution of pressures at the peak wind for this sample is shown in fig. 2. It can be seen that the peak wind occurred most frequently slightly below the 200 mb level (at about 37,000 ft). The range was from 345 to 120 mb (27,000 to 50,000 ft). No relationship was found between the height and speed of the peak wind.

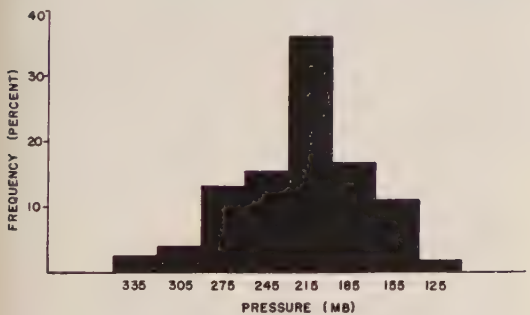

Fig. 2. Distribution of pressures at the peak wind for the period November 1, 1952 through March 31, 1953.

The average vertical profiles plotted against log p for each of the five speed classes are shown in fig. 3. Since this is an approximate height scale, it can be seen that the wind increases with height at an increasing rate to the level of the peak wind. Above the peak wind, speed falls off very rapidly at first, but at a decreasing rate. The shapes of the five curves are similar. If we assume that the speed groups may be arrayed to define a mean cross section perpendicular to a jet stream (highest speeds at the center), it may be inferred that the average shape of the jet profile is the same throughout a broad region on both sides of the jet core.

Statistical reasoning leads to the conclusion that the magnitude of the shear in the immediate vicinity of the peak wind may be somewhat exaggerated because the peak wind was chosen as the reference level. Since the peak wind generally occurs between standard levels, the interpolation immediately above and below

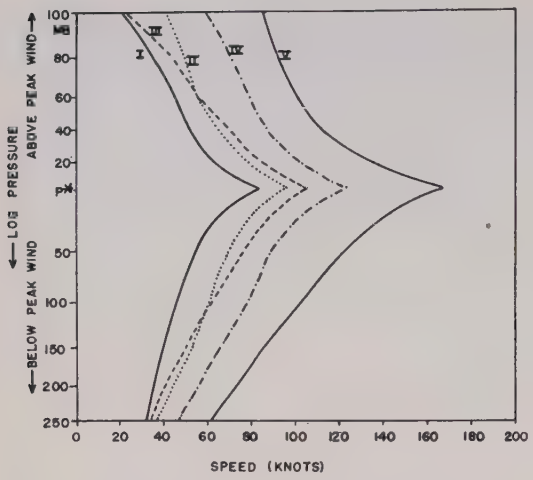

Fig. 3. Average vertical profiles for five equally frequent wind speed groups with the following ranges in peak speeds: 80-90 knots, 91-101, 102-112, 113-135, and > 135 knots.

is over a smaller interval than elsewhere. This fact, together with the fact that the sign of the shear on each side of the peak wind is necessarily consistent, produces an exaggerated average shear in this region. Furthermore, it is a well known statistical principle that if in each case a maximum speed is selected from a group of observations having a given probable error, the average maximum will tend to have a positive error.

In order to show the extent to which the curves may be considered reliable with respect to the zones of greatest shear, the distribution of the point of greatest shear in each sounding (excluding the region from $p^\star + 30$ mb to $p^\star - 30$ mb) was analyzed. It was found that in 78 % of the cases, the maximum shear occurred within, at most, 100 mb of the peak wind and 55 % occurred within 60 mb. Since the region within 30 mb had been deliberately excluded, the maximum shear is probably quite near the peak wind. Thus, for all practical purposes, the shear may be considered discontinuous at the peak wind level.

An exponential equation was found to give the best fit to the observations. In computing the constants for this equation, the peak speeds were ignored for the reasons given above. This amounted to a reduction in peak speeds of approximately 10 %. Below the level of the peak wind the equation is

$$u_p = U \exp\{-k_1(p-p^\star)/100\}; (p-p^\star) \leqslant 260\,mb$$

where u_p is the wind speed in knots at pressure p, U is the peak speed, and k_1 equals 0.33 ± .15. The distribution of k_1 is slightly skewed toward higher values. Above the level of the peak wind the equation is

$$u_p = U \exp\{-k_2(p^\star-p)/100\}; (p^\star-p) \leqslant 100\,mb$$

where the average value of k_2 is 0.56. Its variation is approximately similar to that of k_1. Curves for values of U at 25 knot intervals were calculated using the average values of k_1 and k_2 (fig. 4). These show that, on the average, the peak speed is about 2.4 times the speed at a pressure 260 mb higher (roughly the mid-tropospheric speed).

In most of the soundings, the tropopauses could be grouped into three types which were related to the jet stream in a definite manner. Fig. 5 shows these types. By definition, type A soundings have a high cold tropopause and a lower, weaker tropopause at a temperature at least 10° C warmer. Type C soundings have a single tropopause and an approximately isothermal stratosphere. Both types are characterized by points of marked lapse rate change. In contrast, type B soundings do not have sharp lapse rate discontinuities. The criterion for this type is a tropopause transition layer at least 5,000 ft (1.5 km) thick with a lapse rate more stable than 5° C/km. The curves of fig. 5 were computed at positions A, B, and C in fig. 1. This cross-section and others indicate that type A tropopauses are typical of the high-pressure side of the jet stream, type B of the jet core, and type C of the low pressure side.

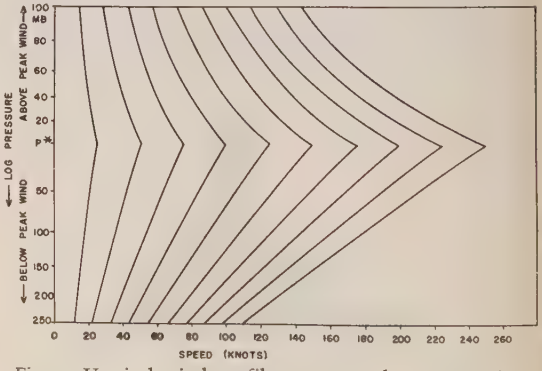

Fig. 4. Vertical wind profiles corresponding to equations (1) and (2) with $k_1 = 0.33$ and $k_2 = 0.56$ for values of U at 25 knot intervals.

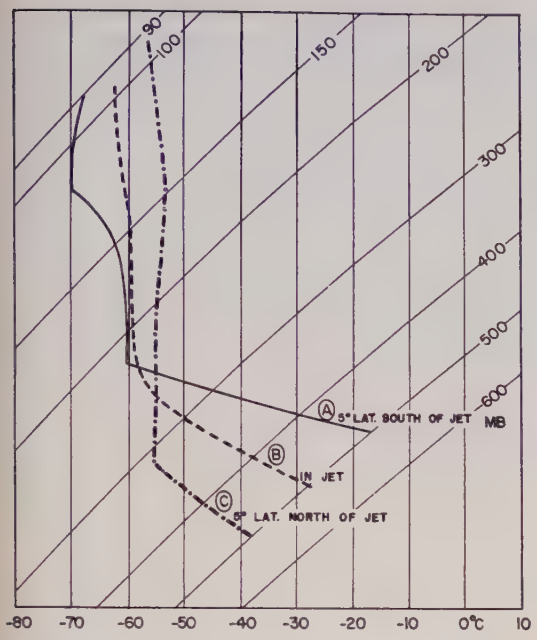

Fig. 5. Soundings at points A, B and C in fig. 1.

The wind soundings were separated into three classes based on the associated tropopause type and average profiles were again prepared. These proved to be identical in shape to those in fig. 3. It was found that for soundings of types B and C, the average tropopause height coincided closely with the average height of the accompanying peak winds. For type A soundings, however, the average height of the lower tropopause was 4,000 ft below the average height of the peak wind. A rather surprising result was that the average height of the lower tropopause of type A was slightly less than the height of the type C tropopause, in contrast to figs 1 and 5. No tests of the significance of this result were made.

Through study of the soundings of wind and temperature an attempt was made to use the height of the tropopause to predict the height of the peak wind. This attempt was unsuccessful since it was found that the correlation between the two was not sufficiently high.

In a recent report, RIEHL and MAYNARD (1954) give horizontal wind profiles for the upper troposphere based on aircraft observations (fig. 6). A jet stream model was constructed by using this horizontal wind distribution at the level of the peak wind and by deriving the vertical wind distribution using the curves of fig. 4. Tropopauses were inserted using the average relationships discussed above. Fig. 7 shows the resulting model.

Comparison of this model with fig. 1 reveals an important difference in both the vertical and horizontal wind profiles, namely the sharp peak at the wind maximum. The rounded vertical profiles of fig. 1 are based on winds computed geostrophically from the observed temperature and pressure fields. For this reason, the region of maximum vertical shear is found in the mid-troposphere where the horizontal temperature gradients are most intense. Near the jet core the indicated shear is relatively small since the gradients are weak. In contradiction to this picture, the results presented herein show the greatest shear near the jet core. Therefore either the thermal field of fig. 1 is not generally representative or the layers in the vicinity of the peak wind are markedly ageostrophic. Since numerous observations verify the thermal field, the ageostrophic alternative follows.

The ageostrophic flow pattern of the model (fig. 7) was derived by comparing its wind field with a geostrophic field computed by means of the thermal wind equation from the 500 mb wind distribution of the model and

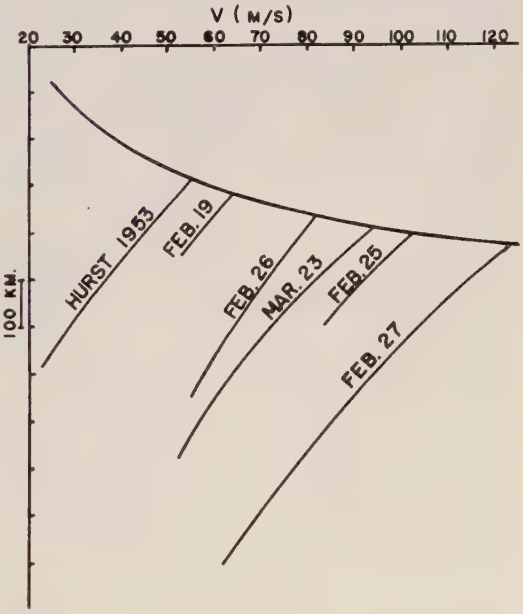

Fig. 6. Composite diagram showing velocity profiles of all observed jet streams. (RIEHL and MAYNARD, 1954).

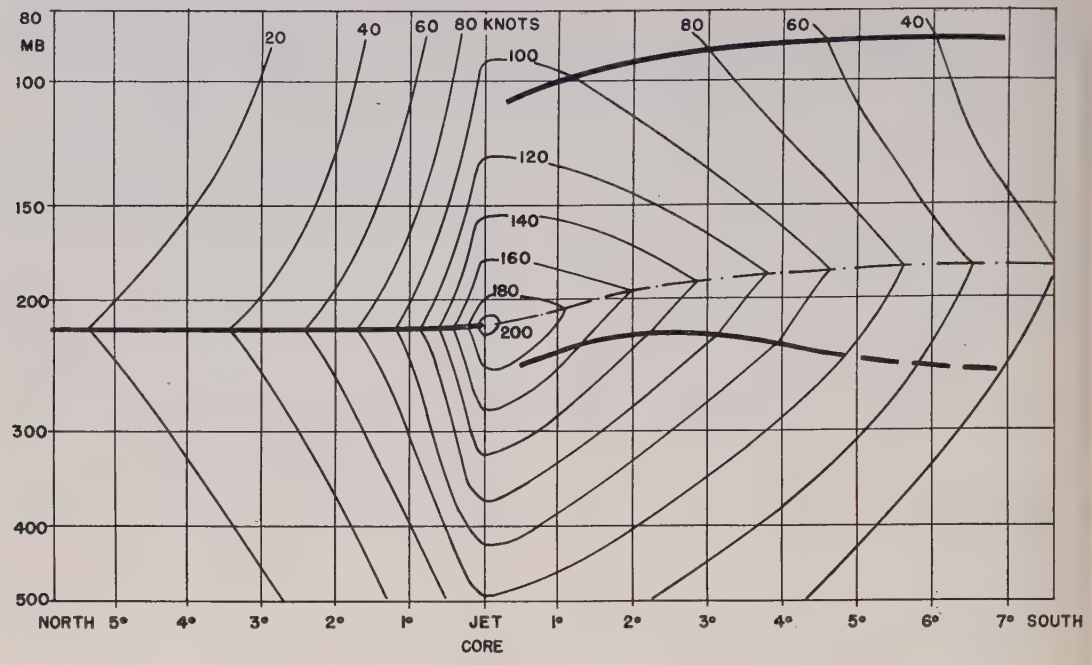

Fig. 7. Model of a jet stream constructed from the curves of fig. 4 and 6. Heavy lines are tropopauses, light solid lines are isotachs (knots), dash-dotted line marks the level of the peak wind.

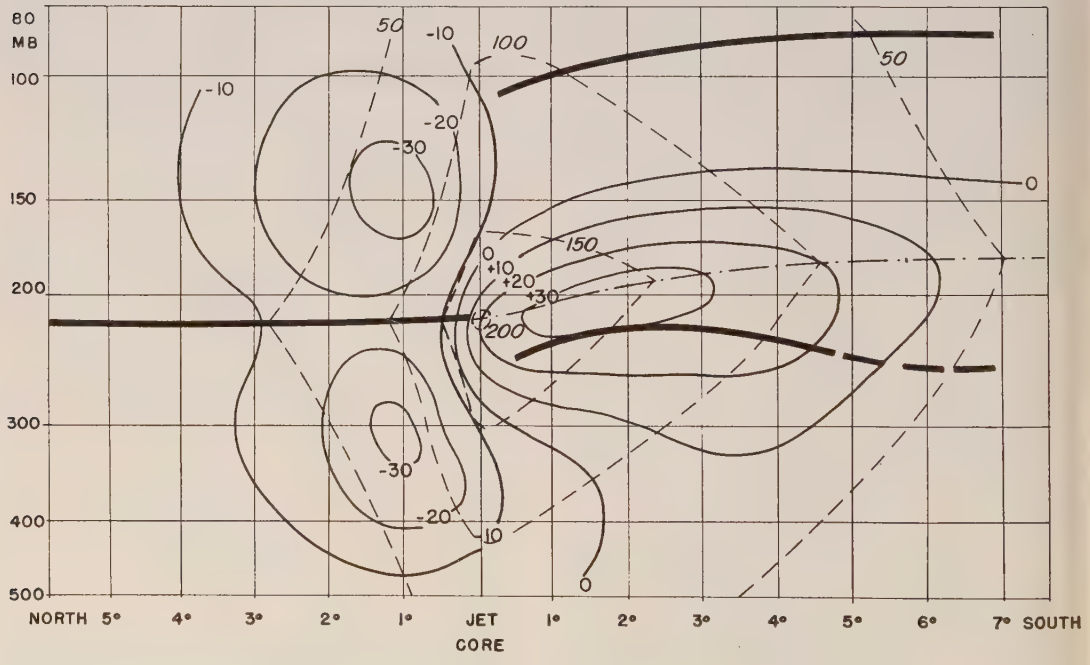

Fig. 8. Ageostrophic components (knots) of the model shown in fig. 7.

Palmén and Nagler's thermal field (fig. 1) slightly modified because of differences in tropopause heights between figs. 1 and 7. The ageostrophic components (fig. 8) have a center of positive (super-geostrophic) flow at the level of the peak wind on the south side of the jet core and two subgeostrophic centers above and below the peak wind on the north side. Recent experience, however, indicates that extreme horizontal shear on the north side of the jet core, as shown in the model, seems to be characteristic of jet streams with cyclonic curvature. In this case, comparison should be made with gradient, rather than geostrophic, flow. Compared to fig. 8, departures from gradient flow would have a slightly more intense positive (super-gradient) center nearer the jet core and smaller, less intense sub-gradient centers.

The ageostrophic (or agradient) flow patterns follow on acceptance of the vertical profiles in fig. 4, the horizontal profiles of Riehl and Maynard, and the thermal field of Palmén and Nagler. A reasonable "geostrophic" thermal field which fits the wind field of the model could not be devised. The assumption of a typical vertical temperature sounding at the south end of the cross-section led to a 30° temperature inversion at the tropopause at the north end. Conversely, the assumption of a typical sounding at the north end of the section resulted in super-adiabatic lapse rates above the lower tropopause south of the jet core. Thus the ageostrophic characteristics of the jet stream can be expressed either in terms of wind or temperature departures from geostrophic models.

Although jet stream characteristics of possible importance (such as tilt in the vertical axis) are not included in fig. 7, we believe that at least qualitatively this model does portray the large scale characteristics of the jet stream. However, the indirect methods used in deriving fig. 8 may to some extent account for the large ageostrophic components found. For this reason, the latter figure should not be accepted without reservations.

Conclusions

Analysis of observed data for the United States for the winter of 1952—1953 reveals the following characteristics of the jet stream:

1. On the average, the rate of wind speed increase below the peak wind is considerably less than the decrease above.
2. The shape of the vertical profiles appears to be independent of the peak wind speed.
3. Strongest vertical shears are found near the level of the peak wind, and shear is nearly discontinuous at this point. This also appears to be true of the horizontal shear.
4. A model of the jet stream based on recent data departs markedly from the classical geostrophic model with sub-geostrophic and super-geostrophic flow respectively on the north and south sides of the core.

Acknowledgments

The writers are grateful for the helpful criticisms of Dr. J. Kuettner and to Mr. George S. McLean for preparing the data and drafting the figures.

REFERENCES

Endlich, R. M., Harney, P., McLean, G. S., Rados, R. M., Tibbets, Maj. O. J., and Widger, W. K., 1954: Project Jet Stream. *Bull. Amer. Meteor. Soc.*, **35**, 143—154.

Palmén, E., and Nagler, K. M., 1948: An analysis of the wind and temperature distribution in the free atmosphere over N. America in a case of approximately westerly flow. *J. Meteor.*, **5**, 58—64.

Riehl, H., and Maynard, H., 1954: Exploration of the jet stream by aircraft during the winter of 1953. *Final Report under Contract No. 189s-88360 between U.S. Navy and Univ. of Chicago.*

Solot, S. B., and Darling, E. M., 1954: A note on the difference method of averaging. *Bull. Amer. Meteor. Soc.* **35**, 484—487.

Staff Members, Dept. of Meteorology, University of Chicago, 1947: On the general circulation of the atmosphere in middle latitudes. *Bull. Amer. Meteor. Soc.*, **28**, 255—280.

A Frontal-Jet Stream Cross Section[1]

By B. W. BOVILLE, W. S. CRESWICK AND J. J. GILLIS, Central Analysis Office, Montreal, Canada

(Manuscript received December 21, 1954)

Abstract

The validity of the thermal wind relationship for determining high level winds in the vicinity of jet streams is discussed.

A cross section wind field was constructed utilizing only the thermal field for levels above 700 mb. This wind field is compared to one obtained from rawin reports.

The results indicate that a reasonable picture of the high level jet winds is obtained when vertical extrapolation is based on the thermal field analysed with respect to three-dimensional fronts.

I. Introduction

A jet-stream isotach analysis at 300 mb is carried out at the Central Analysis Office, Montreal, Canada for an area extending approximately from 30° W to 160° W and 25° N to 80° N. The density of high level wind reports does not permit an *ab initio* analysis of the asymmetric jet wind field over most of the chart. The extension of the analysis into these areas is to a large measure based on the close relationship which exists between the structures of jet streams and three-dimensional fronts. The cross sections contained in this paper were prepared as part of a training program in jet stream analysis techniques.

2. The frontal cross section

To illustrate the validity and use of the thermal wind approximation the cross section given as fig. 2 was drawn on the following basis. A line was chosen which was approximately normal to the flow and where rawin data were sufficiently dense to permit a subsequent check on the true wind structure. Upper air stations on this line were Denver, Colo., Dodge City, Kan., Topeka, Kan., Columbia, Mo., Rantoul, Ill., Dayton, Ohio, and Pittsburgh, Pa. The analysis was carried out utilizing complete tephigram plots but wind data were limited to the levels surface to 700 mb.

The tephigrams (fig. 1) show three air masses (*mT*, *mP* and *mA*) and two fronts with the top and base of each hyperbaroclinic zone being well defined. The major high level thermal contrast is between Rantoul (RAN) and Dayton (FFO) and a jet core is to be expected in the 300—250 mb layer where the thermal gradient becomes zero and then reverses.

The only structure not precisely shown by the tephigrams was for the 400—200 mb layer between Rantoul and Dayton. Inspection of neighbouring tephigrams showed a well defined Polar front to levels above 400 mb so that the extension of the frontal surface to the tropopause was valid. No conclusive evidence was available as to whether the tropopause sloped steeply or was broken in that area. The continuous structure was drawn as an adequate portrayal of the thermal gradients.

The thermal winds were calculated from the isotherms at many points using a scale based on the equation

$$\frac{\partial V_H}{\partial Z} = \frac{g}{fT}\frac{\partial T}{\partial n}$$

[1] Published by permission of the Controller, Meteorological Division, Department of Transport, Canada.

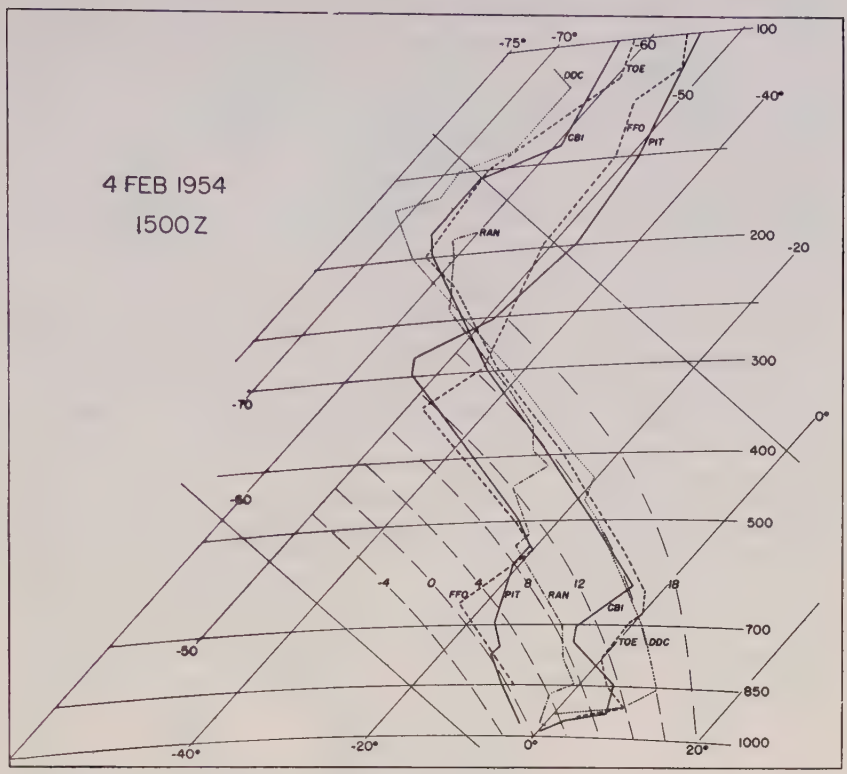

Fig. 1. Tephigrams (dry bulb curves).

Vertical addition from the observed 700 mb winds provided a dense network of calculated winds as a basis for the 20 knot isotachs.

3. Comparison of calculated and observed winds

The observed winds for all levels were plotted on a cross section on which the tropopause and fronts had been entered. The observed wind field was then drawn as shown in fig. 3. There were sufficient winds for an objective analysis except for the layer above 200 mb over Rantoul.

Comparison of the two wind fields reveals a striking similarity indicating the validity of using the thermal-wind relationship even up to levels as high as 100 mb. In general the wind increase through the frontal zones appears to be spread through a deeper layer than the calculation in fig. 2 would indicate. This may be partly real and partly due to the averaging process used in obtaining the observed winds for specific levels. The only significant discrepancy is found in the 400—200 mb layer over Topeka extending to about 250 mb over Columbia. The observed winds are 20—40 knots greater than the calculated winds.

The calculated winds are based on the assumption that addition of the geostrophic-thermal wind to the observed 700 mb wind yields a correct high-level wind. This is, in effect, assuming that any ageostrophic components have the same magnitudes from 700 mb up. For pressure systems with vertical axes this is a reasonable assumption in percentage terms but not in absolute terms due to the higher wind speeds at upper levels (e.g. the curvature term contains the square of the wind speed). Since the wind excess over Topeka is in the same direction as the geostrophic wind its explanation should be sought in terms of anticyclonic curvature.

4. Application of the equation of horizontal motion

From the equation of horizontal motion, after PRIESTLEY (1948), it may be shown that:

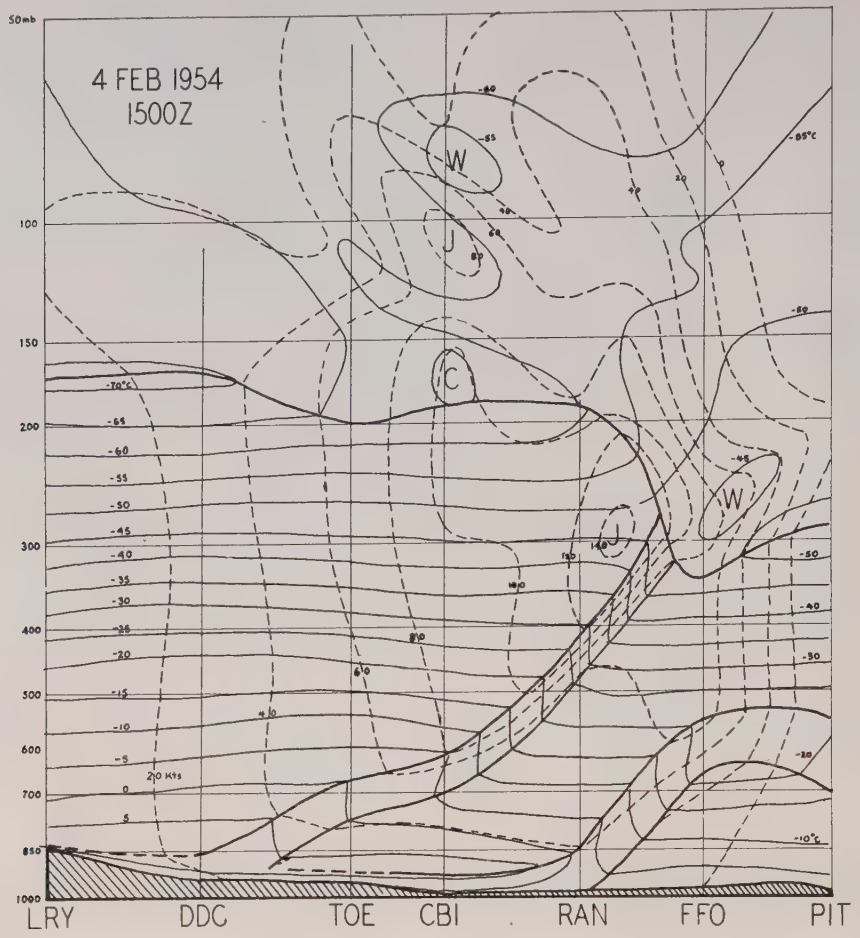

Fig. 2. Vertical Cross Section.
Solid heavy lines—fronts, tropopause.
Solid thin lines—isotherms °C.
Dashed thin lines—isotachs (computed).

$$\vec{\mathbf{V}}_H = \vec{\mathbf{V}}_g - \frac{K_{Ht}}{f} V_H^2 \vec{\mathbf{t}} + \frac{\dot{V}_H}{f} \vec{\mathbf{n}} + \frac{w}{f} \vec{\mathbf{k}} \times \frac{\partial \vec{\mathbf{V}}_H}{\partial Z} + \vec{\mathbf{j}} \cot \varphi w$$

where $\vec{\mathbf{t}}$, $\vec{\mathbf{n}}$, $\vec{\mathbf{k}}$, $\vec{\mathbf{j}}$ are respectively, tangential, normal, vertical and northward unit vectors in relative coordinate systems and the other symbols have their usual meaning.

To show an indication of the relative magnitudes of the geostrophic departures the individual terms of this equation were considered.

4.1. The curvature term $\frac{K_{Ht}}{f} V_H^2 \vec{\mathbf{t}}$

Inspection of the 300 mb contours in the Topeka area indicates a straight or slightly cyclonically curved field which would appear to negate a curvature explanation for the wind excess. However, examination of the actual wind reports reveals considerable cross contour flow and there are sufficient reports to permit an independent streamline analysis for the area. The streamlines, as in fig. 4, do show anticyclonic curvature over a considerable portion of the cross section area. K_H, the curvature of the trajectory, may be related to K_s, the

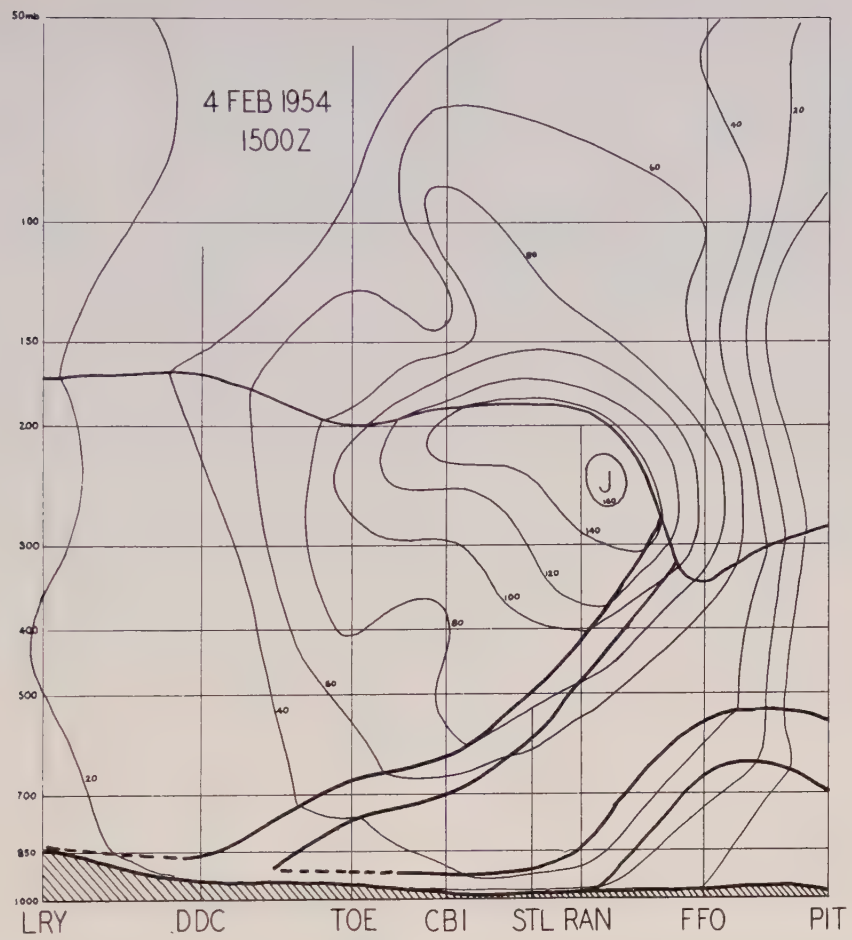

Fig. 3. Vertical Cross Section.
Solid heavy lines—fronts, tropopause.
Solid thin lines—isotachs (observed).

curvature of the streamline, through the equation

$$K_H V_H = K_s (V_H - C \cos \varphi)$$

where $C \cos \varphi$ is the component of motion of the pressure system in the direction of V_H.

Measurements on fig. 4 give anticyclonic streamline curvature of about 1/600 nm east of Dodge City decreasing to zero near Columbia thence the cross section line remains near the inflexion point of the streamlines to the jet axis. Measurements from surface and upper level charts show a short wave system moving through the area, in the direction of the flow, at about 30 knots.

Inspection of fig. 2 and 4 reveals the following: In the vicinity of Dodge City the motion ($C \cos \varphi$) approximates the wind speed (V_H) and also since V_H itself is small the curvature term will be small. Near Topeka there is still considerable curvature combined with strong winds and a strong wind increase above 700 mb and the curvature term may be significant. From St. Louis to Rantoul $K_s = 0$ thus the curvature term will be zero. From the foregoing equations the K_s at Topeka required to give the wind excess of V_H (fig. 3) over V_g (fig. 2) at 300 mb can be computed as follows

	V_H	V_g	$V_H - V_g$	K_t	K_s
TOE	94 kts	68	26	1/1,000 nm	1/680 nm

(300 mb)

The measured K_s in the vicinity of Topeka

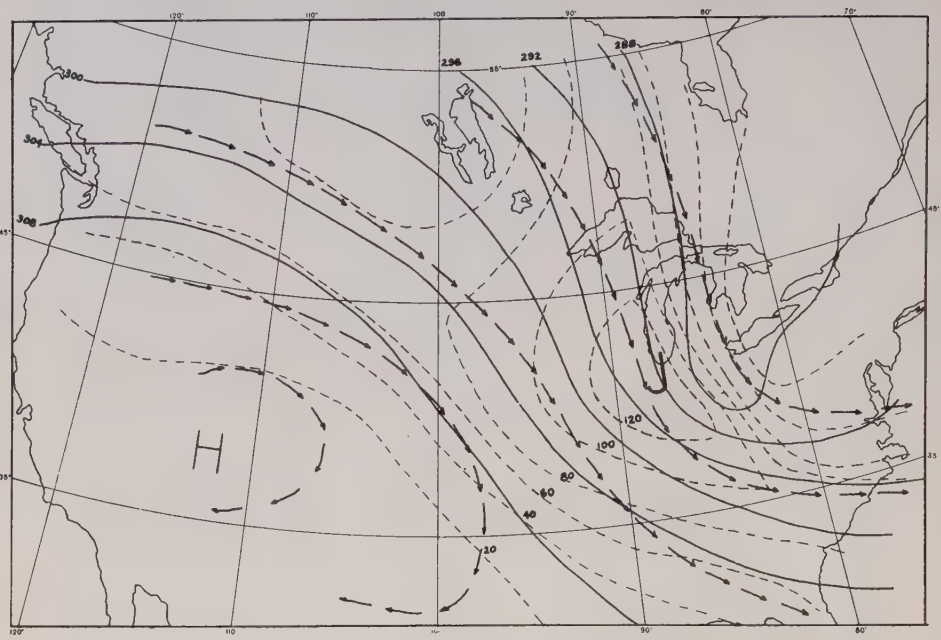

Fig. 4. 300 mb Chart (4 Feb. 1954—1500Z).
—— Contours.
→ → Streamlines.
---- Isotachs (knots).

is of the order of 1/700 nm and thus the wind excess can be adequately explained in terms of streamline curvature.

4.2. The acceleration term $\frac{\dot{V}_H}{f}\vec{\mathbf{n}}$

The action of the acceleration term where n is normal to the trajectory towards lower pressure is strikingly demonstrated in the Bismarck to Memphis area of fig. 4. The streamlines are seen to cross the contours towards lower heights where V_H is increasing along the streamline, become parallel as the maximum is reached and cross towards higher heights where the wind decreases. The following computations were made for Des Moines using:

$$\dot{V}_H = \frac{\partial V_H}{\partial t} + \vec{\mathbf{V}}_H \cdot \frac{\partial \vec{\mathbf{V}}_H}{\partial s}$$

$\frac{\partial V_H}{\partial t} = -20$ kts/6 hours (from successive rawins)

$V_H = 100$ kts, $\frac{\partial V_H}{\partial S} = 20$ kts/200 nm

$$\frac{\dot{V}_H}{f} = \frac{\frac{-20}{6} + 100 \times \frac{20}{200}}{f(\text{hour}^{-1})} = 23 \text{ kts.}$$

This gives an angle between V_H and V_g of 13 degrees.

4.3. The vertical motion term $\left(\frac{w}{f}\vec{\mathbf{k}} \times \frac{\partial \vec{\mathbf{V}}_H}{\partial Z}\right)$

This term will, in general, be of significance when both the vertical motion and vertical shear (of V_H) are relatively large such as in the vicinity of fronts and jet streams.

The term arises from a consideration of the effect of vertical motion in the total differential dV_H/dt

$$\text{i.e. } \frac{dV_H}{dt} = \frac{\partial V_H}{\partial t} + \vec{\mathbf{V}}_H \cdot \frac{\partial \vec{\mathbf{V}}_H}{\partial s} + \vec{\mathbf{w}} \cdot \frac{\partial \vec{\mathbf{V}}_H}{\partial t}$$

Thus it represents an acceleration due to ascent or descent where V_H varies vertically in the same manner as $\vec{\mathbf{V}}_H \cdot \frac{\partial \vec{\mathbf{V}}_H}{\partial s}$ represents motion across the horizontal isotach field.

A qualitative application of this term can be obtained by using the thermal wind relationship as a first approximation for $\frac{\partial \vec{\mathbf{V}}_H}{\partial Z}$. The term can then be assessed in terms of horizontal temperature gradients. Thus ascent gives a horizontal component of motion from warm to cold air; descent gives a horizontal component of motion from cold to warm air.

In the vicinity of jet streams some further assumptions can be made regarding the distribution of V_H. The vertical shears are usually parallel to the wind (wind direction changes little with height) and thus the term can be expressed as a component normal to the streamlines,

$$\text{i. e. } \frac{w}{f}\vec{\mathbf{k}} \times \frac{\partial V_H}{\partial Z}\vec{\mathbf{t}} = \frac{w}{f}\frac{\partial V_{H+}}{\partial Z}\vec{\mathbf{k}} \times \vec{\mathbf{t}} = \frac{w}{f}\frac{\partial V_H}{\partial Z}\vec{\mathbf{h}}$$

In this form the effect of the term is seen to be similar to that of the horizontal acceleration term (4.2).

Since the sign of the vertical shear changes across the jet core it follows that:

(a) above the jet core ascent gives a component of horizontal motion towards higher pressure and subsidence towards lower pressure.

(b) below the jet core the reverse holds.

The requirement for vertical motion in this term makes computations rather difficult. However, two have been attempted with the realization that possible errors may be large.

In the vicinity of Sault Ste. Marie (SSM) the streamlines cross the contours towards lower pressure and at the same time the wind speed decreases along the streamline. If the contour streamline pattern is right then it is clear that the vertical-motion term must be rather strong. There is a sharp tropopause at 300 mb at SSM coinciding with a reversal of vertical wind shear. Since the wind direction remains constant along the streamline from 30,000 to 35,000 feet while the wind speed drops 7 knots an evaluation will be made on this basis.

$$V_H = 45 \text{ kts} \quad \frac{\partial V_H}{\partial Z}\vec{\mathbf{t}} = -7 \text{ kts}/5{,}000 \text{ ft}$$

The angle between V_H and $V_g \simeq 10$ degrees and the required cross component is 45 sin $10° = 8$ kts. The expression can now be solved for w

$$w = \frac{f}{\partial V_H/\partial Z} Vn = -0.32 \; kts \simeq -16 \text{ cm/sec}$$

Thus subsidence of 16 cm/sec just above 300 mb is required to account for the cross-wind component. A somewhat higher figure would be required to balance the horizontal deceleration as well.

At 300 mb over Dayton (FFO) there is appreciable increase of wind with height and judging by the low tropopause and high 300 mb temperature considerable subsidence. For

w negative and $\frac{\partial V_H}{\partial Z}$ positive $\left(\frac{\partial \vec{\mathbf{V}}_H}{\partial Z} // \vec{\mathbf{V}}_H\right)$

this represents a velocity component normal to the flow towards higher pressure.

$\frac{\partial V_H}{\partial Z} = 4$ kts/1,000 ft; using a w calculated on the basis of the observed temperature gradient at 300 mb upstream from Dayton and subsidence along a dry adiabat, $w = -.17$ kts ($\simeq -8.5$ cm/sec). This gives a cross component towards higher pressure = 12 kts and is equivalent to an angle between V_H and $V = 7$ degrees.

Since the computed values of vertical motions and cross-contour flow are of the same order as those usually quoted it appears that qualitatively at least they may be of significance. However, it should be noted that most of the computed values also fall within the range of the possible errors of the observed values.

4.4. The latitude term ($\vec{\mathbf{j}} \cos \varphi w$)

This term is usually very small and represents an easterly component for subsidence and a westerly component for ascent. The value of this term for the subsidence figure in 5.3 is $-.17 \times 1.2 = -0.2$ kts.

4.5. It thus appears that although the thermal approximation gives very good results when used to calculate the overall wind field, other terms in the velocity equation can give appreciable contributions to the total wind. The use of the thermal wind approximation will be most valid when extrapolations are done vertically within a similar pressure and wind

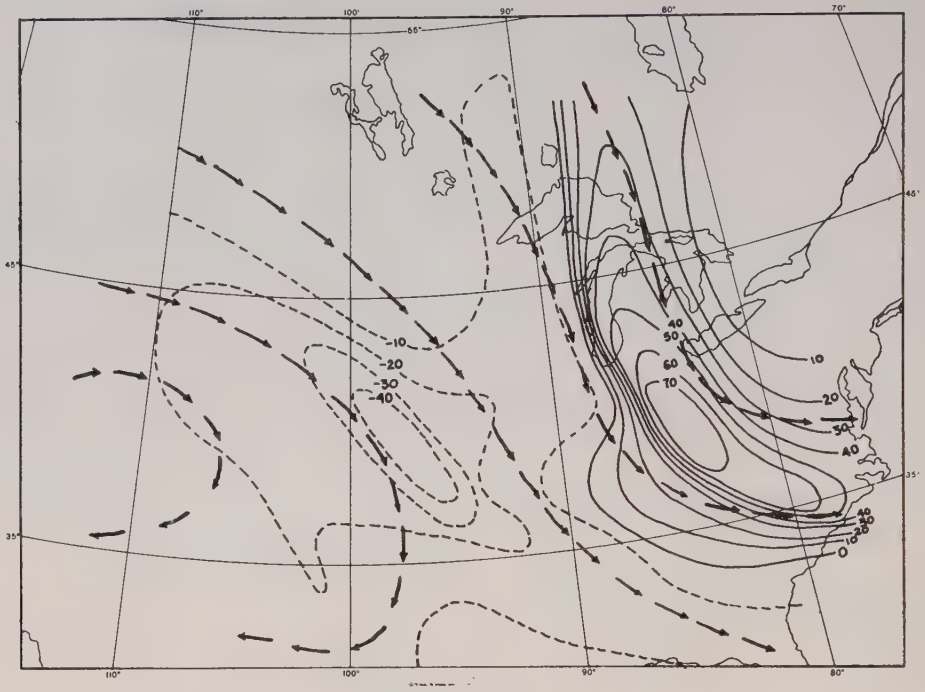

Fig. 5. 300 mb Chart (4 Feb. 1954—1500Z).
——, ---- Isolines of relative vorticity (hour^{-1} × 10^{-2}).
→ → Streamlines.

field, e.g. extrapolation to 300 mb from an observed 500 mb wind will normally have the ageostrophic components incorporated in the 500 mb wind. Absolute errors will increase in areas where there is strong curvature change or strong vertical motion.

5. The vorticity field at 300 mb

The distribution of the vertical component of relative vorticity at 300 mb is given in fig. 5. This field was computed from the data given by fig. 4 using the expression for relative vorticity (e.g. HOLMBOE, 1945).

$$\zeta = \frac{V_H}{R_s} - \frac{\partial V_H}{\partial n}$$

The two terms were computed independently using units of knots and 100 nm and then added to give the total relative vorticity. The data given in fig. 5 are thus in units of hour^{-1} × 10^{-2} which is 36×10^4 times the standard vorticity unit of sec^{-1}. In terms of the units of fig. 5 the coriolis parameter (f) at 40° N is equal to 33.7.

The horizontal wind shear is so strong, in the vicinity of the jet stream at 300 mb, that this term generally predominates in the vorticity calculations. However, the curvature term is strong enough to produce cyclonic vorticity to the west of the jet axis in the vicinity of Nashville (BNA). To the west of Topeka (TOE) where it has the same sign as the shear term the two produce a small region where anticyclonic vorticity exceeds the coriolis parameter.

6. Relation of the vorticity field to surface pressure change

The surface pressure changes, in millibars, between 1230 Z and 1830 Z are given in fig. 6. Since this period overlaps the upper air time of 1500 Z the surface changes and the 300 mb vorticity field can be compared.

The relationship between the surface pressure change and the relative vorticity field has been treated by a number of writers (e.g. SUTCLIFFE, 1947; RIEHL, 1952).

From their derivations the following quali-

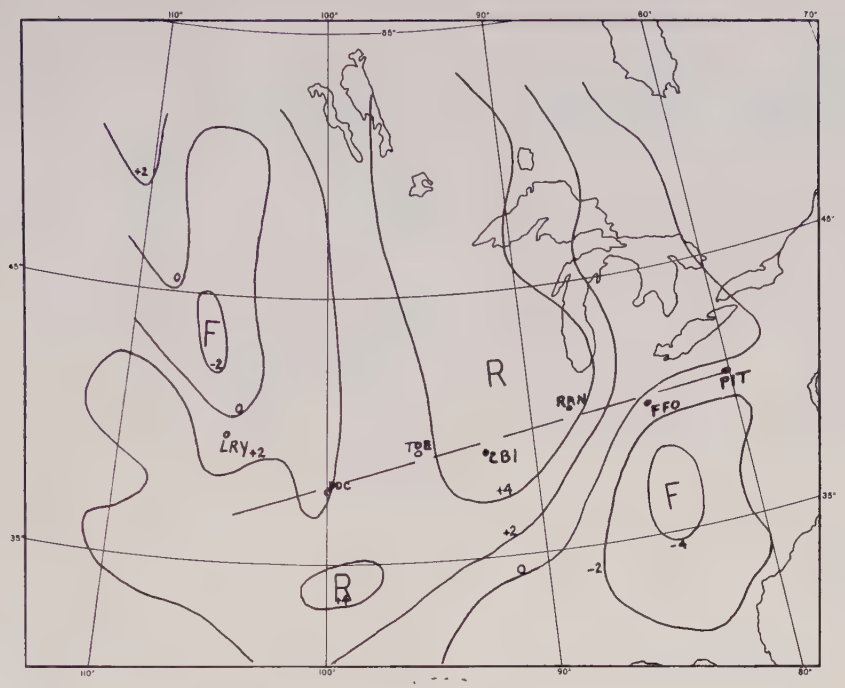

Fig. 6. Surface Pressure Change Chart.
1230Z to 1830Z 4 Fec. 1954 (whole millibars).

tative relationships, applicable to a barotropic atmosphere, can be inferred:

$$\text{sign of } \frac{dP_0}{dt} = \text{sign of } (-\text{div}_{300}\, V_H) = \text{sign of } (\vec{\mathbf{V}}_H \cdot \nabla\, \zeta) \text{ subscript}$$

Thus if the cyclonic (relative) vorticity at 300 mb decreases (or anticyclonic vorticity increases) downstream the contribution of this term is for a surface pressure fall. The opposite is also true.

From figures 5 and 6 it can be seen that there is good agreement between the surface pressure changes and the advection of vorticity. The maximum pressure falls to the southeast of Dayton (CVG)—Nashville (BNA) are just to the south of the normal axis of maximum cyclonic vorticity. The pressure rises in the St. Louis (STL)—Rantoul (RAN) area lie in a region where $(\vec{\mathbf{V}}_H \cdot \nabla \zeta)_{300}$ is positive. Also the line of pressure rises and falls in the Casper (CPR)—Goodlands (GLD)—Oklahoma City (OKC) region is close to the line of vorticity changes associated with anticyclonic maximum.

REFERENCES

HOLMBOE, GUSTIN, and FORSYTH: *Dynamic Meteorology*, Wiley 1945.

PRIESTLEY, C. H. B., 1948: *Australian Journal of Scientific Research*, Vol. 1, pp. 41—57.

SUTCLIFFE, R. C., 1947: *O. J. R. Met. Soc.* **73**, p. 370.

RIEHL, H., et al, 1952: *Meteorological Monograps*, Vol. 1, No. 5.

A Weather Situation with Strong Convection in the Middle Stratosphere

By Lars RAAB, Swedish Meteorological and Hydrological Institute, Stockholm

(Manuscript received June 15, 1954)

Abstract

Two examples of convective cells in the middle stratosphere are demonstrated. They have been measured during two routine aerological soundings in Östersund, Central Sweden. The accuracy of the measurements of the vertical wind velocities (in one case amounting to some ten meters per second) is discussed. The phenomenon is explained from the weather situation, which is characterized by two cold-pools, one in the troposphere moving southwest from Russia and one in the upper stratosphere moving southsoutheast over Scandinavia from the North Pole region.

In early February 1953 two routine radiosondes launched at Östersund in Central Sweden (63° N, 15° E) indicated the existence of strong convective vertical currents in the middle stratosphere, 7 km above the tropopause and about 15 km above sea level.

The sounding result of the first radiosonde, sent up at 1500 GCT 4 February 1953, is illustrated in Fig. 1. The well defined tropopause is at the 8 km level, and in the stratosphere there are two separate temperature regions. The lower one extends up to 14.5 km with temperatures above — 59° C, and the upper region above 15.5 km has temperatures below — 64° C slowly decreasing with height to — 70° C at 20 km.

Between these layers there is an intermediate region with temperature gradients as high as 0.7° C per 100 m, and in the upper part of this region the radiosonde experienced highly variable vertical winds. At first the radiosonde entered a strong downward current, enough strong to force the whole sounding system down. The record suddenly showed an increase of pressure, and the operator assumed the sond to fall due to a bursted balloon. However, half a minute later the sonde left the strong downward current and began to rise again, at first rapidly and then in quite a normal manner. The winddriven commutator increased the angular velocity at time, indicating acceleration of the balloon or wind-shear between the sonde and the balloon. The details of this part of the sounding are examined with extremely care, and the result is shown in Fig. 2 with temperature plotted against pressure. Assuming the buoyancy force of the balloon to vary only slowly during the ascent and the ascending velocity of the balloon to be equal to 5 m/s when passing the convective cell, we obtain from the variations in calculated heights, the vertical velocities in the cell as measured by our sonde. The flight values are tabulated in Table 1 and from these values we obtain the downward wind velocity = 25 m/s and the upward wind velocity = 10 m/s with an error discussed later being about 50 per cent.

The second radiosonde was sent up at 1500

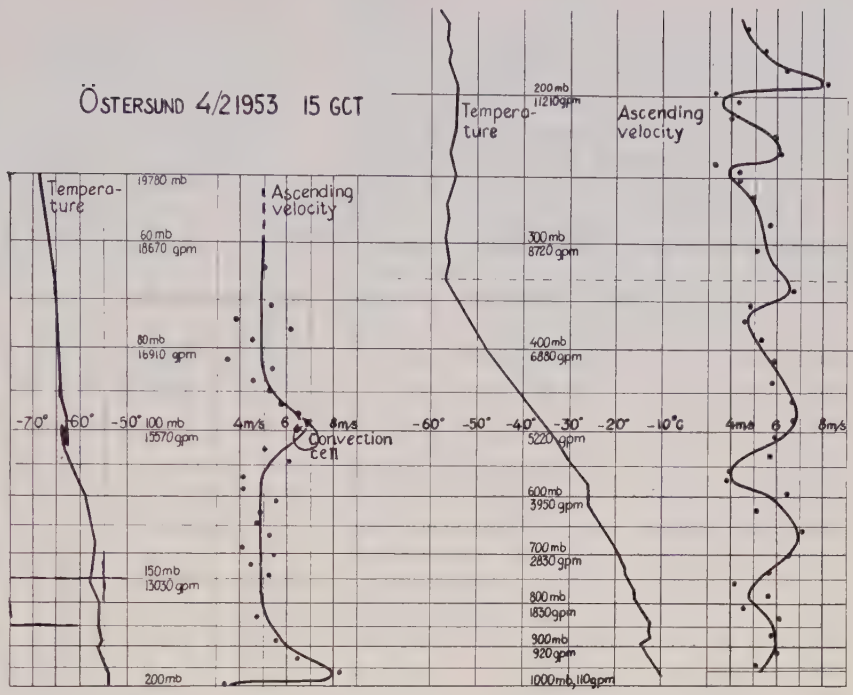

Fig. 1. The sounding made at Östersund (63°N, 15°E). Both temperature curves and curves of ascending velocity of the sonde are shown. The circular arrow indicates the location of the measured conventive cell.

GCT 6 February 1953, and the stratospheric part of the sounding is illustrated in Fig. 3. The temperature curve of the middle stratosphere is similar to that of 4 February, and in the upper part of the most unstable layer now situated between 13.5 and 14.2 km the sonde experienced a motion similar to the first sonde. The downward wind velocity of the cell was here not strong enough to force the sonde down, but the recorded pressure stopped falling and stayed at the same value for some ten seconds. The downward velocity measured here was 5 m/s and the upward velocity 3 m/s with an error of about 50 per cent.

The sounding equipment. The sounding system used at the Swedish aerological stations is the wellknown Finnish system. The reader not familiar with it is referred to a paper of TOMMILA and VÄISÄLÄ (1947). However, a short description of the functioning is necessary here, when discussing the errors in the above measurements.

The radiosonde is a variable radio-frequency oscillator, the variation of the radio-frequency by means of a variable condensor corresponding to the variation of the meteorological element. The receiver is a superheterodyne with variable beat-frequency discrimination. The recording pen is mechanically coupled to the condensor of the beat-oscillator, and by proper manual tuning the variation in the frequency of the radiosonde can be followed on the recording paper. Five intermittent signals of different frequencies are sent by the radiosonde, pressure, temperature, humidity, and two reference frequencies, and the operator has to follow all these signals one by one. Hence there is a limitation in the number o consecutive points in the record of one single element, the limitation depending upon the ability of the operator. It is also customary to devote more care to the record of temperature than to the other elements because of the more rapid random fluctuations in temperature than in e.g. pressure. The reference frequencies vary very slowly, hence it is not common to record them in more than 3—4 points per minute. Nearly the same holds for pressure and humidity, say 4—6 points, and the temperature records generally consist of 10 points per minute. Thus the record of pressure from which height calculations are made will not completely show the details in pressure variations with the sonde passing the convective cell.

The variations are smoothed out due to the sparsely recorded points. Important is, however, that we could state that the pressure variations recorded in this manner are not exaggerated. Another important smoothing influence is the hysterese in the pressure bulb.

The measurement of the vertical wind velocity by means of radiosonde height calculations. The ascending velocity of the radiosonde can be calculated from the consecutive height values of the sounding. This is made for the first entire sounding, and the values are demonstrated in Fig. 1. The sounding is divided into layers of about 300 m thickness, and the ascending velocity is calculated in every layer. The dots around the right curves in Fig. 1 indicate these values. The dispersion error is about 15 per cent at 1,000 mb and 50 per cent at 100 mb in these determinations. The curve drawn is smoothed with regard to this fact.

Some main features in the vertical velocity-height curve can be detected. The mean value of a layer of say 5 km thickness is estimated from the figure to be about 5.5 m/s in the lower troposphere and decreases slowly to 5 m/s or somewhat less in the stratosphere. This slow variation may be due to the variations in the buoyancy and frictional forces of the balloon. In the troposphere and the lower stratosphere there are wave-like patterns indicating gravitational waves in these layers. Above 13 km there is no indication of variations in the velocity up to the end of the sounding in the 19 km level, except in the 15—16 km layer where the convective cell is situated. This fact shows that the buoyancy force is practically constant in this region and that the ascending velocity of the balloon relative to the air is 4.9 m/s ± 0.3 m/s. In the 15—16 km layer there is a general upward motion, which may result of the compensation for the strong downward motions which seem to drive the convection in this layer.

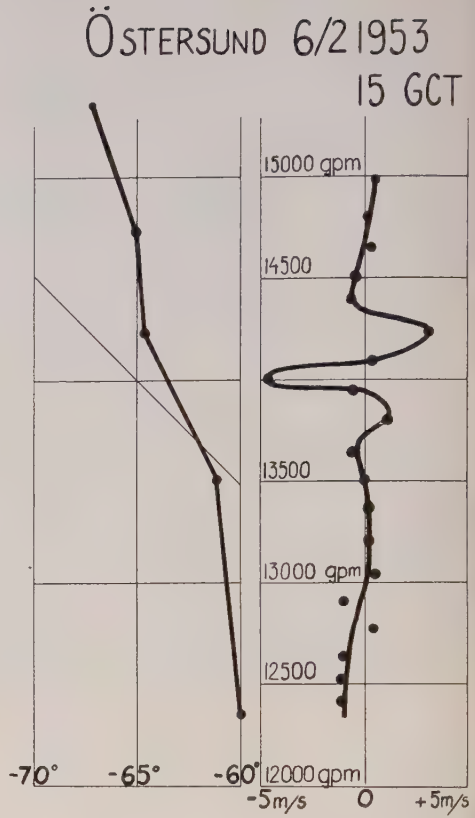

Eig. 3. The stratospherical part of the second sounding in Östersund showing the persistance of the convective layer. Both temperature and vertical wind velocity are shown.

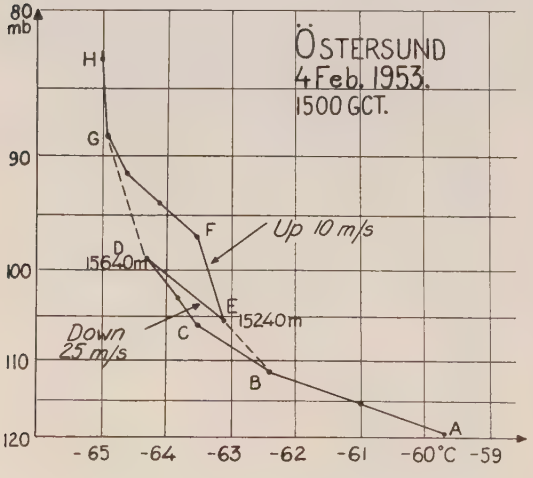

Eig. 2. The details of the sounding in Fig. 1 when the radiosonde passed the convective layer. Full line indicates the real path of the sonde, dashed lines indicate interpolated temperatures in different horizontal regions.

The error in a measurement of the ascending velocity in such a small layer as about 300 m is rather large. It consists of an error in pressure measurement and an error in time interval measurement. The pressure error consists of two distinct parts, the first is an instrumental error which is practically constant throughout the sounding but varies from sonde to sonde. The dispersion of this instrumental error is

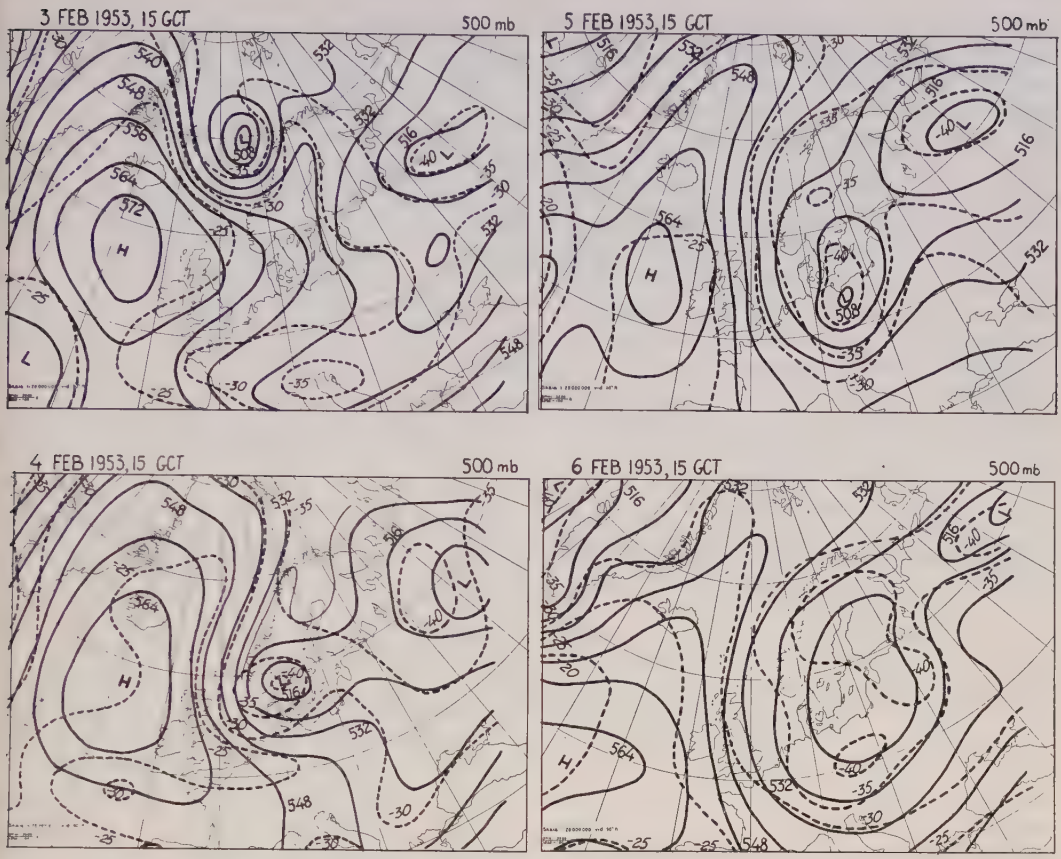

Fig. 4, 5, 6 and 7. Upper air maps showing the development and motion of the intence low mowing from northeast Greenland southeast over Europe.

rather great = 7—10 mb. The second part is due to inaccurate recording and evaluation and will be about 1.5 mb at a pressure of 100 mb if extremely great care is taken in the evaluation. The error in pressure difference will be only 2 mb, because of the elimination of the instrumental error. (See RAAB and RODSKJER, 1950.) In our case the pressure difference when the sonde descended was 6 mb and the relative error is then 33 per cent. The error in time interval measurement is $^1/_{10}$ minute which in $^1/_2$ minute makes an error of 20 per cent. These errors add so that the error in vertical wind velocity will be as large as 53, say 50 per cent. There will also be an error in the pressure measurement as described above due to the sparse number of recorded points and due to the hysterese in the pressure bulb. This error is approximately estimated to 1 mb, that is 15 per cent, which adds to the upper error limit. We may then state that the error is between + 65 per cent and — 50 per cent.

The values of the downward wind velocity will then be between 41 m/s and 12 m/s and the upward wind velocity will be between 17 m/s and 5 m/s.

In the second sounding the corresponding values are 8 and 2.5 m/s (the downward wind velocity) and 5 and 1.5 m/s (the upward wind velocity).

The dynamics of the convective cell. The movement up and down illustrated in Fig. 2 will probably have been accompanied by a horizontal motion of the sonde. At first the sonde seems to have entered a horizontally limited region with a temperature curve ABCDGH. At D the sonde entered the downdraft and followed it to the point E where the sonde

reached another horizontally limited region with the corresponding temperature curve ABEFGH and then followed this upwards. In the colder region the air will begin to sink due to the warmer surroundings.

Is it now possible for an air parcel which starts at G and follows the curve GDE to obtain a final velocity of 25 m/s if the surroundings do not change? The fact that the air parcel falling along the curve GDE does not warm dry-adiabatically may be explained by assuming sufficient entrainment to keep the temperature of the air parcel low enough. The buoyancy force is in our case negative and equal to

$$\frac{\varrho_{\text{surr.}} - \varrho_{\text{parcel}}}{\varrho_{\text{surr.}}} g$$

per unit mass. That is according to the gas law

$$\frac{T_{\text{parcel}} - T_{\text{surr.}}}{T_{\text{parcel}}} g.$$

The energy gained is

$$\int_{\text{GDE}} \frac{T_{\text{parcel}} - T_{\text{surr.}}}{T_{\text{parcel}}} g dz = w^2/2.$$

An integration of the area GDEFG = S gives the value 530 m · °C, and we obtain $w^2 = 2 \cdot 9.81 \cdot S/210 = 50$ (m/s)^2.

$w = 7$ m/s which is somewhat lower but of the right order of the lower error limit of the value w described above. The surface S may be assumed to be twice as large if we assume the starting point a little more to the left of point G. The value of w will then be 10 m/s which is practically in agreement with the lower limit of the measured value of w.

The persistence of the stratosphere with double temperature regions. As the phenomenon with the convective cells repeated on the 6th of February and the temperature soundings still show the double temperature region in the stratosphere there must be some mechanism which sustains the regions, because convection and turbulence would cause an elimination of the sharp border with the great temperature gradient. This mechanism is to be found in the general circulation pattern. The main features of the weather development as seen from the 500 mb upper air maps (Fig.

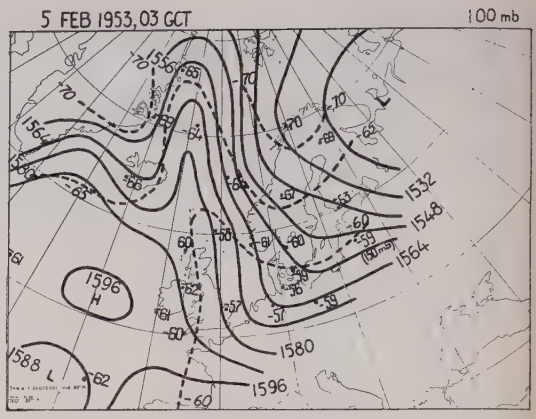

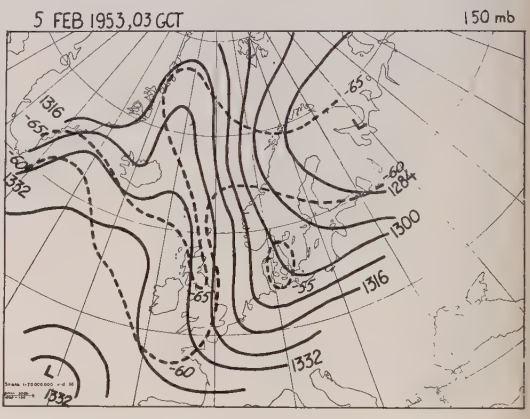

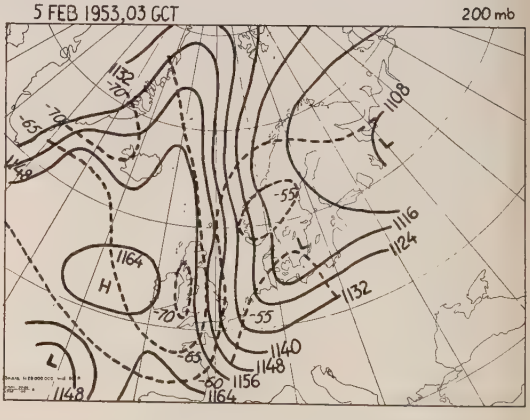

Fig. 8, 9 and 10. Upper air maps showing the distribution of wind and temperature in different levels of the stratosphere.

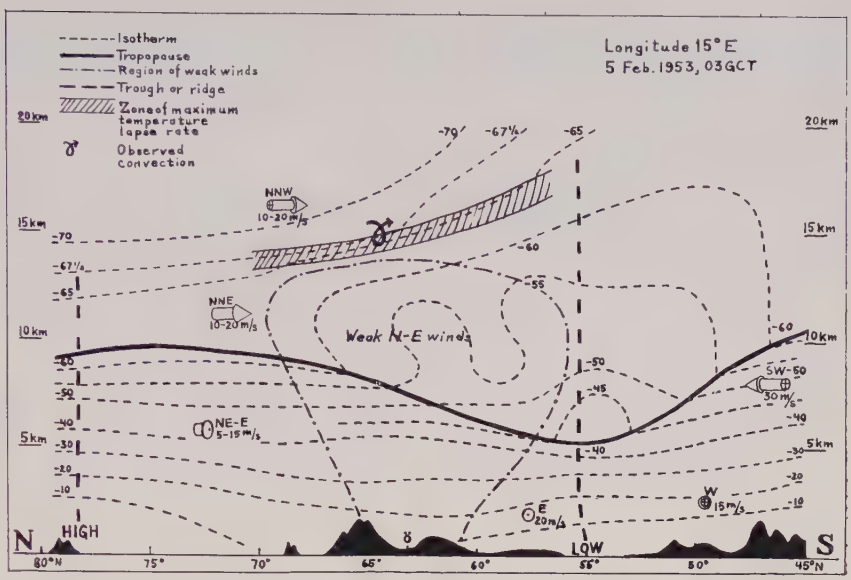

Fig. 11 The vertical section through latitude 15° E showing the mechanism of instabilisation in the middle stratosphere.

4—7) during the days in question are the following:

1. Together with warm air advection over Greenland a strong high pressure ridge is building up from the south over Iceland and eastern Greenland and reaches maximum intensity on the 4th of February.

2. The warm air advection over Greenland forces a relatively small cold-pool to move from Jan Mayen southeast over Scandinavia and form a deepening low.

3. In the morning of the 4th of February the deepening low passes the Scandinavian mountain range and makes contact with a wide cold-pool situated west of the Ural mountains.

4. The 4th of February the cold air from the Russian cold-pool entered the rear side of the Scandinavian low and began to fill it with cold air.

5. The Scandinavian low then retards and spreads out and at 1500 GCT the 6th of February there is a wide cold-pool over central and northern Europe and only a smaller rest west of the Ural mountains.

The variations of the circulation pattern with height is demonstrated in Fig. 8—11 and shows the situation at 0300 GCT the 5th of February instead of 1500 GCT the 4th of February. This because of the satisfactory number of soundings made in the Scandinavian region in the morning of the 5th of February. The network consists of all the ordinary stations in the analysed region of the 100 mb map and can be seen from the temperature values plotted on the 100 mb map (Fig. 8).

6. In the cold-pools and the lower stratosphere above there is a general downward motion causing the specific warm stratosphere, the downward motion being a part of the tropopause circulation. The contrasts between the "warm" and "cold" air masses are expressively shown on the 200 mb map (Fig. 10).

7. Up to the 200 mb level above Östersund there is advection between east and north of this warmed stratospherical air.

8. Arriving to the 100 mb level we can see the weather situation change and a general cold advection taking place over total Scandinavia, especially in the northern and eastern parts. The cold air arrives from northnortheast from Spitzbergen and originates from a cold-pool of the upper stratosphere with its centre north of Spitzbergen. As an example of a stratospherical cold-pool combined with a surrounding stratospherical "jet stream" see for instance HUBERT (1953).

9. With the high pressure ridge over the Atlantic still reaching up in the 100 mb level this ridge forces the cold air from northnorthwest over central Sweden and Östersund and further to the south.

Hence the advection is still there above 100

mb and in the layers below there is the warming effect above the cold-pool of the troposphere.

Hence the contrasts between lower and higher stratosphere are sustained with the described convective phenomenon as a result.

Fig. 11 shows schematically the variation in the vertical of the described circulation pattern together with the equiniveaus of temperature.

Final remarks. Radiosondes entering convective cells have been observed in the tropospheric region, but in the middle of the stratosphere such an event seems a little surprising. At the first glance an instrumental error seems to be the most natural explanation of the behavior of the radiosonde, but the radiosonde worked with both reference frequencies in good conditions and both the temperature and pressure gradient changed the direction at the same time. An instrumental error which enters both in the temperature and pressure sensing elements but not in the reference elements does not seem probable. The repetition of the phenomenon both the 4th and 6th of February makes an explanation due to real effects in the circulation more probable.

Acknowledgments. Thanks are due to Dr A. Ångström and Dr A. Nyberg, Director and Assistant Director of the Swedish Meteorological and Hydrological Institute, for their kind interest in the subject.

The author is also indebted to the Chief Meteorologist of the aerological sounding station in Östersund, S. Hjalmarsson who made and supervised the accurate measurements.

Table 1.

Time of recorded pressure point	Temperature	Pressure	Height	Ascend. vel.	Vertical wind vel.
Minutes	°C	mb	gpm	m/s	m/s
44.25	— 59.7	119.5	14,460		
				+ 4.1	— 0.7
45.15	— 61.0	115.5	680		
				+ 4.1	— 0.7
46.00	— 62.4	111.5	890		
				+ 6.0	+ 1.2
46.90	— 63.5	106.0	15 210		
				+ 5.0	+ 0.2
47.50	— 63.8	103.0	390		
				+ 7.0	+ 2.2
48.10	— 64.3	99.0	640		
				— 22.3	— 27.1
48.40	— 63.1	105.5	240		
				+ 14.2	+ 9.4
49.00	— 63.5	97.0	750		
				+ 6.4	+ 1.6
49.50	— 64.1	94.0	940		
				+ 5.7	+ 0.9
50.00	— 64.6	91.5	16,110		
				+ 5.2	+ 0.4
50.65	— 64.9	88.5	310		
				+ 4.8	0.0
52.00	— 65.0	83.0	16,700		

REFERENCES

Hubert, W.E., 1953: A Case Study of Variation in Structure and Circulation about Westerly Jet Streams over Europe. *Tellus*, **5**, pp. 360, 361 and 365.

Raab, L., and Rodskjer, N., 1950: A Study of the Accuracy of Measurements of the Väisälä Radiosonde. *Arkiv för Geofysik*, **1**. Nr 2.

Tommila, M., and Väisälä, V., 1947: *Handbook of Sounding by means of the Finnish Radiosonde.* Helsinki.

Numerical Weather Map Analysis[1]

By PÁLL BERGTHÓRSSON[2] and BO R. DÖÖS, University of Stockholm

(Manuscript received June 30, 1955)

Abstract

A method to analyze upper air charts numerically is presented. The analysis is expressed by the height values of the pressure surface in gridpoints. The computed height in a gridpoint is obtained as a weighted mean of height values derived from the surrounding height and wind observations, the forecast height in the point and the corresponding normal height. Nine 500 mb maps are analyzed with the aid of the Swedish computor BESK, six of these consecutive. The size of the grid was 32×41 points.

The analyses have been compared with two independent conventional analyses. The mean values of the root mean square of the differences between the numerical and the conventional analyses were 26 m and 24 m respectively and 26 m between the two conventional ones.

The root mean square of the differences between the observed and analyzed heights was 22 m in the mean. This is roughly what should be expected judging from the existing knowledge about observation errors.

Three barotropic forecasts have been computed from the numerical analyses. They are compared with the corresponding numerical forecasts from conventionally analyzed maps.

It was not possible to find any significant difference between the goodness of the forecasts based on the numerical analyses and the conventional analyses.

1. Introduction

The first attempts at numerical weather forecasting on a routine basis have been characterized by a combination of tedious manual work on one hand and electronic computations with extremely high speed on the other. The weather observations are plotted on maps, examined and analyzed. From this manual analysis values are interpolated at a great number of gridpoints and punched on a paper tape, which afterwards is checked and recopied. Finally the electronic computer can start the forecasting procedure.

The manual part of these operations consumes time that is out of proportion to the time required for the machine computation. This, however, is not the only disadvantage. The manual analyst cannot be expected to use systematic and quantitative methods in his interpolations and extrapolations. His work is rather a complicated curve-fitting by the eye based on a number of more or less well-established rules. The analysis will, in other words, be subjective and depending on the skill of the meteorologist. It is furthermore very difficult to avoid wiggles and irregularities of small scale which are neither desirable nor justified by observations. These may frequently amplify in the forecast computation and thus reduce the value of the final forecast. Errors in the reading and punching of values in gridpoints are also highly probable.

This leads to the conclusion that it would be desirable to device a method to perform the analysis with the computer. Already in the early stage of experiments with numerical forecasting, PANOFSKY (1949) presented a method of objective analysis. Later SMAGORINSKY (unpublished), ELIASSEN (1954), GILCHRIST and CRESSMAN (1954), and VÄISÄLÄ (unpublished) have studied this subject. These authors have presented methods which are

[1] Part of the research reported in this document has been sponsered by the Geophysics Research Directorate of the Air Force Cambrigde Research Center, Air Research and Development Command, United States Air Force, under contract No. 61 (514)—648-C, through the European Office ARDC.

[2] Now at the Icelandic Weather Service, Reykjavik, Iceland.

applicable for interpolation between observed values, to obtain the most probable values in gridpoints.

In our investigation of this problem at the University of Stockholm, we reached the conclusion that quite often it is not possible to get a reasonable analysis only by means of interpolation between synoptic observations. It is quite clear that the distance between the observations must be small compared with the size of the systems to be analyzed. This is certainly not the case in many areas as over the oceans. In such cases any *interpolation* method will fail, independent of whether it is linear, quadratic or cubic. If, however, some observations were available in the area 12 hours ago, a twelve hour forecast is probably a better approximation than the interpolated analysis. The application of the forecast for the analysis has indeed been suggested by Smagorinsky and Gilchrist and Cressman, and it is a rather natural way of keeping time continuity in the maps.

If the forecast in the case discussed above is of little value, no observations being available when it was made, it is quite possible that even climatological informations will give the most reasonable solution. This is particularly true in low latitudes, where the deviations from normal patterns are surprisingly low. The suggestion of using the normals is due to Mr. Charasch. At this point it may be adequate to point out, that we can not hope to get a *true* analysis. What we can expect is to obtain the *most probable* analysis. This may serve to justify the use of the climatological informations together with the forecast and the observations.

2. Method of analysis

The following investigation has been restricted to the analysis of the 500 mb flow pattern. However, the same method could in principle be applied to other levels.

As informations we have used the observations of wind and height at the 500 mb surface, the 12 or 24 hour barotropic forecast valid for the same time as the analysis, and the normal height of the 500 mb level for the particular month when the analysis is made.

The principle of the analysis is the following:

We start out with the best available approximation of the 500 mb map. This preliminary field is then modified as far as possible with available observations. The analysis we obtain in this manner can then be used as a preliminary field which again is modified by the observations. We found, however, that in

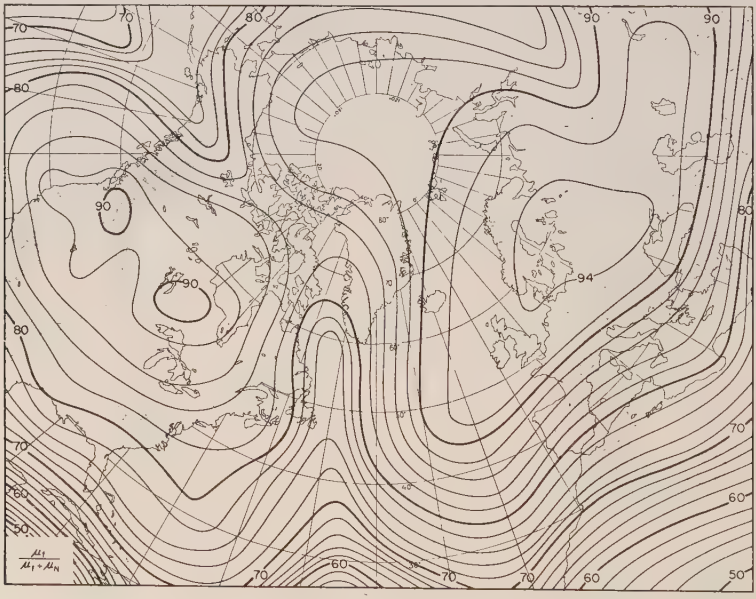

Fig. 1. Percentage contribution of the forecast in constructing the preliminary field.

most cases fairly satisfactory results were obtained in the first try.

The first preliminary 500 mb heights (Z_p) are constructed as a weighted mean of the forecast heights (Z_f) and the normal heights (Z_N). For each gridpoint we thus obtain

$$Z_p = \frac{\mu_f Z_f + \mu_N Z_N}{\mu_f + \mu_N} \qquad (1)$$

μ_f and μ_N being the weights of the forecast and normal heights respectively. We assume that μ_f is only a function of geographical position and season. Assuming furthermore that the deviations from normals are not correlated with the deviations from the forecast, we can put

$$\mu_f = \frac{\text{const.}}{\sigma_f} \qquad (2)$$

in other words, the weight of the forecast is inversely proportional to the root mean square of the differences between observed and forecast heights for a great number of forecasts. In the same manner the weight of the normal in each point is determined as:

$$\mu_N = \frac{\text{const.}}{\sigma_N} \qquad (3)$$

σ_N being the root mean square of the deviation of the daily values Z from Z_N. Fig. 1 shows the geographical distribution of the ratio $\mu_f/(\mu_f + \mu_N)$ expressed in per cent. The computed height in a gridpoint will now be expressed as a *weighted mean of height values derived in three different ways from the surrounding observations and the preliminary Z-field given by* (1). From each station observing the 500 mb height and the wind and not farther away from the gridpoint than about 900 km, these three approximate height values for the gridpoint are derived in the following way:

1) Assuming that the difference between the observed height (Z_{os}) and the preliminary height at the station (Z_{ps}) is the same as the difference between the derived height (Z_1) and the preliminary height (Z_{pg}) in the gridpoint (fig. 2 a), we find:

$$Z_1 = Z_{pg} + (Z_{os} - Z_{ps}) \qquad (4)$$

2) Assuming that the observed wind is geostrophic and representative for the area between the gridpoint and the station, one can compute the corresponding gradient of Z and finds another approximate height value Z_2 in the gridpoint (fig. 2 b)

$$Z_2 = Z_{os} + \left(\frac{\partial Z}{\partial n}\right)_{os} \cdot l \qquad (5)$$

l being the distance between the station and the gridpoint.

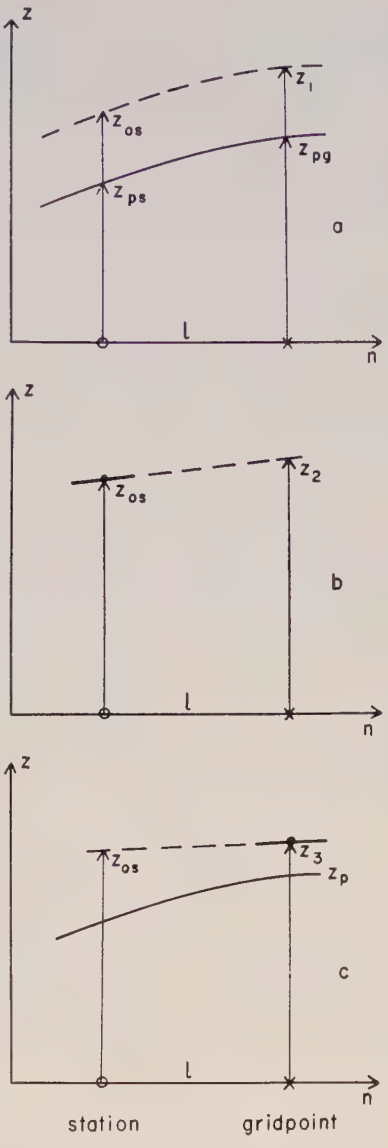

Fig. 2. Schematic illustration of the derivations of the heights Z_1, Z_2 and Z_3.

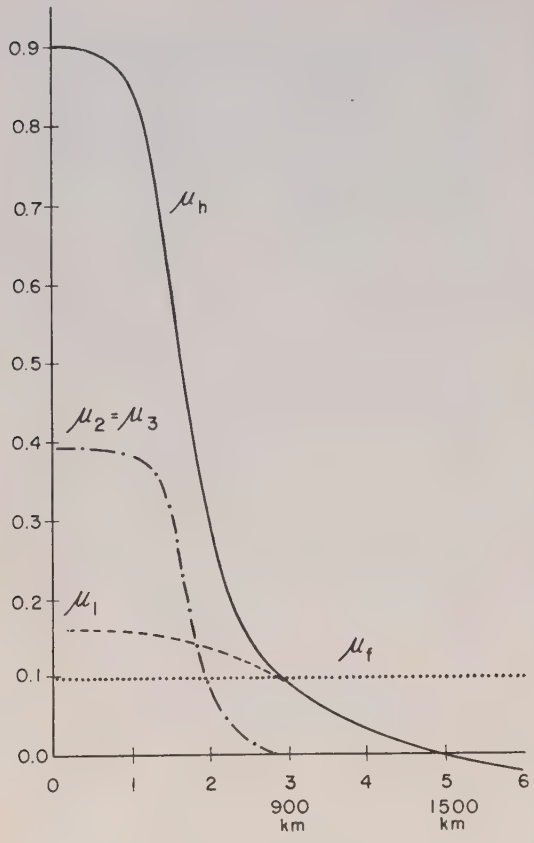

Fig. 3. A graphical representation of the weighting functions.

3) Assuming the gradient of the preliminary field *in the gridpoint* to be representative for the area between the station and the gridpoint, the height in the point will be (fig. 2 c)

$$Z_3 = Z_{os} + \left(\frac{\partial Z}{\partial n}\right)_{pg} \cdot l \qquad (6)$$

We have next assumed that the weights of these three heights, Z_1, Z_2 and Z_3, are functions only of the distance between the gridpoint and the station. These weighting functions can be determined statistically with the following method.

We form the regression equation

$$Z_g = \frac{\mu_1 Z_1 + \mu_2 Z_2 + \mu_3 Z_3 + \mu_f Z_f}{\mu_1 + \mu_2 + \mu_3 + \mu_f} \qquad (7)$$

For a given distance from the station we now require that the mean square difference between Z_g and the conventionally analyzed height shall be a minimum for a great number of cases. This will determine the ratio between the coefficients μ_1, μ_2, μ_3 and μ_f. Since μ_f is assumed to be known from the special investigation of forecast errors this will give μ_1, μ_2 and μ_3. This computation can then be repeated for different distances from the station and thus determines the weighting functions μ_1, μ_2 and μ_3. This investigation gave the result that these weighting factors can be approximated by the following expressions:

$$\mu_1 = \frac{30}{r^4 + 150} - 0.04 \qquad (8)$$

$$\mu_2 = \mu_3 = \frac{27}{r^8 + 70} \qquad (9)$$

where r is given in gridunits. Having modified the preliminary height in one point by one such station we have

$$Z_g = \frac{\mu_f Z_f + \mu_N Z_N + \mu_1 Z_1 + \mu_2 Z_2 + \mu_3 Z_3}{\mu_f + \mu_N + \mu_1 + \mu_2 + \mu_3} \qquad (10)$$

In the case where the station reports height only or if it is so far from the gridpoint, that the wind is of no value as an information (beyond ca 900 km) we only use assumption 1) which was discussed above in connection with stations observing both height and wind. We obtain

$$Z_h = Z_{pg} + (Z_{os} - Z_{ps}) \qquad (11)$$

The weighting function μ_h was found to be quite different from μ_1. This is because Z_h is the only contribution from the station. μ_h will therefore be higher than μ_1 near the station (cf. fig. 3). It was found to be of little use to apply the height Z_h from stations beyond 1,500 km, as the weight μ_h then becomes very small. The function μ_h can be approximated by

$$\mu_h = \frac{2.25}{r^8 + 5} + \frac{10}{r^4 + 20} - 0.01 \qquad (12)$$

Having modified the preliminary height in one point by one such station using the observed height only, one obtains

$$Z_g = \frac{\mu_f Z_f + \mu_N Z_N + \mu_h Z_h}{\mu_f + \mu_N + \mu_h} \qquad (13)$$

In order to test how sensitive the analysis is to the shape of the weighting functions (8), (9) and (12) we changed these functions so that μ_1, μ_2, μ_3 and μ_h were twice as large for $r = 0$. In recomputing one analysis we found that the difference between the analyses was insignificant, at the most 10 m in single points.

In our previous discussion we have only considered one station contributing to the height in a gridpoint. In the case of several stations influencing the height at the point, another factor has to be taken into account. Some of the stations may be very close to each other and therefore give contributions that are correlated, while other stations are isolated and give contributions which are more or less uncorrelated to those of other stations. The weight of the contributions from a station should therefore be reduced. For this reduction we have used a factor inversely proportional to the density of stations surrounding the particular station, i.e. $\frac{1}{\varrho}$. We have evaluated ϱ as the number of stations within a radius of ca 375 km, the station itself also being counted. The ultimate height at the gridpoint will thus be

$$Z_g = \frac{\mu_f Z_f + \mu_N Z_N + \sum_{i=1}^{n} \frac{1}{\varrho_i} [\mu_1 Z_1 + \mu_2 Z_2 + \mu_3 Z_3]_i + \sum_{j=1}^{m} \frac{1}{\varrho_j} [\mu_h Z_h]_j}{\mu_f + \mu_N + \sum_{i=1}^{n} \frac{1}{\varrho_i} [\mu_1 + \mu_2 + \mu_3]_i + \sum_{j=1}^{m} \frac{1}{\varrho_j} [\mu_h]_j} \qquad (14)$$

Here n denotes the number of stations influencing the height at the point and giving the contributions Z_1, Z_2 and Z_3, and m is the number of stations which give contributions from the observed heights only.

This formula is very suitable for numerical computations. One can for example compute the heights in the gridpoints one by one, in every case using all stations that influence the point. We have, however, chosen the method to compute at a time the contributions from one station to the height at all gridpoints affected by the station. Thus it is possible to feed the observations into the machine in an arbitrary order and thus also use stations that arrive during the computations.

Suppose for example that we are going to modify the height at a gridpoint by the contribution Z_h having the weight μ_h. We know the height Z_g before the modification and the sum of weights $\Sigma\mu$ used to compute it. The modified height Z_g' will then be:

$$Z_g' = \frac{\Sigma\mu Z_g + \frac{1}{\varrho_s}\mu_h Z_h}{\Sigma\mu + \frac{\mu_h}{\varrho_s}} \qquad (15)$$

where ϱ_s is the station density at this particular station. After computing Z_g' we store the quantities Z_g' and $\Sigma\mu' = \Sigma\mu\frac{\mu_h}{\varrho_s}$ for this point, and the height can later be modified by another station in a similar way.

3. The computational program

The method of analysis discussed in the previous section has been carried through with the aid of the Swedish computor BESK.

The computational program can be outlined in the following manner (cf. fig. 4).

I. The entire code is read and stored on the magnetic drum.

II. The data tape, which contains the coordinates of the stations, the heights of the pressure surface and the wind direction and speed, is read for the first time. At this moment only the density of stations for each station is computed. These values are stored on the magnetic drum for later use.

III. The twelve-hour forecast, based on the previous map, is read, converted from the decimal to the binary system and stored on the drum. It is possible to use the output tape from the barotropic forecast.

IV. The normal heights are read from tape and converted from decimal to binary. Thereafter the weights μ_f and μ_N for each gridpoint are read. The weighted mean of the normal and the forecast (the preliminary field) is computed and stored.

V. The data tape is read for the second time. In order to save space in the storage only a

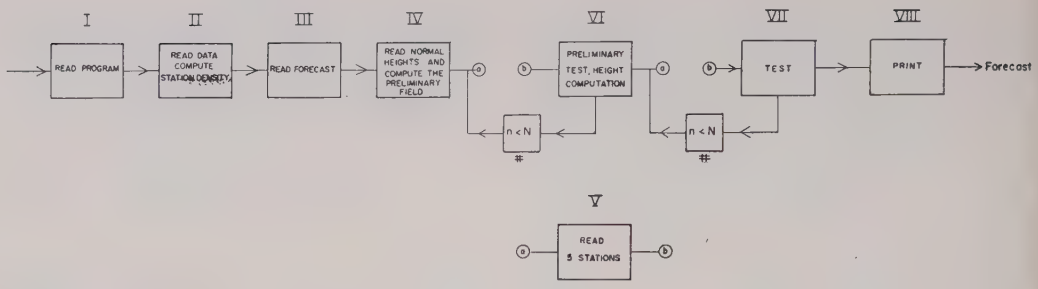

Fig. 4. Flowdiagram of the computations. N denotes the total amount of stations on the data-tape.

few (5) stations are read from the tape at a time. For each one of these stations the height of the pressure level is converted from decimal to binary, the geostrophic gradient of the two components of the wind (if it is a windstation) is computed. The densities, which were computed in part II, are extracted for these stations.

VI. Treating one station at a time, the height and the two components of the wind are compared with the corresponding values of the preliminary field. If the difference between the observed height and the interpolated height of the preliminary field exceeds the tolerance (100 m), the coordinates of the station and the both heights are printed to be available for visual inspection. If the corresponding differences for the wind exceeds the tolerance (30 kts), the coordinates and the observed and interpolated gradient are printed. It is possible at this point to disregard the observation if one can conclude that it is erroneous. Thereafter the observation (if it is accepted) is used to modify the heights in the surrounding grid points according to (15). After these five stations have been treated five new stations are read from the tape using part V. This is repeated until all stations have been considered.

VII. The analysis is now completed. Using part V to read the data tape the observations are now tested in the same manner as in part VI. However, the observations are now tested against the analysis instead of the preliminary field. The tolerances are now more strict (50 m for the height and approximately 25 kts for the geostrophic gradient). If an observation now is suspected to be erroneous it is possible by a correction-tape either to remove the observation or to correct it.

VIII. The result of the analysis is now printed. The analysis is stored in the machine so that it is possible to use it for a barotropic forecast immediately.

4. Results

The computations were made over a rectangular grid consisting of 32×41 points and the gridsize was 300 km at 50°N (fig. 5). The time required to compute the analysis was 22 minutes using about 500 pieces of informations, counting a height as one and a wind as two. For a station which reports both height and wind it takes about two and a half second to modify the heights in the surrounding grid-points and for a station which only reports height about two seconds. (At the BESK the time for addition is 56 microsec and the time for multiplication is 364 microsec).

In all nine analyses have been computed: 26 September 1500 GMT—29 September 0300 GMT 1954, a series consisting of six analyses with 12 hour intervals, 22 January 0300 GMT, 23 January 0300 GMT 1955 and 23 May 1500 GMT 1955. In fig. 6, 8 a and 9 three of these analyses are shown.

The last analysis was carried out on a routine basis in cooperation with the Weather Service of the Royal Swedish Air Force. This was done in order to investigate how much it is possible to gain in time by using this method of analysis. The observations were checked and punched as soon as they arrived. At 2300 GMT (8 hours after the observation time) most of the observations were received. The data tape was then recopied and checked. A few observations, which had arrived in the meantime, were added. At about 24 GMT the data tape was ready for the machine.

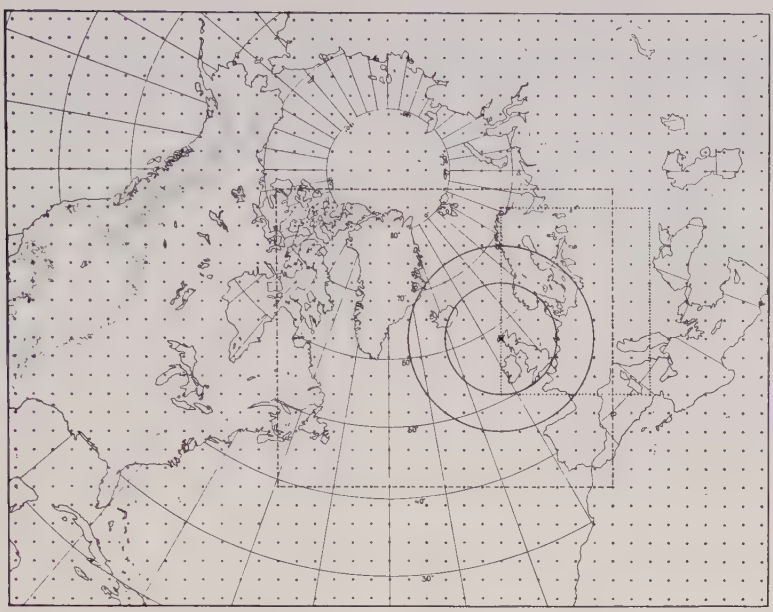

Fig. 5. Location of the grid used in analyses and forecasts. The two circles indicate the areas from which observations can influence the height in a gridpoint. The inner circle represents the influence area of a wind observation, the outer circle the corresponding area for a height observation.
The verification of the forecasts was done over the area inside the dashed line. The dotted line indicates the area used in the comparison presented in table 1, (the values in brackets).

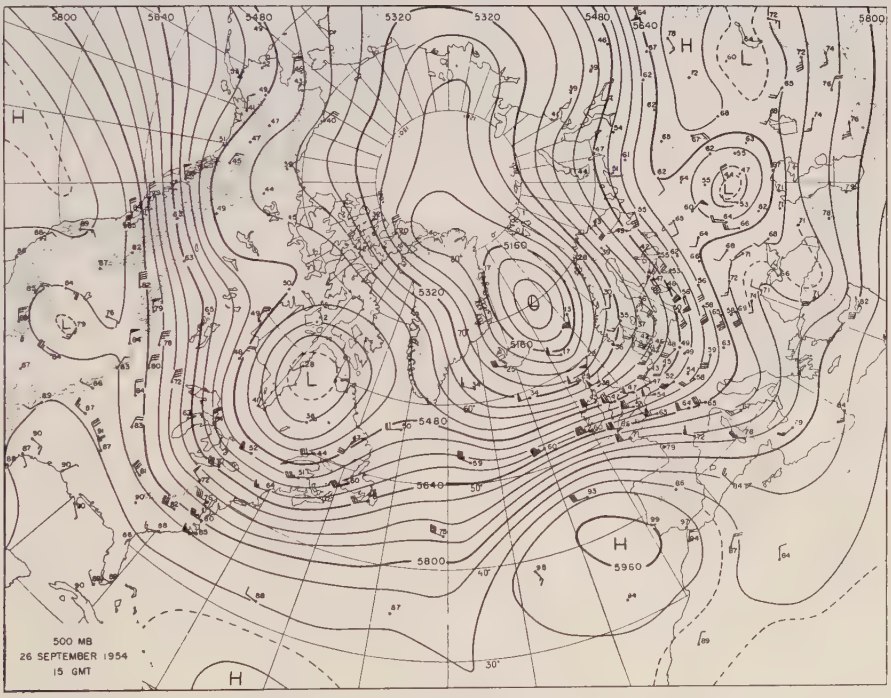

Fig. 6. Numerical analysis of the 500 mb contours on September 26, 1500 GMT, 1954. Heights given in decameters at the stations. Contour lines tabelled in m.

This experiment showed that it is possible to save about $3^1/_2$ hours in comparison with the manual preparation of the analysis. The possibility of clerical errors is also reduced. Further, it may be regarded as an advantage that the same set of observations and a given forecast will give a unique solution of the analysis; it is in other words objective.

The most important question, however, is if this numerical procedure gives us as true a picture of the actual conditions as the conventional method.

This is quite difficult to test. As the manual analysis generally represents considerable synoptic knowledge and experience, it is not unreasonable to require that the numerical analysis show no considerable deviations from the manual analysis.

In order to test this we have compared the numerical analyses (N) with two independent conventional analyses (C_1 and C_2) of the same synoptic situations. The analyses C_1 and C_2 were made in daily service at the Swedish Weather Service (SMHI) and at the Institute of Meteorology of the Stockholm University. The root mean square of the differences $N—C_1$, $N—C_2$, and $C_1—C_2$ were computed and are shown in Table I. The comparison was made over the whole map except in certain areas close to the boundaries where some of the conventional analyses were incomplete. The comparison was also made over a small area (indicated in fig. 5) where the station density is comparatively dense.

In computing the preliminary field 12^h barotropic forecasts were used in all analyses except for 22/1 and 23/1 0300 GMT, 1955, where 24^h barotropic forecasts were used. These forecasts were computed from numerically analyzed maps when it was possible. Thus, in the period from 26/9 1500 GMT to 29/9 0300 GMT, 1954 which consists of 6 consecutive analyses, 12 hours apart, it was only necessary to use a conventionally analyzed map for computing the 12^h forecast from 26/9 0300 GMT 1954. In spite of this the goodness of the analyses did not decrease during the period (cf. tables). *Table I shows that generally the differences between the two conventional analyses are approximately the same as the differences between the numerical and conventional analyses.* It can further be seen th at the analysis is comparable to the conventional analysis also in regions with relatively sparse observations.

Another possible test is to compute the root mean square of the differences between analyzed and observed heights at the stations. The result of this investigation is shown in Table II. If we had obtained the true analyses this root mean square difference should be approximately the same as the standard error in height

Table I.

Date	$\sqrt{\frac{\Sigma(N-C_1)^2}{p}}$ (m)	$\sqrt{\frac{\Sigma(N-C_2)^2}{p}}$ (m)	$\sqrt{\frac{\Sigma(C_1-C_2)^2}{p}}$ (m)
26/9 —54 15	23 (24)	22 (24)	29 (30)
27/9 —54 03	26 (19)	27 (11)	29 (21)
27/9 —54 15	26 (19)	26 (22)	28 (18)
28/9 —54 03	27 (26)	26 (25)	23 (18)
28/9 —54 15	31 (25)	28 (20)	25 (18)
29/9 —54 03	25 (23)	22 (15)	25 (22)
23/5 —55 15[1]	23 (11)	14 (11)	22 (12)
Mean	26 (21)	24 (18)	26 (20)
28/9 —54 03[2]	25 (24)	23 (23)	23 (18)
22/1 —55 03[3]	41 (21)	48 (29)	36 (26)
23/1 —55 03[3]	44 (36)	50 (37)	36 (29)

The values in brackets refer to the comparison in the small region.

[1] This analysis was done on an operational basis.
[2] This analysis was obtained by recomputing the analysis, now using the first analysis as the preliminary field.
[3] In computing these analyses a 24^h forecast was used for the construction of the preliminary field.

Table II.

Date	$\sqrt{\frac{\Sigma (N-O)^2}{q}}$ (m)	Number of stations (q)
26/9 —54 15	23	230
27/9 —54 03	22	231
27/9 —54 15	23	228
28/9 —54 03	24	233
28/9 —54 15	22	213
29/9 —54 03	22	237
23/5 —55 15[1]	20	247
Mean	22	
28/9 —54 03[2]	19	233
22/1 —55 03[3]	26	223
23/1 —55 03[3]	27	209

Footnotes, the same as for table I.

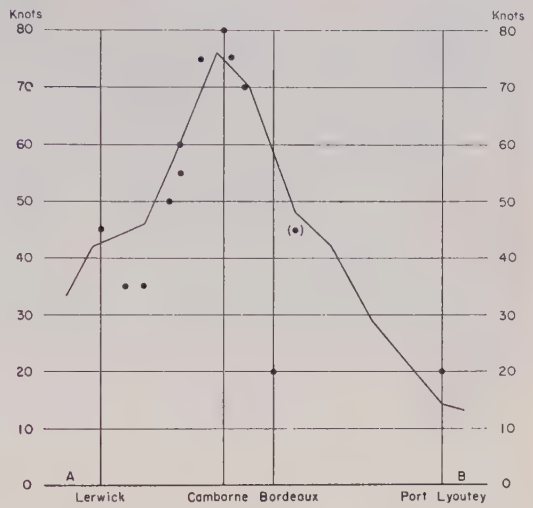

Fig. 7. Geostrophically computed 500 mb windprofile (the curve) compared with wind observations (dots).

observations. Unfortunately the observation errors are not very well known. From the comparison of different types of radiosondes in Payerne 1950 (NYBERG, 1952) and an investigation by RAAB and RODSKJER (1950) one can estimate it to be 20—30 m at the 500 mb level. The results in Table II therefore seem to indicate that the smoothing in the numerical analysis which is responsible for the differences between the analysis and observations, is of the right order of magnitude. In order to study the smoothing we recomputed one of the analyses (Jan. 23, 0300 GMT, 1955). In this

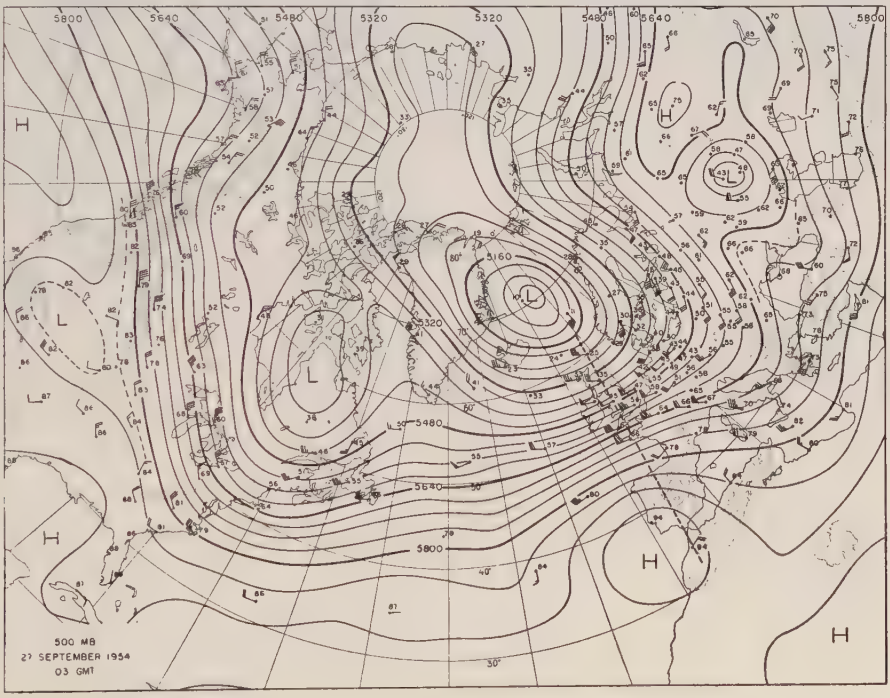

Fig. 8a. Numerical analysis of the 500 mb contours on September 27, 0300 GMT, 1954.

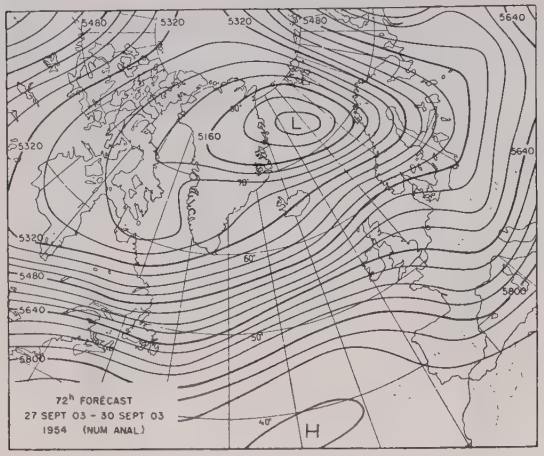

8 b

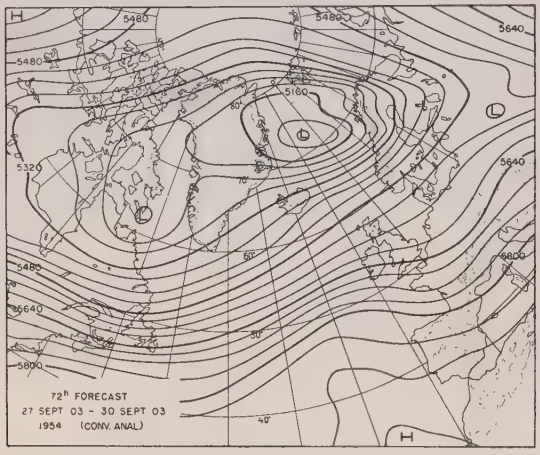

8 c

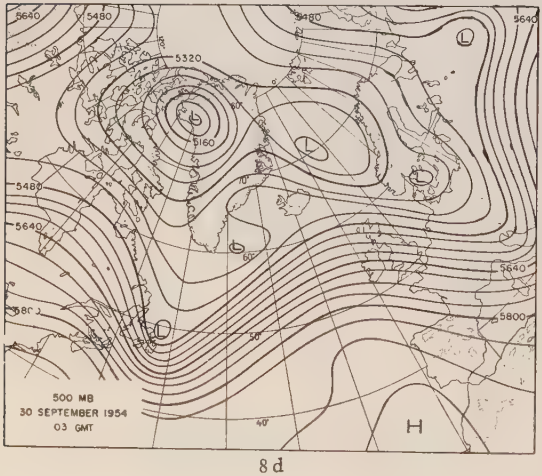

8 d

we introduced one error by increasing the height value at Helsingfors with 270 m. The largest difference between the two analyses was 35 m which occurred in two gridpoints. The difference then decreased roughly by 10 m per gridunit. The decrease was a little less in the direction where the station network was less dense.

This indicates that in areas where the station density is relatively good, the method is relatively insensitive to moderate errors at individual stations.

It is interesting to investigate how the computed height gradients agree with the observed winds. As an example we show here the profile of a jet stream over the English Channel on the 27th of September 1954 at 0300 GMT. In fig. 8 a the position of this cross-section A—B is shown. In fig. 7 the solid curve represents the computed geostrophic velocities in gridpoints close to this line. The dots represent observed winds close to the line. Generally the deviations are not more than about 5 knots. It is of special interest that the peak of the jet stream seems to be very well represented, considering that finite differences over 600 km were used in computing the geostrophic wind. On the whole the computed profile seems to be smoother than the observed one. This is, however, not unreasonable, considering the influence of observation errors and local wind variations, which cannot be represented by the finite differences in the wind computation. In one case, at the station Bordeaux in France, this smoothing results in an almost complete neglection of an observed wind. It is not easy to prove that this neglection of the wind is justified. If the observation were right, it would, however, indicate a relative anticyclonic shear much stronger than the cyclonic shear on the northern side of the jet, and this seems to be unlikely.

Another and perhaps the most important test is how the forecasts based on a numerical

Fig. 8 b. 72h forecast of 500 mb contourfield from September 27, 0300 GMT, 1954. The initial map numerically analyzed.

Fig. 8 c. 72h forecast of 500 mb contourfield from September 27, 0300 GMT, 1954. The initial map conventionally analyzed.

Fig. 8 d. 500 mb contours on September 30, 0300 GMT 1954.

Table III.

Date	24h forecast						48h forecast						72h forecast					
	Numerical Anal.			Conventional Anal.			Numerical Anal.			Conventional Anal.			Numerical Anal.			Conventional Anal.		
	r	ε (m)	$\frac{\varepsilon}{\sigma_x}$	r	ε (m)	$\frac{\varepsilon}{\sigma_x}$	r	ε (m)	$\frac{\varepsilon}{\sigma_x}$	r	ε (m)	$\frac{\varepsilon}{\sigma_x}$	r	ε (m)	$\frac{\varepsilon}{\sigma_x}$	r	ε (m)	$\frac{\varepsilon}{\sigma_x}$
27/9—54 03	0.72	38	0.79	0.53	47	0.89	0.71	63	0.77	0.64	73	0.84	0.74	88	0.85	0.49	98	0.96
28/9—54 03	0.78	39	0.52	0.88	39	0.52	0.77	61	0.67	0.83	57	0.56	0.73	87	0.71	0.76	82	0.67
29/9—54 03	0.82	39	0.57	0.83	39	0.57	0.86	61	0.54	0.80	69	0.63	0.70	113	0.79	0.67	117	0.81
Mean	0.77	39	0.64	0.75	42	0.67	0.78	62	0.66	0.76	66	0.68	0.72	96	0.78	0.64	99	0.81
28/9—54 03[2]	0.84	37	0.52	0.88	39	0.52	0.77	61	0.67	0.83	57	0.56	0.72	88	0.71	0.76	82	0.67

Footnote, the same as for table I.

analysis compare with those based on a conventional analysis. For this test it is, however, necessary to have abundant material. It is quite possible that in single cases a good analysis may give a worse numerical forecast than a forecast based on a bad analysis, due to errors in the model or errors in the verification map.

We have made 24, 48 and 72 hour forecasts from three of the analyses discussed above. Besides the correlation coefficient (r), we have computed the root mean square of the differences between observed and computed changes ε and the ratio $\frac{\varepsilon}{\sigma_x}$, where σ_x is the root mean square of the observed changes.

These results were compared with the results from numerical forecasts based on the same maps but analyzed with conventional methods (Table III).

As far as one can draw conclusions from

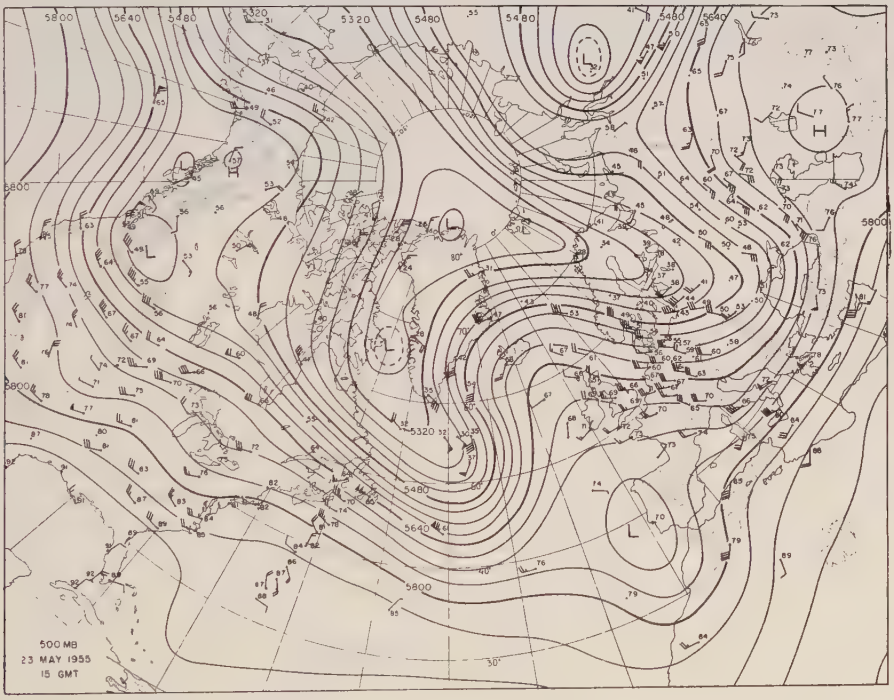

Fig. 9. Numerical analysis of the 500 mb contours on May 23, 1500 GMT, 1955.

these few results there seems to be no significant difference between the goodness of the forecasts based on our analyses and the conventional analyses.

One of the 72^h barotropic forecasts from a numerically analyzed map (fig. 8 a) is shown in fig. 8 b. The corresponding forecast from a conventionally analyzed map is shown in fig. 8 c. The verification map which also is conventionally analyzed is shown in fig. 8 d.

One of the analyses (28 September 0300 GMT, 1954) was recomputed. This time the first analysis was used as the preliminary field. As can be seen from Table I, the difference between the first and second analysis is comparatively small. In certain areas, however, the analysis was improved, especially where the forecast was unsatisfactory. One example: The observed height at the Russian station (28—900) was 5,470 m. In the conventional analysis there was a closed low with its center close to a gridpoint half a gridunit south of that station. The first preliminary height at this gridpoint was 5,580 m, i.e. about 110 m higher than the conventional analysis. The first computed analysis gave the height 5,536 m. The difference between the conventional analysis and the numerical one thus was 66 m. In the second analysis the height in the same gridpoint was 5,514 m. Thus the recomputation reduced the height further 22 m.

Close to Stockholm a similar improvement of the analysis was obtained. The 24^h forecast was slightly better (cf. Table III) when the second analysis was used, while the 48^h and 72^h forecasts did not change appreciably.

Acknowledgement

The authors wish to thank Professor C.-G. Rossby for his great interest and encouragement. To Dr. B. Bolin, who suggested this work, we are greatly indebted for reading the manuscript. We also thank Dr. G. Dahlquist and Mr. E. Charasch for valuable discussions.

Finally we wish to thank Miss S. Back, who prepared all the tapes for the machine computations and Mrs. B. Dahlborg who carried out the drafting.

REFERENCES

Eliassen, A., 1954: An Attempt to formulate the Problems encountered in the Study of the Requirements of Upper Air Network for Numerical Forecasting. *Report from the Institute of Theoretical Astrophysics, Blindern, Norway.*

— 1954: Provisional Report on Calculation of Spatial Covariance and Autocorrelation of the Pressure field. Institute for Weather and Climate Research, *The Norwegian Academy of Science and Letters. Publications and Reports July 1, 1953—June 30, 1954.*

Gilchrist, B. and Cressman, G. P., 1954: An Experiment in Objective Analysis. *Tellus* 6, pp 309—318.

Nyberg, A., 1952: On the comparison of Radiosonde Data in Payerne May 1950. *Sveriges Meteorologiska och Hydrologiska Institut, Communication,* Series B, No. 9.

Panofsky, J., 1949: Objective Weather Map Analysis. *Journal of Meteorology,* 6, pp 386—392.

Raab, L. and Rodskjer, N., 1950: A Study of the Accuracy of Measurements of the Väisälä Radiosonde. *Arkiv för Geofysik,* Bd 1, Nr 2.

Some Aspects of the Flow of Stratified Fluids

III. Continuous Density Gradients

By ROBERT R. LONG, the Johns Hopkins University[1]

(Manuscript received April 5, 1955)

Abstract

The investigations of Parts I and II are extended to include experiments and theoretical considerations relating to the behavior of fluid systems with continuous gradients of density. The general equation of steady-state motion derived in Part I is integrated to yield the flow of a stratified fluid over an obstacle of finite dimensions. The results indicate a more or less complicated laminar wave motion for obstacles of maximum height below a certain value. Larger barriers cause an overdevelopment of the waves to a point where closed circulations and negative horizontal velocities appear. It is shown that this is accompanied by locally unstable distributions of density and eventual turbulence. If the height of the barrier is further increased, the velocity increases indefinitely in some parts of the field, becoming infinite for an obstacle of a certain size. No steady-state solution exists for larger barriers. The two critical values of the obstacle height depend primarily on the Froude number: If this number exceeds $1/\pi$ the solution exists and is stable for all obstacles; for small Froude numbers the barrier must be small if the solution is to exist or be stable.

If the obstacle is small enough to permit laminar or moderately turbulent motion, the accompanying experiments verify all important features of the theory with remarkable fidelity. Larger obstacles cause considerable turbulence and blocking effects which propagate upstream, causing alternate maxima (jets) and minima of horizontal velocity in the vertical.

1. Introduction

Part I of this series of papers (Long 1953) contained a theoretical analysis of the steady-state flow of a stratified fluid over a barrier. Part II (Long 1954) represented an attempt to investigate experimentally the simplest possible system of this type: the flow of two superimposed layers of different density over a smooth boundary of finite dimensions. In the latter investigation it was possible to present an accompanying theory which explained rather well the observed behavior. In general shock waves or internal hydraulic jumps in the lee of the barrier are the only phenomena of any great importance and these occurred as predicted by the theory.

In many applications of stratified theory to natural phenomena, it has been assumed that a fluid system with continuous density gradient may be approximated by layered systems (Abdullah 1954, Tepper 1952). There is really no evidence to support such an assumption and it appeared to be desirable, for this and other reasons, to extend the theory and experiments to systems with continuous density stratification. It is the purpose of this paper to present the results of this investigation.

[1] This research was supported by the U.S. Weather Bureau. Presented at the 5th Congress of the OSTIV (Organisation Scientifique et Technique Internationale du Vol à Voile) at Buxton, England, 1954.

2. Preliminary theory

In Part I it was shown that the steady-state motion of a stratified fluid in a channel was governed by the equation

$$\nabla^2 y_0 + \frac{1}{2}[(\nabla y_0)^2 - 1]\frac{d}{dy_0}\ln(U^2\varrho) - \\ -\frac{g}{U^2\varrho}\frac{d\varrho}{dy_0}(y_0 - y) = 0 \qquad (1)$$

where y_0 is the height of a streamline far upstream, and $U(y_0)$, $\varrho(y_0)$ are the velocity and density distributions far upstream. The assumptions in the derivation of this equation are the following:

(1) The fluid is incompressible.

(2) The flow is steady and two-dimensional.

(3) Sufficiently far upstream from the source of disturbance (obstacle), $y_0 = y$ and the velocity and density distributions (U, ϱ) are known functions of the vertical coordinate.

The significance of assumption (3) should be emphasized. In effect it is assumed that the flow and density are initially given by $U(y)$, $\varrho(y)$. An obstacle is then inserted in the stream and a steady state is awaited. It is not only assumed that the flow reaches a steady state but that the velocity and density fields approach $U(y)$ and $\varrho(y)$ if we go sufficiently far upstream. It is conceivable that the obstacle could cause an alteration of the basic distributions U, ϱ to propagate indefinitely far upstream. In this case either the flow would never come to a steady state or else it would approach a new distribution $U'(y)$, $\varrho'(y)$ upstream.

Equation (1) is highly non-linear if $U(y_0)$, $\varrho(y_0)$ are assigned arbitrarily. If, however, we suppose that we deal with a model in which ϱ is linear in y_0 and $U^2\varrho$ = const we obtain the linear equation

$$\nabla^2\delta + \sigma^2\delta = 0, \quad \delta = y - y_0, \quad \sigma^2 = \frac{g}{U^2\varrho}\left|\frac{d\varrho}{dy_0}\right| \qquad (2)$$

In (2), δ represents the variation in height of the streamline y_0 = const about its equilibrium (upstream) height. A model with a linear density gradient is, of course, of considerable interest physically, but it is perhaps unlikely that we will encounter the condition $U^2\varrho$ = constant in practical applications. In geophysical problems involving stratification ϱ varies very slowly with height (the analogous quantity in the atmosphere is potential density). $U^2\varrho$ = const will then imply a very small increase of velocity with height. It may be hoped then that the present model will contain the essential features of a statified fluid with constant density gradient and uniform velocity. This is the viewpoint adopted in this paper; the experiments show that no sensible error results from the approximation.

3. Theoretical flow of a stratified fluid over an obstacle

The solution of equation (2) for flow in an infinite channel with rigid, parallel, upper and lower boundaries is straightforward provided the obstacle at the bottom of the channel is considered to be infinitesimal in height. The solution turns out to be indeterminate if σ exceeds a certain value, but it has long been recognized that this indeterminancy may be removed by introducing viscosity[1] (Rayleigh 1883). The simplest possible equation for such motion with damping is

$$\frac{\partial}{\partial x}(\nabla^2\delta' + \sigma^2\delta') = \mu\delta' \qquad (3)$$

The solution of (3) for the same boundary conditions is unique and when μ approaches zero, δ' approaches a solution of (2). The only effect of friction that remains when μ vanishes is the absence of wave motions upstream.

We are, however, interested in flow over an obstacle of finite height and this makes the standard approach by Fourier integrals so complicated that it is practically impossible. Lacking a better method, a finite solution was derived in the following manner: The solution was obtained first for an infinitesimal obstacle of some convenient shape. This solution is of the form

$$\delta = a f(x, y; \sigma, b) \qquad (4)$$

where b relates to the length of the barrier and a is the maximum height of the infinitesimal barrier. If in (4) we arbitrarily assign a finite

[1] Recently Stoker (1953) has shown that in the flow of a liquid with free surface, the indeterminancy is also avoided by solving the problem from an initial state, then letting $t \to \infty$.

value to a the resulting solution still satisfies (2) exactly. When the solution is plotted, the material curve $\gamma_0 = 0$ lies on the line forming the bottom of the channel everywhere except in the vicinity of the origin of x, where it rises into the channel, reaching a maximum height and then returning to the line $y = 0$. If we take the $\gamma_0 = 0$ curve as the new channel bottom, (4) represents, in effect, flow of the stratified fluid over a certain obstacle whose height and shape are obtained in the above indirect manner. A disadvantage of this method is that the resulting obstacle is not always symmetric about the line $x = 0$. The asymmetry is usually slight, however, and the height and length of the barrier can be varied by varying a and b.

We assume as the solution of (2) the following:

$$\delta(x \leq -b) = \delta_1 = \sum_{n=n_1+1}^{\infty} A_n e^{a_n x} \sin n\pi y \qquad (5)$$

$$\delta(-b \leq x \leq b) = \delta_2 =$$

$$= \sum_{0}^{\infty} E_n \cos \frac{n\pi x}{b} \sin \left(\sigma^2 - \frac{n^2\pi^2}{b^2}\right)^{1/2} (1-\gamma) +$$

$$+ \sum_{n=1}^{n_1} (F_n \cos a_n x + G_n \sin a_n x) \sin n\pi y +$$

$$+ \sum_{n=n_1+1}^{\infty} (H_n e^{a_n x} + M_n e^{-a_n x}) \sin n\pi y \qquad (6)$$

$$\delta(x \geq b) = \delta_3 = \sum_{n=1}^{n_1} (B_n \cos a_n x +$$

$$+ C_n \sin a_n x) \sin n\pi y +$$

$$+ \sum_{n=n_1+1}^{\infty} D_n e^{-a_n x} \sin n\pi y \qquad (7)$$

In these expressions the height of the channel is taken as 1, and the obstacle has a height $\gamma_s = f(x)$ for $-b \leq x \leq b$, $\gamma_s = 0$ elsewhere. The quantities E_n and a_n are

$$E_n = -\frac{1}{b \sin \left(\sigma^2 - \frac{n^2\pi^2}{b^2}\right)^{1/2}} \int_{-b}^{b} f(x) \cos \frac{n\pi x}{b}\, dx, \quad n \geq 1$$

$$E_0 = \frac{1}{2b \sin \sigma} \int_{-b}^{b} f(x)\, dx, \quad a_n = |\sigma^2 - n^2\pi^2|^{1/2} \qquad (8)$$

The integer n_1 is the last for which $(\sigma^2 - n^2\pi^2)$ is a positive quantity. The assumed solution satisfies equation (2) and the kinematic conditions at the top of the channel $y = 1$, at the bottom, $y = 0$ and, with the assumption that $f(x)$ is infinitesimal, the kinematic condition at the obstacle. Moreover, there are no upstream waves. The constants A_n, B_n, C_n, D_n, F_n, G_n, H_n, M_n are available to establish continuity at the lines $x = \pm b$. They are determined by requiring that δ and δ_x be continuous at these lines. Omitting this straightforward procedure, and choosing a special obstacle

$$f(x) = \frac{a}{2}\left(1 + \cos \frac{\pi x}{b}\right), \quad -b \leq x \leq b$$

$$f(x) = 0 \text{ elsewhere} \qquad (9)$$

we obtain

$$\delta_1 = -a \sum_{n=n_1+1}^{\infty} \frac{\gamma_n}{2} [e^{a_n(x+b)} - e^{a_n(x-b)}] \sin n\pi y \qquad (10)$$

$$\delta_2 = \frac{a}{2 \sin \sigma} \sin \sigma(1-\gamma) +$$

$$+ \frac{a \cos \frac{\pi x}{b}}{2 \sin \left(\sigma^2 - \frac{\pi^2}{b^2}\right)^{1/2}} \sin \left(\sigma^2 - \frac{\pi^2}{b^2}\right)^{1/2} (1-\gamma) +$$

$$+ a \sum_{n=1}^{n_1} \gamma_n \cos a_n(x+b) \sin n\pi y +$$

$$+ a \sum_{n=n_1+1}^{\infty} \frac{\gamma_n}{2} [e^{-a_n(x+b)} + e^{a_n(x-b)}] \sin n\pi y \qquad (11)$$

$$\delta_3 = -a \sum_{n=1}^{n_1} 2\gamma_n \sin a_n b \sin a_n x \sin n\pi y -$$

$$- a \sum_{n=n_1+1}^{\infty} \frac{\gamma_n}{2} [e^{a_n(x-b)} - e^{-a_n(x+b)}] \sin n\pi y \qquad (12)$$

The coefficient γ_n is

$$\gamma_n = \frac{n\pi}{\sigma^2 - n^2\pi^2} - \frac{n\pi}{\sigma^2 - n^2\pi^2 - \frac{\pi^2}{b^2}} \qquad (13)$$

The combined solution δ has the following properties:

(a) δ and its first derivatives with respect to x and y exist and are continuous for all x and y in the field of flow, except when $\sigma^2 = p^2\pi^2$, $p = 1, 2 \ldots$.

(b) Second derivatives of δ with respect to x and y ($\sigma^2 \neq p^2\pi^2$) exist for all x and y in the field of flow, except at the points $(b, 0)$, $(-b, 0)$. Equations (10)—(12) represent, therefore, a solution of (2) for flow in an infinite channel over an infinitesimal obstacle (9). The non-existence of the second derivative at the two boundary points is simply an expression of the non-existence of $f''(x)$ at these points. The significance of the exceptional values of σ will be discussed in section 6.

As previously indicated we may assign a finite value to a and obtain thereby the solution for flow over a certain finite obstacle. Since $\delta = y - y_0$, the equation for the obstacle $y = h(x)$ is

$$h(x) - \delta[x, h(x)] = 0 \qquad (14)$$

If $\sigma < \pi$ it is easily shown that δ has no nodal lines within the fluid running along the direction of the channel. (POCKELS 1891). Therefore the maximum height of the obstacle varies monotonically, being 1 when $a = \infty$. If $\sigma > \pi$, however, such nodal lines exist[1]. In this range the height of the obstacle approaches the height of the first nodal line above it as $a \to \infty$. Therefore, it is clearly impossible to obtain a steady state flow over an obstacle higher than this. The computations based on equations (10)—(12) indicate that the maximum obstacle may be varied somewhat by varying b, but for any reasonable value of b, including an indefinitely large half width, there is a maximum obstacle height when $\sigma > \pi$.

4. Solution for a very long obstacle

The solution for infinite b is very simple and illuminating. We are then only interested in the solution δ_2 (equation 11), which reduces to

$$\delta = \frac{a \sin \sigma(1-y)}{\sin \sigma} \qquad (15)$$

[1] It is apparent from equation (4) that the equation of the nodal curves is independent of a.

If the (nearly) constant height of the barrier is $\beta(x)$,

$$\delta = \beta(x) \frac{\sin \sigma(1-y)}{\sin \sigma(1-\beta)} \qquad (16)$$

It may be noted that this is the solution of the partial differential equation

$$\frac{\partial^2 \delta}{\partial y^2} + \sigma^2 \delta = 0 \qquad (17)$$

which is derived from (2) by assuming infinitely slow variations of δ in the direction along the channel. This is analogous to the hydrostatic assumption made in Part II. The singularities of this equation are the straight lines in fig. 1. We note again that if $\sigma < \pi$, the height, β, may have any value between 0 and 1. As in the full solution there is a singularity for infinitesimal barriers when $\sigma = p\pi$, $p = 1, 2, 3 \ldots$. Aside from these values of σ there is a maximum barrier for every $\sigma > \pi$ given by the distance from the $\beta = 0$ axis to the first straight, sloping line above it (denoted by $R_i = -\infty$). In general the larger σ the smaller the maximum obstacle.

For the solution (16), and for the full solution, non-existence corresponds to an infinite velocity at some points of the fluid. If the obstacle is near its maximum size we will have very high velocities and therefore very high shears. It is to be expected that this will lead to a breakdown into turbulence so that the solution may exist but be unstable. Moreover, in (16) a high obstacle means a negative velocity ($\sigma > \pi$) at some level and this corresponds in the full solution to closed circulations above or in the lee of the barrier. Since the density is constant on a streamline such a closed circulation implies, necessarily, local regions in which density *increases* vertically. This may be shown analytically as follows: Since $\varrho = \varrho_0 (1 - k y_0)$,

$$\frac{\partial \varrho}{\partial y} = -k \varrho_0 \frac{\partial y_0}{\partial y} \qquad (18)$$

However, the local velocity along the channel is

$$u = -\frac{\partial \psi}{\partial y} = -\frac{d\psi}{dy_0} \frac{\partial y_0}{\partial y} = U \frac{\partial y_0}{\partial y} \qquad (19)$$

so that

$$\frac{\partial \varrho}{\partial y} = -k \varrho_0 \frac{u}{U} \qquad (20)$$

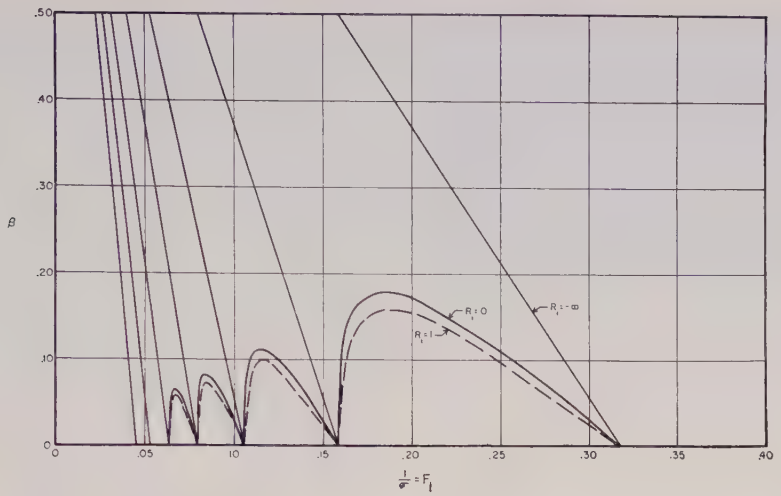

Fig. 1. Graph of solutions for flow over very long obstacle of height $\beta(x)$. The solid, straight lines ($R_i = -\infty$) represent the singularities of the solution (16). At the given Froude number, the distances from the abscissa to the first line, $R_i = -\infty$, above it is the maximum height of the barrier. The solution does not exist for a higher barrier. If the extreme height of the obstacle is the distance from the abscissa to the solid curve labeled $R_i = 0$, the velocity, u, is just zero somewhere in the fluid above the barrier. For a higher obstacle, closed cells appear and the solution is unstable. If the extreme height of the barrier is the distance to the dashed curve labeled $R_i = 1$, the Richardson number (24) falls to one somewhere in the fluid. For higher barriers $R_i < 1$, and shearing instability may arise.

The density increases with height (overturning instability) if $u < 0$. The exact criterion may be derived from (16):

$$\gamma_0 = \gamma - \frac{\beta \sin \sigma(1-\gamma)}{\sin \sigma(1-\beta)} \qquad (21)$$

Differentiating with respect to γ, the necessary and sufficient condition for overturning instability is

$$\min \left[1 + \frac{\sigma\beta \cos \sigma(1-\gamma)}{\sin \sigma(1-\beta)} \right] \leq 0 \qquad (22)$$

An investigation of (22) shows that the minimum occurs at nodal surfaces of the function $\delta = \gamma - \gamma_0$. If $\sigma < \pi$ the velocity u exceeds U everywhere and can never become negative. Hence *no overturning instability can occur for* $\sigma < \pi$ *regardless of the size of the barrier.*

When $\pi < \sigma < 2\pi$ the minimum occurs at the top of the channel where $\gamma_0 = \gamma = 1$ and this minimum will be negative if

$$1 - \frac{\sigma\beta}{|\sin \sigma(1-\beta)|} < 0 \qquad (23)$$

It is easily seen that (23) is the criterion for instability for all $\sigma > \pi$. The inequality (23) corresponds to the area above the curves marked $R_i = 0$ in fig. 1. We note that the lower the Froude number, the smaller the barrier must be to avoid the overturning instability. There is thus a considerable range in which the solution exists but is unstable.

It is possible, of course, that the fluid system may break down for even smaller obstacles than the ones indicated by the curves of (23), due possibly to shearing instability. We have no clear guide for this investigation, although an obvious choice is to plot the maximum obstacle for which the *minimum* Richardson number in the field is just equal to one, i.e. we *assume* for stability that

$$\min R_i \geq 1, \quad R_i = \frac{\frac{-g}{\varrho}\frac{\partial \varrho}{\partial y}}{\left(\frac{\partial u}{\partial y}\right)^2} \qquad (24)$$

Since U is practically constant, the Richardson number then becomes

$$R_i = \frac{\sigma^2 \left(\frac{\partial \gamma_0}{\partial \gamma}\right)}{\left(\frac{\partial^2 \gamma_0}{\partial \gamma^2}\right)^2} =$$

$$= \sin \sigma(1-\beta) \frac{[\sin \sigma(1-\beta) + \beta\sigma \cos \sigma(1-\gamma)]}{\beta^2 \sigma^2 \sin^2 \sigma(1-\gamma)} \quad (25)$$

Furthermore, min $R_i(\gamma) = R_i(\gamma_s)$ where

$$\left(\frac{\partial R_i}{\partial \gamma}\right)_{\gamma_s} = 0, \quad \left(\frac{\partial^2 R_i}{\partial \gamma^2}\right)_{\gamma_s} > 0 \quad (26)$$

These relationships define γ_s by the equation

$$\cos \sigma(1-\gamma_s) = -\frac{1}{\sigma\beta} \sin \sigma(1-\beta) \pm$$

$$\pm \sqrt{\frac{1}{\sigma^2\beta^2} \sin^2 \sigma(1-\beta) - 1} \quad (27)$$

Since the two terms on the right in (27) must be of opposite signs,

$$\cos \sigma(1-\gamma_s) = -\frac{1}{\sigma\beta} \sin \sigma(1-\beta) +$$

$$+ \frac{\sin \sigma(1-\beta)}{|\sin \sigma(1-\beta)|} \sqrt{\frac{1}{\sigma^2\beta^2} \sin^2 \sigma(1-\beta) - 1} \quad (28)$$

Therefore

$$\min R_i = \frac{|\sin \sigma(1-\beta)| \sqrt{\frac{1}{\sigma^2\beta^2} \sin^2 \sigma(1-\beta) - 1}}{2\sigma\beta \left\{1 - \frac{1}{\sigma^2\beta^2} \sin^2 \sigma(1-\beta) + \frac{|\sin \sigma(1-\beta)|}{\sigma\beta} \sqrt{\frac{1}{\sigma^2\beta^2} \sin^2 \sigma(1-\beta) - 1}\right\}} \quad (29)$$

Defining

$$x \equiv \frac{\sin \sigma(1-\beta)}{\sigma\beta} \quad (30)$$

the condition that min $R \geq 1$ is

$$-|x| + 2\sqrt{x^2 - 1} \geq 0 \quad (31)$$

This is satisfied in the regions below the curves marked $R_i = 1$ in fig. 1. We note that the $R_i = 1$ curves and the $R_i = 0$ curves are quite close, so that for practical purposes either may be chosen as the stability criterion.

5. Discussion of solution for flow over obstacle of finite length and height

Returning to the more important case of barriers of finite length, the problem of obtaining the pattern of flow, and information similar to the above, is one of laborious computation. This has been done for a number of values of σ and b, and for values of a yielding well-developed wave motion. The results are contained in figs. 6—13 in which the theoretical and comparable experimental flow patterns are shown together. In many of the calculated flows the obstacle is so large that closed cells appear. It need only be remembered that smaller values of a will eliminate these cells and yield a somewhat smaller barrier. Otherwise the pattern of flow will be unaffected. A discussion of the most important features o the motion is presented in the next section where a comparison is made with the experiments.

Computations were not performed for very small values of b. Such flow would be over very abrupt obstacles and in actual experiment boundary layer separation effects would dominate, rendering the theoretical solution almost useless.

We may observe from the computations leading to the above figures, and additional computations, the maximum obstacle for existence and for eliminating closed circulations. If the parameter a is given such large values that the obstacle approaches its maximum height for existence, the barrier obtained is very asymmetric, rising sharply on the upwind side and dropping very rapidly on the lee. The calculations were restricted then to obtaining the maximum obstacle for overturning stability (no closed circulations). The results are presented in fig. 2. They are analogous to the curves marked $R_i = 0$ in fig. 1. We note that the latter, based on the assumption of an infinitely long barrier, are very similar and provide a close approximation. Except near the singular values of the Froude number, the

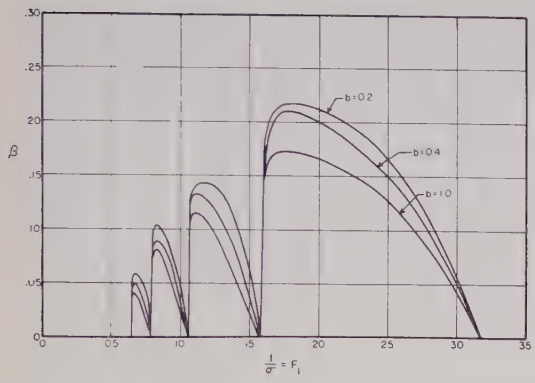

Fig. 2. Maximum obstacle heights for overturning instability in flow over a barrier of half length .2, .4, 1.0. The three curves give the maximum height of the barrier at a given Froude number. Higher obstacles will be associated with the appearance of turbulence at some points of the fluid. Smaller barriers will have laminar flow over them.

curves indicate, roughly, $\beta \cong F_i$ when overturning instability begins.

6. Experiments with a stratified fluid

The fact that the solutions in section 5 satisfy the frictionless equations of motion exactly, eliminates one of the major deficiencies of prior investigations of such systems, namely the assumption of infinitesimal obstacle heights. On the other hand, the basic velocity and density distributions $U^2\varrho = \text{const}$, ϱ linear, are not likely to be encountered in natural phenomena or experiment and the practical question arises as to the applicability to real systems in which the distributions of velocity and density are only approximations to these relationships. One system which can be produced experimentally is a basic velocity distribution $U = \text{const}$ and ϱ nearly linear and very slowly decreasing with height. In such a case the σ of equation (2) is nearly constant and any other terms that enter the complete equation (1) are small compared to the terms of (2). This type of system was investigated and a comparison made below between experimental results and the theory of section 3.

The physical set up is a long channel (fig. 3) containing a mixture of water and salt with a smooth density-height curve. An obstacle is towed by a motor drive at a constant speed along the bottom. The percentage density gradient from top to bottom is small (10 per cent or less). The density-height curve is roughly linear except at the top and bottom of the channel where the fluid tends to have a uniform concentration of salt. Using the speed of the barrier, the depth of the water and a representative density difference, we may compute for each experiment a Froude number

$$F_i = \frac{U}{\left(g \frac{\Delta \varrho}{\varrho} H\right)^{1/2}}$$

which is of the form of $1/\sigma$ in equation (2).

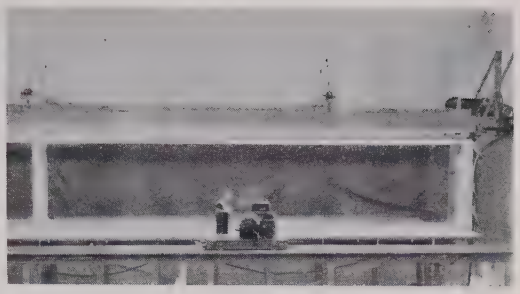

Fig. 3. Channel used for stratified fluid experiments. The entire channel is 20 ft long, 6 in wide and 2.5 ft high.

Considerable question arises regarding the computed Froude number of the experiments. The uncertainty is in the value of $\Delta\varrho/\varrho$. If the density gradients in the experiment were linear this would be simply the measured difference in density from top to bottom divided by the mean density. Actually the density gradients resemble that shown in fig. 4. As mentioned earlier, there is a considerable tendency to have a homogeneous layer at top and bottom. An explanation for this was suggested to the writer

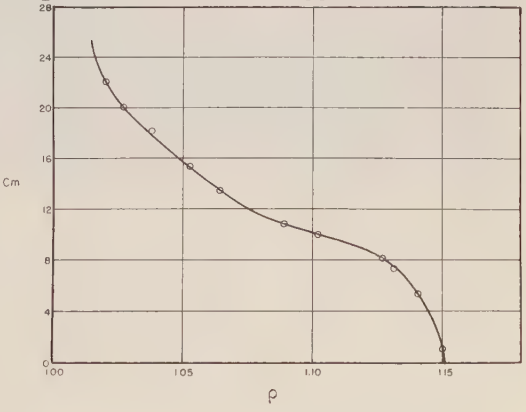

Fig. 4. Density-height curve for fig. 5.

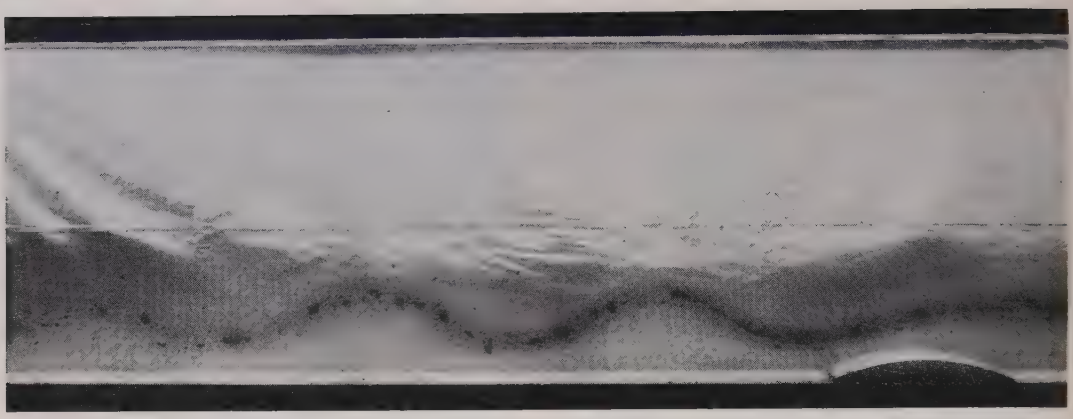

Fig. 5. Sine waves in flow over barrier. $F_i = .220$, $\beta = .137$, $b = .59$. The length of the waves is approximately 1.90.

by Sir Geoffrey Taylor, who remarked that if the mixing of the salt by turbulent diffusion be regarded as Fickian diffusion, the absence of flux of salt through the bottom and top surfaces would require the vanishing of the normal derivative of salt concentration, and a tendency for homogeneous layers at top and bottom.

The observed density distribution offers two possibilities for computing $\Delta\varrho$: the difference in density at top and bottom, or the $\Delta\varrho$ obtained by extrapolating the mean slope of the curve in the interior of the fluid. The flow pattern associated with the density curve in fig. 4 suggests an answer. Fig. 5 is the photograph of this flow. If $\Delta\varrho$ is taken as the density difference from top to bottom, the computed Froude number is .253; using the average gradient in the interior we obtain .220. Since the theoretical wave length is

$$\lambda = \frac{2\pi}{(F_i^{-2} - \pi^2)^{1/2}}$$

we obtain $\lambda = 2.64$, 1.94 respectively. Since the measured length is 1.90 (approximately), the fluid system seems to behave as if it had a linear density gradient equal to the average slope of the density curve in the interior. Because of this, the computed values of F_i in this paper are based on slope of the density curve in the interior of the fluid. It is perhaps of some importance meteorologically that a lower homogeneous layer (adiabatic layer) has no sensible effect on the phenomena.

The obstacles used in the experiments are of various sizes but all have an "easy shape" to reduce the effects of boundary layer separation. The ratio (β) of maximum obstacle height to the total depth is varied by using different obstacles and different fluid depths (H). Observations are made by recording the motion of aluminum tracer particles by a time exposure on a photographic plate. The camera is moved on a track at the speed of the obstacle so that the recorded flow is approximately steady.

The main features of the experiment are revealed in figs. 6—13 in which the flows are shown in the order of decreasing Froude number. Fig. 6 is flow at a very high speed. The motion involves only a symmetrical elevation of the streamlines over the barrier. Experimentally it resembles potential flow very closely. Theoretically, it is obvious that the density gradient generates some negative vorticity as the fluid rises over the barrier. This eliminates the need for the strong decrease of velocity with height that accompanies potential flow. As a result the vertical velocities extend to greater heights and the horizontal component increases by about the same amount at all levels. For purposes of comparison with the atmosphere we note that if we relate the total depth of fluid to the height of the tropopause, the Froude number of .350 corresponds to a mean velocity of 45 m/sec. The theoretical flow is for a somewhat higher Froude number but since both are above the critical number π^{-1} they are very similar.

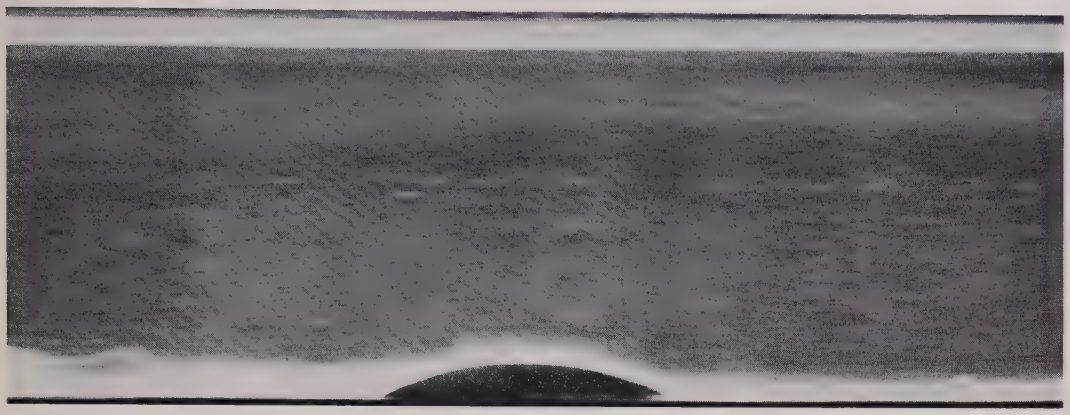

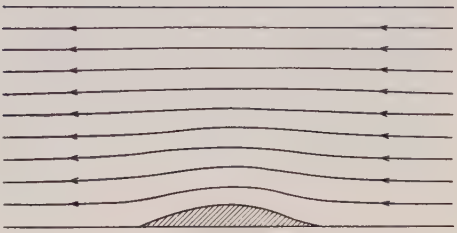

Fig. 6. Observed and calculated flow over an obstacle. Theoretical: $F_i = .500$, $\beta = .100$, $b = .4$, $a = .14$. Experimental: $F_i = .350$, $\beta = .092$, $b = .42$.

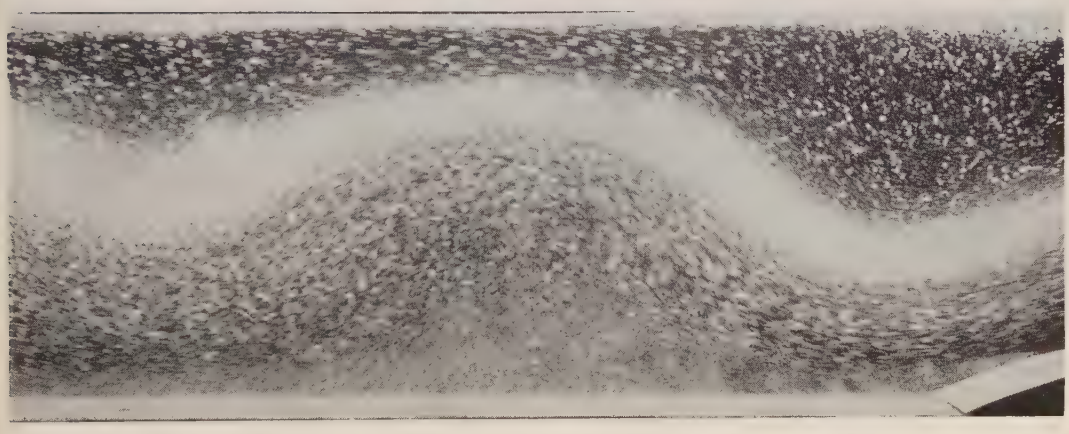

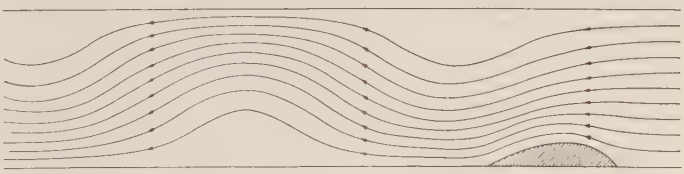

Fig. 7. Observed and calculated flow over an obstacle. Theoretical: $F_i = .250$, $\beta = .150$, $b = .4$, $a = .30$. Experimental: $F_i = .233$, $\beta = .151$, $b = .57$.

Fig. 7 shows a flow pattern at a Froude number in the range $(2\pi)^{-1} < F < \pi^{-1}$. A long wave appears in the lee. The theoretical wave length, at the F_i of the experiment (somewhat smaller than the F_i of the drawing), is 2.1 H, which is very close to the observed length. According to fig. 2 the β of the experiment is just below the value calling for zero horizontal velocities at some places in the field. We see in the photograph that a large region in the upper part of the channel just in thelee contains fluid at rest with respect to the barrier. There is no evidence of turbulence in this region; we would anticipate its onset for a somewhat larger value of β. The turbulence appearing near the bottom under the first crest of the wave is not due primarily to overturning or shearing instability but to boundary layer separation. In all experiments this effect tends to cause turbulence beneath the first crest in the lee. This is to be expected because this area corresponds to a minimum of velocity and therefore a maximum of dynamic pressure. The resulting adverse pressure gradient just upstream will cause separation. The fluid in the boundary layer is then carried into the body of the fluid to form a large turbulent eddy.

Fig. 8 is another example of flow in the range of a single sine wave in the lee. The obstacle is quite large; the waves have developed beyond the point of overturning instability. This is shown by the appearance of turbulence in the reversal region at the free surface just in the lee. This, and the turbulence below the first crest (due partly to boundary layer separation and partly to overturning instability), has removed so much energy that the waves further downstream are greatly weakened. The size of the obstacle is such that a theoretical solution exists although it is unstable. We see, nevertheless, that the obstacle is causing a blocking action upstream. This is evidenced by the shortness of the streaks in the fluid near the bottom ahead of the barrier. We have in this an indication that an alteration of upstream density and velocity distribution takes place in the range where a steady-state solution exists but is unstable.

Fig. 9 is flow below the second critical number, $F_i = 1/2\pi$. As shown in both theory and experiment the streamlines tend to open up in the region midway between top and bottom and just in the lee. At the F_i of the experiment fig. 2 indicates a reversal of velocity above a β of .075. Since the β of the experiment is well above this we have definite, turbulent eddies. The resultant loss of energy prevents the appearance of a second eddy downstream as predicted by the theoretical drawing, although there is evidence of a velocity reduction in the appropriate region downstream.

Fig. 10 represents a further reduction in F_i to the range $(4\pi)^{-1} < F_i < (3\pi)^{-1}$, and shows a remarkable array of eddies downstream, whose positions and distances correspond very closely to those in the theoretical drawing. The discrepancy in the two Froude numbers leads only to a shortening of wave length in the observed flow. Fig. 2 indicates a β of .087 for overturning instability at the F_i of .084. This is verified by the experiment, since the eddies appear slightly turbulent but not enough to prevent repetitions of the pattern downstream. It is interesting to note that the "S"-shaped streamlines above the barrier appear in both theory and experiment.

Fig. 11 is another example of flow in the range $(4\pi)^{-1} < F_i < (3\pi)^{-1}$. The obstacle is very large and the flow is therefore very turbulent. An outstanding feature is the exaggerated crest in the lee where the flow is strongly affected by boundary layer separation. In other respects the experiment and theory agree closely.

Fig. 12 is an example of flow in the range $(5\pi)^{-1} \leq F_i < (4\pi)^{-1}$. The theoretical flow is for a Froude number very close to the critical value $(4\pi)^{-1}$. The result is a well-developed wave motion for a very small barrier. The observed flow is at a Froude number corresponding to a β of .048 in fig. 2. Since the β in the experiment is .056 we would expect the definite turbulence in the eddies seen in the photograph. Moreover the tendency for blocking the lower fluid ahead of the barrier is very evident. The eddies just in the lee appear in the same position in the theoretical and experimental flows, and the other details correspond very closely.

Little effort was made to investigate the singular points of the theoretical solution in sections 4 and 5, i. e., the values of $\sigma = p\pi$. These singularities are expressions of the fact that a long wave of undetermined amplitude can exist at those values of σ in a channel with

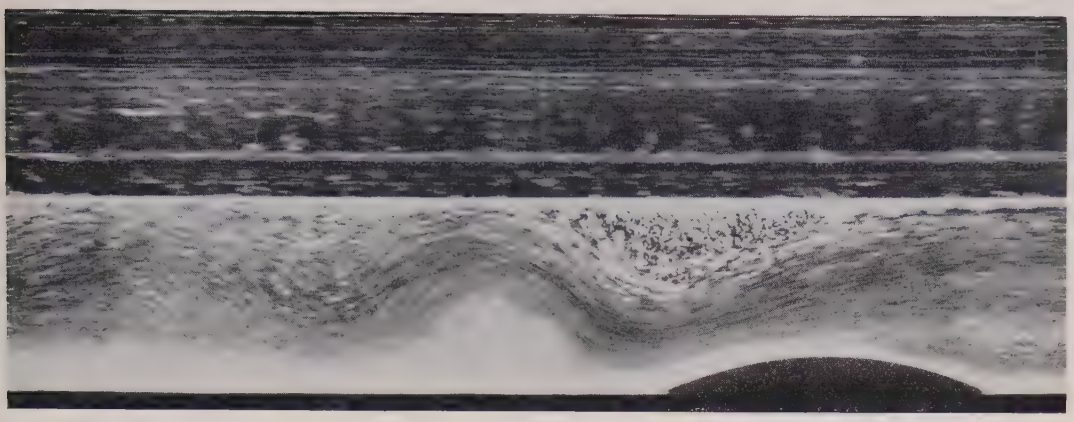

Fig. 8. Observed and calculated flow over an obstacle. Theoretical: $F_i = .200$, $\beta = .200$, $b = 1.0$, $a = .35$. Experimental: $F_i = .204$, $\beta = .200$, $b = .86$.

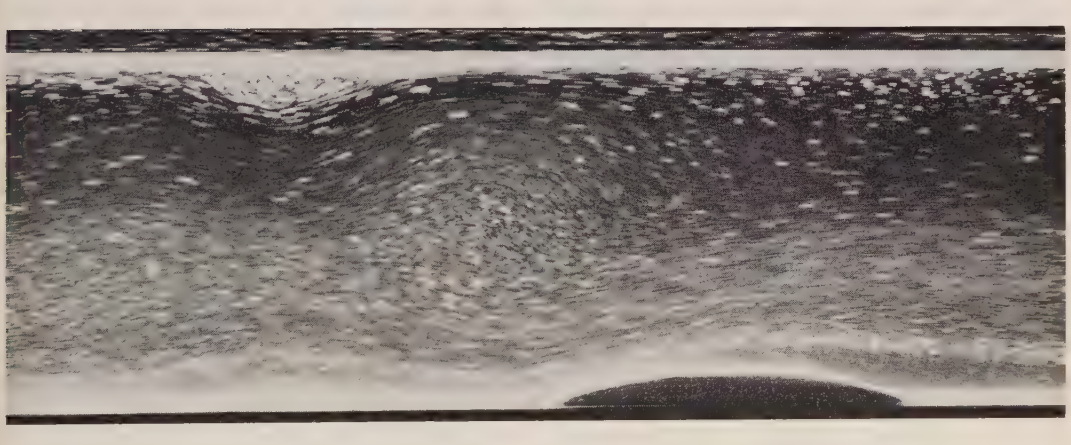

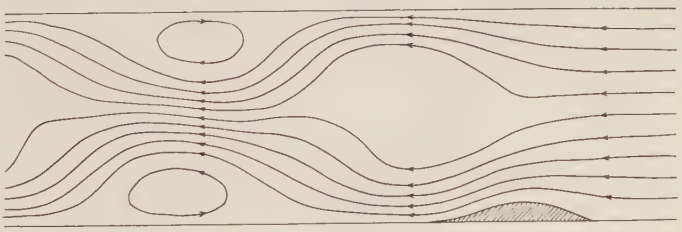

Fig. 9. Observed and calculated flow over an obstacle. Theoretical: $F_i = .143$, $\beta = .100$, $b = .4$, $a = .18$. Experimental: $F_i = .131$, $\beta = .085$, $b = .50$.

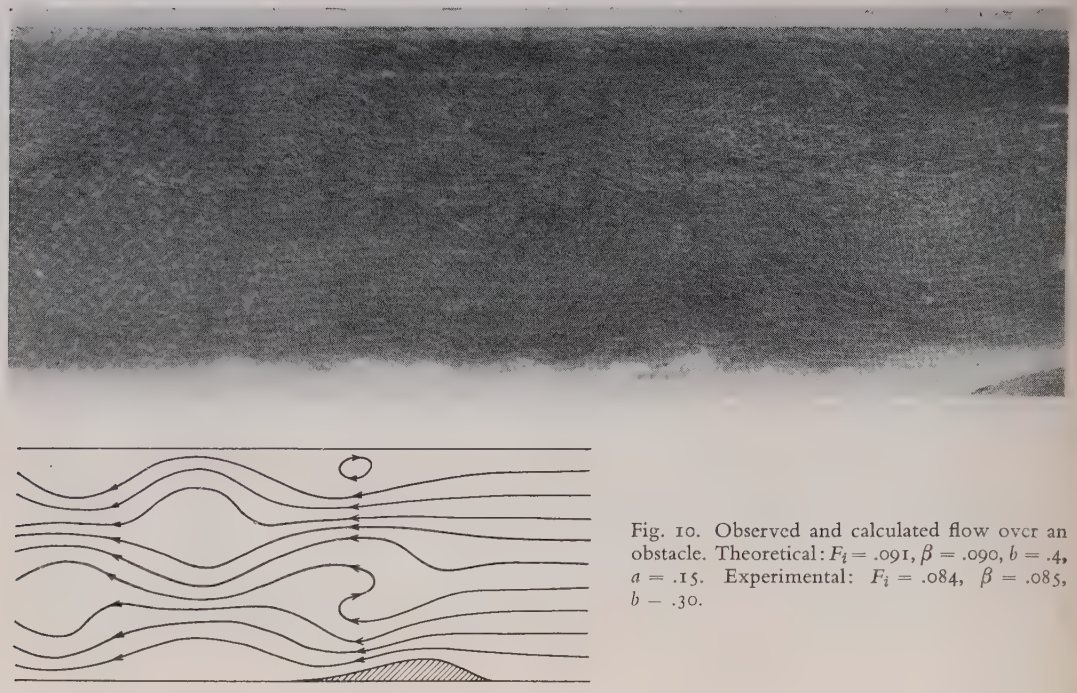

Fig. 10. Observed and calculated flow over an obstacle. Theoretical: $F_i = .091$, $\beta = .090$, $b = .4$, $a = .15$. Experimental: $F_i = .084$, $\beta = .085$, $b = .30$.

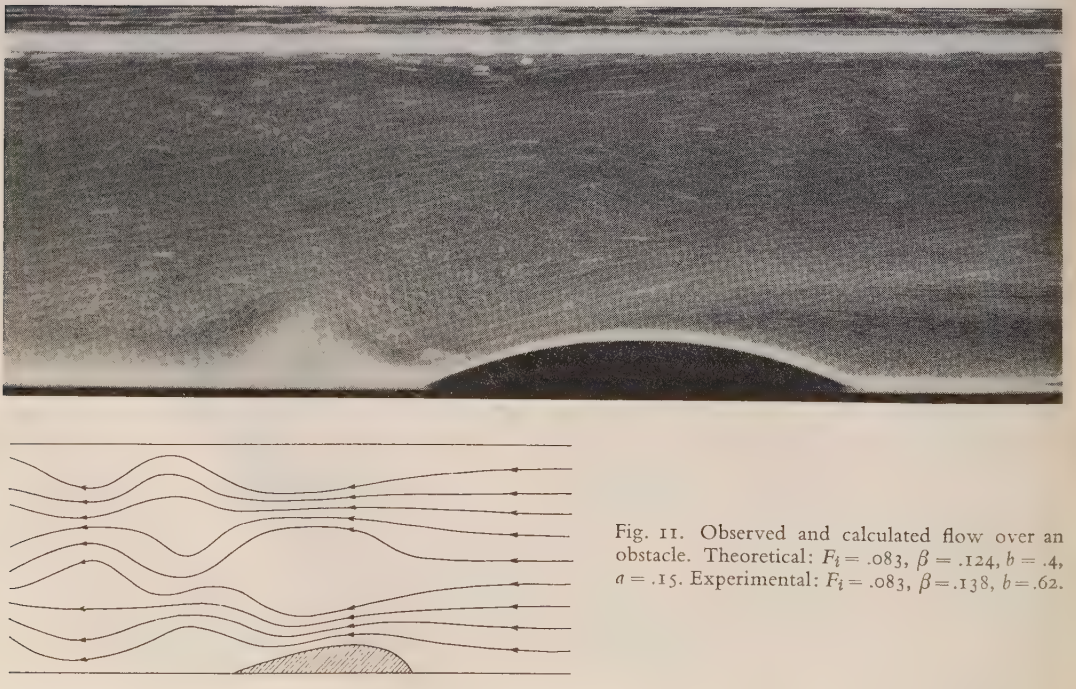

Fig. 11. Observed and calculated flow over an obstacle. Theoretical: $F_i = .083$, $\beta = .124$, $b = .4$, $a = .15$. Experimental: $F_i = .083$, $\beta = .138$, $b = .62$.

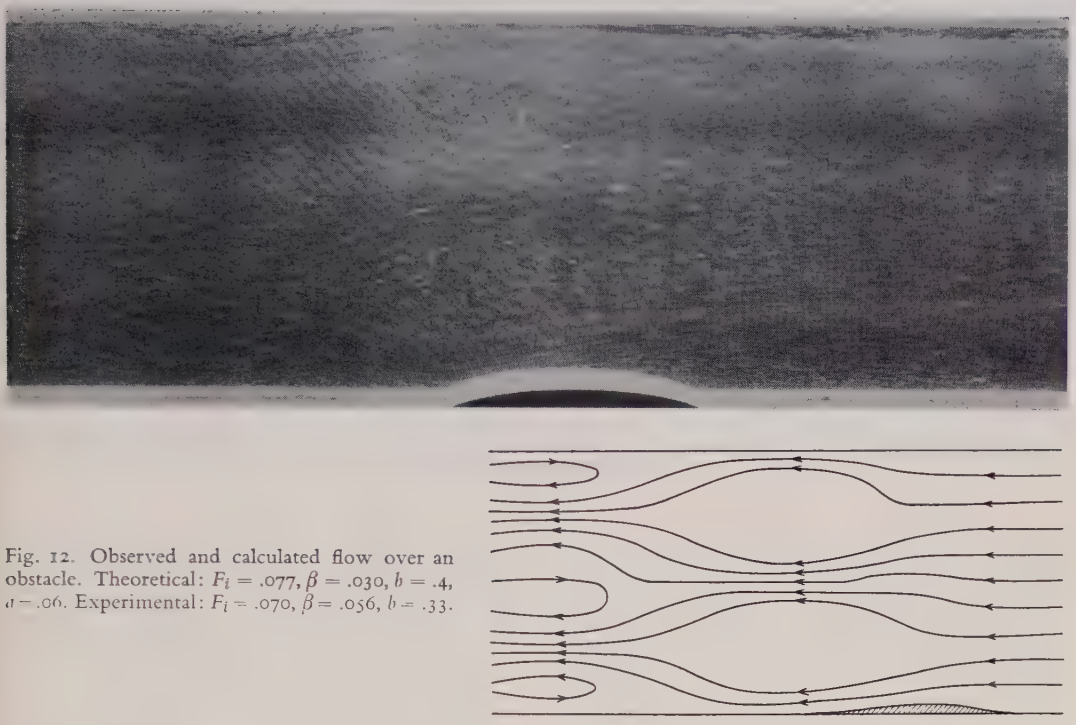

Fig. 12. Observed and calculated flow over an obstacle. Theoretical: $F_i = .077$, $\beta = .030$, $b = .4$, $a = .06$. Experimental: $F_i = .070$, $\beta = .056$, $b = .33$.

plane top and bottom. The same phenomenon occurs in the flow of water with a free surface over an obstacle at the critical Froude number $F^2 = U^2/gH = 1$. The singularity is removed by introducing friction as in equation (3) but the flow patterns remain exaggerated at $\sigma = p\pi$ unless the frictional coefficient is large.

It appears to be impossible to seek for these singularities in the experiment for several reasons: The foremost is the uncertainty in the calculated Froude number. The range of uncertainty is at least as large as the range of σ, on either side of $p\pi$, in which exaggerated wave patterns are indicated for small obstacles. Secondly, the experimental model has distributions of density and velocity upstream which differ from the theoretical model, and if the same kind of singularities exist for the actual conditions of the experiment, they will doubtless occur at Froude numbers sensibly different from $(p\pi)^{-1}$. Thirdly, the time period, from the beginning of the experiment until the recording of the motion by visual or photographic means, is finite and the corresponding time dependent solution may not possess any singularities. Finally it is likely that slight adjustments of the upstream velocity and density fields by blocking effects or other wave propagations upstream will be able to change the "Froude" number to a non-singular value. Such adjustments may not be observable.

An effort was made to investigate the singular value $\sigma = \pi$ by taking a number of photographs in a small range about this value. In this case the quasi-unsteady nature of the experiment made the effort unsuccessful. When σ was slightly less than π, a wave formed in the lee which simply became longer and longer as the experiment progressed. Presumably, it could be made arbitrarily long, and of vanishingly small amplitude, if a channel of very great length were available. Another investigation at values of σ near 2π simply indicated a gradual transition from a simple sine wave pattern for $\sigma < 2\pi$ to the more complex double wave system for $\sigma > 2\pi$.

7. Other experimental results

When the obstacle is very large, in the sense that the solutions of section 3 either do not exist or are unstable, the experiments tend to

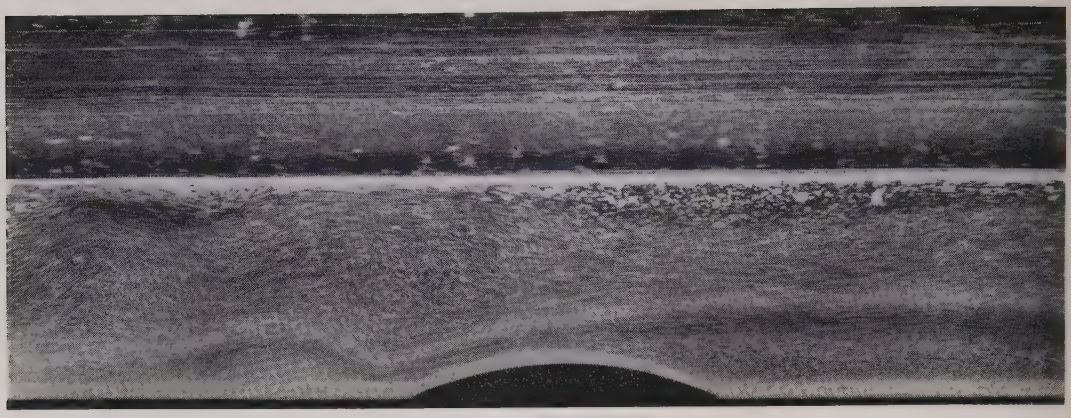

Fig. 13. Jet formation ahead of a large barrier. $F_i = .141$, $\beta = .165$, $b = .71$. Note the stagnation of fluid at top and bottom with jet in between.

indicate that a stable steady-state solution cannot be obtained theoretically even if we drop the assumption of unaffected flow far upstream or include viscosity. As the obstacle is raised in height impulses are sent upstream which lead to alternate jets and stagnation regions in the vertical (fig. 14). At the same time turbulence sets in over the obstacle and in the lee and this persists, at least down to very low Froude numbers. Obviously, this is not a steady state since turbulent fluctuations of velocity are, by their nature, non-steady. It thus appears hopeless to improve on the solution obtained in this paper either by dropping some of the assumptions or by including viscous terms. It is conceivable, of course, that a solution could be obtained as an initial value problem and that it should reveal developments for short time intervals from the initial instant. It is scarcely to be hoped, however, that a solution with viscosity included, is within the realm of possibility even using present high speed electronic equipment. This follows from the fact that the turbulence appears to set in as a large eddy (involving, initially, locally unstable density gradients) and then breaks down rapidly into smaller and smaller cells which would soon become smaller than the distance between grid points in any numerical integration.

It would be well, however, to examine the tendency for jet formation more closely. The fact that jets form and seem to move far upstream is of great importance to meteorology and oceanography. Experiments with homogeneous rotating fluids (Long 1954) indicate that rotation also favors jet formation so that it is likely that atmospheric and oceanic jet streams are due to these two effects. While this is not a new idea (Rossby 1951), it is not known just how rotational and gravitational stability work in creating these velocity maxima. Since the experiments show that the presence of gravitational stability alone is sufficient, it may be argued that a detailed understanding of this simpler phenomenon is a prerequisite for a physical understanding of atmospheric jets.

Such a detailed study has not been made for the purposes of this paper. We may note, however, that a Froude number of less than $1/\pi$ is a necessary requirement, and that the jets become more numerous as F_i is decreased. Fig. 13 is an example of a single jet, forming upstream in the interior of the fluid. The value of (.165) is considerably larger than the maximum for stability at this Froude number. Pronounced eddies therefore are formed in the lee. At the same time the large obstacle blocks the flow of fluid ahead of it both at the bottom and top; to preserve continuity the fluid speeds up in the interior forming a jet. For lower Froude numbers the jets increase in number; as many as 8 or 10 may be seen visually at values of F_i around .01. The ones in the upper part of the fluid are usually weak in such a case and not easily recorded by streak photography. Fig. 14, however, gives some indica-

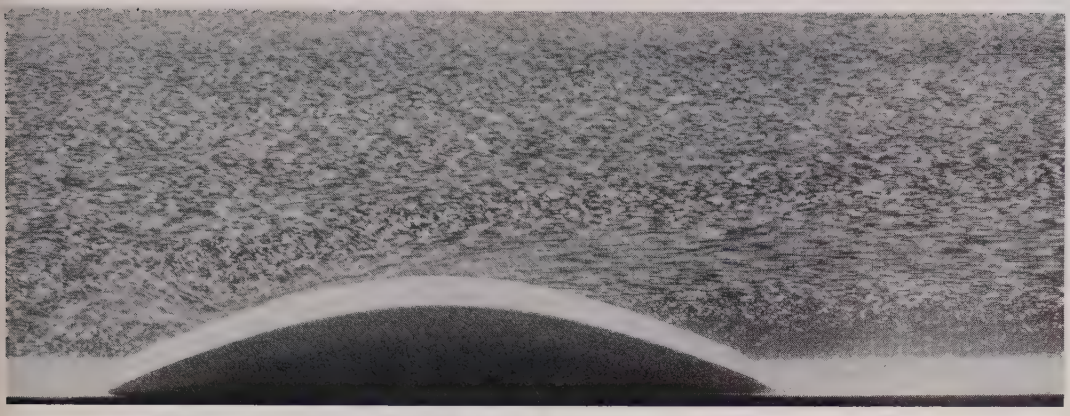

Fig. 14. Multiple jets ahead of the large barrier. $F_i = .017$, $\beta = .150$, $b = .56$. Note the complete blocking of the lowest layer of fluid and sharp velocity shear between this layer and the jet above it.

tion: four jets are visible just over the obstacle, in a depth of about .4 H. All but the lowest one weaken upstream. In many cases the jet nearest the bottom can be seen very easily at distances of 10 H ahead of the barrier, terminating at the end of the channel. The discontinuity of velocity at the bottom of the jet in fig. 14 is extremely sharp. Using the density gradient from top to bottom a local value of the Richardson number at the lower edge of the jet was computed. It is a maximum of .34, and probably smaller, yet no turbulence has appeared in the photograph. However, it is certain that the formation of the jet was accompanied by a very considerably intensification of the density gradient by vertical stretching in the lowest layer of fluid and vertical shrinking in the jet. It is likely that this has increased the Richardson number to a value above 1.0, permitting stability. Thus, the very process by which jets are formed in a stratified fluid presents an agency for their maintenance against turbulent dissipation.

The experiments shed considerable light on the behavior of stratified fluids with other than linear density gradients. If the gradient is confined to a discontinuity or near discontinuity of density across an interface, the phenomena may be expected to be those discussed in Part II, i. e., hydraulic jumps or shock waves in the lee at the interface. In the experiments of this paper the density gradients are obtained by putting first a layer of fresh water in the channel. Another layer of salt water is then inserted at the bottom. Initially a very sharp discontinuity of density exists in the interior. This is destroyed by repeated motions of an obstacle along the bottom. The first run reveals the same phenomena encountered in the flow of two immiscible layers: subcritical motion with little or no disturbance at low Froude numbers, followed by hydraulic jumps at the interface and finally supercritical flow at high Froude numbers. After a few more runs the wave motions typical of continuous gradients begin to appear; the hydraulic jump begins to take on the appearance of the turbulent reversal areas observed in the cases of "linear" gradients. The transition is quite clear if the obstacle is kept at a speed appropriate to the Froude number (.14) of fig. 9. The hydraulic jump develops continuously into the single large eddy in this photograph just downstream in the interior of the fluid. At the same time the more laminar wave motions of fig. 9 begin to appear.

An accompanying theory of non-linear density gradients is necessarily incomplete. If a near-discontinuity of density exists the theory of Part II is available to predict and explain the major features. If the slope of the density curve is smooth the experiments of this paper suggest that the gradient may be considered linear with little error. An intermediate situation involving a general gradient interrupted by one or more inversions (near-discontinuities) is a common one in the atmosphere. Such a model is still governed by equation (2), if we

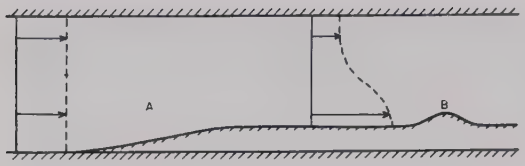

Fig. 15. Obstacle in channel yielding new basic current.

assume a steady state, but this equation is now highly non-linear and intractable. The experiments suggest that the shock-wave phenomenon will dominate if the inversions are very strong, the phenomena of this paper if they are weak.

8. Stratified model with shear and non-linear density gradient

We conclude this paper with a brief discussion of a more general model of a stratified fluid: one that possesses a certain shear of velocity with height in the basic current. In section 4 the solution (16) is valid for the motion of the stratified fluid in a channel whose bottom rises (or falls) very gradually at A in fig. 15, from $y = 0$ to $y = \beta = \text{const.}$ The streamlines and density surfaces will become parallel to the new bottom, but with a velocity and density distribution which we may compute from (16). If, further downstream at B, we disturb the new current in some way, say by inserting an obstacle of finite dimensions, equation (2) will still hold if δ is the variation of the streamline about its old equilibrium height, say y_{00}. However,

$$y_{00} = y_0 - \frac{\beta \sin \sigma(1 - y_0)}{\sin \sigma(1 - \beta)} \qquad (32)$$

where y_0 is now the equilibrium height of the streamline above $y = 0$, upstream of the barrier B but well downstream of A.

This concept leads to another model of a stratified fluid for which equation (1) is linear: In terms of the usual notations of this paper, if we specify a velocity and density distribution in a channel between $y = 0$ and $y = 1$ as

$$U^2\varrho = \alpha\,[1 + A\cos\sigma y_0 + B\sin\sigma y_0]^2 \qquad (33)$$

$$\frac{d\varrho}{dy_0} = \frac{-\sigma^2\alpha}{g}\,[1 + A\cos\sigma y_0 + B\sin\sigma y_0] \qquad (34)$$

we find that equation (1) reduces to

$$(\nabla^2 + \sigma^2)\left(y_0 - y + \frac{A}{\sigma}\sin\sigma y_0 - \frac{B}{\sigma}\cos\sigma y_0\right) = 0 \qquad (35)$$

In this model (which includes $U^2\varrho = \text{const.}$, ϱ linear as a special case), α, A, B, σ may be varied to obtain currents with various shears of wind with height and density gradients. For example, in the range of $2\pi > \sigma > \pi$, an obvious choice of A and B yields a basic current that is a maximum at the top of the channel and decreases to a minimum somewhere near the bottom. The accompanying density distribution is one of high stability in the upper part of the channel and low stability in the region of weak velocities. Evidently we must require that the velocity in the basic current be of one sign if we are to avoid regions of unstable density gradient. We note also that the disturbed configuration of the streamlines is independent of α.

Equation (35) may be solved for flow over a given obstacle in the manner of section 3. In addition the model may be produced experimentally by use of a long obstacle resembling that in fig. 15. Both the theoretical and experimental investigations are major undertakings and are outside the scope of this paper.

Acknowledgments

The author wishes to acknowledge the help of Mr. James F. Haubert in performing the experimental phases of this research. He was assisted by Messrs. Rudolf Kuster and Harry Mottek. The computations leading to the theoretical flow pattern were performed by Mr. William H. Adams.

REFERENCES

Abdullah, A. J., 1954: A proposed mechanism for the development of the eye of a hurricane. *J. of Meteor.* **11**, 189—195.

Long, R. R., 1953: Some aspects of the flow of stratified fluids. I. A theoretical investigation. *Tellus* **5**, 42—58.

— 1954: Some aspects of the flow of stratified fluids. II. Experiments with a two-fluid system. *Tellus* **6**, 97—115.

— 1954: The motion of an obstacle along the axis of a rotating fluid. Technical Report No. **6**, Contract N-onr-248(31).

Pockels, F., 1891: Über die partielle Differentialgleichung $\triangle u + k^2 u = 0$, Teubner, Leipzig, 339 pp.

Rossby, C.-G., 1951: On the vertical and horizontal concentration of momentum in air and ocean currents. *Tellus* **3**, 15—27.

Stoker, J. J., 1953: Unsteady waves on a running stream. *Communications on Pure and Applied Mathematics* **6**, 471—481.

Tepper, M., 1952: The application of the hydraulic analogy to certain atmospheric flow problems. *W. B. Research paper No. 35*, 50 pp.

Hydraulic Jump in a Fluid System of Two Layers

By CHIA-SHUN YIH and C. R. GUHA

Iowa Institute of Hydraulic Research

(Manuscript received October 1, 1954).

Abstract

The number of conjugate states for the flow of a fluid system of two layers is investigated by means of the momentum principle. The uniqueness of the conjugate state is proved for the cases in which the modified Froude number for either layer is predominantly large. Specific experimental results for three special cases demonstrate the uniqueness of the state downstream from the hydraulic jump, and show that, for a first approximation, the simple analysis provides a means for determining the downstream depths, with smaller errors for lower jumps.

Introduction

Although fluid motion in a stratified system was investigated more than a century ago by STOKES (1847), and not long afterwards by HELMHOLTZ (1868), WEBB (1884), GREENHILL (1887) and LOVE (1891), it is only during recent years that it has attracted the serious attention of oceanographers, meteorologists, and hydraulicians. As a result of the revived interest of the geophysicists, the subject is at present enjoying a period of intensive investigation. Among the recent contributors may be mentioned ROSSBY (1951), CRAYA (1951), KUELEGAN (1953), STOMMEL and FARMER (1952), TEPPER (1952), LONG (1953), and BENTON (1953).

In spite of the encouraging advancements of recent years, much is still to be learned about the subject and many questions at issue are yet to be settled. Among these the most important is the one concerning the determination of the state downstream from a hydraulic jump for a completely specified state upstream. It is with a view toward answering this question that an analysis based on simple assumptions was made for the case of two-layer flow and the relevant experiments were performed. The results obtained will be presented in the following sections of this paper.

Analysis

General Considerations

The system under study consists of two superposed layers of fluids flowing over a plane bottom. The upper surface is assumed to be free. For simplicity, the bottom is taken to be horizontal.

As indicated in Fig. 1, the density, the discharge per unit width, and the depths upstream and downstream from the hydraulic jump are respectively denoted by ϱ_1, q_1, h_1, and h_1' for the upper fluid, and by ϱ_2, q_2, h_2, and h_2' for the lower fluid. The gravitational acceleration is denoted by g. For fixed values of the densities, of the discharges, and of g, and for given upstream depths (h_1, h_2), the dynamically possible depths (h_1', h_2') downstream from the jump are said to be conjugate to (h_1, h_2), and the upstream and downstream states are conjugate by definition. A critical state is then defined as one which is conjugate

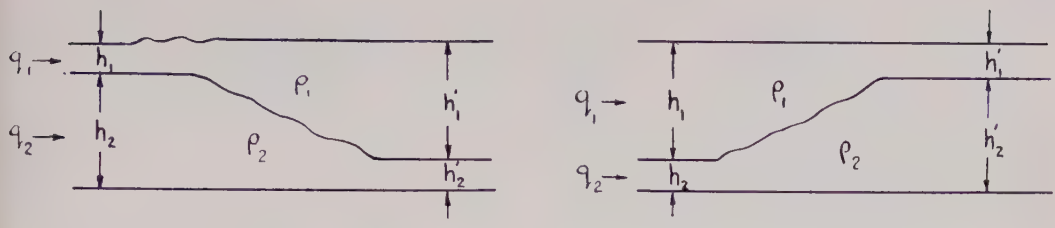

Fig. 1. Definition sketches (a) Normal jump (b) Inverted jump.

to itself, corresponding to an infinitesimal hydraulic jump. The number of conjugate states and the determination thereof will be the chief concern of the present analysis.

If a jump occurs in a fluid system of two layers, there is usually rather violent mixing at the interface. The interfacial shear is generally larger than the shear at the solid boundary, and cannot be neglected without introducing sizable error except under favorable conditions. Furthermore, due to the motion of the fluids the pressure distribution is no longer hydrostatic. As is well known, the distribution of the dynamic part of the pressure at the interface depends directly on the existence and location of the point of separation and therefore indirectly on the distribution of the interfacial shear. Since so little is known about the interfacial shear, it is evident that a rigorous theory cannot be achieved at present. However, if one is content with a first approximation, an *a priori* analysis can be constructed by neglecting the interfacial shear and assuming hydrostatic distribution for the pressure. This analysis will at least yield some conclusions of a qualitative nature which may be expected to hold even if interfacial shear is to be taken into account. Furthermore, for low jumps its conclusions may even be quantitatively correct. Thus, at the present stage of its development, the subject may well benefit from such an analysis.

Neglecting the shear, assuming hydrostatic distribution of pressure, and taking the mean head over the jump section as $^1/_2\,(h_1+h_1')$, one has, by applying the momentum principle to the lower layer,

$$\varrho_2 q_2^2\left(\frac{1}{h_2'}-\frac{1}{h_2}\right)=h_2 h_1 \varrho_1 g+\frac{1}{2}h_2^2\varrho_2 g+\frac{1}{2}(h_1+h_1')\cdot$$

$$\cdot\,(h_2'-h_2)\,\varrho_1 g-h_2'h_1'\varrho_1 g-\frac{1}{2}h_2'^2\varrho_2 g \qquad (1)$$

This can be rewritten as

$$2a_2\,(h_2-h_2')=h_2\,h_2'\,(h_2+h_2')\,[r\,(h_1-h_1')+$$
$$+(h_2-h_2')] \qquad (2)$$

in which

$$a_2=\frac{q_2^2}{g},\quad r=\frac{\varrho_1}{\varrho_2}$$

Similarly, one obtains, for the upper layer,

$$2a_1(h_1-h_2')=h_1h_1'(h_1+h_1')\,[(h_1-h_1')+$$
$$(h_2-h_2')] \qquad (3)$$

in which

$$a_1=\frac{q_1^2}{g}$$

Given h_1 and h_2, one has to solve Eqs. (2) and (3) simultaneously for the conjugate depths h_1' and h_2'. Since these equations are all of the third degree in h_1' and h_2', there are in general nine solutions. One solution is obviously $h_1'=h_1$ and $h_2'=h_2$. Thus at first sight there may be as many as eight other solutions representing eight states conjugate to the given one. However, to have a physical meaning, the solutions must be real and positive. Therefore, the number of conjugate states is decided by that of the positive solutions of Eqs. (2) and (3), aside from the obvious one corresponding to the given state.

It may be noted that since the critical state is conjugate to itself by definition, the differences $h_1'-h_1$ and $h_2'-h_2$ are infinitesimal, and may be replaced by the differentials dh_1 and dh_2. Equations (2) and (3) then become the differential equations

$$\frac{dh_2}{dh_1}=\frac{rh_2^3}{a_2-h_2^3} \qquad (4)$$

$$\frac{dh_1}{dh_2}=\frac{h_1^3}{a_1-h_1^3} \qquad (5)$$

from which it immediately follows that

$$h_1^3 = \frac{a_1(a_2 - h_2^3)}{a_2 - (1-r)h_2^3} \qquad (6)$$

in which h_1 and h_2 are now the critical depths. This equation was already given by BENTON (1953) in an elegant manner from a somewhat different approach. Thus the present definition of a critical state is equivalent to that of Benton.

To investigate the number of conjugate states, one starts by tracing the graphs of Eqs. (3) and (2), using h_1' and h_2' as the variables. For this purpose these equations are rewritten as:

$$h_2' = \frac{2a_1(h_1' - h_1)}{h_1 h_1'(h_1 + h_1')} + h_2 - (h_1' - h_1) \qquad (3\,a)$$

$$h_1' = \frac{2a_2(h_2' - h_2)}{r h_2 h_2'(h_2 + h_2')} + h_1 - \frac{h_2' - h_2}{r} \qquad (2\,a)$$

From Eq. (3 a), it can be seen immediately that h_2' has a discontinuity at $h_1' = -h_1$ and $h_1' = 0$ in such a way that $h_2' = -\infty$ for $h_1' = -h_1 - 0$ and for $h_1' = +0$, and $h_2' = +\infty$ for $h_1' = -h_1 + 0$ and for $h_1' = -0$. Furthermore, for large values of $|h_1'|$, h_2' behaves like $-h_1'$.

Now if h_2' in Eq. (3 a) is differentiated twice and the result equated to zero, the following equation is obtained:

$$h_1'^3 - 3h_1'^2 - 3h_1' h_1^3 - h_1^3 = 0$$

the only real root of which is

$$h_1' = h_1(2^{1/3} - 1)^{-1} \qquad (7)$$

corresponding to a point of inflection of the graph of Eq. (3), located to the right of the h_2'-axis. Differentiating Eq. (3 a) once with respect to h_1' and setting the result to zero, one has

$$2a_1(h_1^2 + 2h_1 h_1' - h_1'^2) - h_1 h_1'^2 (h_1 + h_1')^2 = 0 \qquad (8)$$

the roots of which correspond to the maxima and minima of h_2'. The left side of Eq. (8) is definitely negative for $h_1' < -h_1$, so that there can be no maxima or minima for such values of h_1'. Since $h_2' = +\infty$ for $h_1' = -0$ and $h_1' = -h_1 + 0$, and since there is no point of inflection for negative values of h_1', there is only one minimum of h_2' in the range $-h_1 < h_1' < 0$. For $h_1' = +0$ and $h_1' = +\infty$, Eq. (3 a) shows that $h_2' = -\infty$. With the only point of inflection given by Eq. (7), there can be only one maximum for positive values of h_1'. This can occur only at a value of h_1' smaller than that given by Eq. (7). Furthermore, $h_2' = -\infty$ for $h_1' = -h_1 - 0$, and the function h_2' is monotonic for $h_1' < -h_1$. From the foregoing considerations, the graph of Eq. (3) or (3 a)—with branches I, II, and III—can be traced, and is shown in Fig. 2 in dimensionless terms.

Similarly the graph of Eq. (2) or (2 a) can be traced, as shown in Fig. 2 with branches IV, V, and VI. It is evident that I intersects IV and VI, VI intersects III, and the lower branch of VI intersects the left branch of III. The intersections will be denoted by A, B, C, and F. Furthermore, it should be noted that the left branch of III and the lower branch of VI have no point of inflection. These facts will prove useful in the investigation of the number of intersections of III and VI, which of all possible intersections, alone have positive coordinates and thus determine the number of conjugate states.

If one writes

$$\Delta h_2 = h_2' - h_2^3, \quad \Delta h_1 = h_1' - h_1 \qquad (9)$$

and equates the expressions for $\Delta h_2/\Delta h_1$ obtained from Eqs. (2) and (3), one has

$$\frac{2F_1}{x(x+1)} - 1 = r\left(\frac{2F_2}{2F_2 - y(y+1)} - 1\right) \qquad (10)$$

in which

$$F_1 = a_1/h_1^3,\ F_2 = a_2/h_2^3,\ x = h_1'/h_1,\ y = h_2'/h_2 \qquad (11)$$

By a translation of coordinates Eq. (10) can be reduced to the symmetrical form

$$\left[\xi^2 - \left(\frac{1}{4} + 2F_1'^2\right)\right]\left[\eta^2 - \left(\frac{1}{4} + 2F_2'^2\right)\right] = \frac{4rF_1^2F_2^2}{(1-r)^2} \qquad (12)$$

in which F_1' and F_2' are the modified Froude numbers defined by

$$F_1'^2 = F_1^2(1-r)^{-1},\ F_2'^2 = F_2^2(1-r)^{-1} \qquad (13)$$

and

$$\xi = x + \frac{1}{2},\ \eta = y + \frac{1}{2}$$

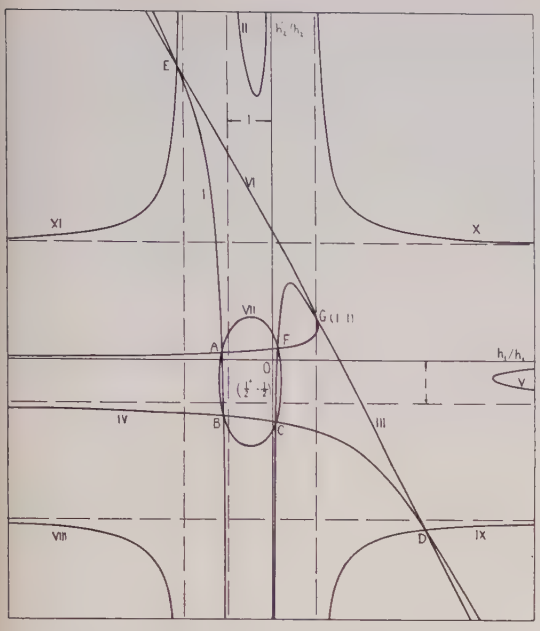

Fig. 2. Graphs of the momentum equations and of Eq. (10) or (12)

The solutions of Eqs. (2) and (3), except the one corresponding to the given state, are those of Eqs. (2) and (10), or those of Eqs. (3) and (10).

The graph of Eq. (10) can be easily traced, and is shown in Fig. 2—branches VII to XI. It is symmetrical with respect to the lines $x = -\frac{1}{2}$ and $y = -\frac{1}{2}$, and consists of one closed convex piece around the center $\left(-\frac{1}{2}, -\frac{1}{2}\right)$ and four branches of a hyperbolic shape with asymptotes

$$x = -\frac{1}{2} \pm \left(\frac{1}{4} + 2F_1'^2\right)^{1/2}$$

$$y = -\frac{1}{2} \pm \left(\frac{1}{4} + 2F_2'^2\right)^{1/2} \qquad (14)$$

It is immediately clear that IX must intersect III at a point D and XI must intersect VI at a point E. Since there are already five intersections A, B, C, D, and E which are not those of III and VI, these two branches can intersect in four points at most. That is, for a given state, there can be at most three conjugate states.

Since there is no point of inflection on I, IV, the left branch of III, and the lower branch of VI, these can intersect VII (which is convex) only at A, B, C, and F, as shown in Fig. 2. It is then obvious that III, VI, and VII cannot intersect simultaneously at any point other than F. For otherwise the point, being on III, would lie to the right of F, and being on both VI and VII, would have an ordinate at once greater and smaller than that of F. Thus, if X does not meet III and VI, there can be only two points at which III intersects VI, namely, G (1, 1) and F, G representing the given state and F representing the unique conjugate state.

A few *sufficient* conditions for the uniqueness of the conjugate state can be easily obtained. From Eqs. (8) and (3a) it is evident that the maximum ordinate on III depends on a_1, h_1, and h_2 only. But from Eq. (14) the horizontal asymptote of X can be so far above the x-axis for predominantly large values of F_2' that X and III, and consequently III and VI, do not intersect. Similarly if F_1' is predominantly large X and VII and consequently III and VII do not meet. Thus, under these conditions, the conjugate state is unique. It should be noted that whenever these conditions are satisfied, the conjugate depths are either both greater or both smaller than the corresponding depths of the given state—in other words, any jump that occurs cannot be primarily internal in character.

The results concerning the finiteness of the number of conjugate states in general and the uniqueness of the conjugate state under special conditions are in direct contrast to Benton's claim (Benton, 1953) that, given a complete description of the upstream state, infinitely many downstream states are possible. It seems improbable that the present conclusions would be invalidated if shear were to be taken into account, since the process involved would still —perhaps *a fortiori*—have a deterministic nature.

If the conjugate state is unique, whether a hydraulic jump can occur is decided, as usual, from energy considerations. Otherwise several situations may present themselves. If the energy flux for the given state is less than that of each of the three conjugate states, a jump cannot occur, whereas if it is greater than that for one of the conjugate states only, a jump can occur and the downstream state is unique if

it occurs. In all other situations a jump can occur but, if it occurs, the downstream state cannot be uniquely determined by momentum and energy considerations alone, and which of the two or three possible conjugate states will be realized after a jump depends primarily on the controls downstream.

Since the validity of the momentum equations and the uniqueness of the downstream state are to be tested for three cases of primarily internal jumps, specific results from Eqs. (2) and (3) will be given here for these cases. For the case in which the downstream velocities are the same for both layers, one has

$$\frac{q_1}{q_2} = \frac{h_1'}{h_2'} = \lambda$$

and Eq. (2) becomes

$$(1 + r\lambda)\left(\frac{h_2'}{h_2}\right)^3 + r\left(-\frac{h_1}{h_2} + \lambda\right)\left(\frac{h_2'}{h_2}\right) -$$

$$-\left(1 + r\frac{h_1}{h_2} + 2F_2^2\right)\left(\frac{h_2'}{h_2}\right) + 2F_2^2 = 0 \qquad (15)$$

This equation has two positive roots: one is $h_2' = h_2$, corresponding to the given state, and the other corresponds to the conjugate state. If the upper layer is at rest, $a_1 = 0$, and from Eqs. (2) and (3) one obtains

$$\frac{h_2'}{h_2} = \frac{1}{2}\left(\sqrt{1 + 8F_2'^2} - 1\right) \qquad (16)$$

Similarly, if the lower layer is at rest, one has

$$\frac{h_1'}{h_1} = \frac{1}{2}\left(\sqrt{1 + 8F_1'^2} - 1\right) \qquad (17)$$

One notes in Eq. (16) that if h_2' is greater than h_2 by a finite amount, F_2' is definitely greater than 1. Physically, this means that the velocity q_2/h_2 must be greater than the celerity of the fastest long waves of infinitesimal amplitude in order to hold the finite jump in place, i.e., finite disturbances progress faster than infinitesimal ones. In this light, Eq. (16) can be considered as a formula giving the celerity of progression of disturbances of finite amplitudes. In fact, the greater the ratio $\Delta h_2/h_2$, the greater the celerity. The same remarks can be made in connection with Eq. (17).

It may be noted also that, if $a_1 = 0$, from Eq. (3) it follows that the free surface is level, whereas if $a_2 = 0$ but $a_1 \neq 0$, Eq. (2) gives $r\Delta h_1 = -\Delta h_2$, and the free surface is not level. Of course, if $a_2 = 0$ and r is very near 1, the change in the free-surface elevation is imperceptible. The truth of the foregoing remarks has been verified in the experiments performed to establish the validity of Eqs. (15) to (17). These experiments will be presented in the following section.

Experimental results

To test the validity of the momentum equations and the uniqueness of the downstream state if a jump occurs, experiments were carried out for three cases[1]. In the first case, the upper fluid was at rest, and the jump of the lower fluid was upward (normal jump). In the second case, the lower fluid was at rest, and the jump of the upper fluid was downward (inverted jump). In the third case, both fluids were in motion, but in such a way that the downstream velocities were the same for both layers. The limitation on the downstream condition for the third case was imposed by an experimental artifice which had to be adopted for the sake of expediency. Experimentally it would be rather difficult and expensive to enable the discharges to vary independently and to realize a stationary jump with two moving layers. Instead of attempting to have a stationary jump, one tried to obtain a surge by filling a channel sealed at the downstream end with the lighter fluid, and discharging the heavier fluid into it at the bottom. As the lower fluid reached the end of the channel, it rose in height to form a surge which moved upstream with a celerity depending on the actual discharge of the lower fluid and the upstream depths. On taking velocities relative to the surge, the situation of two moving layers was achieved, but with the restriction that the downstream velocities were necessarily the same for both layers.

Water was used for the moving fluid in het first two cases (stationary jumps), and for het

[1] The experiments for Cases 1 and 2 were performed by the second author for his M. S. Thesis at the Iowa Institute of Hydraulic Research. The first author is responsible for the rest of the material contained in this paper.

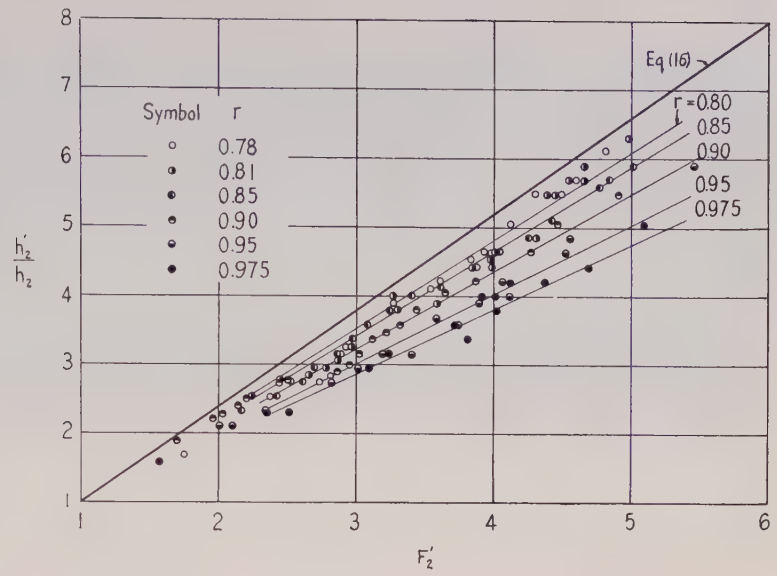

Fig. 3. Experimental results for the normal jump

lower fluid in the third case (surge). The other fluid used was either stanisol (an oil prepared by the Standard Oil Company, with specific gravity 0.777), or a mixture of stanisol and carbon tetrachloride (specific gravity 1.59). Since stanisol has a kinematic viscosity of about 3.4×10^{-5} ft^2/sec, is not highly inflammable, and mixes well with carbon tetrachloride to form a homogeneous mixture, it was found to be quite suitable to use. For easy visualization of the interface, the oil or oil mixture was always dyed red.

The lucite flume used was 4 feet long, 6 inches wide, and 8 inches deep. For stationary jumps the depths were controlled by one upstream gate and one downstream gate. The upstream gate was designed to ensure parallel flow of the water into the channel, and the downstream gate was designed to reduce entrainment of oil. The discharge of water was controlled by a valve upstream and measured by a triangular weir downstream. A supply of oil was maintained to compensate for the loss due to entrainment. For the moving jump the total depth was controlled by horizontal slots on the side of the channel near the upstream end. As the water entered the sealed channel, the oil would spill over the lowest open slot, so that an approximately constant total depth was maintained at the upstream end. The depth of the water at entrance was not controlled, but was found to be about half an inch. With the total depth at the entrance controlled by the slots, different combinations of (h_1, h_2) could be achieved. The discharge was again controlled by an upstream valve, and was measured through the celerity of the moving jump and the water depths upstream and downstream from the jump. All depths were measured either visually or photographically.

Before the experimental results are presented, it may be noted that the variables h_2' and h_2' depend on h_1, h_2, ϱ_1, ϱ_2, g, q_1, q_2, and the dynamic viscocities μ_1 and μ_2. If h_2' is taken as the dependent variable, a dimensional analysis shows that

$$\frac{h_2'}{h_2} = \left(\frac{h_1}{h_2}, \frac{q_1}{q_2}, \frac{\mu_1}{\mu_2}, r, F_2, R_2\right) \qquad (18)$$

in which F_2 is the Froude number for the lower layer and $R_2 = q_2 \varrho_2/\mu_2$ is the Reynolds number for the same layer. Equation (18) can be used to correlate the data obtained for Case 3 and Case 1 (for which $q_1/q_2 = 0$). For Case 2, a similar analysis yields

$$\frac{h_1'}{h_1} = F_1\left(\frac{h_1}{h_2}, \frac{\mu_1}{\mu_2}, r, F_1, R_1\right) \qquad (19)$$

in which F_1 and R_1 are respectively the Froude number and the Reynolds number for the upper layer. From Eq. (2) it follows that h_2'/h_2 does not depend on μ_1/μ_2 and R_2 according to the simple theory. Furthermore,

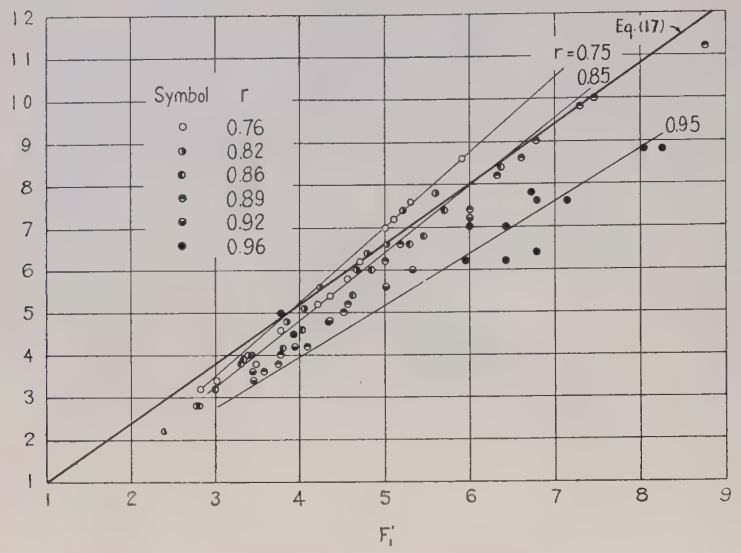

Fig. 4. Experimental results for the inverted jump

Eqs. (16) and (17) indicate that in Cases 1 and 2, respectively, the ratios h_2'/h_2 and h_1'/h_1 depends only on F_2 and F_1'. In other words, according to the simple theory, the parameters h_1/h_2, μ_1/μ_2, and R_2 or R_1 have no effect on h_2'/h_2 or h_2'/h_1, the effect of r and F_2 are embodied in F_2' in Case 1, and those of r and F_1 are embodied in F_1' in Case 2. To what extent the theoretical predictions are valid will be shown by the experimental results.

The results for the normal jump are shown in Fig. 3, from which it can be seen that the ratio h_2'/h_2 depends not only on the modified Froude number F_2', but also on the density ratio r. But F_2' and r seem to determine h_2'/h_2 uniquely in the range of experimentation. The points all lie below the theoretical curve, with increasing deviation for increasing r and F_2'. The results show that for increasing modified Froude number and density ratio, the effect of shear (chiefly interfacial shear) becomes increasingly important. The free surface was found to be level as expected.

Results for the inverted jump (Fig. 4) show similar trend, except that some points lie above the theoretical curve. The greater scatter is partly due to the difficulty of ascertaining the upstream depth h_1, since an undular jump occurred at the free surface. The free surface was observed to be definitely higher after the jump.

Figure 5 shows the result obtained for Case 3, the velocities being taken relative to the surge. The abscissa is the theoretical value of h_2'/h_2 computed from Eq. (15), and the ordinate is the experimental value of the same ratio. Here it can be seen that except for very high jumps the theoretical prediction is very well verified experimentally. Since h_1^3 was always large as compared with a_1, the free surface could be expected to be almost level according to Eq. (3). As can be seen from Plate 1, this expectation was well verified.

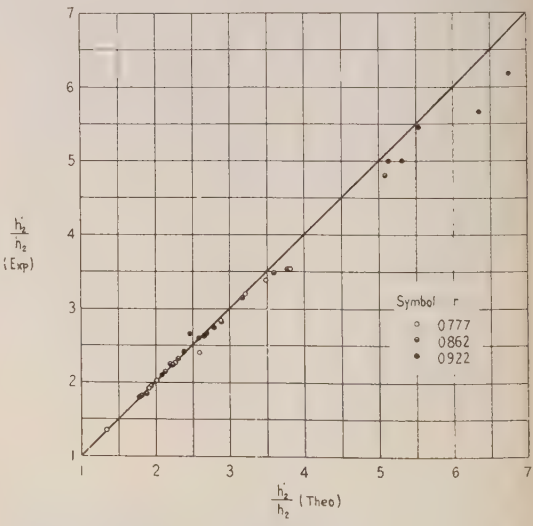

Fig. 5. Comparison of experimental results for the surge with theoretical predictions according to Eq. (15)

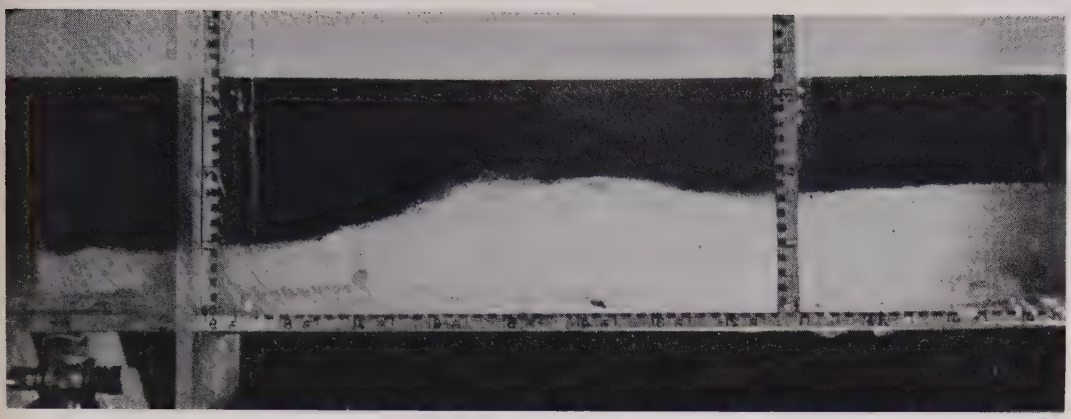

Plate 1. Photograph showing interfacial surge and the almost horizontal free surface between air and oil.

From the same plate it can be seen that the appearance of the surge was fairly smooth, and no violent interfacial mixing existed.

Because of the lack of violent interfacial mixing in Case 3 the neglecting of interfacial shear in the analysis is more nearly justified, and the agreement between theoretical and experimental results is consequently better than in Cases 1 and 2, in which rather violent mixing usually occurred at the interface. In this connection it may also be mentioned that because of the simplicity of the experimental technique employed in Case 3, the experimental limitations encountered in that case are much less severe than in the cases of steady jumps. Why the data for Cases 1 and 2 show a dispersion according to the density ratio whereas those for Case 3 does not, cannot be convincingly explained. This does not, however, prevent one from making the points in regard to the several questions at issue.

From the experiments it is evident that, for the special cases investigated, to a given upstream state there corresponds only one downstream state. Aside from this, it seems that the analysis previously presented provides a means for determining h_2'/h_2 or h_1'/h_1, at least to a first approximation, the absolute errors being small for small theoretical values of $\Delta h_2/h_2$ or $\Delta h_1/h_1$—which correspond to small values of F_2'—1 or F_1'—1 in Case 1 or 2.

Conclusions

From the foregoing investigation of the hydraulic jump in a fluid system of two layers, it can be concluded that:

1. According to a simple analysis based on the momentum principle and the neglecting of shear, there can be at most three states conjugate to a given one. These states can be determined from Eqs. (2) and (3). If the modified Froude number of either layer is predominantly large, there is only one conjugate state. If the conjugate state is unique, and if a jump can occur from the consideration of energy and does occur, the state downstream from the jump is completely determined. If there are more than one conjugate states, merely from momentum and energy considerations it may not be possible to determine uniquely the state downstream from a hydraulic jump.

2. Specific results of experiments performed on primarily internal hydraulic jumps for three special cases, shown in Figs. 3 to 5, demonstrate the uniqueness of the downstream state in these cases, which is expected from the analysis. Furthermore, these results show that the simple analysis provides means for determining the downstream depths to a first approximation, the absolute errors in h_1'/h_1 or h_2'/h_2 being small for small theoretical values of $\Delta h_1/h_1$ or $\Delta h_2/h_2$.

Acknowledgment

This work was sponsored jointly by the Iowa Institute of Hydraulic Research and the Office of Naval Research, under Contract No. N8onr—500. The writers wish to thank Dr Hunter Rouse, Director of the Institute, for his advice in regard to the experimental equipment.

BIBLIOGRAPHY

Benton, G. S., 1953: The occurrence of critical flow and hydraulic jumps in a multi-layered system, Tech. Rep. No. 1, The Johns Hopkins University, Dept. of Civil Eng.

Craya, A., 1951: Critical regimes of flows with density stratification, *Tellus*, **3**, 28—42.

Greenhill, A. G., 1887: Wave motion in hydrodynamics, *Journ. of Math.*, **9**, 62—112.

Helmholtz, H., 1868: Über discontinuirliche Flüssigkeitsbewegungen, *Monatberichte Akad. d. Wiss. Berlin*, 215—228.

Keulegan, G. H., 1953: Characteristics of internal solitary waves, Res. Paper 2442, *Journ. of Res. Nat. Bureau of Standards*.

Long, R. R., 1953: Some aspects of the flow of stratified fluids, I. A theoretical investigation, Tech. Rep. No. 2, The Johns Hopkins University, Dept. of Civil Eng.

Love, A. E. H., 1891: Wave motion in a heterogeneous heavy liquid, *Proc. Lond. Math. Soc.*, **22**, 307.

Rossby, C.-G., 1951: On the vertical and horizontal concentration of momentum in air and ocean currents, *Tellus*, **3**, 15—27.

Stokes, G. G., 1847: On the theory of oscillatory waves, *Trans. Camb. Phil. Soc.*, **8**, 441.

Stommel, H., and Farmer, H. G., 1952: Abrupt changes in width in two-layer open channel flow, *J. Mar. Res.*, **11**, 205—214.

Tepper, M., 1952: The application of the hydraulic analogy to certain atmospheric flow problems, Research Paper 35, U.S. Weather Bureau.

Webb, R. R., 1884: Math. Tripos Papers.

Rotor Phenomena in the Lee of Mountains

By PAUL QUENEY, University of Paris, France

(Presented at the 5th Congress of the OSTIV (Organisation Scientifique et Technique du Vol à Voile) at BUXTON, England, 1954.)

(Manuscript received January 8, 1955)

Abstract

The rotors are explained as a simple "cat's eye effect", or transformation of a stationary wave motion into a system of vortices in the vicinity of a level where the basic wind velocity is vanishing. Some other applications of this same effect to phenomena of smaller or larger scale are also given.

1. Introduction

It is well known that the stationary lee-waves produced by a big mountain often break up into turbulent longitudinal whirls or "rotors" in the lower layers of the air flow. The first detailed study of the phenomena was made by KUETTNER in 1939, in the case of the Riesengebirge (central Europe) by means of airplane observations completed by theoretical considerations. According to this author the lower system is mainly gravitational, associated with the free surface of a cold air layer, and the transformation of the waves into rotors occurs when a certain critical amplitude is attained, while the upper waves may be governed by independant factors, either gravitational, dynamical, or both. However, at least in the first stages of their development, the lower waves have the same phase as the upper ones, so that a definite coupling exists between the two systems. Each rotor produces a stationary roll cloud, very different in aspect from the smooth lenticular ones associated with the upper waves.

More recently some extensive investigations were also made in California on the roll clouds frequently observed in the lee of the Sierra Nevada, and which are particularly big and strong, often exceeding the height of the mountain itself.

Whatever may be the factors governing the wave motion produced by the mountain, some explanation has to be found for the breaking of the waves into separate whirls, and this is properly what we may call the "rotor problem". In the following we shall consider it as a particular case of a more general one, namely the problem of the change of a wave motion into a system of vortices in the vicinity of a level where the basic flow has the same velocity as the waves, and it will be convenient to refer to this change as the "cat's eye effect". For the general theory of this effect it is essential to abandon the so-called infinitesimal assumption used in most of previous theories of mountain waves, and also to take account of the wind shear in the layer under consideration.

The suggestions presented in this paper came us about one year ago, in the course of theoretical researches undertaken at Los Angeles (California) with my colleague Professor J. HOLMBOE and his coo-workers, concerning the two-dimensional perturbations of barotropic flows.

2. Theory of the "cat's eye effect"

Since the earth's rotation is negligible at the scale of the rotors we may adopt the usual assumption of a non-divergent stationary motion taking place in an x, z-vertical plane

parallel to the wind blowing towards the mountain (basic flow). Taking the z-axis vertical upwards and the origin at the ground level in the basic flow, and denoting by $U(z)$ the velocity of this basic flow, the mountain perturbation is then completely defined by the disturbance $\psi(x, z)$ of the corresponding stream-function $\int U dz$, and if these two functions are given the exact equation for the disturbed streamlines is, in any case,

$$\int U dz + \psi(x, z) = \text{const} \qquad (1)$$

However, the analytical form of $\psi(x, z)$ is not simple in general, since this function must satisfy a certain differential equation depending not only on the velocity profile of the basic flow, but also on gravitational stability and viscosity. Therefore, it is convenient to develop the theory only in a simple case, and then to generalize. This simple case will be defined as follows:

i) The basic velocity is an increasing linear function of z, say

$$U(z) = U_0 + \gamma z = \gamma (z - z_0) \quad (\gamma > 0;\ z_0 = -U_0/\gamma) \qquad (2)$$

in other words the basic flow is a Couette flow, vanishing at the level $z = z_0$ (negative if U_0 is positive).

ii) There is no gravitational stability in this basic flow.

iii) Viscosity and turbulence are negligible.

iv) The horizontal scale of the perturbation is large compared with the thickness of the flow under consideration.

Of course these assumptions have only to be valid up to 3 or 4 km about, the average height of the rotors.

According to (ii) the motion is barotropic, and since it is also unviscid the vorticity is conservative. On the other hand this vorticity has the constant value γ in the basic flow, therefore its disturbance must be equal to zero, and accordingly the differential equation for ψ is simply the Laplacian equation $\nabla^2 \psi = 0$. Therefore, the horizontal scale of the perturbation is comparable with its vertical scale, and if we then take account of assumption (iv) we see that ψ may also be considered as a linear function of z, say

$$\psi(x, z) = f(x) + z g(x) \qquad (3)$$

and this means that the horizontal component $u = \partial\psi/\partial z$ of the velocity disturbance is practically independant of z and equal to $g(x)$.

If (2) and (3) are used the equation (1) then gives, for the streamlines,

$$\gamma^2 z^2 + 2[U_0 + g(x)]\gamma z + 2\gamma f(x) = C \qquad (4)$$

where C is a constant along each streamline, and if we solve for γz we get

$$\gamma z = -[U_0 + g(x)] \pm \sqrt{[U_0 + g(x)]^2 - 2\gamma f(x) + C} \qquad (5)$$

It is easy to see that if ψ is small this equation represents a system of unlimited streamlines in the entire flow, except in the vicinity of $z = z_0$ where it gives a system of closed streamlines bounded by particular streamlines intersecting each other: we thus get actually a cat's eye pattern in the vicinity of the level $z = z_0$.

Let us now consider more particularly what happens in the lee of the mountain.

If we assume the existence of lee-waves with a moderate amplitude, we may take for ψ a sinusoidal function of x, and this function must vanish at the ground level $z = 0$. Therefore we can write, if we choose a proper x-origin and denote the wave length by $2\pi/k$,

$$f(x) = 0;\ g(x) = a \sin kx \quad (a > 0) \qquad (6)$$

so that we get for the streamlines

$$\gamma z = -(U_0 + a \sin kx) \pm \sqrt{(U_0 + a \sin kx)^2 + C} \qquad (7)$$

The complete patterns of streamlines given by this equation are shown on fig. 1 (including the virtual portions for $z < 0$, drawn in thin dotted line), they differ according to the value of U_0 as compared to a. For their description it will be convenient to put

$$M = (|U_0| + a)^2;\ M' = (|U_0| - a)^2 \qquad (8)$$

A) If $U_0 < -a$ (fig. 1 A) there is one row of equal cat's eyes located entirely above the ground level, and bounded by the two particular streamlines corresponding to $C = -M'$. The closed streamlines are obtained for $-M < C < -M'$, they are reduced to points for $C = -M$, and their axis is the sine curve

$$z = z_0 - \frac{a}{\gamma} \sin kx \qquad (9)$$

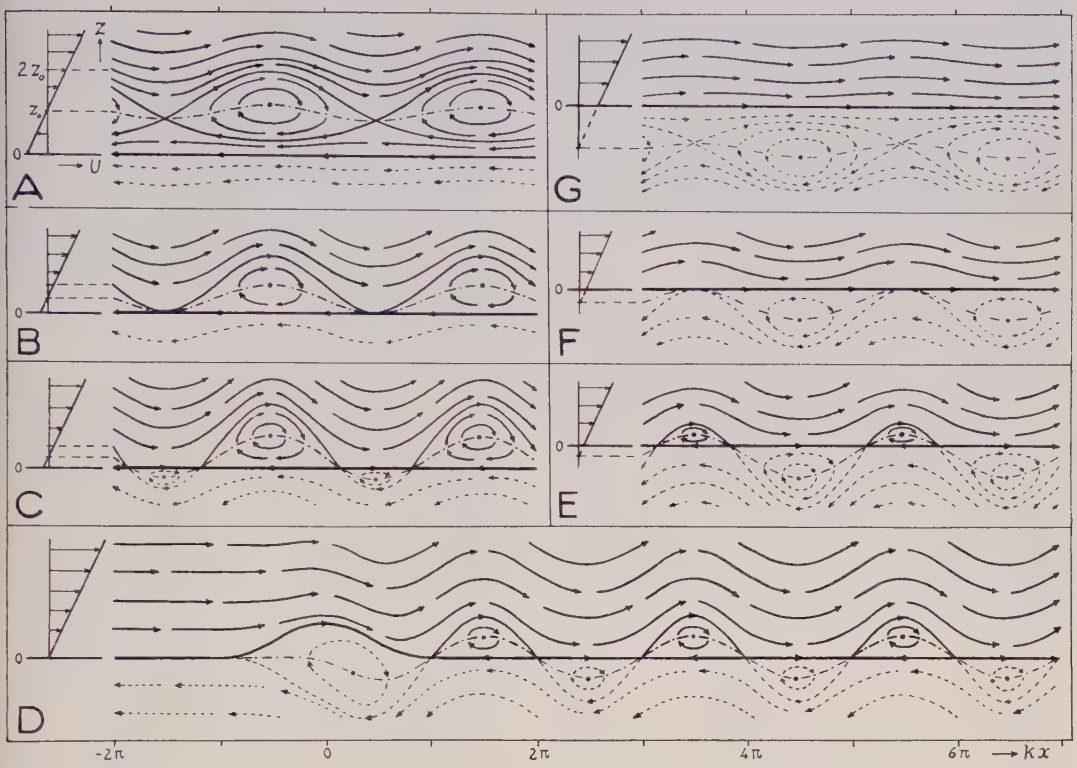

Fig. 1. Stationary wavelike mountain perturbation in a barotropic Couette flow: streamlines corresponding to various wind profiles.

For $C=0$ we get $z=0$ as one particular streamline, at the same time as the sinusoidal streamline

$$z = 2\left(z_0 - \frac{a}{\gamma}\sin kx\right) \qquad (10)$$

All the other streamlines are wavelike, and practically sinusoidal for $C>0$.

B) If $U_0 = -a$ (fig. 1 B), since $M'=0$ the boundary of the cat's eyes is obtained for $C=0$, and it is formed by the x-axis and the sinusoidal streamline (10) which are now tangent to each other. The axis (9) is also tangent to $z=0$. Accordingly the vortices are just in contact with the ground.

C) If $-a<U_0<0$ (fig. 1 C), the boundary of the cat's eyes is again obtained for $C=0$ and formed by the x-axis and the sine curve (10), but these lines are now intersecting each other. Accordingly the cat's eyes are alternately located on the positive and negative side of the x-axis, the axis of the whole system being still formed by the sine curve (9). The positive cat's eyes are larger than the negative one's, their closed streamlines being obtained for $-M<C<0$ whereas those of the latter are obtained for $-M'<C<0$.

D) If $U_0=0$ (fig. 1 D), we have the same situation but the positive and negative vortices are equal, the pattern being skew-symmetrical with respect to the x-axis. The closed streamlines are obtained for $-a^2<C<0$.

E) If $0<U_0<a$ (fig. 1 E), we have again a similar situation, but with the negative vortices larger than the positive ones.

F) If $U_0=a$ (fig. 1 F), the pattern is symmetrical of that of fig. 1 B with respect to the x-axis, so that the cat's eye system is entirely virtual.

G) Similarly, if finally $U_0>a$ (fig. 1 G) the pattern is symmetrical of that of fig. 1 A, and the cat's eyes are again entirely virtual.

In the region between the basic flow and the lee-waves the streamlines can be computed by formula (5) if the mountain profile is given together with the function $g(x)$, for instance, and this formula gives at the same time the virtual streamlines forming the continuation of those described above. In particular the equation for the axis of the closed streamlines is

$$\gamma z = -[U_0 + g(x)] \qquad (11)$$

The result of this computation is represented on fig. 1 D for $U_0 = 0$, in the case of a symmetrical bell-shaped mountain profile: we see that there is an additional virtual cat's eye under the mountain, and the same thing necessarily occurs with any mountain profile.

Remark. It is important to note that the infinitesimal assumption would give no closed streamlines at all: according to this assumption the equation of the disturbed streamline corresponding to a basic streamline $z = h$ would be

$$z = h - \frac{\psi(x, h)}{U(h)} \qquad (12)$$

therefore all the lee-streamlines would be sinusoidal. This formula (12) is actually correct when $|U(h)|$ is large compared to a, in other words when $|h - z_0|$ is large compared to a/γ.

Now we have to examine how the preceding results, derived in the ideal case of an unviscid barotropic Couette flow and a perturbation with a large horizontal scale, can be generalized.

Obviously the transformation of the wave motion into vortices is due to the fact that around $z = z_0$ the basic velocity is overcome by the horizontal component u of the velocity disturbance, and therefore the same must occur with any basic flow provided u is not itself vanishing in the vicinity of $z = z_0$, that is, provided ψ is not maximum or minimum with respect to z. This is certainly the case, whatever may be the scale of the perturbation, if the basic flow remains an unviscid barotropic Couette flow, since ψ is then a solution of the Laplacian equation. Furthermore if the basic flow is modified continuously the streamlines' pattern must also change continuously, and therefore it is undoubtful that the general aspect of the streamlines cannot change as long as such factors as gravitational stability, turbulent viscosity, or vertical variation of the wind shear, are not too much predominant. This restricted generalization will be sufficient for the following applications.

It is also to be noted that this theory of the cat's eye effect may be extended to any two-dimensional basic flow upon which a wave perturbation is superposed, if this perturbation has a definite phase velocity: the waves change into vortices in the vicinity of any basic streamline along which the basic fluid velocity equals this phase velocity.

3. Application to the rotors

The wind soundings made in the Sierra Nevada area have shown that in most of rotor situations the vertical wind shear is roughly independant of height up to more than 5 km, so that the use of a Couette model appears as quite justified at least in this case. In addition the basic wind at the ground level is always very small if not exactly equal to zero. Therefore we may conclude that, unless the gravitational stability or turbulence is an essential factor in the lower layers, the pattern of streamlines associated with a system of lee-waves must be approximately that of fig. 1 D, or eventually that of fig. 1 E. In both cases we have near to the ground a succession of separate equal vorticies, each vortex corresponding with a wave crest: obviously we thus get the explanation of the rotors with their essential properties, and this explanation is very simple indeed, and quite independant of the factors governing the waves themselves. More precisely, the rotors simply appear as a necessary consequence of the fact that the basic wind is vanishing or very small at the ground level, and rapidly increasing upwards.

If we assume $U_0 = 0$ the theoretical height of the rotors, deduced from formula (10), is

$$H_r = \frac{2a}{\gamma} \qquad (13)$$

therefore it is proportional to the amplitude of the lee-waves for a given basic wind. On the other hand if we adopt the model of fig. 1 D, where the mountain crest is at $x = 0$ and the value of $g(x)$ is very small at the same point, the formula (5) gives for the height H of the mountain the approximate value

$$H = \frac{1}{\gamma}\sqrt{-2\gamma f(0)} \qquad (14)$$

whence $$f(0) = -\frac{\gamma}{2} H^2 \qquad (15)$$

Now since ψ satisfies a linear differential equation the amplitude of the lee-waves is roughly proportional to $f(0)$ for a given basic wind and a fixed width of the mountain, and we can therefore conclude that H_r is approximately proportional to H^2. Accordingly the relative importance of the rotors as compared to the mountain increases with the height of this mountain, and we can thus understand why big rotors are only observed with high mountains, and why no definite rotors are to be found in the lee of low mountains.

4. Application to similar phenomena

i) Besides the rotors, the same theory explains more generally all the stationary vortices and wavelike clouds frequently observed around a level where the wind changes sign, whatever may be the origin of the responsible wave motion: if we look at fig. 1 A we note that the vertical displacement of the air is much larger inside of the vortices than outside, and this simple remark may explain why condensation occurs at the upper part of each vortex, in the form of a stationary cloud.

ii) At a smaller scale the many wavelike features commonly seen at the ground surface, such as the sand ripples, the dunes of the deserts, and even the water waves formed by the wind, may also be considered as a simple effect of the transformation of some wave perturbation into stationary vortices as a result of the vanishing of the wind at the ground level.

iii) At the synoptic scale also there are various wave motions that may be considered as two-dimensional at a first approximation (they are mainly horizontal instead of vertical), and therefore the general theory of the cat's eye effect again applies to them. Accordingly a system of vortices is to be expected everywhere the phase velocity equals the fluid velocity. We thus get the explanation of subtropical anticyclones between westerlies and easterlies, and it is possible that the cyclones themselves are essentially nothing but the result of a similar transformation of a wave motion into vortices.

We thus see how so many meteorological phenomena, apparently very different, may be finally related to only one very simple hydrodynamical effect.

Wave Motion in a Rotating Couette Flow of a Viscous Fluid

By SHIH-KUNG KAO, The Johns Hopkins University[1]

(Manuscript received September 27, 1954)

Abstract

With the assumption of non-divergence horizontal flow, a certain class of solutions of the nonlinear hydrodynamic equations are obtained for a viscous Couette flow on an earth whose variation of Coriolis parameter with latitude is constant. These solutions yield waves of transient type, of which the amplitude, wave velocity, and the inclination of the trough and ridge lines vary with time.

For Couette flow with both lateral and vertical velocity-shears, the vertical profile of the amplitude of the waves can either be exponential in z or independent of z, whereas for Couette flow with lateral velocity-shear only it permits to be independent of z, a sinusoidal function, or a hyperbolic sine or cosine of z. These waves will eventually disappear in a Couette flow regardless the fluid is viscous or not, although under certain conditions waves may be amplified within a certain time interval.

Pressure field, geostrophic deviation, meridional transports of energy and westerly momentum are obtained for such a flow system. For reasonable values of the constants for atmospheric systems, geostrophic deviation can be as high as one order magnitude smaller than the actual wind speed.

1. Introduction

The linearized vorticity equation for a rotating inviscid fluid with basic uniform flow was first studied by Rossby (Rossby, 1939), who obtained a solution for the motion of sinusoidal waves of infinite lateral extent on an earth whose variation of Coriolis parameter with latitude is constant.

In a recent paper (Kao, 1954) waves solutions of the nonlinear hydrodynamical equations have been obtained for a rotating viscous fluid with uniform (basic) linear velocity for the plane, and with (basic) uniform angular velocity for the sphere. It was shown that under certain conditions these solutions permit to have a (lateral) sinusoidal velocity profile.

[1] This researchw as supported by the Geophysics Research Directorate, Air Force Cambridge Research Center, under Contract AF 19 (604)—916.

The objective of the present paper is to study a certain class of solutions of the nonlinear vorticity equation for a rotating Couette flow of a viscous fluid. On account of the coordinate dependency of the velocity of a Couette flow, the characteristics of the solutions obtained for a Couette flow are significantly different from that for a (basic) uniform flow.

2. Wave Solutions of the Nonlinear Vorticity Equation for a (Rotating, Viscous) Couette Flow with Both Lateral and Vertical Velocity-Shear

If the vertical velocity is neglected, and zero horizontal divergence and constant density (or an autobarotropic condition) are assumed, the vorticity equation for a rotating, viscous fluid on an earth whose variation of Coriolis parameter with latitude is constant is

$$\left\{\frac{\partial}{\partial t}-\frac{\partial \Psi}{\partial y}\frac{\partial}{\partial x}+\frac{\partial \Psi}{\partial x}\frac{\partial}{\partial y}-\nu\left(\nabla^2+\frac{\partial^2}{\partial z^2}\right)\right\}\nabla^2\Psi+$$

$$+\beta\frac{\partial \Psi}{\partial x}=0 \qquad (1)$$

where x, y, z are the Cartesian coordinates, positive toward the east, north and zenith respectively; Ψ is the stream function, ν the coefficient of kinematic viscosity, $\beta \approx 2\Omega a^{-1}\cos\varphi$ the variation of the Coriolis parameter with latitude φ, a and Ω respectively the radius and angular velocity of the earth, ∇^2 the horizontal Laplacian operator.

For a Couette flow with velocity shear S and Q respectively with respect to y and z, the stream function may be expressed

$$\Psi(x, y, z, t)=-\left(U_0+\frac{1}{2}Sy+Qz\right)y+$$

$$+\psi(x, y, z, t) \qquad (2)$$

where U_0 is the mean zonal velocity at $y = z = 0$. For motions in such a flow system vorticity equation becomes

$$\left\{\frac{\partial}{\partial}+(U_0+Sy+Qz)\frac{\partial}{\partial x}+\frac{\partial \psi}{\partial x}\frac{\partial}{\partial y}-\frac{\partial \psi}{\partial x}\frac{\partial}{\partial x}-\right.$$

$$\left.-\nu\left(\nabla^2+\frac{\partial^2}{\partial z^2}\right)\right\}\nabla^2\psi+\beta\frac{\partial \psi}{\partial x}=0 \qquad (3)$$

Let us find the solutions of the above partial differential equation, which belong to the class

$$\nabla^2\psi=J(t)\psi \qquad (4)$$

Using vorticity equation (3) one can show that harmonic waves in the solution of this class is of the form[1]

$$\psi(x, y, z, t)=$$

$$=F(t)\,G(z)\sin K\{x-h(y, z, t)\} \qquad (5)$$

where $K = 2\pi L^{-1}$ is the wave number, L the wave length.

[1] It can be shown that for flow with uniform (basic) velocity J in (4) becomes independent of time, and waves permit to have finite lateral extent.

To satisfy relation (4) one finds that

$$J(t)=-K^2\left\{1+\left(\frac{\partial h}{\partial y}\right)^2\right\}$$

$$\frac{\partial^2 h}{\partial y^2}=0$$

We may therefore express

$$h(y, z, t)=[I(t)+\xi]\,y+R(z, t) \qquad (6)$$

$$J(t)=-K^2\{1+[I(t)+\xi]^2\} \qquad (7)$$

where $I(t)$ and $R(z, t)$ are functions which will be determined later, ξ is a constant to be determined by the initial condition. Substituting from (6) into (5), then into (3) and making use of relation (4), one finds that

$$\frac{1}{J}\frac{dJ}{dt}+\frac{1}{F}\frac{dF}{dt}-\nu\left\{J(t)-K^2\left(\frac{\partial R}{\partial z}\right)^2+\right.$$

$$\left.+\frac{1}{G}\frac{d^2G}{dz^2}\right\}=0 \qquad (8)$$

and

$$\frac{\partial h}{\partial t}-\left\{U_0+Sy+Qz+\frac{\beta}{J(t)}\right\}+$$

$$+\nu\left\{\frac{2}{G}\frac{dG}{dz}\frac{\partial R}{\partial z}+\frac{\partial^2 R}{\partial z^2}\right\}=0 \qquad (9)$$

By the inspection of (8) one infers that $R(z, t)$ and $G(z)$ are of the following forms:

$$R(z, t)=[H(t)+\eta]\,z+N(t) \qquad (10)$$

$$G(z)=\exp[K\zeta z] \qquad (11)$$

where $H(t)$, $N(t)$ are functions remained to be determined; η and ζ are real constants to be determined respectively by initial and boundary conditions.

Integration of (9) with respect to t, and with the use of (10) and (11) gives

$$h(y, z, t)=(U_0+Sy+Qz)t+\beta\int\frac{dt}{J(t)}+$$

$$+2\gamma K\zeta\int[H(t)+\eta]\,dt+M(y, z) \qquad (12)$$

Substituting from (10) into (6), then comparing it with (12) one finds that

$$H(t) = Qt, \qquad I(t) = St$$

$$J(t) = -K^2[1 + (St+\xi)^2]$$

$$M(y, z) = \xi y + \eta z + B$$

$$N(t) = U_0 t - \frac{\beta}{K^2 S}\tan^{-1}(St+\xi) + \\ + \gamma K\zeta\,(Qt+2\eta)t \qquad (13)$$

If we impose on $h(y, z, t)$ the initial condition

$$\delta = h(0, 0, 0) = -\frac{\beta}{K^2 S}\tan^{-1}\xi + B$$

at $y = z = 0$, we have

$$h(y, z, t) = \\ = (U_0 + Sy + Qz)t - \frac{\beta}{K^2 S}[\tan^{-1}(St+\xi) - \\ - \tan^{-1}\xi] + \gamma K\zeta\,(Qt+2\eta)\,t + \xi y + \eta z + \delta \qquad (14)$$

Integration of (8) with respect to t and with the use of (13) gives

$$F(t) = \frac{-A}{K^2[1+(St+\xi)^2]}\exp\left\{-\gamma K^2[(1 + \\ + \xi^2 + \eta^2 - \zeta^2)t + (S\xi + Q\eta)t^2 + \frac{1}{3}(S^2+Q^2)t^3\right\} \qquad (15)$$

Stream function (2) becomes therefore

$$\Psi(x, y, z, t) = -\left(U_0 + \frac{1}{2}Sy + Qz\right)y - \\ - \frac{AL^2}{4\pi^2[1+(St+\xi)^2]}\exp\left\{K\zeta z - \gamma K^2 \cdot\right. \\ \cdot\left[(1+\xi^2+\eta^2-\zeta^2)t + (S\xi+Q\eta)t^2 + \right. \\ \left.\left. + \frac{1}{3}(S^2+Q^2)t^3\right]\right\}\sin\frac{2\pi}{L}\left\{x - [U_0 + Sy + Qz]\,t + \right. \\ + \frac{\beta L^2}{4\pi^2 S}[\tan^{-1}(St+\xi) - \tan^{-1}\xi] - \\ \left. - \gamma K\zeta(Qt+2\eta)t - \xi y - \eta z - \delta\right\} \qquad (16)$$

The first term of the right hand side of (16) gives the velocity of the Couette flow with lateral velocity-shear s and vertical velocity-shear Q; the last term gives a sinusoidal wave with an amplitude which is exponential in z and varies with time. In (16) $(st + \xi)$ and $(Qt + \eta)$ are respectively the reciprocal of the slope of the trough and ridge lines with respect to y and z. ξ^{-1} and η^{-1} are therefore the initial slope of the trough and ridge lines of the waves.

Inspection of (16) reveals that the wave velocity and the slope of the trough and ridge lines vary with time. These are two characteristic features of wave motions in a Couette flow, whereas there is no change in the wave velocity and the inclination of trough and ridge lines in a (basic) uniform flow.

It is of importance to note that no stationary or quasi-stationary waves are possible to occur in a rotating Couette flow, since waves in such a system move with a speed,

$$C = U_0 + Sy + Qz - \frac{\beta L^2}{4\pi^2[1+(St+\xi)^2]} + \\ + \frac{4\pi\gamma\zeta}{L}(Qt + \eta) \qquad (17)$$

which depends not only on the velocity of the Couette flow, wave length, latitude, but also on the instantaneous slope of the trough and ridge lines, the coefficient of kinematic viscosity and the exponential power of the amplitude of the velocity profile in z.

Examining frequency equation (17) one finds that term containing β has an extreme value at $t = -s^{-1}\,\xi$, which is possible only if $S\xi < 0$, and tends to zero as time tends to infinity, whereas the last term associating with viscosity, exponential power in z and the vertical slope of the trough and ridge lines decreases or increases with time according to the negative or positive sign of $Q\zeta$. It is readily seen that the last term of (17) disappears if the fluid is inviscid, or the velocity profile is independent of z, or when the trough and ridge lines are perpendicular to the zonal current. It is also readily seen that for uniform flow of an inviscid fluid frequency equation (17) reduces to that of Rossby's wave (Rossby, 1939),

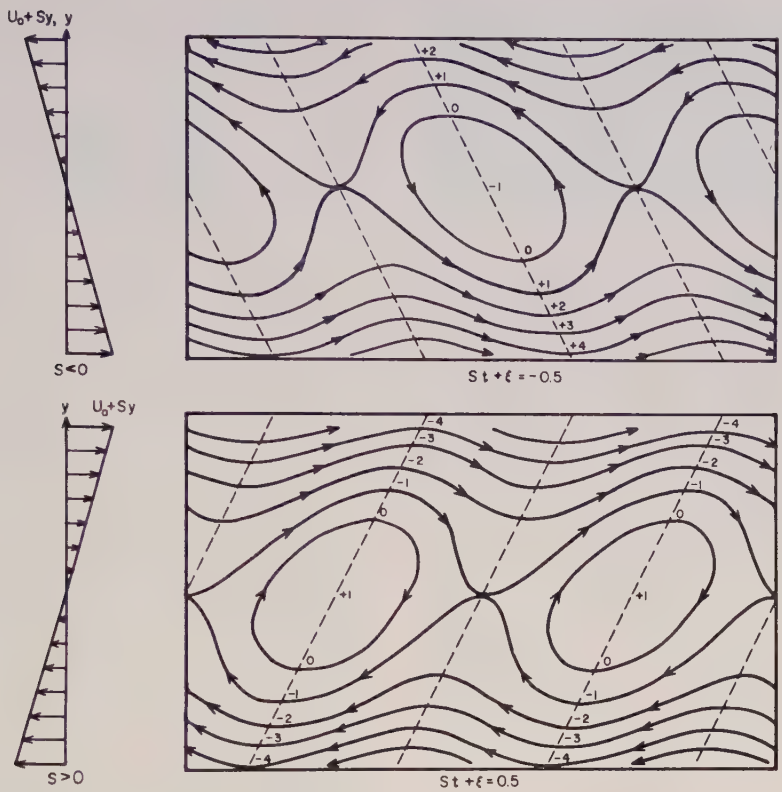

Fig. 1. Distributions of stream function (solid lines), ridge and trough lines (dashed lines).
a. For $S < 0$, $st + \xi = -0.5$, $\gamma = z = 0$
b. For $S > 0$, $st + \xi = 0.5$, $\gamma = z = 0$

$$C = U_0 - \frac{\beta L^2}{4\pi^2}.$$

The amplification and damping of the waves depend on the behavior of the time dependency of the amplitude of the waves. By the inspection of (15) one finds that, for sufficient large value of t, $|F(t)|$ is a monotonic decreasing function of time. Thus *waves will eventually disappear in a Couette flow regardless the fluid is viscous or not.* However, under certain conditions waves may be amplified within a certain time interval. Waves may be damped, unchanged or amplified depending respectively on

$$\frac{d}{dt} \ln F(t) \gtreqless 0$$

or

$$S(St+\xi) + 2\pi^2\gamma L^{-2}[1 + (St+\xi)^2] \cdot$$
$$\cdot [1 - \zeta^2 + (St+\xi)^2 + (Qt+\eta)^2] \gtreqless 0 \quad (18)$$

Let us consider first the wave motion in a Couette flow of an inviscid fluid. For this case only the term $s(st + \xi)$ remains in (18). Waves will be amplified when the slope of the trough and ridge lines is in the opposite sign to the lateral velocity-shear of the Couette flow, i.e. if $S\xi < 0$ and when $t < -S^{-1}\xi$. Wave amplitude reaches its maximum when the trough and ridge lines are perpendicular to the zonal current ($t = -s^{-1}\xi$), and drops when the slope of the trough and ridge lines is of the same sign as the lateral velocity-shear. It is interesting to note that for the inviscid case maximum wave amplitude occurs when the extreme wave velocity is reached.

Now we take into account of the frictional effect and consider the wave motion in a simple Couette flow with $\zeta = 0$. For this case the viscosity term in (18) is always positive. Viscosity tends therefore to suppress the amplification effect and bring the maximum

wave amplitude to an earlier moment than in the case of an inviscid Couette flow. Amplification occurs if $S\xi < 0$ and $\frac{d}{dt} \ln F(t) > 0$. Waves are always damped when the slope of the trough and ridge lines are of the same sign as the lateral velocity-shear of the Couette flow, i.e. $S\xi > 0$.

The negative sign in front of ζ^2 in (15) and (18) indicates that the frictional effect resulted from the vertical exponential profile of the wave amplitude tends to amplify the wave. This is due to the growth of kinetic energy of the system resulted from such an exponential velocity profile. A discussion of the growth of kinetic energy of a system in relation to different velocity profiles may be found in a previous paper (KAO, 1954).

The distribution of the stream functions for different sign of lateral velocity-shears are shown in Fig. 1 a for $s < 0$, $st + \xi = -0.5$, $\gamma = z = 0$, and in Fig. 1 b for $s > 0$, $st + \xi = 0.5$, $\gamma = z = 0$. It is to be noted that the closed cyclonic streamlines occur around zero basic velocity with negative velocity-shear, anticyclonic streamlines around basic velocity with positive velocity-shear.

The pressure field corresponding to a stream function (16) may be obtained by the integration of the equations of motion for the horizontal directions

$$\frac{\partial u}{\partial t} + u\frac{\partial u}{\partial x} + v\frac{\partial u}{\partial y} - fv = -\frac{1}{\varrho}\frac{\partial p}{\partial x} + \gamma\left(\nabla^2 + \frac{\partial^2}{\partial z^2}\right)u,$$

$$\frac{\partial v}{\partial t} + u\frac{\partial v}{\partial x} + v\frac{\partial v}{\partial y} + fu = -\frac{1}{\varrho}\frac{\partial p}{\partial y} + \gamma\left(\nabla^2 + \frac{\partial^2}{\partial z^2}\right)v \qquad (19)$$

where f is the Coriolis parameter, p the pressure, ϱ the density. The result is given by the expression

$$\frac{p}{\varrho} = -\left\{\frac{\beta L(St+\xi)}{2\pi[1+(St+\xi)^2]}\cos\frac{2\pi}{L}\cdot\right.$$

$$\cdot\left(x - [U_0 + S\gamma + Qz]t + \frac{\beta L^2}{4\pi^2 S}[\tan^{-1}(St+\xi) - \tan^{-1}\xi] - \gamma K\zeta[Qt+2\eta]t - \xi\gamma - \eta z - \delta\right) +$$

$$+\left(f_0 + \beta\gamma - \frac{2S}{[1+(St+\xi)^2]}\right)\sin\frac{2\pi}{L}\left(x - [U_0 + S\gamma + Qz]t + \frac{\beta L^2}{4\pi^2 S}[\tan^{-1}(St+\xi) - \tan^{-1}\xi] - \gamma K\zeta[Qt+2\eta]t - \xi\gamma - \eta z - \delta\right)\Bigg\}\cdot$$

$$\cdot\frac{AL^2}{4\pi^2[1+(St+\xi)^2]}\exp\left\{K\zeta z - \gamma K^2\cdot\right.$$

$$\cdot\left[(1+\xi^2+\eta^2-\zeta^2)t + (S\xi+Q\eta)t^2 + \frac{1}{3}(S^2+Q^2)t^3\right]\Bigg\} - \left(f_0 + \frac{1}{2}\beta\gamma\right)\cdot$$

$$\cdot\left(U_0 + \frac{1}{2}S\gamma + Qz\right)\gamma - \frac{1}{12}\beta S\gamma^3 + E(z,t) \qquad (20)$$

in which f_0 is the value of the Coriolis parameter at $\gamma = 0$, and $E(z,t)$ is an arbitrary constant or function of z and t. Equation (20) will be used for the computation of the part of meridional transport of energy due to the work done by the pressure field.

3. Wave Solutions of the Nonlinear Vorticity Equation for a (Rotating, Viscous) Couette Flow with Lateral Velocity-Shear

For a Couette flow with lateral velocity-shear only the vorticity equation may be obtained by putting $Q = 0$ in (3), the stream function and the corresponding pressure field for waves with vertically tilted trough and ridge lines may be obtained by putting $Q = 0$ respectively in (16) and (20). However, for waves without vertical tilt of trough and ridge lines $G(z)$ in (5) becomes less restricted than in a Couette flow with both lateral and vertical velocity-shear. It can be shown that in the former case functions R and h in (9) and (10) become independent of z, and $G(z)$ permits to be a sinusoidal function of z, or a hyperbolic sine or cosine of z, or of course independent of z.

If one follows the similar procedures as in the previous section, one may obtain for this case the stream function

$$\Psi(x, y, z, t) = -\left(U_0 + \frac{1}{2} Sy\right) y - \frac{AL^2}{4\pi^2 [1 + (St+\xi)^2]} \exp\left\{-\gamma K^2 \left[(1 + \xi^2 \pm \zeta^3)t + S\xi t^2 + \frac{1}{3} S^2 t^3\right]\right\} \begin{Bmatrix} \cos K(\zeta z + \varepsilon) \\ \cosh K(\zeta z + \sigma) \end{Bmatrix} \sin \frac{2\pi}{L} \cdot \left\{x - [U_0 + Sy]t + \frac{\beta L^2}{4\pi^2 S} [\tan^{-1}(St+\xi) - \tan^{-1}\xi] - \xi y + \delta\right\} \qquad (21\text{ a, b})$$

and wave velocity

$$C = U_0 + Sy - \frac{\beta L^2}{4\pi^2 [1 + (St+\xi)^2]} \qquad (22)$$

where the positive sign in front of ζ^2 in (21) is associated with the vertical sinusoidal profile of the stream function, the minus sign with the vertical hyperbolic profile; ε and σ are two arbitrary constants. It is worth noticing that for this case the wave velocity is not affected by friction, and is completely determined by the velocity of the Couette flow, wave length, latitude, and the instantaneous slope of the trough and ridge lines. Like the wave motion in an inviscid Couette flow wave velocity reaches its extreme value when the trough and ridge lines are perpendicular to the zonal current.

It is to be noted that for waves with vertical sinusoidal amplitude-profile viscosity tends to damp out the waves, whereas for waves with vertical exponential amplitude-profile viscosity tends to amplify the waves.

For waves in such a Couette flow system the criterion of amplification becomes

$$S(St+\xi) + \frac{\gamma K^2}{2} [1 + (St+\xi)^2] \cdot [1 \pm \zeta^2 + (St+\xi)^2] \gtreqless 0 \qquad (23\text{ a, b})$$

corresponding to waves to be damped, unchanged and amplified. One may find that for waves with vertical exponential amplitude-profile the amplification of waves is similar to that in the Couette flow with both lateral and vertical vorticity-shears. For waves with vertical sinusoidal amplitude-profile viscosity always tends to suppress the amplification effect and bring the maximum wave amplitude to an earlier moment than that in the case of an inviscid Couette flow, although wave velocity in such a system is equal to that in an inviscid Couette flow.

The pressure fields corresponding to the stream functions (21 a, b) can be shown to be

$$\frac{p}{\varrho} = -\begin{Bmatrix} \cos K(\zeta z + \varepsilon) \\ \cosh K(\zeta z + \sigma) \end{Bmatrix} \frac{A}{K^2 (1 + (St+\xi)^2]} \cdot \left\{\frac{\beta (St+\xi)}{K[1 + [St+\xi)^2]} \cos \frac{2\pi}{L} \left(x - [U_0 + Sy]t + \frac{\beta}{K^2 S} [\tan^{-1}(St+\xi) - \tan^{-1}\xi] - \xi y - \delta\right) + \left(f_0 + \beta y - \frac{2S}{[1 + (St+\xi)^2]}\right) \sin \frac{2\pi}{L} \cdot \left(x - [U_0 + Sy]t + \frac{\beta}{K^2 S} [\tan^{-1}(St+\xi) - \tan^{-1}\xi] - \xi y - \delta\right)\right\} \exp\left\{-\gamma K^2 [(1 + \xi^2 \pm \zeta^2)t + S\xi t^2 + \frac{1}{3} S^2 t^3]\right\} - \left(f_0 + \frac{1}{2}\beta y\right)\left(U_0 + \frac{1}{2} Sy\right) y - \frac{1}{12} \beta S y^3 + P(z, t) \qquad (24\text{ a, b})$$

where $P(z, t)$ is an arbitrary constant or function of z and t.

4. Physical Characteristics of Wave Motion in a (Rotating, Viscous) Couette Flow

In the previous sections we have studied the wave solutions of the nonlinear vorticity equation for a rotating Couette flow of a viscous fluid. It may be interesting to investigate the physical characteristics of these waves such as the northward transports of westerly momentum, vorticity and energy, and the geostrophic deviation.

(i) The rate of the northward transport of westerly momentum per wave length in unit height is given by

$$M_T = \int_0^L \varrho uv \, dx$$

where ϱu is the linear westerly momentum per unit volume and the multiplication by v

provides the northward transport of this momentum. By substituting for $u = -\partial\Psi/\partial y$, $v = \partial\Psi/\partial x$ from (16) and (21 a, b) one finds that

$$M_T = \frac{\varrho A^2 L^3 (St+\xi)}{8\pi^2[1+(St+\xi)^2]} \left[\begin{array}{l} \exp\left\{-2\gamma K^2\left[(1+\xi^2+\eta^2-\zeta^2)t+(S\xi+Q\eta)t^2+\frac{1}{3}(S^2+Q^2)t^3\right]\right\} \\ \exp\left\{+2\gamma K^2\left[(1+\xi^2\pm\zeta^2)t+S\xi\, t^3+\frac{1}{3}S^2t^3\right]\right\} \end{array} \right] \tag{25 a, b, c}$$

corresponding respectively for waves represented by the stream functions (16) and (21 a, b). The sign of the transport depends solely on the instantaneous inclination of the trough and ridge lines; positive transport is associated with the northeast—southwest orientation of the trough and ridge lines, negative transport with the northwest—southeast orientation of the trough and ridge lines. Zero transport occurs when the trough and ridge lines are perpendicular to the zonal current, and the transport tends to zero as the trough and ridge lines tend to coincide with the zonal current, i.e. as $t \to \infty$.

It may be interesting to compare the rate of northward transport of westerly momentum due to true wind and the geostrophic wind, and compute the error produced by the geostrophic approximation. Let us denote the rate of the northward geostrophic transport of westerly geostrophic momentum per wave length in unit height by

$$(M_g)_T = \int_0^L \varrho u_g v_g dx$$

where u_g and v_g are the geostrophic wind components respectively in the x- and y-directions. These are obtained from (19) by setting the acceleration and frictional terms equal to zero, and by the use of (20) and (24 a, b). It can be shown that

$$(M_g)_T = \left\{\left(1-\frac{2S}{f[1+(St+\xi)^2]}\right)^2 - \left(\frac{\beta}{fK[1+(St+\xi)^2]}\right)^2\right\} \frac{\varrho A^2 L^3 (St+\xi)}{8\pi^2[1+(St+\xi)^2]} \tag{26}$$

For the convenience of comparing the actual transport and the geostrophic transport we shall neglect the frictional terms in (25), since the frictionel effect is generally small in the atmosphere. The percentage error produced by the geostrophic approximation is thus

$$100\left\{1-\frac{(M_g)_T}{M_T}\right\} = \frac{400}{[1+(St+\xi)^2]}\frac{S}{f} \cdot \left\{1-\frac{1}{1+(St+\xi)^2]}\frac{S}{f}\left(1-\frac{\beta^2}{4S^2K^2}\right)\right\} \tag{27}$$

For middle latitudes $f \sim 10^{-4}$ sec^{-1}, $\beta \sim 10^{-13}$ cm^{-1} sec^{-1}. If we let $L \sim 5 \times 10^8$ cm and $S \sim 5 \times 10^{-6}$ sec^{-1} which corresponds to a velocity shear of 20 m sec^{-1} over a latitudinal distance of 40 degrees, thus $S/f \sim 5 \times 10^{-2}$, $\beta/2\,SK \sim 1$. Since the first term of the right hand side of (27) is generally one to two order of magnitude larger than the other two terms, we may use the first term to estimate the error of transport produced by the geostrophic approximation. The error is about twenty per cent of the true transport for[1] $(st+\xi) = 1$, $= 10^{-1}$ about ten per cent for $(st+\xi) = 1$, the latter corresponds to a 45° inclination of the trough and ridge lines with the x-axis. *The error increases with increasing lateral velocity-shear and with decreasing latitude.*

For waves of tilted trough and ridge lines in a uniform (basic) flow, i.e. $S = 0$ in (27), the error of the northward transport of westerly momentum is only about 0.5 per cent of the actual transport for $\xi = 10^{-1}$, and two-tenths of a per cent for $\xi = 1$. It is significant that the error of transport by geostrophic approximation in a Couette flow is more than ten times larger than that in a uniform flow.

(ii) It can be shown that the rate of the northward transport of mass vorticity is equal

[1] For $(st+\xi) = 0$, $M_T = (Mg)_T = 0$.

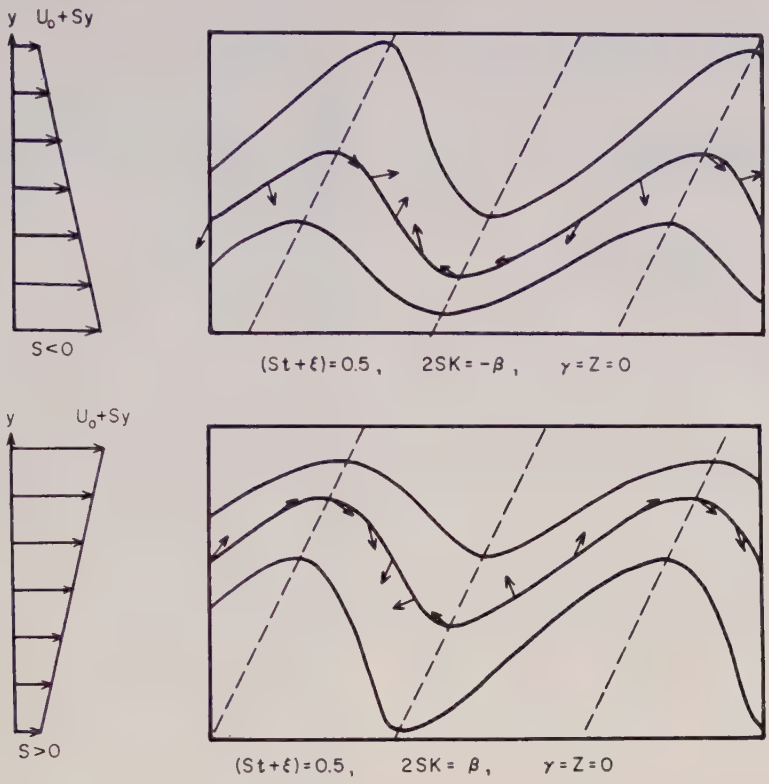

Fig. 2. Distributions of stream function (solid lines), geostrophic deviation (vectors), ridge and trough lines (dashed lines)
a. For $S < 0$, $2SK = -\beta$, $st + \xi = 0.5$, $\gamma = z = 0$
b. For $S > 0$, $2SK = \beta$, $st + \xi = 0.5$, $\gamma = z = 0$

to the rate of the meridional convergence of the northward transport of westerly momentum. Since waves in a Couette flow provide for an equal rate of the northward transport of westerly momentum at all latitudes, no net northward transport of mass vorticity is possible in a Couette flow.

(iii) Harmonic waves with tilted trough and ridge lines produce a north—south transport of energy. Since the motions are assumed horizontal with no net flow of fluid northward, the transport of energy is thus due to advection of kinetic energy and work done by pressure force. The meridional transport of energy integrated over one wave length per unit height is given by

$$E_T = \int_0^L \frac{1}{2}\varrho(u^2+v^2)v\,dx + \int_0^L pv\,dz$$

After substitution from the previous equations and integration, one finds that

$$E_T = \left\{U_0 + Sy + Qz - \frac{\beta L^2}{4\pi^2[1+(St+\xi)^2]}\right\} M_T \quad (28)$$

Thus the rate of meridional transport of energy is equal to the product of the wave velocity and the rate of the meridional transport of westerly momentum. Eastward displacement of waves and northeast—southwest tilting are associated with northward transport of energy, whereas westward displacement and northeast—southwest tilting are associated with southward transport of energy. Other combinations may also occur.

(iv) The difference between the actual and geostrophic wind vectors is called the geostrophic deviation. The components of this deviation are given by

$$u' = u - u_g; \quad v' = v - v_g$$

It can be shown that

$$u' = \frac{2SK}{f[1+(St+\xi)^2]} \frac{AG(z)}{J(t)} \left\{ (st+\xi) \cos K \cdot \right.$$

$$\left. \cdot [x-h(y,z,t)] + \frac{\beta}{2SK} \sin K[x-h(y,z,t)] \right\} \tag{29 a}$$

$$v' = \frac{2SK}{f[1+(St+\xi)^2]} \frac{AG(z)}{J(t)} \cdot$$

$$\cdot \left\{ \cos K[x-h(y,z,t)] - \frac{\beta}{2SK} (St+\xi) \sin K \cdot \right.$$

$$\left. [x-h(y,z,t)] \right\} \tag{29 b}$$

where $J(t)$, $G(z)$ and $h(y, z, t)$ have the same meanings as before, the latter two functions may be different for Couette flows with only lateral velocity-shear, and with both lateral and vertical velocity-shears. The geostrophic deviations depend on velocity-shear, wave length, latitude and the instantaneous slope of the trough and ridge lines. It can easily be shown that for the previous assigned values of the constants for atmospheric systems the geostrophic deviations can be as high as one order of magnitude smaller than that of the actual wind speed. It is particularly to be stressed that different signs of velocity-shear give different geostrophic deviations. Such differences are illustrated in Figs. 2 a and 2 b. Fig. 2 a shows the distributions of stream function (solid curves), geostrophic deviation (vectors), and the trough and ridge lines (dashed lines) for the case: $s < 0$, $st + \xi = 0.5$, $2SK = -\beta$ and $\gamma = z = 0$; Fig. 2 b shows the distributions of the same quantities for $S > 0$, $2SK = \beta$, $st + \xi = 0.5$ and $\gamma = z = 0$. It is to be remarked that these figures do not represent the typical distribution of geostrophic deviations, since the distribution of geostrophic deviation can be quite different for different values of velocity-shear, wave length, latitude and the inclination of trough and ridge lines.

5. Conclusions

It has been shown that the solutions of the nonlinear vorticity equation for a rotating Couette flow of viscous fluid yield waves of transient type, of which the amplitude, wave velocity, and the inclination of the trough and ridge lines vary with time. These waves will eventually disappear in the Couette flow regardless the fluid is viscous or not, although under certain conditions waves may be amplified within a certain time interval.

For Couette flow with both lateral and vertical velocity-shears the vertical profile of the amplitude of the waves can either be exponential in z or independent of z, whereas Couette flow with lateral velocity-shear only permits it to be independent of z, a sinusoidal function, or a hyperbolic sine or cosine of z.

For inviscid Couette flow waves will be amplified when the slope of the trough and ridge lines is in the opposite sign to that of the velocity-shear, but will be damped when they have the same sign. The maximum wave amplitude and the extreme wave velocity occur when the trough and ridge lines are perpendicular to the x-axis. For waves with vertical sinusoidal amplitude-profile viscosity tends to damp out the waves, whereas for waves with vertical exponential amplitude-profile viscosity tends to amplify the waves.

Pressure field, geostrophic deviation, meridional transport of energy and westerly momentum are obtained for such a flow system. It has been shown that for reasonable values of the constants for atmospheric systems the geostrophic deviation and the error resulted from the geostrophic approximation to the northward transport of westerly momentum can be as high as one order of magnitude smaller than the actual values.

Acknowledgment

The writer wishes to thank Drs George S. Benton and Robert R. Long for their critical review of this paper.

REFERENCES

Kao, S. K., 1954: Harmonic Wave Solutions of the Nonlinear Vorticity Equation for a Rotating Viscous Fluid. *J. Meteor*, **11**, No. 5 373—379.

Rossby, C.-G., 1939: Relation between Variation in the Displacement of the Zonal Circulation of the Atmosphere and the Displacement of the Semipermanent Centers of Action. *J. Marine Res.* (Sears Foundation), **2**, 38—55.

Nivellement hydrographique entre six stations danoises

Par AXEL JESSEN, Institut Géodésique, Copenhague

(Manuscript received 21 June 1954)

Abstract.

The annual means of sea-level are considered as consisting of two independent quantities: the height of the zero point in question and the height of the water-surface. An attempt is made to separate these two quantities. The result is a set of diagrams showing the relative secular motion of the zero points and the sea-level.

Les enregistrements marégraphiques dans deux stations 1 et 2 donnent la différence correcte des hauteurs des zéros quand les niveaux observés v_1 et v_2 appartiennent à la même surface de niveau. On est cependant loin d'avoir les moyens de corriger v_1 et v_2 tel que cette condition soit remplie, en dépit de nombreuses recherches. La différence $v_1 - v_2$ n'est donc qu'une approximation à la différence des niveaux des deux stations. D'autre part il semble possible, acceptant l'hypothèse que les v_1 et v_2 soient affectées d'erreurs assez constantes, de suivre les variations de $v_1 - v_2$ en fonction du temps, et c'est un essai dans cette direction qui sera fait.

Une complication intervient cependant, puisque les nombres v_i sont corrélées. Il y a entre deux observations v_1 et v_2 une équation $v_1 - tv_2 = q$, ou t dans beaucoup de cas diffère de 1. C'est-à-dire que la différence des niveaux est une fonction du niveau de la mer, comme l'on voit en écrivant $v_1 - v_2 = q - (1-t)v_2$. La fig. 1 montre ce phénomène. Les moyennes annuelles de v_1 à Aarhus sont portées en ordonnées aux abscisses correspondantes v_2 à Hornbæk. La tendence du groupement autour de la ligne droite $v_1 - 0{,}7\, v_2 = q$ est apparente. Cette corrélation se présente, soit que l'on se base sur des moyennes mensuelles ou annuelles ou 5-annuelles. La condition nécessaire pour qu'une théorie des corrections des v_i soit acceptable est qu'elle rende t égal à 1.

Le présent mémoire s'occupe des stations

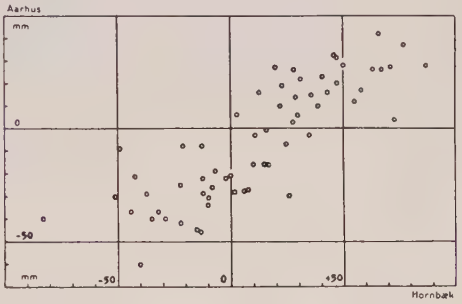

Fig. 1. Corrélation des niveaux de la mer observés à Aarhus et à Hornbæk.

danoises 1 Aarhus, 2 Hornbæk, 3 Köbenhavn, 4 Gedser, 5 Korsör, 6 Slipshavn. Le tableau suivant donne les moyennes annuelles du niveau de la mer en unités de mm; les tableaux correspondantes dans publ. scient. (Association d'oceanographie Physique, 1940) sont augmentés et quelques valeurs changées un peu. Les nombres représentent les hauteurs de la mer au dessus des zéros locaux respectifs.

Le coefficient t est calculé de la manière suivante. On représente l'assemblage des points dans fig. 1 par la droite

$$(a) \quad L(xy) = x \sin A - y \cos A - p = 0$$

Un point $(x_1 y_1)$ a la distance $L(x_1 y_1)$ de cette ligne. On exige que la condition $\sum_{x,y} \big(L(xy)\big)^2 = \text{min.}$ soit remplie, ce qui rend

Année	Aarhus	Horn-bæk	Kôben-havn	Gedser	Korsör	Slips-havn	Année	Aarhus	Horn-bæk	Kôben-havn	Gedser	Korsör	Slips-havn
1892	— 46	— 13	0	— 15	4	— 19	1923	12	55	60	63	57	39
3	— 30	26	37	20	38	20	4	— 16	17	14	26	25	4
4	— 28	6	3	— 7	18	— 17	5	26	67	82	73	67	61
5	— 26	— 8	18	19	25	— 10	6	14	29	44	56	48	51
6	— 34	— 10	4	— 7	4	— 36	7	20	47	61	88	70	56
7	— 45	— 15	— 6	— 22	0	— 32	8	10	22	34	45	50	37
8	10	39	62	48	59	23	9	— 16	10	25	31	41	18
9	28	87	104	125	102	60							
							1930	— 8	— 13	7	27	27	10
1900	— 22	— 12	— 2	20	10	— 15	1	19	23	42	40	45	40
1	— 60	— 40	— 21	— 19	— 8	— 47	2	23	41	53	70	54	37
2	— 22	— 2	3	3	14	— 25	3	— 8	— 21	0	23	30	6
3	37	77	77	91	86	46	4	— 16	15	32	9	36	4
4	— 28	2	— 5	— 13	13	— 21	5	15	36	50	49	54	26
5	— 7	25	25	45	43	10	6	6	3	24	39	44	16
6	3	28	36	28	41	9	7	— 9	— 49	— 21	44	24	— 3
7	— 27	8	14	16	25	— 15	8	26	63	76	81	88	48
8	— 40	— 35	— 25	— 22	— 12	— 43	9	— 37	— 44	— 24	0	9	— 10
9	— 21	0	18	4	28	— 8							
							1940	— 29	— 37	— 9	23	28	1
1910	— 3	11	17	15	35	— 1	1	— 40	— 83	— 27	4	— 4	— 16
1	6	30	46	41	48	26	2	— 37	— 32	2	39	24	0
2	16	43	54	20	39	24	3	17	58	80	81	87	52
3	27	71	83	67	78	58	4	— 1	16	46	77	66	34
4	31	47	64	46	71	51	5	32	46	78	108	101	74
5	— 25	— 22	2	20	16	4	6	27	20	45	84	86	57
6	14	29	49	53	54	30	7	— 30	— 51	— 35	27	24	— 3
7	— 29	— 12	8	21	12	— 8	8	28	50	67	98	105	67
8	— 31	— 10	4	21	14	— 2	9	42	66	87	100	115	80
9	— 40	— 29	— 10	13	8	— 19							
							1950	26	28	40	77	82	51
1920	— 19	— 7	— 2	— 3	15	— 11	1	— 21	— 42	— 38	— 6	19	— 6
1	4	73	76	41	57	39	2	16	13	51	108	92	64
2	— 3	35	45	82	52	28	3	22	31	53	80	90	59

possible le calcul de A et p par les équations

$$\frac{\partial \Sigma}{\partial A} = 0, \quad \frac{\partial \Sigma}{\partial p} = 0.$$

Soit N le nombre des points, tang $A = t$, alors on aura pour t l'équation

$$\text{(b)} \quad t^2 + \frac{N\Sigma x^2 - N\Sigma y^2 - (\Sigma x)^2 + (\Sigma y)^2}{N\Sigma xy - \Sigma x \Sigma y} t - 1 = 0$$

Pour éviter que le résultat soit influencé trop fort par les variations séculaires du niveau des stations, on a calculé t comme moyenne de trois valeurs correspondant chacune à $N = 20$ environ.

Les deux racines de (b) représentent les directions des axes d'une ellipse d'erreur de l'assemblage des points (STUMPFF, 1940). Soient t_a la racine positive, t_b la racine négative, et

$$L_a(xy) = (1 + t_a^2)^{-\frac{1}{2}}(t_a x - y) = 0$$

$$L_b(xy) = (1 + t_b^2)^{-\frac{1}{2}}(t_b x - y) = 0.$$

les droites correspondantes pour $p = 0$. Alors, substituant v_1 et v_2 au lieu de x et y, $L_a(v_1 v_2)$ caractérise la différence des niveaux des deux stations, $L_b(v_1 v_2)$ caractérise la somme des hauteurs de l'eau. L_a et L_b sont non-corrélés. Dans le cas idéal on a $t_a = 1$ et $t_b = -1$, d'où $L_a = (v_1 - v_2)/\sqrt{2}$, $L_b = -(v_1 + v_2)/\sqrt{2}$. C'est donc une idée naturelle d'introduire des niveaux réduites v_1' et v_2' et de calculer des différences de niveau réduites et des hauteurs de l'eau par les équations

(c)

$$h_{12} = L_a\sqrt{2} = \sqrt{2}(1 + t_a^2)^{-\frac{1}{2}}(t_a v_1 - v_2) = v_1' - v_2'$$

$$w_{12} = -L_b\sqrt{2} = -\sqrt{2}(1 + t_b^2)^{-\frac{1}{2}}(t_b v_1 - v_2) = v_1' + v_2'$$

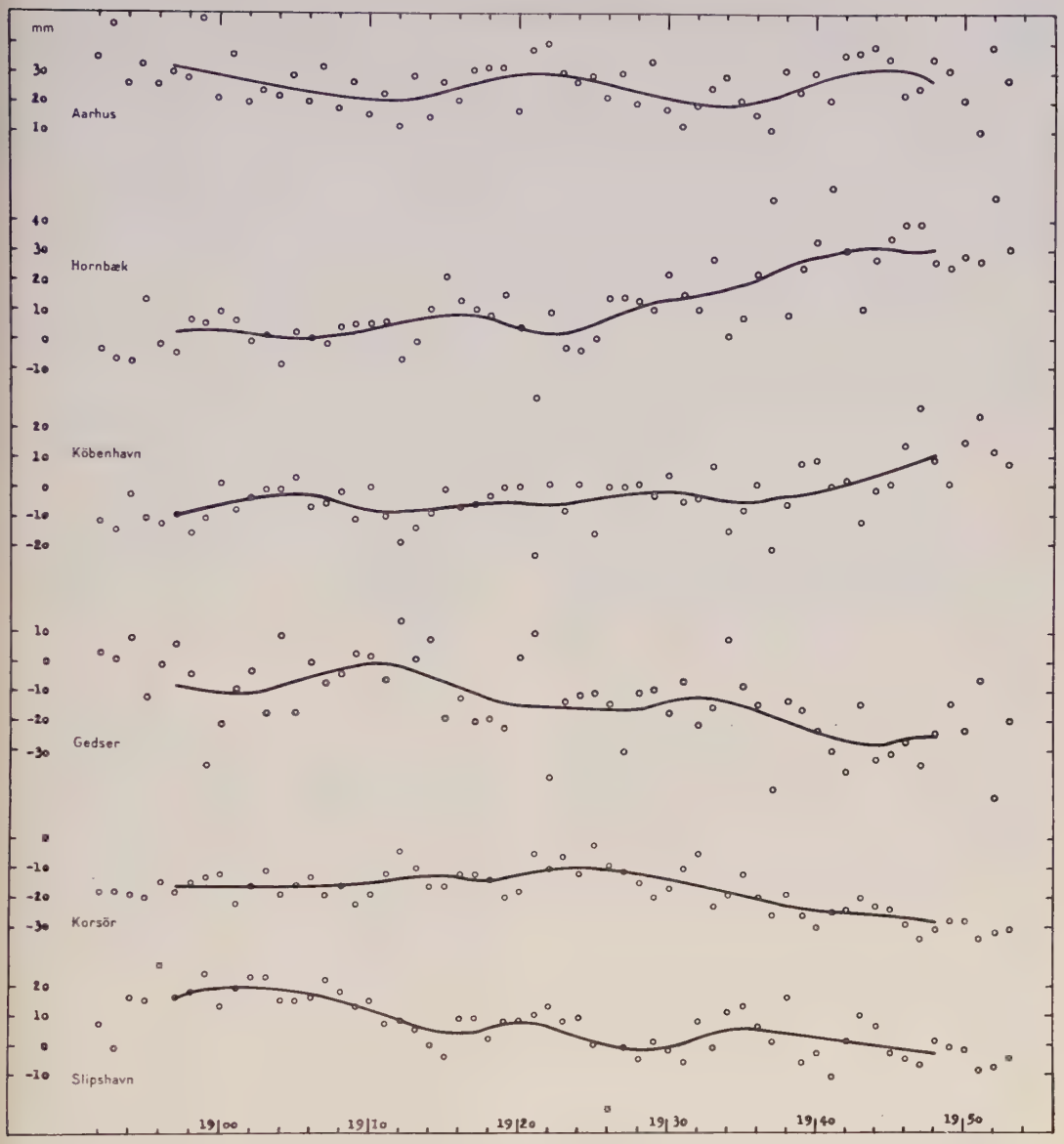

Fig. 2. Variations de la hauteur des zéros locaux.

Par ce procédé on obtient pour les 6 stations mentionnés les équations

$$h_{12} = 0{,}78\,(1{,}5\,v_1 - v_2),$$
$$h_{23} = 1{,}00\,(1{,}0\,v_2 - v_3),$$
$$h_{34} = 1{,}05\,(0{,}9\,v_3 - v_4),$$
$$h_{45} = 1{,}05\,(0{,}9\,v_4 - v_5),$$
$$h_{51} = 1{,}10\,(0{,}8\,v_5 - v_1),$$
$$h_{65} = 0{,}95\,(1{,}1\,v_6 - v_4).$$

$$w_{12} = 1{,}16\,(0{,}7\,v_1 + v_2)$$
$$w_{23} = 1{,}00\,(1{,}0\,v_2 + v_3)$$
$$w_{34} = 0{,}95\,(1{,}1\,v_3 + v_4)$$
$$w_{45} = 0{,}95\,(1{,}1\,v_4 + v_5)$$
$$w_{51} = 0{,}90\,(1{,}2\,v_5 + v_1)$$
$$w_{65} = 1{,}05\,(0{,}9\,v_6 + v_5)$$

Une pair d'équations appartenant ensemble fournit les valeurs correspondantes de v_i'. On

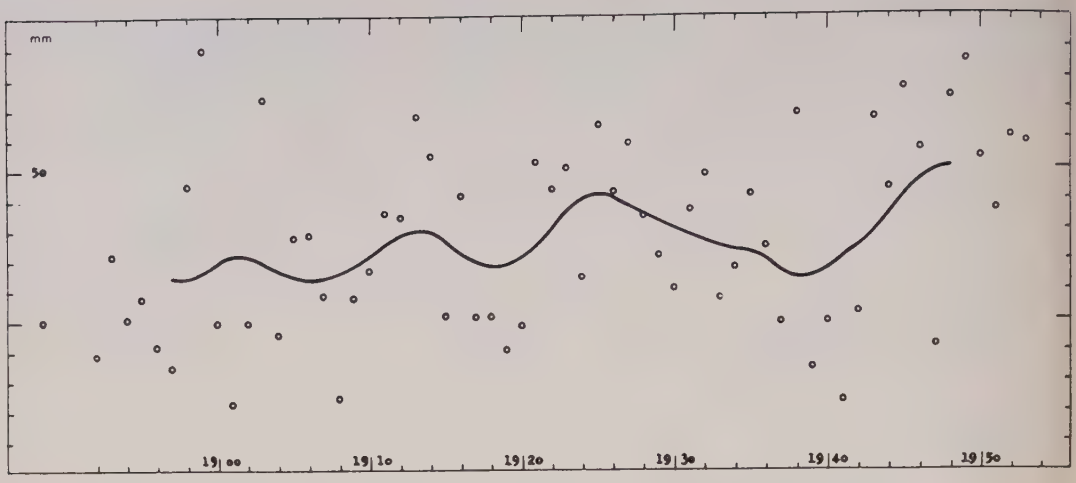

Fig. 3. Variation du niveau de la mer v'.

prend la moyenne de plusieurs v_i' ainsi calculées pour le même indice i pour valeur définitive de v_i'. Finalement on forme la moyenne pesée v' de tous les v_i'; v' représente le niveau réduit de la mer au dessus d'un zéro fictif, dont la hauteur est supposée plus constante que les hauteurs des zéros locaux. La hauteur d'un zéro local au dessus du zéro fictif est $v'—v_i'$.

Les fig. 2 et 3 donnent la représentation graphique de $v'—v_i'$ et v'. L'axe central des diagrammes est supposé d'être la meilleure approximation de la courbe des hauteurs considérées. Pour une valeur fixe de i, il est construit d'après les formules de VERCELLI (1946):

$$^1/_4\,(y_{-1}+2y+y_1),\ ^1/_8\,(y_{-4}+2y_{-2}+2y+2y_2+y_4),$$

appliquées dans l'ordre indiquée. L'axe central de v' est construit sur le même modèle.

Pour chaque courbe on a calculé l'erreur moyenne $m=\sqrt{\frac{1}{n}\sum e^2}$, e étant la différence d'un point de la courbe et la $v'—v_i'$ correspondante. On trouve, en unités de mm, les valeurs suivantes, première colonne.

Aarhus	6,8	9,6
Hornbæk	8,9	10,5
Köbenhavn	7,1	7,9
Gedser	10,4	10,9
Korsör	4,5	4,9
Slipshavn	5,9	6,4
v'	27,8	27,8

Les nombres de la deuxième colonne sont les erreurs moyennes que l'on trouve par un procédé tout analogique au précédant, mais sans tenir compte de la corrélation entre les niveaux donnés v_i. Les courbes construites alors ressemblent beaucoup aux courbes rendues ici, mais peuvent s'en écarter systématiquement de 2—6 mm.

Les erreurs moyennes semblent justifier l'emploi des mm. Les courbes donnent l'impression d'une variation individuelle très marquée des niveaux des zéros locaux. A Korsör, le repère de contrôle qui définie le zéro local, a été remplacé par un autre repère en 1926; ce changement se revèle par un changement dans l'inclinaison de la courbe.

La courbe de v' a ses maxima coïncidant avec les époques des minima des taches solaires.

REFERENCES

ASSOCIATION D'OÉANOGRAPHIE PHYSIQUE, 1940: *Monthly and Annual Mean Heights of Sea-Level.* Up to and including the year 1936. Publication Scientifique No. 5, 86—91.

— *Monthly and Annual Mean Heights of Sea-Level 1937—1946* and unpublished data for earlier years. Publication Scientifique No. 10, 35—36.

STUMPFF, K., 1940: *Ermittlung und Realität von Periodizitäten. Korrelationsrechnung.* Berlin, Handbuch der Geophysik X, 84 pp.

VERCELLI, F., 1946: *Analisi Periodale dei Diagrammi.* Trieste, Istituto Geofisico, Pubbl. n. 221, 5.

NOTES

Note on Simple Assumptions Regarding the Baroclinic Structure of the Atmosphere

By BARRY SALTZMAN, Massachusetts Institute of Technology[1]

(Manuscript received November 11, 1954)

1. Background

In a series of recent articles (STARR 1953, LORENZ 1953, PFEFFER and SALTZMAN 1954) 'local' angular momentum has been used as a basic physical parameter in the study of atmospheric flow. In the last of these references the following approximate dynamical equation was shown to be valid for regions of the atmosphere free of mountain barriers;

$$\frac{\partial M}{\partial t} = \tau, \tag{1}$$

where t is time, M is the total angular momentum within an arbitrarily-located, vertically-oriented, fixed cylindrical volume extending through the depth of the atmosphere, measured relative to the axis of the volume, and τ is the horizontal transport of this 'local' momentum across the fictitious walls of the volume.

LORENZ (1953) has shown that local momentum, M, represents a space-weighted average of the vorticity in a given region of the atmosphere. He has shown, also, that it is possible to make a distinction between displacement and intensification processes by resolving the local momentum transport, τ, into barotropic and baroclinic components, similar to the conventional resolution of the vorticity advection. In more concrete terms we may write,

$$\tau = \frac{p_0}{g} R^2 \int_0^{2\pi} \overline{C_T C_R}\, d\theta \tag{2}$$

or,

$$\tau = \frac{p_0}{g} R^2 \int_0^{2\pi} \overline{C_T} \cdot \overline{C_R}\, d\theta + \frac{p_0}{g} R^2 \int_0^{2\pi} \overline{C_T' C_R'}\, d\theta, \tag{3}$$

where p_0 is the surface pressure (assumed uniform), g is the acceleration of gravity, R is the radius of the cylindrical volume, C_T and C_R are the tangential (positive counter-clockwise) and radial (positive inward) components of the wind velocity respectively, θ is the polar coordinate, the bar denotes a vertical average throughout the atmosphere with respect to pressure, and the primes denote a departure from this average. In (3) the first integral

[1] The research reported in this paper has been sponsored by the Geophysics Research Directorate, Air Force Cambridge Research Center, under Contract No. AF 19(604)-1000.

represents the barotropic component of τ, while the second integral gives the baroclinic contribution resulting from the vertical variation of the horizontal wind field.

It is the purpose of this note to report some observed short-comings of the evaluation of the baroclinic term of (3) by means of an assumption regarding the vertical variation of the wind, as compared with a "three-dimensional" evaluation of the baroclinic contribution by means of data at five levels of the atmosphere. These results may have some bearing on numerical prediction attempts which aim to capture the effects of baroclinicity by similar assumptions.

2. Procedure

In the previous study (PFEFFER and SALTZMAN, 1954) the integral (2) was evaluated directly on a daily basis, using geostrophic winds, for the two-month period January—February, 1949, for a cylindrical volume located over the North Atlantic Ocean. Data at the surface and the 700, 500, 300, and 100 mb levels were employed. The 300, and 100 mb charts were kindly loaned by the U.C.L.A. General Circulation Project and are believed to be one of the best series of maps available at these levels. In addition, the barotropic part of (3) was evaluated for the same region and period, with 500 mb taken as the level of the mean wind.

As an extension of this study it was decided to test whether sufficiently accurate estimates of τ could be obtained by using an assumed wind profile to measure the baroclinic term of (3). Specifically, it was assumed that the tangential and radial components of the wind vary linearly with pressure, the rate of variation (or thermal wind per unit pressure difference) in the troposphere being determined by the 700—300 mb thickness in accordance with the geostrophic principle. Although it does not affect the results appreciably, for greater realism the wind was assumed to decrease above the 200 mb level in a simple linear fashion. These are similar to the assumptions used in the so-called $2^1/_2$-dimensional numerical prediction models.

By subtracting the barotropic component from the "three-dimensional" momentum transport it is possible to obtain a measure of the daily baroclinic contributions. It would be hoped that the baroclinic term computed on the basis of the assumed vertical variation of the wind compares favorably with these values. As it turns out, however, the correlation coefficient between these two quantities for the two-month period is disappointingly small (+.20) and the root mean square deviation is of precisely the same magnitude as the baroclinic term itself. It is recognized that these results may, in part, be attributed to inaccuracies in the estimation of the barotropic term using 500 mb data. It is most likely, however, that the results are mainly a consequence of the crudeness of the representation of the vertical variation of the momentum transport through the use of the assumed wind profile.

One may further inquire as to whether there is an improvement in the verification of the dynamical relationship (1) as a result of using the values of τ based on data at five levels of the atmosphere rather than the values based on the assumed wind profile. Verification of (1) may be measured by the correlation coefficient between the change of local momentum over 24 hours and the time-integrated momentum transport over the same period. As noted in reference 2, estimates of this time-integrated momentum transport over 24 hours, obtained by summing the values of τ at the beginning and end of the period, are far less satisfactory than those obtained when the intermediate (12-hourly) information is incorporated. Unfortunately, in the present case only 24-hourly data were available at upper levels for the "three-dimensional" measurement of the momentum transport and, for comparison purposes, it was necessary to use 24-hourly data in the case of the barotropic and "$2^1/_2$-dimensional" quantities also. Consequently, the correlation coefficients presented in Table 1 are all rather low and can be taken only as a very crude indication of the true relative differences in the verification of the three models[1]. Subject to this reservation, these coefficients suggest that the improvement obtained over the barotropic model by the

[1] When 12-hourly information is included in estimates of $\int_0^{24} \tau dt$ the +.29 correlation coefficient for the barotropic case becomes +.70 (see reference 2).

"2 1/2-dimensional" model is small compared with the improvement obtained when baroclinic effects are taken into account in a more elaborate manner by means of multi-level computations.

Table 1. Correlation coefficients between the time-integrated transport of local momentum and the simultaneous change of local momentum over a 24-hour period, using data at 24-hour intervals. Number of pairs: 58.

barotropic	+ .29
"2 ½-dimensional" baroclinic	+ .32
"3-dimensional" baroclinic	+ .54

As would be expected, it is observed that the greatest improvement over the barotropic verification occurs on specific days when the baroclinic component of the local momentum transport is large. On these same days it is often found that the baroclinic term computed by means of the assumption fails to give an adequate measure of this baroclinicity.

These findings are, of course, of a limited nature and cannot be regarded as a conclusive test of the "2 1/2-dimensional" assumption. Strictly speaking, the results apply to a model which has angular momentum rather than vorticity as the primary physical parameter. The results may be of some general interest, however, in that they suggest possible difficulties in obtaining significant improvement over barotropic numerical forecasting procedures by incorporating simple assumptions regarding the baroclinic structure of the atmosphere.

Acknowledgements

The author wishes to express his appreciation to Professor V. P. Starr for his constant encouragement; to Fil. Lic. G. Arnason for reading the note critically; and, particularly, to Mr. R. L. Pfeffer for his helpful suggestions and stimulating discussions.

REFERENCES

Lorenz, E. N., 1953: Displacement and intensification associated with variations of local angular momentum. *Geophys. Res. Papers*, No. 24, 19—25.

Pfeffer, R. L., and Saltzman, B., 1954: Large-scale rotational flow in a fixed cylindrical volume of the atmosphere. *Final Report, M.I.T. General Circulation Project*, No. AF 19-122-153, 267—284. Also, *J. Meteor.*, 1955 (in press).

Starr, V. P., 1953: Some aspects of the dynamics of cyclones. *Geophys. Res. Papers*, No. 24, 9—17.

Report on the second informal conference on atmospheric chemistry, held at the Meteorological Institute, University of Stockholm, May 31—June 4, 1955

By ERIK ERIKSSON, Institute of Meteorology, University of Stockholm

Last year in May an informal conference in atmospheric chemistry was held at this Institute, a note on which was published in the third issue of Tellus for 1954. In this conference a number of scientists took part, representing studies such as meteorology, oceanography, geology and agriculture. The aim of the conference was to focus attention on the role played by the atmosphere in the circulation, transport and redistribution of certain chemical elements and the possible geochemical, meteorological and practical importance of such processes. It is necessary to establish observational networks in order to study these processes.

As a result of the conference a network of stations was established in the Scandinavian countries, for the collection of monthly air and precipitation samples. Shortly after the conference cooperation with Great Britain was arranged through Prof. P. A. Sheppard of Imperial College (London), which added five stations in England and Scotland. This was originally thought would serve as a link between the Scandinavian network and the United States—North Atlantic net planned by Dr. Chr. Junge from the Air Force Cambridge Research Centre, who also took part in the conference.

A separate network of stations for regular sampling of air for CO_2 was also an outcome of the conference, and this now covers the whole of Scandinavia. Both networks are in operation and the data are published regularly in this journal as a special bulletin.

The present conference was organized by Prof. C. G. Rossby from this Institute and Dr. H. Egnér from the Royal Agricultural College of Sweden, Uppsala, and was attended by the following invited foreign guests:

Dr. W. Bleeker, Koninklijk Nederlands Meteorologisch Instituut, De Bilt, Holland.
Dr. J. Bouquiaux, Institut d'Hygiène et d'Epidemiologie, Bruxelles, Belgium.
Prof. K. Buch, Oceanographic Institute, Helsingfors, Finland.
Dr. L. Facy, Météorologie Nationale, Paris, France.
Dr. J. Grandjean, Institut Royal Météorologique de Belgique, Bruxelles, Belgium.
Dr. Kurmies, Versuchsanstalt Thomasphosphat, Essen, Germany.
Dr. F. Koroleff, Oceanographic Institute, Helsingfors, Finland.
Dr. H. Riehm, Staatliche Landwirtschaftliche Forschungs- und Versuchsanstalt, Augustenberg near Karlsruhe, Germany.

The conference was attended also by Swedish representatives invited from various research institutions and organizations, representing agriculture, forestry, geology, medicine and technical sciences.

The following visitors at the Institute from abroad were also present during the conference:

Dr. J. Adem, Institute of Geophysics, University of Mexico, Mexico City.

Mr. E. Barrett, Woods Hole Oceanographic Institution, Woods Hole, U.S.A.

Mrs. C. Barrett, Institut Royal Météorologique de Belgique, Bruxelles, Belgium.

Mr. P. Bergthorsson, Icelandic Weather Service, Reykjavik, Iceland.

Lt. Col. W. Best, U.S.A.F. Weather Service.

Dr. A. P. Burger, South African Weather Bureau, Pretoria, S. Africa.

Mr. E. Charasch, Meteorological Service, Lod Airport, Israel.

Lt. Cdr. M. Eaton, Office of Naval Research, Washington, U.S.A.

Mr. J. Hughes, Office of Naval Research, Washington, U.S.A.

Lt. Cdr. Masterton, Office of Naval Research, Washington, U.S.A.

Mr. C. Ramaswamy, Weather Service of India, India.

Mr. P. M. Saunders, Imperial College, London, England.

Mr. H. Tabatabay, Iranian Weather Service, Tehran, Iran.

The conference was opened by Prof. C. G. Rossby, who in some introductory remarks outlined its purpose. This was ultimately to discuss and make recommendations on two important questions concerning future cooperative work, namely how to improve and extend the present network and how to maintain it. Before any measures are taken it is, however, necessary to make some kind of list of the various areas to which the results can be applied. After this list has been made the future organization of the network will be discussed. At present it seems reasonable to have the network extended so as to cover France, Belgium, the Netherlands, West Germany and probably Switzerland. The Mediterranean area is also important and an extension so far south is a future goal.

Prof. Rossby also mentioned that Dr. Junge's network will probably be ready this year and that it seems likely that it will be extended south by the cooperation of Dr. Fournier d'Albe, of the Institute of Geophysics, Mexico. It may also be possible to extend it north through cooperation with the Canadians. If all this can be achieved there will be a network for the study of the chemical climate which covers a large part of the northern hemisphere.

Dr. H. Egnér gave a brief outline of the history of the present European network, which dates back to 1945 when the early Swedish network was planned. He also mentioned briefly some practical details concerning the present network.

In the afternoon Prof. Buch discussed the background to the present CO_2 net in Scandinavia. Up to date there are 230 samples of air from this network analysed and the average CO_2-content of these is 3.36×10^{-4} atm. This value, compared with the data compiled by Callendar, indicates a linear increase since 1900. As to the distribution this is remarkable, as the bulk of values are fairly evenly distributed around the mean. A division of the data according to the classified air masses has also been made with the result that the 60 per cent of continental polar and 40 per cent of maritime polar air masses have the same mean value. Unfortunately, no arctic air masses were sampled. He pointed out, however, that the series is too short as yet to be representative.

Prof. Buch also discussed the recent paper by Dingle in Tellus on the rate of exchange of CO_2 between the air and the sea in the North Atlantic. Dingle has used for his calculations a constant value for the CO_2 pressure ($= 3.0 \times 10^{-4}$ atm.). As this pressure in fact, however, is generally considerably higher, one can presume that the CO_2 exchange atmosphere—sea in the northern regions is more rapid and the reverse exchange in the southern parts slower than appears from Dingle's calculations. Better knowledge of the CO_2 concentrations over the North Atlantic would be highly desirable.

Another point Prof. Buch made concerned the influence of combustion of fossil carbon on the C^{14} activity of very recent organic material. If no exchange of the carbon dioxide had occurred it should be revealed by a decrease in the C^{14} activity of the atmospheric CO_2 and indirectly also of the very recent plant material compared to the C^{14} activity of plant material formed 100 years ago.

In the discussion afterwards Dr. G. Arrhenius from the Scripps Oceanographic Institute mentioned that this matter has recently been investigated in USA but that no distinct differences were obtained.

Finally Prof. Buch mentioned the influence of an increase of carbon dioxide in the atmosphere on the heat economy of the earth. The greatest effect would occur in polar regions, where the amount of water vapor is low.

During the discussion Prof. L. G. Romell, from the Swedish Research Institute of Forestry, made some comments on the sampling of air for CO_2 analyses. He pointed out that it would be advisable, in work of the scope now under discussion, to take the samples 100 metres or more above the ground, avoiding the bottom layer of air which has a rapidly fluctuating CO_2 content owing to photosynthesis and soil respiration. Mr. Eriksson replied that the sampling was done at a time of the day when the turbulence in the air could be expected to be at its maximum. Also the sampling sites were chosen as far as possible on gravel grounds, roof tops, etc., where the influence of vegetation would be expected to be small. Further, a probably greater error is introduced during the late fall—early winter seasons, when an accumulation of CO_2 may take place below the rather frequent low inversions.

The last lecture this day was given by Dr. Facy, who reported on present work on atmospheric chemistry in France. He pointed out that the main work so far had been done from the cloud physics point of view, and was concerned therefore mainly with the particulate matter in the atmosphere—the so-called condensation nuclei. In Paris, however, routine investigations on the gases CO_2 and SO_2 are being carried out, and it appears that there is a marked positive correlation between them. The correlation differs in summer and winter, which can be accounted for by variations in industrial and social activities.

As to the particulate matter he described different methods for the collection and the study of these, including the use of the electron microscope. It has been found experimentally that repeated condensation and evaporation on giant nuclei will practically clean the air of very small particles by a mechanism very much like thermal precipitation. When condensation occurs the flux of water vapor towards the surface of the drops causes a flux of very small particles in the same direction. Once they are caught by the drop they will be included with the original condensation nuclei on subsequent evaporation.

As to the sea salt nuclei derived from spray, he mentioned some important observations made on these during evaporation. During slow evaporation a very few cubic crystals, presumably of sodium chloride, form in each drop. When the evaporation is rapid the crystallization occurs explosively, scattering the cubic crystals. In the electron microscope a great number of very small particles can also be seen to have formed, presumably consisting of calcium sulphate crystals in a magnesium chloride solution.

Dr. Facy also mentioned investigations on portions of rain during rainfalls, mainly showers. It was found that the very first portion of the rain contained very high concentrations of substances, especially of sodium chloride. The results also indicated that the last traces at a shower may give information on what was originally in the rain.

In the discussion afterwards Mr. Eriksson said that investigations on portions of rainfall carried out at this Institute in Stockholm did not give any pronounced decrease in concentration with time. The variations within a rainfall were quite large and the only thing which seemed to be reasonably constant was the rate of sodium deposition. The locations of sampling, however, are not comparable and may account for the difference in results.

The second day was devoted to subjects relevant to geochemistry and paleoclimatology. Mr. E. Eriksson from this Institute talked about the chemical composition of river waters in relation to airborne salts. (A paper on this subject is published in the second issue of Tellus 1955.)

Afterwards Dr. Egnér discussed the gaseous equilibria between air and water. He presented a table showing the various gases occurring in the atmosphere and showed on a graph the solubility of these under varying pH conditions. The pH greatly affects the solubility of gases which can form acids or bases in solution like hydrogen sulphide, sulphur dioxide, ammonia and carbon dioxide. The rate at which equilibrium is established varies greatly with the type of gas, being for instance very rapid for amonia and very slow for carbon dioxide.

The importance of these gases in the at-

mosphere to soils, plants, technical constructions and human beings has yet to be assessed. Once we know their amounts, variations and behaviour a good deal can be predicted.

In the afternoon Prof. S. Mattson from the Royal Agricultural College, Uppsala, gave some interesting details on the chemistry of a so-called raised bog in the south-west of Sweden. As such a bog is cut off from nutrient supply from below its growth and composition must reflect the temperature, humidity and chemical climate. Nutrients are supplied practically only from the air. There are many indications of varying climatic conditions since the glacial epoch in these bogs, and with aid of pollen analyses it is possible to date the material to some extent. As to the chemical constituents the common cations such as sodium, potassium, calcium and magnesium occur as fairly easily exchangeable ions and are therefore mobile in the bog. Others such as ammonia, phosphate, silica and aluminium oxide are fairly firmly fixed, especially ammonia, which is intimately bound in the organic matter. The yearly accumulation of such constituents may therefore be calculated and will reflect varying conditions in the chemical climate. As the dating is fairly approximate and can be done only at certain selected levels, the averages have some degree of uncertainty and represent rather long time periods. The most remarkable feature of the bog investigated by Prof. Mattson was that the rate of accumulation of nitrogen (presumably as ammonia) has been fairly constant during most of the time up to the last period when it increases remarkably, a fact which Prof. Mattson interpreted as being due to the increase of population and of domestic animals, and the industrial combustion of coal during the last centuries. He showed that if the increase was assumed to have taken place in the first 30 cm (from the surface), which may correspond to a few hundred years, the increase in nitrogen content is about five-fold. The same though much stronger is indicated by phosphate.

In the discussion Dr. O. Arrhenius pointed out the possibility that the increase in the top part of the bog was due to an accumulation by plant roots from below. Prof. Romell referred to the distribution of phosphorus in a typical heath profile and stressed the fact that the uppermost soil horizon, dominated by living organic matter, is quite generally a zone of accumulation, due to biological action. Mr. Eriksson showed some estimates of the amounts of ammonia released to the atmosphere by domestic animals and industrial activities over Själland, not very far from the bog and in the direction of frequent winds. According to these estimates the annual release of ammonia per unit area has increased by a factor of around six since 1780. Considering the order of magnitude of these estimates he thought that the increase in the top part of the bog could very well be accounted for as being due to an increased rate of delivery from Denmark. Prof. Mattson also pointed out that the increase in the top part of the bog was not only restricted to ammonia and phosphate. A proportional increase of aluminium and silica had also taken place and this could not be attributed to biological enrichment.

The next forenoon was devoted to discussion of practical applications of research in atmospheric chemistry. Dr. U. Trägårdh, Tekniska Högskolan, Stockholm, and member of the Swedish Corrosion Committee, discussed some problems in atmospheric corrosion. Generally, corrosion is much more severe in industrial than in rural areas and more severe in maritime than in continental climates. There is a conventional classification of the climate used in connection with corrosion but there is no close correlation between this classification and the degree of corrosion. The rate of corrosion also seems to vary with the season and with the prehistory of exposure of metal constructions.

Sulphur dioxide gas has been found to have a strong corrosive effect on metals and it is very much enhanced by the presence of particulate matter, especially coal dust.

In the discussion Dr. Facy stressed the importance of the humidity. In desert regions corrosion is no problem whereas in humid areas it may be very severe. The role of microorganisms in corrosion should also be looked into.

Mr. T. Berglund, Sandviken Steel Works, also mentioned the importance of humidity and especially formation of dew on steel constructions. In presence of dust particles

the formation of dew caused by fluctuating temperatures leads to severe corrosion.

Mr. O. Johansson, Royal Agricultural College of Sweden, Uppsala, described some investigations on sulphur compounds in the atmosphere near a slate burning plant. He had found a fairly rapid decrease of these sulphur compounds in the prevailing wind direction. At a distance of 10 km the concentration in the air and in precipitation were quite normal. Another interesting thing brought out by this investigation was the surprisingly high amounts of sulphur taken up by the soil directly from the air. This amount was about twice as large as that received by precipitation.

In the discussion afterwards Dr. Egnér pointed out that the direct transfer of atmospheric constituents to the soil and vegetations seems to be quite considerable. This can of course be expected considering the amount of air which must come into contact with plants and the ground. Estimates from the daily assimilation of CO_2 and transpiration shows that it must be of the order of 500 m^3 of air per m^2 surface and day. The importance of the direct transfer to the ground of chemical constituents has been brought out here in three lectures, namely for ammonia by Prof. Mattson, for chloride by Mr. Eriksson and now for sulphur by Mr. Johansson.

Two of the staff members of the Swedish Public Health Institute reviewed some problems relevant to atmospheric chemistry. Mr. C. E. Holmquist discussed briefly health problems and atmospheric pollution. There are some standards for the tolerable limits of pollutants in industrial plants. The tolerable limit for SO_2 has been set to 10 ppm. However, during a severe smog in London in 1952 it was estimated that 4,000 people were killed by the smog, yet the SO_2 concentration was never more than 1.5 ppm. Therefore tolerable limits for one constituent have no meaning as long as we do not know what role other constituents may play. There are probably many organic compounds which may be of interest. He also mentioned that there is at present no uniformity of sampling methods and gave as an example the measurements of dustiness, which is assessed by different, incomparable methods in different countries.

Mr. G. Sjöström mentioned some recent results of research on iodine in foodstuffs, soils and water, carried out by the Public Health Institute. He mentioned that endemic goitre is at present no problem in Sweden but that there were two areas in which it existed earlier, one on the Highland in the south of Sweden, and the other in the provinces of Dalecarlia, Gästrikland, Hälsingland and Ångermanland. The iodine content of some soil profiles indicated, however, a beginning iodine impoverishment of the top layers of cultivated soils. The atmosphere is generally supposed to be the main iodine source for soils and it would therefore be of interest also from the public health point of view to examine the iodine content of air and precipitation systematically.

In the discussion afterwards Mr. J. Hughes, Office of Naval Research, Washington D. C., mentioned the peculiar circumstances of atmospheric pollution in the Los Angeles Basin where very high ozone contents were found, contrary to what would be expected. As to the iodine. Mr, Eriksson mentioned that the source for iodine in air is most probably the sea and that the iodine chloride ratio in rainwater is much higher than that in sea water. The chemistry of iodine is also more complex than that of chloride. Dr. Egnér asked whether the content of nitrous oxide (laughing gas) and presumably its geographic distribution could have any effect on the behavior of human beings. To this Mr. Holmquist answered that he did not know of any investigations on this.

The afternoon was devoted to a meeting on the European network of stations for air and precipitation samples. Prof. Rossby opened this session by summarizing the preceding events. It seems obvious that the results of synoptic air and precipitation analyses have a very wide application and there is no doubt that an improved and extended network in Europe would give valuable and detailed information over a considerable area. Prior to this conference representatives from France, Belgium, the Netherlands and Germany have expressed their interest in the present network and suggested additional sampling points in their countries. The first step to take now is therefore to make a first decision on the number and position of additional sampling points. As the analytical burden of the Royal

Agricultural College in Sweden cannot be increased further, the future arrangement of the analytical work has also to be decided upon.

As to the analytical data received from the new network, Prof. Rossby suggested that they should be published in the same way as at present, namely quarterly as a special bulletin in Tellus.

Prof. Rossby also gave some information on the financial side of the network. The cost of equipment is about 700 Sw. Krs. per station. To this should be added the cost of necessary electric installations. The operators of the stations in Sweden receive 200 Sw. Krs. yearly, and the present cost of maintenance of the whole net of 50 stations, including the cost of analyses and inspection travels, does not exceed 40,000 Sw. Krs. a year.

Dr. Facy discussed the situation in France. The Meteorological Service in France can set up sxi stations now, and as suitable locations he suggested Rostrenem, Le Mans, Bourges and Ambérieu roughly on a WNW—ESE line and Magny-les Hameaux and Luxeuil to the north of Bourges and Ambérieu respectively.Dr. Facy also mentioned that the Department of Agriculture may become interested and extend the number of stations in France so as to have southern France also represented.

As to Belgium, Dr. Grandjean stated that the Royal Meteorological Institute was willing to set up four stations, namely in Botrange, Dourbes, Uccle and one coastal station which has not yet been chosen.

Finally, Dr. Bleeker representing the Meteorological Service of the Netherlands, suggested that one, and possibly two stations, could be set up in the Netherlands, namely in Witteven, where a magnetic observatory is located (possibly one also in De Bilt). He was not certain, however, in what degree a sampling station in De Bilt would suffer from industrial contamination from the nearby city of Utrecht.

In Germany the number of stations and their position will be worked out later by Dr. Riehm and Dr. Flohn of the Meteorological Service in Germany. Dr. Riehm mentioned that six or seven stations may be established in West Germany. At present there are three planned: two around Feldberg in Baden and one at Augustenberg, near Karlsruhe.

As to the improvements of the network Prof. Rossby mentioned that the number of stations in Norway certainly will be increased, as this is a rather important region. In Britain also the number of stations will be increased and Prof. Sheppard at the Imperial College is at present trying to arrange for the analytical work for these stations to be carried out there.

Prof. Buch mentioned that the number of stations in Finland will be increased, making a total of about ten and that Dr. F. Koroleff will be ready to take over the analytical work for this area on July 1, 1956.

Concerning the analytical work from the remainder of the stations, Dr. Bouquiaux from the Public Health Institute in Bruxelles stated that analyses from about ten stations could be undertaken at his Institute. Prof. Rossby therefore suggested that the French, Belgian and Netherlands samples be analysed at Dr. Bouquiaux's institute, an arrangement to which the representatives for these countries agreed.

The analyses from the German net will be taken care of by Dr. Riehm. He thought it possible to manage samples from about ten stations and suggested therefore that samples which may be collected in Switzerland in future also be analysed in his laboratory.

By this arrangement of analyses centers Sweden can handle the remainder of the net, including additional points in Norway.

The extension of the CO_2 net was also discussed. Dr. Facy suggested Brest in France as a suitable sampling place, the analyses being made in Paris. In Belgium and the Netherlands additional sampling points are available and the analyses can be done at the Public Health Institute in Bruxelles.

Dr. Bleeker discussed some recent measurements of artificial radioactivity in air samples which are being taken on a routine basis in the Netherlands. He described the sampling method and mentioned some very interesting results. He stressed that such measurements are of immediate importance for human welfare and that the undue secrecy around such measurements should be removed. This would facilitate cooperative work on a large scale. Prof. Rossby suggested that this im-

portant question should be taken up for discussion in a letter to the editor of Tellus.

Lt. Col. W. Best, USAF Weather Service, who was not present during this meeting, had given the following information which he wanted made known to those taking part in the conference. The USAF Weather Service make routine weather reconnaissance flights over fixed routes in the northern hemisphere. These aircraft carry weather observing instruments and may well be capable, should the requirement arise, of carrying equipment for both sampling of chemical constituents in the air and for direct measurements of those constituents during flight.

On the last day of the conference, at the Royal Agricultural College of Uppsala, the forenoon was devoted to lectures and discussions. Prof. Rossby discussed some recent results of a study of the chloride to sodium ratio in precipitation in Sweden, as related to the mean monthly circulations (paper by Rossby and Egnér published in the first issue of Tellus 1955).

He mentioned among other things that the yearly variations in the amounts of various constituents is intimately connected to the general circulation and is a much more sensitive indication of circulation changes than for instance temperature and rainfall. He showed that 1949 had very much higher sodium values than later years and that the circulation that year was distinctly characterized by west winds whereas in later years the mean pressure charts show a great deal of continental influence.

In the discussion afterwards Mr. Thuresson from the Becker Co. Paint & Laquer Industry mentioned that 1949 was a rather severe year for corrosion of paints on wood compared to later years. Mr. T. Berglund from the Sandviken Steel Works said that he too had had the same experience concerning steel corrosion.

Mr. Barrett reviewed a recent paper which he had prepared with Mr. G. Brodin of the Royal Agricultural College on the pH in precipitation (to be published in the second issue of Tellus 1955). The pH values at coastal stations are generally on the acid side and are frequently as low as 4.8 on the west coast. Inland the pH values are as a rule on the alkaline side (compared with distilled water in equilibrium with atmospheric carbon dioxide). He also discussed possible explanations for the low coastal values and suggested that H_2S liberated from sea water is oxidized to SO_3 and taken up by the precipitation. He suggested that ozone played a great role in this oxidation.

Mr. Eriksson made some remarks on possible mechanisms for the chemical separation of chloride from sea salt nuclei. Only one such process has been suggested so far, that proposed by Cauer, who thought that ozone in the air might oxidize chloride to chlorine, thus releasing it from sea salt spray. From known data this oxidation seems far too slow to be of any importance. Another process suggested by Mr. Eriksson is that SO_3 when being formed from SO_2 by oxidation is immediately taken up by the condensation nuclei in the air. As H_2SO_4 is formed the pH will drop sufficiently to cause an appreciable vapor tension of HCl (when chloride is present in the nuclei), as indicated by thermodynamic data. As the accumulation of SO_3 will be more important for small nuclei these will be more rapidly depleted of Cl than larger nuclei. The same mechanism is likely to operate in presence of HNO_3 in the air instead of SO_3. As H_2SO_4 is less volatile than HNO_3 and this is less volatile than HCl, HNO_3 will operate mainly on the largest condensation nuclei when both SO_3 and HNO_3 are present.

In the discussion Dr. Bouquiaux doubted that the open sea could be any source for H_2S in the air as the oxygen supply in the sea is ample. He thought, however, that a considerable quantity can come from the part of the sea bottom which is exposed by tidal fluctuations. Mr. Eriksson mentioned that the Hawaian rains also were fairly acid, apparently due to an addition of SO_2 which can hardly be of continental origin.

The afternoon was devoted to demonstrations by Dr. Egnér and Mr. Brodin of the equipment used for sampling air and precipitation in the present network, and of the laboratory used for the analytical work. After this demonstration a sight-seeing tour through Uppsala followed, and the conference was closed by a dinner party at the Royal Agricultural College.

Current Data on the Chemical Composition of Air and Precipitation III

(For further information see Egnér, H., Eriksson, E., *Tellus* **7**, 134—139, 1955.)

D 504

Station	Code	mm	mg/m²								pH	$\frac{\mu val}{l}$	ohm⁻¹ cm⁻¹
			S	Cl	NO_3-N	NH_3-N	Na	K	Mg	Ca		HCO_3^-	$\varkappa \cdot 10^6$
Riksgränsen	Ri	17	18	61	2	2	42	5	6	15	6.3	7	27
Kiruna	Ki	6	7	5	3	1	3	1	2	8	6.2	18	19
Arjeplog	Ar	4	8	8	1	0	11	3	3	14	7.0	111	41
Öjebyn	Öj	12	20	6	2	5	5	5	3	25	6.7	27	25
Röbäcksdalen	Rö	23	25	7	7	4	8	5	3	23	6.0	1	15
Offer	Of	7	16	10	1	3	17	4	3	15	6.8	70	37
Bredkälen	Br	2	—	—	—	—	—	—	—	—	—	—	61
Åre	ÅF	27	21	40	2	2	34	5	5	18	6.3	9	16
Åre, Hummeln	ÅH	16	21	66	5	3	59	5	7	17	6.7	47	37
Sveg	Sv	0.5	—	—	—	—	—	—	—	—	—	—	232
Mora	Mo	6	34	8	3	7	6	14	6	64	7.3	196	90
Åmot	Åm	4	11	5	2	2	15	3	3	15	—	—	67
Sala	Sa	18	31	10	4	5	29	6	8	59	7.1	96	34
Ultuna	Ul	20	25	11	4	8	14	5	4	19	5.6	0	20
Erken	Er	12	13	6	2	2	5	2	2	10	4.9	0	22
Strängnäs	St	28	39	13	6	9	20	5	5	43	6.5	19	22
Forshult	Fo	22	23	9	5	6	18	4	5	31	6.6	37	20
Kvarntorp	Kv1	27	167	17	8	26	17	12	8	210	6.0	12	75
Kvarntorp	Kv7	27	40	12	6	12	10	6	4	27	4.8	0	26
Västra Ny	VN	35	38	13	10	12	17	6	6	35	5.7	5	18
Lanna	La	18	40	19	6	21	20	7	5	33	5.7	6	37
Bornö	Bo	58	87	54	21	33	56	12	12	68	5.5	0	24
Vinga	Vi	20	58	302	14	21	162	13	25	26	4.3	0	116
Falsterbobruk	Fa	52	68	20	12	23	19	7	5	29	4.7	0	26
Flahult	Fl	19	29	14	10	7	21	5	3	25	5.9	14	22
Ambjörnarp	Am	28	48	33	11	18	31	7	5	36	5.5	0	28
Simlångsdalen	Si	30	79	52	20	41	44	6	6	34	4.5	0	53
Plönninge	Pl	19	65	60	14	37	48	8	7	32	4.6	0	69
Söraby	Sö	20	46	14	9	19	13	5	4	24	4.7	0	40
Smedby	Sm	11	50	25	12	19	49	6	7	44	6.8	92	76
Sylfaste	Sy	17	37	26	8	7	62	20	11	71	7.3	267	66
Bräkne-Hoby	BH	12	41	48	11	17	26	32	5	36	5.4	0	63
Hammenhög	Ha	12	43	33	8	10	29	81	9	83	6.9	143	69
Alnarp	Al	32	82	45	14	24	31	16	11	83	5.4	0	43
Hilleshög	Hi	26	139	71	17	17	172	424	5	73	7.1	272	110
Ås	Ås	36	46	14	8	8	21	7	4	47	6.4	16	17
Vågåmo	Vå	2	—	—	—	—	—	—	—	—	—	—	67
Lista	Li	65	102	518	23	28	318	23	36	47	4.5	0	62
Kauhava	Ka	7	13	17	2	6	9	7	2	17	6.7	54	42
Kuopio	Ku	23	20	4	3	5	7	3	3	17	6.0	8	12
Jyväskylä	Jy	29	25	6	4	5	8	4	3	13	5.1	0	13
Tvärminne	Tv	16	20	9	5	7	7	3	2	15	5.4	0	20
Ödum	Öd	16	52	63	7	17	53	26	6	51	6.6	35	58
Askov	As	37	100	105	21	43	65	10	10	45	4.5	0	60
Tystofte	Ty	28	67	87	11	24	85	9	11	61	6.5	33	44
Aberdeen	Ab	27	42	65	8	5	52	6	10	27	5.7	7	30
Edinburgh	Ed	11	27	51	2	0	37	9	7	35	6.6	68	52
Leeds	Le	25	137	122	12	21	48	18	26	123	4.3	0	98

D 505

Station	Code	mm	mg/m²								pH	$\frac{\mu val}{l}$ HCO_3^-	ohm^{-1} cm^{-1} $\varkappa \cdot 10^6$
			S	Cl	NO_3-N	NH_3-N	Na	K	Mg	Ca			
Riksgränsen	Ri	3	—	20	—	—	30	—	—	—	—	100	54
Kiruna	Ki	64	4	14	2	0	5	3	1	10	5.4	0	7
Arjeplog	Ar	21	1	7	2	1	8	1	1	14	7.0	91	18
Öjebyn	Öj	34	2	7	5	11	25	6	3	41	6.8	39	18
Röbäcksdalen	Rö	28	7	9	7	9	29	5	5	37	6.7	26	23
Offer	Of	50	15	10	6	10	25	5	4	23	5.9	11	17
Bredkälen	Br	38	22	10	5	12	16	7	2	21	6.0	15	12
Åre	ÅF	42	7	10	2	2	14	2	2	15	6.3	13	9
Åre, Hummeln	ÅH	9	6	24	2	2	17	2	2	10	6.5	26	27
Sveg	Sv	41	74	35	8	6	52	7	8	53	6.9	64	19
Mora	Mo	68	52	16	10	7	10	9	7	89	6.5	21	16
Åmot	Åm	57	46	16	9	13	24	4	4	29	5.5	0	13
Sala	Sa	53	62	21	9	14	26	9	5	35	5.5	0	18
Ultuna	Ul	55	60	22	13	28	19	7	3	22	4.8	0	23
Erken	Er	55	66	28	10	13	20	11	4	25	4.5	0	26
Strängnäs	St	47	69	22	12	20	29	7	6	53	5.4	0	23
Forshult	Fo	79	70	27	10	18	31	6	5	39	5.1	0	15
Kvarntorp	Kv1	67	638	52	17	114	40	29	20	705	4.8	0	110
Kvarntorp	Kv7	65	128	18	15	29	30	12	8	61	4.4	0	39
Västra Ny	VN	67	82	50	14	26	52	9	8	45	5.0	0	22
Lanna	La	41	69	61	14	29	56	11	8	47	5.8	9	28
Bornö	Bo	69	94	258	20	24	179	13	16	27	5.5	0	33
Vinga	Vi	52	148	1450	20	21	1050	41	97	77	4.6	0	157
Falsterbobruk	Fa	43	54	24	12	12	19	5	4	34	4.6	0	27
Flahult	Fl	83	106	122	20	54	54	28	8	39	5.1	0	23
Ambjörnarp	Am	110	99	209	26	41	137	30	15	53	5.1	0	24
Simlångsdalen	Si	112	117	226	32	46	155	21	19	52	4.7	0	32
Plönninge	Pl	76	96	249	25	35	168	15	22	55	4.8	0	36
Söraby	Sö	91	96	97	26	37	65	13	12	49	4.6	0	28
Smedby	Sm	65	60	41	11	13	56	9	9	48	6.4	17	16
Sylfaste	Sy	44	56	31	15	23	35	7	7	62	6.6	20	23
Bräkne-Hoby[1]	BH	—	—	—	—	—	—	—	—	—	—	—	—
Hammenhög	Ha	57	86	101	23	37	69	16	10	173	7.0	60	37
Alnarp	Al	59	74	151	23	34	95	30	15	186	6.2	15	47
Hilleshög	Hi	53	127	166	28	34	201	353	14	73	7,1	78	63
Ås	Ås	82	53	210	11	19	80	12	9	127	5.7	2	23
Vågåmo	Vå	24	17	6	3	5	19	3	5	28	7.3	51	14
Lista	Li	81	122	900	15	11	648	22	68	60	4.6	0	74
Kauhava	Ka	30	26	10	4	9	6	3	2	13	5.9	4	13
Kuopio	Ku	40	30	0	4	10	8	2	3	22	5.1	0	14
Jyväskylä	Jy	78	51	7	11	23	13	6	3	18	4.9	0	14
Tvärminne	Tv	54	60	18	13	19	22	6	5	35	4.9	0	24
Ödum	Öd	45	86	260	15	29	117	14	14	61	5.3	0	37
Askov	As	85	92	635	23	45	366	26	55	77	4.7	0	55
Tystofte	Ty	72	110	208	29	89	162	19	18	65	5.0	0	36
Aberdeen[2]	Ab	—	—	—	—	—	—	—	—	—	—	—	—
Edinburgh	Ed	57	54	124	8	15	96	15	14	51	5.6	2	25
Leeds	Le	68	159	214	23	37	112	18	57	129	4.6	0	52
Rothamsted	Ro	106	151	176	31	19	92	28	36	120	4.4	0	31
Newton Abbot	NA	105	97	350	13	13	205	16	27	87	5.0	0	29
Augustenberg[3]	Au	—	—	—	—	—	—	—	—	—	—	—	—
Güntherstha l	Gü	125	80	93	21	16	89	31	12	113	5.5	3	13
Feldberg[4]	Fe	—	—	—	—	—	—	—	—	—	—	—	—

[1] Bird droppings in the funnel; sample not analyzed.

[2] Precipitation sample not received.

[3] Will start sampling October 1, 1955.

[4] Will start sampling June 1, 1955.

D 506

Station	Code	mm	mg/m²								pH	$\frac{\mu val}{l}$ HCO_3^-	ohm^{-1} cm^{-1} $\varkappa \cdot 10^6$
			S	Cl	NO_3-N	NH_3-N	Na	K	Mg	Ca			
Riksgränsen	Ri	62	16	20	4	2	17	5	3	18	5.6	4	6
Kiruna	Ki	63	26	14	4	4	5	4	2	23	5.2	0	9
Arjeplog	Ar	41	19	34	4	4	16	4	4	47	6.3	21	12
Öjebyn	Öj	45	42	19	6	11	14	9	6	84	6.3	40	20
Röbäcksdalen	Rö	61	35	10	5	7	17	6	6	33	5.1	0	12
Offer	Of	66	46	26	7	10	40	13	7	52	6.2	16	14
Bredkälen	Br	49	22	5	3	6	7	4	7	19	5.3	0	9
Åre	ÅF	41	20	12	3	2	16	6	3	25	6.1	16	9
Åre, Hummeln	ÅH	25	15	14	3	1	14	3	2	17	6.0	8	10
Sveg	Sv	32	28	23	6	6	46	11	6	51	6.8	75	23
Mora	Mo	25	20	13	1	7	6	13	5	64	6.8	97	24
Åmot	Åm	22	15	8	4	1	16	6	3	30	6.4	25	15
Sala	Sa	31	51	13	7	3	25	13	6	72	6.4	34	27
Ultuna	Ul	24	29	11	5	8	17	5	4	40	6.2	18	24
Erken	Er	23	24	7	3	5	7	10	3	24	5.3	0	17
Strängnäs	St	19	39	12	5	4	24	10	6	51	6.2	22	32
Forshult	Fo	35	37	23	5	2	22	8	5	55	6.1	14	16
Kvarntorp	Kv1	19	330	65	4	29	31	22	37	219	6.0	15	217
Kvarntorp	Kv7	12	45	10	3	8	11	10	13	55	4.8	0	55
Västra Ny	VN	12	18	15	4	1	25	6	6	45	6.8	93	40
Lanna[1]	La	—	—	—	—	—	—	—	—	—	—	—	—
Bornö	Bo	32	48	152	9	6	88	10	33	33	4.8	0	47
Vinga	Vi	7	54	524	12	6	270	22	41	47	5.3	0	390
Falsterbobruk	Fa	13	30	27	5	3	15	28	7	42	6.1	30	44
Flahult	Fl	22	47	23	9	11	29	13	19	37	5.9	12	33
Ambjörnarp	Am	28	59	49	10	15	38	14	7	42	5.2	0	37
Simlångsdalen	Si	32	51	84	11	10	58	13	16	32	4.6	0	47
Plönninge	Pl	17	62	67	13	11	78	10	12	64	6.7	67	68
Söraby	Sö	19	39	22	5	7	23	47	5	32	5.1	0	31
Smedby	Sm	13	18	11	2	1	24	31	15	29	6.7	90	38
Sylfaste	Sy	39	34	13	7	5	20	11	5	68	6.6	54	20
Bräkne-Hoby	BH	23	64	41	16	106	48	35	12	78	7.1	280	95
Hammenhög	Ha	41	87	82	18	27	70	90	19	96	6.4	73	55
Alnarp	Al	36	72	28	14	13	22	12	21	52	6.1	15	33
Hilleshög	Hi	25	96	51	14	13	64	201	6	55	6.9	110	72
Ås	Ås	22	30	38	4	2	40	12	6	56	6.7	66	33
Vågåmo	Vå	20	24	32	1	1	22	22	6	46	6.7	100	28
Lista	Li	52	98	849	18	12	421	39	56	59	4.5	0	103
Kauhava	Ka	23	23	10	2	1	9	10	10	27	5,6	22	17
Kuopio	Ku	14	10	2	2	1	8	4	0	19	6,5	27	14
Jyväskylä	Jy	19	11	22	2	1	9	5	1	25	6.3	29	16
Tvärminne	Tv	22	17	23	3	2	12	10	1	61	5.6	4	16
Ödum	Öd	78	94	79	19	34	60	16	14	52	4.8	0	29
Askov	As	42	86	64	22	26	54	20	46	95	4.9	0	44
Tystofte	Ty	56	106	70	22	36	77	14	12	93	5.7	8	32
Aberdeen	Ab	46	46	108	4	1	174	8	24	101	7.0	306	55
Edinburgh	Ed	14	50	110	7	5	97	2	13	56	5.9	4	90
Leeds	Le	39	85	70	15	15	46	13	57	103	5.6	10	39
Rothamsted	Ro	52	89	56	21	25	43	14	8	66	5.9	55	36
Newton Abbot	NA	68	86	154	26	42	122	17	13	60	5.7	23	31
Augustenberg	Au	—	—	—	—	—	—	—	—	—	—	—	—
Günthersthal	Gü	139	89	28	202	10	28	20	7	64	5.2	0	13
Feldberg	Fe	108	94	20	48	76	16	14	12	70	5.6	8	15

[1] Dirty sample; not analyzed.

L 504

Station	Code	$\mu g/m^3$ (= kg/km^3)						
		S	Cl	NH_3-N	Na	K	Mg	Ca
Riksgränsen[1]	Ri	—	—	—	—	—	—	—
Kiruna	Ki	0.0	0.0	0.1	1.2	0.2	0.2	0.5
Arjeplog[2]	Ar	—	—	—	—	—	—	—
Öjebyn	Öj	3.9	5.5	2.3	0.4	0.8	0.4	7.0
Röbäcksdalen	Rö	6.4	3.6	1.5	0.5	0.6	0.3	6.0
Offer	Of	4.3	0.0	3.5	0.5	2.6	0.4	6.7
Bredkälen[2]	Br	—	—	—	—	—	—	—
Åre	ÅF	3.5	4.2	1.1	0.6	1.2	0.4	4.1
Åre, Hummeln	ÅH	3.1	3.5	0.8	1.2	0.6	0.1	3.0
Sveg[3]	Sv	—	—	—	—	—	—	—
Mora	Mo	5.5	3.4	3.5	0.5	0.4	0.1	5.2
Åmot	Åm	4.9	7.5	1.9	1.0	1.4	0.0	8.1
Sala[2]	Sa	—	—	—	—	—	—	—
Ultuna	Ul	4.9	2.0	1.5	0.2	0.4	0.1	1.8
Erken	Er	3.7	2.0	1.0	0.1	0.3	0.1	2.8
Strängnäs	St	4.7	0.0	2.6	0.4	0.3	0.1	1.4
Forshult	Fo	4.8	0.0	1.6	0.5	1.2	0.8	6.7
Kvarntorp	Kv1	44.0	0.7	6.1	0.2	1.9	1.3	18.0
Kvarntorp	Kv7	2.0	0.0	1.9	0.2	0.0	0.2	2.4
Västra Ny[3]	VN	—	—	—	—	—	—	—
Lanna	La	—	—	—	—	—	—	—
Bornö[2]	Bo	—	—	—	—	—	—	—
Vinga	Vi	9.9	124.0	3.4	52.0	3.5	10.0	19.0
Falsterbobruk	Fa	3.9	4.9	2.0	0.0	0.0	0.8	5.1
Flahult	Fl	3.4	3.7	1.4	0.5	0.5	0.2	2.9
Ambjörnarp[3]	Am	—	—	—	—	—	—	—
Simlångsdalen[3]	Si	—	—	—	—	—	—	—
Plönninge	Pl	8.6	9.2	4.5	0.5	0.0	0.5	4.5
Söraby[3]	Sö	—	—	—	—	—	—	—
Smedby	Sm	2.4	3.3	2.7	0.2	0.0	0.2	3.0
Sylfaste[2]	Sy	—	—	—	—	—	—	—
Bräkne-Hoby[4]	BH	—	—	—	—	—	—	—
Hammenhög[3]	Ha	—	—	—	—	—	—	—
Alnarp	Al	12.0	3.3	3.7	0.9	0.4	0.6	4.6
Hilleshög[3]	Hi	—	—	—	—	—	—	—
Ås	Ås	4.8	5.3	2.3	0.4	0.3	0.4	5.7
Vågåmo	Vå	0.0	3.8	5.6	0.4	0.3	0.6	7.4
Lista	Li	4.4	60.0	1.6	27.0	1.2	3.7	5.7
Kauhava	Ka	2.8	2.5	2.1	0.4	0.7	0.6	5.6
Kuopio	Ku	4.5	3.5	1.7	0.1	0.1	0.3	5.0
Jyväskylä	Jy	3.2	0.0	0.9	0.0	0.0	0.5	3.4
Tvärminne	Tv	1.0	0.0	0.8	0.0	0.0	0.2	1.6
Ödum	Öd	12.0	13.0	5.7	6.1	0.7	0.8	3.7
Askov[4]	As	—	—	—	—	—	—	—
Tystofte	Ty	5.2	2.7	5.8	1.2	0.2	0.5	2.9
Aberdeen	Ab	9.9	9.6	3.1	3.1	0.3	1.1	9.0
Edinburgh	Ed	15.0	20.0	2.1	10.0	3.0	1.9	2.6
Leeds	Le	30.0	12.0	4.9	5.2	1.1	1.8	8.0

[1] Trouble with the aerator.

[2] Samples spoiled at the station.

[3] No equipment for air sampling.

[4] Sampling will start on June 1, 1955.

L 505

Station	Code	μg/m³ (= kg/km³)						
		S	Cl	NH_3-N	Na	K	Mg	Ca
Riksgränsen	Ri	0.0	1.9	1.5	4.6	3.5	1.5	2.8
Kiruna	Ki	0.0	0.0	2.3	1.1	1.3	0.5	4.0
Arjeplog	Ar	1.4	2.6	1.1	1.2	0.0	5.0	13.4
Öjebyn	Öj	0.0	0.3	3.4	1.4	1.1	0.1	2.6
Röbäcksdalen	Rö	1.2	0.9	1.0	1.2	0.7	0.1	2.5
Offer	Of	0.5	0.0	3.3	1.5	0.0	0.2	1.6
Bredkälen	Br	0.8	2.1	1.1	1.2	0.0	0.1	0.9
Åre	ÅF	1.5	0.7	0.9	0.7	0.3	0.0	1.0
Åre, Hummeln	ÅH	0.8	0.0	0.8	1.0	0.3	0.8	1.0
Sveg	Sv	—	—	—	—	—	—	—
Mora	Mo	0.4	0.8	3.0	0.5	0.3	0.1	1.0
Åmot	Åm	0.3	0.0	1.5	0.8	0.6	0.1	1.9
Sala	Sa	4.7	3.2	2.9	2.1	1.5	0.2	1.9
Ultuna	Ul	0.1	1.2	1.7	0.6	0.0	0.0	1.6
Erken	Er	0.5	0.6	1.1	0.8	0.6	0.1	0.7
Strängnäs	St	0.5	0.0	2.1	0.6	0.4	0.0	1.0
Forshult	Fo	1.0	0.0	1.7	0.9	0.0	0.0	2.7
Kvarntorp	Kv1	7.1	6.0	7.1	1.5	2.1	1.3	5.6
Kvarntorp	Kv7	0.9	0.0	1.5	0.6	0.0	1.2	3.3
Västra Ny	VN	—	—	—	—	—	—	—
Lanna	La	1.5	2.7	2.1	1.3	0.4	0.0	3.9
Bornö	Bo	1.3	4.1	1.1	2.6	0.3	0.7	3.6
Vinga	Vi	1.7	11.9	1.1	2.9	0.0	1.1	1.2
Falsterbobruk	Fa	0.3	5.1	1.5	1.4	0.0	13.8	1.1
Flahult	Fl	0.2	1.1	1.1	0.9	0.4	0.9	4.8
Ambjörnarp	Am	—	—	—	—	—	—	—
Simlångsdalen	Si	—	—	—	—	—	—	—
Plönninge	Pl	1.4	7.1	2.7	1.6	0.1	0.2	2.7
Söraby	Sö	—	—	—	—	—	—	—
Smedby	Sm	0.8	0.0	2.0	1.0	0.6	0.0	2.7
Sylfaste[1]	Sy	—	—	—	—	—	—	—
Bräkne-Hoby	BH	—	—	—	—	—	—	—
Hammenhög	Ha	—	—	—	—	—	—	—
Alnarp	Al	3.4	6.7	2.9	1.6	0.2	0.3	1.0
Hilleshög	Hi	—	—	—	—	—	—	—
Ås[1]	Ås	—	—	—	—	—	—	—
Vågåmo	Vå	0.0	0.0	3.7	0.8	1.0	0.0	1.9
Lista	Li	3.0	24.4	1.4	41.3	2.8	4.8	4.5
Kauhava	Ka	0.0	0.0	1.5	1.4	0.3	0.5	1.0
Kuopio	Ku	0.0	0.5	1.7	0.7	0.0	0.3	1.0
Jyväskylä	Jy	0.0	1.0	1.1	0.8	0.6	0.7	2.6
Tvärminne	Tv	0.4	0.0	1.2	1.2	0.0	0.4	1.9
Ödum	Öd	0.7	7.5	3.0	3.9	0.8	3.9	2.7
Askov	As	—	—	—	—	—	—	—
Tystofte	Ty	0.8	0.0	4.5	1.9	0.5	0.7	2.7
Aberdeen	Ab	2.2	11.1	3.3	3.2	0.0	19.4	0.7
Edinburgh	Ed	1.4	0.0	2.0	1.2	0.0	0.6	1.9
Leeds	Le	15.6	4.9	3.9	3.7	0.6	1.2	1.9
Rothamsted	Ro	8.8	4.3	2.6	1.8	0.8	0.7	8.4
Newton Abbot	NA	2.1	2.0	2.9	2.4	0.5	0.0	0.2
Augustenberg	Au	—	—	—	—	—	—	—
Günthersthal	Gü	3.8	0.0	1.0	2.4	0.5	2.5	7.5
Feldberg	Fe	—	—	—	—	—	—	—

[1] Samples spoiled at the station.

L 506

Station	Code	$\mu g/m^3$ (= kg/km^3)						
		S	Cl	NH_3-N	Na	K	Mg	Ca
Riksgränsen[1]	Ri	—	—	—	—	—	—	—
Kiruna[2]	Ki	—	—	—	—	—	—	—
Arjeplog[2]	Ar	—	—	—	—	—	—	—
Öjebyn	Öj	1.8	0.7	1.7	0.7	0.6	0.2	2.5
Röbäcksdalen	Rö	1.8	2.1	1.3	0.6	0.9	1.6	7.2
Offer	Of	2.8	4.0	3.4	1.4	1.5	0.9	15.0
Bredkälen	Br	5.9	8.9	3.7	2.9	2.2	1.0	28.0
Åre	ÅF	0.0	1.2	1.0	1.4	1.4	0.4	7.7
Åre, Hummeln	ÅH	0.1	0.0	0.6	0.7	0.6	0.4	6.0
Sveg	Sv	—	—	—	—	—	—	—
Mora	Mo	1.4	1.3	2.3	1.1	0.8	0.1	3.5
Åmot	Åm	0.1	2.0	2.0	0.7	0.5	0.1	9.0
Sala	Sa	2.9	0.0	3.0	1.7	0.7	0.6	12.0
Ultuna	Ul	1.4	1.9	1.4	0.6	0.8	0.3	6.7
Erken	Er	3.6	0.0	1.0	0.8	0.5	1.1	4.2
Strängnäs	St	1.6	0.0	3.1	1.0	0.7	1.3	3.1
Forshult[2]	Fo	—	—	—	—	—	—	—
Kvarntorp	Kv1	43.0	4.9	8.0	1.6	2.3	21.0	15.0
Kvarntorp	Kv7	5.4	0.8	1.7	0.7	0.3	2.9	6.2
Västra Ny	VN	—	—	—	—	—	—	—
Lanna	La	4.2	2.5	3.4	6.1	15.0	1.7	46.0
Bornö	Bo	—	—	—	—	—	—	—
Vinga[1]	Vi	—	—	—	—	—	—	—
Falsterbobruk	Fa	3.3	6.4	1.6	1.1	0.7	1.5	13.0
Flahult	Fl	1.4	2.8	1.2	0.9	0.6	1.3	6.0
Ambjörnarp	Am	—	—	—	—	—	—	—
Simlångsdalen	Si	—	—	—	—	—	—	—
Plönninge	Pl	4.0	5.0	3.8	2.7	0.7	0.5	8.6
Söraby	Sö	—	—	—	—	—	—	—
Smedby	Sm	0.0	1.0	2.4	3.6	1.8	0.7	8.4
Sylfaste	Sy	2.9	6.3	2.2	0.9	0.8	0.1	8.2
Bräkne-Hoby	BH	0.0	0.0	0.9	1.1	0.3	0.1	6.3
Hammenhög	Ha	—	—	—	—	—	—	—
Alnarp	Al	7.3	3.3	4.0	1.2	0.9	2.0	9.7
Hilleshög	Hi	—	—	—	—	—	—	—
Ås[2]	Ås	—	—	—	—	—	—	—
Vågåmo	Vå	4.0	11.0	12.0	3.4	2.6	2.5	26.0
Lista	Li	6.4	47.0	1.8	37.0	1.4	3.3	21.0
Kauhava	Ka	5.3	2.7	2.3	2.8	3.3	0.5	6.4
Kuopio	Ku	0.8	1.3	2.6	3.4	0.6	0.4	9.4
Jyväskulä	Jy	0.0	2.1	1.5	2.0	1.0	0.9	11.0
Tvärminne	Tv	0.0	0.0	0.8	1.1	0.4	0.1	5.1
Ödum	Öd	5.5	25.0	4.9	27.0	2.1	2.2	8.2
Askov	As	7.9	4.7	5.7	2.2	0.6	0.7	5.3
Tystofte	Ty	8.7	5.5	5.3	3.5	0.6	2.1	8.5
Aberdeen	Ab	18.0	16.0	6.7	12.0	2.0	9.6	24.0
Edinburgh	Ed	7.7	4.8	2.2	3.4	0.6	0.2	2.8
Leeds	Le	19.0	7.1	3.4	2.1	1.0	3.5	4.9
Rothamsted	Ro	14.0	3.5	2.7	1.6	0.6	0.8	3.1
Newton Abbot	NA	5.2	5.3	2.0	2.2	0.7	0.7	4.3
Augustenberg	Au	—	—	—	—	—	—	—
Günthersthal	Gü	4.3	3.3	3.8	2.3	1.6	0.4	2.0
Feldberg	Fe	4.2	1.8	2.3	2.0	1.0	0.2	5.6

[1] Trouble with the aerators.

[2] Samples spoiled at the station.

Uppsala in July 1955.

G. Brodin
Agricultural College, Uppsala

Current Data of CO_2 in the air Febr.—April 1955 in Scandinavia.

(Cf. FONSELIUS, KOROLEFF: *Tellus*, 7, 2, pp. 258—265)

February							March						
Stn	Date	Hour	°C	Wind m/sec.	Weather Pressure	ml/10 l	Stn	Date	Hour	°C	Wind m/sec.	Weather Pressure	ml/10 l
Ab.	1	—	—	—	—	—	Ab.	1	13	— 4	W		3.26
	10	13	— 8	SW 3.5		3.39		10	13	— 19	NNW 3.5		3.23
	20	13	— 8			3.58		20	13	— 9.5	N		3.23
Öj.	1	13	— 13.0	NE		3.29	Öj.	1	13	— 12.0	N		3.33
	10	13	— 17.2	NE	snow	3.23		10	13	— 13.8	SW		3.29
	20	13	— 9.2	N		3.40		20	13	— 5.6	E	snow	3.22
Br.	1	13	— 10	NE	snow	3.51	Br.	1	13	— 2	WNW		3.28
	10	13	— 7	SW		3.46		10	13	± 0	NW		3.28
	20	13	— 10	NW		3.28		20	13	— 5	SE	snow	3.23
Ul.	1	13	+ 0.7	SW		4.32	Ul.	1	13	— 2.2	WSW		3.70
	10	13	— 3.5	W 3.6		3.67		10	13	— 1.8	N		3.68
	20	13	— 9.6	N 3		3.36		20	13	— 3.7	calm		3.59
Fl.	1	13	+ 1.8	S		3.54	Fl.	1	13	— 1.6	W		3.28
	10	13	— 4.6	NNE		3.36		10	13	+ 1.5	NE		3.31
	20	13	— 8.0	NE		3.33		20	13	— 5.2	E		3.29
Pl.	1	13	± 0	E		3.57	Pl.	1	13	— 1	W		3.29
	10	13	— 3	N		3.26		10	13	± 0	calm		3.30
	20	13	— 5	N		3.61		21	13	± 0	E		3.40
Ka.	1	13	— 5.2	NE	751.8	3.01	Ka.	1	13	— 6.3	SSE	762.8	3.36
	10	13	— 5.8	WSW	744.8	3.61		10	13	— 8.3	calm	762.8	3.90
	20	13	— 15.4	NW	752.6	3.25		20	13	— 6.8	SW 6.5	753.9	3.34
Ri.	1	15	— 9.2	calm	747.8	3.03	Ri.	1	15	— 8.2	ESE 5	763.0	3.25
	10	16	— 4.9	S 2.5	742.0	3.72		10	—	—	—	—	—
	20	15	— 18.4	WNW 10	748	3.55		20	—	—	—	—	—
Lu.	1	12	— 8.3	SSE 2	741.0	3.24	Lu.	1	12	— 6.1	SSE 3	754.4	3.38
	10	12	— 5.8	S 3	735.5	3.60		10	—	—	—	—	—
	20	12	— 19.2	NNW 2	741.3	3.41		20	12	— 8.4	NE 3	744.0	3.80
Tv.	1	12	+ 3.0	SW 0	766.0	2.98	Tv.	1	12	— 1.0	SW 1.0	782	3.41
	10	12	— 2.0	NE 0.5	760.0	3.40		10	12	— 5.0	S 0	778	3.67
	20	12	— 12.0	N 0.5	777.8	3.31		20	12	— 2.0	E 1.0	768	3.40
Bo.	1	13	— 5.6	NE 4		3.53	Bo.	1	13	+ 2.4	NNE		3.07
	10	13	— 3.2	NNE 1		3.37		10	13	— 2.2	NE		3.34
	20	13	+ 0.8	6		3.10		20	13	— 5.2	NNE		3.60
Vå.	1	13	+ 1.4	NE		3.38	Vå.	28/2	13	— 12.4	SE		3.49
	10	13	— 3.2	SW		3.32		10	13	+ 0.4	WSW		3.45
	20	13	— 21.6	SW		3.52		20	13	— 10.4	SW		3.45
Be.	1	13	+ 7.6	SSE 2		3.32	Be.	1	—	—	—	—	—
	10	13	— 0.1	NNE 2		3.40		10	13	+ 3.1	calm		3.40
	20	13	— 4.0	S 2		3.63		20	13	— 1.0	SSE		3.49
Öd.	1	13	+ 3.2	NE		3.63	Öd.	1	13	— 1.8	S		3.30
	15	13	— 5.4	NNW		3.29		10	13	+ 4.8	SW		3.34
	20	13	— 4.8	N		3.31		20	13	— 3.4	NW		3.55
As.	1	13	+ 6	SE		3.55	As.	1	13	— 2.0	S 4	3	3.31
	10	13	— 0.5	NNE 3		3.41		10	13	+ 3.5	NW 1		3.35
	20	13	— 4.6	NE 5		3.29		20	13	— 2.0	W 2		3.52

April						
Stn	Date	Hour	°C	Wind m/sec.	Weather Pressure	ml / 10 l
Ab.	1	13	—	NW 2.1	—	3.42
	—	—	—	—	—	—
	20	13	—	NNW 7	—	3.37
Öj.	1	13	— 2.0	N		3.30
	10	13	— 1.5	E		3.09
	20	13	+ 6.3	W		3.49
Br.	1	13	+ 1	NNW		3.23
	10	13	— 5	SE		3.00
	20	13	± 0	NW		3.43
Ul.	1	13	+ 2.3	WNW 5.1		3.34
	10	13	— 2.1	NW 2.0		3.20
	20	13	+ 14.7	SW 2.8		3.43
Fl.	1	13	+ 3.4	NW		3.25
	10	13	+ 2.4	S		3.10
	20	13	+ 14.4	NE		3.29
Pl.	1	13	+ 3	W		3.23
	10	13	+ 4	SE		3.14
	20	13	+ 7	W		3.36
Ka.	1	13	— 3.5	NE 1.5	745.3	3.92
	10	13	— 0.4	N 4.5	758.7	3.21
	20	13	+ 5.5	SW 2.5	749.9	3.10

April						
Stn	Date	Hour	°C	Wind m/sec.	Weather Pressure	ml / 10 l
Ri.	1	—	—	—	—	—
	10	—	—	—	—	—
	20	—	—	—	—	—
Lu.	1	12	— 4.9	E 1.5	737.7	3.76
	10	12	— 3.3	N 4.5	751.6	3.06
	20	13	— 5.0	S 3.0	741.9	3.96
Tv.	1	12	— 2.0	N 1	766	—
	10	12	0.0	N 4	755	3.27
	20	12	+ 5.0	SW 1	768	3.17
Bo.	1	13	— 3.4	NNE 3		3.04
	10	13	+ 0.4	NNE 5		3.08
	20	13	+ 1.7	NNE 2		3.18
Vå.	30/3	13	+ 0.8	SW		3.16
	10	13	+ 1.2	E		3.10
	20	13	+ 4.4	WSW		3.21
Be.	1	13	+ 2	calm		3.43
	10	13	+ 7	SSE		3.18
	20	13	+ 5.5	NNE		3.50
Öd.	1	13	+ 4.2	WSW		3.23
	10	13	+ 4.6	N		3.11
	20	13	+ 13.4	W		3.27
As.	1	13	+ 6	NNW 5		3.18
	10	13	+ 4	SSE 5		3.32
	20	13	+ 12.8	NW 5		3.21

Letters to the Editor

Note on Radioactive Compounds in the Atmosphere

Dear Sir,

I have read with much interest the contribution of Messrs Rossby and Egnér "On the Chemical Climate and Its Variation with the Atmospheric Circulation Pattern" in the preceding issue of Tellus Vol. 7, No 1. It seems as if a new and promising field of meteorological activities has been opened up by the "synoptic" studies made on the basis of the Scandinavian network of sampling stations. I was also interested in the Note of Messrs Egnér and Eriksson on "Current Data on the Chemical Composition of Air and Precipitation" and I highly appreciate your plans of publishing quarterly chemical data, in order to make the material of the enlarged Western European network available to all persons interested in atmospheric chemistry.

The aim of this letter is to call your attention to a field in atmospheric chemistry, which is extremely new, namely that of the artificial radio-activity in air and precipitation. Some work in this field has been done by various authors,[1] mainly in relation to thermonuclear explosions. It is however clear — and here I like to refer to Putnam's fascinating book "Energy in the Future"[2] — that contamination of the atmosphere by artificially created radio-active matter, might in due course also result from such more normal human activities as the operation of nuclear reactors for the generation of energy.

One could of course leave the study of the radio-active pollution of the precipitation and the air to medical and biological workers as they are mainly concerned with the dangers of radio-active contamination to human and animal life. I feel, however, that Meteorological Services also have a responsibility in this field. Their task is twofold, namely 1) to give assistance in collecting the samples to be investigated in special laboratories, and 2) to interpret the results of the obtained measurements.

You may be interested to know that the Royal Netherlands Meteorological Institute, in collaboration with the Medical-Biological Laboratory of the National Defense Research Council, hopes to embark on a programme of continuous supervision of the radioactivity in the atmosphere. Preliminary experiments have shown how strongly such radio-activity of the air can vary. The following table gives the activities, determined 3 — 5 days and 2 — 4 weeks after air samples were taken on days during the last decade of April (μC per liter $\times 10^{-10}$).

	After 3—5 days	After 2—4 weeks
	$\times 10^{-10}$ μC per liter	
April 19—20	10.7	6.9
April 20—21	8.8	8.1
April 21—22	11.3	8.9
April 22—23	11.8	7.0
April 23—24	6.4	3.9
April 24—25	6.4	3.9
April 25—26	3.5	2.6
April 26—27	7.8	7.8
April 27—28	18.7	10.1
April 28—29	27.4	13.5
April 29—30	14.2	10.9
April 30—May 1	4.5	4.3

It is interesting to note that periods of higher activity usually consist of groups of 3 — 5 days; the period of 28 — 30 April, with tropical air transported from the South on the 29th, gave the highest values ever experienced since January 1, 1955, when observations started.

The radio-activity of artificial origin i rainn water or snow also varies considerably from ay tod

---

[1] H. Garrigue, 1951: L'invasion d'air radio actif d'origine atomique et son influence sur les précipitations atmosfériques; *C.R.* **232**, 1003—1004.
M. Abrihat, R. Pinoir, J. Pouradier and A. M. Venet, 1952: Sur l'existence de produits radio actifs artificiels dans les eaux de pluie de la région parisienne; *C.R.* **234**, 1161—1163.
D. C. Rose and J. Kalzmann, 1952: Radio-active deposits found at Ottawa after the atomic explosions of Jan. and Febr. 1951. *Canadian J. of Physics* **30**, 111—128.
N. V. Ryder and C. N. Watson-Munro, 1954: The direction of radio active dust from the British nuclear bombs of October 1953; *N. Zealand J. Sc. and Technol.* **36**, 155—159.
J. F. Gabites, The drift of radio active dust from the British nuclear bomb tests in October 1953; *N. Zealand J. Sc. and Technol.* B **36**, 160—165.
R. J. List, On the transport of atomic debris in the atmosphere; *B.A.M.S.* **35**, 315—325.

[2] P. S. Putnam, 1953: *Energy in the future;* Van Nostrand Co, New York, Toronto, London, 1953.

day; activities of 8×10^{-7} μC per ml have been observed.

It is the intention to place the results of the observations at the disposal of the Royal Netherlands' Academy of Sciences. I would, however, appreciate if you could consider the possibility of publishing these data also in Tellus and in case your reaction to this suggestion is favorable, to invite other countries to follow our example.

I hope you will agree with me that it is of importance to make information on this subject available to scientists, the more so as the study of artificial radio-activity may in the long run lead to interesting meteorological results.

Sincerely yours,

Ir. C. J. WARNERS
Director in Chief of the Royal Netherl. Meteor. Institute

Note on Fjørtoft's Graphical Method of Integrating the Barotropic Vorticity Equation

Dear Sir:

In the graphical method of integration of the barotropic vorticity equation due to FJØRTOFT (1952) the grid length of the finite difference net is chosen to be one quarter of the wavelength of the most rapidly changing Fourier components of the contour field. This ensures the complete damping of those components when the finite difference equivalent is substituted for the Laplacian operator and a fictitious velocity field changing more slowly than the real velocity field can be derived.

If a more accurate determination of vorticity is required than is possible with a 600 km grid, then as Fjørtoft pointed out, a new slowly changing advection field would have to be found to make the graphical method practicable. It can be shown however that where the most rapidly changing component is taken to have a wavelength of about 2,500 km, such a velocity is possible only for a grid length of about 600 km.

For with Fjørtoft's notation, in the conservation formula

$$\frac{d\xi}{dt}=0 \text{ put } z=+z^{\star\star}+z^{\star} \text{ where } z^{\star\star}=c\xi.$$

The constant c has then to be found for some grid length d.

$$\text{Now } \frac{\partial\xi}{\partial t}=\frac{g}{f}\nabla z^{\star}\times\mathbf{k}\cdot\nabla\xi=\frac{g}{f}\nabla\,(z-c\xi)\times\mathbf{k}\cdot\nabla\xi$$

$$=\frac{g}{f}\nabla z\times\mathbf{k}\cdot\nabla\xi$$

$$=\frac{g}{f}\nabla[\bar{z}+J(\phi)]\times\mathbf{k}\cdot\nabla z \qquad (1)$$

The same result can be derived directly from the conservation formula without any substitution for,

$$\frac{\partial\xi}{\partial t}=\frac{g}{f}\nabla z\times\mathbf{k}\cdot\nabla\xi$$

$$=-\frac{g}{f}\nabla z\times\mathbf{k}\cdot\nabla[\bar{z}+J(\phi)]$$

$$=\frac{g}{f}\nabla[\bar{z}+J(\phi)]\times\mathbf{k}\cdot\nabla z \qquad (2)$$

From (1) and (2)

(a) It does not matter what value is given to c for $\frac{g}{f}\nabla c\,\xi\times\mathbf{k}$ has no advective effect on the field of ξ
The substitution $z=z^{\star}+z^{\star\star}$ is not necessary for the same result is found more directly as in (2).

(b) Advection of the ξ field is equivalent to advection of the z field by the geostrophic wind due to the $\bar{z}+J(\phi)$ field.

(c) $\bar{z}+J(\phi)$ is slowly changing only when the most rapidly changing components are suppressed, *i.e.* when $d=$ about 600 km. For any other grid length more slowly changing components are damped out and therefore the time steps would have to be shorter. The graphical method is practicable then for one grid length only.

REFERENCE

FJØRTOFT, R. (1952): On a numerical method of integrating the barotropic vorticity equation. *Tellus* **4**, 179—194.

J. F. DE LISLE, I. S. KERR
New Zealand Meteorological Service, Wellington, New Zealand.

Professor R. Fjørtoft wants to refer to a forthcoming article in Tellus Vol. 7, No. 4 where his results are generalized and where the questions raised by Drs J. F. de Lisle and I. S. Kerr will be discussed in some detail.

The Editor

Results of Detailed Synoptic Studies of Squall Lines

By TETSUYA FUJITA, Kyushu Institute of Technology and University of Chicago[1]

(Manuscript received June 15, 1955)

Abstract

A system of synoptic analysis on a mesometeorological scale has been developed through the combined use of space and time sections applied to all regular and special stations in an area 500 by 900 mi. in the Central United States. Two periods of development of large thunderstorm areas are analyzed. In both of these periods tornadoes occurred. The synoptic model of a squall line in this scale involves three principal features of the pressure field—the pressure surge, the thunderstorm high and the wake depression. Another feature, called the tornado cyclone, accompanies tornado funnels. Divergence values of 10 to $60 \cdot 10^{-5}$ sec $^{-1}$ over areas of 100 to 10,000 sq. mi. are measured. The mesosynoptic disturbances greatly influence the situation as viewed on the regular synoptic scale, which is about 10 times the meso-scale, and make conventional analysis hopelessly difficult.

1. Introduction

Severe storms such as thunderstorms, hail, high wind, and tornadoes usually occur in close relation to disturbances with linear dimensions of 10 to 100 miles. The analysis dealing with this scale is termed mesoanalysis. The term "mesometeorology" has been used in studies of radar meteorology by SWINGLE (1953) and others. The analysis of systems with dimensions of 100 to 1 000 miles or more is involved in the usual daily synoptic practice.

Studies of micro-scale disturbances, smaller than 10 miles, are typified by the Thunderstorm Project (BYERS, BRAHAM, 1949) in Florida (1946) and Ohio (1947). Microanalysis was carried out for weather elements such as pressure, temperature, radar echo, wind direction and speed, divergence, etc. The five-minute interval chart sequences revealed the microstructure of the thunderstorm circulation.

Using the data from the automatic recording stations in Ohio operated by the U.S. Weather Bureau's Cloud Physics Project in 1948, WILLIAMS (1948) studied the microstructure of the squall-lines. In this chart the microstructure of the pressure and temperature systems is well represented by the five-minute interval analysis. TEPPER (1950) studied the microstructure of the "pressure jump" line traversing the area of the 1948 Ohio network. The one-minute interval charts he made show the isallobars for the amount of the pressure increase following the "jump". His study made it clear that there exists a very tight pressure gradient in a narrow zone where the winds are very far from being geostrophic. The micro-analysis of the thunderstorm high of Aug. 24, 1947, over Kyushu, Japan was done by the writer (FUJITA, 1950) on the basis of ten-minute interval charts for an area of 60 by 50 miles. The chart sequence shows that the thunderstorm high, having a very tight pressure gradient, deforms when it passes over mountains.

Other earlier microscale or mesoscale analyses include the well-known Norwegian charts published in the early 1920's leading to the

[1] The research reported in this paper has been sponsored by the Geophysics Research Directorate of the Air Force Cambridge Research Center, Air Research and Development Command, under contract AF 19(604)-618.

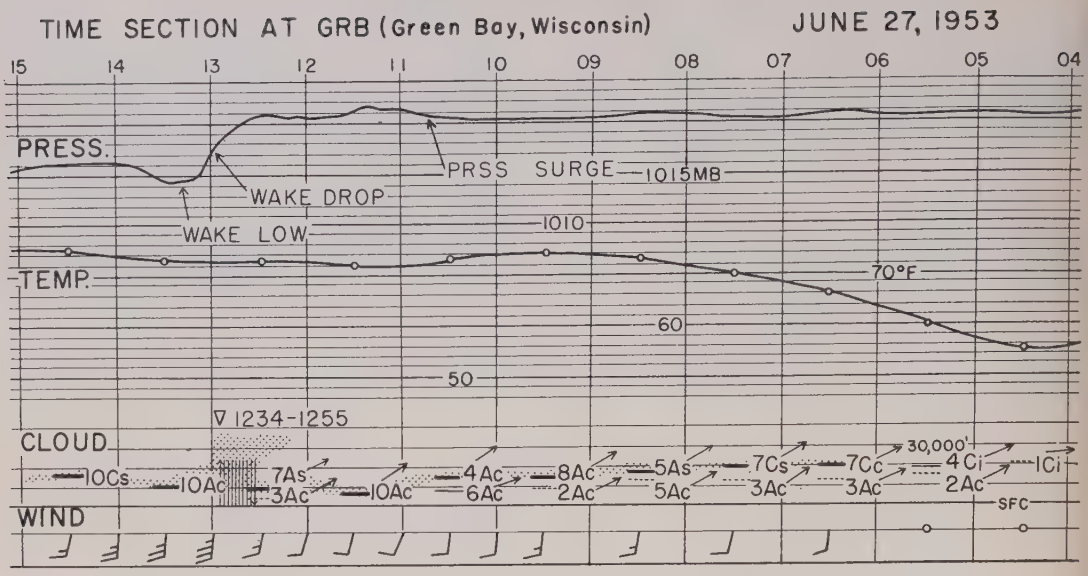

Fig. 1. Example of time section.

discovery of air-mass and frontal analysis, the micro-studies of SUCKSTORFF (1953) in connection with thunderstorms, the charts of the U.S. Soil Conservation Service in the Muskingum Valley, used by BYERS (1942), and studies by C. F. BROOKS (1922). The author asks forgiveness for failing to mention others.

The cold front of September 26—27, 1948 was also analyzed by the writer (FUJITA, 1951). From the pressure, temperature, wind and rain traces of stations in Western Japan, the 20-minute interval charts for pressure, temperature, and rain were constructed. The area covered by the study was 300 by 200 miles. In that area, the stations were scattered, the average separation being 60 miles. This was an early stage of meso-analysis.

BERGERON (1954) made analyses of a pseudo-cold-front over the Middle West, and emphasized the importance of the cooling effect of rain, in order to explain the divergence field beneath squall-line thunderstorms.

In the studies carried out by the writer at the University of Chicago under the general guidance of Dr Horace R. Byers, many important features of the meso-scale disturbances became clear. Most of the tight pressure gradients associated with squall line activity, which Tepper calls "pressure jumps", are now known to be the result of the huge thunderstorm high produced by squall-line thunderstorms. To distinguish the pressure rise at the front of the thunderstorm high from the hydraulic jump, which demands adherence to an analogy from hydraulics, Dr Byers and the writer chose to call it "the pressure surge."[1] Following the surge, "the thunderstorm high" comes, then the pressure falls gradually or very rapidly. This fall is due to effects in the wake of the thunderstorm high which usually moves rapidly with the direction of the wind aloft. The low pressure areas following the "wake drop" in pressure we will designate as the "wake depression." These features are illustrated in Plate 4.

2. The time and space section

The average separation of the teletype stations in the Middle West of the United States is about 100 miles. If one plots the data in the usual way employed on daily synoptic charts,

[1] Definition of "surge" in the *Meteorological Glossary*: First used by Abercromby to denote a general change of pressure superposed upon the changes which are due to the movement of DEPRESSIONS and ANTICYCLONES.

In the *Weather Glossary*, U.S. Dept. of Commerce, Weather Bureau, it is said that "surge means any change of pressure over a wide area, the precise cause of which is unknown, but which is not due to the passage of low or high pressure areas or to diurnal barometric variation".

using the hourly reports from these stations, it would be very difficult to analyze the meso-scale disturbances.

The time section of the weather elements from each station will give added information about the weather conditions in the areas between stations. An example of the time section is shown in Fig. 1. As will be seen in the figure, the time runs from right to left, so that in the zone of the westerlies the time section becomes very similar to the space section running through the station in question. In the time section, we must enter all available observations. To this end, the original data used in this study include:

(1) Hourly Teletype Sequences. Report of the amount and the height of the cloud base, sea-level pressure, temperature and dew point, wind, remarks, etc. The time of observation is about 28 minutes after the hour.

(2) Special Weather Report on Teletype. Report of the events occurring between the regular hourly observations. Usually, pressure and temperature do not appear. In the 1130 Form kept in the National Weather Record Center, Asheville, all of the hourly and the special observations not sent out by teletype are shown.

(3) Self-recorded Traces. Pressure, temperature, humidity, wind, and precipitation traces kept in the National Weather Records Center.

(4) Traces from the Severe Storm Research Unit in the U.S. Weather Bureau. About 200 accelerated barograph, 30 hygrothermograph and some wind and precipitation from stations maintained in the Middle West. The traces from these stations are excellent material for the meso-analysis.

(5) Hourly precipitation data and Climatological Data. These are published by the U.S. Weather Bureau. In the Hourly Precipitation Data, the hourly amounts of the rain from stations all over the United States are tabulated. Average separation of the stations is 30 to 40 miles. The daily amount of precipitation measured either in the a.m. hour or the p.m. hour is shown in the Climatological Data. Average distance of the stations is 10 to 20 miles.

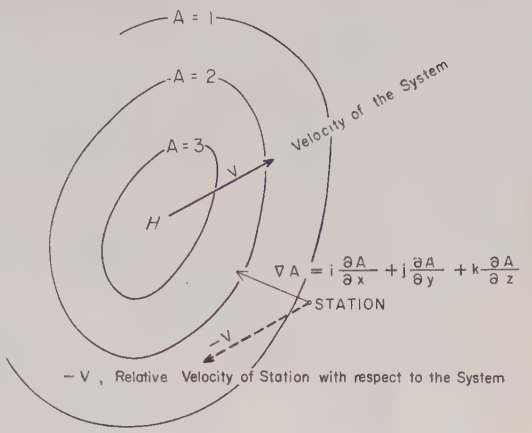
A = 1
A = 2
A = 3
Velocity of the System
V
H
$\nabla A = i\frac{\partial A}{\partial x} + j\frac{\partial A}{\partial y} + k\frac{\partial A}{\partial z}$
STATION
−V
−V , Relative Velocity of Station with respect to the System

Fig. 2. Relative velocity of a station with respect to a moving system.

Making use of these data, one must construct the time section for each station before the meso-analysis is carried out. As will be seen in Fig. 1, pressure, temperature, height and amount of cloud, movement and type of cloud, and wind speed are plotted carefully. After making the time section, it is better to indicate the significant points such as pressure surge, wake drop, wake low, temperature break, etc.

Time sections made for each station can be changed into a space section on the synoptic chart. As shown in Fig. 2, the relative velocity of a station with respect to a moving system is $-V$. It is convenient to use the conventional relationship used in hydrodynamics for the local and individual change in a moving system. If we regard the station as moving with respect to the system, the individual change of the element A, that is, dA/dt may be considered as the change at the station moving with relative velocity $-V$. Then $\partial A/\partial t$ is the change in the system. The formula is

$$dA/dt = \partial A/\partial t + (-V \cdot \nabla A)$$
$$= \partial A/\partial t - V \cdot \triangle A$$

In the case, where the system does not change rapidly, the formula can be reduced to

$$\frac{dA}{dt} = -V \cdot \text{grad } A$$

From this equation, the time change can be converted into the space change. Practically,

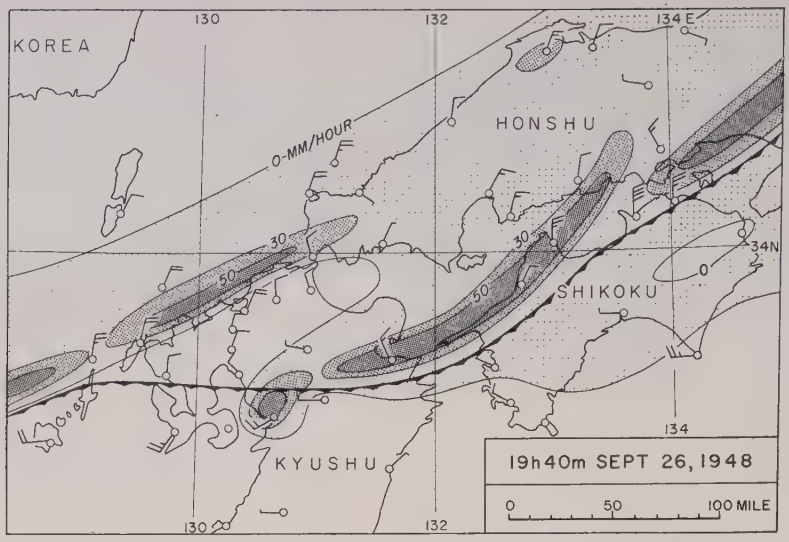

Fig. 3. Rain intensity chart of the cold front at 1940, Sept. 26, 1948 over West Japan.

however, the change of the system is taking place rather quickly. Techniques dealing with this problem will be discussed in the chapter on pressure analysis.

3. Analysis of precipitation

The precipitation traces show the amount of the accumulated rain. In the meso-analysis, we are interested in the distribution of the rain intensity. The traces must be differentiated with respect to time. The rain-intensity curve obtained by the careful differentiation are entered in the time section charts. An example of the rain intensity charts for the squall-line over West Japan in 1948 is shown in Fig. 3. To draw the isohyets, the traces from the 60 stations in the areas are used. The two rain bands are pushing toward the east-south east.

The available precipitation traces in the Middle West are not sufficient in number to permit construction of the rain intensity pattern. Isohyets for the hourly precipitation amount can be drawn in this case.

Before making the hourly precipitation charts, it is useful to draw the isohyets for the total amount of the rainfall accompanying the storm under study. The total precipitation chart shows the areas where the heavy rain showers have passed and thus gives an important clue to the areal distributions.

Percentage Method

A percentage method is used in which the precipitation reported by the daily observation station can be converted into the total rainfall amount for a particular storm. Consider the hourly rain from the hourly observation stations in Fig. 4. R_1, R_2, ... are the rain accompanied by the storm B in which we are interested. If these were the daily observation stations, they would report the rainfall amounts R_1', R_2', ... on the 23rd, for instance. The amount of R is not always equal to that of R', since the period is different. Taking the ratios

$$\frac{R_1}{R_1'} = r_1, \quad \frac{R_2}{R_2'} = r_2, \quad \frac{R_3}{R_3'} = r_3 \quad \ldots \ldots$$

for each hourly observation station, we plot them on the map. An example will be seen in Fig. 5, in which the values of r computed by the formula,

$$r = \frac{R}{R'27+28} = \frac{\text{amount of rain accompanying storm of 26—28 June, 1953}}{\text{sum of daily amounts measured at 6 p.m. on 27 and 28 June, 1953}}$$

The iso-percentage lines in the figure show that the ratios are 1.00 (charted as 100) in most of the areas. The sum of the daily precipitation

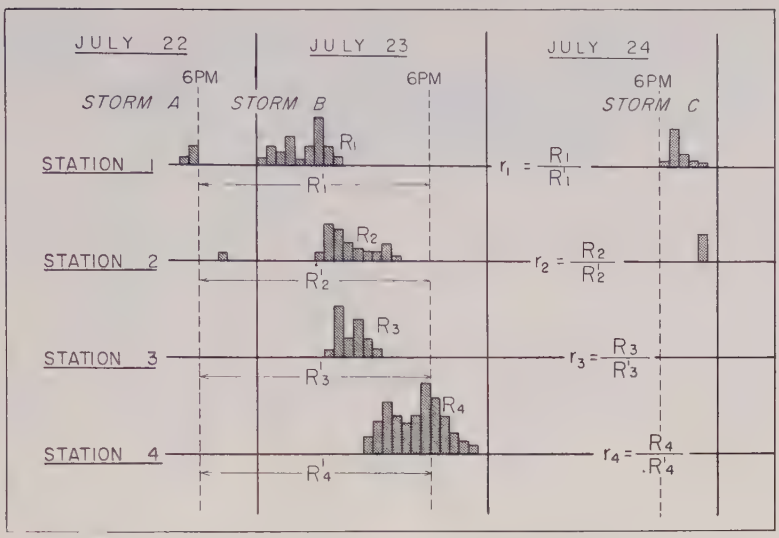

Fig. 4. Example of rainfall plot for applying the "percentage method".

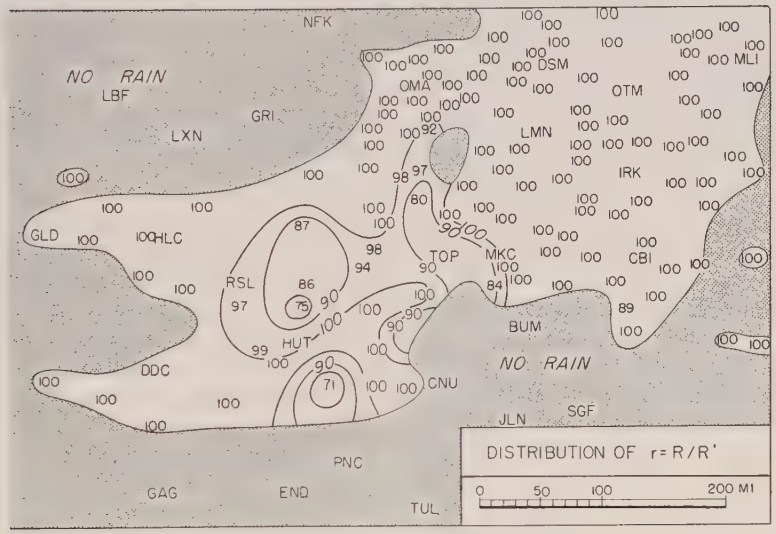

Fig. 5. Distribution of the ratio $r = R/R'$ for the period of June 27—28, 1953. (Center of map near Kansas City—MKC.)

amounts on 27th and 28th June, 1953 can in such circumstances be used as the total amount of rain brought by the storm of 26—28 June. In the other areas where the ratios are not equal to 100, we plot the location of the daily observation station on the iso-percent chart and read the value of r for each station. Let r_0 be the ratio for the daily observation station where the daily rainfall of R_0' was observed. R_0, the rainfall accompanied by the particular storm, can be computed by the relation,

$$R_0 = R_0' r_0$$

As an example, the total rainfall for the storm of 26—28 June, 1953 is shown in Fig. 6. Isohyets in the chart are contoured for every 0.20 inch. In the map area, we have about 600 hourly observation stations. By using the

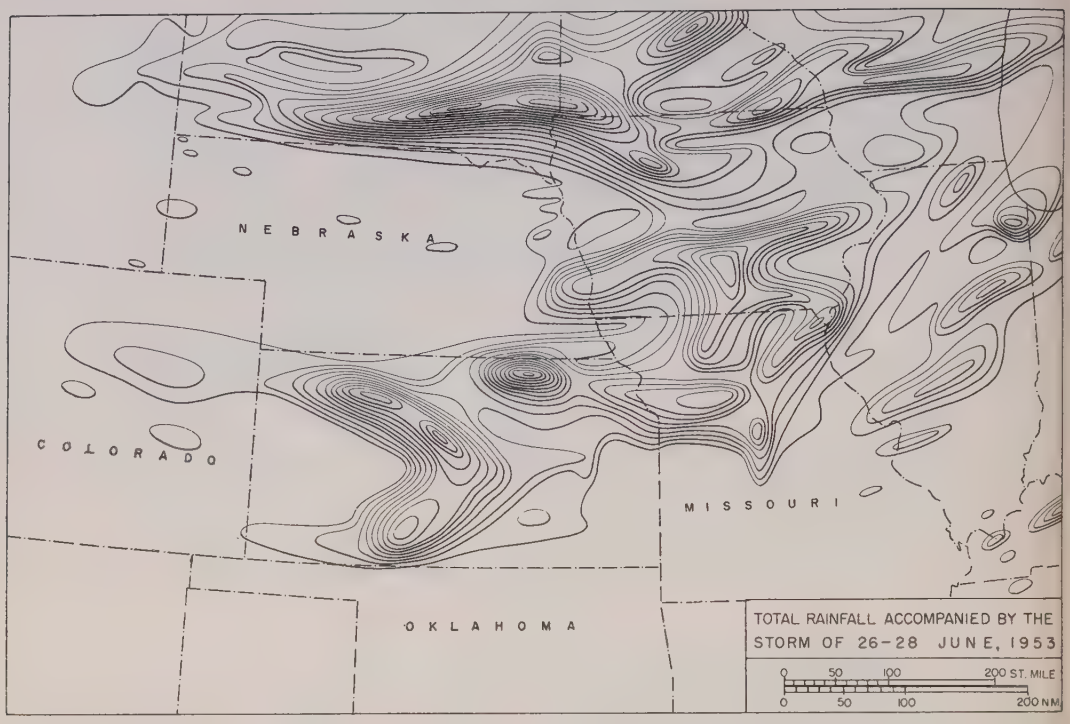

Fig. 6. Total precipitation amount caused by the storm of June 26—28, 1953. The amounts are contoured for every 0.20″.

percentage method, 2,400 daily observation stations are used in addition to the hourly observation stations.

The percentage method can be utilized also in obtaining the hourly precipitation amount from the total precipitation. For this purpose, the ratios of the hourly precipitation to the total precipitation are computed for all the hourly observation stations. Then we plot them on the chart, and draw the iso-percentage lines. Superimposing the iso-percentage lines on the isohyet chart made for the total precipitation amount, we make the multiplication of

(total amount of rain) × (percentage of $\frac{\text{hourly rainfall}}{\text{total rainfall}}$). In this process, the total amount of rain is separated into the hourly amount.

4. Analysis of wind

The time section of the observed winds must be converted into the space section in the scale of the wind map. The direction of the line in the wind chart, along which the winds for each station will be plotted, is that of the movement of the particular system we want to analyze. Usually, the winds for one hour on both sides of the map time are entered on the chart. If several winds are available in the immediate vicinity, the one observed closest to the map time should be used when changing the time section into the space section. From these winds plotted on the chart, the isotachs and the stream lines are drawn.

Divergence and convergence of the wind field are computed next. The computation of the values can be done by using the formula

$$\text{div}_2 = \frac{\Delta u}{\Delta x} + \frac{\Delta v}{\Delta y}$$

The writer developed the method of obtaining convergence from the balance of the net inflow and the outflow.

Method of Computation

Consider the streamlines CA and DB in Fig. 7. The curves AB and CD are the orthogo-

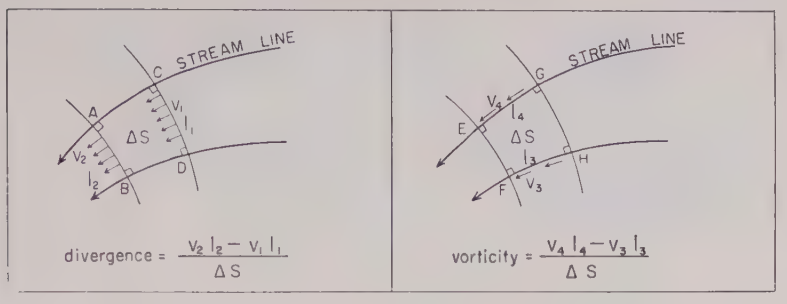

Fig. 7. Method of computation of divergence and vorticity.

nal trajectories to the streamlines with intercepts of length l_1 and l_2 between the streamlines. If the mean speed of the winds passing across CD and AB be v_1 and v_2 respectively, the convergence inside the area $\triangle S$ is given by

$$\text{Conv}_2\, V = \frac{v_1 l_1 - v_2 l_2}{\Delta s}$$

or

$$\text{Div}_2\, V = \frac{v_2 l_2 - v_1 l_1}{\Delta s}$$

As shown in Fig. 7, the vorticity of the wind field can also be computed in a similar way.

Computation Scale

It is possible for us to compute these quantities by using the celluloid computation scale reproduced in Fig. 8. The scale has a straight indicator OQ movable around the eyelet at o. On the celluloid plate, the speed, speed × length, and the area scales are shown. As will be seen in the figure, the vertical lines with

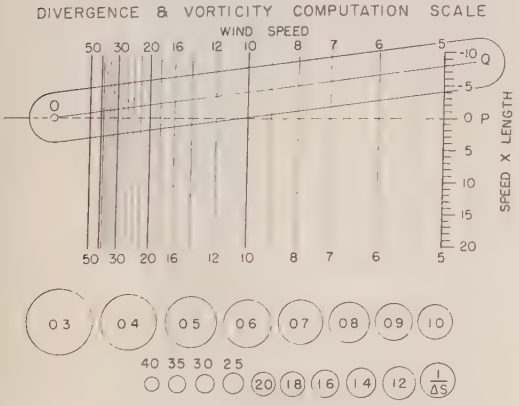

Fig. 8. Computation scale for divergence and vorticity.

wind speed at the top and the bottom are so spaced that the distance from the point o is inversely proportional to the wind speed. To the right, the scale of the speed times length $(v \cdot l)$ is shown. At the bottom, the various areas are shown by the circles with the numbers showing the values of $l/\triangle S$.

Drawing the streamlines and the orthogonal trajectories, we divide the whole area of meso-analysis into areas $(\triangle S)$ like those in Fig. 7. To compute the convergence, we put the celluloid scale, for instance, on Fig. 7, so that the point A comes just under the intersection of the horizontal line OP and the vertical line having the wind speed v_2. Then we rotate the celluloid plate around A, until B comes right under the line of v_2. The value of $v_2 l_2$ can be read on the right scale by moving Q downward until OQ passes through the point B. It is evident, from the law of triangles, that the product, windspeed × length $(v \cdot l)$ is obtained on the righthand scale.

An example of the computed result is shown in Fig. 9. This is the micro-analysis of the wind field beneath the thunderstorm in its dissipating stage. The chart in the lower left is made first, and the isotachs shown in the lower right are drawn. Superimposing the streamline chart on the isotach chart, we read the wind speed values in the upper right chart. Finally, the divergence and convergence are obtained by using the celluloid scale.

Examples of the divergence chart for a squall-line system are presented in the color plates 2 and 3.

5. Analysis of temperature

Micro-scale temperature disturbances are usually superimposed upon the meso-scale temperature field. To represent the meso-dis-

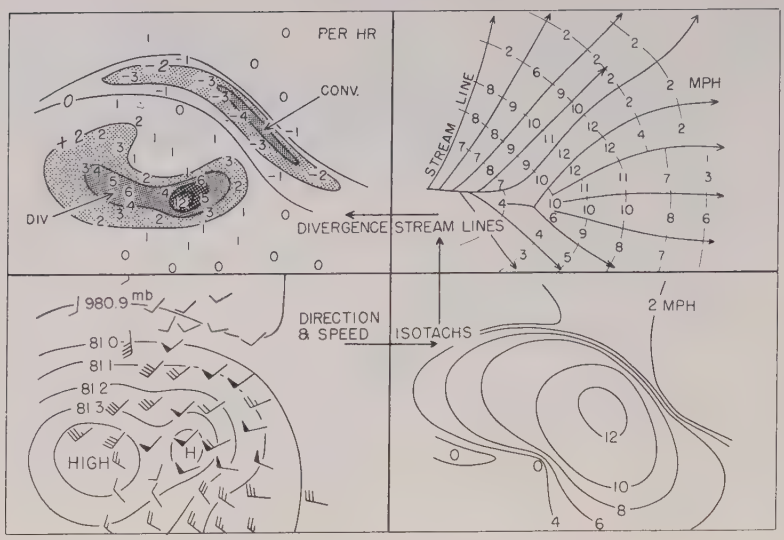

Fig. 9. Example of micro-scale divergence pattern.

turbances effectively, the micro-disturbances, which are caused by the cloudiness, ground condition, vegetation, minor topography or small lakes, shelter exposure problems, etc., must be suppressed.

The isotherms in the upper chart of Fig. 10 are drawn so that they satisfy the plotted values of the mean maximum temperature in June, 1953. One might consider that the drawing of the isotherms is quite adequate, since they are drawn to fit the observed values. This conception is not true. In the middle chart, it is shown that the temperature observed in the small area *A*, having the same scale as of the upper chart, is different from place to place. Isotherms for the temperature field in question are shown in the same area enlarged. There is no doubt that the isotherms in the upper chart would become just like these which are seen in *B*, if we could have as many observation stations as in the micro-analysis. The frequency distribution of the observed temperatures in the area *A* shows the fact that the variation reaches as much as 5 degrees Fahrenheit, as shown on the right of the figure.

The smoothed isotherms shown in the lower chart are the only reasonable ones which can be expected from the data available. The positive and negative values are the amount of correction that must be added to the station temperature, in order to fit the smoothed isotherms.

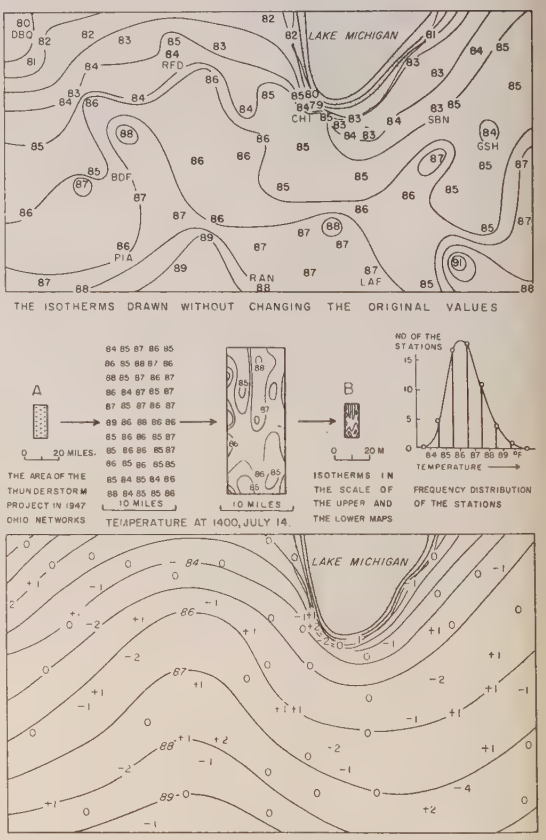
LAKE MICHIGAN
THE ISOTHERMS DRAWN WITHOUT CHANGING THE ORIGINAL VALUES
A
B
0 20 MILES.
THE AREA OF THE THUNDERSTORM PROJECT IN 1947 OHIO NETWORKS
10 MILES
TEMPERATURE AT 1400, JULY 14.
ISOTHERMS IN THE SCALE OF THE UPPER AND THE LOWER MAPS
NO OF THE STATIONS
TEMPERATURE
FREQUENCY DISTRIBUTION OF THE STATIONS
LAKE MICHIGAN
THE ISOTHERMS FOR THE GENERAL TEMPERATURE FIELD FREE FROM THE UNKNOWN LOCAL DISTURBANCES. (DRAWN BY SMOOTHING THE ABOVE SHOWN CHART)

Fig. 10. Application of smoothing method for correction of the mean temperature.

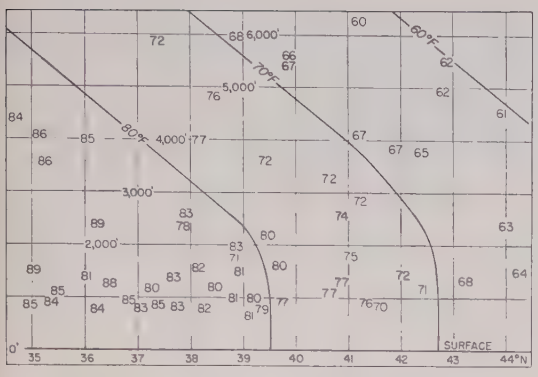

Fig. 11. Chart illustrating reduction of station temperature to sea-level.

Mean Temperature Correction

First, we consider the sea-level correction. The correction will be done by assuming the lapse rate. If we use the lapse rate in the free atmosphere, overcorrection occurs. The writer obtained the lapse rate along the surface for the stations in the Middle West of the United States by plotting the station temperature with respect to the elevation and the latitude. From the inclination of the isotherms drawn in Fig. 11, the lapse rates are known to be 1° F/1000 ft., up to 2000 ft., and 3° F/1000 ft. above 2000 ft.

Let the sea-level temperatures obtained by the sea-level correction be T, T', T'', ... etc. They can be written as

$$T = T_0 + T_1 \sin \omega t + \ldots . T_m \sin m\omega t + \ldots$$
$$T' = T'_0 + T'_1 \sin \omega t + \ldots . T'_m \sin m\omega t + \ldots$$
$$T'' = T''_0 + T''_1 \sin \omega t + \ldots . T''_m \sin m\omega t + \ldots$$

where ω is the angular velocity of the earth. In the formulae, T_0, T'_0, T''_0, ... are the mean sea-level temperature, and T_1, T'_1, T''_1, ... are the diurnal variations for each station. The meso-scale disturbances having the period of several hours appear in the terms such as T_{m-1}, T_m, T_{m+1} ... etc. As has been shown in the upper chart of Fig. 10, the isotherms, before they have been smoothed, are very irregular. We can easily imagine that the meso-disturbances analyzed on such an irregular mean temperature field will not show their true features. For the first approximation, the mean temperatures T_0 must be plotted on the chart and then must be corrected by drawing the smooth isotherms.

The smoothed isotherms for T_0 during the period of June 26—28, 1953 are shown in Fig. 12. The mean station temperatures and the amount of correction, smoothed sea-level temperatures minus station temperature are entered on the chart. It will be seen that the amount of correction in the states of Colorado and New Mexico is at most stations more than

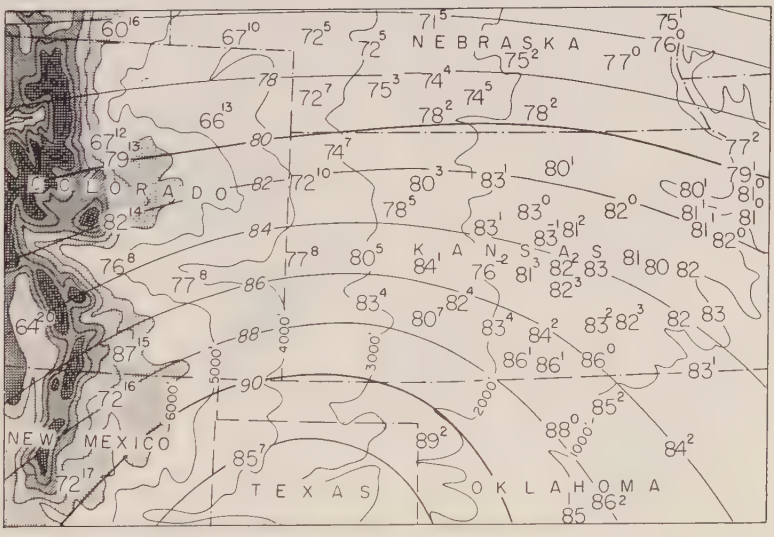

Fig. 12. Distribution of mean station temperature and the smoothed isotherms of sea-level temperature.

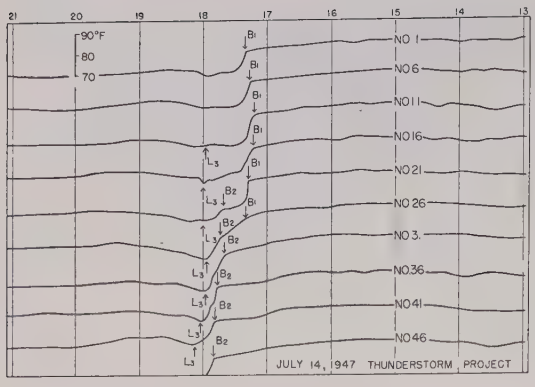

Fig. 13. Propagation of the temperature breaks over the Thunderstorm Project stations.

10° F. When we plot the temperature values on the hourly meso-scale chart, for instance, the amount of correction mentioned above must be added to the temperatures on the trace.

The second approximation is the correction of the value of T_1, the diurnal variation. This is based on the fact that the variation is very large on the bare ground and small on the water. These local effects must be eliminated if possible. To make the correction easier, the smoothed isotherms may be drawn for the maximum and minimum temperatures, and they are corrected.

Experience shows that the mean value correction is enough for the meso-analysis, and the correction to the diurnal variation is not always necessary.

In the meso-analysis of temperature, the thermograph traces must be used together with the corrected temperature values. Looking at the traces from each station, the points of break, maximum and minimum are checked first. The significant points are then termed as B_1, B_2, ... L_1, L_2, ... H_1, H_2, ..., in which the numbers 1, 2, ... indicate the numbering of the disturbances by which the significant points are produced.

In Fig. 13, the breaks and the minimum temperatures are indicated on the traces from the Thunderstorm Project stations. The distance from stations No. 1 to No. 46 is 18 miles. When the temperature break travelled in this short distance, B_1 dissipated and B_2 appeared. It happens sometimes, when the distance between stations is large, that the significant points are very difficult to follow from station to station. In the micro-analysis, such breaks will appear to be double or triple lines, but in the meso-analysis no such fine structure can be shown.

For each significant point on the time-section isochrone charts are made. Then, the time-section can be converted into the space-section running through each station. An example is shown in Fig. 14, in which the traces are so oriented that time increases toward the per-

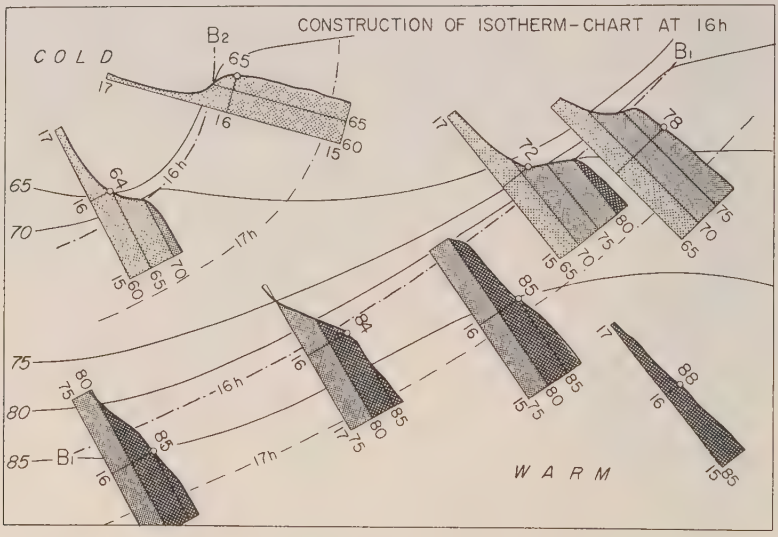

Fig. 14. Arrangement of the thermograph traces for the construction of an isotherm chart.

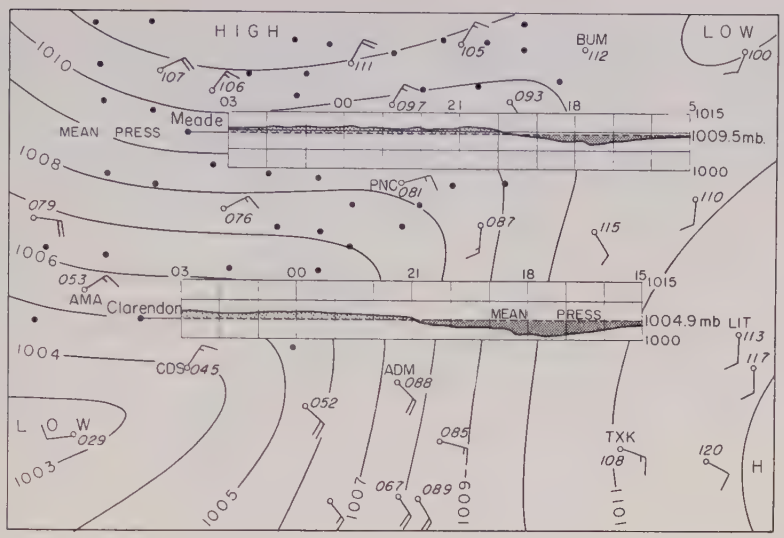

Fig. 15. Chart used in the reduction of the barograph traces to sea-level.

pendicular to the isochrone for the map time. The length of the trace corresponding to one hour is equal to the displacement of the isochrone in one hour. The traces are very helpful in determining the interval of the isotherms on the chart. The area under the trace is stippled by the different tones. They will help the drawing of the isotherms and their spacing. In the actual analysis, several different colors can be used, which show the temperatures 50—55, 55—60, 60—65, 65—70, 70—75, 75—80, . . .

Examples of the temperature analyses will be seen in sections 7 and 8.

6. Analysis of pressure

The barograph traces from the stations in the area of meso-analysis are the most important material we should have. As has been mentioned in the chapter section 2 of the time and the space section, the barograph traces from the Severe Storm Research Unit, U.S. Weather Bureau are used.

By using these traces, the writer tried to make sea-level charts. Unfortunately, most of the barograph stations have neither thermographs nor mercury barometers by which the station pressure could be obtained. Moreover, the elevation of the barograph stations is not accurately determined. Therefore, the formula of sea-level reduction is not available. Even if we could have enough information for the sea-level reduction, we could not use the method of ordinary reduction; because a rise of the sea-level pressure occurs due to the drop in the station temperature, even if the station pressure remains unchanged. We are interested in the pressure pattern satisfying the original trace. This means that the traces must be reduced to sea-level without changing their shapes.

The reduction of the barograph traces from the Severe Storm Unit is done by drawing the isobars of the mean pressures from the teletype stations. As shown in Fig. 15, mean wind and mean pressure are mapped together. The isobars for the mean pressure show the mean sea-level pressure of each barograph station indicated by the dots. Barographs from Meade and Clarendon, for instance, are shown in the map, which are reduced to sea-level by shifting them upward or downward until the mean sea-level pressure, 1009.5 and 1004.9 mb, respectively, coincides with the mean pressure of the barograph traces. With the trace thus shifted, the sea-level pressures can be read directly on the pressure scale.

With a similar technique, shown in Fig. 14, the pressure values and the traces are used for the construction of the isobar chart. Another technique of changing the time section into the space section is provided. As will be seen in

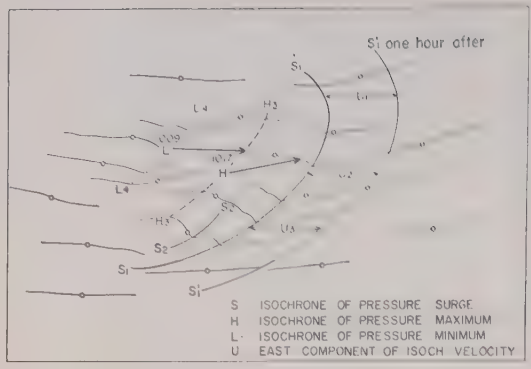

Fig. 16. Arrangement of the barograph traces for analysis of the pressure field.

Fig. 16, the isochrones for the time of the analysis are drawn first, which are Surge 1, Surge 2, High 3, Low 4. Making use of the characteristic that the eastward component of the displacement U_1, U_2, U_3 of the isochrone of the surge are similar, we enter the barograms on the chart keeping the barograph horizontal but with time increasing to the left. The length of the barograms in one hour is equal to the length of U. In the area where the pressure falls, the traces on the chart will increase eastward, so that the tendencies can be known immediately. When we enter the traces on the chart, some adjustments must be done so that the significant points come on the isochrones. Most of the recent analyses by the writer were done by using this technique.

When we examine the significant points on the original traces for squall-line systems, certain characteristics are apparent in many of them. Five different stages of the pressure profile of a rapidly moving squall-line thunderstorm high are shown in Fig. 17. The traces are characterized by the "pressure surge", "thunderstorm high", "pressure drop" and "wake depression". These disturbances are superimposed upon the undisturbed field. The deviation from the undisturbed pressure field is termed "the pressure excess," which may have either a positive or a negative sign.

Figure 18 shows how these characteristics are related to the horizontal and the vertical structure of the squall-line thunderstorm. The high-momentum air aloft is cooled and brought down by the downdraft, and spreads over the ground forming a large thunderstorm high. The descending speed of the downdraft will contribute to the increment of the horizontal momentum. Meanwhile, the pressure gradient produced by the downdraft itself will accelerate the descending air before it reaches the ground. Even if the wind aloft is very light, it will be understood that the downdraft gust has a large speed at which it spreads out.

A mass of high-speed air following the pressure surge line will act much as if it were a solid body moving in a fluid. The wake flow is induced in the rear of the thunderstorm high if that happens to be the prevailing downwind side for low-level winds. The low pressure area thus produced is termed "the wake depression". Usually, the depression appears in the mature stage of a squall-line, forming, with the thunderstorm high, a positive and negative pressure dipole. If the winds in the low levels around the thunderstorm are moving in the same direction but faster than the pressure surge line, the wake depression will be found ahead of the thunderstorm.

When the system is changing rapidly, the change in the system itself will contribute to the tendency. To analyze such a case, the isobar charts for both undisturbed pressure and the excess pressure are made independently and they are superimposed. Fig. 19 was made in such process. The dashed isobars passing through the disturbed area show the undisturbed isobars of 1010 and 1008 mb.

The separation of the pressure excess from the original traces must be done very carefully. After the separation, the amount of the pressure excess for each barograph station is plotted on the chart. In Fig. 20, the heavy isobars are envelopes of the maximum amount of the

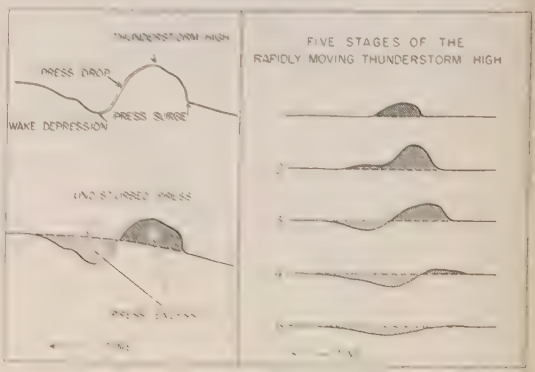

Fig. 17. Schematic diagram of the barograph trace for a squall-line thunderstorm. Time runs from right to left.

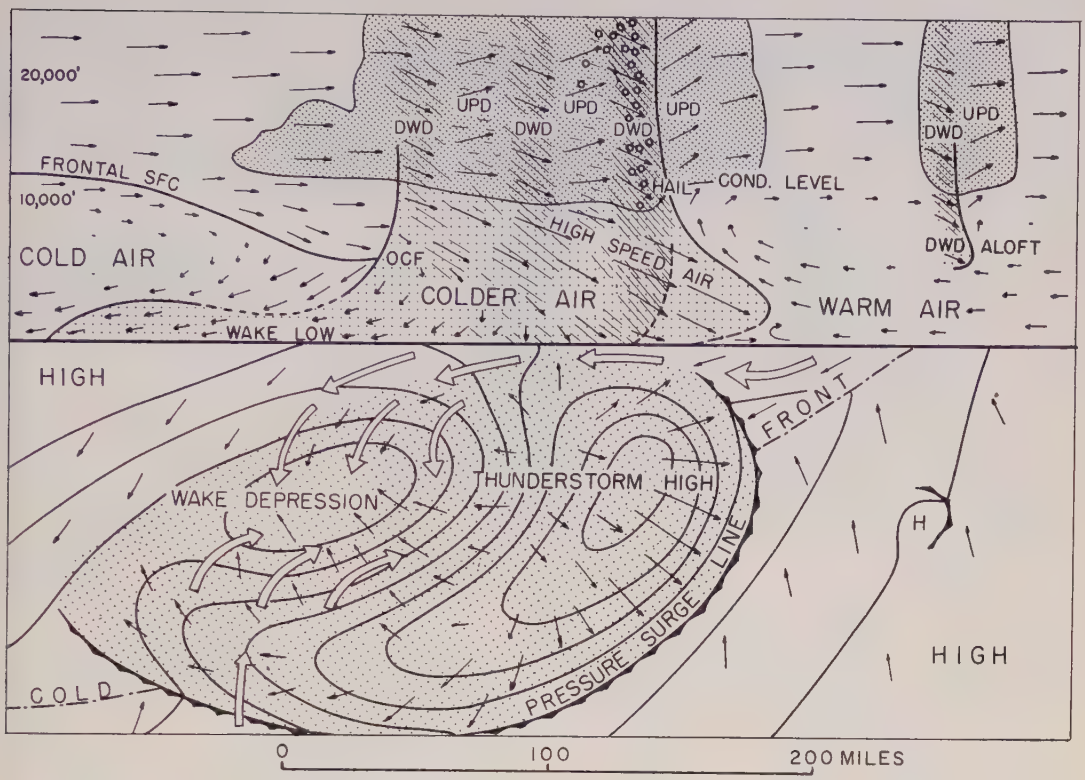

Fig. 18. Schematic section through a squall-line thunderstorm, and illustration of the wake depression.

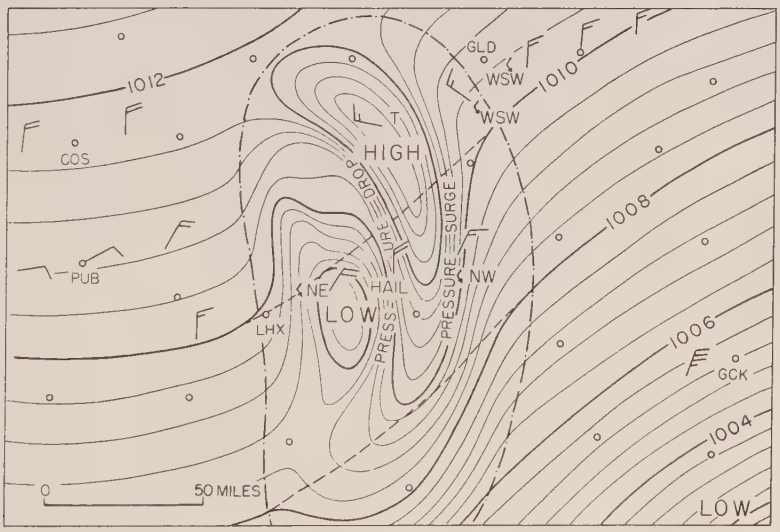

Fig. 19. Details of a meso-analysis of a rapidly moving thunderstorm high.

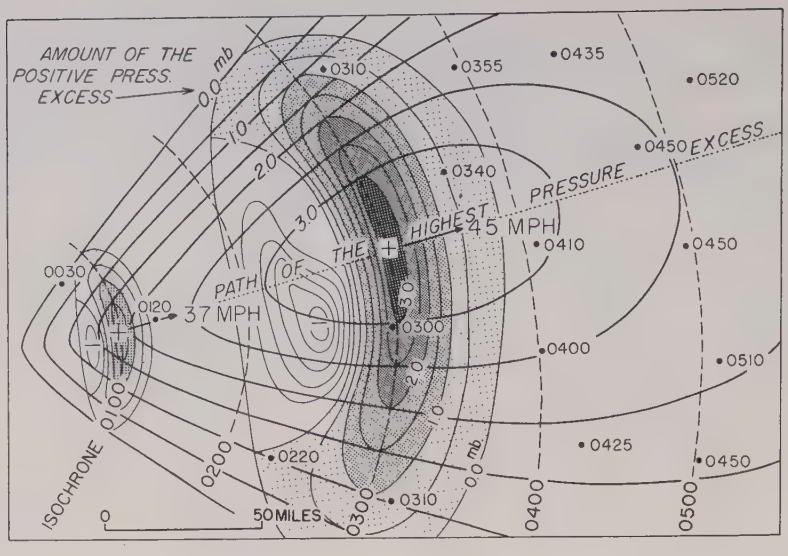

Fig. 20. Isobars of pressure excess.

pressure excess as it swept over the map. The analyses show that the system started to develop between 0000 and 0100 CST. Within three hours, the maximum pressure excess reached more than 3 mb. From these isochrones and the isobars for the excess pressure, the amount and the location of the highest point of the excess pressure are known for any hour. The isobars of the excess pressure for 0300 and 0100 CST are contoured on the chart. The 0300 isobars of pressure excess superimposed upon the undisturbed pressure chart produce the actual sea-level isobars in Fig. 19. Using a similar method, the negative disturbances are analyzed.

7. Analysis of squall line of June 5—6, 1953

In the afternoon and evening of June 5, a very strong squall line accompanied by heavy rains, hail and tornadoes swept over the entire state of Oklahoma and the southern portion of Kansas. Eleven tornadoes were reported. Hailstones of the size of golf balls piled up to a depth of seven inches on the highway north of Ardmore, Oklahoma (see index map, Fig. 21).

The tornadoes reported in the National Summary of the Climatological Data are shown in Fig. 22. The locations and times of the tornadoes indicate the existence of five tornado sequences. They are ABDC, EFG, HI, J, and KL. The events suggest the displacement of a "tornado cyclone." Brooks (1949, 1954) called the micro-low, intermediate in size between the regular cyclone and the tornado funnel within it, "the tornado cyclone". Fulks (unpublished) emphasized the initiation of the upper vortex in his model of tornado initiation.

The writer considered from the distribution of the tornadoes shown in Fig. 22, that there exists a tornado cyclone inside of which tornadoes develop periodically. The paths of the five tornado cyclones related to the five tornado sequences of June 5 are shown in Fig. 23. These tornado cyclones are fixed also by the traces from the barograph stations available. To know the relation between the tornadoes and the pressure surge, the isochrones of the surge are shown on the same chart. It will be seen that the tornado cyclones No. 1 and No. 2 were initiated before the pressurel-surge line was organized.

Hourly Meso-synoptic Chart. Hourly meso-synoptic charts are made from 14 h to 24 h of June 5, and they are shown in Figs 24—34. At 1400, tornado cyclone No. 1 is already seen near the western border of Oklahoma and Texas. About 30 minutes prior to the map time, tornado clouds were observed, with one touching the ground. On the chart, the isobars are drawn for every one mb, and the isotherms for every 2° F. The meteorological conditions

Fig. 21. Map of areas used in analysis of the two cases.

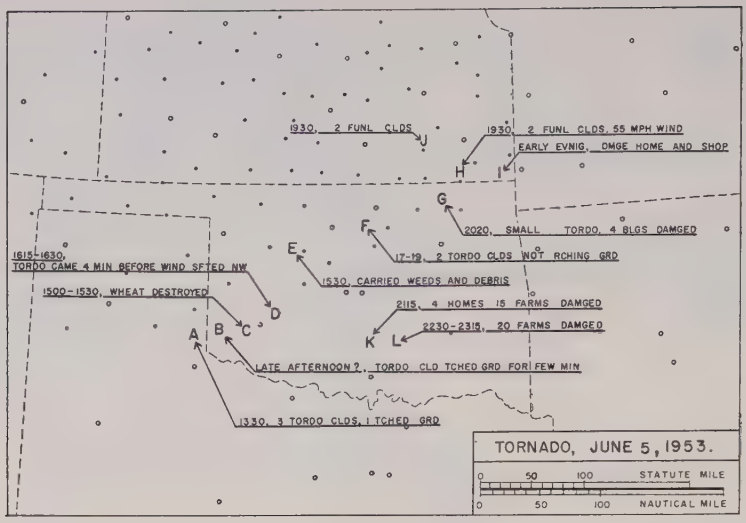
1930, 2 FUNL CLDS
1930, 2 FUNL CLDS, 55 MPH WIND
EARLY EVNIG, DMGE HOME AND SHOP
2020, SMALL TORDO, 4 BLGS DAMGED
17-19, 2 TORDO CLDS NOT RCHING GRD
1530, CARRIED WEEDS AND DEBRIS
2115, 4 HOMES 15 FARMS DAMGED
2230-2315, 20 FARMS DAMGED
1615-1630, TORDO CAME 4 MIN BEFORE WIND SFTED NW
1500-1530, WHEAT DESTROYED
LATE AFTERNOON ?, TORDO CLD TCHED GRD FOR FEW MIN
1330, 3 TORDO CLDS, 1 TCHED GRD
TORNADO, JUNE 5, 1953.
STATUTE MILE
NAUTICAL MILE

Fig. 22. Distribution of the tornadoes on June 5, 1953.

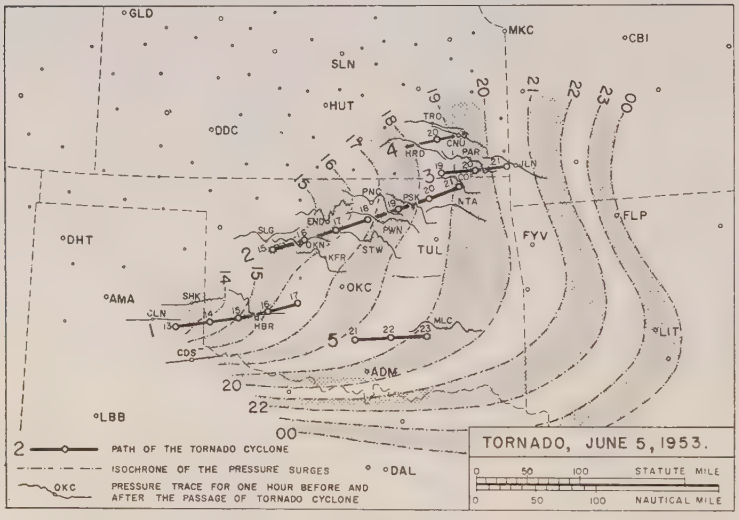

Fig. 23. Relation between the movement of pressure surge line and tornado cyclone.

of the initiation of tornado cyclone No. 1 will be discussed later.

Rain areas spread out and the tornado cyclone of No. 2 appeared to the north of No. 1. A pressure-surge line was formed east of the rain area, which started to move eastward. A temperature break line seen in Kansas is moving southeastward. By 16 h the two rain areas in Oklahoma are combined into one. The two tornado cyclones are moving almost at the same speed; but the northern part of the surge line is moving faster than the southern, so the

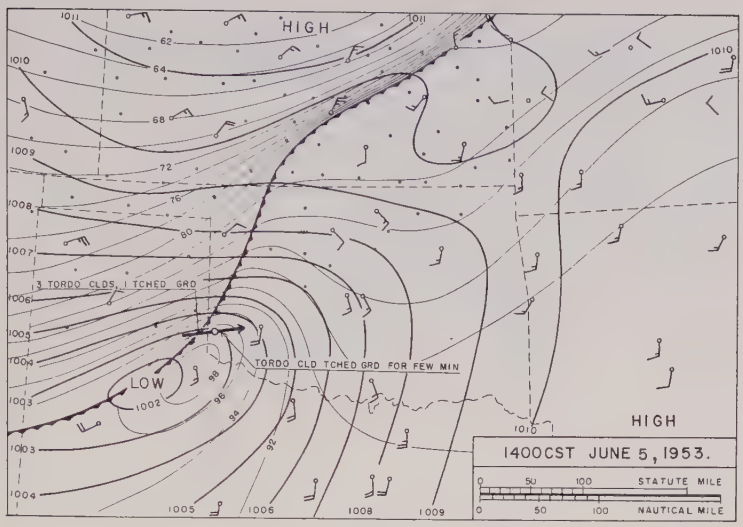

Fig. 24.

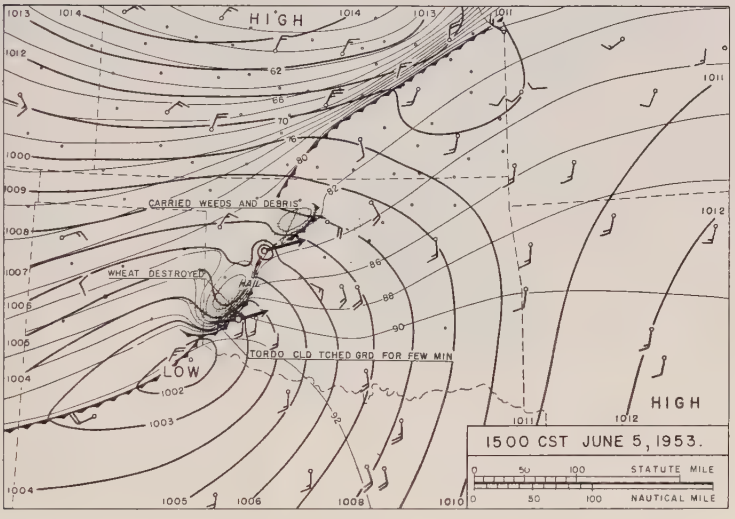

Fig. 25.

tornado in the north was engulfed in the cold air. Between 1615 and 1630, the tornado in the south came 4 minutes before the wind shifted to northwest. This means that the southern tornado moved slightly earlier than the surge line.

By 17 h, tornado No. 2 travelled east-northeastward above the cold dome. A tornado cloud not reaching the ground was reported. Probably, the underlying cold air prevented the dipping of the funnel cloud down to the ground. Usually, a horizontal vortex inside the upper layer of a twofluid system sucks up the lower fluid, in a similar manner to that we see on the sea surface in a hurricanecenter. This situation continued till 18 h.

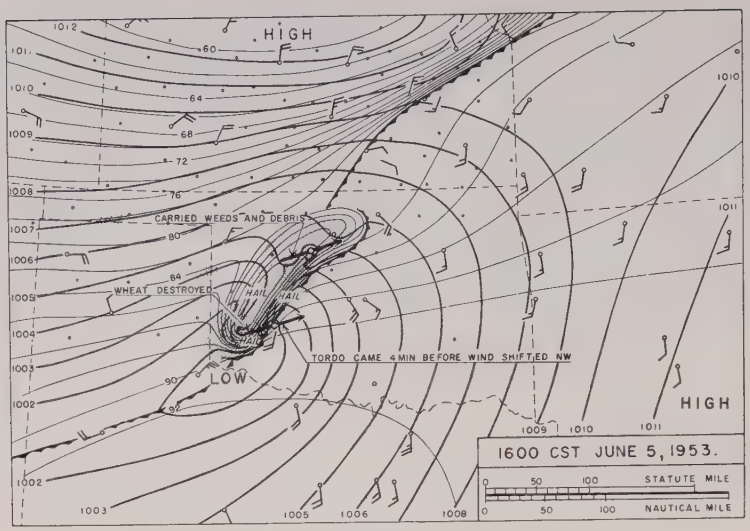

Fig. 26.

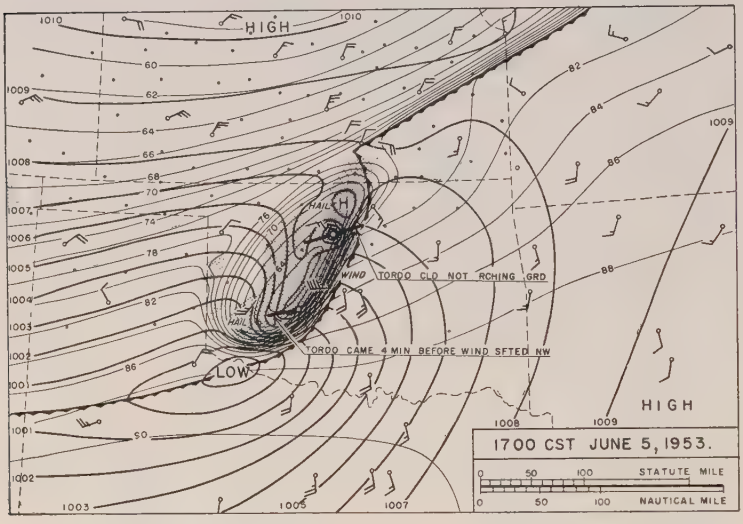

Fig. 27.

At 19 h, another small system entered into the map area from the west. Two new tornadoes (Nos 3 and 4) appeared in the northern part of the big thunderstorm high. While the tornado cyclone No. 2 is travelling over the cold dome during this hour the tornado funnel apparently managed to reach the ground. In the Climatological Data (1953), it is reported that four buildings were damaged or destroyed. The funnel observed appeared to be smaller than most tornadoes. This tornado would have spent much energy to make a vortex in the cold air.

A wake trough had developed by 2100, and tornado cyclone No. 5 appeared inside the cold air to the south. Prior to the appearance

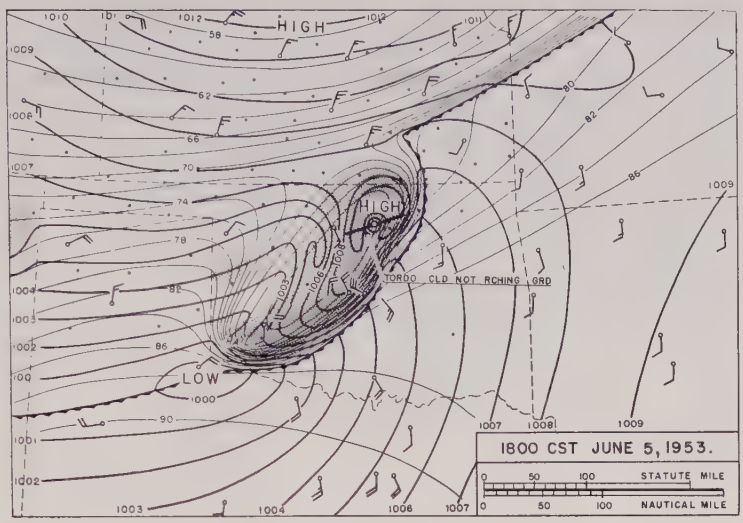

Fig. 28.

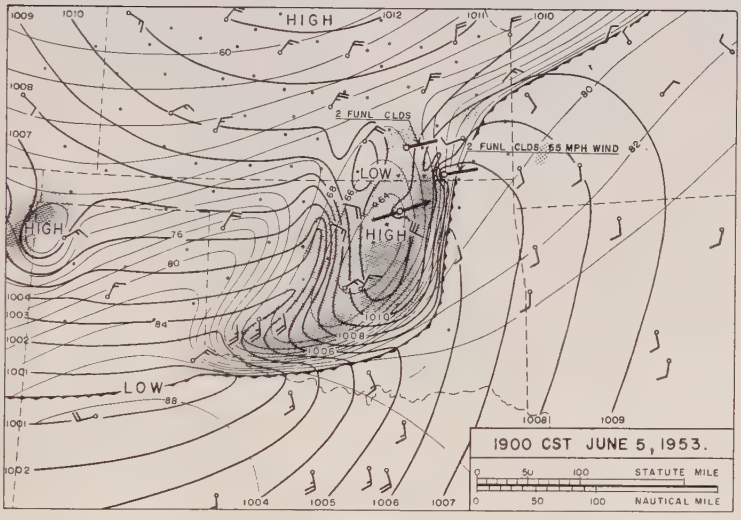

Fig. 29.

of the tornado cyclone, hail was reported in the area where the initiation of the cyclone probably occurred, Strong heil moved eastward with the tornado cyclone. Hailstones of 1/2 to 1 inch in diameter piled up seven inches deep on the highway. A wake depression center, having a higher temperature inside, appeared at 22 h. By this time, the squall-line activity became weaker; meanwhile, the surge line moved far eastward from the rain areas.

At 2300 and 0000 next day, the thunderstorm high associated with the main storm became weaker. The thunderstorm high in the north was intensified by the heavy rain in that area. A well developed wake depression is seen in

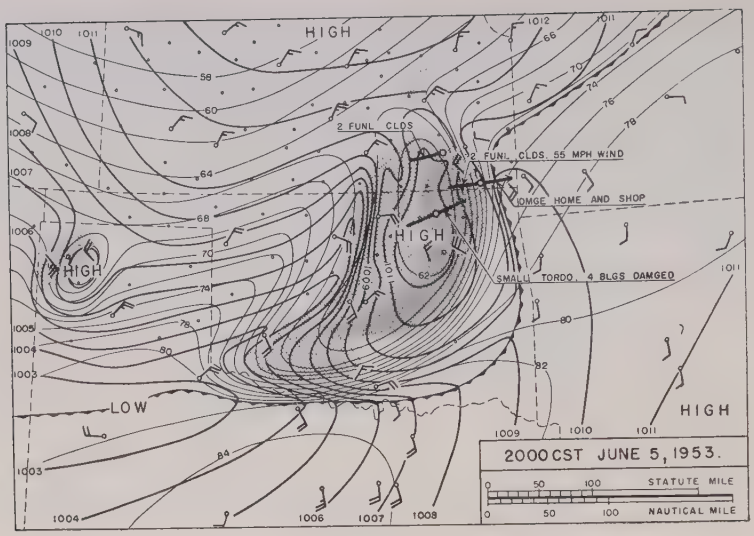

Fig. 30.

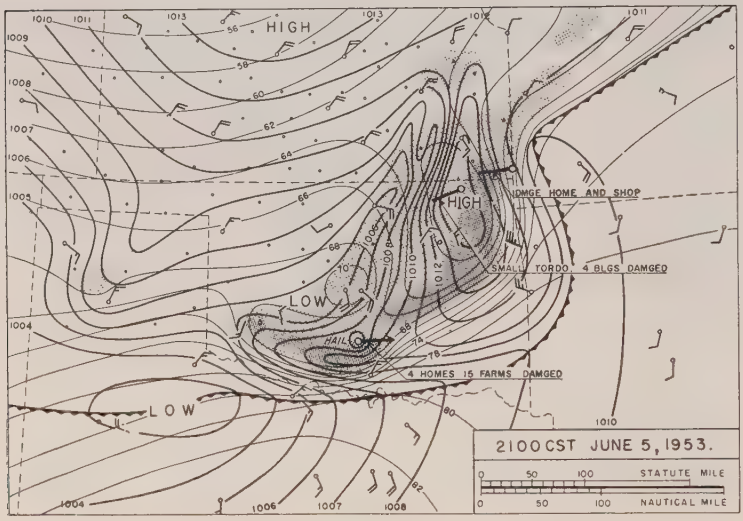

Fig. 31.

the rear. Hail is continuing in southern Oklahoma, but no tornadoes are reported in the storm areas.

Condition of the Tornado Initiation. — Meteorological conditions which gave rise to the development of the tornado sequence No. 1 are shown in Fig. 35. The tornado was reported at 1300 in the Texas Panhandle near the Oklahoma border. Amarillo radar reported "PPI NO ECHO" at 1305, then at 1335, "scattered circular echo 8 miles diameter" is reported to the south of the tornado, which had been observed as a tornado by that time. The echo moved north-eastward developing into an eliptical, scattered, 20 by 8 mile echo. At Childress, thundering cumuli were observed

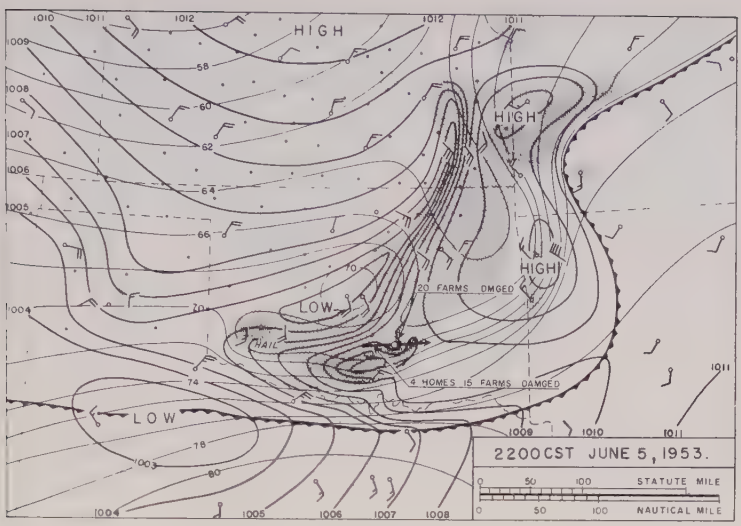

Fig. 32.

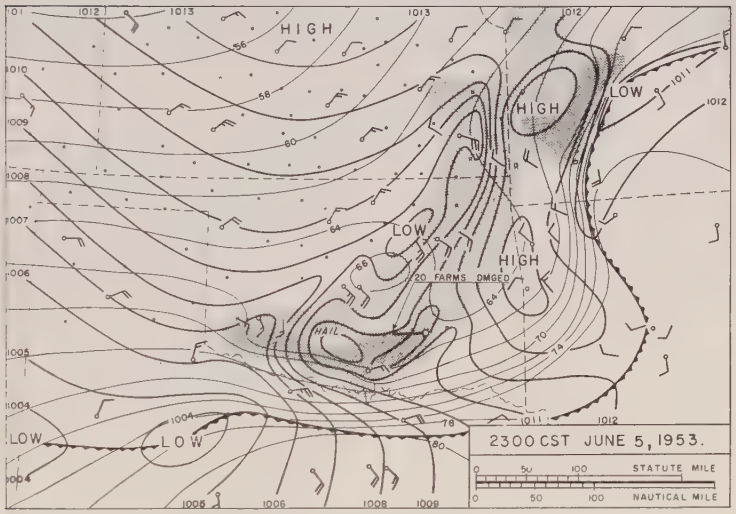

Fig. 33.

at 1230, then at 1330, when the tornado was reported, a rain shower was visible to the north. A pilot reported, at 1219, that he met light turbulence in the line of cumulus oriented SW—NE on the Oklahoma and Texas border.

From the traces of the three barograph stations in the area, no indication of pressure surge was seen, which might have moved into the tornado area from the west. From these facts the space section of the clouds and of the pressure from CDS to TUL in Fig. 36 are constructed. The tornado cyclone is believed to have been initiated at 1330 in the area where an isolated shower of 8 miles in diameter existed. No appreciable pressure-surge lines are recognized in that area. One or two hours

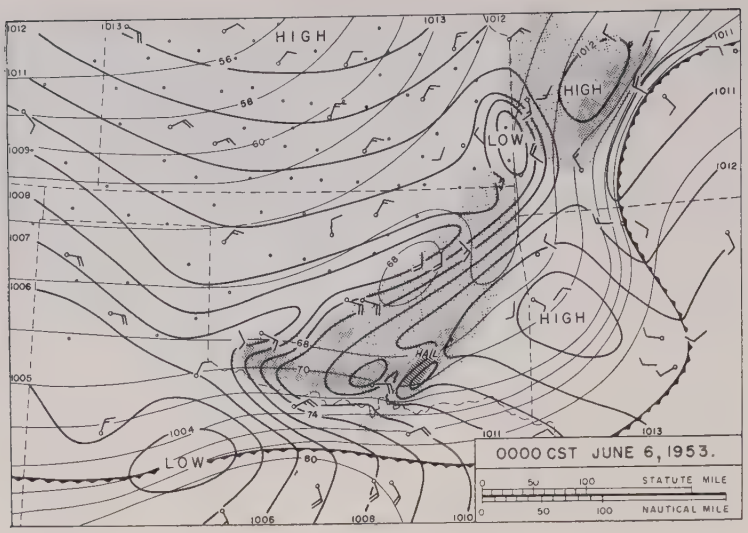

Fig. 34.

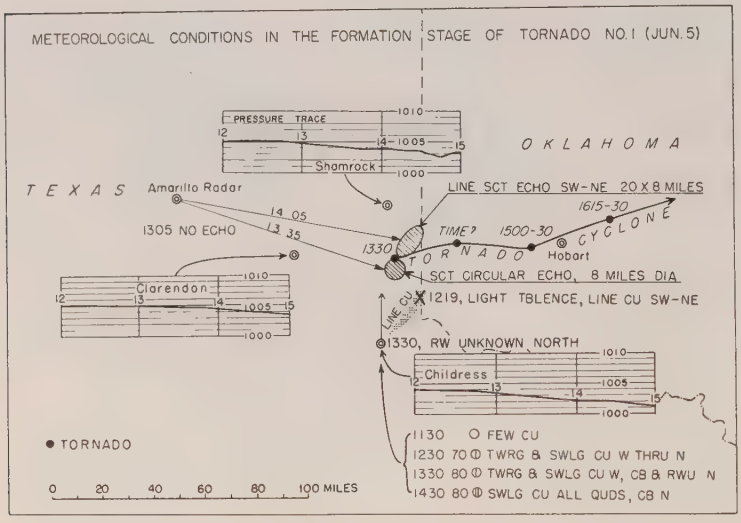

Fig. 35. Meteorological conditions in the formation stage of tornado No. 1.

after the development of the tornado, a surge line became intense.

The conditions of the initiation of the tornado cyclone No. 2 are shown in the chart to the right in Fig. 36. In this case, however, the surge line moved faster than the tornado. Such a case is unfavourable for the extension of the funnel cloud down to the ground. Therefore, the tornadoes of this sequence either were very small or did not reach the ground.

8. Analysis of squall line of june 27, 1953

In this study, the meso-analyses were carried out in a large area of 600 by 1000 miles. Hourly charts were made for a 36-hour period, seven of which are presented.

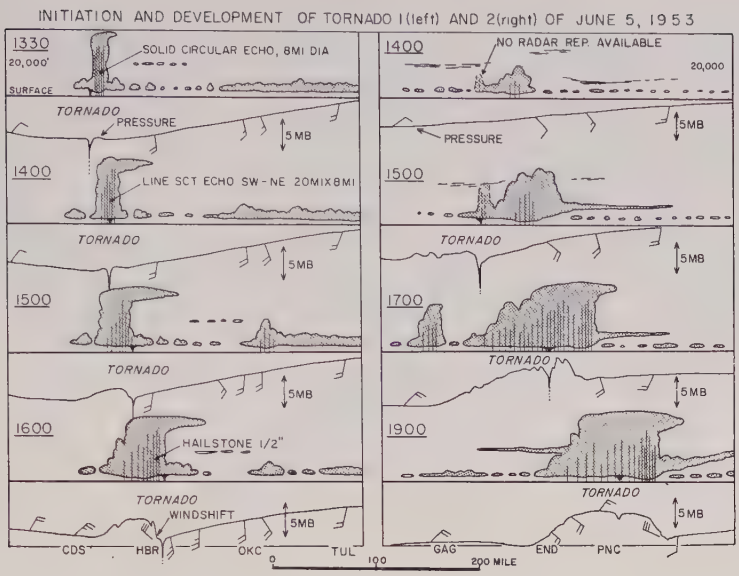

Fig. 36. Schematic section of cloud and pressure related to the tornado initiation.

At 15 h on the 27th (Fig. 37), a post-mature thunderstorm high was travelling over the Chicago area. It was followed by a very deep wake depression, having a pressure drop of about 8 mb. Along the cold front passing across the middle portion of Kansas, several rain showers and thunderstorm highs were being formed. The isotherms for every 2° F show no discontinuity at the front of the cold air. One hour later, at 16 h (Fig. 38), a strong shower accompanied by a tornado developed in southwestern Iowa. In the chart, the barograph traces are entered in a manner similar to that of Fig. 16. These traces show the gradual drop in pressure east of the front.

The thunderstorm high over the Chicago area became weak, reaching the "Stage 4" of Fig. 17. The barograph traces showed an appreciable pressure surge. Three thunderstorm highs located along the cold front have not yet developed a wake depression. They are now in "Stage 1." The tornado in Iowa is moving almost at the same speed as the pressure surge. By 17 h the trough associated with the front has deepened in some places in the expected positions of wake depressions.

By 18 h pressure-surge lines of the three thunderstorm highs were combined into a lone one. Heavy thunderstorm rains are moving behind the surge. On the other hand, the thunderstorm high near Chicago has reached the "Stage 5", in which the pressure surge dissipates and the wake depression remains. Tornadoes are still active in Iowa.

The pressure-surge lines moved far to the east from the cold front. According to the diurnal variation of the pressure, which is positive at 19 h, a gradual rise in pressure is seen to the east of the surge line.

A wake depression in Iowa became pronounced at 20 h. The rapid movement of the surge line left the rain areas far to the west.

The large thunderstorm highs reached the post-mature stage by 21 h. The characteristics of this stage are the separation of the lines of pressure surge, temperature break, and the beginning of rains. In case of a strong daytime squall line, these three lines occur almost at the same time. In the night-time squall lines, however, the surface inversion prevents the sinking of the cold-dome air down to the ground. Especially in the post-mature stage, the absence of rain immediately behind the surge line means an absence of precipitation cooling following the pressure surge. It is usual in this stage that the temperature breaks one half to one hour after the pressure has surged. It will be seen in the chart at 21 h, that the surge line is about 30 to 40 miles ahead of the line of the temperature break.

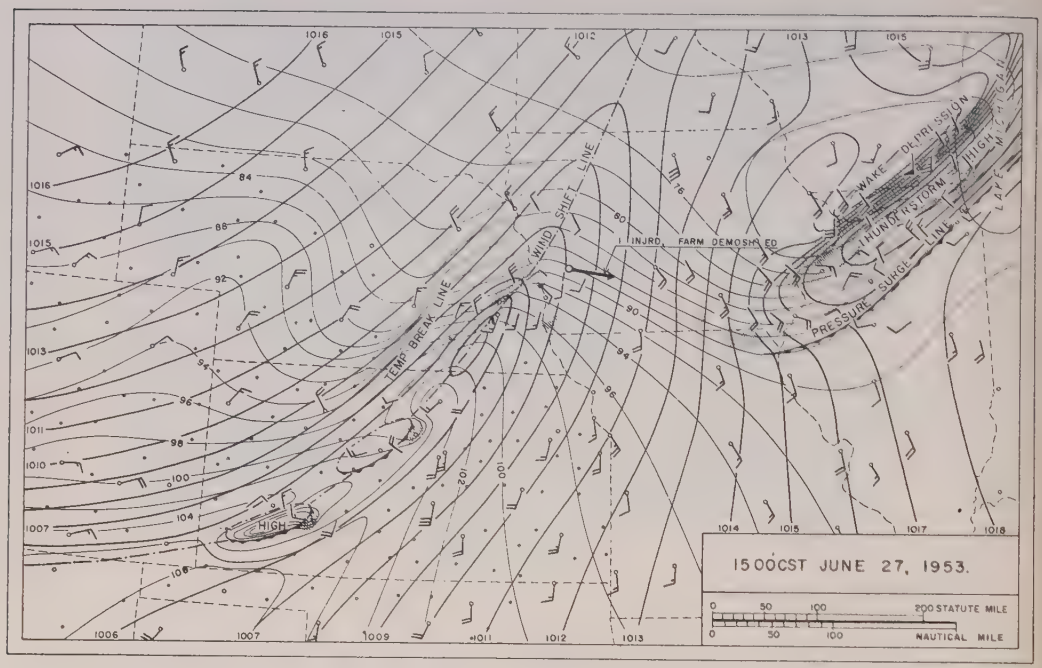
1 INJRD, FARM DEMOSHED
WIND SHIFT LINE
TEMP. BREAK LINE
WAKE DEPRESSION
THUNDERSTORM HIGH
PRESSURE SURGE LINE
HIGH
1500CST JUNE 27, 1953.
200 STATUTE MILE
NAUTICAL MILE

Fig. 37.

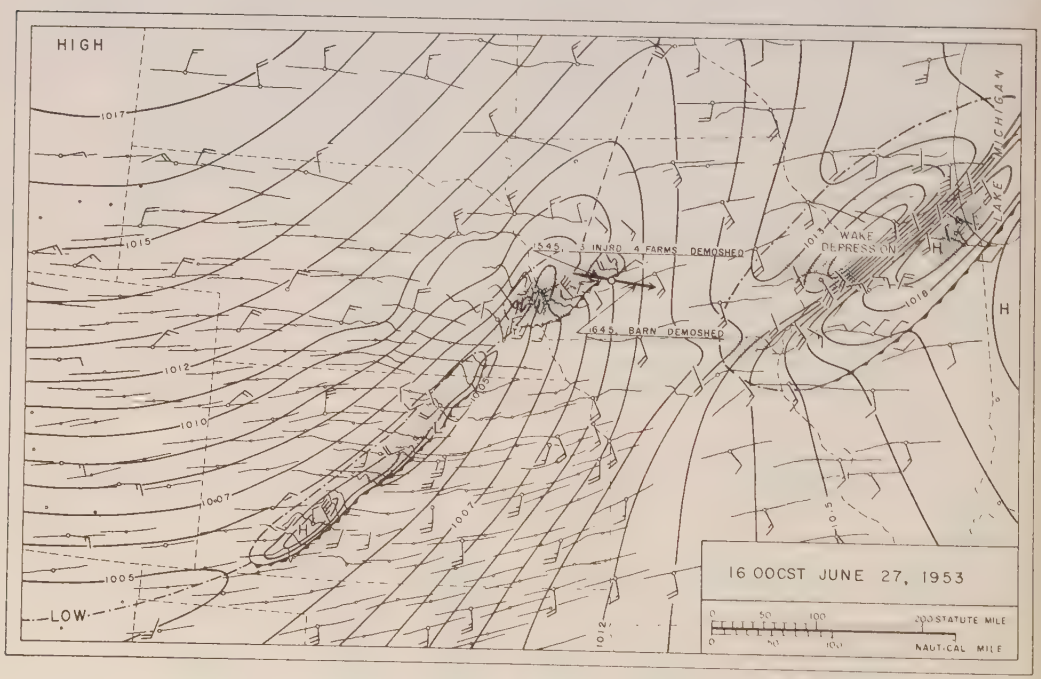
HIGH
LOW
1645, 3 INJRD 4 FARMS DEMOSHED
1645, BARN DEMOSHED
WAKE DEPRESSION
LAKE MICHIGAN
16 00CST JUNE 27, 1953
200 STATUTE MILE
NAUTICAL MILE

Fig. 38.

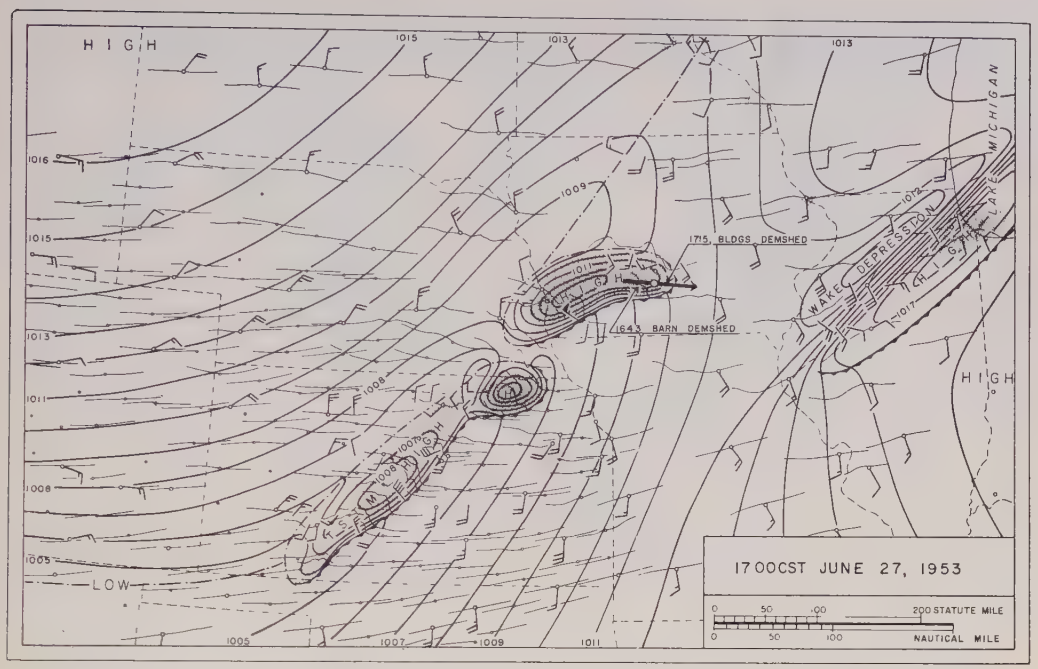
HIGH
1015
1013
1013
LAKE MICHIGAN
1016
1009
1012
1715, BLDGS DEMSHED
WAKE DEPRESSION
1015
1017
1643 BARN DEMSHED
HIGH
1013
1011
1008
1005
LOW
1005
1007
1009
1011
1700CST JUNE 27, 1953
0 50 100 200 STATUTE MILE
0 50 100 NAUTICAL MILE

Fig. 39.

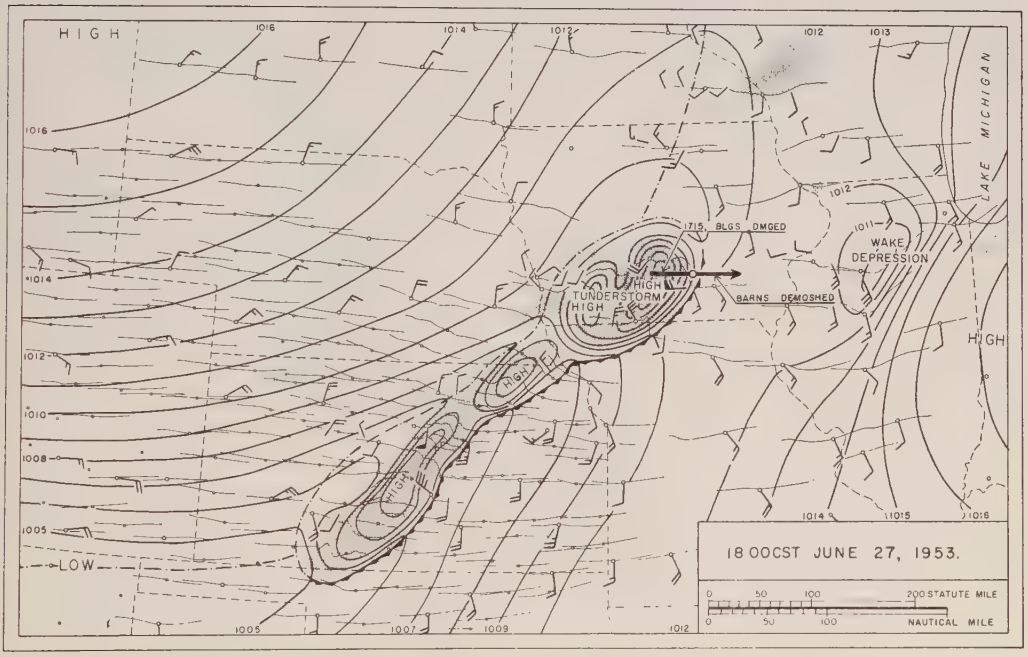
HIGH
1016
1014
1012
1012
1013
LAKE MICHIGAN
1016
1012
1715 BLGS DMGED
1011
WAKE DEPRESSION
1014
HIGH
THUNDERSTORM HIGH
BARNS DEMOSHED
HIGH
1012
1010
1008
HIGH
HIGH
1005
LOW
1014
1015
1016
1005
1007
1009
1012
1800CST JUNE 27, 1953.
0 50 100 200 STATUTE MILE
0 50 100 NAUTICAL MILE

Fig. 40.

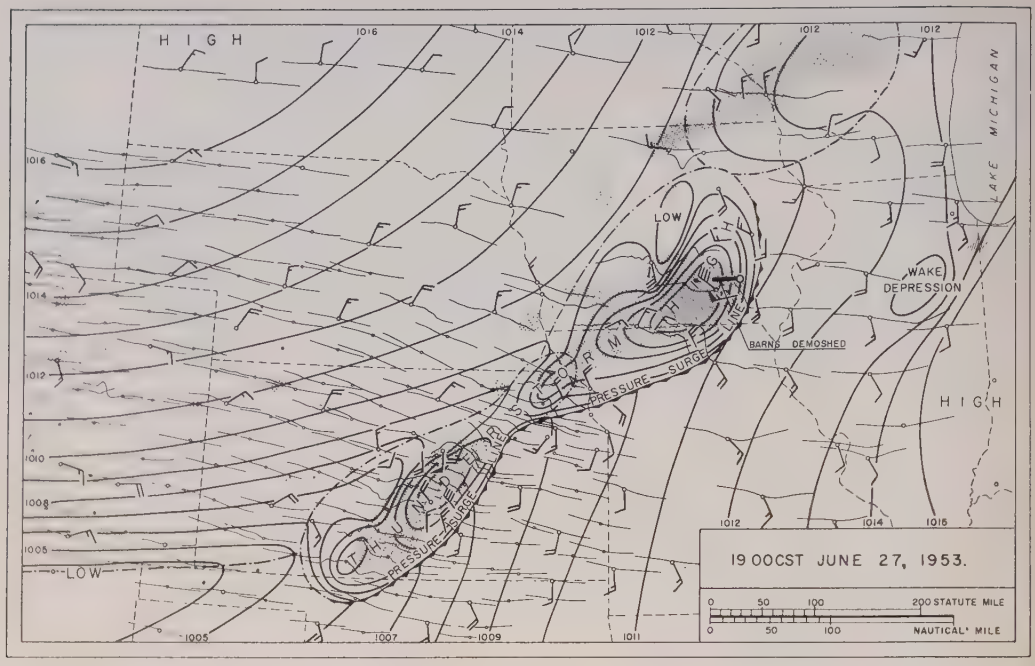
HIGH
LOW
LOW
WAKE DEPRESSION
BARNS DEMOLISHED
PRESSURE SURGE LINE
PRESSURE SURGE LINE
HIGH
LAKE MICHIGAN
1900CST JUNE 27, 1953.
200 STATUTE MILE
NAUTICAL MILE

Fig. 41.

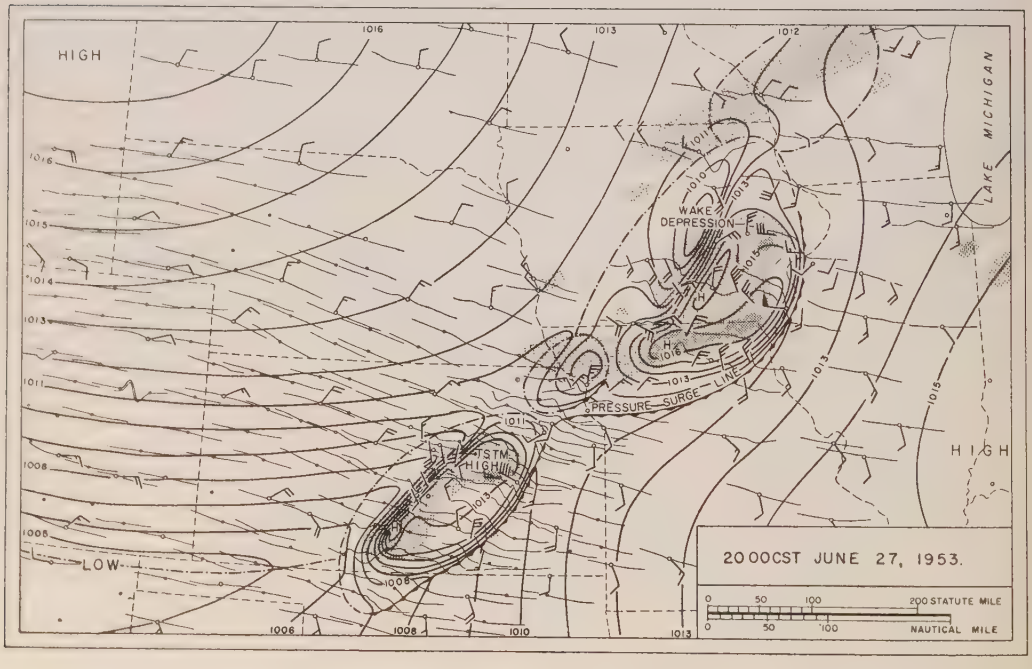
HIGH
LOW
WAKE DEPRESSION
PRESSURE SURGE LINE
HIGH
LAKE MICHIGAN
2000CST JUNE 27, 1953.
200 STATUTE MILE
NAUTICAL MILE

Fig. 42.

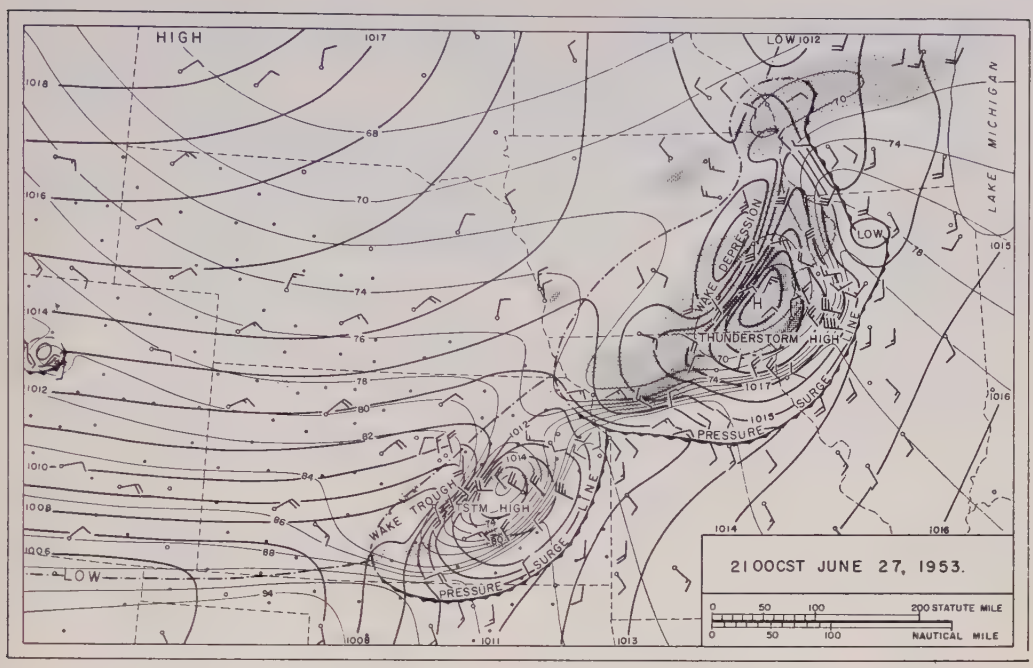

Fig. 43.

Meteorological conditions of the early stage of the tornado occurrence in Iowa are shown in Fig. 44. Norfolk, Nebraska, radar reported a line echo at 1440. Within one hour it developed into a large echo, bringing in a heavy rain represented by the isohyets for 1500—1600. The tornado was reported at 1545 at the position shown on the chart. It can be considered that the tornado cyclone associated with the tornado would have been formed at 1500 or 1530. The initiation of the tornado cyclone would be related to the heavy rain of 0.86° seen in the figure north of the cyclone path. Pierce (13) has pointed out that tornadoes tend to form at the southwestern part of a large thunderstorm, as suggested also by this case. From the fact that we had no rain before 15 h, except 0.02° at Omaha, it is concluded that this tornado cyclone must be related to a very early stage of the squall-line development.

The time section for Omaha shows the pressure surge at 1530 and the temperature break at 1450. The station is so far from the tornado area that we cannot expect to find any further information about the tornado.

9. Some representations in color

The cloud chart at 21 h, June 27, 1953 is shown in Plate 1. The blue bands indicate vertical cross-sections up to 30,000 ft. which pass through the teletype stations. The shapes of the clouds were estimated by changing the time section, such as in Fig. 1, for example, into a space section. To make the relative positions of the clouds with the surface systems clear, the surface winds and isobars are shown in the areas outside of the blue bands. It will be seen that the developed squall line thunderclouds are moving over the thunderstorm highs shown in pink. Surface rains of the past hour are shown by the blue areas. The lightning, schematically represented by red arrows, and the rain inside the clouds (blue vertical lines) is also entered. This chart was made for demonstration purposes; however, the antecedent charts now to be examined show the developments leading up to this peak of squall-line activity.

With the technique introduced in the section on wind analysis, divergence and convergence were computed for the hours 15 and 20, June

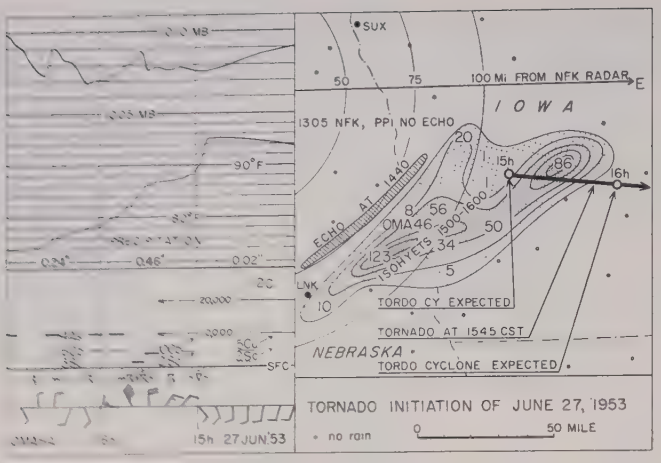

Fig. 44. Meteorological conditions of the tornado initiation in Iowa.

27, 1953. In Plates 2 and 3, divergence areas are represented by different intensities of red, while convergence is indicated in the blue areas. In the chart at 15 h (Plate 2), a convergence zone is seen along the cold front. Five hours later, at 20 h, four thunderstorm highs had developed. The most important feature of the divergence pattern in the chart is the very high values of the velocity divergence existing inside the meso-scale thunderstorm highs. It is known by the "Thunderstorm Project" that a very large divergence exists inside the meso-scale thunderstorm high. The meso-scale divergence of 10 to 60×10^{-5}/sec is shown for the first time by this analysis. Actually, the thunderstorm highs are increasing despite the large value of divergence near the ground. This fact suggests the existence of a very strong converging flow aloft, which must more than compensate the surface divergence as shown also to be the case in individual cells examined by Byers and Hull (7). It will be necessary to consider that the inversion layers which might have existed originally should be destroyed by the vertical motion.

A thermodynamical section of the squall line at 20 h is shown in Plate 4. In the upper chart representing the soundings, the area between the temperature (T) and dew point (T_d) curves is colored in pink. The pressure-surge line to the right is moving eastward at the rate of 55 knots. The cold front surface fixed by the aircraft reached the 10,000 foot level. Location of the surface cold-front, which is not visible in the surface chart, is determined by extrapolating the profiles of undisturbed pressure on both sides of the thunderstorm high into the thunderstorm area as indicated in the space section of pressure in the center chart. Winds in the lower chart are the ones *relative* to the system which is moving eastward at the rate of 30 knots, at which speed the thunderstorm high is moving. The front of the cold thunderstorm air, moving at 55 knots eastward, is faster by as much as 25 knots than the speed of the high. It will be seen that the upper winds obtain some additional momentum through their descending motion and the effect of the pressure gradient near the surface. Inside the wake depression, the air is accelerated eastward due to the wake friction of the thunderstorm high. The main low-level flow relative to the thunderstorm high is in the sense that the wake is to the west of the thunderstorm mass.

10. Conclusions

The detailed analysis methods developed by the author in Japan, extended and refined in their application to the Central United States, give as true a picture of meso-scale phenomena as can possibly be obtained from the data and records. The scheme of analysis described enables one to make inferences concerning the magnitudes and times of weather changes or events not specifically given in the data as, for example, in the crude reporting of climatological co-operative stations. Meso-scale pat-

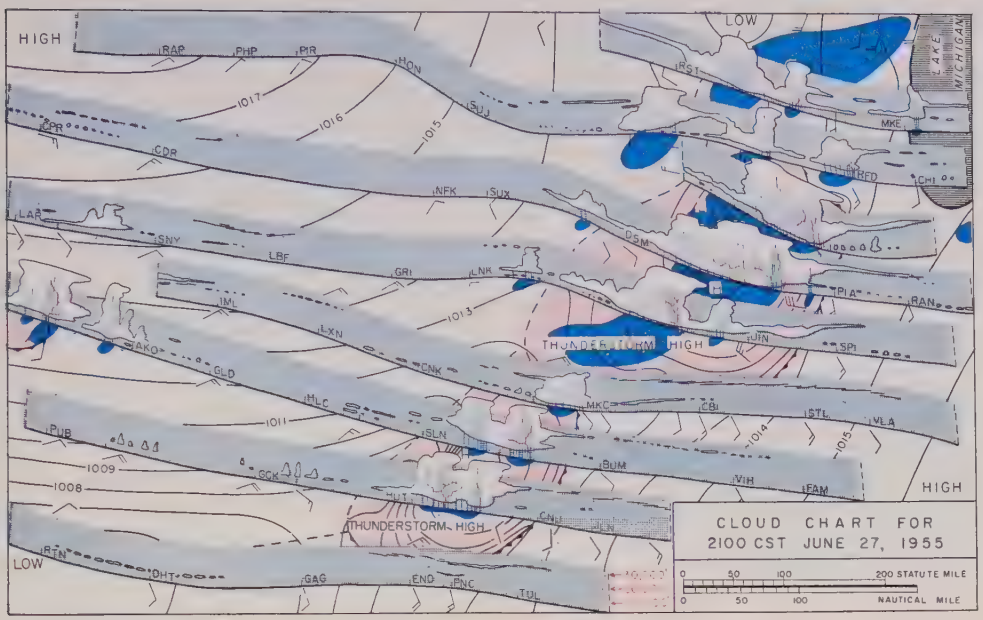

Plate I. Squall-line clouds and weather at 2100, June 27, 1953.

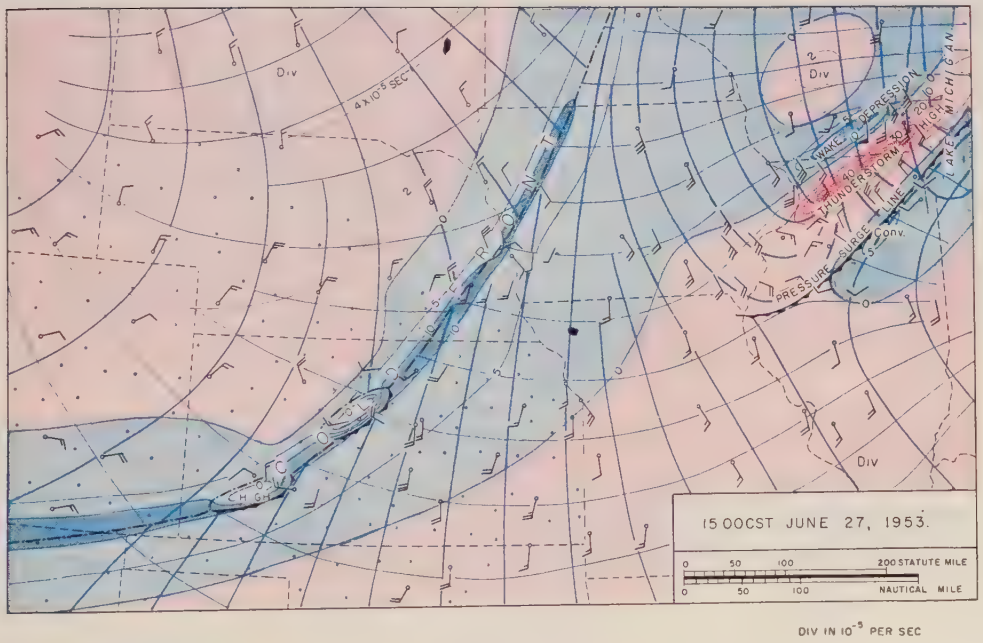

Plate II. Divergence and convergence pattern for 1500, June 27, 1953.

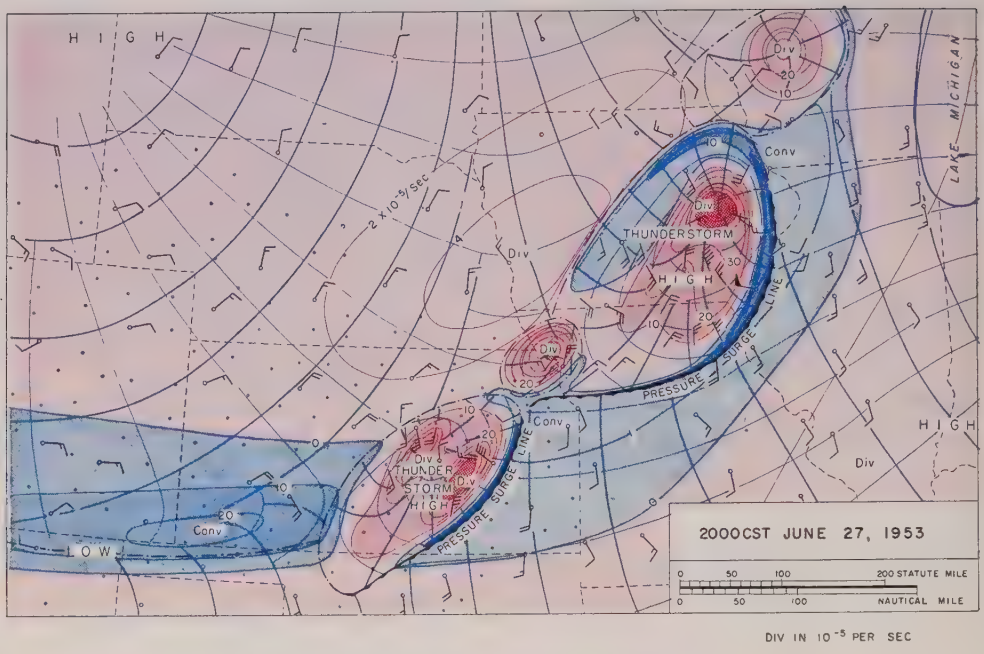

Plate III. Divergence and convergence pattern for 2000, June 27, 1953.

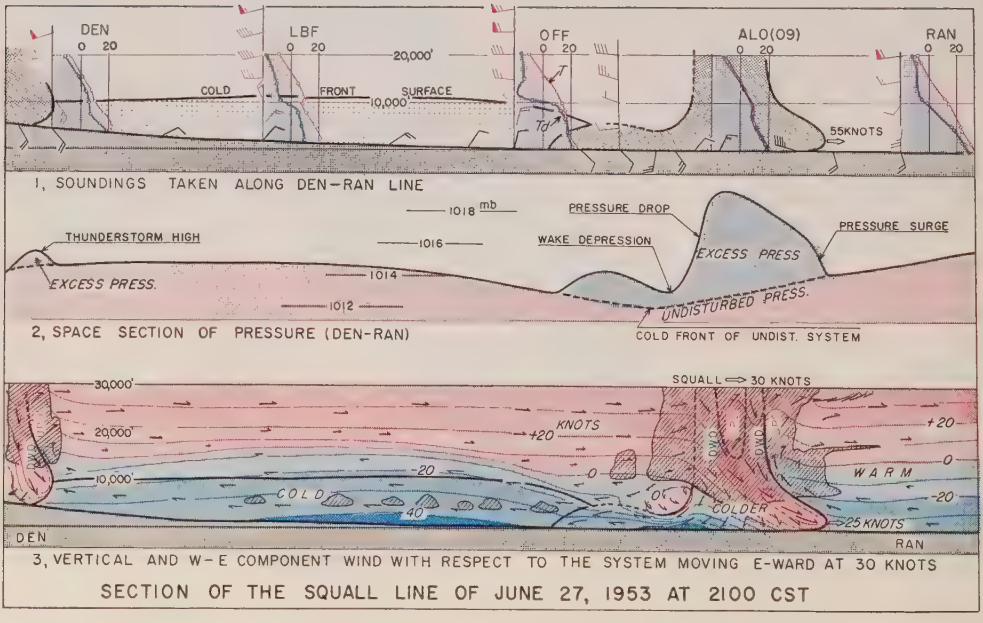

Plate IV. East-west cross section of the squall-line of June 27, 1953 at 2100 CST.

terns such as squall lines lead themselves admirably to this type of interpretation.

In the analysis of the squall line of June 5—6, 1953 five tornado sequences were noted, each associated with an intense tornado cyclone in which the tornado funnels intermittently appeared. This intense system of storms was initiated *before* a pressure-surge line was orgaganized. This suggests the futility of seeking a "trigger" mechanism in the pressure field at the initial stage.

The analysis shows that tornado cyclones can move either faster or slower than the pressure-surge line. In the slower moving case, the tornado cyclone becomes surrounded in the low levels by cold air of the thunderstorm high and the penetration of tornado funnels down to the surface is inhibited.

A low pressure center or trough, much larger in dimensions than the tornado cyclone but much weaker, appears as the "wake depression". This depression was well marked in the second case analyzed, that of June 27, 1953. Another feature of this case was the lack of coincidence, during the night, of the lines of pressure surge, temperature break and beginning of rains. This appears to be characteristic of night thunderstorms and is explainable as an effect of the nocturnal inversion in preventing the downdraft and outflow from reaching the ground.

Colored charts and diagrams are an essential feature of the type of analysis treated here. In the interests of economy in printing, only a few maps are reproduced in color in this article. The charts in Plates 2 and 3 show the unusually high values of divergence (10 to $60 \cdot 10^{-5}$ sec^{-1}) obtained in this scale. The vertical analysis in Plate 4 demonstrates that the rapid displacements of the lines are in agreement with the winds above the frictional layer. This suggests that the speed does not have to be explained by a mysterious upper impulse-type wave.

If the charts analyzed in this article were to be considered in the usual synoptic scale of 1:10,000,000 or less with stations 50 to 100 mi. (80 to 160 km) apart, a highly confusing picture would result. In drawing the isobars one could, of course, ignore the pressure report of a station that might happen to be in the thunderstorm high, the wake depression or, highly improbably, the tornado cyclone. But since the recognizable features of the true front are completely obliterated, its location on the map would be impossible to find.

In the short-period forecasting or extrapolation of the weather on the meso-synoptic scale, the complete data such as used in this paper are not available on a current basis, so it is necessary to rely on other tools. On this basis, the most helpful information is that to be obtained from a network of continually operating radar stations.

Acknowledgements

The study was carried out at the University of Chicago under the supervision of Dr Horace R. Byers, chairman of the Department of Meteorology. Sincere gratitude is expressed to Dr Byers for his kind guidance and comments in the development of the writer's mesoanalyses.

The writer wishes to express his thanks to Dr Morris Tepper, Severe Storm Research Unit, U.S. Weather Bureau, for making the traces from the Severe Storm Network available; to Mr Leslie Smith and Mr Lawrence M. Dye, National Weather Records Center for their kind help in the collection fo the weather data; and to Dr George W. Platzman, University of Chicago, for his suggestions for the advancement of the studies. The writer is also very grateful to Mr Krishna Murti for his assistance in the analyses.

TABLE OF ABBREVIATIONS

(a) Station Names

ADM	Ardmore, Oklahoma	CHI	Chicago, Illinois	DBQ	Dubuque, Iowa
AKO	Akron, Colorado	*CLN	Clarendon, Texas	DDC	Dodge City, Kansas
ALO	Waterloo, Iowa	CNK	Concordia, Kansas	DEN	Denver, Colorado
BDF	Bradford, Illinois	CNU	Chanute, Kansas	DHT	Dalhart, Texas
BUM	Butler, Missouri	COS	Colorado Springs, Colorado	DSM	Des Moines, Iowa
CBI	Columbia, Missouri			END	Enid, Oklahoma
CDR	Chadron, Nebraska	CPR	Casper, Wyoming	FAM	Farmington, Missouri
CDS	Childress, Texas	DAL	Dallas, Texas	FLP	Flippin, Arkansas

FYV	Fayetteville, Arkansas	LXN	Lexington, Nebraska	RAP	Rapid City, South Dakota
GAG	Gage City, Oklahoma	*MKC	Kansas City, Missouri	RFD	Rockford, Illinois
GCK	Garden City, Kansas	MKE	Milwaukee, Wisconsin	RST	Rochester, Minnesota
GLD	Goodland, Kansas	MLC	McAlester, Oklahoma	RTN	Raton, New Mexico
GRB	Green Bay, Wisconsin	*MLI	Moline, Illinois	SBN	South Bend, Indiana
GRI	Grand Island, Nebraska	NFK	Norfolk, Nebraska	SGF	Springfield, Missouri
GSH	Goshen, Indiana	*NTA	Nowata, Oklahoma	*SHK	Shamrock, Texas
HBR	Hobart, Oklahoma	OFF	Offutt, Nebraska	*SLG	Seiling, Oklahoma
HLC	Hill City, Kansas	OKC	Oklahoma City, Oklahoma	SLN	Salina, Kansas
HON	Huron, South Dakota			SNY	Sidney, Nebraska
HUT	Hutchinson, Kansas	*OKN	Okeene, Oklahoma	SPI	Springfield, Illinois
IML	Imperial, Nebraska	OMA	Omaha, Nebraska	STL	St. Louis, Missouri
*IRK	Kirksville, Missouri	OTM	Ottumwa, Iowa	*STW	Stillwater, Oklahoma
JLN	Joplin, Missouri	*PAR	Parsons, Kansas	SUJ	Sioux Falls, South Dakota
KNR	Kingfisher, Oklahoma	PHP	Philip, South Dakota	SUX	Sioux City, Iowa
LAF	Laytette, Indiana	PIA	Peoria, Illinois	TOP	Topeka, Kansas
LBB	Lubbock, Texas	PIR	Pierre, South Dakota	*TRO	Toronto, Kansas
LBF	North Platte, Nebraska	PUB	Puebro, Colorado	TUL	Tulsa, Oklahoma
LHX	La Junta, Colorado	PNC	Ponca City, Oklahoma	TXK	Texarkana, Arkansas
LIT	Little Rock, Arkansas	*PSK	Pawhuska, Oklahoma	UIN	Quincy, Illinois
LMN	Lamour, Iowa	*PWN	Pawnee, Oklahoma	VIH	Vichy, Missouri
LNK	Lincoln, Nebraska	RAN	Rantoul, Illinois	VLA	Vandalia, Illinois

(b) Words in Figures

BLGS	buildings	GRD	ground
CLDS	clouds	INJRD	injured
COND	condensation	OCF	occluded front
CY	cyclone	QUDS	quadrants
DEMSHED	demolished	RCHING	reaching
DIA	diameter	REP	report
DMGD	damaged	RW(U)	rainshower (unknown)
DWD	downdraft	SCT	scattered
ELNL	funnel	SFC	surface
		SFTED	shifted
		SWIG	swelling
		TCHED	touched
		TORDO	tornado
		TSTM	thunderstorm
		TWRG	thundering
		UPD	updraft

* Automatic Barograph Station.

REFERENCES

Baldwin, T., 1954: Tropical hurricanes, *Quart. J. Roy Met. Soc.*, No 344, pp. 131—104.

Bergeron, T. and Solberg, H., 1923: Meteorological conditions for the formation of rain, *Geophysiske Publikasjoner*, II, pp. 4—60.

Brooks, C. F., 1922: The local, or heat, thunderstorm, *Mo. Weath. Rev.*, U.S. Weather Bureau No. 50, pp. 28—30.

Brooks, E. M., 1940: The tornado cyclone, *Weatherwise*, 2, 4, pp. 32—33.

Brooks, E. M., 1954: Characteristics of thunderstorm microbarographs, *Trans. Amer. Geoph. Union*, **35**, 3, pp. 413—420.

Byers, H. R., 1942: Nonfrontal thunderstorms, *Dep. Meteor. Univ. Chicago, Misc. Rep.*, No. 3.

Byers, H. R. and Hull, E. C., 1949: Inflow patterns of thunderstorms as shown by wind aloft, *Bull. Am. Met. Soc.*, **30**, 3, pp. 90—99.

Byers, H. R. and Braham, R. R. Jr., 1949: *The Thunderstorm*, Report of the Thunderstorm Project, 1946 and 1947, Government Printing Office, Washington, D.C.

Climatological Data, *National Summary*, 4, 6, 1953, p. 181.

Fujita, T., 1950: Microanalytical study of thundernose, *Geoph. Mag. of Japan*, **22**, 2, pp. 71—88.

Fujita, T., 1951: Microanalytical study of cold front, *Geoph. Mag. of Japan*, **22**, 2. pp. 237—277.

Fulks, J. R.: On the mechanics of the tornado (unpublished).

Penn, S., Pierce, C., and McGuire, J. K., 1955: The squall line and Massachusetts tornadoes of June 9, 1953, *Bull. Am. Met, Soc.*, **36**, 3, pp. 109—122.

Suckstorff, G. A., 1953: Die Strömungsvorgänge in Instabilitätsschauern, *Meteor. Zeitschrift*, **52**, Heft 12, pp. 449—452.

Swingle, D. M. and Rosenberg, L., 1953: Mesometeorological analysis of cold front passage using radar weather data, *Proc. Conf. on Radar Meteor.*, Univ. of Texas, Ch. XI-5.

Tepper, M., 1950: A proposed mechanism of squall-line: the pressure jump, *J. Met.*, **7**, pp. 21—29.

Williams, D. T., 1948: Surface micro study of squall-line thunderstorms, *Mo. Wea. Rev.*, **76**, 11, pp. 239—246.

Tests of the Salt-Nuclei Hypothesis of Rain Formation

By A. H. WOODCOCK and D. C. BLANCHARD, Woods Hole Oceanographic Institution,[1] Woods Hole, Massachusetts

(Manuscript received May 18, 1955)

Abstract

Atmospheric chlorides in sea-salt nuclei and the chlorides dissolved in shower rainwaters were recently measured in Hawaii. A comparison of these measurements reveals the remarkable fact that the weight of chloride present in a certain number of nuclei in a cubic meter of clear air tends to be equal to the weight of chloride dissolved in an equal number of raindrops in a cubic meter of rainy air. This result is explained as an indication that the raindrops grow on the salt nuclei in some manner which prevents a marked change in the distribution of these nuclei during the drop-growth process.

The data presented add new evidence in further support of the salt-nuclei raindrop hypothesis previously proposed by the first author (WOODCOCK, 1952).

1. Introduction

The earlier study of atmospheric salt particles at cloud levels over Florida (WOODCOCK, 1952) showed that the number of the larger of these particles per cubic meter of air was similar to the average number of raindrops found during rain storms in other locations. This study also showed that the chloride in these nuclei, assuming that each raindrop forms around a single salt nucleus, was sufficient to account for the range of chloride concentrations usually observed in rains. This similarity of the number and chloride content of salt nuclei and the number of raindrops and the chloride content of rain waters led to the suggestion that raindrops form on the large salt nuclei. It was suggested that further studies should reveal a close relation between the salt in the clear air and salt in the rain falling from clouds subsequently formed in this air.

The purpose of this paper is to present the results of the first field tests of the salt-particle raindrop hypothesis. These tests were carried out during 1952 in Hawaii, where the salt nuclei content of the trade winds is well known and where shower rains occur with great regularity from orographic clouds over the mountains. These clouds form in the wind stream as it flows over the islands, and are usually restricted in vertical development to the lower atmosphere up to the trade-wind inversion at about 2,000 meters.

Rain samples were taken within the clouds at positions 1, 3, 4, and 5 (see fig. 1) on the island of Hawaii. Sampling of rain within the clouds made it possible to avoid the difficult problems of evaporation of raindrops and of the coalescence of drops with salt particles, which exists in rains which are sampled far below cloud base (MIYAKE, SUGUIRA, 1950). The sampling positions were selected because positions 1 and 4 are within the bases of the clouds near the area where many of the first shower rains reach the ground, and because

[1] Contribution no. 768 of the Woods Hole Oceanographic Institution. Work supported by the Office of Naval Research, under contract number Nonr-798(00) (NR-082-124).

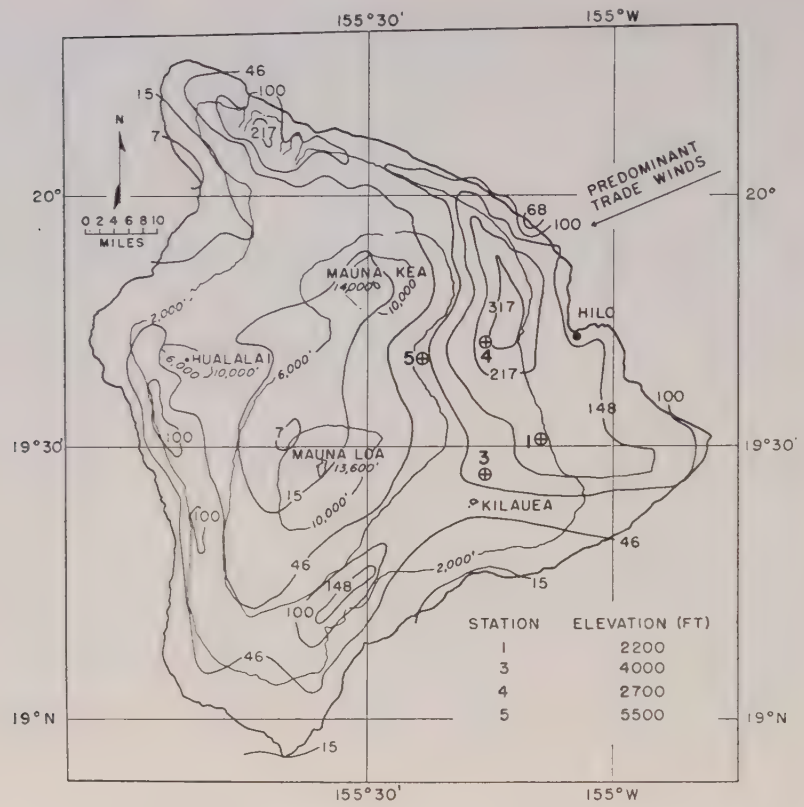

Fig. 1. Isohyetal map of the island of Hawaii, with the locations of the rain-sampling stations used in the present study. The rain-fall contours represent inches annually.

positions 3 and 5 are approximately downwind from 1 and 4 respectively and also within the clouds.

If the salt nuclei were growing to raindrop sizes in these shower clouds, we supposed that the larger less numerous nuclei, which are initially the larger of the cloud droplets (KEITH, ARONS, 1954), might become larger raindrops and fall out of the clouds at the windward stations 1 and 4. The remaining small and numerous drops, formed upon the smaller and more numerous nuclei, would be expected to fall more slowly and to reach the ground further downwind near positions 3 and 5. Thus it was anticipated that the raindrop number and the rain water chlorinity at stations 1 and 4 might be found to be related to the number of the larger salt nuclei in the air and that the rain at stations 3 and 5 might be similarly related to the smaller nuclei in the air.

The observations presented below give reasonably consistent support to this anticipated pattern of interrelationship of salt nuclei and rain.

2. Sampling rains and atmospheric salt in Hawaii

In this phase of our work in Hawaii the field problems were first, to measure from aircraft the number and the weight of the salt particles in the air stream before it arrived over the islands and second, to measure on the mountainside the drop size distribution, the salt content and intensities of the rains within the orographic clouds.

The filter-paper technique was used for measuring the sizes of the raindrops. Exposure of these filter papers was made at about the same time that bulk rain-water samples were

Table 1. Intensities, chlorinities, and drop size distributions in rains at stations 1 and 4. Sampling by filter-paper and bulk-water techniques

Position	Date (1952)	Time (LCT)	Bulk water samples		Rain drops sampled by filter paper technique										
			Rate mm hr^{-1}	Chloride mg l^{-1}	Rate mm hr^{-1}	Number of rain drops m^{-3} within various diameter ranges (mm)									
						.2—.4	.4—.6	.6—.8	.8—1.	1.—1.2	1.2—1.4	1.4—1.6	1.6—1.8	1.8—2.	2.—2.2
Part 1—Rain intensity range 0.4 to 2.0 mm/hour															
1	May 4	1810	1.9	6.3	0.71	4320	855	21							
1	» 4	1815	1.9	6.2	0.90	3200	1300	43							
1	» 4	1827	0.5	5.7	0.21	2620	19								
1	» 4	1832	1.8	2.8	1.00	6900	971	21	8						
4	» 6	1655	1.9	13.7	1.30	3210	890	287	20						
4	» 6	1706	0.4	24.8	0.71	4050	790	41							
4	» 6	1716	0.4	22.9	0.38	1600	580								
			1.26	11.8	0.74	3700	770	59	4						
Part 2—Intensity range 2.0 to 5.0 mm/hour															
1	May 1	1339	2.9	6.8	3.4	1500	385	390	265	52	26				
1	» 4	1835	2.3	2.9	3.2	1700	850	620	225	40					
1	» 4	1842	2.4	3.2	2.0	1800	1770	390	41	6					
4	» 6	1722	3.2	8.9	2.3	2170	524	590	168						
4	» 6	1734	3.9	8.0	3.8	1080	137	355	550	31					
			2.6	6.0	2.9	1650	733	468	250	26	5				
Part 3—Intensity range 5 to 10 mm/hour															
1	May 4	1848	7.0	1.3	8.0	111	520	690	670	194	54				
4	» 6	1735	7.9	7.7	8.4	790	280	82	87	121	65	125	14		
			7.45	4.5	8.2	450	400	386	379	158	60	63	7		
Part 4—Intensity range > 10 mm/hour															
1	May 1	1344			20.6	1282	369	76	206	164	198	202	23	55	7
1	» 4	1846	12.9	1.5	25.0	290	196	251	710	850	410	85	11		
			12.9	1.5	22.8	786	282	163	458	507	304	144	17	28	4

taken for chloride analysis. One-half square meter stainless steel funnels were used to obtain these bulk-water samples. Adequate volumes of water for chloride analysis could be taken with these funnels in from 10 to 300 seconds, the time depending upon the rain intensity. The filter-paper and funnel samples were taken only at times when the rain rate appeared to be constant. During the sampling periods rain showers were not observed to be drifting in over the land from the windward sea. Thus the samples were taken in orographic showers, with little rain falling to windward of stations 1 and 4.

The results of the rain sampling at stations 1 and 4 are shown on Table 1, and those at stations 3 and 5 on Table 2. In these tables averages are made from data which are separately tabulated into "parts" having similar rain intensities. The average raindrop distribution from the different rain intensities shown on Table 1 were plotted cumulatively as shown on the lower left part of figure 2.

In the present study it is also necessary to know the liquid water content and the rate of fall of the rain sampled with the filter papers. These quantities were derived as illustrated on Table 4, where rate of fall and liquid water content (columns 6 and 7) are determined from the raindrop distributions found in the highest intensity rains at stations 1 and 4 (see Table 1, part 4).

The chlorinities of the rains, which are given on Tables 1 and 2, were determined by the standard Mohr method, using a microburette and a one-hundredth normal silver nitrate solution.

Atmospheric salt particles were sampled in

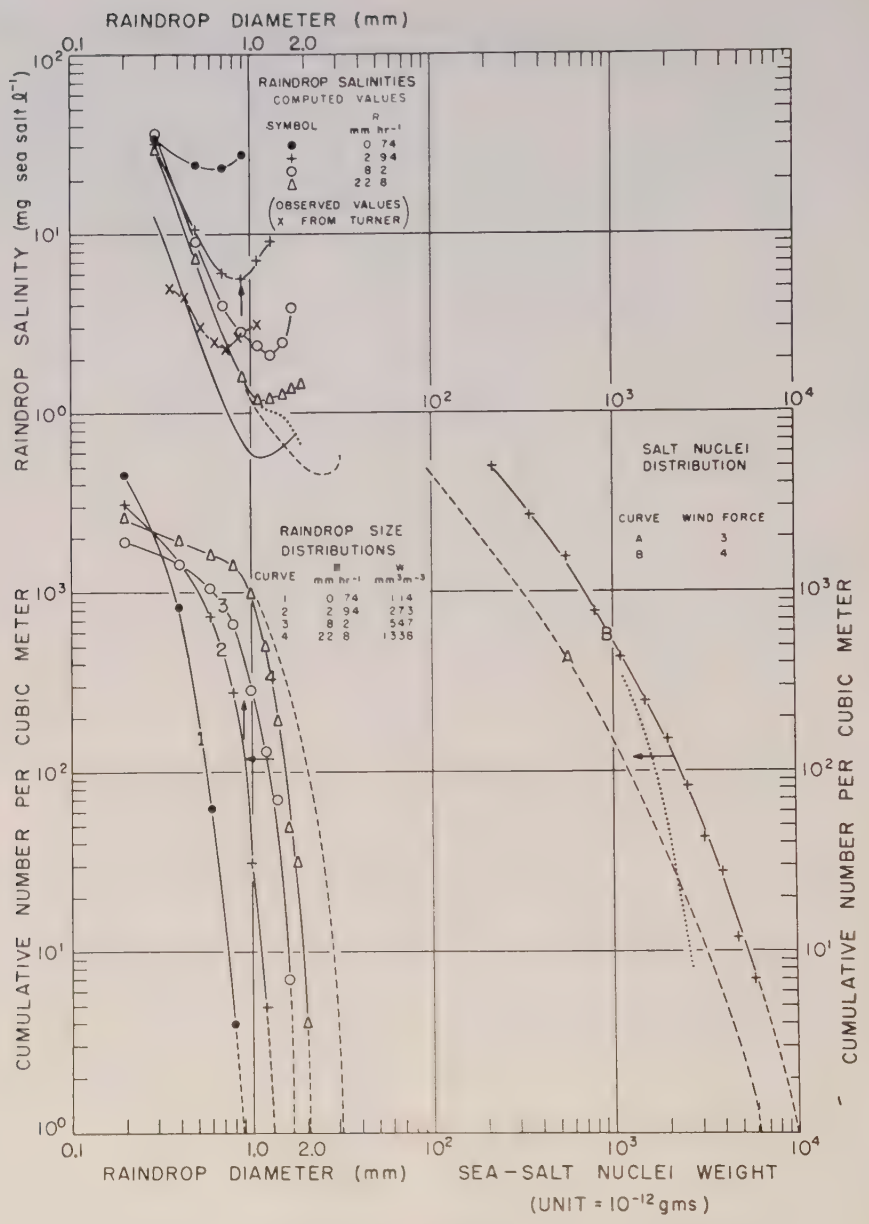

Fig. 2. The lower part of this figure shows cumulative average number distribution curves for salt nuclei and for drops in rains of various intensities (R). These curves are used, as described in the text, to compute the average chlorinity of the rain waters (fig. 5) and to compute the raindrop salinity values which are given above.

clear air at cloud levels over the sea by exposing small glass slides from aircraft. The methods used to sample atmospheric salt and those used to sample the rains have been described previously (Blanchard, 1953; Woodcock, Gifford, 1949; Woodcock, 1952), and will not be discussed further in this paper.

It proved impracticable, during the 1952 field trip, to obtain simultaneous observations of airborne salt and of rain. This difficulty was

Table 2. Intensities, chlorinities and drop size distributions in rains at stations 3 and 5. Sampling by filter-paper and bulk-water techniques

Position	Date (1952)	Time (LCT)	Bulk water samples		Rain drops sampled by filter paper technique						
			Rate mm hr^{-1}	Chloride mg l^{-1}	Rate mm hr^{-1}	Number drops m^{-3} in various diameter ranges (mm)					
						< 0.2	0.2—0.4	0.4—0.6	0.6—0.8	0.8—1.0	1.0—1.2
Part 1—Intensity range 0.1 to 1.0 mm/hr											
5	Apr. 28	1702	0.13	2.10	0.09	48,700	85				
5	» 28	1740	0.22	2.3	0.19	41,500	2,040				
5	» 28	1812	0.23	6.8	0.06	25,400	243				
5	» 28	1819	0.23	6.8	0.19	78,500	930				
5	» 28	1834	0.33	2.9	0.18	110,000					
3	May 1	1513	1.00	0.8	0.58	800	5,800	485			
3	» 4	1710	0.74	0.8	0.87	20,000	8,600	56			
3	» 4	1737	0.29	0.4	0.37	28,500	5,400				
5	» 5	2043	0.80	0.6	0.65	101,000	7,030	144			
5	» 5	2116	1.00	0.3	0.53	80,800	6,400	33			
5	» 5	2138	0.22	0.4	0.19	66,200	1,360				
5	» 5	2149	0.11	1.4	0.25	149,000					
5	» 5	2222	1.00	0.2	0.26	29,500	3,600				
5	» 5	2235	0.92	0.2	0.45	51,000	6,100				
			0.52	1.9	0.35	59,400	3,400	51			
Part 2—Intensity range 1.0 to 3.0 mm/hour											
5	Apr. 28	1727	1.09	2.00	1.43	116,000	11,500	1,150			
5	» 29	1759	2.28	1.2	1.95	2,450	5,400	2,060	270	24	
3	May 1	1455	2.70	0.7	2.40		8,300	3,860	31		
5	» 5	2053	1.10	0.4	1.34	65,000	11,200	1,120	27		
			1.79	1.1	1.78	45,800	9,100	2,050	82	6	

eliminated because it had been found, during many previous salt-sampling airplane flights, that a clear relationship existed between the wind force and the quantity of salt nuclei in the air at cloud levels. Figure 3 shows the averaged results from the salt nuclei samples taken in Hawaii on twenty-three different days between June 1951 and July 1952. Differences in the distribution of mass of salt among the nuclei on these days are shown cumulatively on figure 4. This figure also shows that the smoothed curves on figure 3 are based upon from nine to twenty-seven measured size-range categories.

Thus by using these salt-nuclei data and the average wind force observations from U.S. Weather Bureau surface maps (see Table 3), we were able to make a quantitative estimate of the average weight of salt as nuclei in the air during the interval of days when we sampled rain. This average salt amount was compared to the average weight of salt in the rain on these days.

3. Relating the salt in the nuclei to the salt in the rain at the windward stations 1 and 4

As previously stated, the purpose of the present study is to test the idea that a close relationship exists between the weight of the larger salt nuclei per cubic meter of clear air and the weight of salt dissolved in the rain in a cubic meter of rainy air. Expressed differently the above idea would mean that the largest salt nuclei form the raindrops, and that the individual drops which make up the first rains coming from a shower cloud should contain the salt found in an equal number of the largest salt nuclei.

The average numbers and sizes of raindrops for various rain intensities at stations 1 and 4 are plotted cumulatively on figure 2 (see curves, lower left), starting with the largest drops observed. On the same figure the average distribution of number and weight of salt nuclei is similarly presented at the lower right. This salt nuclei curve, taken from the data shown on figure 3 is used because the

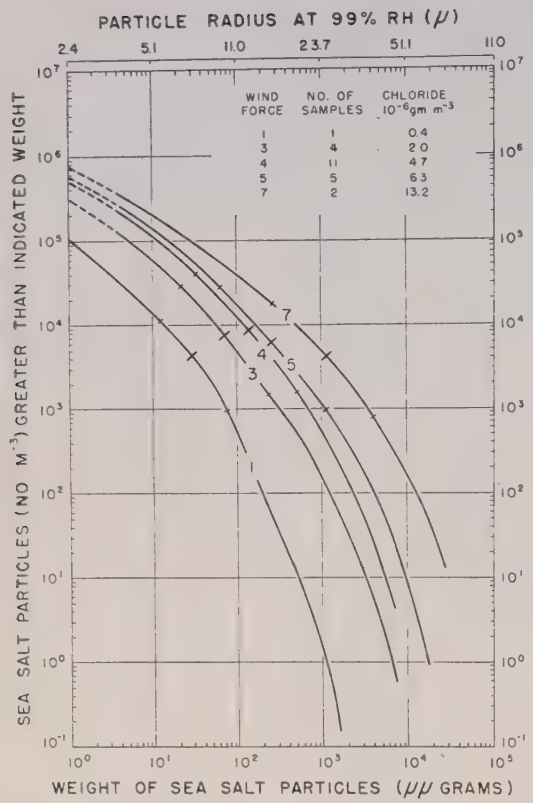

Fig. 3. Cumulative distribution curves for averaged salt nuclei number during winds of various forces in Hawaii. (Taken from WOODCOCK, 1954.)

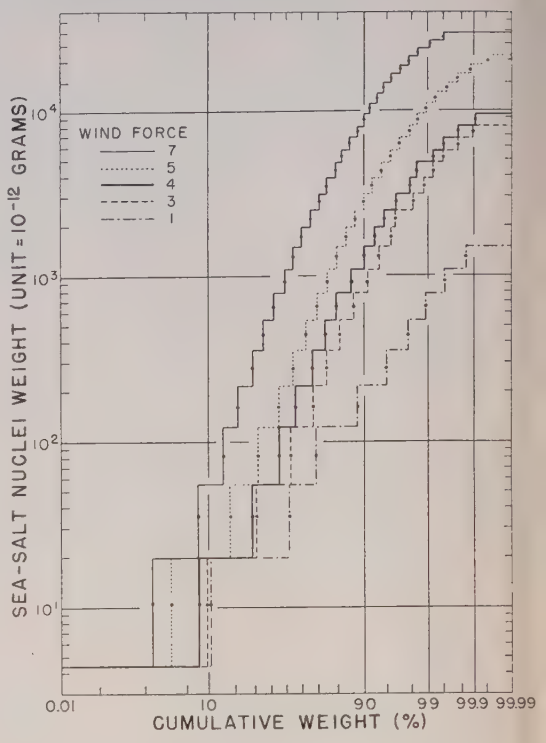

Fig. 4. Averaged cumulative per cent weight distribution curves for salt nuclei present in the atmosphere in Hawaii under varying wind conditions (forces 1 through 7).

observed average wind force during the days when the rains samples were taken was very nearly force 4 (see Table 3).

Figure 2 and Table 4 contain the information required to compute the chloride concentration which should be observed in rains if each of the larger salt particles has become a raindrop and if, in the process, little change has occurred in their distribution in the air. For example: rains averaging 6,328 $mm^3\ m^{-2}\ sec^{-1}$ intensity were made up of a definite number of drops of each size range falling per square meter per second (see Table 4, columns 4 and 5). The approximate weight of sea salt in the nucleus of each of these raindrops is taken from the force 4 cumulative salt nuclei curve on figure 2, using the appropriate cumulative raindrop curve to establish, in each case, this nucleus weight. These weights are shown on Table 4, column 8. As an indication of the derivation of these weights, note on salt curve B (fig. 2)

Table 3. Surface winds over the sea, during the days when rain was sampled, as reported by ships and planes within 400 nautical miles of Hilo, Hawaii. Taken from the four daily surface maps of the North Pacific, which were obtained from the US Weather Bureau, Honolulu, Hawaii

Date 1952	Number of servations reported	Average wind force
April 28.....	14	4.9
April 29.....	5	3.6
May 1.....	11	3.3
May 4.....	8	3.8
May 5.....	14	3.8
May 6.....	9	3.8
		av. = 3.9

that salt particles weighing 420 $\mu\mu$g, occur at the cumulative number 2150, which corresponds to the same number of 0.3 mm drops on raindrop curve number 4. Thus 420 $\mu\mu$g is entered on Table 4, column 8, as the weight

Table 4. Averaged rain data derived from filter paper samples, table 1, part 4

1	2	3	4	5	6	7	8	9
Drop dia.	Drop no.	Drop vol.	Drop fall rate	Drop no. falling	Rain rate mm^3	Rain water in air	Wt. sea salt in each drop. Unit=	Total sea salt falling in drops
mm	m^{-3}	mm^3	m sec^{-1}	m^{-2} sec^{-1}	m^{-2} sec^{-1}	mm^3 m^{-3}	10^{-12} g	10^{-6} gm m^{-2} sec^{-1}
0.3	786	.0141	1.17	920	13	11.1	420	0.386
0.5	282	.065	2.06	581	38	18.3	485	0.282
0.7	163	.180	2.90	473	85	29.4	530	0.251
0.9	458	.375	3.65	1,670	628	172	600	1.000
1.1	507	.700	4.30	2,180	1,523	354	830	1.810
1.3	304	1.14	4.90	1,490	1,700	347	1,350	2.010
1.5	143	1.73	5.45	780	1,348	248	2,270	1.770
1.7	17	2.56	5.95	100	256	43	3,500	0.350
1.9	28	3.59	6.35	175	628	99	5,100	0.892
2.1	3	4.85	6.75	22	108	16	10,000	0.220
					6,328	1,338		8.971

of sea salt to be found in a 0.3 mm raindrop and in rains of the indicated average intensity. Column 9 gives the product of these nucleus weights and the numbers of raindrops (column 5). The computed salinity of the rain (S_c) is now simply the ratio of the total weight of sea salt falling, to the total amount of water falling.

$$S_c = \frac{Ms}{W} \qquad (1)$$

where S_c = computed sea-salt concentration of rain (mg l^{-1})

Ms = sea salt falling m^{-2} sec^{-1} (mg)

W = liquid water falling m^{-2} sec^{-1} (liters)

For the high-intensity rains averaged on Table 4, the amounts of sea salt and water falling are 8.97 μg m^{-2} sec^{-1} and 6,328 mm^3 m^{-2} sec^{-1} respectively. The ratio of these quantities, with the units adjusted, yields a computed sea-salt concentration of 1.42 mg l^{-1}, or a chloride concentration 0.8 mg l^{-1}.

The above computed value for the average chloride concentration, plus other concentrations similarly computed from the averaged data concerning rains of lower intensity (see Table 1) are plotted on figure 5[1]. This also shows the observed average chlorinities of the rains at stations 1 and 4. These observed chloride concentrations are remarkably similar to the computed concentrations, and this similarity is regarded as suggesting that each large salt particle has formed a raindrop.

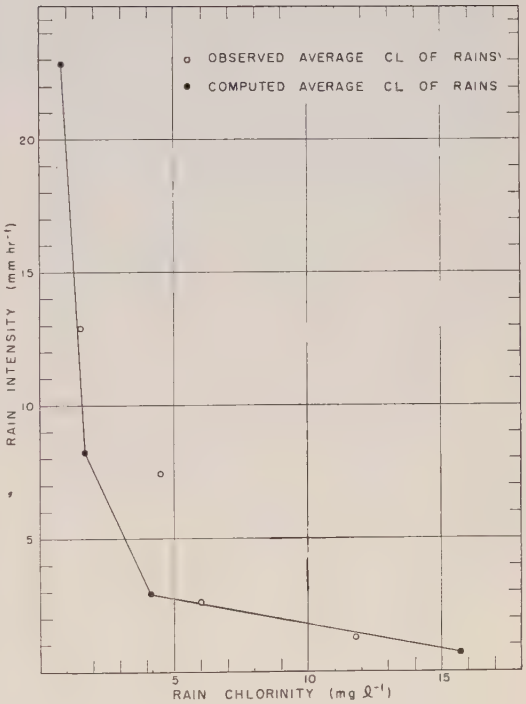

Fig. 5. Observed and computed chlorinities of rains related to rain intensity.

[1] These computed chloride concentrations for the rains of other intensities were derived in the manner shown on Table 4, but are not tabulated here in order to save space.

Table 5. Summary of averaged rain data from windward stations 1 and 4, Hawaii. May 1, 4, and 6, 1952

A	B	C	D	E	F	G	H	J	K	L
Rain from funnel sampler		Rain from filter paper samples			Rain Cl computed from nuclei	Rain Cl m^{-3} of air (ExF)	Wt. of Cl falling in rain 10^{-6} g	Ratio of Cl in rain to Cl in air	Raindrop size range	Total number of raindrops
Rate mm hr^{-1}	Cl conc. mg l^{-1}	Rate mm hr^{-1}	Rate mm m^{-2} sec^{-1}	Water content mm^3 m^{-3}	mg l^{-1}	10^{-6} g	m^{-2} sec^{-1}	G/4.7	mm dia.	m^{-3}
1.26	11.8	0.74	206	114	15.7	1.79	5.68	0.38	0.3—0.9	4,533
2.60	6.0	2.94	821	273	4.1	1.12	6.09	0.24	0.3—1.3	3,132
7.45	4.5	8.20	2,279	547	1.7	0.93	6.80	0.19	0.3—1.7	1,903
12.90	1.5	22.80	6,329	1,338	0.8	1.07	9.0	0.23	0.3—2.1	2,693

4. Relating the salt nuclei to the salinity of the rains at the leeward stations 3 and 5.

As previously suggested on pages 437 and 438 the rains falling at the leeward stations 3 and 5 were found to be made up of great numbers of small drops containing relatively little chloride (see Table 2). This character of these leeward rains tends to support the idea that they are composed of drops which have formed on the very numerous salt nuclei found among those particles weighing from about 5 to 20 $\mu\mu$g. The average chloride in these rains (see Table 6, column G) equals 6.2 per cent of the total chlorides found during force 4 winds (total $= 4.7 \times 10^{-6}$ g m^{-3}). On figure 4 it can be seen that during force 4 winds about 7.5 per cent of the chlorides in the air are between 4.5 and 20 $\mu\mu$g in weight, and in figure 3 the salt nuclei curve for force 4 winds shows that there are about 1.4×10^5 particles present in this weight range. Thus the chloride content and the numbers of the small salt nuclei are quite adequate to account for the chloride content and the numbers of the raindrops in the leeward rains.

Due to the nature of the techniques used to measure these small raindrops and small nuclei, it is not possible, with the present data, to relate the raindrops to the nuclei more precisely. Such precision could be obtained in future measurements by dividing the smaller raindrop and salt nuclei number distributions during the measuring process into greater numbers of size-range categories. Note on Table 2 that the greatest numbers of the raindrops at stations 3 and 5 are in the first size category, while figure 4 shows that all of the appropriate salt nuclei fall within a single measured size-range category.

Most of the raindrops sampled at stations 3 and 5 are so small that due to evaporation it is very unlikely that they would survive a fall through many hundreds of meters of clear air. This probably explains why these small drops have not been reported in such great numbers by other observers.

5. Computed raindrop salinity compared to observed salinity

During the spring of 1954, TURNER (1955) measured the salinity of individual raindrop size ranges in Hawaii. For obtaining rain waters

Table 6. Summary of averaged rain data from leeward stations 3 and 5, Hawaii. April 28 and 29, and May 1, 4, and 5, 1952

A	B	C	D	E	F	G	H	J
Rain-water samples					Rain Cl m^{-3} of air (BxE)	Ratio of Cl in rain to Cl in air	Raindrop size range	Raindrop number m^{-3} of air
funnel collector		filter-paper samples						
Rate mm hr^{-1}	Chloride mg l^{-1}	Rate mm hr^{-1}	mm^3 m^{-2} sec^{-1}	Rain in air mm^3 m^{-3}	10^{-6} g	F/4.7	mm dia.	
0.52	1.9	0.35	97	119	0.22	.047	0.1—0.3	62,850
1.79	1.1	1.78	494	331	0.36	.077	0.1—0.9	57,038
					av. = 0.29			

from different drop size-range categories, he used a simple modification of the raindrop spectrograph which has been described by BOWEN and DAVIDSON (1951). Turner determined the sodium content of drops in many rain samples at cloud base near station 4, and it is useful here to compare his interesting observations to the raindrop salinities computed from our raindrop size distributions obtained at the same location. For this purpose his sodium chloride concentration values[1] were converted to total sea-salt concentration by multiplying by 1.3, the approximate ratio of total salts in the sea to the sodium chloride present.

On figure 2 (top) his average raindrop salinity values for 39 samples are compared to similar values computed from the average rain and salt nuclei data (lower curves on figure 2) used in the present paper. The method used to derive these latter raindrop salinities is given in equation (1) and is applied, for example, as follows. A nucleus, having a mass of approximately 2,100 $\mu\mu$g, corresponds in cumulative number per cubic meter of air, to the number of 0.9 mm diameter raindrops shown on one of the raindrop distribution curves (see arrow marks near lower curves on fig. 2). The ratio of this nucleus mass (2.1×10^{-6} mg) to the volume of a 0.9 mm raindrop ($.375 \times 10^{-6}$l), equals a concentration of 5.6 mg l^{-1}. This drop salinity is indicated by the arrow mark beside the second raindrop salinity curve at the top of figure 2. The other computed values for raindrop salinity were similarly derived.

It is interesting that the form of Turner's average observed raindrop salinity curve and those computed from our raindrop and salt nuclei data is similar, despite the differences in the sampling times, sampling durations, and in the methods used to derive the salinity values.

The occurrence of the pronounced salinity minimum in Turner's results and in our computed values is apparently a reflection of the average slopes and relative values of the cumulative raindrop and salt nuclei curves. For instance, if the observed cumulative average raindrop distribution curve represented by curve 4 (see figure 2, lower left) had actually followed the adjacent dashed line, then the computed raindrop salinity minimum would not have occurred at a drop diameter of 1.1 mm (see triangular symbols, upper diagram, fig. 2). Instead a different salinity curve would have occurred (see extended dashed line), with the salinity minimum falling at a drop diameter of about 2.5 mm. As an indication of the effects of changing nuclei distribution, the assumption of a force 3 salt-nuclei curve instead of the average force 4 curve (see curve A, fig. 2), simply shifts the computed drop salinity curves down. The unbroken drop salinity curve on figure 2 shows the dilution effects of the reduced nucleus sizes upon drop salt concentrations for the highest intensity rains. As a final example of the effects of the shape of the salt nuclei curve, note that the use of the dotted line modification of curve B in computing raindrop salinity, removes the salinity minimum from the drop salinity curve (see dotted line at top of fig. 2). This removal of the salinity minimum is mentioned here because Turner has remarked that about one-third of his results showed no salinity minimum. Thus the form and, of course, the slope of the computed raindrop salinity curves is clearly dependent upon the relative slopes and magnitudes of the cumulative raindrop and salt-nuclei curves.

Turner's raindrop salinity curve is based upon many hours of sampling, during which time the rain intensity probably varied greatly. Had he been able to collect his rain water during short periods of time (i.e., in about 100 seconds) and, in each case during rains of nearly constant intensity, it is supposed that he would have obtained different salinity curves for different rain rates similar to those which we compute from our observed raindrop and salt nuclei curves.

Turner's average values for the salinity of raindrops of each size range, probably represent an integrated quantity. Note for instance on figure 2 that the salinity of the 0.9 mm diameter raindrops computed from our curves may vary from 1.6 to 28 mg l^{-1}, depending upon the rain intensity in which they are sampled. The raindrop salinity values which will be obtained during a prolonged sampling period in orographic rains at station 4 would seem to depend, in part at least, upon the relative

[1] Sodium concentrations, measured by flame photometry, were converted by Turner to equivalent NaCl values.

frequency of occurrence of rains of different intensities. They will also presumably depend upon the extent to which the samples are taken in the first rains from the showers, or in rains which are the winnowed remnants of showers occurring to windward of the raindrop spectrograph sampling position.

In future physical-chemical studies of rain, it would be very useful to combine raindrop spectrograph measurements of drop salinity, with simultaneous determinations of raindrop size distribution and of salt nucleus size distributions.

6. Discussion and conclusions

Clearly many more observations, such as those given on Tables 1 and 2, are needed in order to thoroughly test the consistancy of the pattern of interrelationship of nuclei to raindrops which has evolved from the present study. Data deficiencies are especially great among the higher intensity rains (see Table 1), and the lack of simultaneity of the rain and salt-nuclei observations introduces a further element of uncertainty. However, the authors feel that the data and ideas presented here, when considered as a whole, are sufficiently useful to justify publication at this time

Some of the above observational deficiencies were eliminated in further measurements recently made (1954) in Hawaii in connection with the co-operative cloud physics work of "Project Shower". These numerous measurements, which will require much time to completely analyse, will be presented in a later study of this problem.

A rather obvious result of the present study is the emphasis which is given to the importance, in the understanding of Hawaiian shower rain formation, of detailed knowledge of the salt particle size distribution in the clear air and the distribution of raindrop size and raindrop salinity within the clouds. It is also important to know where the rain samples are taken in relation to the stage of development of the showers. In the present study an effort was made to sample the first and the last rains falling from showers moving up the mountain slope. The authors feel that this detailed knowledge of the nuclei, the raindrops and the rain-sampling position, is essential to a further understanding of the evolution of raindrops in the shower rains of marine air masses. The techniques used here should also prove useful in exploring the role of sea-salt nuclei in the formation of raindrops in continental rains.

It should be pointed out that in the analysis presented here, the quantities of salt falling in the rains at stations 1 and 4 amount to only about 20 to 40 per cent of the total salt in the air (see summary Table 5, column J). Since, of the remaining 60 to 80 per cent of the atmospheric salt, only about 6 per cent falls at stations 3 and 5 (see summary Table 6, column G), it is supposed that the remaining salt rained-out in the drops falling between these stations, as the rain showers were carried by the winds up the mountain from the lower to the upper stations. In a later publication (of "Project Shower" observations) the authors plan to include an analysis of the effect of wind and wind shear upon the distribution of raindrops at various locations on the mountainside.

In the Hawaiian shower rains, rapid changes in intensity with time are very common, as shown on Tables 1 and 2, and by BLANCHARD (1953; see fig. 2). Most of this change is thought to be due to winds transporting the showers over the sampling stations. For instance the average clouds which were producing the showers in the present study were probably moving at about 7 meters per second up the mountain slope. During a sixty second interval between rain samples a shower-producing cloud could thus move almost one-half kilometer. The showers are seldom large in diameter, and in aircraft a flight of one-half kilometer is often sufficient to carry the observer from the misty peripheral regions to the relatively intense rains of the center.

The interpretation of the measurements presented here, in terms of the details of the raindrop-forming processes operating in these Hawaiian rains, is uncertain. They seem, however, to be clearly useful in narrowing the areas of search for these "details". One can say from the present measurements that a drop-forming process seems to be required which will, (a), involve most of the larger salt nuclei in a simultaneous growth, (b) cause this growth to occur, presumably very rapidly, in a manner which prevents marked changes in the distribution of the nuclei (or drops), and (c) add water to the nuclei without at the same time greatly adding to their salt content.

Table 7. Weights of sea salt added to a 0.9 mm diameter raindrop due to coalescence with 10 and 20 μ radius cloud droplets containing sea-salt nuclei of various sub-micron sizes

Cloud droplet radius μ	Cloud droplet no. required to form 0.9 mm diameter raindrop	Weight sea salt (10^{-12} g) in 0.9 dia. raindrops (cloud droplet no × nucleus wt.)				
		(0.5 μ) 10^{-12} g	(0.2 μ) 10^{-13} g	(0.1 μ) 10^{-14} g	(0.05 μ) 10^{-15} g	(0.02 μ) 10^{-16} g
10	91,000	91,000	9,100	910	91	9.1
20	11,400	11,400	1,140	114	11.4	1.1

In the present study the quantities of salt in the individual large salt nuclei are adequate to account for all of the salt found in the rains. This suggests that the drops have grown entirely by condensation processes, or through coalescence with relatively chloride-free cloud droplets[1]. If one assumes, for instance, that the 0.9 mm diameter raindrops (which, on rain curve 2, fig. 2, are supposed to have formed on 2,100 $\mu\mu$g salt nuclei) have grown through coalescence with 10 μ radius cloud droplets, about 91,000 of these droplets would be required. Table 7 shows amounts of salt which would be added to the initial giant (2,100 $\mu\mu$g) nucleus due to coalescence with cloud droplets which have formed on sea-salt nuclei of various sub-micron sizes. On this table it is evident that the quantities of salt added through accretional growth might in some instances equal or greatly exceed the weight of the giant nucleus upon which the raindrop initially formed. The very small nuclei would, of course, require rather large water vapor supersaturations in the clouds to become activated.

Junge's work at Round Hill (Junge, 1954) indicates that most of the numerous nuclei which are less than about 0.8 μ in radius (or $< 5 \times 10^{-12}$ g, as shown on fig. 2) are composed largely of ammonium sulfate. However, in Hawaii Junge recently sampled aerosols which were less than 0.8 μ radius, and he found relatively very little ammonium sulfate present.

[1] Hawaiian clouds, which are not producing rain, have been found to contain from 30 to 140 cloud droplets per cubic centimeter, though the air at sea level usually contains several hundred Aitken nuclei in an equal volume.

From the results of this paper, we cannot say that the raindrops in Hawaii do or do not grow by accretion. If the nuclei smaller than about 10^{-12} g are sea salt, then accretion would seem to be ruled out unless the nuclei are very small (see Table 7). Thus we feel that one of the important steps in future physical-chemical studies of raindrop formation in shower clouds is to determine the chemical nature and the number of the majority of the individual cloud-droplet nuclei which are smaller than about 0.8 microns and to relate these particles to the solutes found in the cloud and rain waters.

A conservation of the number of the larger nuclei per unit volume of air, during their growth to raindrops, is indicated by the results given here. This number conservation is not consistent with the model proposed by Bowen (1950), in which accretional growth involves marked alterations in drop distributions. If these Hawaiian raindrops grow largely by accretion, or by condensation, the authors feel that it is necessary to suppose that this growth occurs very rapidly in turbulent volumes of air which are ascending within clouds in a way similar to the "bubble parcels" proposed by Scorer and Ludlam (1953).

Acknowledgments

The writers are indebted to Mr W. A. Mordy, of the Pineapple Research Institute, the Hawaiian Sugar Planters Association and the Territorial Cattleman's Council, for the opportunity to work in Hawaii, and to the Honolulu office of the U.S. Weather Bureau for supplying north Pacific weather charts.

REFERENCES

Blanchard, D. C., 1953: Raindrop size distribution in Hawaiian rains. *Jour. Meteor.*, **10**, 457—473.

Bowen, E. G., 1950: The formation of rain by coalescence. *Aust. Jour. Sci. Res.*, A, **3**, 193—213.

Bowen, E. G. and Davidson, K. A., 1951: A raindrop spectrograph. Quart. *J. R. Met. Soc.* **77**, 445—449.

Junge, C. E., 1954: The chemical composition of atmospheric aerosols, I: Measurements at Round Hill field station, June—July 1953. *J. Meteor.*, **11**, 323—333.

Keith, C. H. and Arons, A. B., 1954: The growth of sea-salt particles by condensation of atmospheric water vapor. *J. Meteor.* **11**, 173—184.

Miyake, Y. and Suguira, Y., 1950: The mechanism of the dissolution of the atmospheric chloride into rain water. *Pap. Meteor. Geophys.*, **1**, 222—226.

Scorer, R. S. and Ludlam, F. H., 1953: Bubble theory of penetrative convection. *Quart. J. R. Meteor. Soc.*, **79**, 94—103.

Sugawara, K., Oana, S., and Koyama, T., 1949: Separation of the components of atmospheric salt and their distribution. *Bull. Chem. Soc. Japan*, **22**, 47—52.

Turner, J. S., 1955: The salinity of rainfall as a function of drop size. *Quart. J. R. Meteor. Soc.*, **81**, 418—429.

Woodcock, A. H. and Gifford, M. M., 1949: Sampling atmospheric sea-salt nuclei over the ocean. *Jour. Marine Research*, VIII, 177—197.

Woodcock, A. H., 1952: Atmospheric salt particles and raindrops. *J. Meteor.*, **9**, 200—212.

— 1954: Salt nuclei in marine air as a function of altitude and wind force. *J. Meteor.*, **10**, 362—371.

The Water Content of Cumuliform Cloud

By J. WARNER, Radiophysics Laboratory, C.S.I.R.O., Sydney

(Manuscript received April 5, 1955)

Abstract

Measurements have been made of liquid water content throughout many cumuliform clouds. The amount of water present at any level was always less than the adiabatic value, and the ratio of these two quantities decreased with height above cloud base. This ratio was found to be independent of the horizontal extent of the cloud except in the case of very small clouds. The transition between clear air and dense cloud was frequently abrupt.

1. Introduction

Our state of knowledge of the physical properties of clouds is far from complete, and as a result, ideas about cloud formation and growth can at best only be tentative. Apart from isolated observations of liquid water content at unspecified points in cloud, the only detailed studies known to the author are those of ZAITSEV (1950) and WEICKMANN and AUFM KAMPE (1953). In neither of these cases was a continuous record of water content available at any one level in the cloud.

In most reported observations it has been noted that the value of the liquid water content at any level above the base of the cloud has been less than the amount that would be released by simple adiabatic lifting of the cloud air and condensation of the surplus water vapour. STOMMEL (1947, 1951) followed by AUSTIN and FLEISHER (1948), HOUGHTON and CRAMER (1951) and MALKUS (1949, 1952 a, 1952 b) put forward and elaborated a theory of entrainment of the environmental air into the cloud which could account for the observed deficiency in liquid water. In no case were suitable observations of cloud water content available to give quantitative support to the theory. MALKUS (1954) calculated updraft velocities in cloud from the observed temperatures on the basis of the theory and found them to be in good agreement with the observed values. A particular defect of the theory, namely its assumption of a steady state in a cumulus cloud, was commented upon by SCORER and LUDLAM (1953) in putting forward their alternative "bubble theory". Some support for this bubble theory is given by MALKUS and SCORER (1954) from an analysis of time-lapse motion picture studies of the development of cumulus towers. At present this theory can give only a qualitative guide to the variation of water content that might be expected throughout a cumulus cloud, and no attempt has been made to interpret existing observations in terms of the theory.

An instrument developed by WARNER and NEWNHAM (1952) has been used to measure liquid water content of cumuliform clouds at all levels. This investigation was made on maritime and landward clouds along the eastern Australian coast. The present investigation was restricted to cumulus or stratocumulus clouds, wholly or almost wholly warmer than freezing from 2,000 to 10,000 ft deep, and for the most part, to single clouds well isolated from their neighbours.

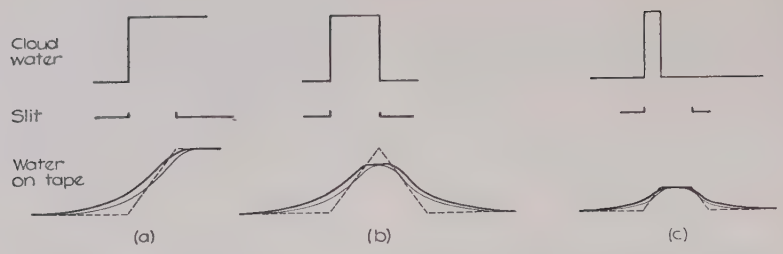

Fig. 1. Pictorial representation of effect of sudden changes of water on instrument for 10″/min tape speed, 140 knots air speed. (a) Sudden rise to steady value; (b) Peak 140 ft across; (c) Peak 50 ft across.
Legend: - - - Effect of slit alone. —— Slit plus spreading of water on tape. —— Overall effect of slit plus spreading of water plus contact width.

2. Method of measurement

The method of measurement as described by WARNER and NEWNHAM (1952) consists essentially of continuously recording the electrical resistance of a paper tape moved past a narrow slit open to the airstream and moistened by the cloud droplets. The instrument used in the present series of measurements differs only slightly from that described earlier. It was housed, together with other meteorological instruments, in an aerofoil-shaped section suspended below and slightly forward of the leading edge of the starboard wing of a DC3 aircraft. One of the main differences in the present instrument was that the resistance of the tape was measured on the moistened side of the paper, resulting in lower resistance values being obtained. This change lessened the effect of water vapour on the readings and also gave a more rapid response to changes in liquid water content.

Further calibration of the instrument was undertaken, particularly with a view to determining its response time. A very simple method was used, since previous investigations had indicated that for a given amount of water deposited on the paper its method of application did not significantly effect the resistance. This method consisted of applying water to the paper through a wick which was fed through a capillary tube, and determining the rate of application by a measurement of the movement of a small air bubble introduced into the capillary. Measurements of resistance were made at different tape speeds and flow rates, and the calibration deduced from a calculation of the cloud water content that would result in a given amount of water being deposited on the paper under known conditions of slit size, air speed and tape speed. The calibration obtained in this manner agreed with that obtained previously using a spray in a small wind tunnel (under similar conditions of the instrument) and was very much simpler to perform.

The factors influencing the response time of the instrument are: the width of the slit and the rate of movement of the tape past it, any spreading of the water on the tape, the width of the measuring contacts, and the time constant of the recording ohmmeter. Since the slit is 0.1 inches wide the usual tape speed of 10 inches per minute results in any point on the tape taking 0.6 seconds to cross the slit. Thus a sharp-edged cloud would appear as one in which the water content rose from zero to maximum in 0.6 seconds of tape travel, corresponding to a distance in the cloud of 140 ft at the usual aircraft speed of 140 knots. When the water is deposited on the paper it is absorbed and tends to spread. The amount of spread varies with the amount of water deposited on the paper, but usually corresponds to a further 200-ft extension of the sharp-edged cloud postulated above. The width of the resistance measuring contacts makes any change of tape resistance commence to record earlier and finish recording later than it otherwise would, the total extension being equivalent to 60 ft for the conditions under discussion. For the case of a sharp peak of liquid water a similar argument leads to the likely form to be taken by the record. The overall effects are summarized pictorially for different cloud conditions in Fig. 1. The values suggested will vary with tape and aircraft speeds and will also change with the cloud water content itself.

The discussion above has ignored the time

constant of the recording ohmmeter. This varies with the amplitude of the signal and slightly with the position of the pointer on the scale. For a signal equal to 5 per cent of full scale deflection, half amplitude is reached in 1 second and full response occurs after 10 seconds. Optimum response occurs with signals of about half full scale amplitude which record fully in 0.8 second. Owing to overshoot, larger signals take longer to reach their final value, a full scale deflection signal achieving a steady state in 5 seconds after a 5 per cent overshoot.

All these effects are clearly not additive and if fine structure of clouds is under investigation the limitations of the instrument need to be considered in detail, bearing in mind the nature of the variation being looked for. However, an overall time constant of the instrument can well be regarded as $^1/_2$ second.

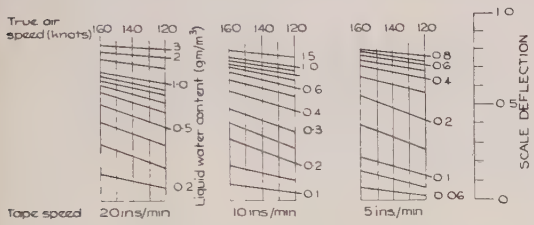

Fig. 2. Calibration of instrument at different aircraft speeds and tape speeds. (For collection efficiency 1.0).

For completeness it is as well to summarize the other important characteristics of the instrument.

(a) The overall accuracy of a water content measurement is about ± 20 per cent, though the comparative accuracy is much better.

(b) The calibration is non-linear, being shown in Fig. 2.

(c) The calibration is sensibly independent of temperature within the range 2° C to 28° C.

(d) The salinity of the cloud water does not affect the calibration at least over the range normally experienced.

(e) The collection efficiency of the instrument is 0.75 for 10 μ diameter drops, and for most clouds 80 per cent or more of the liquid water is collected. A figure of 0.8 has been taken in the results described below.

(f) For the drop size range experienced in clouds the calibration is unaffected by drop size once the drops have been collected.

(g) Readings taken in rain are unreliable owing to splashing and loss of most of the larger drops.

(h) Readings cannot be made at sub-zero temperatures owing to icing.

The flight procedure usually followed was to climb to about 1000 ft above the cloud tops to choose a suitable cloud, the choice being governed by the degree of isolation of the cloud from its neighbours and by a guess as to the probability that it would grow or decay only slightly during the half hour or so required for measurement. Most clouds did, in fact, change during the measurement, both growing and decaying cyclically, but even in cases of continuous slow dissipation the base was affected last and it was sometimes possible to obtain a satisfactory series of observations. Once a cloud was chosen, a series of traverses was made at appropriate height intervals (usually 500 or 1000 ft) starting a few hundred feet below the top and finishing just above cloud base. If during a traverse the liquid water readings exceeded about 0.75 of full scale deflection, where the scale is becoming very crowded owing to saturation of the paper, the traverse was normally repeated using a higher tape speed. Subsequently a climb was made to cloud top height to examine the cloud again, and a sounding was then made of the environmental air from above the cloud top to ground level, measuring temperature and humidity. Special flights at constant height in one cloud, or at a series of heights through many clouds, were also made.

3. Results

Measurements have been made in large numbers of clouds throughout the year, but owing to the limitations of the instrument no data are available on clouds extending markedly above freezing level, and most of the observations were made in summer. In general they were made in clouds that either had no rain in them, or in which the rain was light or restricted to a small part of the cloud. Data have been rejected when they were obtained in heavily raining clouds and when gross changes occurred in the cloud during the course of the observations. Observations have also been rejected when the variation of water content with height was found to be very erratic. This occurred mainly in measurements made in a complex cloud situation and frequently cor-

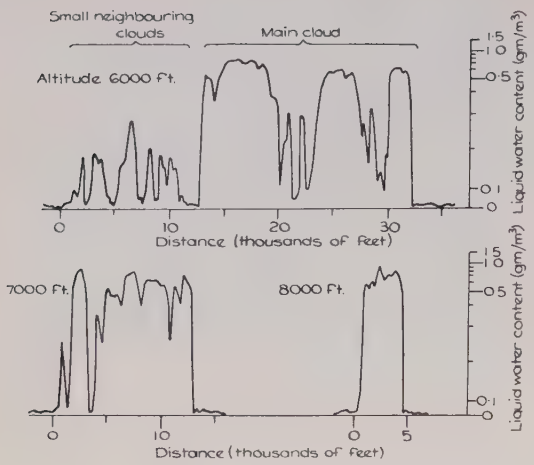

Fig. 3. Successive traverses through cumulus cloud at 6,000, 7,000 and 8,000 ft. Cloud base 3,000 ft, temperature 18·3° C; top 9,300 ft, 7·2° C.

responded to big changes in the appearance of the cloud.

(a) *Peak liquid water content*

The most obvious characteristic of the records of water content at a given height in one cloud was the variability during the traverse as is shown in Fig. 3. It became necessary to decide on the most significant feature of the record. Since the water content sometimes descended to zero well inside cloud, the cloud being defined by failure to see the ground or sky, it was thought inadvisable to use the average value throughout the traverse. It was found that the peak value, or possibly the mean of the series of peaks, was fairly reproducible from traverse to traverse at a fixed height

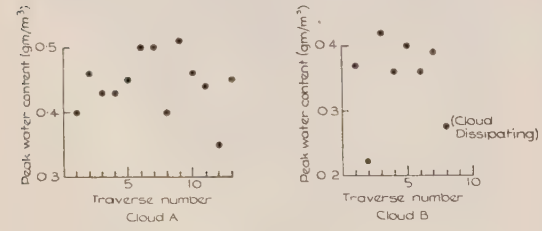

Fig. 4. Constancy of peak liquid water content at given height. Successive traverses through two different clouds, the total period of observation being about 30 minutes in each case.

	Cloud A	Cloud B
cloud base	2,500 ft	3,000 ft
height of traverses	5,900 ft	8,000 ft

and appeared to be a definite characteristic of the cloud. This is well indicated in Fig. 4 which shows, over a period of roughly 30 minutes, the peak values on successive crossings through two different clouds on different days. The recorded peak is not necessarily the maximum liquid water content since the instrument averages over a distance of a hundred or so feet, but it probably does not differ markedly from it in most cases.

(b) *Variation of water content during any traverse*

The water content may rise slowly from the edge of the cloud to its peak value, or it may increase very rapidly. In general, however, there is no steady rise from the edge towards the middle, and the peak value can often be reached very rapidly, the liquid water content

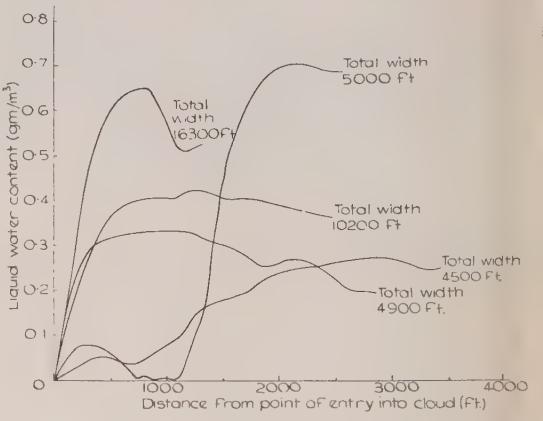
Liquid water content (gm/m³)
Total width 5000 ft
Total width 16300 ft
Total width 10200 ft
Total width 4500 ft.
Total width 4900 ft.
Distance from point of entry into cloud (ft.)

Fig. 5. Variation of water content with distance.

remaining near that figure almost throughout the cloud. There does not appear to be any relation between the size of the cloud and the rate of change of water content near the edges, since on one side of the cloud the change may take place rapidly and on the other slowly, depending largely on the time and place at which the aircraft enters the cloud. Some typical results showing the rate of change of water content near the point of entry into cloud are shown in Fig. 5. When it is remembered that the instrument's response time is such that a sharp-edged cloud would appear as one in which the liquid water increased gradually to its maximum over a distance of the order of 400 ft, it can be seen that in some

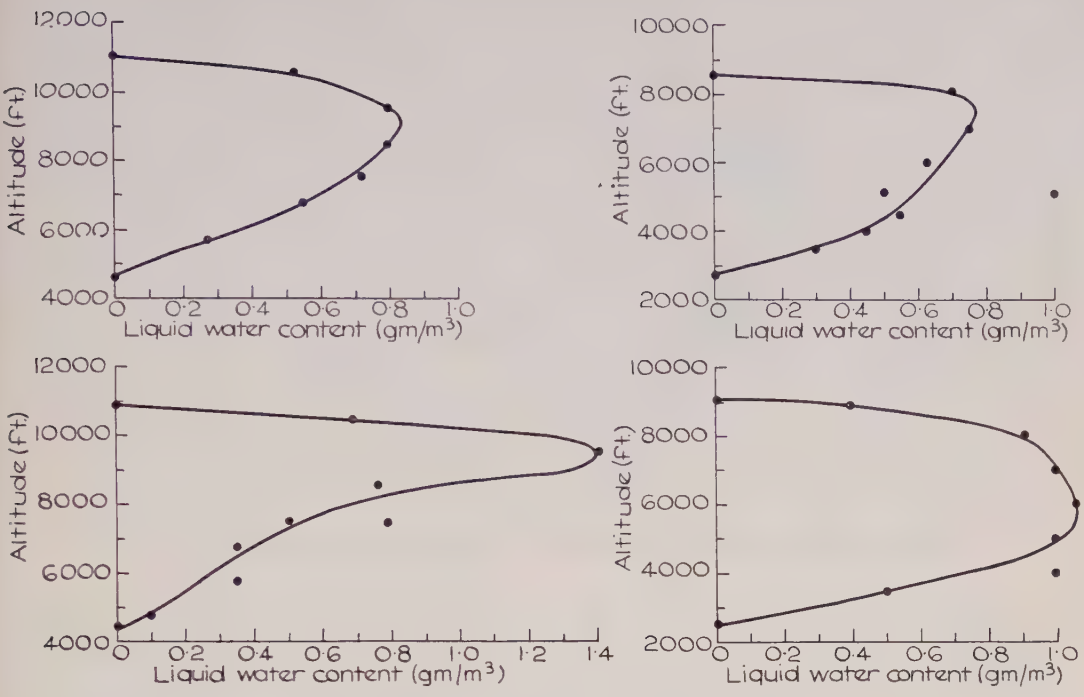

Fig. 6. Variation of peak water content with height.

cases the full transition between cloud and environment must occur over a few tens of feet.

(c) *Variation with height above cloud base*

When the peak value is plotted against height above cloud base it is generally found to increase fairly steadily until a point about 1000 ft below the top of the cloud, after which it falls rapidly to zero. Typical cases of this result are given in Fig. 6. The magnitude of the peak water content is always less than the adiabatic value appropriate to that level. If the ratio of the observed liquid water content W to the adiabatic value W_a is plotted as a function of height above cloud base, it is found in general to decrease from near unity at cloud base to a value approaching 0.2 at 5000 ft above the base. There is, however, a great variation from cloud to cloud, particularly near cloud base. In Fig. 7 the value of this ratio is plotted against height for about 25 clouds. A line is drawn through a series of points each of which represents the peak value of W/W_a on a traverse at a given height in one cloud to represent the conditions throughout the depth of that cloud. The values are taken only in that part of the cloud in which the observed water content is increasing with height. The top one or two thousand feet of cloud in which the water content is decreasing is not represented. The mean value of this ratio for all the clouds is plotted in Fig. 8.

(d) *Mean value of W/W_a throughout a cloud*

If in any cloud the average value of W/W_a is taken from near the base to the point where the water content begins to decrease, it is found to vary markedly from one cloud to the next. Fig. 9 shows a plot of this mean value against the range of W/W_a from the highest observed value, generally found near the base, to the lowest which occurs usually at the point of maximum liquid water content. From consideration of this figure and Fig. 7 it is seen that clouds tend to be either "wet" or "dry" throughout. A cloud which is on the average "wet" is not so because of the presence of an isolated very wet area. The biggest variation from cloud to cloud of W/W_a does, however, occur near the base of the cloud.

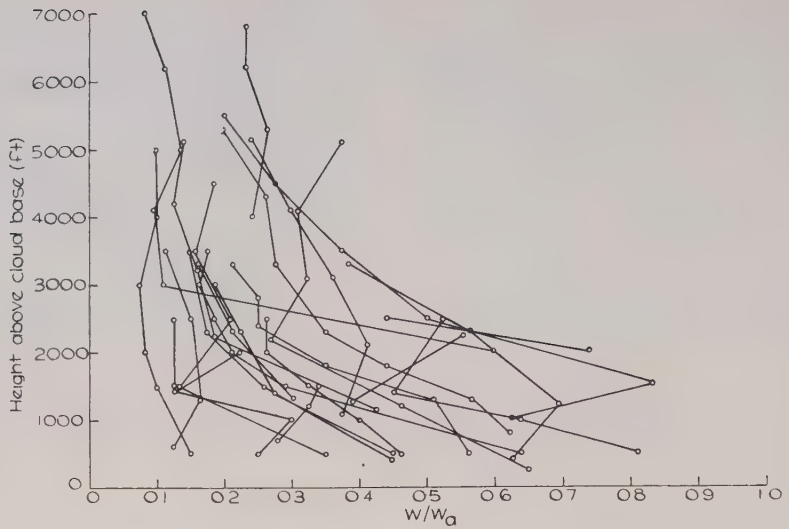

Fig. 7. Ratio of observed liquid water content to adiabatic value versus height above base.

(e) *Variation of W/W_a at a given height with cloud width*

A study was made of the variation of W/W_a at a given height above cloud base with the horizontal width of the cloud under observation. Only clouds greater than 2000 ft across were considered and the observations were grouped into 5000-ft width and 1000-ft height intervals. The result of this examination is shown in Fig. 10 from which it can be seen that there is no evidence that the cloud width affects the value of W/W_a at any given level. When observations were made on many clouds on the one day there was again little evidence that the cloud width affected W/W_a. This statement does not apply to small clouds, however: clouds less than about 1,500 ft across appear to be significantly drier than the bigger clouds at a given height above their bases, and their "wetness" increases with their horizontal extent.

(f) *Effect of environmental parameters on mean W/W_a*

An examination of the data available to the author failed to reveal any correlation between

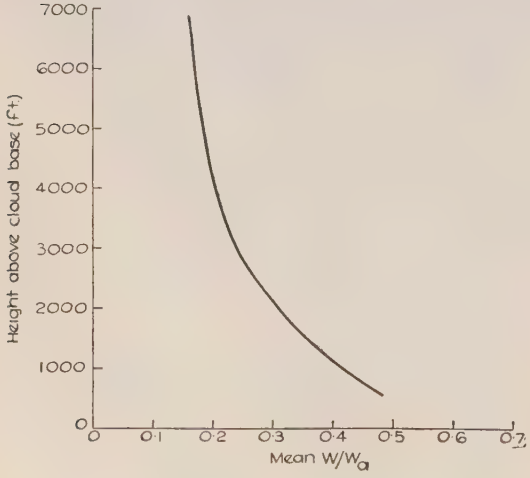

Fig. 8. Mean ratio W/W_a versus height above base.

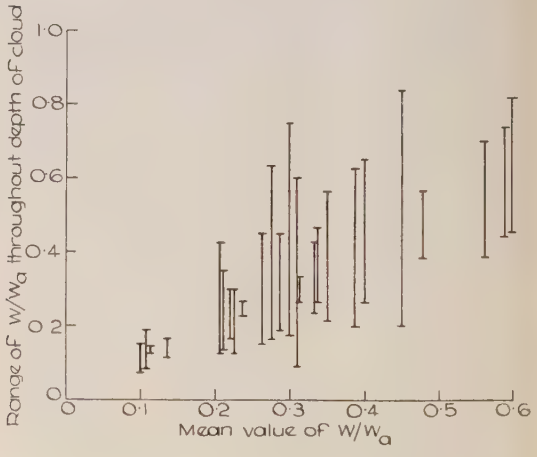

Fig. 9. Range of W/W_a versus mean value W/W_a.

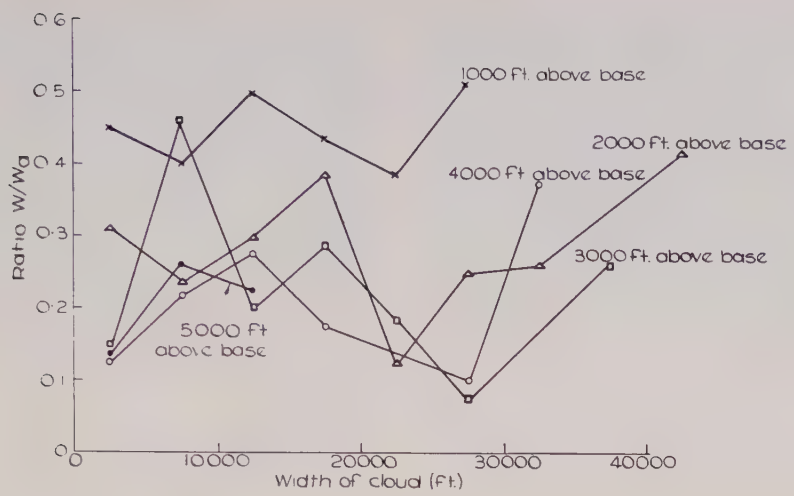

Fig. 10. Relationship between W/W_a and cloud width at given height above base.

the mean value of W/W_a throughout the cloud and either cloud base temperature or mean environmental lapse rate over the first 5,000 ft above ground.

Thus, to summarize the results that have been obtained it can be stated that:

(a) The peak water content considered is a characteristic of the cloud and does not vary with time except when the cloud is consistently dissipating.

(b) In many clouds the transition from clear air to dense cloud is abrupt.

(c) The value of W/W_a in general decreases with height above base but the value varies greatly from cloud to cloud. It is, however, always less than 1.

(d) Clouds tend to be either "wet" or "dry" throughout.

(e) The width of the cloud, provided it is greater than about 1500 ft, has no effect on W/W_a at a given level.

(f) The mean value of W/W_a throughout the cloud is not strongly correlated with either lapse rate or cloud base temperature.

4. Discussion of results

Perhaps the most significant features of the results are the facts that at no point above the base, even in the largest clouds examined, does the observed liquid water content approach the adiabatic value; that the deficiency in water is not a function of the horizontal dimension of the cloud except for very small clouds; and that the edges of clouds are frequently as wet as the centre.

Since in large measure the reliability of these observations depends on the accuracy of the calibration of the instrument, it is considered desirable to discuss this aspect a little further. As was mentioned in Section 2 of this paper, it is thought that the accuracy of measurement of water content is about ± 20 per cent. Several different laboratory calibration techniques all agreed within this accuracy, but unfortunately it has not been possible to calibrate the instrument in flight or at speeds approaching that of the aircraft. However, the fact that the observed liquid water content is sometimes found to approach the adiabatic value near cloud base suggests that the calibration is not seriously in error. Since both "wet" and "dry" clouds give results of the same general character it appears unlikely that saturation effects or splashing are of importance. This view is further supported by the lack of discontinuity between the figures for the lower drier areas of "wet" clouds and those for their upper regions.

The response time of the instrument will also affect the results to a degree dependent on the rate of variation of water content in the cloud under examination. Thus a cloud in which the water content fluctuated very rapidly might

appear drier than one in which a steady somewhat lower peak value obtained. In this regard there did not appear to be any significant difference in the character of the records obtained in large and small clouds, except in the case of very small clouds 1,000 ft or less in width which always showed only a single peak. Visibility records obtained by WEICKMANN and AUFM KAMPE (1953) with an instrument having a very short time constant show small flucutations in distances of about 30 ft, but the bigger changes occur over a distance of more than 100 ft.

The magnitude of the error due to the time constant of the instrument is not known, but in view of these facts it is thought to be comparatively small. In any event it is considered unlikely that probable instrumental errors could affect the general nature of the results obtained.

The steady decrease of W/W_a above cloud base thus appears to be a real and normal phenomenon. Where it did not occur, as in some of the observations not reported, it was associated with a complex cloud situation in which two or more layers of cloud tended to mix, or with the raining out of the cloud during the course of the observations. Pronounced changes in the cloud under observation sometimes occurred and were associated with departures of the W/W_a versus height relationship from the general pattern.

In a cloud undergoing periodic growth and decay, such as those instanced in Section 2(a) and Fig. 4, the water content at a level well removed from the top and base of the cloud remains relatively constant and no increases up to the adiabatic value have been observed. Since in the case of Cloud A of Fig. 4, traverses were made roughly every $1^1/_2$ minutes, it is unlikely that any significant feature would have been missed. Thus, if the growth period is due to the rise of a fresh bubble of air from beneath, that bubble must be well mixed with its environment by the time it reaches the cloud and must continue to mix vigorously during its further ascent through cloud. This view is of course supported by the observation that clouds tend to be "wet" or "dry" throughout their whole vertical depth; there are not regions of excessive wetness well removed from the base. There could of course be very small wet regions to which the instrument would not fully respond. An idea of the effect of such small regions on the record can be gained from a consideration of the earlier discussion of the time constant of the instrument. This would suggest that at an initial liquid water content level of 1 g/m³ a wetter region 140 ft across would record only 0.3 to 0.5 of its increased water content, assuming increases from 0.5 to 2 g/m³ respectively. A larger wet region 500 ft across would record 0.8 or more of its increased water. While these estimates are undoubedly very rough they do suggest that if the full adiabatic value of liquid water is achieved in a cloud it can only be so over a very small region for the instrument not to record the increase. For example, in a cloud where the observed peak water content was 0.9 g/m³ at a height of 4,000 ft above the base and the adiabatic value, assuming ascent from cloud base, was 2.6 g/m³ a wet patch must be only about 30 ft across for the increase to be reduced to below 0.1 g/m³ on the record and thus possibly to have passed unnoticed.

The facts, that the edges of a cloud can frequently be as wet as the middle and that the deficiency in water content is largely independent of cloud width, tend to suggest either that there is no significant horizontal mixing of the cloud air with the environment, or that the mixing is rapid compared with the rate of growth of the cloud and extends over its whole width. The author's observations in this regard are in conflict with those of ZAITSEV (1950) which were, however, restricted to isolated readings, and it is considered doubtful if the contours of liquid water shown in his figures can really be justified. While WEICKMANN and AUFM KAMPE (1953) did not measure water content directly, it is interesting to note that their transmissometer records are very similar in character to the author's own water content records and demonstrate clearly the sharp edge of a cloud and the absence of a central wet region. It should be noted, however, that their computed values of liquid water are markedly higher than those at present being reported. The presence of "holes" well inside cloud in which the liquid water is very low is a feature of many records obtained in both single and multicelled clouds. Sometimes these "holes" appear to extend vertically for a considerable distance since they repeat for two

or three traverses spaced 500 ft or more apart. Their presence may correspond with downdrafts in the cloud, but the author's own accelerometer records are not sufficiently extensive to give adequate support to this idea.

It appears to the author that there is a need to investigate the nature of the air circulation in and around cloud, and that it is only through such an investigation that a better understanding of the process of cloud development and growth will occur. In this regard it is suggested that the technique described by WARNER and BOWEN (1953) may prove useful.

5. Acknowledgements

The author wishes to thank Mr T. D. Newnham for his valuable work in designing the instrument with which these measurements were made and for his help in making the observations. The measurements were made in an aircraft lent and flown by the Royal Australian Air Force.

REFERENCES

AUSTIN, J. M. and A. FLEISHER, 1948: A thermodynamic analysis of cumulus convection. *J. Met.*, **5**, pp. 240—243.

HOUGHTON, H. C. and H. E. CRAMER, 1951: A theory of en rainment in convective currents. *J. Met.*, **8**, pp. 95—102.

MALKUS, J. S., 1949: Effects of wind shear on some aspects of convection. *Trans. Amer. Geophy. Union*, **30**, pp. 19—25.

MALKUS, J. S., 1952 a: Recent advances in the study of convective clouds and their interaction with the environment. *Tellus*, **4**, pp. 71—87.

MALKUS, J. S., 1952 b: The slopes of cumulus clouds in relation to external wind shear. *Quart. J. R. Met. Soc.*, **78**, pp. 530—542.

MALKUS, J. S., 1954: Some results of a trade-cumulus cloud investigation. *J. Met.*, **11**, pp. 220—237.

MALKUS, J. S. and SCORER, R. S., 1954: Marine meteorology—Erosion of cumulus towers. *Woods Hole Oceanographic Inst.*, Ref. No. 54—55. Unpublished manuscript.

SCORER, R. S. and LUDLAM, F. H., 1953: Bubble theory of penetrative convection. *Quart. J. R. Met. Soc.*, **79**, pp. 94—103.

STOMMEL, H., 1947: Entrainment of air into a cumulus cloud. Pt. I. *J. Met.*, **4**, pp. 91—94.

STOMMEL, H., 1951: Entrainment of air into a cumulus cloud. Pt. II. *J. Met.*, **8**, pp. 127—129.

WARNER, J. and NEWNHAM, T. D., 1952: A new method of measurement of cloud-water content. *Quart. J. R. Met. Soc.*, **78**, pp. 46—52.

WARNER, J. and BOWEN, E. G., 1953: A new method of studying the fine structure of air movements in the free atmosphere. *Tellus*, **5**, pp. 36—41.

WEICKMANN, H. K. and AUFM KAMPE, H. J., 1953: Physical properties of cumulus clouds. *J. Met.*, **10**, pp. 204—211.

ZAITSEV, V. A., 1950: Water content and distribution of drop in cumulus clouds. *Glav. geofiz. Observ., Trudy*, **19**, pp. 122—132.

The Production of Condensation Nuclei by Crystallizing Salt Particles

By S. TWOMEY and K. N. McMASTER, Division of Radiophysics, C.S.I.R.O., Sydney. Australia

(Manuscript received 26 May 1955)

Abstract

Experiments were conducted to examine the possibility of condensation nuclei being produced by salt droplets when the environmental humidity was lowered sufficiently for crystallization to take place. It was found that condensation nuclei were in fact produced when salt particles crystallized, each salt particle producing at least several hundred nuclei. It is suggested that these nuclei consisted of minute salt crystals, with mass in the range 10^{-18} to 10^{-14}g, released from the main mass of salt during crystallization.

Introduction

DESSENS (1946) has reported that microscopic salt droplets may crystallize explosively when the environmental humidity is lowered, causing the nucleus to fracture into two or more visible fragments. LODGE and BAER (1954) recently reported experiments which led them to conclude that shattering of salt particles into fragments (greater than an unspecified detection limit) did not take place. On many occasions one of the writers has observed under a microscope the behaviour of salt particles when the environmental humidity is varied, and although crystallization has often been observed, on no occasion was visible frag-mentation noticed. However, it seemed possible that, during the crystallization of a large salt nucleus, very minute fragments might become detached, too small to be detected directly. Tiny particles of this kind should, however, be effective as condensation nuclei. It was hence decided to test this hypothesis by setting up an experiment in which an enclosed volume of air containing a few salt particles could be subjected to variations in relative humidity and its condensation nucleus content examined by adiabatically expanding the air and observing whether clouds formed on expansion.

Apparatus

In order to carry out this experiment, it was necessary to construct an apparatus in which a volume of air could be desiccated or humidified as required, without coming into contact with outside air or any other source of nuclei (chemical compounds or solutions, electric heating elements, etc.). Means also had to be provided for compressing and expanding the air and observing for cloud formation during adiabatic expansions.

The apparatus finally took the form shown in Figure 1. It consisted of an expansion chamber A, a drying chamber B and humidifier chamber C. Pressurization of the expansion chamber was accomplished by an airtight metal bellows which could be expanded by pressurizing it from an external source of compressed air. Chamber pressure was read on the gauge G. The air was dried by circulating cooled alcohol through coils within chamber B. The humidifier chamber C contained a small volume of water and could be warmed by an external heating element; the resulting increase in vapour pressure brought about an increase of relative humidity in the expansion chamber.

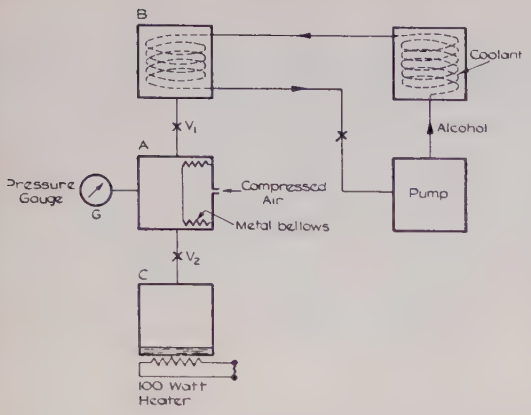

Fig. 1. Schematic representation showing the layout of the apparatus.

The cycle of operations was as follows:

(1) Filtered air was passed through the apparatus for some time before sealing.

(2) The air was humidified and any condensation nuclei remaining in the system were removed by successive adiabatic expansions.

(3) With V_2 closed, cooled alcohol was circulated through the drying chamber. A gradient of vapour pressure was thereby set up which gradually lowered the relative humidity in the expansion chamber. The relative humidity was measured by a metal-plastic dial hygrometer within the expansion chamber.

(4) When the required degree of desiccation was reached, V_2 was opened, V_1 closed, and the humidifying period begun. (The time variation of relative humidity during desiccating and humidifying periods is shown in Fig. 2(a) to 2(d).)

(5) When a relative humidity of 90 % to 92 % had been reached the air was subjected to an adiabatic expansion. Cloud droplets forming in the chamber could readily be observed in the intense heat-filtered beam from a mercury vapour lamp which illuminated the chamber at an angle of 150° to the direction of observation. The expansion ratio normally used represented a theoretical supersaturation in the chamber of 11 % (1·7° C).

Experimental

The actual experiments consisted of a series of tests following the operation cycle described above. Where salt particles were to be included in the expansion chamber, a spider web mounted on a perspex frame was sprayed with a concentrated solution of sea-salt and clipped to a removable panel in the expansion chamber.

In the absence of salt particles, nucleus-free

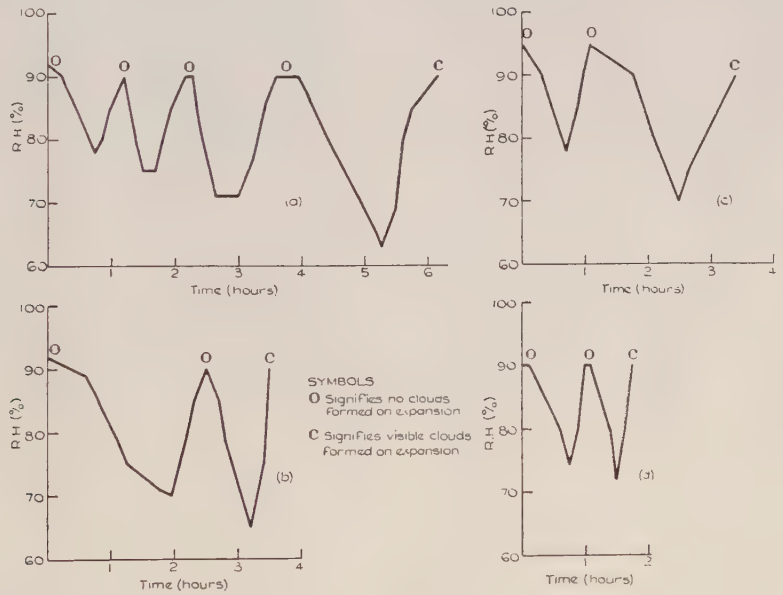

Fig. 2. Graphical illustration of the results of four experiments which were carried out to determine the threshold value of relative humidity for the appearance of nuclei in the chamber. Variation of R.H. with time is shown, and the results of adiabatic expansions are indicated at the appropriate points.

Table 1.

Experiment No.	1	2	3	4	5	6	7	8
Salt particles present	Yes	No	Yes	No	Yes	Yes	No	Yes
Initial R.H.	95 %	90 %	91 %	90 %	91 %	97 %	97 %	97 %
Period of desiccation (min.)	135	110	135	120	130	95	90	125
R.H. after desiccation	62 %	60 %	57 %	69 %	62 %	61 %	61 %	60 %
Period of humidifying (min.)	70	65	30	20	70	30	100	35
R.H. after humidifying	90 %	90 %	90 %	90 %	90 %	90 %	90 %	90 %
Expansion ratio (p_1/p_2)	1.042	1.042	1.042	1.042	1.042	1.042	1.042	1.042
Theoretical supersaturation	11 %	11 %	11 %	11 %	11 %	11 %	11 %	11 %
Cloud observed	Yes	No	Yes	No	Yes	Yes	No	Yes

air was dried to 60 % relative humidity, and then humidified. On expanding, no clouds were observed in the chamber. On the other hand, when salt particles had been introduced, fairly dense clouds were observed on expansion. A series of eight experiments in which salt was alternately included and omitted showed that nuclei were produced *only* when air *containing salt particles* was *desiccated*, humidified and expanded. An average of 20 expansions was required to clear the chamber of the clouds produced on these nuclei. These results are tabulated in Table 1.

Experiments were carried out to determine approximately the threshold relative humidity, to which the air containing the salt particles should be desiccated in order that nucleus production might take place. In these experiments, represented graphically in Figure 2, the chamber remained free of nuclei when the relative humidity had been lowered to 71, 70, 78 and 74 %, while nuclei were produced when the relative humidity had reached 63, 65, 70 and 72 % respectively. It is probable therefore, that the threshold for this effect was between 68 % and 72 % R. H. (The accuracy of the hygrometer was probably about ± 2 % R. H.)

An attempt was made to determine the critical supersaturation of the nuclei produced. It was not possible to determine this limit with accuracy, as the measurement of relative humidity within the chamber was liable to errors, and the characteristics of the expansion system with respect to deviations from the true adiabatic were not known. The theoretical supersaturation, deduced from temperature, humidity and critical pressure measurements was usually about 2·5 % (0·4° C), ranging from < 1 to 11 % (< 0·15 to 1·8° C) for individual experiments. Although the actual supersaturation would certainly have been smaller than the preceding adiabatic values, it seems likely that a supersaturation at least of the order of 0·2° C is necessary for these nuclei to grow to cloud droplet size. The relationship between nucleus size and critical supersaturation has been computed by many investigators (e. g. SQUIRES 1952). The following relationships are quoted for liquid drop nuclei and for hygroscopic salt nuclei.

Nucleus mass	Supersaturation for water droplets	Supersaturation for salt nuclei
10^{-11}g	0.1 % (0.015° C)	0.002 % (0.00025° C
10^{-14}g	1 % (0.16° C)	0.06 % (0.008° C)
01^{-17}g	12 % (1.85° C)	2 % (0.25° C)
10^{-20}g	300 % (19° C)	60 % (8° C)

It seems most likely, therefore, that the nuclei produced during the desiccation of salt particles are of the order of 10^{-14} to 10^{-18} g. It follows that a single salt particle of mass 10^{-10} g could produce several hundreds or more such nuclei without undergoing any appreciable reduction in size.

The density of the clouds observed in the chamber was of course somewhat variable, but a very conservative estimate of the droplet concentration would be 100 per cm³. As the volume of air in the chamber was of the order of 1 litre and the number of particles on the spider webs seldom reached 100, it is seen that the crystallization of each salt particle must have produced many hundreds of minute nuclei.

A rough estimate of size was obtained by considering the velocity of fall of the nuclei when only a few were present in the chamber. The droplets formed on the nuclei fell out at

a few mm per sec, the supersaturation theoretically reached in the expansion being 1·7° C. This indicates that the nuclei had grown to a radius of 5 μ in about 1 sec. From theoretical computations of droplet growth (SQUIRES loc. cit.) it was found that to achieve this degree of growth, the nucleus mass should be greater than 10^{-18} g; the fact that the nuclei could remain in suspension in the chamber for an hour or so during humidifying periods suggested that their mass did not exceed 10^{-14} g.

Discussion

When a particle of sea-salt or common salt is placed in a stream of air whose humidity can be controlled, it undergoes a transition to the liquid state when the environmental relative humidity reaches 75 % (TWOMEY 1953, 1954). The relative humidity at which droplets of salt solution crystallize when the humidity is being lowered is not as well defined. This transition is of course dependent on the degree of supersaturation which the solution can tolerate and is probably critically dependent on the impurities present both in the solution and in the nearby air. During investigations in this Laboratory, it was observed that well-ventilated droplets 1 to 10 μ in radius usually crystallized around 70 % R.H. This figure agrees quite well with the threshold relative humidities at which condensation nuclei have been found to appear. It is therefore suggested that these nuclei were formed during the crystallization of the larger salt particles, and that they consisted of minute salt crystals released from the main mass during the crystallization process.

This result provides an alternative hypothesis for explaining the increased numbers of nuclei observed over land. It is not unreasonable to suppose that sea-salt nuclei travelling over land are subjected to greater and more frequent variations in environmental humidity than they are likely to encounter while over the ocean, so that the process of crystallization may at least partly explain the increase in the condensation nucleus count. The observations of CAUER (1949) concerning the escape of chlorine from droplets of salt spray (which CAUER attributed to a photochemical reaction) might well be explained by the release of condensation nuclei from crystallizing salt droplets.

It should be pointed out that the rate at which desiccation occurred within the expansion chamber (1 % to $^1/_2$ % R.H. per minute) corresponds to the rate of change of humidity occurring in the free air for adiabatic vertical movements with velocities which are quite low (less than 1 metre per second).

Conclusion

The crystallization of a few microscopic salt particles produces several hundred or more minute nuclei, which are effective condensation nuclei at moderate supersaturations. These nuclei are probably minute salt crystals with masses in the range 10^{-14} to 10^{-18} g.

REFERENCES

CAUER, H., 1949: Ergebnisse chemisch-meteorologischer Forschung. *Archiv f. Met. Geophysik u. Bioklimat.* (B) **1**, 221—256.

DESSENS, H., 1946: Les noyeaux de condensation de l'atmosphère. *C. R. Acad. Sci.*, 223, 915.

LODGE, J. P., and F. BAER, 1954: An experimental investigation of the shatter of salt particles on crystallization. *J. Meteor.*, **11**, 420—421.

SQUIRES, P., 1952: The growth of cloud drops by condensation. *Aust. J. Sci. Res. A*, **5**, 59—86.

TWOMEY, S., 1953: The identification of hygroscopic particles in the atmosphere by a phase-transition method. *J. appl. Physics*, **24**, 1099—1102.

TWOMEY, S., 1954: The composition of the hygroscopic particles in the atmosphere. *J. Meteor.*, **11**, 334—338.

On the Use of Space-Smoothing in Physical Weather Forecasting

By RAGNAR FJØRTOFT, University of Copenhagen

(Manuscript received April 15, 1955)

Abstract

In section 1—2 a certain space-smoothing operation is defined and its usefulness in solving elliptic equations is demonstrated in the case of a Poisson equation. It leads to solutions in a closed form which possess the numerical simplicity of the ordinary iteration methods, but is converging more rapidly. The reverse operation of unsmoothing is also defined as far as it can be done, and it is mentioned that the combined processes of smoothing and unsmoothing are convenient tools for obtaining a spectral analysis of horizontal scalar fields, and also to remove systematical errors which are made when derivatives are taken as finite differences.

In sections 3—6 the application of smoothing is shown in the barotropic forecasting problem. At first a general theorem is proved concerning trajectories of two-dimensional non-divergent flow. It states that if the streamfunction ψ_1 of such a flow can be decomposed into two components ψ_2, α of which α is individually conserved in the ψ_1-motion, then the displacements of the fluid particles up to any time can be found by at first displacing in the *stationary* flow $\alpha_{t=0}$ = const and then adding from the resulting positions the displacements in the flow with the streamfunction ψ_2. The theorem is first applied to barotropic flow. In this case the first stationary field to displace in is the deviation between the actual and smoothed flow, while the second field to displace in is the smoothed flow.

The space-smoothing is next applied to an equation expressing the individual conservation of a quantity s in a two-dimensional non-divergent flow. The Reynolds term belonging to the smoothed equation is studied and found to depend essentially upon the deformation properties of the velocity field. The role of deformation for the net spectral flow of energy in the s-field is studied. The smoothing is in particular applied to the vorticity equation to show how this possibly can be utilized in the integration problem.

In sections 7—11 the baroclinic case is considered. In sections 7—8 is shown the fundamental role of deformation for the interchange of potential and kinetic energy. It is found that in the advective model there is direct proportionality between the change in total kinetic energy and total thermal wind energy, and also a direct proportionality between the change in kinetic energy for the vertically mean motion and the thermal wind energy.

In section 9 is discussed the possible importance of non-linear interference for the understanding of the creation and local distribution of disturbances in the atmosphere.

The integration problem is discussed in sections 10—12. At first an extension of the barotropic displacement rule is given for the vertically mean motion. The trajectory problem for levels other than the mean level is touched in section 12, and a simple non-advective model discussed shortly in section 11.

Introduction

In an article in Tellus (FJØRTOFT, 1952) it was shown that a certain operation of space-smoothing of the horizontal streamfield could be utilized in connection with the barotropic forecasting problem. On the one hand it led to rapidly converging solutions of the elliptic equation appearing in the problem. On the other hand the smoothing was of such a character that vorticity would be conserved in the smoothed motion as well. This reduced considerably the number of iterations which are necessary for a forecast over a certain period, provided the numerical problem was treated in a Lagrangian sense. Since the appearance of the mentioned article the further

work with the method has continued along the following directions: First, the method has been improved for the barotropic case, and extended to simple baroclinic models. Secondly, it has been tested to a number of 50 cases of which some also have been treated on numerical computers. By comparison the results hitherto seem to be practically equally good.

The application of the developed integration methods will be brought in a second part of this paper because all the additional problems which arise as soon as theory is applied to practical cases deserve a separate treatment. Instead, however, is included in this part some results of more general theoretical interest which are closely related to the integration problem.

On a certain space-smoothing operation

1. Definition of the smoothing operator

Let β be any function of position on a spherical surface, ∇_h the spherical nabla-operator, and β_q the eigenvalues of the eigenvalueproblem

$$\nabla_h^2 \beta_q + a_q \beta_q = 0 \tag{1}$$

$$\beta_q = \text{unique on a spherical surface} \tag{2}$$

The a_q's are, as is known, given by

$$a_q = \frac{q(q+1)}{R^2}, \quad q = 1, 2, \ldots \tag{3}$$

where R is the radius of the sphere. It will be supposed that β satisfies the conditions for an expansion after the eigensolutions of (1), (2):

$$\beta = \sum_{q=1}^{\infty} \beta_q \tag{4}$$

We now define as $\beta^{(r)}$ an operation performed on β which is given by

$$\beta^{(r)} = \beta + \frac{\nabla_h^2 \beta}{a_r} \tag{5}$$

Inserting here from (4) and using (1) we arrive at

$$\beta^{(r)} = \sum_{q=1}^{\infty} \left(1 - \frac{a_q}{a_r}\right) \beta_q \tag{6}$$

Hence it is seen that the operation which has been introduced smooths out entirely the r-component of β and damps all β_q for which $a_q < a_r$, e.i. according to (3) for $q < r$. Therefore if (4) is approximated by a finite series

$$\beta = \sum_{q=1}^{N} \beta_q \tag{7}$$

it is seen that $\beta^{(N)}$ will imply a smoothing of all components of β, since then

$$\beta^{(N)} = \sum_{q=1}^{N} \left(1 - \frac{a_q}{a_N}\right) \beta_q \tag{8}$$

where now $0 \leq 1 - \frac{a_q}{a_N} < 1$.

For the following arguments it will be supposed that β is given or approximated by a finite series (7). It should be mentioned that in the practical applications to be treated in the second part of this paper, the differential operation $^{(r)}$ will be replaced by a corresponding finite difference operation $^{-r}$ which satisfies the following conditions

$$\bar{\beta}_q^r = \text{or} \simeq \beta_q^{(r)} \text{ when } q \gtrless r \tag{9}$$

and

$$|\bar{\beta}_q^r| \simeq 0 \text{ when } q > r. \tag{10}$$

In the following we shall make such use of the operation $^{(r)}$ which makes it effective for components β_q with $q \leq r$ only. Whether we use (9) or (5) will therefore not change the results we arrive at essentially. However, for the theoretical reasoning in this paper it will be simpler to use the operation$^{(r)}$ because of the simple way in which the eigenvalues a_q enter into the coefficients of the expansion of $\beta^{(r)}$.

A repeated smoothing will now imply the relationship

$$\beta^{(r),(s)\dots(t)} = \sum_{q=1}^{N} \left(1 - \frac{a_q}{a_r}\right)\left(1 - \frac{a_q}{a_s}\right)\dots \left(1 - \frac{a_q}{a_t}\right)\beta_q \qquad (11)$$

and thus result in a complete damping out of the components β_q with the indexes $q = r, s, \dots, t$.

The identity (5) may also be written

$$\beta = -\frac{\nabla_h^2 \beta}{a_r} + \beta^{(r)} \qquad (12)$$

If we write a similar identity for $\beta^{(r)}$ we obtain

$$\beta^{(r)} = -\frac{\nabla_h^2 \beta^r}{a_s} + \beta^{(r)(s)} \qquad (13)$$

where s may be taken equal to or different from r. Combining (12) and (13) we obtain

$$\beta = -\frac{\nabla_h^2 \beta}{a_r} - \frac{\nabla_h^2 \beta^{(r)}}{a_s} + \beta^{(r)(s)}$$

Iterating this procedure we arrive at

$$\beta = -\left[\frac{\nabla_h^2 \beta}{a_r} + \frac{\nabla_h^2 \beta^{(r)}}{a_s} + \dots + \frac{\nabla_h^2 \beta^{(r),(s)\dots(t)}}{a_u}\right] + \beta^{(r)(s)\dots(t)(u)} \qquad (14)$$

We observe that

$$\nabla_h^2 \beta^{(r)(s)\dots(t)} = (\nabla_h^2 \beta)^{(r)(s)\dots(t)} \qquad (15)$$

Let us now first take $r, s, \dots, t, u, \dots = N$. We then have

$$\beta^{(r)(s)\dots(t)(u)\dots} \equiv \beta^{(N)p} = \sum_{q=1}^{N} \left(1 - \frac{a_q}{a_N}\right)^p \beta_q \to 0$$

when $p \to \infty$. In this case therefore, using (15), we may write (14) in the limit as

$$\beta = -\frac{1}{a_N} \lim_{p\to\infty} \left[\nabla_h^2 \beta + (\nabla_h^2 \beta)^{(N)} + \dots + (\nabla_h^2 \beta)^{(N)p} + \dots\right] \qquad (16)$$

In the second case we choose successively $r = N, s = N-1, \dots, t = 2, u = 1$. Since now

$$\beta^{(N)(N-1)\dots(2)(1)} = \sum_{q=1}^{N} \left(1 - \frac{a_q}{a_N}\right)\left(1 - \frac{a_q}{a_{N-1}}\right)\dots\left(1 - \frac{a_q}{a_2}\right)\left(1 - \frac{a_q}{a_1}\right)\beta_q,$$

(14) can by reference to (15) be written

$$\beta = -\left[\frac{\nabla_h^2 \beta}{a_N} + \frac{(\nabla_h^2 \beta)^{(N)}}{a_{N-1}} + \dots + \frac{(\nabla_h^2 \beta)^{(N)(N-1)\dots(2)}}{a_1}\right] \qquad (17)$$

The solution of a Poisson equation

$$\nabla_h^2 \beta = F \qquad (18)$$

with the boundary conditions (2) and correct for the N first components can now be obtained by replacing $\nabla_h^2 \beta$ with the known function F in either (16) or (17). In the former case the form of the solution corresponds completely to the one of successive iterations used in Richardsons method (19). In (17), however, the solution is given in a closed form while at the same time maintaining the computational simplicity which characterizes the method of successive iterations. The main advantage, however, in using (17) for numerical purposes is explained by the fact that taking a few terms in (17) gives a much closer approximation to the solution than taking the same number of terms in (16).

2. The "reverse" operation of unsmoothing

Suppose now that β is an unknown function satisfying a relation

$$\beta^{(N)} = f \qquad (19)$$

where f is known. While obviously β_N cannot be found because $\beta_N^{(N)}$ must be zero, the other components can be determined by a reverse process of unsmoothing. For instance is

$$\beta = \beta_N + \lim_{p \to \infty} \left[\beta^{(N)} - \frac{\nabla_h^0 \beta^{(N)}}{a_N} + \frac{\nabla_h^4 \beta^{(N)}}{a_N^2} + \cdots + (-1)^p \frac{\nabla_h^{2p} \beta^{(N)}}{a_N^p} + \cdots \right] \qquad (20)$$

as can be verified by substituting $\beta = \sum_{q=1}^{N} \beta_q$ on both sides. It can be shown that there exists also a similar relationship between β, β_N, and $\beta^{(N)}$ in a closed form. The combined process of smoothing and unsmoothing will prove very useful in the numerical work of obtaining a spectral analysis of a field β as will be demonstrated in an article to appear later. It has also been used to remove systematical errors arising when space derivatives are obtained by taking finite differences.

The barotropic forecasting problem

3. Formulation of the integration problem

In the so-called barotropic case velocity $\mathbf{v}$ is supposed to be horizontal and non-divergent

$$\mathbf{v} = -\nabla_h \psi \times \mathbf{k} \qquad (21)$$

and the motion governed by the equation

$$\frac{D}{dt} \nabla_h \times \mathbf{v} \cdot \mathbf{k} = 0. \qquad (22)$$

For simplicity the motion will be considered in an absolute coordinate system. $\frac{D}{dt}$ is defined from

$$\frac{D}{dt} = \frac{\partial}{\partial t} + \mathbf{v} \cdot \nabla_h$$

Eq. (22) then simply expresses the individual conservation of the vertical component of absolute vorticity. Using (21) we can also write (22) as

$$\frac{D}{dt} \nabla_h^2 \psi = 0. \qquad (23)$$

Suppose now that ψ and hence $\nabla_h^2 \psi$ is known initially. Suppose further that on the basis of this information the trajectories of the fluid particles, or rather their displacements up to a time t_1 are known with some accuracy. In accordance with (23) we will then be able to find the distribution of $\nabla_h^2 \psi$ at time t_1 with a corresponding accuracy by simply letting the fluid particles carry along the vorticities they possess initially. If $F(\mathbf{r})$ denotes this distribution of $\nabla_h^2 \psi$ at time $t = t_1$, $\mathbf{r}$ being the position vector for points in the considered horizontal surface, a solution of the Poisson equation

$$\nabla_h^2 \psi^\star = F(\mathbf{r})$$

will yield the field $\psi_{t=t_1}$ with some accuracy. By n iterations of the operations above we will obtain a forecast for the period $n\,t_1$.

According to the integration scheme outlined above the integration problem consists of two essentially distinct parts. The second part has already been dealt with in some detail in section 1. In the following section the first part will be considered more closely.

4. The trajectory or displacement problem for barotropic flow

If $\mathbf{p}$ denotes the displacement of a particle up to a time t and $\mathbf{p}_1'$ the corresponding displacement in the stationary flow $\mathbf{v} = \mathbf{v}_{t=0}$, we obviously have

$$\lim_{t \to 0} \frac{\mathbf{p}'}{t} = \lim_{t \to 0} \frac{\mathbf{p}}{t}$$

For $t \leq t_1$ we can therefore, if t_1 is taken sufficiently small consider $\mathbf{p}'$ as a sufficiently good approximation to $\mathbf{p}$, meaning thereby that $\mathbf{p}' - \mathbf{p}$ then will be small of higher order than $\mathbf{p}$ itself. In other words, the approximation

$$\mathbf{v} = \mathbf{v}_{t=0}; \quad t \leq t_1 \qquad (24)$$

will be sufficiently accurate as a basis to find $\mathbf{p}$, if only t_1 is taken sufficiently small.

Applied to the atmosphere we probably have to take t_1 not > 2 h. if we shall avoid serious errors in a 24 h. forecast, thus making it necessary with a total of 12 iterations for a forecast over this period. In the following a method will be given by means of which t_1 can be increased considerably. The method is based upon a certain theorem which will find repeated use in this paper. For that reason it will be most convenient to give the proof of it in general terms. Let then ψ_1 symbolize a streamfunction defining a velocity $\mathbf{v}_1$ in some motion by

$$\mathbf{v}_1 = -\nabla_h \psi_1 \times \mathbf{k},$$

while $\frac{D_1}{dt}$ is defined from: $\frac{D_1}{dt} = \frac{\partial}{\partial t} + \mathbf{v}_1 \cdot \nabla_h$. Suppose further that it is possible to write

$$\psi_1 = \psi_2 + \alpha \tag{25}$$

$$\frac{D_1 \alpha}{dt} = 0. \tag{26}$$

With $\mathbf{v}_\alpha$, $\mathbf{v}_2$, $\frac{D_2}{dt}$ defined by

$$\mathbf{v}_\alpha = -\nabla_h \alpha \times \mathbf{k}$$

$$\mathbf{v}_2 = -\nabla_h \psi_2 \times \mathbf{k}$$

$$\frac{D_2}{dt} = \frac{\partial}{\partial t} + \mathbf{v}_2 \cdot \nabla_h$$

we obtain

$$\frac{D_1 \alpha}{dt} = \frac{\partial \alpha}{\partial t} + (\mathbf{v}_2 + \mathbf{v}_\alpha) \cdot \nabla_h \alpha = \frac{D_2 \alpha}{dt} + \mathbf{v}_\alpha \cdot \nabla_h \alpha$$

Since now $\mathbf{v}_\alpha \cdot \nabla_h \alpha = 0$ we obtain by comparing with (26):

$$\frac{D_2 \alpha}{dt} = 0. \tag{27}$$

Hence, α which according to (26) is individually conserved in our motion, is also so in the fictitious motion with the velocities $\mathbf{v}_2$.

We consider now a particle which at time $t = 0$ is at some arbitrary point A on some arbitrary level line $\alpha_{t=0} = \alpha_1$ (fig. 1). In accordance with (26) this particle moves with the level line and hence must at time $t = T$ be at some point C at $\alpha_{t=T} = \alpha_1$. In the fictitious motion with the velocities $\mathbf{v}_2$ the "particle" which at time $t = T$ also arrives at C must in accordance with (27) have originated from some point, say B, at the level line $\alpha_{t=0} = \alpha_1$. We can now find the point B in a simple way, using only the *initial* conditions, by the following arguments: We consider all particles which at time $t = 0$ are on the line $\alpha_{t=0} = \alpha_1$. The set of trajectories of these particles in the *fictitious* motion are next considered. If these are labelled in some unique fashion by a set $\{l\}$ this will introduce a function $f(\mathbf{r})$ such that $f(\mathbf{r}) = \text{const} = l$ will represent the equation for the trajectory numbered l. Particularly we shall label the

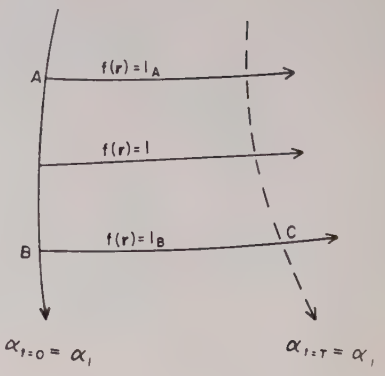

Fig. 1. Illustration to the text in section 4.

trajectories through A and B with l_A and l_B, respectively. Now, according to definition

$$\frac{\partial f}{\partial t} = 0 \tag{28}$$

Hence $\frac{D_1 f}{dt} = \mathbf{v}_1 \cdot \nabla_h f$. Substituting here $\mathbf{v}_1 = \mathbf{v}_2 + \mathbf{v}_\alpha$ we obtain

$$\frac{D_1 f}{dt} = \mathbf{v}_2 \cdot \nabla_h f + \mathbf{v}_\alpha \cdot \nabla_h \tag{29}$$

Suppose now that in particular $\left(\frac{D_1 f}{dt}\right)_A$ denotes the individual derivative for the particle which initially is at A. In this case, repeating the arguments from earlier, $\mathbf{v}_2$ must be the velocity of a "particle" in the fictitious motion which is initially at $\alpha_{t=0} = \alpha_1$, and hence must be parallel to the trajectory $f(\mathbf{r}) = l$ which passes through the considered point. Hence $\mathbf{v}_2 \cdot \nabla_h f = 0$, and accordingly (29) can be written when applied to the particle in question

$$\left(\frac{D_1 f}{dt}\right)_A = \mathbf{v}_\alpha \cdot \nabla_h f,$$

or if we recall that $\mathbf{v}_\alpha \cdot \nabla_h f = \nabla_h \alpha \times \nabla_h f \cdot \mathbf{k}$

$$\left(\frac{D_1 f}{dt}\right)_A = \nabla_h \alpha \times \nabla_h f \cdot \mathbf{k} \tag{30}$$

If next $\mathbf{v}_3$ is defined as the stationary velocity $\mathbf{v}_3 = -\nabla_h \alpha_{t=0} \times \mathbf{k}$, and $\frac{D_3}{dt}$ is the correspond-

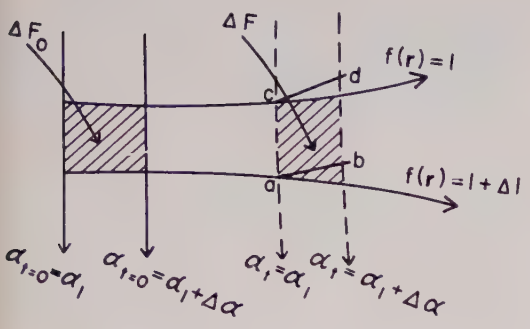

Fig. 2. Illustration for the text below.

ing "individual" derivative: $\frac{D_3}{dt} = \frac{\partial}{\partial t} + \mathbf{v}_3 \cdot \nabla_h$, we obtain by reference to (28)

$$\left(\frac{D_3 f}{dt}\right)_A = \mathbf{v}_3 \cdot \nabla_h f$$

or

$$\left(\frac{D_3 f}{dt}\right)_A = \nabla_h \alpha_{t=0} \times \nabla_h f \cdot \mathbf{k} \qquad (31)$$

We have as is known

$$\nabla_h \alpha \times \nabla_h f \cdot \mathbf{k} = \lim_{\Delta\alpha,\, \Delta l \to 0} \frac{\Delta\alpha \, \Delta l}{\Delta F} \qquad (32)$$

and

$$\nabla_h \alpha_{t=0} \times \nabla_h f \cdot \mathbf{k} = \lim_{\Delta\alpha,\, \Delta l \to 0} \frac{\Delta\alpha \, \Delta l}{\Delta F_0} \qquad (33)$$

Here ΔF is the area between the level lines $\alpha_t = \alpha_1$, $\alpha_t = \alpha_1 + \Delta\alpha$, some fictitious trajectory $f(\mathbf{r}) = l$, and the neighbour one $f(\mathbf{r}) = l + \Delta l$, (fig. 2), while ΔF_0 correspondingly is the area between the level lines $\alpha_{t=0} = \alpha_1$, $\alpha_{t=0} = \alpha_1 + \Delta\alpha$, some fictitious trajectory $f(\mathbf{r}) = l'$, and the neighbour one $f(\mathbf{r}) = l' + \Delta l$. Let now ΔF_1 denote the area of the surface element $a\,b\,c\,d$ into which ΔF_0 transforms in the $\mathbf{v}_2$-motion. Because of (27) and the definition of $f(\mathbf{r})$ the corners a, b, c, d must be situated as the diagram shows. Since $\nabla_h \cdot \mathbf{v}_2 = 0$, $\Delta F_1 = \Delta F$. On the other hand if in particular $l' = l$, from continuity reasons $\Delta F / \Delta F_1 \to 1$ when $\Delta\alpha \to 0$. Accordingly also $\Delta F_0 / \Delta F \to 1$ when $\Delta\alpha \to 0$. This in connection with (33), (32), (31), and (30) gives

$$\left(\frac{D_1 f}{dt}\right)_A = \left(\frac{D_3 f}{dt}\right)_A \qquad (34)$$

provided f assumes the same value on both sides. Since now both particles, namely the one of the real motion and the one of the stationary field $\alpha_{t=0}$, initially have the same value l_A for $f(\mathbf{r})$, we obtain by integration of (34) that also at any later time the two particles assume identical values of f. Particularly, the particle moving in the stationary field will arrive at B on the trajectory $f(\mathbf{r}) = l_B$ at the same time as the particle in the real motion arrives at C on the same fictitious trajectory. To summarize we have therefore obtained the following result:

If a flow is determined from a stream-function ψ_1 which satisfies the conditions

$$\psi_1 = \psi_2 + \alpha$$

$$\frac{D_1 \alpha}{dt} = 0$$

we can find the displacements of the fluid particles up to any time t by displacing at first in the stationary velocity field $-\nabla_h \alpha_{t=0} \times \mathbf{k}$ and then adding from the resulting positions the corresponding displacements in the fictitious motion with the velocities $\mathbf{v}_2 = -\nabla_h \psi_2 \times \mathbf{k}$. (35)

The result that trajectories can be added in this way seems surprising at first sight. For usually trajectories can not be added by virtue of the highly non-linear operations involved in finding them. When we nevertheless can do so in the present case it must be due to the rather special conditions expressed in (25), (26). However, it should be borne in mind that the order in which we let the displacements take place is not arbitrary. This can easily be seen by for instance taking a particle initially in a stagnation point of the field $\alpha_{t=0}$. Then the first displacement is zero, and the net displacement is accordingly determined from the ψ_2-flow alone. If we had started with this displacement the next displacement in the $\alpha_{t=0}$-field would, however, in general not have been zero.

In this section we shall make a first use of the above theorem in an application to barotropic flow. We then write down the identity

(12) applied to the streamfunction ψ, taking $r = N$, together with eq. (23) after this has been divided by $-a_N$. This gives

$$\psi = \psi^{(N)} - \frac{\nabla_h^2 \psi}{a_N} \tag{36}$$

$$\frac{D}{dt}\left(-\frac{\nabla_h^2 \psi}{a_N}\right) = 0 \tag{37}$$

This system is a special case of (25), (26), as it is seen if we let $\psi_1 \to \psi$ and $\alpha \to -\frac{\nabla_h^2 \psi}{a_N}$. We obtain therefore the following rule:

The displacements in barotropic flow up to any time may be found by at first displacing in the stationary velocity field with the streamfunction $-\left(\frac{\nabla_h^2 \psi}{a_N}\right)_{t=0}$, and then from the resulting positions adding the corresponding displacements in the smoothed motion with the streamfunction $\psi^{(N)}$. (38)

We now put as an approximation

$$\mathbf{v}^{(N)} = \mathbf{v}^{(N)}_{t=0}; \quad t \leqq t_1' \tag{39}$$

Since there is no upper limit to the period over which we can find the displacements in the stationary field, the upper limit to the period over which we can find the displacements of the particles according to the combined displacement rule above, will be given by t_1' in (39). Since $\mathbf{v}^{(N)}$ represents a smoothed flow in space, it must be less timevariable than the velocities $\mathbf{v}$ themselves. Accordingly we may take t_1' in (39) larger than t_1 in (24). Precisely how large we can take t_1' must depend upon the spectral distribution in space of ψ, partly because this among other things will determine the number N of the component at which we will break the expansion after eigensolutions ψ_q in (7). When applied to the flow near the 500 mb surface experience has shown that the 2 h. for t_1 can be increased approximately to 24 h. for t_1'.

We may now take advantage of this in any forecasting problem of the following nature: Let s denote a quantity which is individually conserved in barotropic motion:

$$\left.\begin{aligned} \frac{Ds}{dt} &= 0 \\ \frac{D\nabla_h^2 \psi}{dt} &= 0 \end{aligned}\right\} \tag{40}$$

If now s and ψ are given initially the displacement rule above will determine the distribution of s after the period t_1'. If particularly $s = \nabla_h^2 \psi$, the first displacement of the level lines $(\nabla_h^2 \psi)_{t=0} = \text{const}$ in the stationary field with the streamfunction $-\left(\frac{\nabla_h^2 \psi}{a_N}\right)_{t=0}$ yields zero changes. In this case it is therefore sufficient with a displacement only in the smoothed flow. This is simply another expression of (27), which, when $\alpha \to -\frac{\nabla_h^2 \psi}{a_N}$, $\frac{D_2}{dt} \to \frac{D^N}{dt}$, after multiplication by $-a_N$ transforms to

$$\frac{D^N}{dt} \nabla_h^2 \psi = 0 \tag{41}$$

$\frac{D^N}{dt}$ being defined by

$$\frac{D^N}{dt} = \frac{\partial}{\partial t} + \mathbf{v}^{(N)} \cdot \nabla_h \tag{42}$$

For any other conservative quantity s, however, the level lines $s_{t=0} = \text{const}$ must generally at first be displaced in the stationary field with the streamfunction $-\left(\frac{\nabla_h^2 \psi}{a_N}\right)_{t=0}$.

5. A few studies of the dynamical equations of the smoothed flow

The operation of space smoothing$^{(N)}$ was introduced in section 1 at first merely as a method of solving a Poisson equation. In the section above this operation of smoothing has also got dynamical interest in the sense that it can be utilized with considerable advantage in the problem of finding trajectories of fluid particles in barotropic motion. The question then naturally arises to what extent the dynamics of such a smoothed motion is determined in terms of the smoothed motion itself. This is essentially a question of the relative importance of certain additional Reynold

terms which appear in the dynamical equation as soon as they are being smoothed. Some inquiry into the nature and interpretation of the Reynold term is the chief object of this section.

Suppose now that we have

$$\frac{Ds}{dt} = H \tag{43}$$

where H is a source for s which is a known function of space and time. For the following argumentation it does not matter if we put $H = 0$, giving

$$\frac{Ds}{dt} = 0 \tag{40}$$

or alternatively

$$\frac{\partial s}{\partial t} = -\mathbf{v} \cdot \nabla_h s. \tag{44}$$

Applying here the smoothing $^{(N)} = 1 + \frac{\nabla_h^2}{a_N}$ on both sides we get after some computation

$$\frac{D^N s^{(N)}}{dt} = (R_s)_N \tag{45}$$

where

$$(R_s)_N = (\mathbf{v} - \mathbf{v}^{(N)}) \cdot \nabla_h (s - s^{(N)}) + \frac{2}{a_N} A(\psi, s) \tag{46}$$

with

$$A(\psi, s) = \frac{\partial^2 \psi}{\partial x \partial y}\left(\frac{\partial^2 s}{\partial y^2} - \frac{\partial^2 s}{\partial x^2}\right) + \frac{\partial^2 s}{\partial x \partial y}\left(\frac{\partial^2 \psi}{\partial x^2} - \frac{\partial^2 \psi}{\partial y^2}\right) \tag{47}$$

In (47) the derivatives with respect to x, y refer to a locally cartesian coordinate system in the considered horizontal surface. It should be noted that $A(\psi, s)$ depends entirely upon the mutual deformation properties of the vector fields $-\nabla_h \psi \times \mathbf{k}$ and $-\nabla_h s \times \mathbf{k}$. The interpretation of $A(\psi, s)$ is seen from the following arguments: Recalling that $\frac{D}{dt} = \frac{D^N}{dt} + (\mathbf{v} - \mathbf{v}^{(N)}) \cdot \nabla_h$, (45) can also be written

$$\frac{Ds^{(N)}}{dt} = (\mathbf{v} - \mathbf{v}^{(N)}) \cdot \nabla_h s + \frac{2}{a_N} A(\psi, s) \tag{48}$$

Multiplying here both sides by s and integrating over the total spherical surface F we obtain by reference to (40):

$$-\frac{d}{dt}\int_F s(s - s^{(N)})\, dF = \int_F s(\mathbf{v} - \mathbf{v}^{(N)}) \cdot \nabla_h s\, dF + \int_F \frac{2s}{a_N} A(\psi, s)\, dF \tag{49}$$

However, since $\nabla_h \cdot (\mathbf{v} - \mathbf{v}^{(N)}) = 0$, we obtain

$$\int_F s(\mathbf{v} - \mathbf{v}^{(N)}) \cdot \nabla_h s\, dF = \int_F \nabla_h \cdot \frac{s^2}{2}(\mathbf{v} - \mathbf{v}^{(N)})\, dF$$

and hence by Gauss's theorem

$$\int_F s(\mathbf{v} - \mathbf{v}^{(N)}) \cdot \nabla_h s\, dF = 0 \tag{50}$$

Then, after multiplication by a_N in (49), recalling that in accordance with (5) $\nabla_h^2 s = -a_N(s - s^{(N)})$, we obtain

$$\frac{d}{dt}\int_F -s\nabla_h^2 s\, dF = -\int_F 2s A(\psi, s)\, dF \tag{51}$$

From (40), however, we obtain simultaneously

$$\frac{d}{dt}\int_F s^2 dF = 0 \tag{52}$$

If we introduce the expansions $s = \sum_{q=1}^{\infty} s_q$ and $\nabla_h^2 s = -\sum_{q=1}^{\infty} a_q s_q$ into (51), (52) and recall the orthogonality properties of the s_q's,

$$\int_F s_q s_r dF = 0, \quad q \neq r,$$

we obtain

$$\sum_{q=1}^{\infty} \frac{d}{dt}\int_F a_q s_q^2 dF = -\int_F 2s A(\psi, s)\, dF$$

$$\sum_{q=1}^{\infty} \frac{d}{dt}\int_F s_q^2 dF = 0$$

Using these equations together with the condition $a_{q+1} > a_q$ we obtain that there will be a net flow of s_q^2 to the higher or lower frequency end of the spectrum according as $-\int_F s\Lambda(\psi, s)\,dF \gtrless 0$. The term $\Lambda(\psi, s)$, which depends entirely upon the mutual deformation properties of the vector fields $\mathbf{v}$ and $-\nabla_h s \times \mathbf{k}$, is therefore solely responsible for a contingent net flow of amplitude squared, s_q^2, in the one or other direction of the spectrum.

If H in (43) were not zero, such net flows of s_q^2 could of course also take place with $\Lambda(\psi, s) \equiv 0$. However, this kind of spectral changes would not depend directly upon the properties of the velocity field.

The interpretation of $\Lambda(\psi, s)$ may be formulated in a somewhat different manner by using the following arguments: We have

$$\frac{d}{dt}\int_F -s\nabla_h^2 s\,dF = \frac{d}{dt}\int_F (\nabla_h s)^2 dF$$

so that by comparison with (51):

$$\frac{d}{dt}\int_F (\nabla_h s)^2 dF = -\int_F 2\,s\Lambda(\psi, s)\,dF \qquad (53)$$

Further, if $\frac{Ds}{dt} = 0$, then, since $\nabla_h \cdot \mathbf{v} = 0$, the area between adjacent level lines $s = s_1$, and $s = s_1 + \triangle s$ must be conserved during the motion. Then, evidently $\frac{d}{dt}\int_F (\nabla_h s)^2 dF \gtrless 0$ according as the lengths of the level lines $s = \text{const}$ are on an average either increased or decreased. We may therefore say that $\Lambda(\psi, s)$ may be interpreted as in an integrated sense to be responsible for whether on an average the lengths of the level lines $s = \text{const}$ will increase or decrease, if $\frac{Ds}{dt} = 0$, or at least tend to do so if $\frac{Ds}{dt} = H \neq 0$. Whether there is locally an equally clear interpretation of $\Lambda(\psi, s)$ is not as yet clear to the author.

If we put $s = \nabla^2\psi$, eq. (45) becomes

$$\frac{D^N}{dt}\nabla_h^2\psi^{(N)} = (\mathbf{v} - \mathbf{v}^{(N)}) \cdot \nabla_h \nabla_h^2 (\psi - \psi^{(N)}) + \\ + \frac{2}{a_N}\Lambda(\psi, \nabla_h^2\psi) \qquad (54)$$

We will discuss this equation from a particular point of view in the next section.

6. Further inquiry into the displacement problem for barotropic motion

While the Reynolds term in eq. (54) may be a very important one in characterizing important features of the motion, its magnitude on the other hand may be such that it can be neglected in connection with the displacement problem for a period t_1'' which may possibly be greater than the period t_1' over which $\mathbf{v}^{(N)}$ was put constant. For the period t_1'' we may now write down the approximation

$$\frac{D^N}{dt}\nabla_h^2\psi^{(N)} = 0; \quad t \leq t_1''. \qquad (55)$$

It is readily seen that this equation can be used in connection with the displacement problem. For writing down the system

$$\psi^{(N)} = \psi^{(N)(N-p)} - \frac{\nabla_h^2\psi^{(N)}}{a_{N-p}} \qquad (56)$$

$$\frac{D^N}{dt}\left(-\frac{\nabla_h^2\psi^{(N)}}{a_{N-p}}\right) = 0, \qquad (57)$$

the latter having been obtained by division by $-a_{N-p}$ in (55), we obtain by identifying ψ_1 with ψ^N, and α with $-\frac{\nabla_h^2\psi^{(N)}}{a_N}$ in eqs. (25), (26):

Under the condition (55) the displacements in the smoothed motion with the velocities $\mathbf{v}^{(N)}$ may be found up to a time $t \leq t_1''$ by at first displacing in the stationary flow with the streamfunction $-\left(\frac{\nabla_h^2\psi^{(N)}}{a_N}\right)_{t=0}$ and then adding from the resulting positions the corresponding displacements in the doubly smoothed flow with the velocities $\mathbf{v}^{(N)(N-p)}$. (58)

Putting now as an approximation

$$\mathbf{v}^{(N)(N-p)} = \mathbf{v}^{(N)(N-p)}_{t=0}; \quad t \leq t_1''' \qquad (59)$$

it will be understood that we can take the t_1''' in (59) larger than the t_1' in (39), because $\mathbf{v}^{(N)(N-p)}$ as a doubly smoothed flow must be less time-variable than $\mathbf{v}^{(N)}$. Let T denote the

larger of t_1'' and t_1'''. The slight experience we have had hitherto with forecasting by the aid of this triple displacement rule seems to indicate that we can choose at least $\frac{a_N}{a_{N-p}} = 2$, and that in this case with the proper choice of N, T may be taken as large as about 48 h.

A discussion of the spectral distribution of ψ which is most unfavourable to a neglect of the Reynolds term in eq. (54) has been carried out and will be presented in a separate paper.

We can now combine the displacement rule (58) above with the earlier rule (38), giving a triple displacement rule:

To find the displacements of fluid particles in barotropic motion up to a time $t \leq T$, we may at first displace in the stationary field $-\left(\frac{\nabla_h^2 \psi}{a_N}\right)_{t=0}$, then from the resulting positions add the displacements in the stationary field $-\left(\frac{\nabla_h^2 \psi^{(N)}}{a_{N-p}}\right)_{t=0}$, and then finally add the displacements in the doubly smoothed flow $\psi^{(N)(N-p)}$, which may be taken stationary and equal to $\psi_{t=0}^{(N)(N-p)}$ when $t \leq T$. (60)

Obviously we could continue these arguments and find the displacements in the doubly smoothed flow by neglecting the Reynolds term $R_{N,N-p}$ belonging to a doubly smoothed vorticity equation,

$$\frac{D^{N,N-p}}{dt} \nabla_h^2 \psi^{(N)(N-p)} = R_{N,N-p}.$$

However, since we have as yet no practical experience in the use of the doubly smoothed vorticity equation we shall abstain from a further discussion of this at the present moment.

Before proceeding to the baroclinic motions we shall mention an other aspect of the results arrived at with respect to displacements of fluid particles in barotropic motion. Let then $\mathbf{p}^\star$ denote the approximate displacements up to any time which would be found in accordance with the methods developed above, as compared to the true displacements $\mathbf{p}$. Provided

$$\mathbf{p}^\star \simeq \mathbf{p}; \; t \leq T \tag{61}$$

the distribution of $\nabla_h^2 \psi$ at time t and thereby by integration ψ and $\mathbf{v}$, will be found with a corresponding accuracy by simply displacing $\nabla_h^2 \psi_{t=0}$ the vector distances $\mathbf{p}^\star$. However, the integration of the Poisson equation becomes altogether unnecessary if we also have

$$\frac{\partial \mathbf{p}^\star}{\partial t} \simeq \frac{\partial \mathbf{p}}{\partial t}; \; t \leq T'. \tag{62}$$

Now (62) does not necessarily follow from (61). On the other hand (61) could not be true if (62) was unsystematically untrue. The unsystematical errors in (62) are relatively easy to get rid of. Provided this has been accomplished we should therefore expect it possible to find velocity $\mathbf{v}$ approximately, directly from

$$\mathbf{v} = \frac{\partial \mathbf{p}^\star}{\partial t} \simeq \frac{\mathbf{p}^\star(t+\triangle t) - \mathbf{p}^\star(t-\triangle t)}{2\triangle t}; t \leq T' \tag{63}$$

Here probably, T' has to be taken somewhat smaller than T in (61).

Experience has shown that T' at least can be taken as large as 24 hrs. when we use the triple displacement rule (60).

The baroclinic case

7. The equation for vertical velocity

In the present case we shall not any longer have the restriction that velocity $\mathbf{v}_3$ shall be horizontal and non-divergent. We may express this by writing

$$\mathbf{v}_3 = \mathbf{v} + \mathbf{v}_\alpha$$

where

$$\mathbf{v} = -\nabla_h \psi \times \mathbf{k}$$

$$\mathbf{v}_\alpha = -\nabla_h \alpha + w\mathbf{k}$$

We shall a priori exclude sound phenomena. Since we in this paper are mainly concerned with the matter from a theoretical point of view we shall do this in the simplest way by assuming

$$\nabla \cdot \mathbf{v}_3 = 0 \tag{64}$$

The boundary conditions to be considered will be taken as

$$w = 0 \text{ for } z = -h, \; z = h \tag{65}$$

where h is the depth of the atmosphere.

We shall next make use of certain equilibrium conditions, essentially in the manner demonstrated by CHARNEY (1948) and ELIASSEN (1948). One of the essential consequences of the method of Charney and Eliassen is the fact that the component $\mathbf{v}_\alpha$ of the velocity field cannot be chosen arbitrary, but is in fact instead determined from a knowledge of the pressure distribution and the boundary conditions alone. In this paper we shall derive the equations for the components of $\mathbf{v}_\alpha$ by at first eliminating $\frac{\partial \ln \vartheta}{\partial t}$ and $\frac{\partial \psi}{\partial t}$ between three equations. The first of these expresses the relation which must exist between ψ and potential temperature ϑ if the $\mathbf{v}_\alpha$-component of the velocity field shall be in equilibrium:

$$\frac{d}{dt}\int_\tau \frac{1}{2}\mathbf{v}_\alpha^2 d\tau \equiv 0 \tag{66}$$

Here it is integrated over the total volume τ of the atmosphere. Considering the coriolis parameter $2\Omega_z$ as a virtual constant under the gradient $\nabla_h \cdot 2\Omega_z \frac{\partial \psi}{\partial z}$,

$$\nabla_h \cdot 2\Omega_z \frac{\partial \psi}{\partial z} \simeq 2\Omega_z \nabla_h \frac{\partial \psi}{\partial z} \tag{67}$$

and considering also the convective acceleration $\mathbf{v} \cdot \nabla_h \mathbf{v}$ negligible in comparison with $2\Omega_z \mathbf{k} \times \mathbf{v}$ when differentiated with respect to height z,

$$\left| \frac{\partial}{\partial z}(\mathbf{v} \cdot \nabla_h \mathbf{v}) \right| \ll \left| \frac{\partial 2\Omega_z \mathbf{k} \times \mathbf{v}}{\partial z} \right|, \tag{68}$$

it has been shown elsewhere (unpublished), that the necessary and sufficient condition for (66) is:

$$2\Omega_z \frac{\partial \psi}{\partial z} + g \ln \vartheta = k(z, t) \tag{69}$$

where k is independent of the horizontal coordinates.

The second of the three equations is the thermodynamic equation

$$\frac{\partial \ln \vartheta}{\partial t} = -\mathbf{v} \cdot \nabla_h \ln \vartheta - \mathbf{v}_\alpha \cdot \nabla \ln \vartheta + Q \tag{70}$$

where Q is proportional to the supply of heat per unit time and mass. Using (67) and including a horizontally constant function in the definition of ψ, elimination of $\ln \vartheta$ between (69), (70) gives:

$$\frac{\partial}{\partial t}\frac{\partial \psi}{\partial z} = -\mathbf{v} \cdot \nabla_h \frac{\partial \psi}{\partial z} - \frac{g}{2\Omega_z}\mathbf{v}_\alpha \cdot \nabla \ln \vartheta + \frac{gQ}{2\Omega_z} \tag{71}$$

The third of the equations is the equation for the vertical component of absolute vorticity $\nabla_h \times \mathbf{v} \cdot \mathbf{k} = \nabla_h^2 \psi$,

$$\frac{\partial}{\partial t}\nabla_h^2 \psi = (\nabla_h^2 \psi)\frac{\partial w}{\partial z} - \mathbf{v}_\alpha \cdot \nabla \nabla_h^2 \psi + (\nabla \times \mathbf{v})_h \cdot$$

$$\cdot \nabla_h w + \nabla_h \times \mathbf{F} \cdot \mathbf{k} - \mathbf{v} \cdot \nabla_h \nabla_h^2 \psi. \tag{72}$$

$\mathbf{F}$ denotes a horizontal frictional force. In the vorticity equation the only non-linear term in $\mathbf{v}_\alpha$ together with the solenoid term have been neglected as presumably small terms. Eliminating $\frac{\partial \psi}{\partial t}$ between eqs. (71), (72) we then obtain

$$L(\mathbf{v}_\alpha) = F \tag{73}$$

where $L(\mathbf{v}_\alpha)$ is a certain linear differential expression of at most second order in the components of $\mathbf{v}_\alpha$, and F a non-homogeneous term which is given by

$$F = \frac{\partial}{\partial z}(\mathbf{v} \cdot \nabla_h \nabla_h^2 \psi) - \nabla_h^2 \left(\mathbf{v} \cdot \nabla_h \frac{\partial \psi}{\partial z} \right) +$$

$$+ \frac{g}{2\Omega_z}\nabla_h^2 Q - \frac{\partial}{\partial z}\nabla_h \times \mathbf{F} \cdot \mathbf{k}$$

The two other equations for the components of $\mathbf{v}_\alpha$ are obtained from the continuity equation and the condition that according to definition $\nabla_h \times \mathbf{v}_\alpha = 0$. This gives respectively

$$\frac{\partial u_\alpha}{\partial x} + \frac{\partial v_\alpha}{\partial y} + \frac{\partial w}{\partial z} = 0 \tag{74}$$

$$\frac{\partial v_\alpha}{\partial x} - \frac{\partial u_\alpha}{\partial y} = 0. \tag{75}$$

The condition that the system (73), (74), (75) above is elliptic can be shown to be given by

$$\left(\frac{\partial \mathbf{v}}{\partial z}\right)^2 < \frac{g \nabla_h^2 \psi}{2\Omega_z} \cdot \frac{\partial \ln \vartheta}{\partial z} \tag{76}$$

This condition is usually satisfied in the atmosphere. With the boundary conditions (65) we must therefore obtain $w \equiv 0$ when $F \equiv 0$. The coefficients in (73), at least in the terms which are the most dominating, are relatively permanent in character as compared to the non-homogeneous term F. The variable conditions for F will therefore be the main factor in creating the variable conditions for the systems of vertical velocities we can have in the atmosphere. We shall now look a little more closely at this non-homogeneous term. Effectuating the differentiation with respect to z it turns out that we can write F on the form

$$F = a_N \left[2(\mathbf{v} - \mathbf{v}^{(N)}) \cdot \nabla_h \frac{\partial \psi}{\partial z} + \frac{2}{a_N} A\left(\psi, \frac{\partial \psi}{\partial z}\right) \right] + \frac{g}{2\Omega_z} \nabla_h^2 Q - \nabla_h \times \frac{\partial \mathbf{F}}{\partial z} \cdot \mathbf{k} \qquad (77)$$

where $^{(N)}$ is defined as in (6) and $A\left(\psi, \frac{\partial \psi}{\partial z}\right)$ is the function $A(\psi, s)$ defined in (47) when we put $\frac{\partial \psi}{\partial z}$ for s. It is an interesting fact that here besides heating and friction, and an advection term $(\mathbf{v} - \mathbf{v}^{(N)}) \cdot \nabla_h \frac{\partial \psi}{\partial z}$, now a term $A\left(\psi, \frac{\partial \psi}{\partial z}\right)$ appears which in accordance with (6) only depends upon the mutual deformation properties of $\mathbf{v}$ and $-\nabla_h \frac{\partial \psi}{\partial z} \times \mathbf{k}$. The relative importance of this and the advection term will be investigated more closely in the following section.

8. The importance of deformation investigated for a simplified baroclinic model

By a partial elimination of u_α, v_α between (73), (74), (75) we obtain the following equation for vertical velocity:

$$(\nabla_h^2 \psi) \frac{\partial^2 w}{\partial z^2} + 2 \frac{\partial u}{\partial z} \frac{\partial^2 w}{\partial y \partial z} - 2 \frac{\partial v}{\partial z} \frac{\partial^2 w}{\partial x \partial z} + \left(g \frac{\partial \ln \vartheta}{\partial z} \Big/ 2\Omega_z \right) \nabla_h^2 w = F \qquad (78)$$

The terms containing the first derivatives of u_α, v_α, w are small if the relative variation in space of the coefficients in (78) are negligible in comparison with the corresponding variations in the first derivatives of $\mathbf{v}_\alpha$, and have been neglected. It is understood that for the components of vertical velocity which have sufficiently large horizontal scales, eq. (78) can under the boundary condition (65) be approximated by

$$2\Omega_z \frac{\partial^2 w}{\partial z^2} = F \qquad (79)$$

When we make the corresponding simplifications in the vorticity equation (72) and in the eq. (71) we obtain

$$\frac{\partial}{\partial t} \nabla_h^2 \psi = -\mathbf{v} \cdot \nabla_h \nabla_h^2 \psi + 2\Omega_z \frac{\partial w}{\partial z} + \nabla_h \times \mathbf{F} \cdot \mathbf{k} \qquad (80)$$

and

$$\frac{\partial}{\partial t} \frac{\partial \psi}{\partial z} = -\mathbf{v} \cdot \nabla_h \frac{\partial \psi}{\partial z} + \frac{g}{2\Omega_z} Q \qquad (81)$$

For the following arguments it does not matter whether we ignore friction and heating, or not. For simplicity we shall therefore put both zero: $\mathbf{F} = 0$; $Q = 0$. Eq. (81) can then also be written

$$\frac{\partial}{\partial t} \frac{\partial \psi}{\partial z} = -\mathbf{v} \cdot \nabla_h \frac{\partial \psi}{\partial z} \qquad (82)$$

Let us next assume that

$$\frac{\partial^2 \psi}{\partial z^2} = 0. \qquad (83)$$

We can then write

$$\psi = \hat{\psi} + \left(\frac{\partial \psi}{\partial z}\right) z; \quad \mathbf{v} = \hat{\mathbf{v}} + \left(\frac{\partial \mathbf{v}}{\partial z}\right) z, \qquad (84)$$

where

$$\hat{\psi} = \psi_{z=0} = \frac{1}{2h} \int_{-h}^{h} \psi dz. \qquad (85)$$

Substituting $\mathbf{v} = \hat{\mathbf{v}} + z \frac{\partial \mathbf{v}}{\partial z}$ in (82) and observing that $\frac{\partial \mathbf{v}}{\partial z} \cdot \nabla_h \frac{\partial \psi}{\partial z} = 0$, we obtain

$$\frac{\partial}{\partial t} \frac{\partial \psi}{\partial z} + \hat{\mathbf{v}} \cdot \nabla_h \frac{\partial \psi}{\partial z} = 0. \qquad (86)$$

Differentiating (86) with respect to height and using (83) we obtain

$$\frac{\partial}{\partial t}\frac{\partial^2 \psi}{\partial z^2} = 0,$$

showing that (83), when once satisfied will also be so at any later time. Substituting from (84) in the terms on the r.h.s. of (79) and recalling that

$$\Lambda\left(z\frac{\partial \psi}{\partial z}, \frac{\partial \psi}{\partial z}\right) = 0$$

in accordance with the definition (47), we obtain

$$2\Omega_z \frac{\partial^2 w}{\partial z^2} = a_N\Big[2\left(\hat{\mathbf{v}} - \hat{\mathbf{v}}^{(N)}\right)\cdot\nabla_h\frac{\partial \psi}{\partial z} + \\ + \frac{2}{a_N}\Lambda\left(\hat{\psi}, \frac{\partial \psi}{\partial z}\right)\Big] + a_N z\left(\frac{\partial \mathbf{v}}{\partial z} - \frac{\partial \mathbf{v}^{(N)}}{\partial z}\right)\cdot\nabla_h\frac{\partial \psi}{\partial z} \tag{87}$$

With the boundary conditions (65) the solution of (87) becomes

$$2\Omega_z w = a_N\Big[2\left(\hat{\mathbf{v}} - \hat{\mathbf{v}}^{(N)}\right)\cdot\nabla_h\frac{\partial \psi}{\partial z} + \\ + \frac{2}{a_N}\Lambda\left(\hat{\psi}, \frac{\partial \psi}{\partial z}\right)\Big]\frac{1}{2}(z^2 - h^2) + a_N\left(\frac{\partial \mathbf{v}}{\partial z} - \frac{\partial \mathbf{v}^{(N)}}{\partial z}\right)\cdot \\ \cdot\nabla_h\frac{\partial \psi}{\partial z}\frac{1}{6}(z^2 - h^2)\,z \tag{88}$$

This solution will now be used in order to find an expression for the increase in total "volume" kinetic energy. Ignoring friction we may in accordance with a result obtained by Fjørtoft (6) write

$$\frac{d}{dt}\int_\tau \frac{1}{2}\mathbf{v}_3^2 d\tau = \int_\tau g \ln\vartheta w d\tau$$

Substituting here for $\ln\vartheta$ from the balance condition (69) obtained from (66) we also obtain

$$\frac{d}{dt}\int_\tau \frac{1}{2}\mathbf{v}_3^2 d\tau = \frac{d}{dt}\int_\tau \frac{1}{2}\mathbf{v}^2 d\tau = \int_\tau \frac{\partial \psi}{\partial z} 2\Omega_z w d\tau,$$

since because of the continuity equation (64) and the boundary conditions (65)

$$\int_\tau k(z,t) w d\tau = 0$$

Substituting for $2\Omega_z w$ the solution (88), the antisymmetrical part of the solution falls out under the integration and we are left with the equation

$$\frac{d}{dt}\int_\tau \frac{1}{2}\mathbf{v}^2 d\tau = \Big[-\int_\tau 2\frac{\partial \psi}{\partial z}\Lambda\left(\hat{\psi}, \frac{\partial \psi}{\partial z}\right)\partial\tau - \\ - \int_\tau \frac{\partial \psi}{\partial z}\left(\hat{\mathbf{v}} - \hat{\mathbf{v}}^{(N)}\right)\cdot\nabla_h\frac{\partial \psi}{\partial z}\,d\tau\Big]\frac{h^2}{3}$$

However, using (50) this equation reduces to

$$\frac{d}{dt}\int_\tau \frac{1}{2}\mathbf{v}^2 d\tau = -\frac{2}{3}\int_\tau \psi_T \Lambda\left(\hat{\psi}, \psi_T\right) d\tau \tag{89}$$

having for convenience introduced the quantity ψ_T defined from

$$\psi_T = h\frac{\partial \psi}{\partial z}. \tag{90}$$

Recalling now the definition of $\Lambda(\psi, s)$, we have obtained the result that changes in the total kinetic energy in our model depend entirely upon the mutual deformation properties of the velocity field $\hat{\mathbf{v}} = -\nabla_h\hat{\psi}\times\mathbf{k}$ and the "thermal" wind field $\mathbf{v}_T = -\nabla_h\psi_T\times\mathbf{k}$.

After multiplication by h eq. (86) can be written

$$\frac{D\psi_T}{dt} = 0; \quad \frac{D}{dt} = \frac{\partial}{\partial t} + \hat{\mathbf{v}}\cdot\nabla_h. \tag{91}$$

In agreement with (53) we now get

$$\frac{d}{dt}\int_\tau \frac{1}{2}\mathbf{v}_T^2 d\tau = -\int_\tau \psi_T \Lambda\left(\hat{\psi}, \psi_T\right) d\tau. \tag{92}$$

Eq. (89) can therefore also be written

$$\frac{d}{dt}\int_\tau \frac{1}{2}\mathbf{v}^2 d\tau = \frac{2}{3}\frac{d}{dt}\int_\tau \frac{1}{2}\mathbf{v}_T^2 d\tau. \tag{93}$$

There is accordingly in the absence of friction and heating direct proportionality between the increase in total kinetic energy and total energy in the thermal wind field. We may now also take over the other results of section 5, thus giving:

(a) The total thermal wind energy and hence also the total kinetic energy increases or decreases in the absence of friction and heating according as the lengths of the isolines $\psi_T =$ = const, essentially the horizontal isotherms, are on an average either increased or decreased.

(b) The total thermal wind energy, and hence also the total kinetic energy, increases or decreases in the absence of friction and heating according as there is a net flow of amplitude $(\psi_T)_q^2$ to either lower or higher wavelengths.

Substituting from (84) $\mathbf{v} = \hat{\mathbf{v}} + z\frac{\partial \mathbf{v}}{\partial z}$ in $\int_\tau \frac{1}{2}\mathbf{v}^2 d\tau$ we obtain

$$\frac{d}{dt}\int_\tau \frac{1}{2}\mathbf{v}^2 d\tau = \frac{d}{dt}\int_\tau \frac{1}{2}\hat{\mathbf{v}} d\tau + \frac{1}{3}\frac{d}{dt}\int_\tau \frac{1}{2}\mathbf{v}_T^2 d\tau \quad (94)$$

By elimination of $\frac{d}{dt}\int_\tau \frac{1}{2}\mathbf{v}^2 d\tau$ between (93), (94) we get

$$\frac{d}{dt}\int_\tau \frac{1}{2}\hat{\mathbf{v}}^2 d\tau = \frac{1}{3}\frac{d}{dt}\int_\tau \frac{1}{2}\mathbf{v}_T^2 d\tau. \quad (95)$$

All what was said above for the total kinetic energy is therefore also valid for the kinetic energy of the vertically mean flow.

According to (b) above an increase in the total kinetic energy necessarily is connected with a decrease in thermal wind kinetic energy on the larger scales. Whether actually the total kinetic energy also shall decrease on the same scales will, however, according to (94) also depend upon in which direction and with what magnitude the kinetic energy of the vertically mean flow changes on these scales. The results above do, however, only give a clue to an understanding of the conditions for the changes in the *total* kinetic energy, and the *total* kinetic energy of the vertically mean flow, and not of the nature of the changes in their spectral distribution.

9. On the possible importance of non-linear interference for the understanding of the creation and geographical distribution of disturbances

Let now $\hat{\psi}^{(N)\ldots(N-p)}$ and $\psi_T^{(N)\ldots(N-p)}$ denote repeatedly smoothed fields. We do then know that neither of these fields contain components with wavenumbers above $N-p-1$. The function $A(\psi^{(N)\ldots(N-p)}, \psi_T^{(N)\ldots(N-p)})$ however, may by interference contain "energy" on wavenumbers which are excluded in the smoothed fields. The distribution of the bulk of energy in these higher components must essentially depend upon the mutual deformation properties of the smoothed $\hat{\mathbf{v}}$ – and $\mathbf{v}_T$-fields. The author of this article has some experience in forecasting on the basis of initially smoothed fields. It has repeatedly turned out as a result of the displacements of the ψ_T-isolines, that the field ψ_T, though smoothed initially, ends up with "energy" on smaller scales, the bulk of which has a typical distribution relative to the smoothed fields. These smaller scale phenomena which thus enter the picture, are generally also verified. While we will return to this in the practical examples to be brought in the second part of this paper, we shall here study the same phenomenon by investigating the function $A(\hat{\psi}, \psi_T)$ for the normal maps of November. Using the ordinary geostrophic approximation $\psi = \frac{gZ}{2\Omega_z}$, where Z denotes the height of a pressure surface we may write

$$A(\hat{\psi}, \psi_T) = k_1 \cdot A(Z_0, Z_7 - Z_0)$$

and

$$\int_\tau \psi_T A(\hat{\psi}, \psi_T) d_\tau =$$

$$= k_2 \int_F (Z_7 - Z_0)\, A(Z_0, Z_7 - Z_0)\, dF$$

where k_1, k_2 are certain positive proportionality factors. Here, Z_0, Z_7 denote the normal heights of the 1,000 mb and 700 mb surfaces, respectively, smoothed so as to give zero energy on wavelengths below approximately 5,000 km. In fig. 3 the function $A(Z_0, Z_7 - Z_0)$ is illustrated together with the normal, smoothed thickness field $Z_7 - Z_0$. It is clearly seen that the integral above will obtain a negative value when F is taken as the area represented on the map. According to the results of the preceding section we can therefore conclude that the normal fields of essentially pressure and temperature are such as to give a flow of "energy" in the horizontal temperature field towards the high-frequency end of the spectrum, thereby increasing the total kinetic energy.

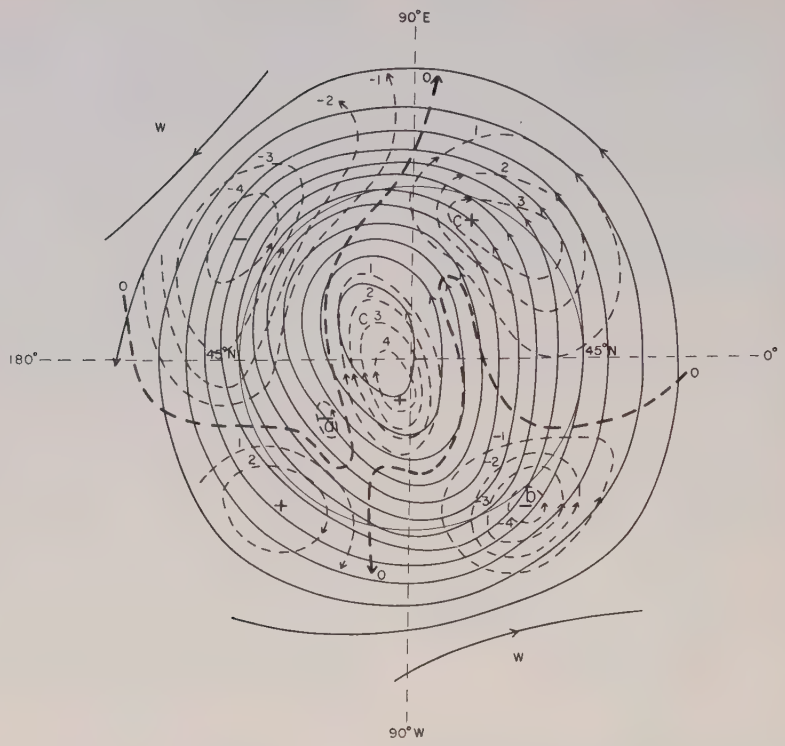

Fig. 3. Spacely smoothed normal 700—1000 mb thickness field (full lines) together with the field of A (Z_0, $Z_7 - Z_0$) (broken lines).

In fig. 4 we have drawn the component A' of $A(Z_0, Z_7 - Z_0)$ which only have energy on the scales which were discluded in the fields Z_0 and $Z_7 - Z_0$ themselves.

Much remarkably the field of A' consists of three pairs of centers centered around localities which coincide rather closely with the three main centers of mean diurnal variability of the height of the 500 mb surface found by Nyberg (1949) for the single month of November 1947.

The above investigations indicate that the phenomena of non-linear interference in the above sense may have a bearing on our understanding of the creation and local distribution of disturbances and is now being taken up for systematical study.

10. The integration problem

When we treated the integration problem for barotropic motion we developed methods which clearly represented an advantage when we undertook to find the displacements of the fluid particles. When we are now turning to the integration problem for baroclinic flows our main problem will be to investigate how much of these advantages, if anything, can be maintained. The following is not a complete treatment of this problem. The general baroclinic problem is so difficult that it is best to start with simple models. It is thought however, that even these will reveal the most fundamental features of baroclinic flows, and that the manner in which we are going to treat the integration problem may be rather typical for more general models.

It is an explainable fact that the barotropic model applies best to the vertically mean flow represented approximately by the horizontal flow between the 500 mb and 600 mb surfaces, while the flows in greater distances above and below certainly are very little barotropic. It is therefore natural to direct the attention at first to the vertically mean flow where the results obtained for barotropic flow must be expected to be least altered.

Maintaining the assumption (83) and averaging the vorticity equation (80) in the vertical, we obtain

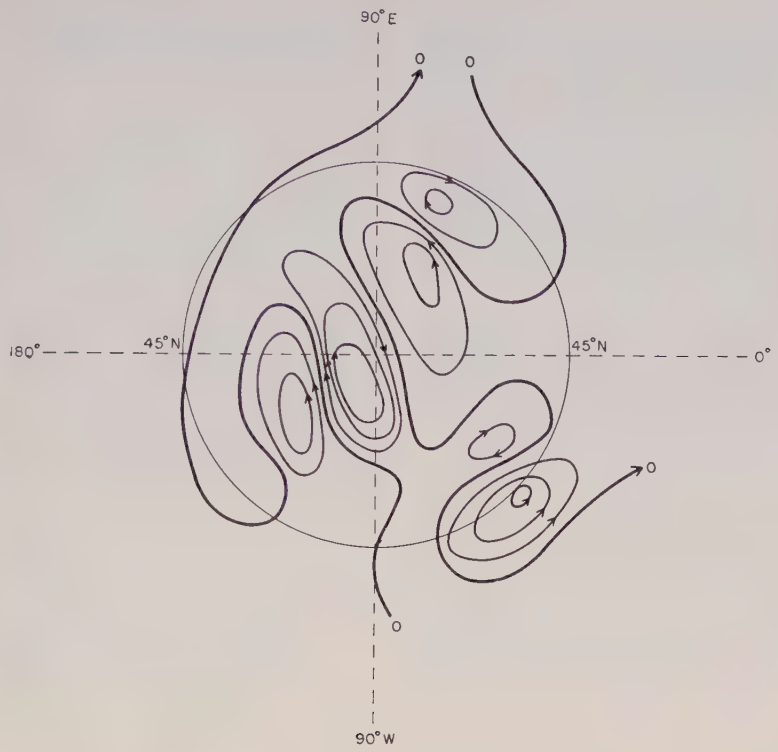

Fig. 4. The field of A' defined in section 9.

$$\frac{\partial}{\partial t}\nabla_h^2\hat{\psi} + \hat{\mathbf{v}}\cdot\nabla_h\cdot\nabla_h^2\hat{\psi} = H \qquad (96)$$

where

$$H = -\frac{1}{3}\mathbf{v}_T\cdot\nabla_h\nabla_h^2\psi_T. \qquad (97)$$

For an illustration of the integration methods we shall at first make the advective assumption (91):

$$\frac{D\psi_T}{dt} = 0. \qquad (91)$$

If, now $\mathbf{r}_0$ denotes the position vectors at time $t = 0$ for particles moving with the velocities $\hat{\mathbf{v}}$, we may use $\mathbf{r}_0$ to define the Lagrangian particle variables in contrast to $\mathbf{r}$ which has been used to define the coordinates of position on the horizontal surfaces. Eq. (96) may then be written in Lagrangian coordinates as

$$\frac{\partial}{\partial t}\nabla_h^2\psi(\mathbf{r}_0, t) = H(\mathbf{r}_0, t) \qquad (98)$$

and in Eulerian variables as

$$\frac{\partial}{\partial t}\nabla_h^2\psi(\mathbf{r}, t) = -\hat{\mathbf{v}}\cdot\nabla_h\nabla_h^2\hat{\psi} + H(\mathbf{r}, t) \equiv I(\mathbf{r}, t). \qquad (99)$$

Let us assume that

$$\left|\frac{\partial}{\partial t}H(\mathbf{r}_0, t)\right| \ll \left|\frac{\partial I(\mathbf{r}, t)}{\partial t}\right|. \qquad (100)$$

If now $(\Delta t)_0$ and Δt denote the maximum grid distances in time which can be used for a numerical description of $H(\mathbf{r}_0, t)$ and $I(\mathbf{r}, t)$, respectively, we could take $(\Delta t)_0 \geqslant \Delta t$ if (100) were true. This would so far be an advantage in the numerical work of integration. However, to get a prognosis based on (98) we must also know where the individual particles move in the course of time, a problem which does not arise in (99). If it should now happen that in order to find the displacements $\mathbf{p}(\mathbf{r}_0, t)$, iterative operations of some nature were required with a maximum iteration period T

which could not be taken larger than Δt, then there would certainly be no advantage in using a Lagrangian method. If, however, on the contrary $T > \Delta t$, then under the assumption (100), and provided the operations involved in finding $\mathbf{p}(\mathbf{r}_0, t)$ are not too complicated, there would be an advantage in using (98), because the number of iterations required for a forecast over a certain period would be less than the one required if we used (99).

In the *barotropic* case where $H = \text{const} = 0$, there is no upper limit to $(\Delta t)_0$. Further, it has been shown in this article that it is possible to find in a relatively simple manner the displacements $\mathbf{p}(\mathbf{r}_0, t)$ using an iteration period $T \simeq 24$—28 hours. Since now Δt cannot be taken larger than between 1—2 hours because of the rapidity with which $-\mathbf{v} \cdot \nabla_h \nabla_h^2 \psi$ changes in the atmosphere, there would in fact be an advantage in using a Lagrangian numerical method in the barotropic case.

In the *baroclinic* case $I(\mathbf{r}, t) = -\mathbf{v} \cdot \nabla_h \nabla_h^2 \psi + H(\mathbf{r}, t)$. Since there is no general tendency in the atmosphere for a compensation between these two terms, and further because as a matter of observation

$$\left| \frac{\partial H(\mathbf{r}_0, t)}{\partial t} \right| \leqslant \left| \frac{\partial H(\mathbf{r}, t)}{\partial t} \right|,$$

the assumption (100) would certainly also be fulfilled in the baroclinic case. Recalling that

$$\frac{D}{dt} \nabla_h^2 \psi = \frac{D^N}{dt} \nabla_h^2 \psi$$

and letting $\mathbf{r}_0^N$ denote Lagrangian particle variables for the smoothed motion, (98) can also be written

$$\frac{\partial}{\partial t} \nabla_h^2 \psi(\mathbf{r}_0^N, t) = H(\mathbf{r}_0^N, t) \qquad (101)$$

It is an observational fact that generally

$$\left| \frac{\partial H(\mathbf{r}_0^N, t)}{\partial t} \right| < \left| \frac{\partial H(\mathbf{r}_0, t)}{\partial t} \right|.$$

It will therefore also fror this reason be an advantage to connect the integration problem with (101). Suppose now that T' represents the maximum grid distance in time which can be used for a numerical description of $H(\mathbf{r}_0^N, t)$. This means that for particles moving in the smoothed motion we may consider H an approximate constant for $t \leqq T'$

$$\frac{D^N H}{dt} = 0; \quad t \leq T'. \qquad (102)$$

In order to utilize (101) we must now be able to find the trajectories in the smoothed flow, and next H as a function of time. Since H is determined when we know ψ_T, and ψ_T is found in accordance with (91) when we know the displacements together with the initial conditions, we are left therefore essentially with a displacement problem.

A relatively simple displacement rule can be found by considering the system (36), (96), and (102), dividing the latter equations by $-a_N$:

$$\begin{aligned} \hat{\psi} &= \hat{\psi}^{(N)} - \frac{\nabla_h^2 \psi}{a_N} \\ \frac{D}{dt}\left(-\frac{\nabla_h^2 \psi}{a_N} \right) &= -\frac{H}{a_N} \qquad (103) \\ \frac{D^N H}{dt} &= 0. \quad t \leqq T'. \end{aligned}$$

On the basis of this system the following rule can now be proved which is an extension to the baroclinic case of the rule (38):

To find the displacements up to a time $t' \leq T'$, we may at first displace in the velocity field with the streamfunction

$$-\left(\frac{\nabla_h^2 \psi}{a_N}\right)_{t=0} - \left(\frac{H_{t=0}}{a_N}\right) t, \qquad (104)$$

and then add from the resulting positions the displacements in the smoothed flow.

It is seen that the only difference from the barotropic displacement rule (38) is that the first displacements must be carried out in a field which has got the additional non-stationary component $-(H_{t=0}/a_N)t$. However, because this field maintains its form and also possesses a simple dependency on time, the displacement will not be difficult to carry out. In most cases it will be sufficient to displace in the stationary field

$$-\left(\frac{\nabla_h^2\psi}{a_N}\right)_{t=0}-\left(\frac{H_{t=0}}{a_N}\right)\frac{t'}{2}$$

because in most cases $(H_{t=0}/a_N)t'$ will be relatively weak in comparison to $-\nabla_h^2\psi_{t=0}/a_N$.

Again we should remember that the results depend upon the choice of a_N. For if a_N is very large the smoothed flow $\mathbf{v}^{(N)}$ wont be very much different from the actual flow $\mathbf{v}$ in the range of wavelengths containing most of the energy. Then $\mathbf{v}^{(N)}$ would be practically as much time-variable as $\mathbf{v}$, and we could accordingly not displace in the smoothed flow $\mathbf{v}^{(N)}_{t=0}$ much longer than we could have done in the actual flow $\mathbf{v}_{t=0}$. By the proper chcise of a_N, however, the time scale of $\mathbf{v}^{(N)}$ becomes such that we can put as an approximation

$$\mathbf{v}^{(N)}=\mathbf{v}^{(N)}_{t=0};\quad t\leq 24\,\text{hours.},\qquad (39)$$

like we did in the barotropic case.

To make a prognosis for the period T' in accordance with what has been outlined above we proceed now in theory as follows.

Using the displacement rule (104) we displace the "thickness"-lines $(\psi_T)_{t=0}=\text{const}$ to find $\psi_T(\mathbf{r}, T')$. This gives us also $H(\mathbf{r}_0^N, T')$. Thereafter, we find

$$\nabla_h^2\hat{\psi}(\mathbf{r}_0^N, T')=\nabla_h^2\hat{\psi}(\mathbf{r}_0^N, 0)+\left[H(\mathbf{r}_0^N, 0)+\right.$$
$$\left.+H(\mathbf{r}_0^N, T')\right]\frac{T'}{2}$$

Knowing the displacements in the smoothed flow we then also know the distribution $\nabla_h^2\hat{\psi}(\mathbf{r}, T')$, say $=F(\mathbf{r}, T')$. By a solution of

$$\nabla_h^2\hat{\psi}(\mathbf{r}, T')=F(\mathbf{r}, T')$$

we find $\hat{\psi}(\mathbf{r}, T')$. The flow in any other level will be determined from

$$\psi=\hat{\psi}+\frac{z}{h}\psi_T.$$

11. A simple non-advective model

If we also include the convection term in the thermodynamic equation it becomes

$$\frac{\partial}{\partial t}\frac{\partial\psi}{\partial z}=-\hat{\mathbf{v}}\cdot\nabla_h\frac{\partial\psi}{\partial z}-\frac{g}{2\Omega_z}\frac{\partial\ln\vartheta}{\partial z}w\qquad (105)$$

An equation for vertical velocity is now obtained from an elimination between (80) and (105), giving

$$2\Omega_z\frac{\partial^2 w}{\partial z^2}+\frac{g}{2\Omega_z}\frac{\partial\ln\vartheta}{\partial z}\nabla_h^2 w=F.\qquad (106)$$

We shall now make use of the assumption (83). The deviations from a linear distribution with height for ψ which now necessarily must develop because of the inclusion of the convective term in (105) will be supposed to be small enough to justify the use we shall make of (83) below. In this connection we should mention that in a so-called two-parametric model where the solution for ψ is obtained by linear interpolation between the values of ψ in two distinct levels, (83) is by assumption automatically satisfied.

Using (83), the vertically averaged vorticity equation (96) will be unchanged. However, the deviations from a linear distribution with height of velocity makes it natural to define ψ_T as

$$\psi_T=\frac{1}{2}(\psi_{z=h}-\psi_{z=-h})$$

The equation for ψ_T is obtained by integrating(105) from $z=-h$ to $z=h$ and divide by 2. Using (83) we obtain then:

$$\frac{D\psi_T}{dt}=-\frac{g}{2\Omega_z}\frac{\partial\ln\vartheta}{\partial z}\int_{-h}^{h}\frac{1}{2}w\,dz.\qquad (107)$$

Smoothing eq. (105) on both sides we obtain in accordance with (48) and (83):

$$\frac{D}{dt}\left(\frac{\partial\psi}{\partial z}\right)^{(N)}=\left(\hat{\mathbf{v}}-\hat{\mathbf{v}}^{(N)}\right)\cdot\nabla_h\frac{\partial\psi}{\partial z}+$$
$$\frac{2}{a_N}A\left(\hat{\psi},\frac{\partial\psi}{\partial z}\right)-\frac{g}{2\Omega_z}\frac{\partial\ln\vartheta}{\partial z}w^{(N)}.\qquad (108)$$

Substituting in (106) $\nabla_h^2 w=a_N(w^{(N)}-w)$ and the expression (87) for F this equation can also be written:

$$2\Omega_z\frac{\partial^2 w}{\partial z^2}-\frac{ga_N}{2\Omega_z}\frac{\partial\ln\vartheta}{\partial z}w=a_N\left[2\left(\hat{\mathbf{v}}-\hat{\mathbf{v}}^{(N)}\right)\cdot\right.$$
$$\left.\cdot\nabla_h\frac{\partial\psi}{\partial z}+\frac{2}{a_N}A\left(\hat{\psi},\frac{\partial\psi}{\partial z}\right)\right]-\frac{ga_N}{2\Omega_z}\frac{\partial\ln\vartheta}{\partial z}w^{(N)}+$$
$$+a_N z\left(\frac{\partial\mathbf{v}}{\partial z}-\frac{\partial\mathbf{v}^{(N)}}{\partial z}\right)\cdot\nabla_h\frac{\partial\psi}{\partial z}.\qquad (109)$$

Eliminating $w^{(N)}$ between (109) and (108), we obtain

$$2\Omega_z \frac{\partial^2 w}{\partial z^2} - \frac{g a_N}{2\Omega_z} \frac{\partial \ln \vartheta}{\partial z} w = a_N \left(\hat{\mathbf{v}} - \hat{\mathbf{v}}^{(N)}\right) \cdot$$

$$\cdot \nabla_h \frac{\partial \psi}{\partial z} + a_N \frac{D}{Dt}\left(\frac{\partial \psi}{\partial z}\right)^{(N)} + a_N z \left(\frac{\partial \mathbf{v}}{\partial z} - \frac{\partial \mathbf{v}^{(N)}}{\partial z}\right) \cdot$$

$$\cdot \nabla_h \frac{\partial \psi}{\partial z}. \qquad (110)$$

This equation is now solved under the earlier mentioned assumption that $\frac{\partial}{\partial t}\frac{\partial \psi^{(N)}}{\partial z}$ and hence $\frac{D}{dt}\frac{\partial \psi^{(N)}}{\partial z}$ may be considered as approximately independent of height.

If next the solution is introduced into (107), the unsymmetrical part of the solution falls out under the integration and we are left with

$$\frac{D\psi_T}{dt} = k_N \left(\hat{\mathbf{v}} - \hat{\mathbf{v}}^{(N)}\right) \cdot \nabla_h \psi_T + k_N \frac{D\psi_T^{(N)}}{dt} \qquad (111)$$

where

$$k_N = \left[1 - \frac{Tg\lambda}{\lambda}\right]; \quad \lambda^2 = \frac{h^2 a_N g}{4\Omega_z^2} \frac{\partial \ln \vartheta}{\partial z}. \qquad (112)$$

Assuming an average constant value for $\frac{h^2}{4\Omega_z^2}\frac{\partial \ln \vartheta}{\partial z}$, k_N becomes for the proper choice of N equal to one half:

$$k_N = \frac{1}{2} \text{ for the proper choice of } N.$$

Under these assumptions it is easy to show that eq. (111) can be written

$$\frac{D^N}{dt}\left(\psi_T - \frac{1}{2}\psi_T^{(N)}\right) = -\frac{1}{2}\left(\hat{\mathbf{v}} - \hat{\mathbf{v}}^{(N)}\right) \cdot$$

$$\cdot \nabla_h \left(\psi_T - \psi_T^{(N)}\right). \qquad (113)$$

Here the source term on the r.h.s. is according to its nature under most circumstances negligible in its effect on the prognosis of the thickness lines and may be neglected with good approximation:

$$\frac{D^N}{dt}\left(\psi_T - \frac{1}{2}\psi_T^{(N)}\right) = 0. \qquad (114)$$

Accordingly the quantity $\psi_T - \frac{1}{2}\psi_T^{(N)}$ may be considered conserved in the smoothed motion $\psi^{(N)}$ when N is given the proper value. Experiments have shown that eq. (114) has proved useful in overcoming in a simple way the main errors in the thickness forecasts caused by the advective assumption.

12. The trajectory problem for levels other than the vertically mean level

This problem can be treated with success by means of the theorem (35). We shall illustrate this for the advective model. The streamfunction in an arbitrary level is $\psi = \hat{\psi} + (z/h)\psi_T$. We have therefore the system

$$\psi = \hat{\psi} + (z/h)\psi_T$$

$$\frac{D}{dt}\left(\frac{z}{h}\psi_T\right) = 0; \quad \frac{D\psi}{dt} \equiv \frac{\partial}{\partial t} + \mathbf{v} \cdot \nabla_h. \qquad (115)$$

According to the theorem (35) we may therefore find the displacements in an arbitrary level by at first displacing in the stationary field $(z/h)(\psi_T)_{t=0}$, and then add the displacements in the motion in the mean level which can be found by means of any of the earlier rules.

LIST OF REFERENCES

Charney, J. G., 1948: On the scale of atmospheric motions. Geofysiske Publikasjoner. Vol. XVII No. 3.

Eliassen, A., 1948: The quasi-static equations of motion with pressure as independent variable. Geofysiske Publikasjoner. Vol. XVII. No. 4.

Fjørtoft, R., 1951: Stability properties of large-scale atmospheric disturbances. Compendium of Meteorology.

Fjørtoft, R., 1952: On a numerical method of integrating the barotropic vorticity equation. *Tellus*, **4**, 3.

Nyberg, A., 1949: An aerological study of large-scale atmospheric disturbances. *Tellus*, **1**, 1.

Richardson, L. F., 1922: The approximate arithmetical solution by finite differences of physical problems involving differential equations, with an application to the stresses in a masonry dam. *Phil. Trans. roy. Soc.* London, A, **210**, 307—357.

Physical Aspects of Rapid Cyclogenesis in the Gulf of Alaska

By JAY S. WINSTON, Extended Forecast Section, U.S. Weather Bureau, Washington, D.C.

(Manuscript received October 5, 1954)

Abstract

The Gulf of Alaska is often the site of rapid development of large-scale cyclonic activity which can have profound effects on the long-wave pattern over North America in a matter of 24 to 48 hours. During much of the year such cyclogenesis takes place in the presence of a large heat source associated with rapid modification of cold Arctic air masses moving from Alaska out over the warmer sea surface of the Gulf. In order to get some insight into the mechanism of cyclogenesis under these special conditions a case of intense development occurring early in February 1950 has been studied, mainly in terms of the vorticity equation. The effects of barotropic redistribution of vorticity seem to account for much of the development. However, it is found that there exist pronounced fields of divergence and vertical motion, which particularly at the time of most rapid development reflect the influence of heat sources on the circulation.

1. Introduction

The Gulf of Alaska is frequently the site of rapid development of intense cyclonic activity. Much of this cyclogenesis occurs on such a large scale that the basic planetary wave pattern is often radically altered in a few days, especially downstream over North America and the Atlantic. The synoptic aspects of a frequent type of trough development in the Gulf of Alaska and its importance in changing the long-wave pattern over broad areas of the Northern Hemisphere were recognized at an early stage in extended forecasting practice (NAMIAS and CLAPP, 1944). Namias has attributed this type of trough intensification in the area to the rapid modification of cold Arctic air masses which are advected over the open water surface of the Gulf in the northerly flow to the east of a ridge situated over the Bering Sea or the northeast Siberian peninsula. The rapid addition of heat and moisture to the frigid air striking the relatively warm waters of the Gulf was postulated to lead to widespread, organized convection and horizontal convergence, thereby creating sufficient cyclonic vorticity to produce a deep trough. However, this sequence of events depends on the initial establishment of the upstream ridge and the associated northerly current to its east which directs the flow of Arctic air over the Gulf. Since this ridge frequently appears to be formed by the barotropic redistribution of absolute vorticity, it is likely that barotropic effects are also influential in cyclogenesis in the Gulf of Alaska.

These qualitative considerations give some ideas about the physical processes at work in such cyclogenesis, and indeed these concepts have been extremely useful in making many successful medium- and long-range forecasts. However, knowledge of the influence of heat sources on changes in circulation is at best extremely limited, and the quantitative determination of these effects, especially in relation to other dynamic processes, is still in its early stages. Recently SMAGORINSKY (1953) calculated the dynamical influence of large-scale heat sources on the steady-state mean motions and found that these account for some of the gross features of the monthly normal circula-

tion patterns at sea level and in mid-troposphere. Also, recent attempts to make numerical predictions for medium-range time periods have included some indirect estimates of the influence of heat sources (CLAPP, 1953). The effects of non-adiabatic heating have been virtually neglected, however, in short-range prediction methods. For example, SUTCLIFFE (1947) made the adiabatic assumption in order to simplify the use of thickness patterns for prediction of development arising from the baroclinic nature of the atmosphere. Even in the increasingly complex numerical prediction models heating effects have not as yet been incorporated although it has been suggested that they may be taken into account without serious numerical complication (cf., CHARNEY and PHILLIPS, 1953). In those cases which have thus far been subjected to numerical calculation the adiabatic assumption has apparently proved to be satisfactory since some rather good predictions of severe storm developments have been made. Up to now, however, there is little evidence that the application of adiabatic models can be markedly successful in cases of explosive cyclogenesis where large heat sources are involved, as in the Gulf of Alaska.

The main reason for the neglect of heat sources in quantitative methods of prediction stems from the woeful lack of precise knowledge of heating at any given time. In evaluating turbulent transfer of heat from a warmer water surface to colder air (the process which is presumably most important in the Gulf of Alaska) one might attempt to use the type of equation employed by JACOBS (1951), which depends on an assumed heat exchange coefficient and the temperature difference between sea and air. But there is generally insufficient information about these quantities to attempt to compute heating on a day-to-day synoptic basis thereby. As an alternative, heating can probably be calculated to a reasonably good approximation from the three-dimensional field of motion itself, but unless vertical motion can be computed independently of the vorticity and energy equations the consideration of heat sources in a numerical prediction scheme is immediately precluded. Obviously this poses a knotty problem.

Nevertheless before delving into such difficult questions it is desirable to learn more about how heat sources influence circulation changes and just how important these effects are. The Gulf of Alaska region in the cold season provides a good testing ground in that heat sources are large and cyclonic development is often quite explosive. If heating is of importance then surely its effects should be apparent on circulation developments in this locale. In order to get some further insight then into the mechanism of development associated with a large heat source, a case of intense cyclonic development in early February 1950 was chosen for detailed study. The quantitative approach in this work concentrates mainly on the vorticity equation, because of its usefulness in numerical prediction work and its ready adaptability to the geostrophic approximation, a practical necessity with the data available over the Gulf of Alaska region.

2. Broad-scale features of cyclogenesis

The broad-scale circulation changes associated with intense cyclonic development over the Gulf of Alaska in early February 1950 are portrayed clearly by the series of 5-day mean 700-mb charts at one-half week intervals shown in Fig. 1. Note how the Gulf of Alaska trough developed in conjunction with the retrogression to the central Aleutians and the Bering Sea of a large ridge originally in the eastern Aleutians. This resulted in northerly flow of cold air over the Gulf of Alaska. The trough in the Gulf of Alaska was essentially a new perturbation since the initial broad northerly flow east of the large ridge split into two by the period, February 1—5, while the subpolar low over eastern Canada maintained and moved eastward. In other words, the downstream half wave length between ridge and trough was shortened in a discontinous fashion as the Gulf of Alaska trough developed. Farther south over the United States similar radical changes in circulation took place. Prior to Gulf of Alaska trough development a broad cyclonic flow, associated with the trough extending southwestward from the Canadian low, dominated western and central sections of the United States with attendant storminess and cold weather in the west. With the establishment of the trough extending southward from the Gulf of Alaska heights rose rapidly, anticyclonic circulation developed, and consequently more moderate weather set in over the western United States. Such substantial adjust-

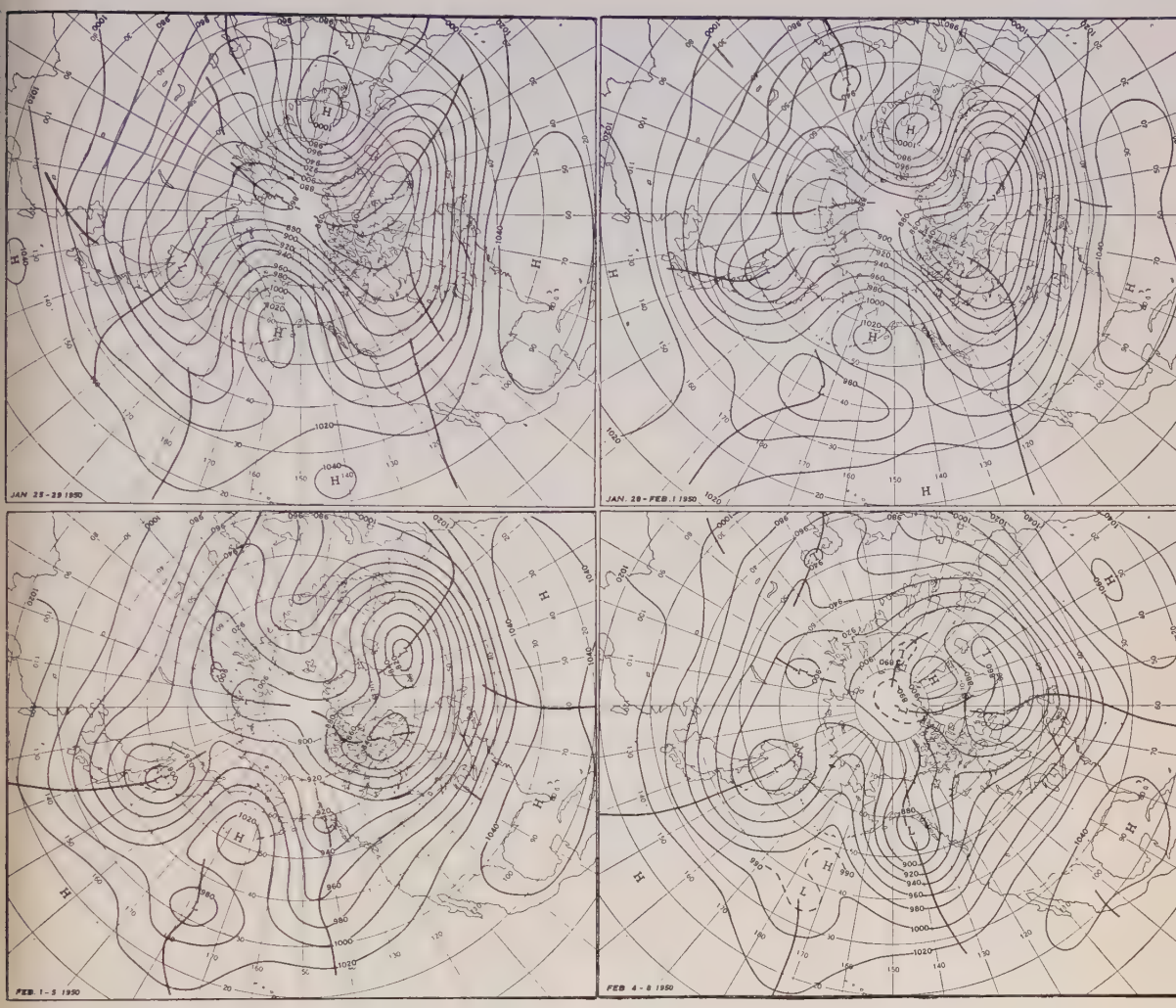

Fig. 1. Series of 5-day mean 700-mb charts illustrating large-scale aspects of strong cyclonic development in the Gulf of Alaska. Charts are at twice-weekly intervals beginning with period January 25—29, 1950. Trough lines are indicated by heavy solid lines; contours in tens of geopotential feet.

ments in circulation over North America are rather typical following rapid cyclogenesis over the Gulf of Alaska.

It has already been pointed out that trough development in this case was apparently dependent upon retrogression of the ridge over the Aleutians and the Bering Sea. The westward motion of this ridge in turn appears to be related to at least two other developments in the western and central Pacific which are evident in Fig. 1. One was the intensifying southerly flow in the vicinity of Kamchatka beginning in the period January 28—February 1 as compared with January 25—29. The other was the closed low in the central Pacific at lower latitudes which was most intense in the period January 28—February 1. Qualitatively it appears that barotropic vorticity flux from both the broad southeasterly current north of this closed low and the increasing southerly current east of Japan played a major role in the retrogression of the ridge over the Bering Sea, and consequently in the subsequent development of the Gulf of Alaska trough.

The sequence of events following the establishment of strong southerly flow at a longitude farther west than previously in the western Pacific is portrayed somewhat more clearly by a time-longitude chart (Fig. 2). This chart shows the variation of meridional components of the 5-day mean geostrophic wind at 700 mb along

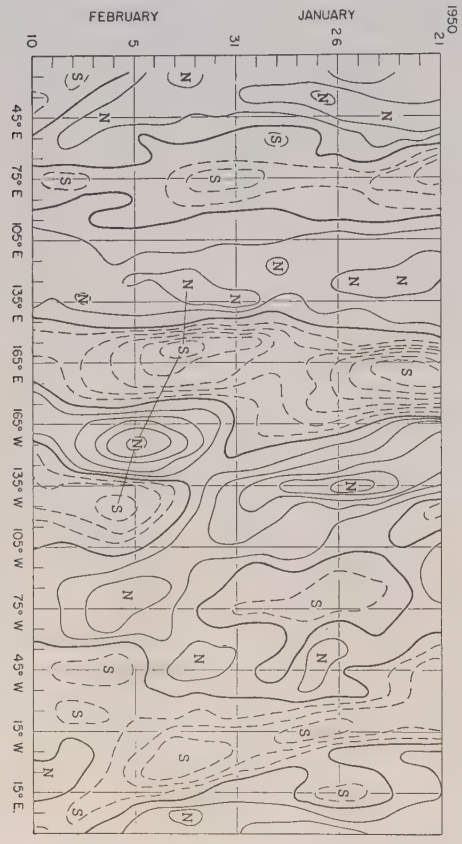

Fig. 2. Time-longitude chart of meridional components of 5-day mean geostrophic wind at 700 mb along the 50°N latitude circle. Isopleths of constant wind speed are drawn at intervals of 100 feet of height difference over 10° of longitude (i.e., approximately at intervals of 3.7 m/sec) with dashed lines showing southerly flow and solid lines northerly flow. Dark solid lines represent zero values of meridional flow and generally mark positions of troughs and ridges.

the 50° N latitude circle. Isopleths of constant wind speed were drawn at intervals of 100 feet of height difference over 10° of longitude (i.e., approximately at intervals of 3.7 m/sec). Five-day mean values centered one day apart were used in Fig. 2 so that the continuity of meridional flow components could be clearly established.

Of primary interest in Fig. 2 is the establishment of a new axis of southerly flow about January 30 near longitude 155° E, some 20° of longitude west of the intense southerly stream which existed from January 21 to 26. This southerly flow reached a maximum between February 2 and 3 and was subsequently followed by a maximum of northerly flow in the Gulf of Alaska (155° W) on February 5 and a maximum of southerly flow on February 6 at 125° W. This downstream progression of increasing meridional flow is similar to many other cases of what has been described as dispersion of energy through the planetary wave train at the speed of the group velocity. A clearcut case of such energy dispersion was recently treated by Carlin (1953), Basically this phenomenon is but another way of considering the adjustments in the contour pattern associated with barotropic flux of absolute vorticity. It is apparent that from the large-scale point of view, as expressed by 5-day mean data, barotropic influences of previous developments in the upstream wave train were of considerable significance in the Gulf of Alaska trough development.

3. History of cyclogenesis from viewpoint of daily synoptic charts

The detailed day-to-day synoptic developments associated with this case of cyclogenesis may be found in the Daily Series of Synoptic Weather Maps of the U.S. Weather Bureau for February 1950. These maps are prepared once daily for sea level and 500 mb at 1230 G.M.T. and 1500 G.M.T., respectively. Owing to space limitations only a selected few of these charts are shown here in Fig. 3.

On January 30 and 31, 1950 (not shown) anticyclonic circulation at sea level and aloft dominated the region of Alaska, the Gulf of Alaska, and much of the Bering Sea and the Aleutians. The individual perturbation which set off the Gulf of Alaska development was located in the Bering Straits on February 1 (Fig. 3 a) and moved through Alaska into the northern Gulf by February 2 (Fig. 3 b). This system was an old occlusion which could be clearly traced from a position northwest of Kamchatka on January 30. This occlusion transformed into a cold front as it moved

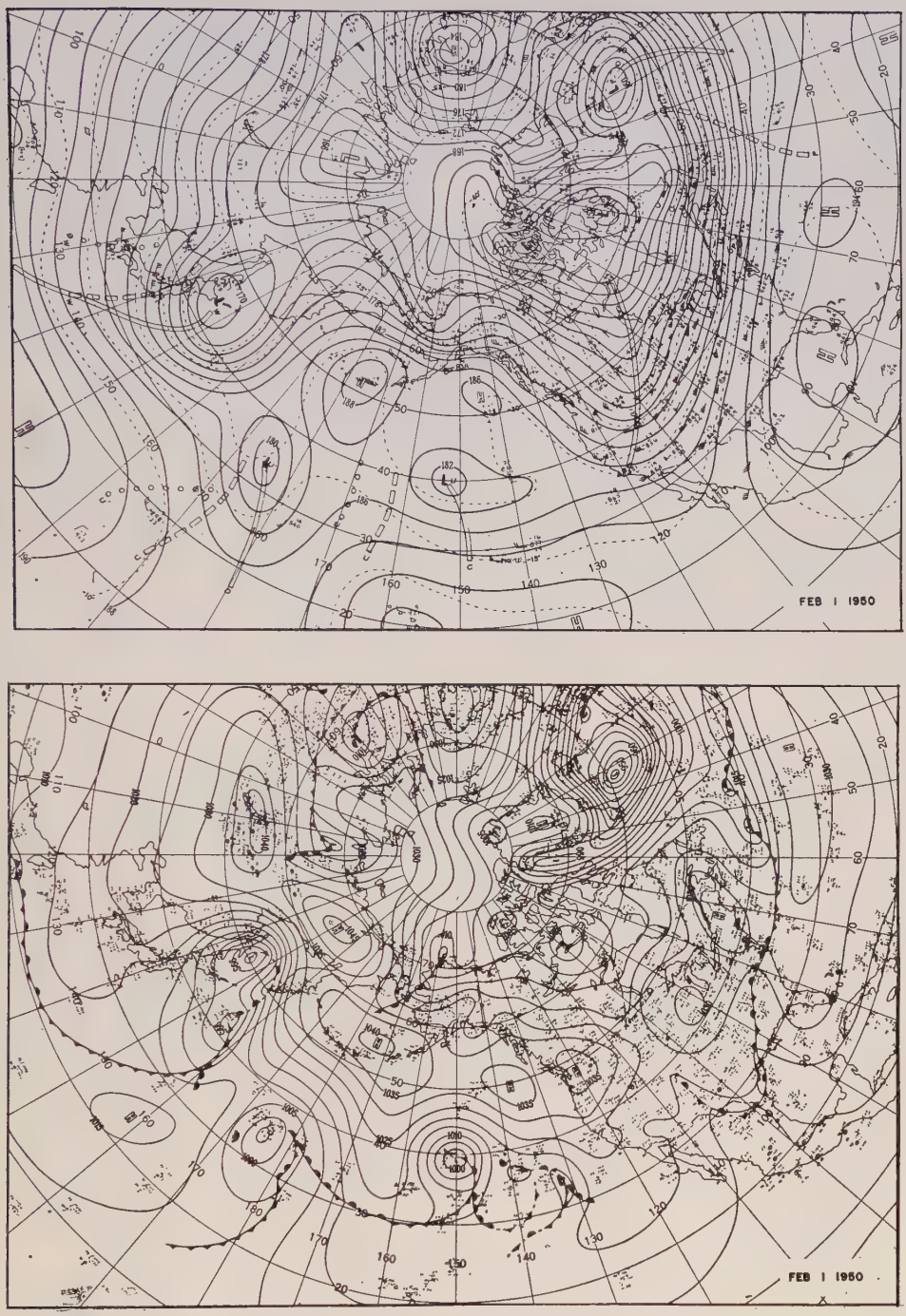

3 a

Fig. 3. Sequence of daily maps for 500 mb (upper) and sea level (lower) portraying details of cyclonic development in the Gulf of Alaska. Maps are reproductions from Daily Series Synoptic Weather Maps published by U.S. Weather Bureau. 500-mb charts are for 1500 GMT and sea-level charts for 1230 GMT.
3 a. February 1, 1950; 3 b. February 2, 1950; 3 c. February 3, 1950; 3 d. February 4, 1950.

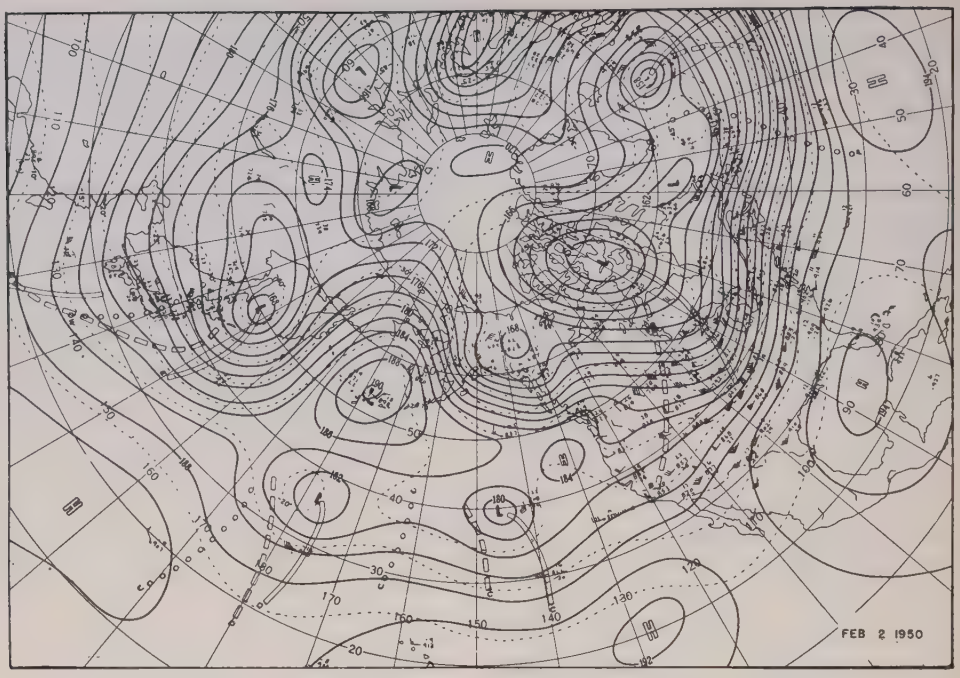

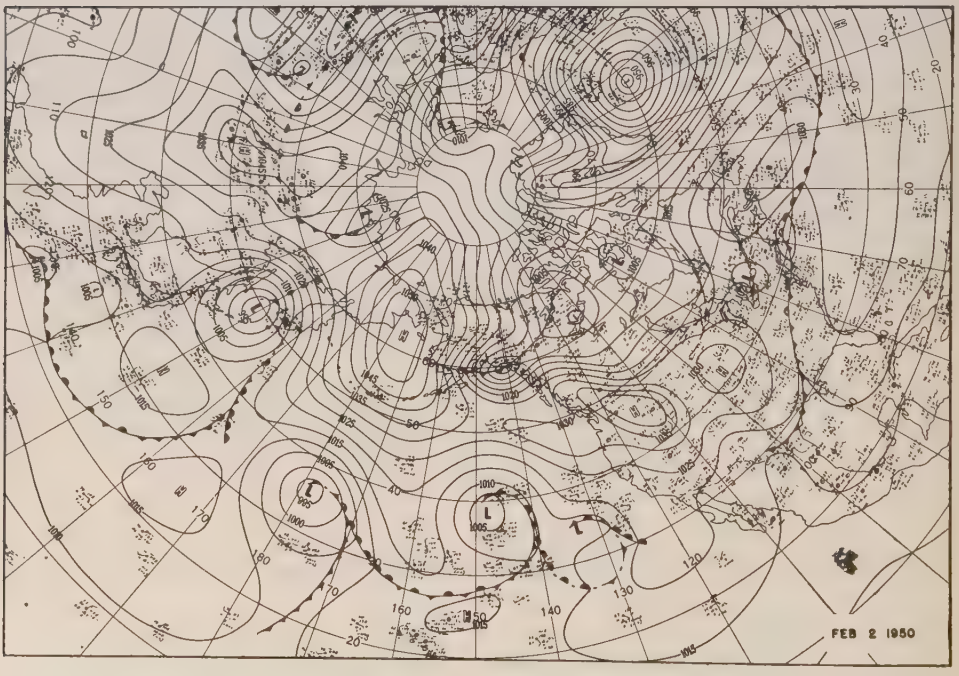

3 b

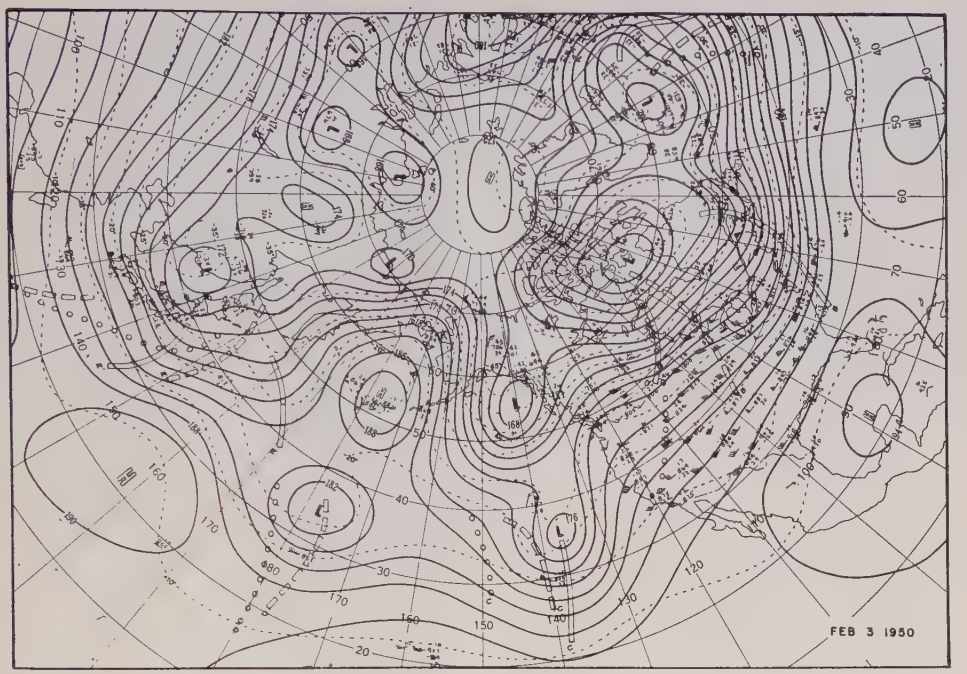

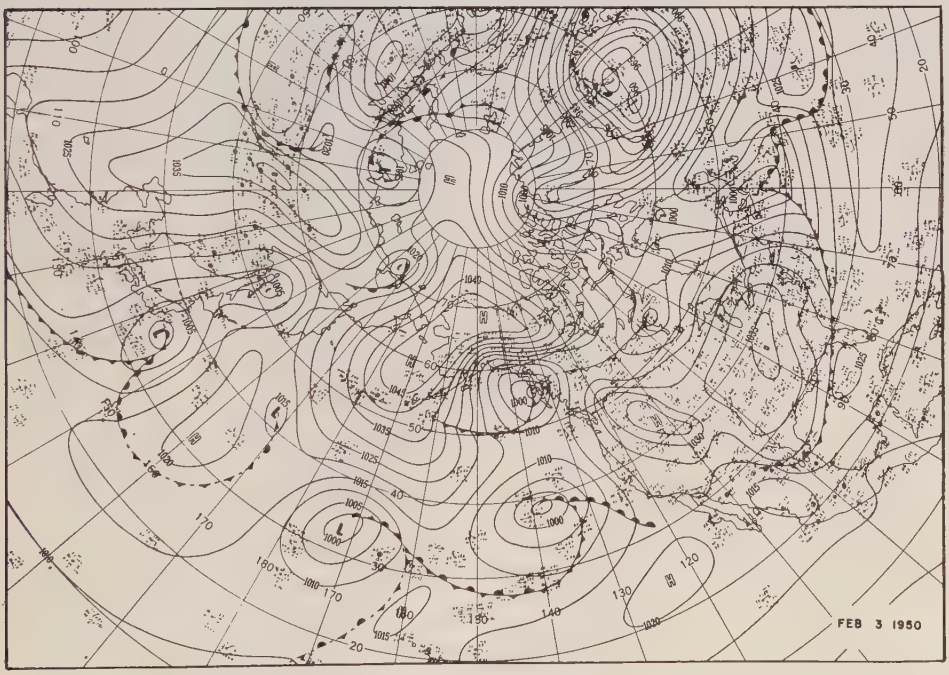

3 c

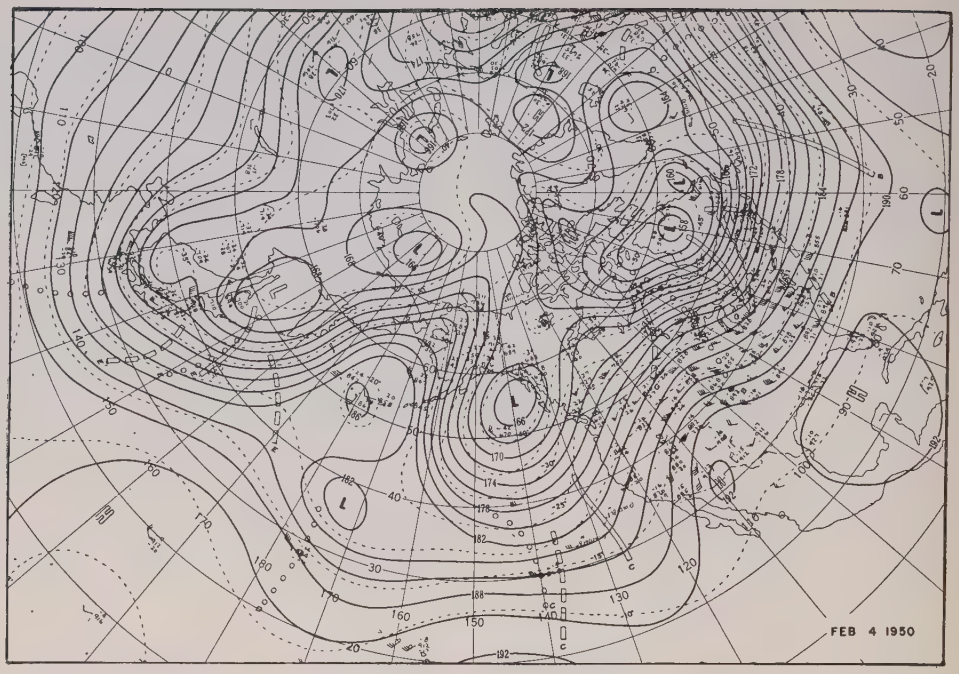

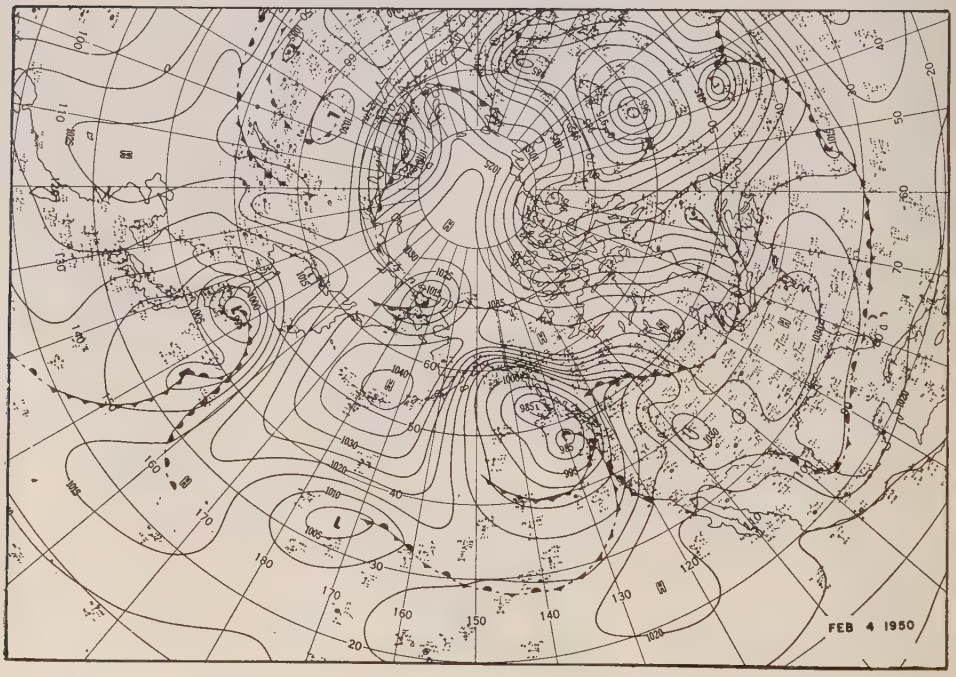

3 d

southeastward across Alaska. Behind this front was a very cold Artic air mass which first reached the Gulf of Alaska very close to map time of February 2 (Fig. 3 b). The intensifying cyclonic center in the northeastern Gulf at sea level formed along the front, and was not the same low which was in northwestern Alaska in Fig. 3 a. Further deepening of this new cyclone followed in the next two days (Figs. 3 c and 3 d).

At 500 mb this trough was very weak as it crossed the Bering Sea on January 31, but it began intensifying as it came into Alaska (Fig. 3 a), and a closed low center formed on February 2 (Fig. 3 b). This center drifted southward into the Gulf over the developing sea level cyclone by the next day (Fig. 3 c), and continued deepening through the next two days. The developing trough in the Gulf of Alaska extended its influence to rather low latitudes of the eastern Pacific as it became longitudinally superimposed over the pre-existing low latitude trough which had been drifting slowly eastward. This juncture of the two troughs occurred on February 3 and 4 (Figs. 3 c and 3 d) and was accompanied by deepening and northeastward motion of the low-latitude cyclone.

Rapid rises in sea-level pressure and 500-mb height had been occurring over the Aleutians, the Bering Sea, and northeast Siberia around February 1 (Fig. 3 a). These rises had been preceded on January 30 and 31 by cyclonic development near Japan (not shown) and accompanying initiation of strong southerly flow to the east of Japan at both sea level and 500 mb. The maximum intensity of the ridge over the Aleutians was reached on February 2 (Fig. 3 b) just as cyclogenesis got under way in the Gulf. Subsequently, the ridge aloft weakened slightly, but underwent little change in basic position in the next few days (Figs. 3 c and 3 d).

The events occurring on the daily charts give the same basic impression that has already been derived from inspection of the 5-day mean data (Figs. 1 and 2). This impression is that the development of a new trough in the vicinity of the Gulf of Alaska could be anticipated qualitatively from antecedent large-scale circulation changes upstream in the planetary wave pattern. Furthermore, it can also be reasonably estimated that the transmission of these influences downstream into the Gulf of Alaska was effected to a great extent by barotropic flux of absolute vorticity. However, these deductions are as yet all qualitative. The next step is to see how much influence barotropic effects have quantitatively, and thence to estimate the relative importance of the heat source in the Gulf of Alaska.

4. Barotropic tendency computations

The effects on the mid-tropospheric contour patterns due to advection of absolute vorticity alone may be measured approximately by tendency computations based on the simple barotropic form of the vorticity equation,

$$\frac{\partial \zeta}{\partial t} = - \underset{\rightarrow}{V} \cdot \nabla \eta \,, \qquad (1)$$

where ζ is the vertical component of relative vorticity, t time, $\underset{\rightarrow}{V}$ horizontal wind vector, $\nabla \eta$ the horizontal gradient of the vertical component of absolute vorticity. The absolute vorticity, η, is simply $(\zeta + f)$, where f is the Coriolis parameter. When the geostrophic approximation is made the left side of (1) can be expressed in terms of a height tendency so that we may write

$$\frac{\nabla^2 \partial z}{\partial t} = - \frac{f}{g} \underset{\rightarrow}{V} \cdot \nabla \eta \,, \qquad (2)$$

where ∇^2 is the horizontal Laplacian operator, z height of a constant pressure surface, and g acceleration of gravity. The right-hand side of (2) can also be expressed in terms of the height field (cf. CHARNEY, FJØRTOFT and VON NEUMANN, 1950; BOLIN and CHARNEY, 1951) and is actually evaluated in that manner, but this transformation has been omitted here for the sake of simplicity.

Equation (2) has been applied here in much the same fashion as in recent work of BOLIN and CHARNEY (1951), STAFF MEMBERS OF THE UNIVERSITY OF STOCKHOLM (1952), and ELIASSEN and HUBERT (1953). The advection of geostrophic vorticity (right side of equation 2) was computed over a square grid on a polar stereographic map projection with a grid interval of approximately 575 km at latitude 45°.[1]

[1] It is possible that this fairly large grid size may be somewhat too coarse to yield sufficient detail of the vorticity field. However, it is believed that the spacing between available observation stations is generally so

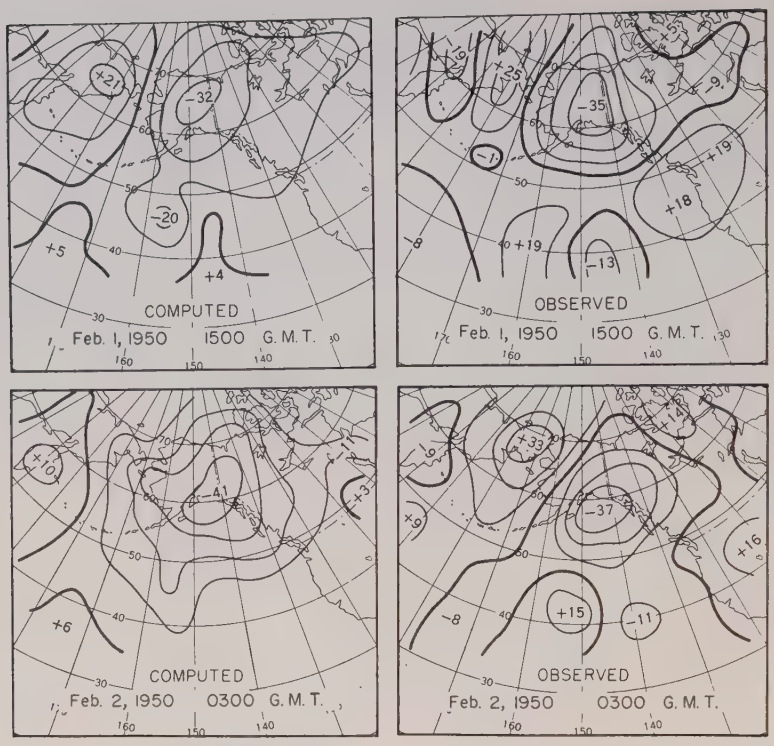

Fig. 4. Computed and observed 700-mb height changes in units of 10 ft/12 hr for early phases of Gulf of Alaska development.

The height tendencies were then determined by relaxation of this field of vorticity advection assuming that the tendencies were zero on the boundary of the area. The computational area was approximately coincident with the total region outlined in Figs. 4—6. The calculations were carried out at the 700-mb level using the twice-daily Northern Hemisphere analyses prepared by the Extended Forecast Section. The reason for the choice of the 700-mb level over the more usual 500-mb level lies mainly in the sparsity of available data over the Pacific Ocean area. Since the upper-level analysis in such regions must depend to a considerable degree upon extrapolation upward from sea-level data, it was felt that the analysis at 700 mb might be somewhat more reliable than at 500 mb. Even if upper-level data were adequate there is no conclusive evidence that the 500-mb level has any basic advantages over 700 mb in regard to the application of the barotropic model. Several empirical findings (e.g., FLEAGLE, 1948; CHARNEY, 1949; PALMÉN and NEWTON, 1951) have indicated that 700 and 500 mb are about equidistant from the average level of nondivergence at which equation (2) is most applicable. It should also be mentioned that CHARNEY, FJØRTOFT, and VON NEUMANN (1950) concluded that the appropriate level lies between 500 and 400 mb. On the other hand, recent empirical data of CRESSMAN (1953) indicate that the equivalent barotropic surface is found between 650 and 600 mb. Considering all of these assorted findings it is probably safe to assume that 700 mb and 500 mb are equally amenable on the average to application of the barotropic model.

The computed barotropic tendencies are compared here with the corresponding observed 24-hour change in 700-mb height centered at the time of the map from which computations were

great in this case that a smaller grid might pick up spurious detail of the derivatives of the height field. This danger may exist even with the grid size used here, of course.

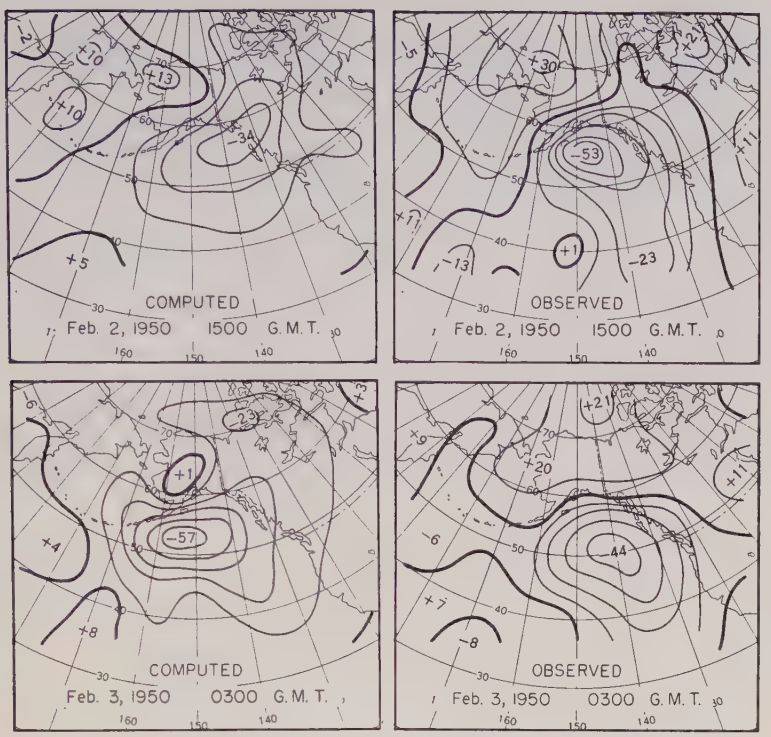

Fig. 5. Computed and observed 700-mb height changes in units of 10 ft/12 hr during periods of most rapid deepening over Gulf of Alaska.

made. It is believed that this method of comparison is somewhat preferable to that used by Bolin and Charney (1951) since their averaging of two successive 12-hour barotropic computations may automatically include some non-barotropic effects which have modified the circulation in the 12-hour interval between maps. On the other hand, the use of an observed 24-hour height change may be a somewhat poorer approximation to an instantaneous tendency than is a 12-hour change.

The results of these barotropic tendency computations as compared with observed height changes are shown in Figs. 4–6. The units in these three figures are tens of feet/12 hours. In Fig. 4 it is immediately apparent that the sizable height falls observed over Alaska and the northern Gulf of Alaska centered at 1500 G.M.T., February 1 and 0300 G.M.T., February 2 are caught fairly well by the computed barotropic tendencies. Note that the computed and observed centers of these negative height changes correspond very well in both intensity and location. Other aspects of the agreement between computed and observed tendencies are not so good, especially over the northern Bering Sea at 0300 G.M.T. of February 2 and in both periods over the United States and near latitude 40° N over the Pacific. These errors are very likely partly attributable to boundary assumptions of zero tendencies, which can cause errors when the relaxation technique is applied.

During the next two twelve-hour periods (Fig. 5) the barotropic tendencies still call for falling heights over the Gulf of Alaska region which compare rather well with the observed tendencies. However, it is notable that the centers of maximum height fall are no longer predicted as well as in Fig. 4. At 1500 G.M.T., February 2 (Fig. 5, top) the maximum computed height fall of −34 was found along the southeast Alaskan coast while the observed height fall of −53 was located near the middle of the Gulf of Alaska. This was the time when the cold Arctic air had begun streaming out

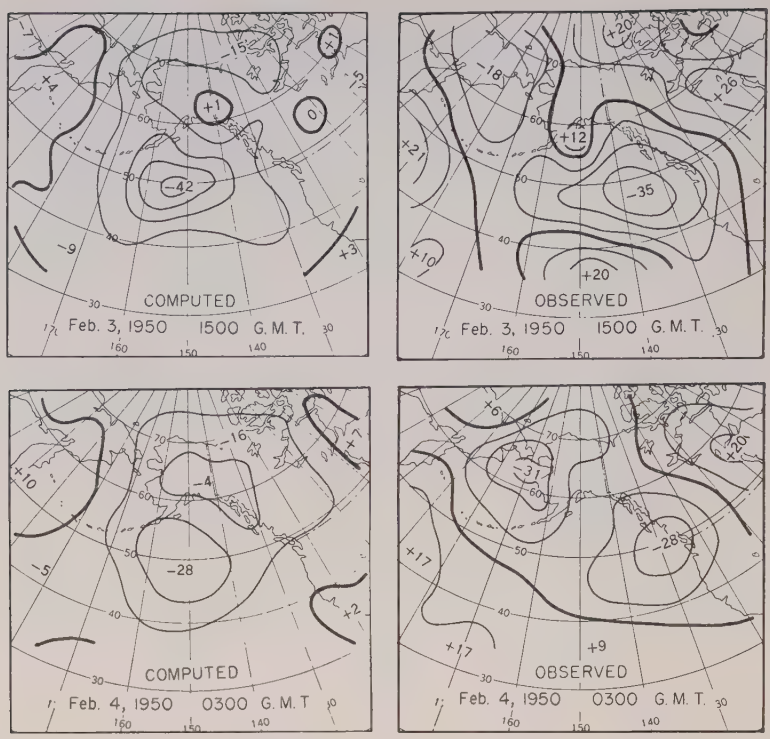

Fig. 6. Computed and observed 700-mb height changes in units of 10 ft/12 hr for two periods subsequent to rapidly deepening stage.

over the Gulf of Alaska, thereby introducing abruptly a large heat source into the atmospheric circulation. By 0300 G.M.T., February 3 (Fig. 5, bottom) a deep closed low had become established over the Gulf of Alaska at 700 mb. Barotropic computations from this flow pattern now indicated large height falls over the extreme western Gulf of Alaska, whereas the observed fall center was located considerably to the east at 50° N, 140° W and was somewhat less in central intensity. A similar discrepancy between the computed and observed fall centers was found at 1500 G.M.T., February 3 (Fig. 6, top). By 0300 G.M.T., February 4 (Fig. 6, bottom) the barotropic tendency computations had deteriorated considerably.

These computations indicate that horizontal advection of absolute vorticity was responsible for much of the cyclonic development in the Gulf of Alaska. This was especially true in the initial stages, but substantial errors in the location and intensity of the maximum height falls began to show up at the time when cold air reached the Gulf of Alaska. In other words, simple advection of vorticity could not explain the rapidity and the exact location of the intense cyclonic development over the Gulf, but did indicate that cyclogenesis would take place in the general area. At the time of most rapid deepening the computed height falls were to the east of and weaker than the observed falls, whereas following establishment of the deep closed low computed falls were to the west and stronger than the observed falls. These errors of the barotropic computations can be attributed largely to divergence and hence to the vertical motion field. These effects will be discussed in the next section.

5. Vertical motion fields associated with cyclogenesis

The importance of the vertical motion field in determining non-advective local changes in vorticity may be seen in the complete vorticity equation written in the form

$$\frac{\partial \zeta}{\partial t} = -\underset{\rightarrow}{V}\cdot\nabla\eta - \omega\frac{\partial \eta}{\partial p} + \eta\frac{\partial \omega}{\partial p} + \underset{\rightarrow}{k}\cdot\nabla\omega\times\frac{\partial \underset{\rightarrow}{V}}{\partial p} \quad (3)$$

This equation applies to isobaric surfaces since pressure, p, has been used as the vertical co-ordinate (see ELIASSEN, 1952, for the derivation in this form). Hence, ∇ means differentiation along an isobaric surface, and $\partial/\partial t$ represents local rate of change on an isobaric surface. ω is the individual rate of change of pressure, dp/dt, which is essentially the vertical motion in this co-ordinate system. $\underset{\rightarrow}{k}$ is a unit vertical vector and the other symbols have the meanings given previously. In the derivation of this equation Eliassen has neglected friction and the horizontal component of the earth's rotation.

Equation (3) states then that local vorticity changes are a result of not only horizontal advection of vorticity [first term on right of (3)], but also three additional terms: vertical advection of vorticity $(-\omega\partial\eta/\partial p)$, divergence $\left(\eta\frac{\partial \omega}{\partial p}\right)$, and transformation of horizontal vorticity into vertical vorticity $\left(\underset{\rightarrow}{k}\cdot\nabla\omega\times\frac{\partial \underset{\rightarrow}{V}}{\partial p}\right)$. Although the latter term has been shown to have on occasion a relatively large magnitude (cf. REED, 1951) it was decided that it could be neglected in this case since vertical shear of the horizontal wind over the Gulf of Alaska region was generally small between 1,000 and 500 mb. If this tilting term is neglected we then have from (3)

$$\frac{\partial}{\partial p}\left(\frac{\omega}{\eta}\right) = \frac{\frac{\partial \zeta}{\partial t} + \underset{\rightarrow}{V}\cdot\nabla\eta}{\eta^2}, \quad (4)$$

which upon integration becomes

$$\left(\frac{\omega}{\eta}\right)_{p_1} = \left(\frac{\omega}{\eta}\right)_{p_0} - \int_{p_1}^{p_0}\frac{\frac{\partial \zeta}{\partial t} + \underset{\rightarrow}{V}\cdot\nabla\eta}{\eta^2}\,dp, \quad (5)$$

where p_1 and p_0 are arbitrary pressure surfaces. In practice p_0 is assumed to be 1,000 mb and the integral is approximated by values of $\left(\frac{\partial \zeta/\partial t + \underset{\rightarrow}{V}\cdot\nabla\eta}{\eta^2}\right)$ at certain standard isobaric surfaces. The vertical motion at 500 mb was obtained from the expression

$$\omega_5 = \eta_5\left[\left(\frac{\omega}{\eta}\right)_{10} - \frac{150}{\eta_{10}^2}\left(\frac{\partial \zeta}{\partial t} + \underset{\rightarrow}{V}\cdot\nabla\eta\right)_{10} - \frac{250}{\eta_7^2}\left(\frac{\partial \zeta}{\partial t} + \underset{\rightarrow}{V}\cdot\nabla\eta\right)_7 - \frac{100}{\eta_5^2}\left(\frac{\partial \zeta}{\partial t} + \underset{\rightarrow}{V}\cdot\nabla\eta\right)_5\right] \quad (6)$$

and for 700 mb by

$$\omega_7 = \eta_7\left[\left(\frac{\omega}{\eta}\right)_{10} - \frac{150}{\eta_{10}^2}\left(\frac{\partial \zeta}{\partial t} + \underset{\rightarrow}{V}\cdot\nabla\eta\right)_{10} - \frac{150}{\eta_7^2}\left(\frac{\partial \zeta}{\partial t} + \underset{\rightarrow}{V}\cdot\nabla\eta\right)_7\right], \quad (7)$$

where the subscripts 5, 7, 10 refer to the 500, 700, and 1,000-mb surfaces respectively. In the computations it was assumed that ω_{10} was zero, i.e., no vertical motion near ground level. This assumption is justified over the level surface areas, but is probably somewhat open to question over the mountain ranges of Alaska and western Canada. However, since the grid interval of 575 km is in many cases large enough to encompass both leeward and windward slopes of a mountain barrier $\omega_{10} = 0$ may be the most appropriate assumption even over the mountain zones. Perhaps more restrictive over these higher elevations is the somewhat fictitious nature of the sea-level or 1,000-mb chart where substantial reductions to sea level must be made. No adjustments in equations (6) or (7) were made over these areas so that vertical motion estimates over mountainous terrain are probably somewhat less reliable than over the oceans and flatter land areas.

A few words may be in order here about the possible influence of surface friction, which is neglected in the equations. Simple assumptions about friction (cf., PANOFSKY, 1951) indicate that frictional inflow would produce upward motion at the top of the friction layer near a sea-level pressure minimum. This effect would generally enhance the upward motions calculated here near low centers and increase the downward motion near high centers. However, a recent observational study of frictional flow over an ocean surface by SHEPPARD et al. (1952) indicates that the whole classical concept of a frictional boundary layer has little validity

over the sea surface. These findings raise considerable doubt then as to whether a simple assumption of frictional inflow across isobars at the surface would have added much accuracy to vertical motion estimates made here.

In evaluating equations (6) and (7) local vorticity changes were approximated by the observed 24-hour changes centered around each given 12-hour period, while the advection of vorticity was computed from the chart at the middle of this 24-hour period. The grid used for these computations was the same as described earlier for the barotropic tendency calculations. In order to express the vertical motions in more familiar units the values of ω were converted into the true vertical velocity w, in cm/sec through use of the hydrostatic equation. It should be pointed out by the way, especially when considering equations (6) and (7), that w is opposite in sign to ω. The results of some of these computations of vertical motion are shown in Figs. 7—9 superimposed on the appropriate contour patterns.

Before considering some of the individual details of these vertical motions, it is of interest to point out that in general the various areas of upward and downward motion are similar in magnitude and areal extent to values calculated by other investigators in a variety of situations. This holds not only for studies where the vorticity equation was used in the calculations (e.g., SAWYER, 1949; ELIASSEN and HUBERT, 1953), but also for computations by adiabatic and kinematic methods (e. g., FLEAGLE, 1947; PANOFSKY, 1951).

Turning our attention now to Fig. 7 and concentrating on the higher latitude wave train we see that a broad area of relatively small upward motion was located in and east of the developing trough over southern and southwestern Alaska at both 700 mb and 500 mb. The maxima at both levels were over the northeastern Gulf of Alaska. In the northwesterly flow to the rear of the trough over western Alaska and the Bering Straits pronounced downward motion occurred.

Twelve hours later (Fig. 8) upward motion continued over most of the Gulf of Alaska and became somewhat more intense. Note that these positive vertical velocities extended well back into the northwesterly flow west of the developing trough over the Gulf of Alaska at both 700 and 500 mb. The centers of maximum upward motion were now located over the middle of the Gulf of Alaska, to the southwest of the maxima in Fig. 7, even though the trough had moved eastward. Also, the downward motion east of the ridge over western Alaska and the Bering Sea had decreased markedly from its indicated intensity twelve hours earlier.

These changes in the vertical motion distribution relative to the trough were undoubtedly associated with the deepening of the cyclonic circulation over the Gulf, but this association does not provide an explanation for these vertical motion adjustments. Rather, one must look for the cause of the vertical motion-divergence fields to get a better understanding of why rapid deepening took place in the Gulf of Alaska. Since the maximum upward motion now appeared in the northwesterly flow off the Alaskan coast (Fig. 8) and since this northwesterly flow through most of the troposphere was now carrying extremely cold air out over the Gulf of Alaska, it seems most logical to postulate that the large low-level heat source introduced in the Gulf of Alaska at this time was responsible for large-scale convergence and upward motion in this area. The mechanism for production of upward motion through heating may be attributed in simplest terms to a thermal circulation where vertical expansion of heated columns of air relative to non-heated or cooled columns leads to outflow at high levels and inflow in the lower portion of the atmosphere. This classical thermal theory of pressure change has recently been summarized by AUSTIN (1951).

In the ensuing period (Fig. 9) the vertical motion fields once more took on a more familiar appearance relative to the deep trough in the Gulf of Alaska. Generally, pronounced downward motion developed west of the trough and upward motion now dominated the area east of the trough. However, upward motion persisted in the vicinity of the trough-line itself. Positive vertical velocities also developed to the rear of the trough south of 50° N, in advance of the surface cold front. During the three subsequent 12-hour periods (not shown), fairly similar conditions prevailed, i.e., downward motion behind the trough, and upward motion ahead, as the trough moved slowly eastward.

This return to what might be considered a more typical distribution of vertical motion

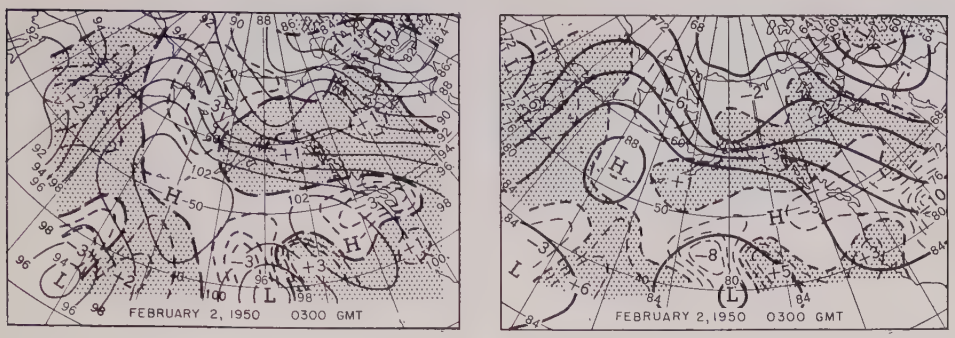

Fig. 7. Vertical motion (in cm/sec) at 700 mb (left) and 500 mb (right) for 0300 GMT, February 2, 1950. Shaded areas indicate upward motion, unshaded areas downward motion. Dashed isopleths of vertical motion are drawn at intervals of 1 cm/sec at 700 mb and 2 cm/sec at 500 mb. Contours of 700-mb surface are drawn for every 200 ft while 500-mb contours are at intervals of 400 ft.

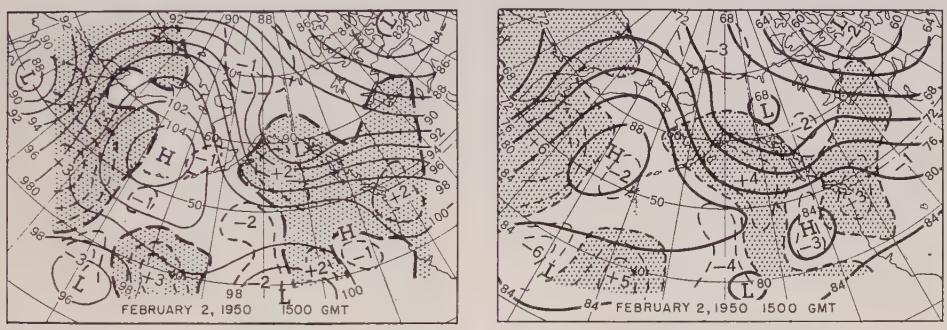

Fig. 8. Vertical motion (in cm/sec) at 700 mb (left) and 500 mb (right) for 1500 GMT, February 2, 1950. See legend to fig. 7.

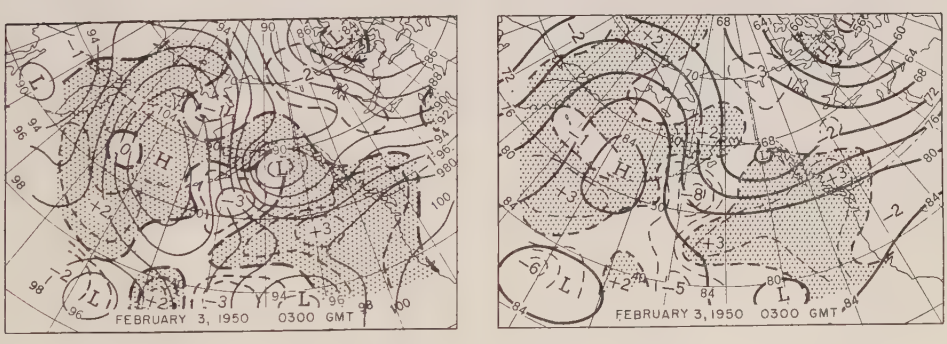

Fig. 9. Vertical motion (in cm/sec) at 700 mb (left) and 500 mb (right) for 0300 GMT, February 3, 1950. See legend to fig. 7.

relative to the trough in the Gulf of Alaska seems to imply that the usual effects of subsidence and horizontal divergence of the cold air mass in its southward drift, and lifting and horizontal convergence of the warmer air mass east of the trough once again became dominant even though a pronounced heat source still existed as cold air continued to stream out over the Gulf. Thus, the tentative conclusion one can draw from this series of vertical motion computations (and also from the essentially dependent barotropic tendency computations)

is that the effects of heating in this cyclogenetic development were most influential during a relatively short period (i.e., of the order of some 12—24 hours) following the initial establishment of the heat source. After the cold dome moved out over the ocean in greater depth, both horizontally and vertically, the more powerful effects of sinking and spreading of the cold air counteracted the convergence effects of heating from the ocean surface.

6. Calculations of atmospheric heating in the Gulf of Alaska

In view of the apparent influence of heating in Gulf of Alaska cyclogenesis, it is important to obtain some quantitative information about the amount of heat added to the air in this situation. In fact, if the heating could be specified *a priori* in some simple functional form, it would be feasible to include heating effects in current numerical forecasting techniques (e.g., CHARNEY and PHILLIPS, 1953). As yet there does not seem to be any practical way of writing down the true heating function, but empirical studies of heating may provide the basis for some approximate heating model in certain specific cases. In regard to the particular problem of heating of cold air masses over the sea, with which we are primarily concerned in the case of Gulf of Alaska cyclogenesis, there have been several pertinent studies. JACOBS (1951) calculated sensible heat exchange between ocean and atmosphere from long-term average values of differences between sea and surface air temperatures. WEXLER (1944) and MÖLLER (1950) determined normal regions of heating from mean circulation data, while AUBERT and the present author (1951) calculated heating in similar fashion for individual months. Studies of heating of Polar or Arctic air in its passage over the North Atlantic have been made by BURKE (1945) and KLEIN (1946) and more recently by CRADDOCK (1951). There have also been similar studies of air mass heating over other water bodies such as Hudson Bay (BURBIDGE, 1951). Except for Jacobs' work all of these studies have suffered (aside from practical computational difficulties in the techniques used) from their inability to separate adiabatic warming and cooling from the true heat sources. In the heating calculations made here vertical motions obtained in the previous section have been applied to yield what, it is hoped, is a better approximation to the true non-adiabatic heating of the air.

The heating of a layer of air may be expressed as

$$\left(\frac{dQ}{dt}\right)_L = \frac{c_p \Delta p}{g}\overline{\frac{d\vartheta}{dt}} = \frac{c_p \Delta p}{g}\left(\overline{\frac{\delta\vartheta}{\delta t}}\right)_p + \frac{c_p \Delta p}{g}\overline{\omega\frac{\partial\vartheta}{\partial p}} = H + V. \tag{8}$$

Here, $\left(\frac{dQ}{dt}\right)_L$ is the rate at which heat is added to a square centimeter column of depth L, ϑ is potential temperature, c_p specific heat at constant pressure, Δp pressure difference between top and bottom of layer under consideration. $\left(\frac{\delta\vartheta}{\delta t}\right)_p$ is the change of potential temperature following an isobaric trajectory. The bars represent vertical averages through the layer. Other terms have meanings previously defined. H and V have been introduced as shorthand notations for heating measured by temperature change in the horizontal trajectory of the air and heating measured by the vertical advection of potential temperature, respectively.

Isobaric trajectories were constructed on the 1,000, 850, 700, and 500-mb surfaces originating at Anchorage, Alaska, which was generally located near the middle of the stream of cold air pouring out of Alaska. In constructing these trajectories the geostrophic wind field on a particular map was considered to be representative of the flow field for a period of twelve hours centered at map time. An example of these computed trajectories is given in Fig. 10. Temperatures were interpolated from analyzed temperature fields at each of the pressure surfaces at the end of 12 (dots) and 24 hours (arrow heads). These temperature readings were then used to construct two "synthetic" soundings for 12 and 24 hours later which when compared with the original observed sounding at Anchorage showed the amount of heating of the air column as it moved in its isobaric trajectory. An example of the initial sounding as compared with "synthetic" soundings is also shown in Fig. 10.

As exemplified by Fig. 10 the trajectories at the various levels had diverged considerably by the end of 24 hours, but were fairly close together at the end of the first 12 hours. Since the assumption that we are following a vertical

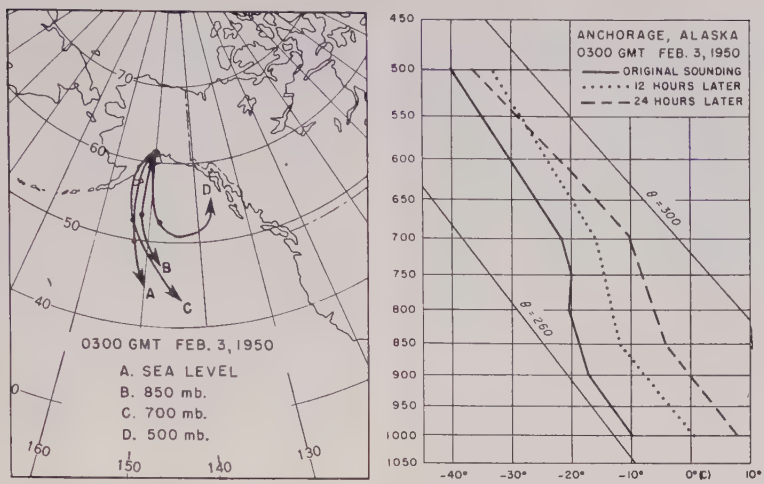

Fig. 10. Example showing trajectories and soundings used in arriving at heating calculations (term H of equation 8) Computed trajectories originating from Anchorage, Alaska at 0300 GMT, February 3 for four indicated isobaric surfaces are shown at left. Dots along paths indicate positions of air parcels after 12 hours and arrow heads show positions at the end of 24 hours. Pseudo-adiabatic chart at right shows initial sounding at Anchorage and »synthetic» soundings 12 and 24 hours later obtained from temperatures interpolated from isotherms on analyzed constant pressure charts at indicated points on trajectories.

column of air is tenuous at best, it was considered that reliable computation of H (see equation 8) could be carried out only for the first 12 hours of the air's travel southward from Anchorage. The vertical term (V of equation 8) was estimated from the average vertical motions (as calculated in the previous section) and the average vertical gradient of potential temperature along the trajectories. These heating calculations for five twelve-hour periods starting shortly after the cold air first broke out in force over the Gulf of Alaska are shown in Table 1.

Of considerable significance in this table are the large magnitudes of the total heating in the layer from 1,000 to 500 mb. These estimates include the effects of all heat sources of course, but it is fairly certain that the greater part of this heating is due to sensible heat gain from the ocean surface. Comparison of these figures with normal daily heating for winter (cf., Fig. 59, JACOBS, 1951) shows that the maximum daily heating observed here is an order of magnitude greater than normal for the Gulf of Alaska region and more than five times as great as the maximum normal heating found at any point in the Northern Hemisphere. However, the heating calculations of Table 1 agree fairly well with those of CRADDOCK (1951) who studied similar air-mass heating following trajectories in the northeastern Atlantic. At any rate these figures emphasize that there is little doubt that sensible heating of air from the sea surface is the most potent atmospheric heat source that is encountered on a relatively large scale.

Table 1. Heating of air associated with cyclogenesis in the Gulf of Alaska, February 2—4, 1950 as calculated using equation (8). Subscripts 7—10, 5—7, and 5—10 refer to layers 700—1,000 mb, 500—700 mb, and 500—1,000 mb, respectively. Units are ly/day

12-Hour Period Beginning	H_{7-10}	V_{7-10}	$\frac{dQ}{dt}_{7-10}$	H_{5-7}	V_{5-7}	$\frac{dQ}{dt}_{5-7}$	$\frac{dQ}{dt}_{5-10}$
1500 GMT, Feb. 2	+ 1,100	+ 170	+ 1,270	+ 590	+ 350	+ 940	+ 2,210
0300 GMT, Feb. 3	+ 1,190	— 170	+ 1,020	+ 700	— 290	+ 410	+ 1,430
1500 GMT, Feb. 3	+ 1,050	— 200	+ 850	+ 550	— 310	+ 240	+ 1,090
0300 GMT, Feb. 4	+ 840	— 140	+ 700	+ 50	— 230	— 180	+ 520
1500 GMT, Feb. 4	+ 600	— 100	+ 500	+ 100	— 200	— 100	+ 400

As might be expected from the nature of the heat source the greater part of the heating is found in the layer below 700 mb, but the contribution in the layer 700 to 500 mb is by no means negligible. Since sensible heating from the sea is concentrated at the surface, turbulent vertical exchange up to rather high levels of the troposhere must account for much of the sizable values of heating found in the upper layer during the first three periods. It is also likely that the release of heat of condensation contributes to this heating at these levels as well as below 700 mb.

Table 1 shows also that the contributions of net vertical advection of potential temperature, V, to the total heating, dQ/dt, are of relatively little importance (although not negligible) in the layer 1,000 to 700 mb while the horizontal term, H, is large. However, as H becomes smaller V takes on an increasing relative importance. In the layer 700 to 500 mb V is generally of equal importance as compared with H since the former is generally larger as one goes aloft while the latter becomes smaller. Thus, during the last two periods V becomes dominant between 700 and 500 mb and net cooling is indicated in the layer. Cooling of the order of 100—200 ly/day can very likely be attributed to radiation.

The calculations point very clearly to the fact that heating over the Gulf reaches its peak immediately after the cold air outbreak and decreases in intensity in the ensuing periods. This is probably due to the setting in of subsidence which restricts vertical turbulent transfer mainly to lower tropospheric layers.

The data in Table 1 may be drawn upon to demonstrate the importance of considering heating in numerical prediction models. In baroclinic models the first law of thermodynamics [equation (8)] has been used as the second prediction equation in order to take care of the unmeasurable divergence term in the vorticity equation [equation (4)]. In these models the adiabatic assumption has generally been made, i.e., $\frac{dQ}{dt} = 0$. If this is done in (8) "adiabatic" vertical motion can be calculated as follows:

$$\bar{\omega}_A = -\frac{(\overline{\delta\vartheta}/\delta t)_p}{\overline{\partial\vartheta}/\partial p}. \qquad (9)$$

Vertical motions along the trajectories calculated by this adiabatic method are given in Table 2. These are compared with the corresponding vertical motions which were obtained from the vorticity equation in the preceding section and which were used to evaluate the vertical terms (V) in Table 1.

Table 2. Comparison of vertical motions determined from the vorticity equation (w) with vertical motions obtained by making the adiabatic assumption w_A. These vertical velocities are averages for the layers 700—1,000 mb and 500—700 mb and for 12-hour isobaric trajectories originating at Anchorage. These were derived from data of Table 1. Units are cm/sec (positive sign indicates upward motion)

12-Hour Period Beginning	700—1,000 mb		500—700 mb	
	w	w_A	w	w_A
1500 GMT, Feb. 2	+ 0.5	— 3.3	+ 1.8	— 3.1
0300 GMT, Feb. 3	— 0.5	— 3.6	— 1.5	— 3.6
1500 GMT, Feb. 3	— 0.7	— 3.7	— 1.7	— 3.0
0300 GMT, Feb. 4	— 0.6	— 3.6	— 1.7	— 0.4
1500 GMT, Feb. 4	— 0.5	— 3.1	— 1.4	— 0.7

The most striking fact shown in Table 2 is that the adiabatic assumption in this case would have generally led to values of vertical motion markedly in error, presuming that those computed diagnostically from the vorticity equation were much closer to the truth. The adiabatic assumption would have been especially bad in the first period since strong downward motion would have been indicated when upward motion actually occurred. At this time the error was greater in the layer 700—500 mb than in the 700—1,000 mb layer. In the other periods the error was not as great, but it was consistently greater in the layer below 700 mb than in the layer above 700 mb. These differences in vertical motion indicate that baroclinic models neglecting nonadiabatic heating would very likely have yielded rather poor results in the prediction of this cyclogenesis, especially during the early stages of rapid deepening and in the lower layers during the later stages of development.

7. Conclusion

In summary, the following mechanism is indicated for Gulf of Alaska cyclogenesis of the type studied in this case:

1. The development is initiated largely by barotropic flux of absolute vorticity as a result of antecedent upstream readjustments in the planetary wave pattern. The upstream ridge shifts far enough west so that a new broad stream of northerly flow is established. This northerly flow transports a deep layer of extremely cold air out over the Gulf of Alaska.

2. As this cold air travels over the open waters of the Gulf it is heated at a rate of as much as 2,000 ly/day in the layer from sea level to 500 mb. Large-scale convergence and upward motion develop in the lower and middle troposphere in the region of this newly established heat source. This convergence creates new cyclonic vorticity and hence rapid deepening of the cyclone center and the associated trough. Most of the major circulation changes occur in the short period of less than 24 hours. Even in this stage, however, barotropic vorticity advection still accounts for a considerable part of the deepening.

3. Following this rapid transition in the circulation pattern further deepening occurs, but vorticity changes and vertical motion are more in accord with the usual dynamics of large-amplitude waves.

These findings raise the question as to whether heating effects of large magnitude can be neglected in short period forecasting by dynamical methods any more than they can be in extended period forecasting. A definitive answer to this question can only be obtained by testing complex baroclinic numerical forecasting models (both including and excluding heat sources) on situations where large heat sources exist. If heating proves to be of major importance, some substantially improved means of calculating the distibution of heating independently of the field of motion must be devised. This goal may indeed be unattainable in the near future since the circulation and heat sources are so closely and complexly interdependent and since knowledge of the physical processes involved in turbulent transfer of heat, condensation and evaporation, radiation, and conversion of energy is so meager. The alternative may well be some empirical method of incorporating heat sources based on extensive observational programs which would attempt to determine atmospheric heating associated with various types of flow patterns, thermal distributions, and geographical features.

8. Acknowledgments

The author wishes to express his gratitude to Mr J. Namias for suggesting this study of Gulf of Alaska cyclogenesis and his continuing interest in the work. The encouragement and helpful advice of Mr Philip F. Clapp in many phases of this study are sincerely appreciated. Thanks are also due Mr R. A. Green for his careful assistance in analysis of data and Mrs Mildred Matthews for her aid in the laborious computations.

REFERENCES

Aubert, E. J., and Winston, J. S., 1951: A study of atmospheric heat-sources in the northern hemisphere for monthly periods. *J. Meteor.*, **8**, 111—125.

Austin, J. M., 1951: Mechanism of pressure change. *Compendium Meteor.*, Boston, Amer. Meteor. Soc., 630—638.

Bolin, B., and Charney, J. G., 1951: Numerical tendency computations from the barotropic vorticity equation. *Tellus*, **3**, 248—257.

Burbidge, F. E., 1951: The modification of continental polar air over Hudson Bay. *Quart. J. R. meteor. Soc.*, **77**, 365—374.

Burke, C. J., 1945: Transformation of polar continental air to polar maritime air. *J. Meteor.*, **2**, 94—112.

Carlin, A. V., 1953: A case study of the dispersion of energy in planetary waves. *Bull. Amer. meteor. Soc.*, **34**, 311—318.

Charney, J. G., 1949: On a physical basis for numerical prediction of large-scale motions in the atmosphere. *J. Meteor.*, **6**, 371—385.

Charney, J. G., Fjørtoft, R., and von Neumann, J. 1951: Numerical integration of the barotropic vorticity equation. *Tellus*, **2**, 237—254.

—, and Phillips, N. A., 1953: Numerical integration of the quasi-geostrophic equations for barotropic and simple baroclinic flows. *J. Meteor.*, **10**, 71—99.

Craddock, J. M., 1951: The warming of arctic air masses over the eastern North Atlantic. *Quart. J. R. meteor. Soc.*, **77**, 355—364.

Cressman, G. P., 1953: An application of absolute-vorticity charts. *J. Meteor.*, **10**, 17—24.

Eliassen, A., 1952: Simplified models of the atmosphere designed for the purpose of numerical weather prediction. *Tellus*, **4**, 145—156.

—, and Hubert, W. E., 1953: Computation of vertical motion and vorticity budget in a blocking situation. *Tellus*, **5**, 196—206.

Fleagle, R. G., 1947: The fields of temperature, pressure, and three-dimensional motion in selected weather situations. *J. Meteor.*, **4**, 165—185.

Fleagle, R. G., 1948: Quantitative analysis of factors influencing pressure change. *J. Meteor.*, **5**, 281—292.

Jacobs, W., 1951: The energy exchange between sea and atmosphere and some of its consequences. *Bull. Scripps Inst. Oceanog. Univ. Cal.*, **6**, 27—122.

Klein, W. H., 1946: Modification of polar air over water. *J. Meteor.*, **3**, 100—101.

Möller, F., 1950: Die Wärmebilanz der freien Atmosphäre im Januar. *Meteor. Rundschau*, **3**, 97—108.

Namias, J., and Clapp, P. F., 1944: Studies of the motion and development of long waves in the westerlies. *J. Meteor.*, **1**, 57—77.

Palmén, E. and Newton, C. W., 1951: On the three-dimensional motions in an outbreak of polar air. *J. Meteor.*, **8**, 25—39.

Panofsky, H., 1951: Large-scale vertical velocity and divergence. *Compendium Meteor.*, Boston, Amer. Meteor. Soc., 639—646.

Reed, R. J., 1951: A study of atmospheric vorticity. Tech. Rpt. No. 10, *Research on atmospheric pressure changes, M. I. T.*, 20 pp.

Sawyer, J. S., 1949: Large scale vertical motion in the atmosphere. *Quart. J. R. meteor. Soc.*, **75**, 185—188.

Sheppard, P. A., Charnock, H., and Francis, J. R. D., 1952: Observations of the westerlies over the sea. *Quart. J. R. meteor. Soc.*, **78**, 563—582.

Smagorinsky, J., 1953: The dynamical influence of large-scale heat sources and sinks on the quasi-stationary mean motions of the atmosphere. *Quart. J. R. meteor. Soc.*, **79**, 342—366.

Staff Members, University of Stockholm, 1952: Preliminary report on the prognostic value of barotropic models in the forecasting of 500 mb height changes. *Tellus*, **4**, 21—30.

Sutcliffe, R. C., 1947: A contribution to the problem of development. *Quart. J. R. meteor. Soc.*, **73**, 370—383.

Wexler, H., 1944: Determination of the normal regions of heating and cooling in the atmosphere by means of aerological data. *J. Meteor.*, **1**, 23—28.

Sunspot Areas, Flares and Filaments Observed at the Stockholm Observatory and at its Station in Anacapri in the Years 1952 and 1953

By Y. ÖHMAN and L. O. LODÉN

(Manuscript received December 12, 1954)

Abstract

Tables are presented giving sunspot areas and filaments according to the solar routine observations carried out at the Stockholm Observatory in Saltsjöbaden in 1952 and 1953. The sunspot areas are obtained from plates secured with a solar camera equipped with an ultra-violet filter, whereas indications of activity through the presence of bright Hα faculae and measures of filaments are obtained from spectroheliograms. Tables are presented also of flares observed in Saltsjöbaden and at the Swedish Solar Station on Capri.

A. Sunspots and faculae. In two earlier publications[1] tables of sunspot areas observed at the Stockholm Observatory have been given for the years 1948, 1949, 1950 and 1951. These observations have been made in connection with a local solar patrol service started in Sweden 1947 in order to give Swedish geophysical institutions and the Royal Swedish Board of Telegraph informations of the solar activity in addition to the Ursigrams and other similar information bulletins from abroad.

The photographic observations of sunspots have been made as before, with a Zeiss objective with a focal length of 800 mm combined with a camera giving solar images with a diameter of 56 mm. In order to obtain a uniform quality of the images, reducing as much as possible the effects of different seeing, the aperture of the lens was kept as small as 30 mm, which in ultraviolet light still gives a fairly good resolution.

The U.G. 2 filter used for selecting a passband of about 200 Å in the H and K region of the spectrum gives with Ilford Lantern contrasting plates some of the characteristics of the low chromosphere. In fact these plates show faintly the faculae all over the surface of the sun and not only near the limb, as on ordinary photographs.

Other details of interest is a low contrast structure of dark filaments or alignments which can be followed out to the very solar limb and indeed sometimes crossing the bright faculae. This suggests a high level for these phenomena. The structure shows great variations with time and has sometimes been found to be particularly apparent, when regions with strong intensity of the λ 5303 Corona line are situated above the surface.

In table I and table II a presentation is given of sunspot areas for 1952 and 1953 according to our measurements. These tables are arranged in the same way as those presented in the two previous publications quoted above. The sunspot areas are thus measured in 10^{-5} of the half sphere of the sun as unit and the figures refer to the first day-sector after the sun's central meridian observed at about 8^h30^m U.T.

[1] *Tellus* **2**, 255, 1950 and **4**, 241, 1952.

Table I. 1952. Sunspot areas in the first day-sector after the sun's central meridian together with signs of active groups + or non active groups —. Interpolated values are given within parenthesis.

	Jan.	Febr.	March	April	May	June	July	Aug.	Sept.	Oct.	Nov.	Dec.
1	4 + 0 —	(0) (—) (0) (—)	0 — 0 —	(0) (—) (0) (—)	(0) (—) (0) (—)	(0) (—) (0) (—)	0 — 0 —	0 — 0 —	0 — 0 —	0 — 0 —	(2) (+) (0) (—)	0 (—) 0 (—)
2	(1) (+) (1) (—)	0 — 0 —	0 — 0 —	0 — 0 —	0 — 0 —	(0) (—) (0) (—)	0 — 19 —	0 — 24 +	16 + 45 +	(0) (—) (0) (—)	(0) (—) (0) (—)	(0) (—) (0) (—)
3	0 — 0 —	0 — 0 —	0 (—) 0 (—)	0 — 0 —	0 — 0 —	0 — 0 —	0 — 0 —	0 — 0 —	0 — 0 —	(0) (—) (0) (—)	(0) (—) (0) (—)	(0) (—) (0) (—)
4	(0) (—) (0) (—)	0 (—) 0 (—)	0 — 0 —	0 — 0 —	0 (—) 0 (—)	0 — 0 —	0 — 0 —	0 — 0 —	0 — 0 —	(0) (—) (0) (—)	(0) (—) (0) (—)	0 — 0 —
5	0 — 0 —	(0) (—) (0) (—)	(0) (—) (0) (—)	0 — 0 —	0 (—) 0 (—)	0 — 0 —	0 — 0 —	0 — 0 —	0 — 0 —	(0) (—) (0) (—)	(0) (—) (0) (—)	0 — 0 —
6	(0) (—) (0) (—)	0 — 8 —	0 — 0 —	0 (—) 0 (—)	(0) (—) (0) (—)	0 — 0 —	0 (—) 0 (—)	0 — 0 —	(0) (—) (0) (—)	0 — 0 —	0 — 0 —	5 (—) 0 (—)
7	(0) (—) (0) (—)	0 — 0 —	0 — 0 —	0 — 0 —	(0) (—) (0) (—)	0 — 0 —	0 (—) 0 (—)	0 — 0 —	(0) (—) (0) (—)	(0) (—) (0) (—)	(0) (—) (8) (+)	0 (—) 0 (—)
8	0 — 0 —	(0) (—) (6) (—)	0 — 0 —	28 + 0 —	0 — 0 —	0 — 0 —	0 (—) 0 (—)	(0) (—) (0) (—)	0 (—) 0 (—)	(0) (—) (0) (—)	(0) (—) (0) (—)	0 (—) 0 (—)
9	(0) (—) (0) (—)	0 — 0 —	0 — 0 —	0 — 0 —	0 — 0 —	0 — 0 —	0 — 0 —	(0) (—) (0) (—)	0 (—) 0 (—)	0 — 0 —	0 — 0 —	(0) (—) (0) (—)
10	0 — 0 —	(0) (—) (0) (—)	0 — 0 —	0 — 0 —	0 — 0 —	0 — 0 —	5 — 0 —	0 (—) 0 (—)	0 — 0 —	32 + 0 —	0 — 10 —	(0) (—) (0) (—)
11	0 — 0 —	0 — 0 —	0 — 0 —	0 (—) 0 (—)	0 — 0 —	0 — 0 —	0 — 0 —	9 (—) 0 (—)	0 — 0 —	0 — 0 —	(0) (—) (0) (—)	— —
12	(0) (—) (0) (—)	0 — 0 —	0 — 0 —	0 — 0 —	0 — 0 —	0 — 0 —	0 — 0 —	0 — 3 —	0 — 0 —	(0) (—) (0) (—)	0 (—) 0 (—)	— —
13	0 — 0 —	0 — 0 —	0 (—) 0 (—)	0 — 0 —	(0) (—) (0) (—)	0 — 0 —	0 (—) 0 (—)	0 (—) 10 (+)	0 — 0 —	0 (—) 0 (—)	(0) (—) (0) (—)	— —
14	(16) (—) (0) (—)	0 — 0 —	0 — 0 —	0 — 0 —	0 — 0 —	0 (—) 15 (+)	0 (—) 0 (—)	27 + 0 —	0 — 0 —	(0) (—) (0) (—)	(0) (—) (0) (—)	(0) (—) (0) (—)

15	(41) (+) (0) (—)	0 — 0 —	0 — 0 —	0 — 0 —	0 — 0 –	0 (—) 0 (—)	23 (+) 74 (+)	0 (—) 0 (—)	0 — 0 —	(0) (—) (0) (—)	(0) (—) (0) (—)	(0) (—) (0) (—)
16	0 — 0 —	0 (—) 0 (—)	0 — 0 —	0 — 0 —	0 – 0 —	0 — 0 —	0 — 0 —	0 — 0 –	(0) (—) (0) (–)	(0) (—) (0) (—)	(0) (—) (0) (—)	0 — 0 —
17	0 — 0 —	0 — 0 —	0 (–) 7 (|)	0 — 0 —	0 — 0 —	0 — 0 —	(0) (—) (0) (—)	0 (—) 0 (–)	0 — 0 —	(0) (—) (0) (—)	0 (—) 0 (—)	0 — 12 +
18	(0) (—) (0) (—)	0 — 0 —	(0) (—) (0) (—)	0 — 0 –	(0) (—) (0) (—)	4 + 0 –	0 (—) 0 (—)	0 — 0 —	0 — 0 —	(0) (—) (0) (—)	0 — 0 —	(38) (+) (0) (—)
19	(7) (–) (0) (–)	(7) (+) (49) (+)	0 — 0 —	0 — 28 +	0 — 0 –	(1) (—) (0) (–)	(0) ( ) (0) ( )	0 — 0 —	0 — 0 —	(0) (—) (0) (—)	(0) (—) (0) (—)	(0) (—) (0) (—)
20	(8) (—) (0) (—)	0 — 0 –	0 — 0 —	0 ( ) 0 (–)	0 — 0 —	0 — 0 —	(0) (—) (0) (—)	0 — 0 —	0 — 0 —	(0) (—) (0) (—)	(0) (—) (0) (—)	— —
21	0 — 0 —	0 — 0 –	0 — 0 —	2 — 0 –	0 — 9 +	0 — 0 —	0 — 0 —	0 — 0 —	(0) (—) (0) (—)	0 — 0 —	— —	— —
22	0 — 0 —	(0) ( ) (0) (–)	0 — 0 —	0 – 0 —	0 — 0 —	0 (—) 12 (+)	(0) (—) (0) (–)	0 — 3 —	(0) (—) (0) (—)	(0) (—) (0) (—)	— —	— —
23	0 — 0 -	(0) (–) (0) (—)	(0) (–) (0) (–)	0 — 0 –	(0) (—) (0) (—)	1 — 0 —	0 — 0 –	0 — 0 —	0 – 0 —	(0) (—) (0) (—)	— —	— —
24	(0) (–) (0) (—)	0 – 0 —	0 (—) 0 (–)	(0) (—) (0) ( )	(0) (–) (0) (—)	0 (—) 0 (—)	0 — 0 —	(0) (—) (0) ( )	0 (—) 0 (—)	(0) (—) (0) (—)	— —	— —
25	0 – 0 —	(0) ( ) (0) (—)	(0) (–) (0) (—)	0 — 0 —	(0) (—) (0) (—)	0 — 0 —	0 — 0 —	0 — 0 —	(0) (—) (2) (—)	(23) (+) (0) (—)	— —	— —
26	(0) (–) (0) (—)	(0) (—) (0) (—)	0 — 0 —	0 — 0 —	0 — 0 —	0 — 0 —	0 — 17 —	33 + 0 —	0 — 0 —	(17) (+) (0) (—)	(0) (—) (0) (–)	— —
27	(0) (—) (0) (—)	(0) (—) (0) (—)	0 (—) 8 (+)	(6) (+) (0) (–)	0 — 0 —	(3) (+) (0) (–)	(0) (—) (0) (—)	(5) (+) (0) (—)	17 (—) 17 ( )	(0) (–) (0) (—)	(0) (—) (0) (—)	— —
28	(0) (—) (0) (–)	(0) (—) (0) (—)	0 (—) 0 (—)	0 — 0 —	0 — 22 +	0 — 0 —	0 — 0 —	0 — 24 +	(0) (–) (0) (—)	(0) (—) (0) (–)	0 — 0 —	— —
29	0 — 8 —	(0) (—) (0) (—)	0 — 0 —	0 — 0 —	0 — 0 —	0 — 80 +	(0) (–) (0) (–)	0 — 2 +	0 — 12 —	0 — 0 —	0 — 0 —	(0) (—) (0) (—)
30	(0) (—) (0) (–)		0 — 0 —	0 — 0 —	0 — 0 —	0 — 0 —	0 — 0 —	(0) (—) (0) (—)	0 — 0 —	0 — 0 —	(0) (—) (0) (—)	(0) (–) (0) (—)
31	(0) (—) (0) (–)		0 — 7 +		0 — 0 —		0 — 0 —	0 — 0 —		0 — 0 —		0 — 0 —

Table II. 1953. Sunspot areas in the first day-sector after the sun's central meridian together with signs of active groups + or non active groups —. Interpolated values are given within parenthesis.

	Jan.	Febr.	March	April	May	June	July	Aug.	Sept.	Oct.	Nov.	Dec.
1	(0) (—)	(0) (—)	0 —	0 —	0 —	(0) (—)	0 (—)	0 —	0 —	0	(0)	0 —
	(0) (—)	(0) (—)	0 —	0 —	0 —	(0) (—)	0 (—)	0 —	0 —	0	(0)	0 —
2	(0) (—)	(0) (—)	0 —	(2) (—)	15 —	(0) (—)	0 (—)	(0) (—)	(0) (—)	0	0	0 —
	(0) (—)	(0) (—)	0 —	(0) (—)	0 —	(0) (—)	0 (—)	(0) (—)	(0) (—)	0	0	0 —
3	(7) (—)	(0) (—)	0 —	0 (—)	0 —	(0) (—)	0 —	0 —	0 —	(0)	(0)	0 —
	(0) (—)	(0) (—)	0 —	0 (—)	0 —	(0) (—)	0 —	0 —	0 —	(0)	(0)	0 —
4	0 —	(0) (—)	0 —	16 (—)	0 —	0 (—)	0 (—)	0 —	0 —	(0)	(0)	(0) (—)
	0 —	(0) (—)	0 —	0 (—)	0 —	0 (—)	0 (—)	0 —	0 —	(0)	(0)	(0) (—)
5	0 —	(0) (—)	0 —	23 (+)	(0) (—)	0 —	0 (—)	0 (—)	0 —	0	(0)	0 —
	0 —	(0) (—)	0 —	0 (—)	(0) (—)	19 —	0 (—)	0 (—)	0 —	0	(2)	0 —
6	(0) (—)	0 —	0 —	(2) (+)	0 —	0 —	0 —	0 (—)	(0) (—)	0	(0)	0 —
	(0) (—)	0 —	0 —	(0) (—)	0 —	0 —	0 —	0 (—)	(0) (—)	0	(0)	0 —
7	(0) (—)	0 —	(0) (—)	(0) (—)	0 —	(14) (—)	0 (—)	0	0 —	0	0	(0) (—)
	(0) (—)	0 —	(0) (—)	(0) (—)	0 —	(0) (—)	0 (—)	0	0 —	0	0	(0) (—)
8	(0) (—)	(0) (—)	(0) (—)	0 —	0 —	0 —	0 (—)	(0)	0 (—)	0	(0) (—)	(0) (—)
	(0) (—)	(0) (—)	(0) (—)	0 —	0 —	0 —	0 (—)	(0)	0 (—)	0	(0) (—)	(0) (—)
9	(0) (—)	(0) (—)	0 —	0 —	(0) (—)	0 —	0 —	8 +	(0) (—)	0	0 (—)	—
	(0) (—)	(0) (—)	0 —	0 —	(0) (—)	0 —	0 —	0	(0) (—)	10	0 (—)	—
10	22 +	(0) (—)	0 —	0 (—)	0 —	0 —	0 —	(0)	0 (—)	(0)	0 —	—
	0 —	(0) (—)	0 —	0 (—)	0 —	0 —	0 —	(0)	0 (—)	(0)	0 —	—
11	(0) (—)	(0) (—)	0 (—)	0 (—)	0 —	0 —	(0) (—)	0	0 —	(0)	0 (—)	—
	(0) (—)	(0) (—)	0 (—)	0 (—)	0 —	0 —	(0) (—)	0	0 —	(0)	0 (—)	—
12	(16) (—)	(0) (—)	(0) (—)	0 —	0 —	0 —	(0) (—)	0	0 —	0	0 —	—
	(0) (—)	(0) (—)	(0) (—)	0 —	0 —	0 —	(0) (—)	0	0 —	0	0 —	—
13	(0) (—)	(0) (—)	0 —	0 —	(0) (—)	0 —	0 —	0	(21) (—)	0	0 —	—
	(0) (—)	(0) (—)	0 —	0 —	(0) (—)	0 —	0 —	0	(0) (—)	0	0 —	—
14	0 —	(0) (—)	(0) (—)	0 —	0 (—)	0 —	0 —	0	0 —	0	0 —	—
	0 —	(0) (—)	(0) (—)	0 —	0 (—)	0 —	0 —	0	0 —	0	0 —	—

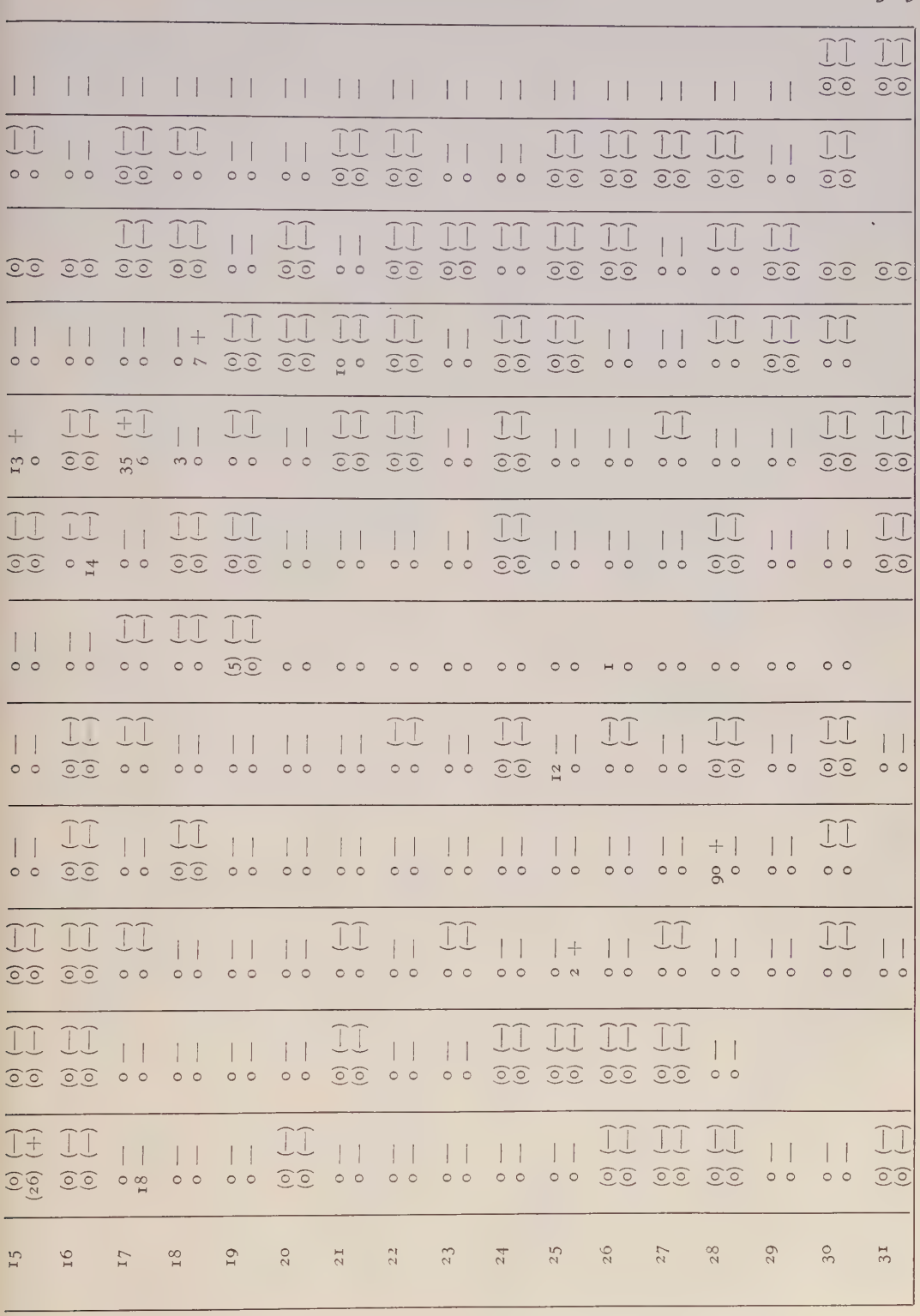

Tellus VII (1955), 4

The upper number in the tables refers to the north hemisphere and the lower number to the south hemisphere. When a number is given within parenthesis no observation has been possible that day but the value has been obtained from interpolation. Zero means that no spot is situated in the day-sector after the central meridian and — that a long period of cloudy weather has made the determination impossible or very uncertain. As to systematic differences in our determinations of sunspot areas compared with the Greenwich Observatory sunspot areas reference is made to the second of the publications quoted above.

The reason why sunspot areas are given only for the first day-sector after meridian is the following: The small scale of our photographs does not allow the same accuracy in the determination of sunspot areas as for instance the Greenwich photographs. Notably near the limb the drawback of the smaller scale is more apparent, whereas the measurements near the centre compare better with determinations from larger images. Now the informations concerning sunspots near or after the sun's central meridian is often required by geophysicists for studying different kinds of terrestrial disturbances of solar origin. We have found from correspondence that our previous tables in this respect have served a useful purpose, even if they must be considered as giving only a very limited part of the complexity of solar phenomena called solar activity.

In order to increase the value of the figures presented here we have tried as before to indicate if brilliant Hα chromospheric faculae are present in these day-sectors or not. These indications have been obtained from the inspection of our patrol spectroheliograms in Hα obtained with the small spectroheliograph described in the earlier publications. These activity figures must not be identified with the rigorous classification of active groups presented for instance in the Quarterly Bulletin.

When the numbers in Table I and II are followed by a + sign, this means that the sunspot group is surrounded by a bright Hα facula according to spectroheliograms obtained the same day with our patrol spectroheliograph. A + sign within parenthesis means that no spectroheliogram has been obtained the same day, but that the activity of the group has been judged from spectroheliograms obtained before or after that date. A – sign after the numbers means that no noticeable bright Hα facula is seen on our patrol spectroheliograms, and when the – sign is within parenthesis earlier or later observations have been used when judging the activity. When no sign is following the number, a long period of cloudy weather has made even an interpolation impossible.

To the observations made with the spectroheliograph in Saltsjöbaden have been added the observational data secured with the 1.0 Å polarizing Hα monochromator at the solar station in Anacapri, Italy, at such periods when this station has been in operation. During 1952 supplementary data were thus obtained from Anacapri for July, August and September and during 1953 from the beginning of April to the end of August. During a period in June 1953 and during another period in August 1953 the spectroheliograph in Saltsjöbaden was dismounted as the celostat was being used for other research.

That the activity signs given from the estimated intensity of the Hα chromospheric faculae really have some significance is apparent from table III, giving a comparison between our classification and a classification of groups from the appearance of solar flares, according to the Quarterly Bulletin, during an interval of time including four days earlier and later

Table III. Comparison between the Stockholm Observatory activity signs + and — and a corresponding activity signs *p* and *n* according to the appearance of flares during a period including four days before and after the observing date

Half year	Number of areas	Percentage			
		$+p$	$-p$	$-n$	$+n$
2nd 1948.....	139	39	21	34	6
1st 1949.....	149	33	25	35	7
2nd 1949.....	134	37	16	36	11
1st 1950.....	103	38	12	32	18
2nd 1950	56	45	5	29	21
1st 1951.....	63	51	5	28	16
2nd 1951.....	50	52	0	14	34
1st 1952.....	26	42	4	35	19
2nd 1952.....	30	50	7	33	10
1st 1953.....	15	33	27	27	13
2nd 1953.....	5	20	20	40	20
All	770	40	15	32	13

Table IV. Flares observed at the Stockholm Observatory (S) and the station on Capri (C)

Day	First obs.	Last obs.	Area sq.deg.	Imp.	Lat.	Long.	Remarks
1952							
July 29.....	10^h52^m			1	12 S	53 E	C
30.....	10 57			1	12 S	40 E	C
Aug. 22.....	15 01			1+	8 N	49 E	C
23.....	15 10			1	13 S	63 E	C
26.....	13 18			1+	8 N	5 E	C With surge
1953							
June 3.....	13 25	14^h15^m	2	1	18 N	46 E	C
6.....	12 58	13 15	1	1	18 N	10 E	C
15.....	12 11	12 30	1	1	10 N	66 E	C
16.....	13 40	14 29	8	2	10 N	53 E	C Two objects
22.....	10 25	10 44	1	1	13 N	40 E	C
25.....	10 00	10 23	2	1+	9 N	0	C Three objects
July 12.....	*16 55*	*17 06*	1	1	12 S	47 E	C
14.....	13 06	*13 55*	2	1	10 S	11 E	C
15.....	14 18	*14 46*	1	1	10 S	3 W	C
15.....	*15 13*	*16 36*	10	2	10 S	4 W	C
17.....	*14 30*	*16 18*	2	1+	11 S	27 W	C
19.....	13 15	*15 18*	2	1+	11 S	63 W	C Four objects
20.....	*10 48*	*11 29*	4	1+	9 S	68 W	C
22.....	15 32	*15 56*	2	1	1 N	85 W	C With bright surge prominence
Aug. 3.....	10 12	*10 21*	2	1	15 N	60 E	C
3.....	11 33	*12 19*	3	1	16 N	60 E	C
4.....	*14 27*	*15 25*	3	1	17 N	42 E	C With surge
6.....	*13 56*	*14 30*	6	1+	17 N	26 E	C Low intensity
6.....	*15 50*	*16 52*	6	1+	17 N	25 E	C Low intensity
7.....	*8 12*	*8 20*	5	1	17 N	15 E	C
7.....	*10 17*	*10 47*	4	1	17 N	14 E	C
7.....	*13 49*	*16 10*	8	2	17 N	13 E	C With large surge
8.....	*9 15*	*9 53*	2	1	18 N	2 W	C
8.....	*11 45*	*12 53*	2	1	17 N	3 W	C
9.....	*12 35*	*12 51*	1	1	18 N	12 W	C
9.....	13 17	*14 05*	3	1	18 N	13 W	C
11.....	*9 43*	*11 10*	6	1	15 N	40 W	C With bright and dark surges
11.....	10 24	*11 27*	2	1	14 N	85 E	C
11.....	*12 44*	*12 59*	1	1	15 N	41 W	C With surge
11.....	*13 20*	*14 10*	2	1+	14 N	83 E	C With bright surge
11.....	*14 07*	*14 25*	1	1	15 N	42 W	C
11.....	*15 35*	*15 55*	2	2	15 N	43 W	C Brilliant. With large surge
14.....	*11 01*	*12 16*	20	2+	12 N	33 E	C Brilliant
Oct. 14.....	10 14	10 47	15	2	9 S	40 W	S

than the date quoted. Most of our + groups are indeed found to have had flares whereas most – groups are found to have had no flares. The agreement is so striking that it may be taken as an indication that a strictly photometric classification of chromospheric faculae might be a useful activity index. (According to a private communication this fact has been established also from a similar rutin work carried out by Professor Kiepenheuer in Freiburg.)

When all the plage areas are taken together it is found from this table that 40 per cent of all the 770 cases are active according to both classifications whereas 32 per cent are non active according to both classifications. Now it

is well possible that a plage area which has low intensity in the 1st day-sector after the central meridian gets a higher intensity only next or following days and with flares. It is possible as well that some bright plage areas really have had flares though they have escaped detection. Finally the appearance of flares may not be the only criterion of a high activity region. The indications of table III may, therefore, be considered rather convincing if we remember also that the quality of the spectroheliograms may be subject to variations, introducing in this way some faults in the classification. No doubt real measurements would be more satisfactory. It seems to us that the variations in the intensity of faculae are more apparent when working with a rather broad pass-band in the spectrum of the order of 0.8 Å for Hα than when working with a more narrow pass band.

B. Solar flares. In table IV a presentation is given of all flares observed at the Stockholm Observatory in Saltsjöbaden and at the Swedish Solar Station in Anacapri during 1952 and 1953. A continuous visual flare patrol was tried on Capri by Y. Öhman in collaboration with Mr N. E. Öhman during the summer of 1953. During this period the number of flares observed with the 1.0 Å polarizing monochromator is considerable. Our scale of importance is perhaps somewhat higher than the international one according to comparisons kindly made for us by Dr L. d'Azambuja in Meudon, and to some extent the use of a rather broad passband in the monochromator may have caused some minor systematic differences from the international scale. The times for the beginning and ending of the flares have been given in Universal Time. Figures in italics mean real beginning or ending of the phenomenon.

At the Stockholm Observatory the observations of flares have been made with the spectroheliograph described before, used as spectrohelioscope. The flare observed on October 14, 1953 was recorded after an announcement made by the Royal Swedish Board of Telegraph of a fade out.

Some of the more interesting flares have been described before in special publications[1].

C. Filaments. A presentation is made in table V and table VI of large filaments which have been recorded with the spectroheliograph of the Stockholm Observatory during 1952 and 1953. The date is given when the centre of the filament has been situated in the first day-sector after the sun's central meridian. From a comparison with the + and − signs in tables I and II it is possible to see which periods are complete and which are not complete. Dates given within parenthesis mean that the appearance of the filament has been judged from earlier or later observations.

[1] Observatory, Vol. 73, p. 203 and p. 236, 1953. Populär Astronomisk Tidskrift 35, p. 25, 1954.

Table V. Filaments observed in 1952

Jan.	Febr.	March	April	May	June	July	Aug.	Sept.	Oct.	Nov.	Dec.
(2)	(10)	1	5	15	9	(27)	12	(8)	(26)	29	—
16	13	2	16	16	10		21	20			
17	14	11	(27)	(18)			25				
(18)	18	29		30							
22											

Table VI. Filaments observed in 1953

Jan.	Febr.	March	April	May	June	July	Aug.	Sept.	Oct.	Nov.	Dec.
(13)	6	19	(23)	2	5	6	26	16	(20)	24	2
(16)	(7)			3				(24)		(28)	
				10				26			

All-Sky Camera Auroral Research during the Third Geophysical Year 1957—58

By WILLY STOFFREGEN, Upsala Jonosfärobservatorium, Section of Research Institute of National Defence, Stockholm, Sweden.

(Manuscript received May 20, 1955)

Abstract

A new type of auroral camera covering the whole sky is developed. Continuously running cameras of this type will be installed in Northern Scandinavia during the Geophysical Year in order to get a complete view of all aurorae occurring over this area. The film material obtained will be analyzed to give height and position of the auroral displays.

1. Introduction

During the Third Geophysical Year 1957—58 (AGI), a strong effort will be made to enlarge our knowledge of the physical properties of the aurorae. According to the recommendations of CSAGI[1], studies of the ionosphere, the earth's magnetism, cosmic rays and solar activity will be greatly extended during the AGI, and a network of expeditions will be placed in and near the polar regions. A great part of these have auroral research on their programmes.

The aurorae are greatly influencing ionospheric conditions at high latitudes, and radio communication through the auroral zones is considerably dependent on the presence of aurorae. This is one of the actual problems, and there is hope that the collected material from the AGI will shed light upon the whole mechanism from the disturbance on the sun to the appearance of aurorae and the resulting ionosphere disturbances, furthermore to a more exact determination of the central lines of the auroral zones and the distribution of aurora around these. Strong earth-magnetic activity results in a shift of the aurorae to lower latitudes and there is also a tendency of displacement of the auroral zones depending on season and time of day.

Visual observations and sporadic photography of aurorae are not sufficient for the study of these problems. The photographic work with ordinary narrow-angle cameras, however, has great importance when studying aurorae on a smaller part of the sky.

During the last 50 years, the different auroral forms have been analyzed by this photographic work and height and position determinations based upon thousands of photographs have been made. Despite the highly developed methods, there has been need for a network of all-sky cameras which gives a continuous survey of an aurora season also including periods without visible aurorae. In order to arrive at a practical realization of such a project which is expedient with regard to the costs of film, personnel and evaluation of the records, a compromise must be made, resulting in a limitation of film size and the number of exposures per minute.

[1] Commission Scientifique de l'Année Géophysique Internationale.

Assuming a mean of 12 hours' running each day during September—April and using a chain of six cameras constructed for 16 mm film and one exposure per minute, the total film consumption will be 6750 meters per year. Since it is not possible to photograph each night because of poor visibility and weather conditions there may be a loss of say 25 % and a resulting consumption of about 5,000 meters a year. The total costs of film and developing will then be about Sw. cr. 8,500 a year.

It has already appeared during the film tests in March—April 1955 that sometimes it would be of advantage to extend the number of exposures up to two per minute. This would give better records of rapidly changing auroral displays. On the other hand, this change would not be enough reason to double the total film costs.

2. Some Problems in Auroral Research

The aurora is a physical phenomenon which mainly occurs in the lower part of the ionosphere. The minimum and maximum heights of observed aurorae range between 75 and 700 km with an approximate centre of the distribution around 110 km height. About 94 % of all aurorae are observed between 90 and 130 km height.

The corpuscular theory of the aurorae has been established by Birkeland and experimentally verified by his laboratory experiments about 1905 with artificial aurorae on the *terrella*. His experiments gave an explanation of the auroral zones, lying at approximately 67° magnetic latitude, and their displacement to lower latitudes during periods of strong earth-magnetic activity.

Great effort has been made in Norway since many years to study the location and distribution of aurorae by simultaneous photography from two or more places, the first such photographs being made by Störmer at Bossekop in 1910 using a base line of about 5 km. Later a chain of stations has been established and is still in operation in Southern Norway and at Tromsö.

By using stars on the photographs it was possible to calculate the position of the aurorae. A summary of the Norwegian observational methods is given by HARANG (1951).

Different theories have been tried for explaining what is happening in the interval between the approach of the corpuscular stream from the sun to the earth and the appearance of a luminous aurora.

There is no discrepancy that the primary source of the aurorae is a radiation from disturbance centres on the sun's surface. There is a marked correlation between sunspot periods, aurorae and periodical variations of the earth's magnetic field. The general view is that the charged particles follow the lines of force of the earth-magnetic field towards the polar regions thus producing aurorae. There is still controversy on what is happening in space at a distance of a few earth-radii from the earth's equator.

The form and position in space of aurorae give some necessary information for the study of the charged particles which produce aurorae. An all-sky camera is doubtless an ideal tool for the study of auroral forms and their changes. The small picture-size and the 180° angle reproduced on the picture may cause small details such as ray structures to be lost, but the great advantage of the camera lies in that the aurorae are photographed over the whole sky. A network of about four all-sky cameras in Northern Sweden will give sufficient accuracy for a determination of the position in space of the aurorae.

3. Aurorae and Ionospheric Conditions

One of the aims of ionosphere research is to get a world-wide survey of ionospheric conditions and a more complete understanding of the influence on the ionosphere from solar disturbances and enhanced geomagnetic activity. The aurorae are an indication that a disturbance on the sun has appeared and the aurorae are changing the structure of the ionosphere in such a way that severe interference on radio communication through the auroral zones will be present. The F1 and F2 layers commonly show a decrease in critical frequencies and an increase in height, and ionospheric records taken during such disturbances show that the lower border of the ionosphere, the D-region, is blanketing the layers above by *high absorption of radio waves*, and the loss of echoes will often be total on all frequencies. Sporadic layers of high ionization often appear in the E-region at high latitudes during aurorae. These correlations were systematically

studied already during the Second Polar Year 1932—33.

In figure 1 an illustration is given of the different disturbances caused by the solar flare on October 14, 1953, and what part the aurorae play in this connection.

Immediately after the flare, the ionosphere at Upsala showed a direct effect due to the intense ultra-violet radiation from the sun. The absorption was very high (high $f_{min.}$-value). No aurora occurred this day and the sky was clear. On October 15 the corpuscular stream had reached the earth giving raise to a strong auroral display with arcs, rays, draperies and corona. The following disturbances were simultaneously noted:

1. Strong aurorae observed at Malmberget, lat. 67.3° N, long. 20.6° E.
2. Enhanced geomagnetic activity. K_p = geomagnetic planetary index.
3. Poor radio propagation conditions; the CRPL Q-values indicate radio propagation conditions in the North Atlantic area. The vertical lines represent the approximate upper and lower limit of the frequency band in Mc/s on which radio stations are received at Upsala.
4. Decrease of critical frequencies of the F-layer at Upsala and pronounced ionospheric storm tendency.
5. Improved reception of a long wave station (Warsaw, 227 kc/s) due to the high D-region ionization.

Upsala Ionosphere Observatory makes continuous ionosphere records at Upsala since 1952. In the near future two ionosphere recorders of panoramic type, taking rapid film records synchronously with the all-sky camera, will temporarily be installed at about 64° latitude in North Sweden, near Lycksele. The combination of rapid ionosphere records and the planned network of auroral cameras during the AGI will give possibilities for the detailed study of the ionosphere during aurorae. The recorders are of new construction with an extended frequency range down to 0.3 Mc/s and are accordingly suited for observation of the lower part of the ionosphere.

The map in figure 2 shows the approximate location of the Northern auroral zone and the positions of ionosphere recorders and aurora cameras during the AGI.

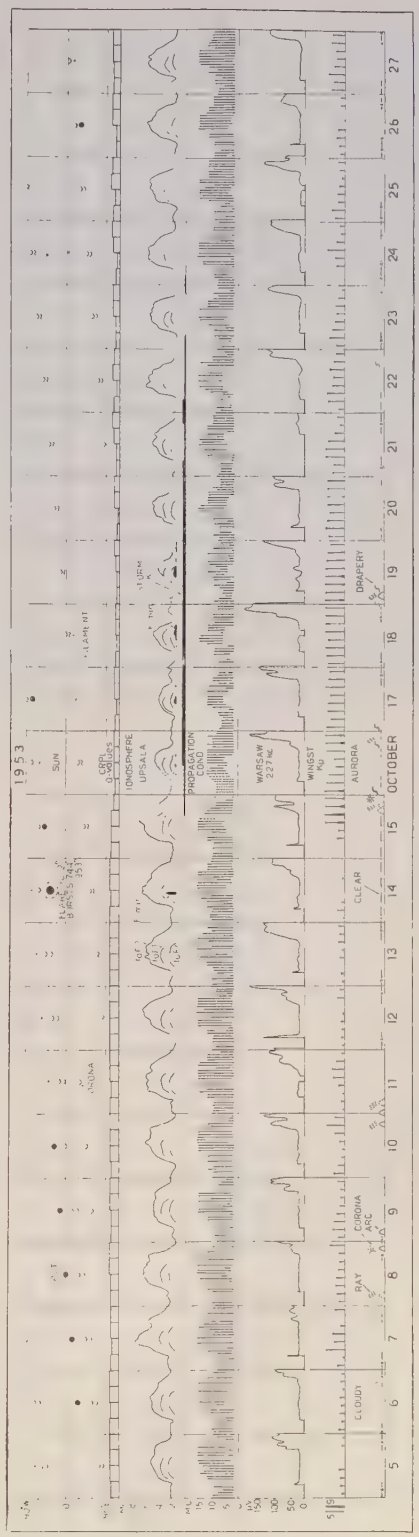

Fig. 1. An example of enhanced auroral activity and other geophysical disturbances caused by the solar flare on October 14, 1953.

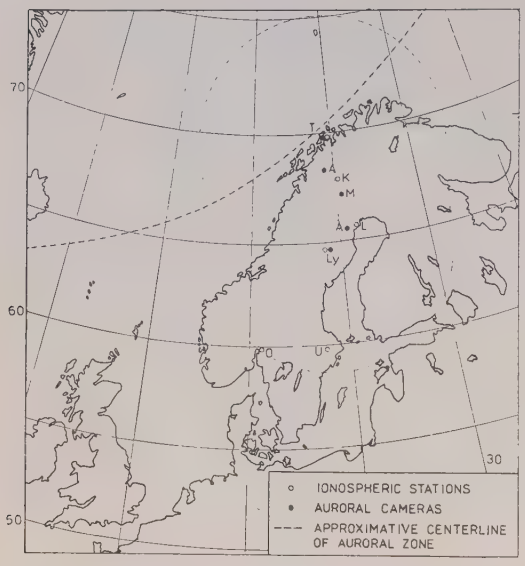

Fig. 2. Map showing the net of ionosphere stations and aurora cameras in Scandinavia during the AGI.

Ionosphere recorders:

T = Tromsö, Tromsö Auroral Observatory
O = Oslo, Ionosphere Station Kjeller, Norwegian Defence Research Establishment.
K = Kiruna, Chalmers University of Technology, Gothenburg.
L = Luleå, Royal Board of Swedish Telegraphs, Stockholm.
Ly = Lycksele, Upsala Ionosphere Observatory.
U = Upsala, Upsala Ionosphere Observatory.

All-sky cameras:

T = Tromsö, Upsala Ionosphere Observatory
A = Abisko, Upsala Ionosphere Observatory
M = Malmberget, Upsala Ionosphere Observatory
Ä = Älvsbyn (Luleå) Upsala Ionosphere Observatory
Ly = Lycksele, Upsala Ionosphere Observatory.

The places for the all-sky cameras have been chosen because of the possibilities of getting assistance from already existing institutions. The dotted line around the observational network indicates the approximate area covered by the auroral cameras. As a reasonable limit aurorae lower than 10° declination are not taken into account. Otherwise the range will be much more extended.

Radio reflections on very short wave-lengths have been obtained during aurorae since 1940 and this technique has been developed after the war by making use of radar equipment with some modifications. There is still discussion between different workers in this field whether the echoes are direct reflections or backscatter after reflection at an intense sporadic E-layer formed along the auroral zone. For the study of this an all-sky camera must be of great value for comparison of the distances measured by radar and the photographic observations.

4. Visual Observations

During 1953 a visual observational method was tried using prepaid postcards for reporting (figure 3).

A number of about 20 observers in Middle and North Sweden made regular observations. In this way the time, approximate direction, approximate height, type and brightness of the aurorae were reported. A summary of the observations showed that this method had some value for a coarse survey of the auroral activity. An experience was also gained of the difficulties of this method.

It is a great problem to find a staff of observers with sufficiently identical manner of reporting observations and it is further difficult to obtain observations without interruptions.

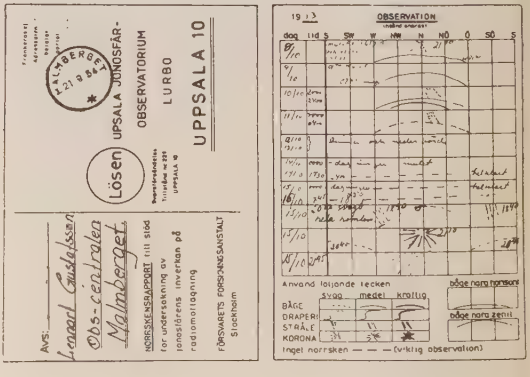

Fig. 3. Sample of aurora report on special cards.

The method can only be based on observations at fixed times or the cost will be prohibitive.

The accuracy of the visual observations by only looking at the sky is not great enough. A typical mistake is reporting the aurorae at much higher angles than they really are. From these reasons it was decided in the same year to use all-sky cameras instead of visual observations in North Sweden. The visual observations will continue, however, and will be a supplement to the photographic methods. Since it is too expensive to arrange photographic observations from South Sweden, visual observations from this part of the country will be of great supplementary value. Instructions for the observations will be given and simple mechanical means for a better determination of the position in the sky of aurorae are recommended. It is hoped that a great number of observers from schools and institutions will participate in this way during the AGI.

5. The All-Sky Camera

The requirements of the camera are as follows:

Great light power of the optical system in order to get short-time exposures.
An aperture of 180 degrees.
The best possible resolution despite the wide-angle coverage.
Avoiding of complicated optical arrangements.
Possibility of using a commercially manufactured 16 mm camera or parts of it.
A construction which is easy to handle and suited for the climate at high latitudes.
Synchronous exposures of all cameras in action.

A camera has been developed for meeting above demands with reasonable costs. Figure 4 shows the complete arrangement consisting of a hut, 2 × 2 meters with a hinged roof which is easy to let down. The camera is mounted on a heavy stand and two crossed arcs with small light bulbs built in for every 10th degree elevation angle are arranged to give a coordinate system for facilitating the evaluation of the films.

An ordinary objective Switar 1 : 1.4 is used. The spherical mirror is aluminized on the outside and provided with a hole in the centre great enough to pass the image to the camera placed below. The plane mirror on the top of the camera is of 110 mm diameter and the camera photographs the sky up to 78° elevation. By this arrangement only a small part of the sky is lost, contrary to some earlier systems which have the camera in the place of this plane mirror. Both mirrors are electrically heated, controlled by a thermostat. The camera is driven by a synchronous motor for 50 c/s and it will be easy to run several cameras synchronously at places which have the same mains frequency—this is the case in almost whole Sweden. Special arrangements will be made at those places not connected to the same net, as Tromsö and Abisko, The start of the cameras is made at an agreed time using chronometers. In this way the cameras will be running the whole night with synchronous exposures. The new cameras now under construction will be furnished with a clock, which is photographed on each picture. All films will also be marked with date and initials giving the place of observation.

Fig. 4. The complete camera arrangement opened for observation. Figures 5 a, b show the arrangement of the mirrors and figure 6 shows the optical details.

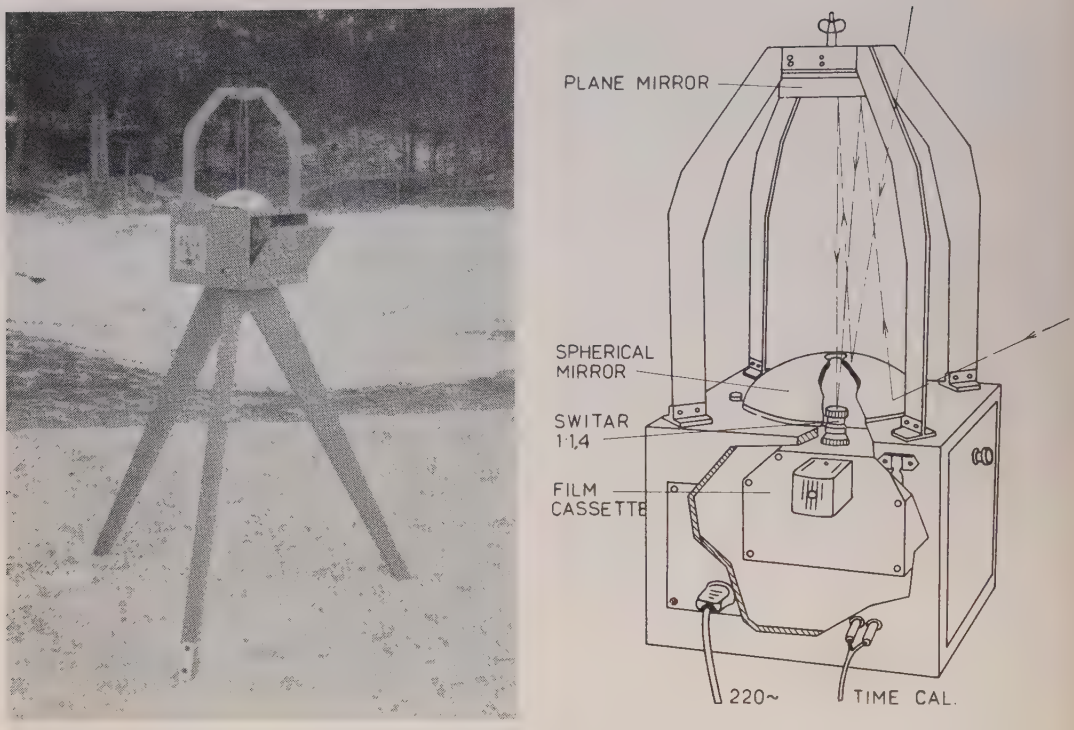

Fig. 5 a. The camera mounted on its stand.
b. The optical principle of the camera.

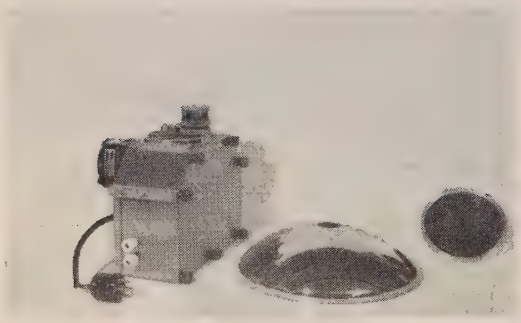

Fig. 6. The optical system of the camera.

6. The optical properties of the camera

During the construction of the camera two principal optical problems had to be solved. The first was to get a nearly linear reproduction of the whole sky and the second to get sufficient resolution despite the small picture size. The mirrors were constructed using a graphical method; the radius and diameter of the spherical mirror were found in this way. The mirror received from the manufacturer had some minor deviations from the calculated dimensions, but nevertheless the linearity is good as seen in figure 7 below.

After some experiments the different dimensions of the optical system were fixed and a calculation of the optical properties was made by A. Bring. The camera reproduces a virtual picture situated on a plane at a certain distance from the objective. The problem is whether the picture is deformed on this plane. The calculation shows, however, that this deformation is not severe and it further shows that the optical resolution on the film surface is about 100 lines per mm, which is of the same magnitude as the resolution of the film emulsion used. Several stars have been identified on the films and this is a good test on the resolution.

Figure 7 shows a picture with a very interesting auroral display.

The lamps are seen clearly and the black lines in NE, NW, SE, and SW are markings

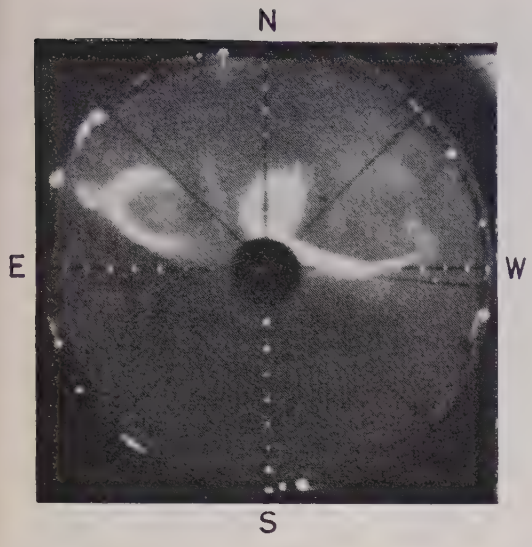

Fig. 7. An aurora of unusual type.

from the supports for the plane mirror. The picture clearly shows the efficiency of this type of photography.

The Western part of this aurora is situated over the Norwegian coast, near Lofoten, and the Eastern part is over Northern Russia, southeast of Kirkenes. This picture is subject for special studies. According to the theory (ALFVÉN, 1950), this trochoidal aurora form may be developed in either an inhomogeneous field or a combination of an homogeneous magnetic field and an electric field. The trochoid is in such a case the result of a circular motion with a superimposed drift motion.

The details of the picture are such that three stars can be detected. One of these can be seen near the antenna mast in the Western direction.

The film strip in figure 8 contains nearly all principal forms of aurorae. Pictures 1—5 show some phases in the development of the auroral form in figure 7. The ray structure is clearly visible in picture 4. Pictures 6—9 show arcs and draperies. Picture 11 resembles a bright flame from zenith to the northern horizon. Pictures 14—18 show different phases of a corona.

These film strips are a good example of the change appearing between each picture when using one exposure per minute. All these pictures were taken with 7 seconds time of exposure, this time being most suitable for this camera and the film used (Gevapan 32°). There is no intention of varying the exposure time depending on auroral brightness. A time of 7 seconds secures that even weak aurorae are photographed, and there is no severe danger of over-exposure. A fixed time of exposure makes it easier to classify the aurorae according to their brightness.

7. The interpretation of the aurora films

The great number of aurora films from the winter 1957—58 will make special arrangements necessary for the interpretation of this material. Moreover, the aurora cameras will also, to some extent, be running during other years. As mentioned before a chain of cameras will be installed at such distances from each other (120—150 km) that it will be possible to find the height and position of recorded aurorae by easy means. Different ways may be tried to find the most effective method of interpretation and at present an arrangement according to the following is under construction. A film projector will be built with 6 identical optical systems. Using this projector 6 pictures of 6×6 cm size, representing simultaneous records from the 6 stations in operation, will be projected side by side on a measuring table. The 6 projector units can be coupled together and each picture of the films may be studied without further synchronization. Each series of 6 pictures can be copied if wanted.

The primary result of one picture series will consist of a table containing time of exposure, elevation and bearing for a number of chosen points of the aurora for each observing station. This table will then be used for a determination of the position of the aurora by means of a mechanical device according to figure 9.

A horizontal rotating disk with an azimuth dial is mounted at the place of each observing station on a large curved map. Each of these disks supports a vertical dial with a steel pointer, which can be put in any direction between 0°—90°. After adjusting each of the 6 pointers to directions given by corresponding film pictures, the point of intersection of the pointers will give the geographical position and height over the earth surface of the chosen point of the aurora considered. These

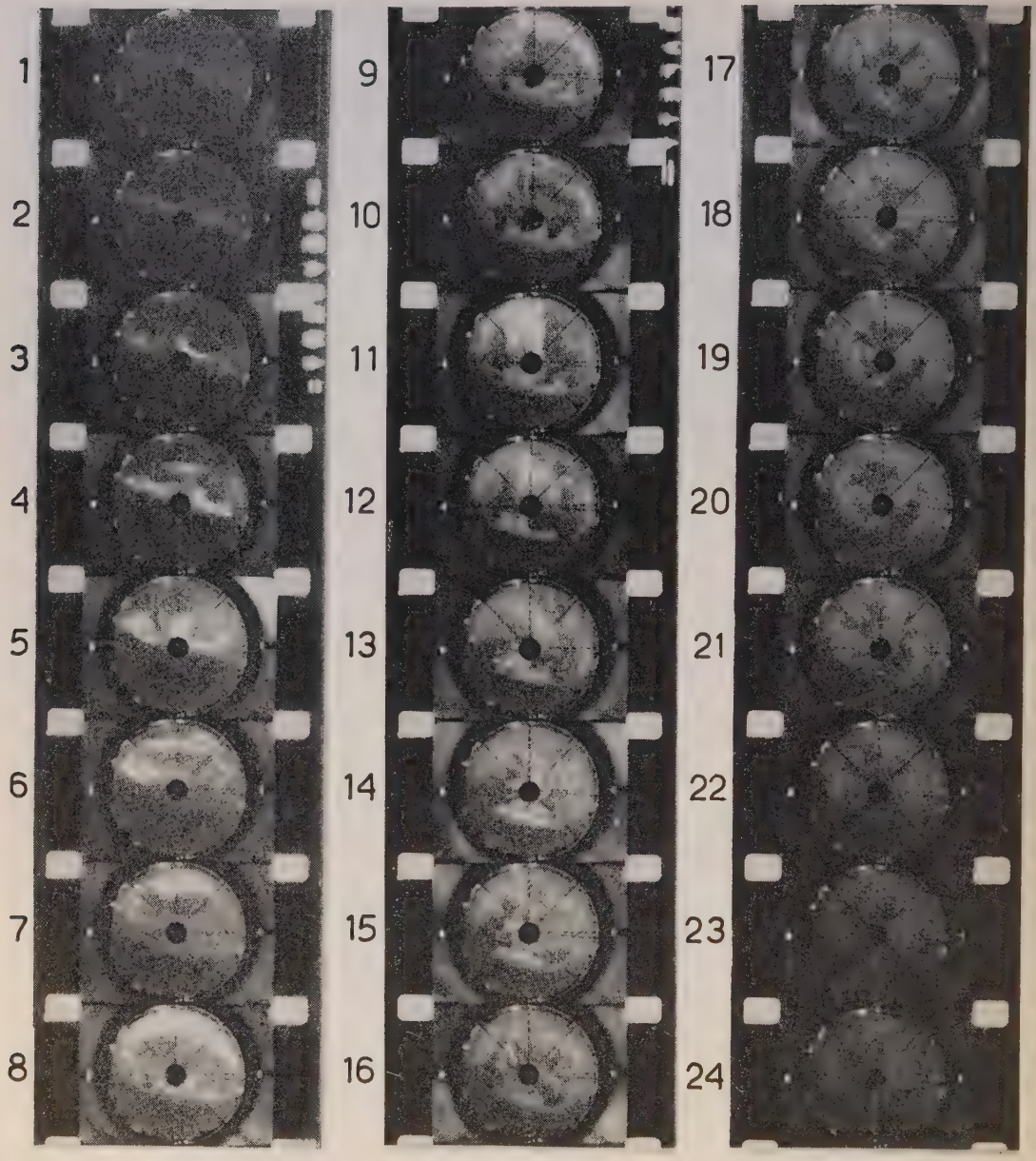

Fig. 8. Film strip of an aurora.

data will be put into a final map. The final result of the aurora films taken during the AGI will be brought together in a catalogue containing a survey of all aurorae observed and maps of their positions together with typical pictures. For statistical studies a great number of aurora observations may be brought together in three-dimensional models. The method of evaluation indicated above does not require personnel of high training.

This special projector arrangement is even usable for the study of the ionospheric records made at the same time.

Acknowledgement

I am much indebted to Mr A. Bring for his mathematical treatment of the optical system and to Mr H. Derblom for his assistance during the construction of the camera and the tests in Northern Sweden.

REFERENCES

Alfvén, H., 1950, *Cosmical Electrodynamics*, Chapter II, Oxford, Clarendon Press.

Harang, L., 1951: *The Aurorae*, The International Astrophysics Series, London, Chapman & Hall.

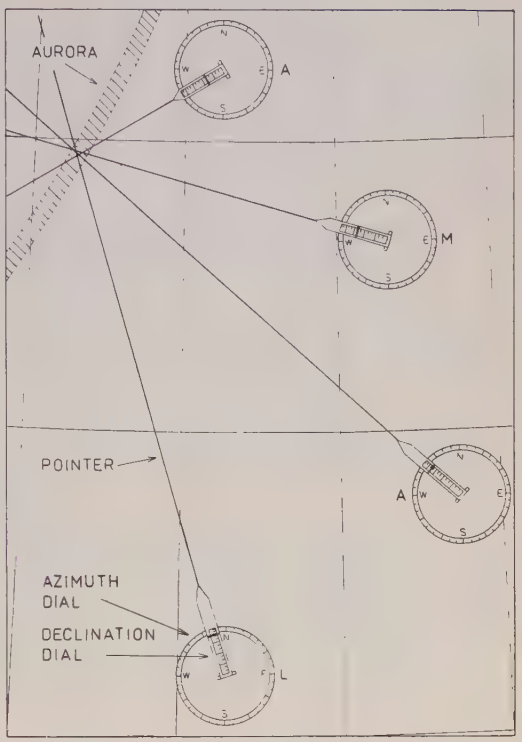

Fig. 9. Principle for determination of the position of aurorae.

—508697

The Equatorial Undercurrent in the Light of the Vorticity Equation[1]

By Dr N. P. FOFONOFF[2] and Prof. R. B. MONTGOMERY[3], Brown University, Providence

(Manuscript received 23 July 1954)

Abstract

The Equatorial Undercurrent, recently observed in the central Pacific Ocean by Cromwell, Montgomery, and Stroup, is a narrow eastward current occupying the lower part of the surface layer at the equator. In the present study the Undercurrent, treated as a permanent feature of the oceanic circulation, is found to be consistent with the conservation of absolute cyclonic vorticity in the equatorward flow comprising one segment of the meridional circulation. The continental barriers permit the formation of the longitudinal pressure-gradient component essential for the existence of the Undercurrent.

Cromwell, Montgomery, and Stroup (1954), in a preliminary account of drogue observations in the central Pacific Ocean, have reported the discovery of the Equatorial Undercurrent. Although this current appears to be a normal feature of the oceanic circulation, further study is required to test this tentative conclusion. The Undercurrent was observed in the zone from the equator to latitude 1° N and at depths from 50 m to 150 m. The velocity was eastward and exceeded 1 knot at the axis. As the bottom of the surface layer or top of the thermocline was at about 100 m, the Undercurrent was found both in the lower part of the surface layer and in the upper part of the thermocline. Previous meridional sections of serial oceanographic observations in this region have been published by Cromwell (1953), Jerlov (1953), and Montgomery (1954).

[1] This study was sponsored by the Office of Naval Research. U. S. Department of the Navy, under contract with Brown University.

[2] Now with Pacific Oceanographic Group, Nanaimo, British Columbia, Canada.

[3] Now with Chesapeake Bay Institute, The John Hopkins University, Baltimore 18, Maryland, USA.

In the present paper the Equatorial Undercurrent is found to agree with a simple application of Rossby's (1936) vorticity equation, that for a horizontal layer of fluid displaced frictionlessly

$$\frac{d}{dt}\frac{f+\zeta}{D} = 0, \qquad (1)$$

where D is the thickness of the layer, ζ is the vertical component of vorticity in the cyclonic sense—or simply *cyclonic vorticity*—relative to the earth's crust, and f is the Coriolis parameter, equal to $2\omega \sin\varphi$, where ω is the angular speed of the earth's rotation and φ is latitude. The absolute cyclonic vorticity is $f+\zeta$. By using cyclonic vorticity and the convention that latitude and Coriolis parameter are positive on both sides of the equator, the discussion can be so worded as to apply in either hemisphere. Fluid crossing the equator forms an exception to (1), for ζ reverses sign.

Let x be distance eastward and y be distance from the equator. Let u and v be the eastward and poleward components of velocity. Then, to a good approximation in low latitudes,

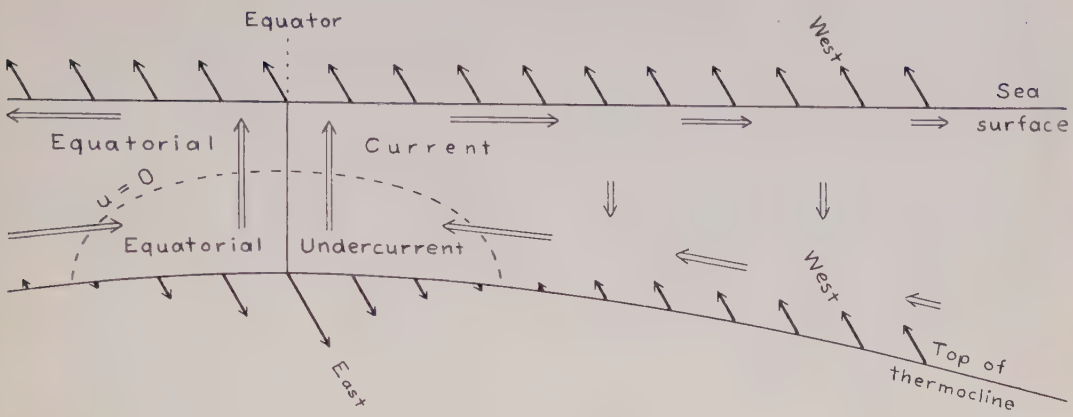

Fig. 1. Meridional section showing idealized currents in surface layer (about 100 m deep) within about 3° of equator, reader looking west. Arrows with double shafts give flux components in the plane of the section. Longitudinal component of velocity at top and bottom of layer is given by diagonal arrows in perspective. Vertical exaggeration 10^3.

$$\zeta = \frac{\delta v}{\delta x} - \frac{\delta u}{\delta y}.$$

One important assumption in the present discussion is that longitudinal gradients are small compared with meridional gradients. In the Pacific Ocean the system of equatorial currents at the surface parallels the equator for some 130 degrees of longitude, so this assumption is strongly supported. As a consequence, the cyclonic vorticity reduces to simply

$$\zeta = -\frac{\delta u}{\delta y} = -\frac{1}{a}\frac{\delta u}{\delta \varphi}, \qquad (2)$$

where a is the earth's radius. This assumption is not to be construed as making conditions longitudinally uniform. The thermocline's upward slope to the east, though small compared with the meridional slope, is an essential characteristic, made possible by the continental barriers. The upward slope of the thermocline is accompanied by a downward slope of the sea surface, and in the surface layer $\partial p/\partial x < 0$, where p is pressure. The longitudinal component of pressure gradient was considered by MONTGOMERY and PALMÉN (1940) to be essential for the existence of the Equatorial Countercurrent and is found in the present study to be essential for the existence of the Equatorial Undercurrent.

The second assumption is that within the surface layer there is a meridional circulation basically like that described by CROMWELL (1953). Easterly winds everywhere within 5 degrees of the equator both drive the west current (South Equatorial Current) and produce drift currents that transport water away from the equator. The poleward transport of the drift current at first increases with distance from the equator, as the deflection due to the earth's rotation becomes effective. Outside an equatorial zone the earth's rotation is fully effective; the transport of the drift current is directed normal to the wind, and the unit-length transport equals τ_0/f, where τ_0 is wind stress, and thus decreases with increasing latitude. At some such latitude as 1° (CROMWELL, 1953, Fig. 7), therefore, there as a maximum poleward transport of the drift current.

As another segment of the meridional circulation, water flows equatorward in the part of the surface layer below the drift current. There is upward flow at the equator, downward flow poleward of latitude 1°.

The actual winds and currents are not symmetrical about the equator, and southeast trades prevail at the equator. As far as the basic features of the Undercurrent are concerned, however, an adequate model seems to consist of a uniform east wind and an ocean symmetrical about the equator. This model is sketched in Fig. 1. The surface layer in this model contains a closed meridional circulation on each side of the equator.

The longitudinal component of surface current is represented as uniform, the relative cyclonic vorticity being zero. The justification for this simplification is that current charts

depict the South Equatorial Current as comparatively broad and uniform; for the entire zone from 5° S to 5° N the surface current is west with maximum speed less than 1.5 knots. The actual lateral shear is small, therefore, compared with what it would be in such a zone if the absolute cyclonic vorticity were uniform (as will be seen from Fig. 2).

If a water layer moves frictionlessly from an initial state f_0, ζ_0, D_0 to a new state f, ζ, D, the vorticity equation gives the relation

$$\frac{f+\zeta}{D} = \frac{f_0+\zeta_0}{D_0}. \tag{3}$$

For water sinking from the surface in the model described, $\zeta_0 = 0$. If this water flows to the equator, the properties become ζ_E, D_E, where

$$\frac{\zeta_E}{f_0} = \frac{D_E}{D_0}. \tag{4}$$

Hence, the water arrives at the equator with positive cyclonic vorticity, regardless of the ratio D_E/D_0.

If the thickness D is assumed constant during displacement and if all the water is assumed to have started from the initial state f_0, $\zeta_0 = 0$, u_0, the exact distribution of zonal component of velocity is easily found by integration of

$$f+\zeta = f_0 \tag{5}$$

to be

$$u - u_0 = 2a\omega[(\varphi_0 - \varphi)\sin\varphi_0 + \cos\varphi_0 - \cos\varphi]. \tag{6}$$

The result is given in terms of the speed of the earth's crust at the equator, $a\omega = 465$ m/s. The minimum eastward component is u_0 (which is negative in the model).

For small latitudes the last equation may be written in the approximate and simpler form

$$u - u_0 = a\omega(\varphi - \varphi_0)^2 \tag{7}$$

(accurate within one per cent in a zone from the equator to latitude $11^1/_2°$), which is drawn in Fig. 2. This convenient graph is valid for any value of u_0 and for any small value of φ_0.

Suppose surface water in a west current (South Equatorial Current) of, say, 0.5 knot with no lateral shear sinks and flows frictionlessly and without change in thickness to the equator. To reach the equator as the east Undercurrent of, say, 1.5 knots, a change of 2 knots, Fig. 2 shows that the water must have come from latitude 2.7°. If frictional losses are allowed for, the average latitude of origin is greater.

The Undercurrent and Cromwell's meridional circulation therefore fit in with the conservation of absolute cyclonic vorticity in the equatorward flow. It is not sufficient to consider the vorticity equation alone, however, for the gain of eastward momentum by the water flowing toward the equator must also be explained. The source of this eastward momentum is to be found in the longitudinal component of pressure gradient, already mentioned. The existence of the longitudinal component of pressure gradient (other than locally) is made possible by the presence of the continental barriers. The conclusion is reached that the Equatorial Undercurrent could not be set up by meridional circulation in a uniform zonal canal encircling the earth.

The longitudinal component of pressure gradient can be expressed in terms of the longitudinal slope of isobaric surfaces. In the lower part of the surface layer in the Pacific Ocean, Montgomery and Palmén (1940, Table IV) found this slope to be about 3×10^{-8}, which is roughly substantiated by Jerlov (1953, Fig. 4).

The equatorward component of velocity in the water moving from latitude φ_0 (say, 3°) to the equator can now be calculated. The longitudinal component of the momentum equation is

$$\frac{du}{dt} = fv - \alpha\frac{\delta p}{\delta x}, \tag{8}$$

where α is specific volume. As

$$fv - \frac{du}{dt} = fv - v\frac{\delta u}{\delta y} = (f+\zeta)v = f_0 v,$$

(8) can be written in the form

$$v = \frac{\alpha}{f_0}\frac{\delta p}{\delta x} = \frac{g}{f_0}\left(\frac{dz}{dx}\right)_{\varphi,p} \approx \frac{g}{2\omega\varphi_0}\left(\frac{dz}{dx}\right)_{\varphi,p}, \tag{9}$$

where g is gravity. As $\partial p/\partial x$ is presumably uniform within the zone from the equator to φ_0, v is also uniform. Furthermore, v is seen to be inversely proportional to φ_0. For $\varphi_0 = 3°$ ($f_0 = 7.6 \times 10^{-6}\ s^{-1}$) and a slope $(dz/dx)_{\varphi,p} =$

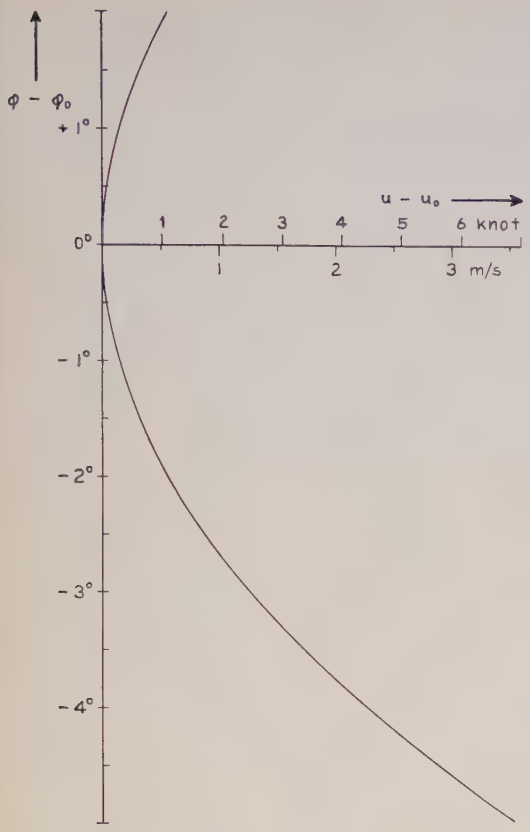

Fig. 2. Eastward speed in zonal flow near equator when the absolute cyclonic vorticity is uniform. The minimum speed (u_0) and the latitude of minimum speed (φ_0) are arbitrary.

$= -3 \times 10^{-8}$, the equatorward component of velocity is calculated to be
$-v = 4$ cm/s $= 2$ nautical miles per day.
The time required for the water to travel from latitude φ_0 to the equator is

$$-\frac{a\varphi_0}{v} = -\frac{2a\omega\varphi_0^2}{g}\left(\frac{dz}{dx}\right)^{-1}_{\varphi,p} \qquad (10)$$

and, therefore, is proportional to the square of φ_0. For the values already assumed, this time is

$$-a\varphi_0/v = 87 \times 10^5 s = 100 \text{ days}.$$

There is another noteworthy restriction of the Undercurrent. As is well known, most oceanic and atmospheric flow is quasi-geostrophic. Over most of the earth, one current does not underly an opposite current within the same homogeneous layer. An undercurrent opposite to the surface current, both in the surface layer, can occur only very close to the equator. Off a coast facing poleward at a moderate latitude, east winds would be expected, therefore, to produce upwelling but no undercurrent.

In summary, the Equatorial Undercurrent is found to be consistent with the equatorward flow in the lower part of the surface layer close to the equator if this flow is approximately frictionless so that absolute cyclonic vorticity is conserved. Continental barriers, which permit a longitudinal component of pressure gradient, are essential for the extensive development of the Undercurrent. In general, an undercurrent within the surface layer can occur only in a narrow equatorial zone. The theoretical latitude of origin of the equatorward flow, calculated from the observed axial speed of the Undercurrent, is about 3°, which may be regarded as a minimum estimate. With the additional use of the observed longitudinal component of pressure gradient, the theoretical equatorward component of velocity is calculated to be 4 cm/s, and the time of travel from 3° to the equator is calculated to be 100 days.

REFERENCES

Cromwell, Townsend, 1953: Circulation in a meridional plane in the central equatorial Pacific. *J. mar. Res.*, **12**, 196—213.

—, Montgomery, R. B., and Stroup, E. D., 1954: Equatorial Undercurrent in Pacific Ocean revealed by new methods. *Science*, **119**, 648—649.

Jerlov, N. G., 1953: Studies of the equatorial currents in the Pacific. *Tellus*, **5**, 308—314.

Montgomery, R. B., and Palmén, E., 1940: Contribution to the question of the equatorial counter current. *J. mar. Res.*, **3**, 112—133.

—, 1954: Analysis of a Hugh M. Smith oceanographic section from Honolulu southward across the equator. *J. mar. Res.*, **13**, 67—75.

Rossby, C.-G., 1936: Dynamics of steady ocean currents in the light of experimental fluid mechanics. *Pap. phys. Oceanogr. Meteor., Mass. Inst Tech. & Woods Hole oceanogr. Instn*, **5**, no. 1, 43 pp.

Current Data on the Chemical Composition of Precipitation and Air IV

(For further information see Egnér, H., Eriksson, E., *Tellus* **7**, 134—139, 1955.)

Precipitation July 1955. D 507

Station	Code	mm	mg/m²								pH	$\frac{\mu val}{l}$ HCO_3^-	ohm⁻¹ cm⁻¹ $\varkappa \cdot 10^6$
			S	Cl	NO_3-N	NH_4-N	Na	K	Mg	Ca			
Riksgränsen	Ri	31	17	76	5	2	46	7	5	21	6.0	15	14
Kiruna	Ki	18	6	32	2	2	21	7	1	26	6.2	30	19
Arjeplog	Ar	3	—	—	—	—	—	—	—	—	—	—	61
Ojebyn	Oj	14	15	21	3	5	26	11	3	45	7.1	156	43
Robäcksdalen	Rö	31	10	10	4	5	18	12	3	27	6.7	33	14
Otter	Ot	31	22	15	3	5	32	9	5	41	6.9	80	21
Bredkälen	Br	24	16	4	2	3	10	4	1	14	5.7	4	11
Åre	ÅE	31	8	13	3	4	33	8	5	34	6.6	104	22
Åre, Hummeln	ÅH	27	7	12	4	3	19	3	3	16	6.4	28	12
Sveg	Sv	40	26	9	8	16	18	10	4	30	6.0	13	13
Mora	Mo	37	33	9	3	5	8	24	5	43	5.9	16	12
Ämot	Äm	43	23	9	3	9	26	8	4	29	6.4	26	11
Sala	Sa	49	37	15	9	1	32	9	6	40	6.3	22	13
Ultuna	Ul	4	10	4	2	2	12	3	2	17	—	—	51
Erken	Er	13	15	4	2	6	7	21	3	15	6.8	46	27
Strängnäs	St	7	11	2	0	0	15	3	2	15	7.0	91	33
Bosshult	Bo	38	30	9	2	0	25	8	5	31	6.2	13	10
Kvamtorp	KvA	38	181	95	5	23	17	17	9	218	4.6	0	83
Kvamtorp	Kv*	60	60	13	5	8	27	10	4	25	4.5	0	25
Västra Ny	VN	25	60	97	8	117	58	103	17	27	6.9	120	85
Lanna	La	18	28	66	4	13	38	12	5	34	6.9	102	39
Hörö	Hö	10	10	23	2	2	25	3	3	22	7.0	70	30
Visby	Vi	17	22	241	3	6	169	11	19	24	6.4	22	78
Falsterbokrok	Fa	33	13	13	0	0	10	12	5	26	6.5	37	11
Hörby	Hö	10	22	16	2	3	26	5	3	24	6.4	22	22
Ängelsmark	Äm	34	18	41	2	4	39	5	5	23	6.3	20	15
Stenungsön	Sö	16	16	27	3	3	19	5	5	14	4.7	0	32
Hönningen	Hö	19	18	35	4	3	37	4	5	24	6.5	50	27
Skrädv	Sk	44	44	25	6	5	34	8	6	43	5.2	0	19
Smedby	Sm	32	37	14	0	4	34	34	6	42	5.9	25	14
Svitsen	Sv	11	8	15	3	0	11	12	4	58	7.4	282	51
Blakse-Hoby	BH	13	20	6	0	0	13	5	3	22	5.6	17	22
Hammenhög	Hä	20	44	20	10	10	48	72	8	55	6.8	77	38
[illegible]	[illegible]	[illegible]	[illegible]	[illegible]	[illegible]	[illegible]	[illegible]	[illegible]	[illegible]	[illegible]	[illegible]	[illegible]	[illegible]
[illegible]	[illegible]	[illegible]	[illegible]	[illegible]	[illegible]	[illegible]	[illegible]	[illegible]	[illegible]	[illegible]	[illegible]	[illegible]	[illegible]
As	As	16	13	8	0	0	18	5	4	24	6.7	56	19
[illegible]	[illegible]	[illegible]	[illegible]	[illegible]	[illegible]	[illegible]	[illegible]	[illegible]	[illegible]	[illegible]	[illegible]	[illegible]	[illegible]
Lista	Li	2	—	—	—	—	—	—	—	—	—	—	170
Karlskrona	Ka	55	30	9	1	0	35	16	5	38	5.8	15	10
[illegible]	[illegible]	[illegible]	[illegible]	[illegible]	[illegible]	[illegible]	[illegible]	[illegible]	[illegible]	[illegible]	[illegible]	[illegible]	[illegible]
Jyväskylä	JY	58	8	32	0	0	16	7	7	44	6.3	30	16
Ylämme	Yl	12	0	13	0	1	12	7	4	25	6.6	57	26
Oulu	OU	11	21	14	4	0	26	4	3	19	4.8	0	36
Ås	Ås	19	27	25	7	4	20	9	17	27	5.5	0	32
Ås	Ås	44	43	20	8	0	45	9	9	52	6.3	30	20
Abborre	Ab	16	22	20	0	1	52	6	7	30	6.8	143	38
Edinburgh	Ed	34	35	40	0	0	44	7	7	39	5.5	0	14
Leeds	Le	19	48	20	3	2	12	7	9	47	4.5	0	50
Rothamsted	Ro	4	16	10	2	1	12	6	3	34	—	—	73
Newton Abbot	NA	85	150	30	35	44	52	17	13	59	4.3	0	48
Augustenborg	Au	[illegible]	[illegible]	[illegible]	[illegible]	—	—	—	—	—	—	—	—
Gartenthal	Ga	128	124	28	23	23	19	19	14	75	4.9	0	20
Edinburg	Ed	141	141	93	39	55	20	29	10	94	4.9	0	23

* Start 1.8.55

Precipitation August 1955. D 508

Station	Code	mm	mg/m²								pH	$\frac{\mu val}{l}$ HCO_3^-	ohm⁻¹ cm⁻¹ $\varkappa \cdot 10^6$
			S	Cl	NO_3-N	NH_3-N	Na	K	Mg	Ca			
Riksgränsen	Ri	105	51	83	8	12	53	11	8	57	5.1	0	13
Kiruna	Ki	6	7	56	3	1	11	6	3	49	—	—	73
Arjeplog	Ar	4	2	61	1	0	22	3	3	48	—	—	109
Öjebyn	Öj	14	6	19	2	2	5	3	3	31	6.7	72	24
Röbäcksdalen	Rö	72	47	30	9	17	25	12	7	35	5.2	0	14
Offer	Of	46	27	34	3	2	34	10	7	49	6.5	45	15
Bredkälen	Br	33	11	4	1	0	5	2	2	35	5.8	10	6
Åre	ÅF	88	22	10	3	0	17	7	3	20	5.9	7	5
Åre, Hummeln	ÅH	105	28	14	4	1	18	7	7	16	5.9	13	4
Sveg	Sv	90	25	15	5	3	21	4	4	40	5.8	7	5
Rättvik[1]	Rä	58	73	23	2	0	13	7	5	122	6.6	80	21
Åmot	Åm	42	40	16	7	12	23	8	5	29	5.9	17	17
Sala	Sa	26	46	12	7	7	24	8	10	59	6.7	72	33
Ultuna	Ul	11	26	21	5	6	10	8	4	46	6.7	101	55
Erken	Er	3	—	—	—	—	—	—	—	—	—	—	61
Strängnäs	St	36	62	11	8	10	28	11	8	49	5.8	12	25
Forshult	Fo	69	50	14	9	12	26	9	8	30	5.4	0	12
Kvarntorp	Kv1	53	575	120	11	49	25	35	19	670	6.4	37	128
Kvarntorp	Kv7	67	114	26	12	41	14	16	7	67	4.4	0	41
Västra Ny	VN	13	81	53	10	160	65	113	17	30	7.4	800	198
Lanna	La	78	60	22	12	30	35	18	14	57	6.5	37	15
Bornö	Bo	29	37	90	8	2	70	9	15	43	6.4	40	35
Vinga	Vi	61	114	477	22	40	275	36	40	49	4.6	0	66
Falsterbobruk	Fa	39	42	21	7	8	13	10	16	31	5.1	0	20
Flahult	Fl	29	38	10	7	13	21	12	6	38	6.3	38	24
Ambjörnarp	Am	42	47	45	9	11	38	11	9	48	6.0	19	22
Simlångsdalen	Si	86	83	60	18	33	45	13	9	40	5.3	0	21
Plönninge	Pl	82	96	54	17	24	70	19	13	53	5.6	0	18
Söraby	Sö	40	57	23	9	15	25	12	7	38	5.3	0	22
Smedby	Sm	30	36	9	7	13	23	9	6	36	6.4	38	23
Sylfaste	Sy	4	—	—	—	—	—	—	—	—	—	—	95
Bräkne-Hoby	BH	53	68	20	12	17	21	15	8	42	5.0	0	23
Hammenhög	Ha	36	48	20	10	5	22	19	7	60	5.9	16	25
Alnarp	Al	8	18	17	3	2	10	3	4	27	6.8	—	47
Hilleshög	Hi	54	46	21	7	5	20	6	12	33	5.0	0	11
Ås	Ås	22	43	20	10	9	31	10	7	35	6.4	34	33
Vågåmo	Vå	7	13	34	0	0	27	15	6	42	7.2	—	75
Lista	Li	55	64	258	15	18	122	17	57	21	4.9	0	41
Kauhava	Ka	36	26	17	6	6	14	10	4	28	5.3	0	16
Kuopio	Ku	11	21	9	9	58	14	34	6	15	7.5	490	79
Jyväskylä	Jy	17	18	60	4	2	18	7	3	39	6.3	41	31
Tvärminne	Tv	16	22	10	5	2	13	12	5	21	5.9	22	24
Ödum	Öd	39	52	52	12	9	36	18	8	59	5.2	0	28
Askov	As	52	71	67	13	34	50	22	9	94	6.4	53	31
Tystofte	Ty	28	37	73	7	0	129	18	14	69	7.2	356	61
Aberdeen	Ab	7	29	53	2	0	74	7	15	49	6.6	—	145
Edinburgh	Ed	28	49	40	7	5	31	15	9	70	5.7	33	31
Leeds	Le	20	88	70	12	5	43	17	24	107	6.3	46	73
Rothamsted	Ro	19	49	44	12	9	24	14	7	77	5.9	20	53
Newton Abbot	NA	17	33	24	6	17	16	8	29	33	6.4	84	42
Augustenberg[2]	Au	44	114	43	27	28	47	23	23	124	6.2	31	45
Güntersthal	Gü	53	75	15	18	28	9	10	5	35	4.3	0	36
Feldberg	Fe	55	83	14	17	24	12	12	6	38	4.5	0	33

[1] The station Mora is moved to Rättvik (Rä), 35 km E of Mora.
[2] The station is situated 5 km W of Karlsruhe.

Precipitation September 1955. D 509

Station	Code	mm	mg/m²								pH	$\frac{\mu val}{l}$ HCO_3^-	ohm^{-1} cm^{-1} $\varkappa \cdot 10^6$
			S	Cl	NO_3-N	NH_3-N	Na	K	Mg	Ca			
Riksgränsen	Ri	62	18	51	2	0	28	6	4	28	5.2	0	7
Kiruna	Ki	121	73	16	11	56	12	24	4	20	6.1	21	8
Arjeplog	Ar	66	41	21	6	11	16	7	4	24	5.4	0	9
Öjebyn	Öj	136	88	15	11	20	32	16	7	69	5.5	0	10
Röbäcksdalen	Rö	59	43	43	6	10	38	9	6	37	6.0	16	12
Offer	Of	42	42	29	4	6	31	28	9	44	6.0	20	17
Bredkälen	Br	71	34	11	4	7	14	5	3	17	5.8	7	6
Åre	ÅF	68	16	30	2	5	32	9	4	23	6.2	17	7
Åre, Hummeln	ÅH	56	19	27	4	4	32	5	4	15	6.1	8	7
Sveg	Sv	70	34	11	6	7	18	6	4	16	5.6	0	7
Rättvik	Rä	53	34	29	7	13	14	8	7	113	6.8	100	23
Åmot	Åm	40	35	22	5	11	19	5	5	23	6.0	14	12
Sala	Sa	32	38	14	5	5	22	6	8	49	6.3	24	20
Ultuna	Ul	34	47	32	8	14	20	9	5	58	6.3	26	22
Erken	Er	91	82	55	14	22	39	19	9	47	4.8	0	20
Strängnäs	St	52	71	56	9	33	41	34	16	37	5.9	14	21
Forshult	Fo	41	44	20	6	11	31	6	8	31	6.0	12	15
Kvarntorp	Kv1	41	574	45	8	31	33	29	23	760	6.0	18	152
Kvarntorp	Kv7	46	65	57	5	14	30	10	8	41	5.0	0	22
Västra Ny	VN	58	51	29	13	49	27	14	5	50	6.2	40	18
Lanna	La	34	50	57	9	15	42	11	7	47	6.0	16	25
Bornö	Bo	94	107	299	20	29	198	15	28	43	5.0	0	28
Vinga	Vi	47	113	1420	21	16	815	38	122	75	4.7	0	138
Falsterbobruk	Fa	73	69	62	13	18	67	11	17	50	5.2	0	17
Flahult	Fl	88	79	79	15	26	48	14	8	50	4.9	0	19
Ambjörnarp	Am	99	89	132	18	29	95	14	12	47	5.0	0	19
Simlångsdalen	Si	132	127	206	27	40	144	19	18	51	4.7	0	22
Plönninge	Pl	73	95	224	18	27	158	48	28	109	6.4	60	34
Söraby	Sö	75	86	63	18	76	41	71	11	48	6.2	40	24
Smedby	Sm	51	40	66	9	10	55	13	13	44	5.9	19	18
Sylfaste	Sy	69	77	98	16	22	49	25	9	94	6.2	28	22
Bräkne-Hoby	BH	97	124	124	16	13	72	28	17	61	5.2	0	17
Hammenhög	Ha	82	76	175	20	16	49	236	39	104	6.4	75	29
Alnarp	Al	133	148	170	30	34	120	35	22	219	6.1	25	24
Hilleshög	Hi	59	57	89	14	27	53	9	9	39	5.4	0	20
Ås	Ås	100	74	43	15	15	46	14	12	42	5.2	0	14
Vågåmo	Vå	27	28	23	2	1	12	13	6	53	6.6	58	20
Lista	Li	116	151	2040	30	24	1260	66	138	80	4.8	0	90
Kauhava	Ka	83	77	16	11	18	14	9	14	59	5.0	0	14
Kuopio	Ku	87	80	16	11	16	12	6	5	50	5.3	0	11
Jyväskylä	Jy	106	80	15	12	20	14	10	4	33	4.9	0	12
Tvärminne	Tv	68	61	60	10	12	38	11	7	47	5.3	0	14
Ödum	Öd	77	73	163	16	23	108	16	12	43	5.0	0	22
Askov	As	85	136	236	29	72	167	19	20	73	5.0	0	35
Tystofte	Ty	82	104	312	19	25	245	33	59	112	6.5	75	35
Aberdeen	Ab	45	32	56	3	5	55	11	8	31	6.5	88	16
Edinburgh	Ed	41	39	69	1	1	51	11	14	34	5.7	0	18
Leeds	Le	31	82	116	10	12	47	11	27	98	5.4	0	49
Rothamsted	Ro	44	73	68	9	9	36	12	8	63	5.2	0	25
Newton Abbot	NA	23	49	201	2	3	105	13	27	87	6.8	150	67
Augustenberg	Au	49	99	45	15	35	33	14	17	80	5.8	21	32
Güntersthal	Gü	57	49	13	11	10	22	10	5	35	5.4	0	13
Feldberg	Fe	49	52	29	12	12	19	7	7	31	4.9	0	20

Air July 1955. L 507

Station	Code	$\mu g/m^3$ (= kg/km^3)						
		S	Cl	NH_3-N	Na	K	Mg	Ca
Riksgränsen	Ri	—	—	—	—	—	—	—
Kiruna	Ki	2.6	6.6	1.8	1.7	1.7	0.2	4.5
Arjeplog	Ar	—	—	—	—	—	—	—
Öjebyn	Öj	1.8	5.5	2.9	1.8	1.5	0.1	5.7
Röbäcksdalen	Rö	1.7	0.9	1.3	1.3	0.8	0.9	2.8
Offer	Of	6.2	7.3	4.9	1.8	2.4	1.3	4.0
Bredkälen	Br	0.0	0.0	0.8	1.0	0.9	0.0	0.5
Åre	ÅF	0.8	0.0	1.0	0.7	0.7	0.2	6.1
Åre, Hummeln	ÅH	4.4	2.4	1.7	1.1	1.0	0.6	8.0
Sveg	Sv	—	—	—	—	—	—	—
Mora	Mo	9.3	0.0	3.3	1.5	1.1	0 0	3.3
Åmot	Åm	3.9	0.8	3.2	1.6	1.2	0.0	3.1
Sala	Sa	11.	0.0	5.4	1.9	0.8	0.7	5.7
Ultuna	Ul	3.5	0.0	1.7	0.7	0.9	3.5	4.3
Erken	Er	6.9	2.6	1.8	1.0	1.1	1.5	2.6
Strängnäs	St	5.4	1.3	4.1	2.3	2.2	0.5	2.2
Forshult	Fo	4.9	1.3	4.3	1.6	1.3	0.4	5.9
Kvarntorp	Kv1	—	—	—	—	—	—	—
Kvarntorp	Kv7	0.3	1.2	2.6	0.6	0.3	0.5	4.2
Västra Ny	VN	—	—	—	—	—	—	—
Lanna	La	0.8	5.4	3.7	2.4	1.4	0.0	4.9
Bornö	Bo	9.1	26.	3.5	15.	1.4	2.4	8.8
Vinga	Vi	—	—	—	—	—	—	—
Falsterbobruk	Fa	3.4	15.	2.4	1.8	1.2	1.1	5.4
Flahult	Fl	1.0	0.0	0.2	0.2	0.0	0.2	1.1
Ambjörnarp	Am	—	—	—	—	—	—	—
Simlångsdalen	Si	—	—	—	—	—	—	—
Plönninge	Pl	4.5	3.1	5.2	1.2	0.8	0.3	3.0
Söraby	Sö	—	—	—	—	—	—	—
Smedby	Sm	2.3	4.4	3.6	1.1	0.2	0.0	5.0
Sylfaste	Sy	0.9	1.6	4.7	1.0	3.0	0.6	4.4
Bräkne-Hoby	BH	0.2	1.1	0.5	26.	0.0	0.0	3.6
Hammenhög	Ha	—	—	—	—	—	—	—
Alnarp	Al	6.2	1.1	5.0	1.7	0.9	1.1	3.6
Hilleshög	Hi	—	—	—	—	—	—	—
Ås	Ås	—	—	—	—	—	—	—
Vågåmo	Vå	2.0	1.0	3.9	0.9	1.2	0.3	7.5
Lista	Li	5.4	11.	1.6	6.9	0.9	1.6	4.4
Kauhava	Ka	0.3	4.9	3.1	2.2	1.7	2.0	5.5
Kuopio	Ku	4.2	0.0	2.4	1.0	0.6	0.6	6.8
Jyväskylä	Jy	—	—	—	—	—	—	—
Tvärminne	Tv	0.0	3.2	2.5	1.6	1.1	3.1	13.
Ödum	Öd	—	—	—	—	—	—	—
Askov	As	1.8	0.6	6.0	2.7	1.2	0.5	2.8
Tystofte	Ty	7.3	0.0	6.4	2.6	1.3	0.7	2.9
Aberdeen	Ab	16.	4.4	5.0	1.9	0.5	1.7	9.2
Edinburgh	Ed	11.	2.7	2.6	1.9	0.7	0.7	3.7
Leeds	Le	13.	0.0	2.9	1.8	0.8	3.2	5.3
Rothamsted	Ro	15.	5.4	5.4	1.8	1.2	1.6	7.4
Newton Abbot	NA	10.	4.9	5.1	1.7	0.4	0.8	5.5
Augustenberg[1]	Au	—	—	—	—	—	—	—
Güntersthal	Gü	8.9	7.0	4.3	1.7	1.6	0.7	8.7
Feldberg	Fe	4.5	0.0	1.6	0.5	0.5	0.6	0.9

[1] Start 1.8.55.

Air August 1955. L 508

Station	Code	$\mu g/m^3$ (= kg/km^3)						
		S	Cl	NH_3-N	Na	K	Mg	Ca
Riksgränsen	Ri	0.3	8.2	1.2	2.6	1.1	3.1	7.6
Kiruna	Ki	0.7	1.8	2.2	0.8	0.5	0.8	5.1
Arjeplog	Ar	—	—	—	—	—	—	—
Öjebyn	Öj	3.8	3.1	3.6	1.7	2.7	0.7	4.3
Röbäcksdalen	Rö	2.2	3.2	1.9	1.8	1.1	0.8	3.7
Offer	Of	0.7	2.2	4.1	1.8	2.3	1.6	10.
Bredkälen	Br	0.0	1.9	1.3	0.4	0.3	0.3	2.0
Åre	ÅF	0.2	2.0	1.3	0.6	0.5	0.4	2.9
Åre, Hummeln	ÅH	1.2	0.6	1.5	1.0	0.6	1.8	4.5
Sveg	Sv	—	—	—	—	—	—	—
Rättvik[1]	Rä	1.7	1.4	3.6	1.4	1.2	0.6	4.2
Åmot	Åm	3.3	5.5	4.5	1.7	0.9	1.3	8.1
Sala	Sa	2.5	2.8	4.3	1.3	1.5	2.0	6.5
Ultuna	Ul	1.4	3.7	3.0	0.8	1.4	0.6	1.5
Erken	Er	1.7	2.7	1.8	1.0	1.6	1.7	3.5
Strängnäs	St	1.8	0.0	4.1	1.5	2.4	1.4	4.7
Forshult	Fo	—	—	—	—	—	—	—
Kvarntorp	Kv1	—	—	—	—	—	—	—
Kvarntorp	Kv7	1.7	3.6	3.1	2.3	0.7	1.0	4.0
Västra Ny	VN	—	—	—	—	—	—	—
Lanna	La	0.1	4.3	5.4	0.8	2.1	0.7	5.0
Bornö	Bo	—	—	—	—	—	—	—
Vinga	Vi	—	—	—	—	—	—	—
Falsterbobruk	Fa	0.7	4.3	3.3	1.1	0.8	0.7	4.0
Flahult	Fl	—	—	—	—	—	—	—
Ambjörnarp	Am	—	—	—	—	—	—	—
Simlångsdalen	Si	—	—	—	—	—	—	—
Plönninge	Pl	0.6	0.6	6.2	1.1	0.8	0.3	7.3
Söraby	Sö	—	—	—	—	—	—	—
Smedby	Sm	2.0	0.0	3.0	2.0	1.4	0.5	4.3
Sylfaste	Sy	2.2	11.	7.1	2.8	0.5	0.7	8.9
Bräkne-Hoby	BH	0.5	0.0	3.0	1.3	0.5	0.5	5.0
Hammenhög	Ha	—	—	—	—	—	—	—
Alnarp	Al	12.	5.1	7.8	1.3	1.5	2.0	11.
Hilleshög	Hi	—	—	—	—	—	—	—
Ås	Ås	4.0	16.	6.4	3.9	4.5	1.2	14.
Vågåmo	Vå	3.2	7.0	7.7	1.4	4.5	2.5	16.
Lista	Li	5.0	22.	3.9	9.0	1.4	2.4	7.1
Kauhava	Ka	0.0	0.6	2.5	2.8	2.4	0.6	1.7
Kuopio	Ku	—	—	—	—	—	—	—
Jyväskylä	Jy	2.5	3.3	2.2	1.4	0.7	0.7	4.9
Tvärminne	Tv	0.0	0.0	1.8	1.0	0.3	0.0	1.4
Ödum	Öd	6.3	1.2	6.8	1.4	1.4	0.5	3.8
Askov	As	5.8	3.4	7.6	1.4	1.2	0.6	2.6
Tystofte	Ty	2.2	5.6	9.6	2.9	1.5	1.2	7.3
Aberdeen	Ab	10.	0.9	5.4	5.3	1.0	3.6	15.
Edinburgh	Ed	7.3	3.9	4.2	1.5	1.2	1.2	3.4
Leeds	Le	4.6	8.3	7.6	2.3	1.6	3.1	9.0
Rothamsted	Ro	19.	4.2	7.2	2.3	1.4	1.7	5.1
Newton Abbot	NA	7.1	2.4	7.7	1.8	1.6	5.9	20.
Augustenberg	Au	—	—	—	—	—	—	—
Güntersthal	Gü	7.0	5.9	4.6	1.2	1.5	1.0	8.7
Feldberg	Fe	1.1	5.4	2.4	1.1	1.1	0.7	4.5

[1] The station Mora moved to Rättvik (Rä), 35 km E of Mora.

Air September 1955. L 509

Station	Code	$\mu g/m^3$ (= kg/km^3)						
		S	Cl	NH_3-N	Na	K	Mg	Ca
Riksgränsen	Ri	0.0	19.0	1.3	2.8	1.9	0.7	4.8
Kiruna	Ki	0.4	3.4	1.1	0.7	0.8	1.4	2.3
Arjeplog	Ar	—	—	—	—	—	—	—
Öjebyn	Öj	1.5	0.1	2.4	0.7	1.0	0.2	0.4
Röbäcksdalen	Rö	3.0	3.7	1.1	0.9	0.7	0.3	2.9
Offer	Of	2.8	7.5	3.5	1.4	1.1	5.5	4.0
Bredkälen	Br	1.2	0.8	1.0	0.5	0.2	0.3	2.7
Åre	ÅF	0.7	1.0	1.0	0.8	0.4	0.3	2.4
Åre, Hummeln	ÅH	4.7	1.2	1.7	0.9	0.7	1.6	5.4
Sveg	Sv	—	—	—	—	—	—	—
Rättvik	Rä	1.9	5.2	2.0	1.6	1.6	0.3	4.9
Åmot	Åm	—	—	—	—	—	—	—
Sala	Sa	4.4	7.2	3.5	1.6	1.8	1.0	7.7
Ultuna	Ul	5.9	4.3	3.5	0.5	0.4	0.7	1.9
Erken	Er	0.0	5.6	0.1	0.0	0.2	0.2	0.8
Strängnäs	St	5.1	0.3	2.4	0.6	0.5	1.7	1.2
Forshult	Fo	—	—	—	—	—	—	—
Kvarntorp	Kv1	90.0	0.8	8.0	0.9	1.1	4.0	18.0
Kvarntorp	Kv7	6.9	3.1	2.1	0.7	0.6	0.6	4.0
Västra Ny	VN	—	—	—	—	—	—	—
Lanna	La	1.6	5.1	4.5	3.7	1.3	5.9	17.0
Bornö	Bo	3.6	5.2	1.6	3.2	0.5	1.1	5.7
Vinga	Vi	—	—	—	—	—	—	—
Falsterbobruk	Fa	4.4	2.3	2.4	1.5	1.0	1.4	3.6
Flahult	Fl	4.8	0.4	2.7	2.6	1.6	0.5	2.2
Ambjörnarp	Am	—	—	—	—	—	—	—
Simlångsdalen	Si	—	—	—	—	—	—	—
Plönninge	Pl	5.0	3.6	4.1	1.6	0.9	1.4	4.6
Söraby	Sö	—	—	—	—	—	—	—
Smedby	Sm	0.0	0.9	2.2	1.0	0.8	0.4	3.4
Sylfaste	Sy	0.9	6.0	11.0	2.2	3.8	1.1	4.4
Bräkne-Hoby	BH	2.8	1.6	3.6	0.8	0.5	1.1	1.3
Hammenhög	Ha	—	—	—	—	—	—	—
Alnarp	Al	11.0	3.4	4.2	2.1	1.4	0.7	3.9
Hilleshög	Hi	—	—	—	—	—	—	—
Ås	Ås	—	—	—	—	—	—	—
Vågåmo	Vå	—	—	—	—	—	—	—
Lista	Li	3.5	28.0	2.2	16.0	2.3	2.2	4.3
Kauhava	Ka	3.3	6.2	2.2	0.6	1.6	1.0	5.4
Kuopio	Ku	1.6	4.2	1.4	1.0	1.4	2.5	4.0
Jyväskylä	Jy	0.0	1.9	1.6	1.3	1.4	2.0	7.6
Tvärminne	Tv	3.4	7.7	2.3	1.1	2.2	5.1	9.5
Ödum	Öd	7.2	1.0	5.8	1.5	1.1	1.0	2.0
Askov	As	5.2	4.1	5.0	1.3	0.7	3.2	1.6
Tystofte	Ty	3.5	8.9	7.6	6.8	1.6	1.8	6.6
Aberdeen	Ab	6.0	7.5	4.0	2.6	3.0	2.5	5.6
Edinburgh	Ed	7.8	3.8	3.0	1.8	0.7	1.8	2.5
Leeds	Le	18.0	11.0	5.2	1.2	1.4	3.2	10.0
Rothamsted	Ro	15.0	7.0	3.0	1.3	0.7	1.9	4.2
Newton Abbot	NA	1.6	5.9	6.1	1.6	0.7	1.3	5.4
Augustenberg	Au	9.7	7.7	8.6	1.4	2.5	19.0	18.0
Güntersthal	Gü	5.3	5.8	3.7	0.8	1.0	1.0	5.2
Feldberg	Fe	1.6	2.7	1.7	0.4	0.4	0.4	1.6

Uppsala in November 1955

G. Brodin
Agricultural College, Uppsala

Current Data of CO_2 in the air

(Cf, Fonselius, Koroleff:

	May					June				
	Date	°C	Wind	Weather	CO_2 ml/10 l	Date	°C	Wind	Weather	CO_2 ml/10 l
Ab	1	2.0	NNW, 0	0	3.15	1	8,2	NW, 3	3	3.28
	10					10	3.5	N, 2	5	3.15
	20	0.9	NNW, 2	● 10	3.10	20	5.8	WNW, 4	2	3.21
Öj	1	5.9	SE, 1	5	3.16	1	20.4	E, 1	0	3.26
	10	4.0	SE, 1	5	3.23	10	11.5	SE, 1	10	3.10
	20	6.0	calm	● 10	3.31	20	14.0	SE, 1	3	3.11
Br	1	9.0	SW, 1	6	3.13	1	22.0	NE, 1	0	3.46
	10	4.0	N, 1	0	3.19	10	8.0	NE, 1	5	2.91
	20	10.0	NW, 1	8	3.10	20	12.0	NW, 1	2	3.03
Ul	1	8.8	ESE, 4	6	3.22	1	17.5	E, 2	4	3.17
	10	9.7	SW, 5	10	3.09	10	12.0	NNW, 3	5	2.92
	20	10.0	WSW, 3	10	(4.00)	20	13.8	N, 1	6	3.10
Fl	1	7.0	SE	●° 10	(3.87)	1	14.4	N	2	3.23
	10	8.7	SW	●° 10	3.10	10	12.2	NE	5	3.07
	20	9.4	NW	5	3.28	20	19.4	NE	0	2.90
Pl	1	10.0	W, 1	8	3.72	1	16.0	E, 1	2	3.18
	10	11.0	W, 4	10	3.04	10	14.0	NW, 1	5	3.09
	20	10.0	W, 4	5	3.25	20	25.0	SW, 1	3	3.00
Ka	1					1	19.8	NNE, 3	0	3.57
	10					10	8.6	NW, 3	5	3.40
	20	4.4	SE, 3	● 10	3.10	20	11.0	N, 4	0	3.45
Ri	1					1	15.6	ESE, 3	0	3.66
	10	3.9	E, 2	● 10	3.30	10	10.0	SSW, 3	10	3.26
	20	7.2	ESE, 3	● 10	3.40	20	10.1	NW, 4	0	3.12
Lu	1	6.4	NW, 5	5	3.48	1	14.7	NNE, 3	4	3.49
	10					10	8.8	SW, 2	5	3.39
	20	2.3	NW, 3	● 10	3.20	20	7.7	W, 1	4	3.50
Tv	1	5.0	S, 0	0	3.30	1	13.0	S, 1	0	3.89
	10	6.0	WSW, 6	0	3.70	10	9.0	S, 1	0	3.57
	20	6.0	SW, 2	● 9	3.33	20	12.0	SW, 3	0	3.48
Bo	1	4.8	SSE, 3	=° 0	2.93	1	16.7	N, 1	0	3.17
	10	1.7	N, 3	=° 4	3.04	10	5.6	NNE, 2	▽̇ 9	2.95
	20	8.9	NNE, 3	=° 7	3.02	20	4.4	NE, 3	=° 7	3.35
Vå	1	5.6	NE, 1	10	3.27	1	19.4	NNE	0	3.29
	10	3.5	WSW, 2	5	3.40	10	10.2	SSW	10	3.17
	20	7.9	WSW, 2	5	3.29	20	17.1	ENE	4	2.97
Be	1	11.1	S, 4	10	3.23	1	20.0	WSW, 1	0	3.24
	10	4.0	SW 3	10	3.50	10	11.5	NNW, 3	6	3.21
	20	6.1	W, 5	10	3.43	20	19.4	W, 2	3	3.68
Öd	1	9.0	SSW	5	3.43	1	16.2	SE	0	2.77
	10	11.4	W, 5	5	3.26	10	13.2	SE	10	3.05
	20	7.8	SW, 4	5	3.31	20	15.2	SW	● 10	3.16
As	1	14.2	S, 1	5	3.04	1	17.8	SE, 2	7	3.13
	10	8.2	WSW, 3	● 10	3.19	10				
	20	8	W, 4	6	3.15	20	14.0	SE, 2	● 10	2.95

Symbols used for description of weather conditions, are those, internationally used. The numbers in the weather column gives the cloudiness.

May—Aug. 1955 in Scandinavia
Teltus **7**, pp. 258—265)

	July					Aug.				
	Date	°C	Wind	Weather	CO_2 ml/10 l	Date	°C	Wind	Weather	CO_2 ml/10 l
Ab	1	18.1	calm	0	3.19	1	9.0	NNW, 6	3	3.19
	10	8.5	NNW, 2	2	3.09	10	8.5	NNW, 5	8	3.18
	20	8.3	NNW, 3	10	3.02	20	20.0	WSW, 1	0	3.20
Öj	1	22.0	SE, 1	5	3.05	1	26.2	SW, 1	2	3.17
	10	24.2	W, 1	0	2.94	10	21.8	SW, 1	0	3.20
	20	16.4	W, 1	10	3.18	20	22.4	S, 1	0	3.24
Br	1	20.0	E, 1	6	3.10	1	19.0	W, 4	5	3.06
	10	25.0	E, 1	2	3.09	10	18.0	W, 4	0	3.10
	20	12.0	W, 5	●° 10	3.24	20	22.0	SE, 1	= 8	3.13
Ul	1	20.0	SE, 1	10	3.26	1	28.4	SW, 2	0	3.32
	10	27.6	N, 0	5	3.03	10	24.8	N, 2	5	3.09
	20	21.7	NNW, 1	5	3.15	20	23.9	SE, 1	10	3.28
Fl	1	17.0	SW	● 10	3.53	1	26.4	W, 0		3.07
	10	22.8	N	0	2.98	10				3.12
	20	26.4	N	0	3.00	20	24.0	NW, 5		2.99
Pl	1	20.0	W, 1	5	3.21	1	21.0	W, 1	10	3.25
	10	28.0	W, 1	0	3.24	10	24.0	NE, 1	0	3.14
	20	21.0	W, 1	0	3.20	20	23.0	W, 1	0	3.29
Ka	1	20.8	N, 2	4	3.26	1	22.6	SW, 2	0	3.29
	10	24.0	NW, 4	0	3.52	10	21.2	N, 2	0	3.22
	20	16.2	W, 3	5	3.66	20	26.0	SSW, 1	0	3.40
Ri	1	22.0	NW, 2	0	3.39	1	22.6	SW, 3	0	3.70
	10	23.8	NW, 4	0	3.66	10	15.3	E, 2	9	3.51
	20	14.0	WSW, 2	● 10	3.37	20				
Lu	1	21.0	SW, 3	4	3.70	1	22.0	S, 1	9	3.84
	10	25.0	NW, 4	0	3.84	10	15.2	NNW, 3	10	3.30
	20	15.1	W, 3	9	3.56	20				
Tv	1	17.0	S, 1	5	3.48	1	22.0	SW, 2	0	3.30
	10	23.0	SW, 2	0	3.50	10	23.0	NE	0	3.42
	20	19.0	W, 5	0	3.30	20	22.0	S, 1	0	3.81
Bo	1	14.1	ENE, 1	∞° 7	3.18	1	10.3	NNE 4	=° 9	3.18
	10	13.4	NNE, 1	= 1	2.98	10	12.5	NNE, 4	=° 10	3.11
	20	10.4	ENE, 3	● 10	3.20	20	18.4	NNE, 3	=° 1	3.27
Vå	1	15.1	NE, 2	● 10	3.61	1	24.0	SW, 2	0	3.12
	10	20.0	SW, 1	10	3.29	10	18.2	SW, 1	0	3.10
	20	20.0	WSW, 3	0	3.18	20	17.2	SW, 1	● 10	3.21
Be	1	14.8	E, 1	10	3.17	1	15.3	ESE, 2	10	3.26
	10					10	20.2	WNW, 1	= 7	3.30
	20	16.4	W, 1	5	3.23	20	15.4	calm. 0	10	3.26
Öd	1	15.8	SW	2	3.32	1	17.2	SW	10	3.09
	10	25.8	NE	0	3.20	10	24.8	NNE	0	3.13
	20	25.7	W	0	3.16	20	26.4	NE	0	3.20
As	1	16.2	W, 2	6	3.49	1	17.2	W, 2	0	3.10
	10	23.2	E, 3	3	3.21	10	25.0	E, 3	0	3.02
	20	21.6	NW, 2	0	3.29	20	23.6	SSW	10	3.27

Symbols used for description of weather conditions, are those, internationally used. The numbers in the weather column gives the cloudiness.

INDEX

Acidity of precipitation, Barrett, Brodin, 251.
Alaska, cyclogenesis, Winston, 481.
ALFVÉN, H.: On the Electric Field Theory of Magnetic Storms and Aurorae, 50.
Antarctic, temperatures, Schumacher, 87.
ÁRNASON, G.: A Two-Parameter Representation of the Normal Temperature Distribution of the 1,000—500 mb Layer, 189.
ARRHENIUS, G.: Distribution of Radioactivity in Pelagic Clays, 226.
aurorae, Alfvén, 50.
—, Block, 65.
auroral research 1957—58, Stoffregen, 509.

BARRETT, E.: The Acidity of Scandinavian Precipitation, 251.
baroclinic disturbances, Fleagle, 168.
—, structure, Saltzman, 385.
barotropic model, Bolin, 27.
BERGTHORSSON, P.: Routine Forecasting with the Barotropic Model, 272.
—: Numerical Weather Map Analysis, 329.
BLANCHARD, D. C.: Tests of the Salt-Nuclei Hypothesis of Rain Formation, 437.
BLOCK, L.: Model Experiments on Aurorae and Magnetic Storms, 65.
BOLIN, B.: Numerical Forecasting with the Barotropic Model, 27.
BOVILLE, B. W.: A Frontal-Jet Stream Cross Section, 314.
BRODIN, G.: The Acidity of Scandinavian Precipitation, 251.
BUCH, K.: Microdetermination of CO_2 in the Air, with Current Data for Scandinavia, 258.

Camera, auroral, Stoffregen, 509.
carbondioxid, Fonselius, Koroleff, Buch, 258.
—, current data, 401, 528.
cellular convection, Nakagawa, Frenzen, 1.
CHARNEY, J.: The Use of the Primitive Equations of Motion in Numerical Prediction, 22.
chemical climate, Rossby, Egnér, 118.
chemistry, conference, Eriksson, 388.
circulation, atmospheric, Rossby, Egnér, 118.
—, maintenance of, Lorenz, 157.
—, wind-driven, time-dependant, Veronis, Morgan, 232.
climate, chemical, Rossby, Egnér, 118.
cloud, water content, Warner, 449.
clouds, jet-stream, Schaefer, Hubert, 301.
composition of air, current data, Egnér, Eriksson, 134.
— — —, — —, 266, 395, 522.
— — river waters, Eriksson, 243.
condensation, nuclei, Twomey, McMaster, 458.
conference, atmospheric chemistry, Eriksson, 388.
convection, cellular, Nakagawa, Frenzen, 1.
—, stratosphere, Raab, 322.
cosmic rays, Sandström, 204.
Couette Flow, rotating, Kao, 372.
CRESWICK, W. S.: A Frontal-Jet Stream Cross Section 314.
crystallizing salt, condensation-nuclei, Twomey, McMaster, 458.
cumuliform cloud, Warner, 449.
current data, air and precipitation, 134, 266, 395, 522.
— —, CO_2, 401, 528.
— —, CO_2, Fonselius, Koroleff, Buch, 258.
cyclogenesis in Alaska, Winston, 481.
cyclone, in upper levels, Kleinschmidt, 96.
cyclones, tropical, Palmén, Jordan, 186.

DAGEL, Y.: Upper Mean Flow over the North Atlantic during January 1952, 111.
disturbances, baroclinic, Fleagle, 168.
diurnal variation of cosmic rays, Sandström, 204.
DÖÖS, B.: Routine Forecasting with the Barotropic Model 272.
—: Numerical Weather Map Analysis 329.
EGNÉR, H.: On the Chemical Climate and its Variation with the Atmospheric Circulation Pattern, 118.
—: Current Data on the Chemical Composition of Air and Precipitation, 134.
electric field theory, Alfvén, 50.
ENDLICH, R. M.: The Mean Vertical Structure of the Jet Stream, 308.
energy in general circulation, Lorenz, 157.
— in tropical cyclones, Palmén, Jordan, 186.
ERIKSSON, E.: Current Data on the Chemical Composition of Air and Precipitation, 134.
—: Airborne Salts and the Chemical Composition of River Waters, 243.
—: Report on the second informal conference on atmospheric chemistry held at the Institute of Meteorology, Stockholm, 31 May—4 June 1955, 388.

Equatorial undercurrent, Fofonoff, 518.
Estoque, M. A.: The Spectrum of Large-scale Turbulent Transfer of Momentum and Heat, 177.

Field theory, electric, Alfvén, 50.
filaments, sunspot, Öhman, 501.
Fjørtoft, R.: On the Use of Space-Smoothing in Physical Weather Forecasting, 462.
flares, sunspot, Öhman, 501.
Fleagle, R. G.: Instability Criteria and Growth of Baroclinic Disturbances, 168.
flow of stratified fluids, Long, 341.
—, wave motion, Kao, 372.
fluid, hydraulic jump, Yih, Guha, 358.
—, ideal, Welander, 141.
—, viscous, Kao, 372.
fluids, stratified, Long, 341.
Fofonoff, N. P.: The Equatorial Undercurrent in the light of the Vorticity Equation, 518.
Fonselius, S.: Microdetermination of CO_2 in the Air, with Current Data for Scandinavia, 258.
forecasting, barotropic model, Bergthorsson, Döös, Fryklund, Haug, Lindquist, 272.
—, numerical, Bolin, 27.
—, space-smoothing, Fjørtoft, 462.
Frenzen, P.: A Theoretical and Experimental Study of Cellular Convection in Rotating Fluids, 1.
frontal jet stream, Boville, Creswick, Gillis, 314.
Fryklund, S.: Routine Forecasting with the Barotropic Model, 272.
Fujita, T.: Results of Detailed Synoptic Studies of Squall Lines, 405.

Geomagnetic activity, Sandström, 204.
Geophysical Year 1957—58, Stoffregen, 509.
Gillis, J. J.: A Frontal-Jet Stream Cross Section, 314.
Goldberg, E. D.: Distribution of Radioactivity in Pelagic Clays, 226.
Guha, C. R.: Hydraulic Jump in a Fluid System of Two Layers, 358.

Haug, O.: Routine Forecasting with the Barotropic Model, 272.
heat, turbulent transfer of, Estoque, 177.
hydraulic jump in a fluid, Yih, Guha, 358.
hydrographic levelling, Jessen, 371.
Hubert, W.: Upper Mean Flow over the North Atlantic during January 1952, 111.
—: A Case Study of Jet Stream Clouds, 301.

Ideal Fluid, Two-dimensional, Welander, 141.
instability criteria, Fleagle, 168.

Jerlov, N. G.: The Particulate Matter in the Sea as Determined by Means of the Tyndall Meter, 218.
Jessen, A.: Nivellement hydrographique entre six stations danoises, 381.
jet stream clouds, Schaefer, Hubert, 301.
— —, frontal, Boville, Creswick, Gillis, 314.
— —, vertical structure, Endlich, Solot, Thur, 308.
Jordan, C. L.: Note on the Release of Kinetic Energy in Tropical Cyclones, 186.

Kao, S.-K.: Wave Motion in a Rotating Couette Flow of a Viscous Fluid, 372.
Kleinschmidt, E.: Die Entstehung einer Höhenzyklone über Nordamerika, 96.
Koroleff, F.: Microdetermination of CO_2 in the Air, with Current Data for Scandinavia, 258.
Kullenberg, B.: Restriction of the Underflow in a Transition, 215.

Layer, 1,000—500 mb, Árnason, Vuorela, 189.
—, fluid systems, Yih, Guha, 358.
levelling, hydrographic, Jessen, 381.
Lindquist, R.: Routine Forecasting with the Barotropic Model, 272.
Long, R. R.: Some Aspects of the Flow of Stratified Fluids. III. Continuous Density Gradients, 341.
Lorenz, E. N.: Available Potential Energy and the Maintenance of the General Circulation, 157.
Ludlam, F. H.: Artificial Snowfall from Mountain Clouds, 277.

Magnetic storms, Alfvén, 50.
— —, Block, 65.
McMaster, K. N.: The Production of Condensation Nuclei by Crystallizing Salt Particles, 458.
microdetermination of CO_2, Fonselius, Koroleff, Buch, 258.
model experiments, Block, 65.
momentum, turbulent transfer of, Estoque, 177.
Montgomery, R. B.: The Equatorial Undercurrent in the light of the Vorticity Equation, 519.
Mordy, W. A.: Salt Nuclei, Wind and Daily Rainfall in Hawaii, 291.
Morgan, G. W.: A Study of the Time-Dependant, Wind-Driven Circulation in a Homogeneous, Rectangular Ocean, 232.

Nakagawa, Y.: A Theoretical and Experimental Study of Cellular Convection in Rotating Fluids, 1.
normal temperature distribution, Árnason, Vuorela, 189.

numerical analysis, Bergthorsson, Döös, 329.
—, forecasting, Bolin, 27.
—, prediction, Charney, 22.

Ocean, circulation of, Veronis, Morgan, 232.

Palmén, E.: Note on the Release of Kinetic Energy in Tropical Cyclones, 186.
particulate matter in the sea, Jerlov, 218.
pelagic clays, Arrhenius, Goldberg, 226.
precipitation, composition of, Egnér, Eriksson, 134.
—, current data, 266, 395, 522.
—, the acidity of, Barrett, Brodin, 251.
prediction, numerical, Charney, 22.
primitive equations, Charney, 22.

Queney, P.: Rotor Phenomena in the Lee of Mountains, 367.

Raab, L.: A Weather Situation with Strong Convection in the Middle Stratosphere, 322.
radioactivity in clays, Arrhenius, Goldberg, 226.
rainfall and salt nuclei, Woodcock, Mordy, 291.
rain, formation, salt nuclei, Woodcock, Blanchard, 437.
river waters, Eriksson, 243.
Rossby, C.-G.: On the chemical climate and its variation with the atmospheric circulation pattern, 118.
rotating fluids, Nakagawa, Frenzen, 1.
rotor phenomena, Queney, 367.

Salt, crystallizing, Twomey, McMaster, 458.
salt nuclei in Hawaii, Woodcock, Mordy, 277.
— —, rain formation, Woodcock, Blanchard, 437.
salts, airborne, Eriksson, 243.
Saltzman, B.: Note on Simple Assumptions Regarding the Baroclinic Structure of the Atmosphere, 385.
Sandström, A. E.: On the Correlation between Geomagnetic Activity and the Diurnal Variation of Cosmic Rays, 204.
Schaefer, V. J.: A Case Study of Jet Stream Clouds, 301.
Schumacher, N. J.: Upper-Air Temperatures over an Antarctic Station, 87.
snowfall, artificial, Ludlam, 277.
Solot, S. B.: The Mean Vertical Structure of the Jet Stream, 308.
space-smoothing, Fjørtoft, 462.
squall lines, Fujita, 405.
Stoffregen, W.: All-Sky Camera Auroral Research during the Third Geophysical Year 1957—58, 509.
stratified fluids, Long, 341.
stratosphere, convection, Raab, 322.
sunspot areas, 1952, 1953, Öhman, 501.
synoptic studies, squall lines, Fujita, 405.

Temperature distribution, normal, Árnason, Vuorela, 189.
temperatures over Antarctic, Schumacher, 87.
Thur, H. A.: The Mean Vertical Structure of the Jet Stream, 308.
transition, underflow in, Kullenberg, 215.
tropical cyclones, Palmén, Jordan, 186.
turbulent transfer of momentum, Estoque, 177.
Twomey, S.: The Production of Condensation Nuclei by Crystallizing Salt Particles, 458.
Tyndall meter, Jerlov, 218.

Undercurrent, equatorial, Fofonoff, 518.
underflow in a transition, Kullenberg, 215.
upper air temperatures, Schumacher, 87.
upper cyclone, Kleinschmidt, 96.
upper mean flow, Hubert, Dagel, 111.
Veronis, G.: A Study of the Time-Dependant Wind-Driven Circulation in a Homogeneous, Rectangular Ocean, 232.
vertical structure, jet stream, Endlich, Solot, Thur, 308.
vorticity equation, Fofonoff, 518.
Vuorela, L.: A Two-Parameter Representation of the Normal Temperature Distribution of the 1,000—500 mb Layer, 189.

Warner, J.: The Water Content of Cumuliform Cloud, 449.
water content in clouds, Warner, 449.
wave motion in Couette flow, Kao, 372.
Welander, P.: Studies on the General Development of Motion in a Two-Dimensional, Ideal Fluid, 141.
wind-driven circulation, Veronis, Morgan, 232.
Winston, J. S.: Physical Aspects of Rapid Cyclogenesis in the Gulf of Alaska, 481.
Woodcock, A. H.: Salt Nuclei, Wind and Daily Rainfall in Hawaii, 291.
—:Tests of the Salt-Nuclei Hypothesis of Rain Formation, 437.

Yih, C.-S.: Hydraulic Jump in a Fluid System of Two Layers, 358.

Öhman, Y.: Sunspot Areas, Flares and Filaments observed at the Stockholm Observatory and at its station in Anacapri in the Years 1952 and 1953, 501.